

Diss. ETH No. 16429

Numerical Investigation of the Buckling Behaviour of Axially Compressed Circular Cylinders Having Parametric Initial Dimple Imperfections

A dissertation submitted to the
SWISS FEDERAL INSTITUTE OF TECHNOLOGY ZURICH

for the degree of
Doctor of Technical Sciences

presented by
LUC WULLSCHLEGER
Dipl. Masch.-Ing. ETH
born June 11, 1970
citizen of Zofingen AG (Switzerland)

accepted on the recommendation of

Prof. Dr. Paolo Ermanni, examiner

Prof. Dr. Hans-Reinhard Meyer-Piening (emeritus), co-examiner

Zürich, 2006

für meine Eltern

Vorwort

Die hier vorliegende Dissertation entstand im Anschluss an ein europäisches Projekt über die Zuverlässigkeit von analytischen Beullasten für laminierte Schalen, an welchem das ehemalige Institut für Leichtbau und Seilbahntechnik (ILS) der ETH Zürich zusammen mit der Empa Dübendorf partizipiert hatte. Aufgabe dieser beiden schweizerischen Partner war es, die Beullasten von einigen dünnwandigen Kreiszyklindern aus Kohlefaserlaminat experimentell zu bestimmen. Zudem hatten sie es übernommen, die lokalen Abweichungen vom Nennradius (Imperfektionen) dieser Versuchszylinder zu vermessen und in die numerischen Analysen einzubringen, mit dem Ziel, den Einfluss dieser gemessenen Imperfektionen zu evaluieren. Als ich 1997 am ILS eine Stelle als wissenschaftlicher Assistent antrat, wurde ich vom damaligen Institutsleiter, Prof. Dr. H.-R. Meyer-Piening, mit der Durchführung von linearen und nichtlinearen Finite-Elemente-Analysen zur Berechnung der Beullasten dieser Zylinder betraut. Diese Beulanalysen bestätigten die Anfälligkeit axialgedrückter Kreiszyklinder auf geometrische Imperfektionen, konnten doch gute Resultate erst erreicht werden, wenn bei der Finite-Elemente-Modellierung der Zylinder jeweils die gemessenen Imperfektionsmuster ihrer Innenflächen als Netzgeometrie übernommen wurden. Unter Verwendung dieser speziellen Finite-Elemente-Modelle gelang es schliesslich, mit transient-dynamischen Analysen die Stauch-Versuche der Zylinder erfreulich exakt zu simulieren.

Die verschiedenen Instabilitäts-Phänomene und die nichtlinearen numerischen Beulanalyse-Methoden weckten mein Interesse und meine wissenschaftliche Neugierde, besonders die transient-dynamische Finite-Elemente-Analyse, welche es ermöglicht, Verformungsprozesse von Schalen oder anderen, auch komplexen Strukturen rechnerisch abzubilden. Schliesslich wollte ich auch in einem Studium der nichtlinearen Kontinuumsmechanik und der nichtlinearen Finite-Elemente-Methode ergründen, was es mit den verschiedenen Formulierungen und Parametern in Programm-Kodes auf sich hat. Deshalb nahm ich nach Abschluss des erwähnten europäischen Projekts anfangs 1999 die sich mir bietende Gelegenheit, die Beulanalysen imperfekter Zylinder als Doktorand in eigener Regie für die vorliegende Dissertation weiterzuführen, gerne wahr.

Das schliesslich daraus ein Buch von über 560 Seiten entstehen sollte, war allerdings nicht geplant. Es schien vielmehr vernünftig, in der

Zeit bis zur Pensionierung von Prof. Dr. H.-R. Meyer-Piening die exzellente EDV-Infrastruktur der ETH und die bereits erworbenen Kenntnisse und gewonnene Erfahrung im Umgang mit den numerischen Beulanalyse-Methoden möglichst intensiv weiter zu nutzen. Da die Finanzierung für Grundlagenforschung im Leichtbau zunehmend schwierig wurde (insbesondere für Beulanalysen von Kreiszyinderschalen), musste angenommen werden, dass künftig wohl kaum mehr weitere Arbeiten in diesem Gebiet angefangen werden. Deshalb sollte im Rahmen dieser Dissertation das Forschungsgebiet um das Beulverhalten von Zylindern mit einer Einzel-Vorbeule so umfassend und vollständig wie möglich bearbeitet werden. Um dieses Ziel zu erreichen wurden in diversen Parameterstudien eine sehr grosse Zahl von Beul- und Finite-Elemente-Analysen durchgeführt, deren Resultate alle verarbeitet und publiziert werden wollten. Die vielleicht etwas unattraktive Seitenzahl dieses Buches ist somit die Konsequenz aus der grossen Menge an Rechenergebnissen und dem Vorsatz, diese alle in dieser einen Dissertation zu beschreiben und, mit vielen Bildern, darzustellen. Aber die hier vorliegende Dissertation beinhaltet auch relativ umfangreiche Erläuterungen zur nichtlinearen Finite-Elemente-Methode, zu den involvierten Eigenproblemen und deren numerischen Lösungsmethoden sowie zu der so genannten Klassischen Beulanalyse mit ihren Lösungen von Schalengleichungen. Die zugehörigen Kapitel entstanden aus Literaturstudien zu Beginn meines Doktorats. Verfasst in einer einheitlichen Terminologie mögen diese vielleicht der geeigneten Leserschaft den Zugang zur Beulanalyse imperfekter Schalen erleichtern.

Die numerischen Untersuchungen des Beulverhaltens von Zylindern mit Einzel-Vorbeulen hatten ihren Anfang also im letzten Jahrtausend! Bis zu meinem Doktorexamen am 19. Januar 2006 war somit genügend Zeit für einige organisatorische Änderungen an der ETH Zürich. Für die Entstehung dieser Dissertation von Belang ist einmal die Umwandlung des Instituts für Leichtbau und Seilbahntechnik (ILS) auf Januar 2000 in den Bereich Leichtbau des Instituts für Mechanische Systeme (IMES). Dann, nach der Pensionierung von Prof. Dr. H.-R. Meyer-Piening per Ende März 2002, folgte schliesslich die Auflösung des Bereichs Leichtbau und dessen Integration in das Zentrum für Strukturtechnologien des IMES unter der Leitung von Prof. Dr. P. Ermanni. Mag sein, dass mit Umstrukturierungen, finanziellen Engpässen und anderen Widrigkeiten während eines Doktorats gerechnet werden muss. Sonderlich hilfreich sind sie jedoch kaum. Aber trotz gelegentlichem Gegenwind: die Arbeit war interessant, sehr lehrreich und hat mir durchaus auch Spass gemacht!

Merci viilmol!

Mein besonderer Dank gilt meinem Doktorvater, Prof. Dr. Hans-Reinhard Meyer-Piening, für seine langjährige über seine Pensionierung hinausreichende tatkräftige Unterstützung, sein offenes Ohr und seine stets offene Türe, seine Anregungen und sein Vertrauen. Er hat diese Dissertation überhaupt erst ermöglicht und mir bei ihrer Durchführung sehr viele Freiheiten gelassen.

Ebenfalls bedanken möchte mich bei Prof. Dr. Paulo Ermanni für sein Interesse und die Übernahme des Referates. Speziell danken möchte ich ihm für die Verlängerung meiner Anstellung als Assistent bis Ende Februar 2003, was die Bereitstellung der Infrastruktur und Finanzierung für meine Dissertation bis dahin ermöglichte.

Meinen Institutskollegen danke ich für die familiäre und freundschaftliche Atmosphäre während meiner Assistenzzeit an der Leonhardstrasse.

George Sigut und Tonko Racic der ETH Informatikdienste möchte ich für ihre kompetente und prompte Hilfestellung bei meinen speicherplatz- und rechenzeitintensiven Finite-Elemente-Analysen auf den HP Superdome Rechnern der Hochschule danken.

Bedanken möchte ich mich zudem bei meinen heutigen Kollegen und Vorgesetzten in der Empa Dübendorf für ihr Interesse an meiner Dissertation und die freundliche Förderung meiner Promotion.

Dave Hunziker, Thisly Kohler, Markus Lutz und Patrick Zwimpfer danke ich herzlich für ihre langjährige wertvolle Freundschaft und dafür, dass sie mir regelmässig halfen, von "terra cylindrica" zurück zu finden.

Meiner Tante Michèle Siegrist einen herzlichen Dank für ihre spontane finanzielle Unterstützung. Herzlichen Dank auch meiner Schwester Pascalina für unsere gemeinsamen Wanderungen in der tensorfreien Bergwelt.

Abschliessend eine herzliches Dankeschön an meine Eltern. Ohne ihre Förderung und Anerkennung meines Studiums und meiner Arbeit über die vielen Jahre hinweg wäre der Abschluss dieser Dissertation undenkbar gewesen.

Contents

Abstract	xiii
Kurzfassung	xix
List of Symbols	xxv
1 Introduction	1
1.1 Shell Buckling in Brief	7
1.1.1 On Instability Phenomena	8
1.1.2 On Buckling Analyses	14
1.2 Outline of the Thesis	17
2 Classical Buckling Analysis of Axially Compressed Cylinders	31
2.1 Shell Theory for Thin Circular Cylinders	32
2.1.1 Kinematic Relations	32
2.1.2 Constitutive Laws	39
2.1.3 Systems of Differential Equations	43
2.2 Buckling of Perfect Cylinders – the Classical Solutions	45
2.2.1 Boundary Conditions	48
2.2.2 Orthotropic Cylindrical Shells	50
2.2.3 Laminated Cylindrical Shells	54
2.3 Approximate Solutions	57
3 Buckling Analyses with Finite Elements	63
3.1 Basic Concept of the Finite Element Method	65
3.2 Static Linear Formulation	67
3.3 Static Nonlinear Formulations	70
3.3.1 Total Lagrangian Formulation	71
3.3.2 Updated Lagrangian Formulation	79
3.3.3 Solutions of the Nonlinear FE Equations	83
3.4 Transient Dynamic Formulations	88
3.4.1 Explicit Methods	90

3.4.2	Implicit Methods	92
3.5	Buckling Analyses	97
3.5.1	Linear Buckling Analysis	99
3.5.2	Nonlinear Buckling Analysis	106
3.5.3	Transient Dynamic Analysis	112
4	Buckling Analysis Results for Ideal Cylinders	117
4.1	The Cylinders and their Modeling	119
4.1.1	Isotropic Shells	119
4.1.2	Laminated Shells	119
4.1.3	Type and Number of Elements	123
4.1.4	Boundary Conditions	124
4.2	Static FE Analysis Results	125
4.2.1	Results for the Isotropic Cylinders	127
4.2.2	Results for the Laminated Cylinders	131
4.3	Transient Dynamic Analysis Results	143
5	Buckling of Cylinders with Distributed Imperfections	153
5.1	Asymptotic Post-Buckling Theory	161
5.2	Nonlinear Analysis Approaches	169
5.2.1	Application of Measured Imperfections	171
5.2.2	Application of Stochastic Imperfections	174
5.3	FE Analysis Results for Cylinders with Measured Imperfections	175
5.3.1	Buckling Analysis Results	178
5.3.2	Transient Dynamic Analysis Results	179
6	Buckling of Cylinders with Localized Imperfections	187
6.1	Local Imperfections	191
6.2	Definition of a Localized Dimple with Free Parameters	196
6.3	Limitations of the Investigation	198
6.4	FE Models and Boundary Conditions	200
6.5	Adaptations to the Buckling Analyses	203
6.5.1	Nonlinear Buckling Analysis with Adaptive Load Step Control	204
6.5.2	Transient Dynamic Analysis	215
6.5.3	Accompanying Data Collection	217
6.6	Isotropic Cylinders with Dimples	222
6.6.1	Inward Dimples	225
6.6.2	Outward Dimples	296
6.6.3	Lateral Dimensions of Dimples Provoking Minimal Cylinder Stability	325
6.6.4	Minimum Buckling Loads for Isotropic Cylinders with Single Dimples	347
6.6.5	Stress Distributions	364

6.6.6	Isotropic Cylinders with Two Dents	398
6.6.7	Alternative Conditions and Models	426
6.7	Laminated Cylinders with Dimples	445
6.7.1	Variation of the Initial Dimple Amplitude	447
6.7.2	Lateral Dimensions of Dimples Provoking Minimal Cylinder Stability	456
6.7.3	Minimum Buckling Loads for Laminated Cylinders with Single Dimples	471
7	Conclusions	479
A	Nonlinear Continuum Mechanics	497
A.1	Deformation and Rotation	497
A.2	Strain Measures	500
A.3	Stresses	502
A.4	The Principle of Virtual Displacements	504
A.5	Constitutive Equations	507
B	Bending of Plates	513
B.1	Pure bending of plates	515
B.1.1	Mindlin-Reissner plate theory	516
B.1.2	Kirchhoff thin-plate theory	517
B.2	Combination of bending and in-plane loading	519
B.2.1	Large deflections of plates	522
B.3	Buckling of plates	525
C	Initial Stress Stiffness Matrices for Plate Elements	527

Abstract

Accurate analysis concerning static instability and reliable appointment of the buckling loads is important for safe design of thin-walled shell structures. Real shells contain geometric imperfections and other deviations from nominal values which have to be considered, as for buckling analyses on the basis of ideal conditions extreme discrepancies between prediction and test data can result. This thesis deals with the buckling behaviour of thin-walled, unstiffened cylinders under pure axial compression because of their extraordinary sensitivity to imperfections in the shell geometry. The parameters required for an application of real imperfections in a buckling analysis are difficult to be specified. And measured values of real imperfections for the design of any new cylinder shell are hardly available. In the absence of such data in most cases buckling patterns are used that result for perfect geometry and whose buckling patterns can be described with harmonic displacement functions. For safe shell design that imperfection shape is significant which yields the minimum buckling load. But, in general neither the geometry nor the amplitudes of the buckling patterns which contribute to the most damaging imperfection shape are known a priori. In addition, the monotone wavelike dimples forming the buckling patterns of perfect cylinders enclose the entire shell surface, and hence localized irregularities like single dents or bulges of different amplitude are insufficiently included. Consequently, due to the lack of adequate imperfections parameters, cylindrical shells still have to be designed by use of reduction factors to be applied to the analytical buckling loads for perfect cylinders. These reduction factors consider smallest empirical values and therefore provide critical loads which appear to be rather conservative. Moreover, such instructions exist for steel and other isotropic shell materials but not for laminated composite cylinders, for instance.

For these reasons the thesis on hand focusses on cylinders having lo-

calized imperfections in form of local inward or outward dimples. To investigate the influences of a single initial dimple on the instability behaviour of such cylinders, and separate from any effect of other irregularities, discrete parametric dents or bulges were added to FE models of unstiffened circular cylinders of otherwise perfect geometry. The chosen shape of a parametric dimple allowed to investigate the influence of its initial amplitude, its initial axial height, its initial circumferential width, and its axial position systematically and independently of other parameters. With regard to the absence of practical design recommendations for laminated composite cylinders the thesis on hand covers analyses of isotropic as well as of laminated CFRP shells.

Several parameter studies were conducted for a number of cylinders having dimples of different initial amplitude but fixed initial circumferential width and axial height. In addition, for a few cylinders and for some predefined initial amplitudes the initial axial height and circumferential width to the dimple was searched which reduce the axial cylinder stability the most. Finally the influence of the relative position of a second identical dent to the load carrying capacity was investigated. These series of analyses aimed at investigating whether there are single, localized initial dimples which reduce the nominal axial buckling load of an unstiffened circular cylinder more than imperfections derived from classical buckling patterns of ideal shells, and whether there is a worst geometry of such a single dimple imperfection. Further: is the instability behaviour the same for isotropic shells as for laminated composite shells having such a localized dimple imperfection? And, is there an important interaction between two initial dimples?

The dimple-parameter studies required a large amount of static and transient dynamic FE analyses. Most of the calculations performed were nonlinear buckling analyses, i.e. nonlinear static stress analyses under consideration of large displacements and rotations using Updated Lagrangian formulations with additional linear eigenvalue calculations, conducted after a selected number of small loading steps to determine the stability of pre-buckling states of stress and deformation. To manage the large number of shells with different buckling loads and behaviour considered, the nonlinear buckling analysis was adapted for an adaptive load step control which utilizes the intermediately extracted eigenvalues. For a selection of cylinders and dimples additional nonlinear transient dynamic analyses were conducted in order to research into the particular deformation processes of such shells under axial loading. Because of the relatively slow compression velocities assumed the implicit “single-step

HOUBOLT” method for time integration was preferred to the more common explicit operators. To reduce the number of time increments needed for stepwise convergence significant inertia damping was introduced.

In a classical analysis, for ideal, thin-walled unstiffened isotropic circular cylinders of medium length under pure axial compression the load-carrying capacity can be predicted analytically by means of simple equations. These equations follow from solving the coupled partial differential equations for equilibrium and compatibility in simply-supported cylinder with harmonic functions. There are also close-form solutions of the DONNELL-type shell equations available for thin-walled orthotropic composite cylinders. Such a classical analysis, however, is applicable exclusively for perfect cylinder geometry.

For the imperfection shapes and sizes considered no test results were available against which the FE analysis results could have been benchmarked. Instead, they are supported by convincing results of such calculations for similar cylinders with perfect geometry and for laminated CFRP cylinders with their measured imperfections included. The results of the ideal cylinders could be compared with values achieved with classical analyses, whereas for the analysis results of the CFRP shells with measured imperfections test data was available for comparisons.

The asymmetrically laminated CFRP cylinders analysed stem from a preceding European project which focussed on the correlation of measured buckling loads of test cylinders with analytical and numerical buckling load predictions. The FE analyses of these shells have shown that for such cylinders calculated buckling loads close to test values may be attained if measured imperfections are included in the analysis. It was further found that the consideration of imperfections requires the use of FE analysis methods which take geometric nonlinearity into account. The nonlinear buckling and transient dynamic FE analyses of these CFRP cylinders with perfect geometry and with measured imperfections applied finally provided the basis for the FE analyses of such cylinders having a single localized dimple.

The FE analyses of cylinders with an initial local dent or bulge yielded particular deformation processes including different local buckling phenomena which were hardly known from unstiffened circular cylinders with neither perfect geometry nor with imperfections distributed over the entire shell surface. Nevertheless, by means of systematic parameter variation some interrelationships between the results and the nominal dimensions of the cylinder and the dimple could be derived.

The initial circumferential curvature of a shell in the dimple plays a decisive role in the deformation process of the cylinders and in the run of their FE analyses. The differences in the behaviour pattern and the initial curvature led to a distinction between “shallow” and “deep” dents. Shallow dents with an initial amplitude smaller than a certain marginal depth provoke a distinct local buckling with a sudden snapping inwards of the dent to form a local flattened shell strip of reduced geometric axial stiffness. Deep dents, in turn, result in a continuous local flattening of the shell without any dynamic local-buckling incident prior to the total cylinder collapse.

Localized, shallow dents of particular initial circumferential width and axial height reduce the buckling load as much as axisymmetric inward dimples of identical initial amplitude. And a non-axisymmetric, shallow dent of adequate initial width and height may be as damaging as an imperfection-pattern that is given by a classical buckling mode of initial amplitude that is half the initial amplitude of the dent. Further, localized non-axisymmetric bulges impair the load carrying capacity less than localized dents of the same absolute initial amplitude, width, and height. Finally, the buckling load of a cylinder with single localized dent is only little different from that of a cylinder having two dents of identical size.

For isotropic cylinders the initial axial heights of dimples that reduces the buckling load the most for a preselected initial depth is close to the wavelength for classical axisymmetric buckling of a perfect cylinder. The initial circumferential widths of the worst dent is between two to three times the initial height, whereas the worst bulge is always axisymmetric.

The studies yielded that the cylinder length is also decisive for the local deformation processes of the shell in and in the adjacency of the initial dimples (local buckling) observed. The design recommendations in standards and literature considered for thin-walled, unstiffened isotropic cylinders under axial compression are conservative if the nominal radius and wall-thickness as well as the nominal cylinder length are taken into account.

For the laminated cylinders investigated accurate and general predictions of minimal buckling loads and of critical dimple dimensions could not be derived on basis of the cylinder geometry alone as the buckling behaviour patterns of such shells depend strongly on the laminate stacking. However, there was no indication that any laminated cylinder with any non-axisymmetric dimple results in a lower buckling load than an isotropic cylinder of identical radius, length and wall thickness also

having a non-axisymmetric dimple.

Kurzfassung

Die korrekte Analyse der statischen Stabilität und das zuverlässige Bestimmen der Beullasten spielen eine wichtige Rolle beim Konstruieren von dünnwandigen Schalenstrukturen. Echte Schalen beinhalten geometrische Imperfektionen und andere Abweichungen von Sollwerten. Diese sind bei einer Analyse zu berücksichtigen, da Traglastberechnungen aufgrund idealer Zustände zu extremen Unterschieden zwischen rechnerischer Vorhersage und Tests führen können. Die vorliegende Dissertation befasst sich mit dem Beulverhalten von dünnwandigen, unversteiften Kreiszylindern unter reiner Axiallast wegen der ausserordentlichen Imperfektionsempfindlichkeit dieser Schalen. Die Parameter, die es für eine Anwendung echter Imperfektionen in einer Beulanalyse braucht, sind schwierig zu bestimmen. Und Messwerte solcher Imperfektionen für die Auslegung neuer Zylinderschalen sind kaum erhältlich. In Ermangelung solcher Daten werden meist Beulformen verwendet, welche für perfekte Schalengeometrie resultieren und deren Muster durch harmonische Funktionen beschrieben werden können. Für eine sichere Schalenkonstruktion ist dasjenige Imperfektionsmuster massgebend, welches die tiefste Beullast verursacht. Im Allgemeinen sind jedoch weder die Geometrie noch die Amplituden der Beulformen, welche zum schädlichsten Imperfektionsmuster beitragen, von vornherein bekannt. Zudem umhüllen die Beulformen perfekter Zylinder gleichmässig die ganze Schalenfläche. Folglich werden lokale Abweichungen wie einzelne Dellen oder Beulen nur ungenügend berücksichtigt. Mangels passender Imperfektionsparameter müssen zylindrische Schalen deshalb noch immer mittels Abminderungsfaktoren konstruiert werden, mit denen die analytischen Beullasten der perfekten Schalen entsprechend zu reduzieren sind. Diese Abminderungsfaktoren berücksichtigen kleinste empirische Werte und liefern so eher konservative Traglasten. Ausserdem existieren solche Auslegungs-Richtlinien für Stähle und andere isotrope

Schalenmaterialien, aber nicht für Zylinder aus orthotropem Faserverbund, beispielsweise.

Aus diesen Gründen behandelt die vorliegende Arbeit das Instabilitätsverhalten von unversteiften Kreiszyklindern unter reiner Axiallast, welche mit örtlich begrenzten Imperfektionen in Form einer einzelner Delle oder Beule behaftet sind. Um die Wirkung einer einzelnen derartigen Vorbeule getrennt vom Einfluss anderer Geometrieabweichungen zu untersuchen, wurden diskrete, parametrische Dellen oder Beulen an FE-Zylindermodellen mit ansonsten perfekter Geometrie angebracht. Die gewählte Form einer parametrischen nach innen oder nach aussen gerichteten Vorbeule ermöglichte es, den Einfluss ihrer Anfangsamplitude, ihrer Anfangsbreite in Umfangsrichtung, ihrer Anfangshöhe in axialer Richtung sowie ihre Anfangsposition systematisch und unabhängig von anderen Parameter zu untersuchen. Im Hinblick auf das Fehlen zweckmässiger Konstruktionsempfehlungen für Komposit-Zylinder umfasst diese Dissertation die Analyse von isotropen wie auch von laminierten CFK-Schalen.

Es wurden zahlreiche Parameterstudien an Zylindern mit einer Vorbeule von unterschiedlicher Anfangsamplitude aber fester Anfangsbreite und -höhe durchgeführt. Zudem wurde für einige Zylinder und einzelne gewählte Anfangsamplituden diejenigen Anfangshöhen und Anfangsbreiten gesucht, welche jeweils die axiale Festigkeit der Schale am meisten reduziert. Schliesslich wurde auch der Einfluss der relativen Lage einer zweiten, identischen Vorbeule auf die Tragfähigkeit eines Zylinders untersucht.

Ziel dieser Analysen war es, zu untersuchen, ob es einzelne, örtlich begrenzte Vorbeulen gibt, die die nominale axiale Beullast eines unversteiften Kreiszyklinders mehr reduzieren als Imperfektionen, die auf klassische Beulmuster idealer Zylinder beruhen. Und: Existieren ungünstigste Geometrien von solchen Vorbeulen? Zudem: Ist der Effekt einer Vorbeule der gleiche für isotrope Zylinder wie für laminierte Komposit-Zylinder? Und schliesslich: Gibt es eine wesentliche Interaktion zwischen zwei identischen Vorbeulen in einer Zylinderschale?

Die Vorbeulen-Parameterstudien erforderten eine grosse Zahl von statischen und transient-dynamischen FE-Analysen. Die meisten durchgeführten Berechnungen waren Nichtlineare Beulanalysen, d.h. nicht-lineare statische Spannungsanalysen unter Berücksichtigung grosser Verschiebungen und Rotationen mittels Umgeformter Lagrangesche Formulierungen und zusätzlichen linearen Eigenwertanalysen, welche nach

ausgewählten kleinen Lastschritten ausgeführt wurden, um die Stabilität der Vorbeulzustände zu bestimmen. Um die grosse Zahl von Schalen mit unterschiedlichen Beullasten und Verhaltensmuster besser bewältigen zu können wurde die Nichtlineare Beulanalyse so modifiziert, dass die regelmässig, jeweils nach einigen Lastschritten berechneten Eigenwerte die Grösse der nachfolgenden Lastschritte automatisch passend einstellt. Für eine Auswahl von Zylindern und Vorbeulgeometrien wurden zusätzlich auch nichtlineare transient-dynamische FE-Analysen durchgeführt, um die speziellen Deformationsprozesse solcher Schalen näher zu untersuchen. Wegen der angenommenen relativ langsamen Kompressions/-geschwindigkeit wurde dazu der impliziten “Einzelschritt-Houbolt-Methode” zur Zeit-Integration gegenüber den gebräuchlicheren expliziten Methoden den Vorzug gegeben. Durch Aufbringen erheblicher Trägheitsdämpfung konnte die Anzahl der benötigten Zeitschritte reduziert werden.

In einer Klassischen Beulanalyse kann die Tragfähigkeit von idealen, dünnwandigen, unversteiften isotropen Kreiszyinderschalen mittlerer Länge unter reinem Axialdruck mit Hilfe einfacher Gleichungen analytisch berechnet werden. Diese Gleichungen entstammen der Lösung der gekoppelten partiellen Differentialgleichungen für Gleichgewicht und Kompatibilität in gelenkig gelagerten Zylinder mittels harmonischer Funktionen. Geschlossene Lösungen solcher Donnell’scher Schalengleichungen stehen auch für dünnwandige orthotrope Composite-Zylinder zur Verfügung. Eine solche Klassische Beulanalyse ist jedoch ausschliesslich für perfekte Zylindergeometrie anwendbar.

Für die untersuchten Imperfektionsmuster standen keine Testresultate zur Verfügung, mit welchen die Resultate der FE-Analysen hätten verglichen werden können. Stattdessen gründet deren Qualität auf überzeugenden Resultaten solcher Berechnungen von ähnlichen Zylinder mit idealer Geometrie und von laminierten CFK-Zylinder, deren gemessene Imperfektionen in ihr FE-Modell eingefügt wurden. Die Resultate zu den idealen Zylinder konnten mit Werten aus Klassischen Beulanalysen verglichen werden. Für Vergleiche mit den Analyseresultaten der CFK-Schalen mit gemessenen Imperfektionen konnten Testwerte herangezogen werden.

Die untersuchten unsymmetrisch laminierten CFK-Zylinder entstammen einem vorangegangenen europäischen Projekt, in welchem die Korrelation zwischen den Beullasten aus Tests und aus numerischen Berechnungen im Mittelpunkt stand. Die FE-Analysen dieser Schalen hatten gezeigt, dass für solche Zylinder sehr gute Resultate erzielt werden

können, falls in der Analyse gemessene Imperfektionen berücksichtigt werden. Es wurde weiter erkannt, dass eine Berücksichtigung von Imperfektionen der Anwendung von FE-Analyse-Methoden bedarf, welche sich für geometrische Nichtlinearitäten eignen. Die Nichtlineare Beulanalysen und die transient-dynamischen FE-Analysen dieser CFK-Zylinder mit perfekter Geometrie und mit gemessenen Imperfektionen dienten schliesslich als Basis für die Analysen von solchen Zylinder, die mit einzelnen parametrischen Vorbeulen behaftet sind.

Die FE-Analysen von mit einer einzelnen Vorbeule behafteten Zylinder brachten spezielle Verformungsprozesse, inklusive verschiedene lokale Beulphänomene, hervor, die sonst von unversteiften Kreiszyylinder kaum bekannt waren – weder für perfekte Geometrie noch für über die ganze Schalenfläche verteilte Imperfektionen. Dennoch konnten mittels systematischer Parametervariation einige Zusammenhänge zwischen den Resultaten und den nominalen Dimensionen der Zylinder und der Vorbeulen eruiert werden.

Die Anfangskrümmung der Schale in der Vorbeule in Umfangsrichtung spielt eine entscheidende Rolle im Verformungsprozess der Zylinder und dem Ablauf ihrer FE-Analysen. Die Unterschiede im Verhaltensmuster und der Anfangskrümmung führte zu einer Unterscheidung zwischen “tiefen” und “seichten” Dellen. Eine seichte Delle mit einer Anfangstiefe kleiner als ein gewisser Grenzwert verursacht ein ausgeprägtes lokales Beulen mit einem plötzlichen Durchschlagen der Zylinderschale in der Delle weiter nach innen, um so einen abgeflachten Schalenstreifen von reduzierter geometrischer axialer Steifigkeit zu erzeugen. Eine tiefe Delle hingegen resultiert in einem kontinuierlichen lokalen Abflachen der Zylinderschale ohne dynamischen lokalen Beulvorgang bei Lasten unterhalb der Kollapslast des gesamten Zylinders.

Örtlich begrenzte seichte Dellen von kritischer Anfangsbreite und -höhe reduzieren die axiale Beullasten gleich stark wie axialsymmetrische, ringförmige Dellen von gleicher Anfangstiefe. Und eine lokale, unsymmetrische seichte Delle von kritischer Anfangsbreite und -höhe kann gleich schädlich sein wie ein Imperfektionsmuster, das von einem Beulmuster eines idealen Zylinders abgeleitet ist und deren Anfangsamplitude der Hälfte der Anfangstiefe der Delle entspricht. Ferner schwächen lokale, unsymmetrische Beulen die Tragfähigkeit weniger als lokale Dellen von gleicher absoluter Anfangshöhe, -breite und -amplitude. Des Weiteren ist die Beullast eines Zylinders mit einer einzelnen lokalen Delle nur unwesentlich höher als mit einer zusätzlichen zweiten Delle gleicher Grösse.

Die Studien ergaben, dass die nominale Zylinder-Länge ebenfalls ausschlaggebend ist für die lokalen Verformungsprozesse der Schalen in den Vorbeulen und in deren Umgebung (lokales Beulen). Die Ausführungsempfehlungen in Normen und in der Fachliteratur für dünnwandige, unversteifte isotrope Zylinder unter Axiallast sind denn insoweit konservativ, als in der Analyse der nominale Zylinderradius, die nominale Wandstärke wie auch die nominale Zylinderlänge berücksichtigt sind.

Für isotrope Zylinder ist die Anfangshöhe in axialer Richtung der Vorbeulen, die die Beullast für eine gegebene Anfangsamplitude am meisten reduzieren, nahe der Wellenlänge für klassisches axialsymmetrisches Beulen eines perfekten Zylinders. Die Anfangsbreite in Umfangsrichtung der "schlimmsten" Delle ist auf etwa zwei bis drei mal der Anfangshöhe begrenzt, die "schlimmste" Beule hingegen ist immer axialsymmetrisch (Ringbeule). Für die laminierten CFK-Zylinder konnte keine genaue und allgemeine Vorhersage über die Dimensionen der jeweils "schlimmsten" Vorbeulen nur auf der Basis der nominalen Zylindergeometrie abgeleitet werden, da deren Beulverhalten auch stark von der Reihenfolge und Orientierung der Laminatschichten abhängt. Indes gibt es kein Anzeichen dafür, dass ein laminiertes Zylinder mit einer lokalen unsymmetrischen Vorbeule in einer tieferen Beullast resultiert als ein isotroper Zylinder gleicher Länge, gleichen Radius und gleicher Wandstärke, ebenso behaftet mit einer lokalen unsymmetrischen Vorbeule.

List of Symbols

Notation

x, X	scalar
\mathbf{x}, \mathbf{X}	tensor
x_{ij}, X_{ij}	components of \mathbf{x} and \mathbf{X} , resp.; $i = 1, 2, 3$; $j = 1, 2, 3$
\mathbf{x}, \mathbf{X}	vector or Matrix
$\{x_{ij}\}$	vector representation of \mathbf{x} or \mathbf{x}
$[X_{ij}]$	matrix representation of \mathbf{X} or \mathbf{X}
\mathbf{X}^T	transpose of \mathbf{X}
\mathbf{X}^{-1}	inverse of \mathbf{X}
$ x $	absolute value of x
$\det \mathbf{X}$	determinant of \mathbf{X}
$\operatorname{div} \mathbf{X}$	divergence of \mathbf{X}
dx	infinitesimal quantity of x
δx	virtual quantity of x
$\mathbf{X} \cdot \mathbf{Y}$	scalar product; eg. $\mathbf{Z} = \mathbf{X} \cdot \mathbf{Y} \rightarrow Z_{ij} = \sum_k X_{ik} Y_{kj}$
$\mathbf{X} : \mathbf{Y}$	double contraction; eg. $z = \mathbf{X} : \mathbf{Y} \rightarrow z = \sum_i \sum_j X_{ij} Y_{ij}$
\mathbf{x}_i	matrix or vector \mathbf{x} at iteration step i
${}^b \epsilon \mathbf{x}$	b actual increment number; ℓ reference increment number; $\ell = 0 \rightarrow$ Total Lagrange; $\ell = s \rightarrow$ Updated Lagrange
$\epsilon \mathbf{x}$	increment of \mathbf{x} with reference state ℓ

Symbols

Symbol	Description
A	area
\mathbf{A}	membrane stiffness matrix
\mathbf{a}	flexibility matrix; membrane compliance matrix; $\mathbf{a} = \mathbf{A}^{-1}$
a_b	initial circumferential dimple width
$a_{\bar{b}}$	most damaging initial dent width for a given w_b
$a_{\bar{b}}^*$	estimations of $a_{\bar{b}}$
\mathbf{B}	extension-bending coupling stiffness matrix
\mathbf{b}	eccentricity matrix; $\mathbf{b} = \mathbf{A}^{-1}\mathbf{B}$
\mathcal{B}	matrix containing spatial derivatives of the functions in \mathbf{H}
${}_{\ell}^s\mathcal{B}_{\ell}$	linear strain-displacement transformation matrix
${}_{\ell}^s\mathcal{B}_{nl}$	nonlinear strain-displacement transformation matrix
\mathbf{b}	body force vector
\mathcal{C}	material tensor
\mathbf{C}	material matrix
\mathcal{C}	damping matrix
c	any constant (may be zero)
\mathbf{D}	bending stiffness matrix
$\tilde{\mathbf{D}}$	modified bending stiffness matrix; $\tilde{\mathbf{D}} = \mathbf{D} - \mathbf{B}^T\mathbf{A}^{-1}\mathbf{B}$
\mathbf{E}	GREEN-LAGRANGE strain tensor; $\mathbf{E} = 1/2[\mathbf{F}^T \cdot \mathbf{F} - \mathbf{I}]$
E_{ij}	GREEN-LAGRANGE strain components
${}_{\ell}\mathbf{E}$	linear strain increment
e	EULERIAN or ALMANSI strain tensor
E	YOUNG's modulus
E_1, E_2	orthotropic YOUNG's moduli
\mathbf{F}	deformation gradient tensor; $\mathbf{F} = \partial\mathbf{x}/\partial\mathbf{X}$
\mathcal{F}	AIRY stress function with $N_x = \partial^2\mathcal{F}/\partial y^2$, $N_y = \partial^2\mathcal{F}/\partial x^2$, $N_{xy} = -\partial^2\mathcal{F}/\partial x\partial y$
\mathcal{F}_0	AIRY stress function of the initial state

Symbol	Description
${}^s\mathbf{f}$	internal resisting force vector
G	shear modulus
G_{12}	orthotropic shear modulus
h	shell wall thickness, plate thickness
\mathbf{H}	matrix containing interpolation or shape functions
\mathbf{I}	unit tensor
\mathbf{I}	identity matrix
J	JACOBIAN determinant; $J = \det \mathbf{F}$
\mathbf{K}	system stiffness matrix
${}^s\mathbf{K}_l$	linear stiffness matrix
${}^s\mathbf{K}_{nl}$	initial-stress or geometric stiffness matrix
${}^s\mathbf{K}_T$	tangent stiffness matrix
${}^e\Delta\mathbf{K}_{nl}$	incremental initial-stress stiffness matrix
L	nominal cylinder length
ΔL	axial compression; cylinder length reduction
l_c	axial half-wavelength for axisymmetric buckling
l_b	initial axial dimple height
$l_{\bar{b}}$	most damaging initial dent height for a given w_b
$l_{\bar{b}}^*$	estimations of $l_{\bar{b}}$
\mathbf{M}	bending and twisting moments per unit length
M_x, M_y, M_{xy}	bending and twisting moments per unit length
m	number of half-waves in axial direction
m_c	number of half-waves in axial direction linked with the smallest buckling load; buckling mode
\mathcal{M}	mass matrix
\mathbf{n}	normal vector
\mathbf{N}	membrane forces per unit length
N_x, N_y, N_{xy}	membrane forces per unit length
$\tilde{N}_x, \tilde{N}_y, \tilde{N}_{xy}$	membrane forces per unit length of the initial state

Symbol	Description
N_{axial}	axial membrane force per unit length; approx. N_x
N_{hoop}	circumferential membrane force per unit length; approx. N_y
N_{shear}	shear membrane force per unit length; approx. N_{xy}
\bar{N}_{axial}	mean N_{axial} in a finite element
\bar{N}_{hoop}	mean N_{hoop} in a finite element
\bar{N}_{shear}	mean N_{shear} in a finite element
$-N_{cr}$	axial buckling load per unit length
n	number of waves in circumferential direction
n_c	number of waves in circumferential direction linked with the smallest buckling load; buckling mode
p	pressure
p_z	lateral area load
\mathbf{p}	force vector; external forces
$\Delta \mathbf{p}^{s+1}$	load increment vector at increment $s + 1$
\mathbf{P}_{cr}^{s+1}	intermediate buckling load vector; result of eigenvalue extraction at increment $s + 1$
\mathbf{p}_{cr}	buckling load vector
P	compressive force
P_{cr}	axial buckling force; compressive: $P_{cr} = -2\pi RN_{cr}$
P_{cl}	classical axial buckling force; buckling load by classical analysis
$P_{cr id}$	buckling load for ideal geometry
$P_{cr L}$	lower buckling load; local buckling load
$P_{cr U}$	upper buckling load; cylinder collapse load
\mathbf{r}	residual forces
R	nominal cylinder radius; radius of reference surface
r	radius coordinate
r_k	local radius of nodal point
\tilde{r}_k	local radius of curvature; local curvature: $1/\tilde{r}_k$; approximation
\mathbf{S}	2nd PIOLA-KIRCHHOFF stress tensor

Symbol	Description
S_{ij}	2nd PIOLA-KIRCHHOFF stress components
s	increment number
\mathbf{t}	stress vector; surface traction vector
\mathbf{T}	transformation matrix
t	time
Δt	time step
U	strain energy
\mathbf{u}	displacement vector; $\mathbf{u} = \mathbf{x} - \mathbf{X}$
u	component u_1 of the displacement vector \mathbf{u}
\bar{u}	displacement u in the reference surface
$\tilde{\mathbf{u}}$	vector of discrete displacements and rotations; DOF
$\overset{s}{\mathbf{u}}$	total displacements at increment s
\mathbf{u}	displacement increment
$\tilde{\mathbf{u}}_\delta$	eigenvector; eigenmodes
$\dot{\mathbf{u}}$	velocity vector
$\ddot{\mathbf{u}}$	acceleration vector
V	body volume
v	component u_2 of the displacement vector \mathbf{u} ;
\bar{v}	displacement v in the reference surface
W	work
W_{ex}	external work
w	component u_3 of the displacement vector \mathbf{u} ; lateral displacements
\bar{w}	displacement w in the reference surface; assumption: $\bar{w} \approx w$
w_0	lateral displacement of the initial state
w_b	initial dimple amplitude; initial dent depth; initial bulge elevation
w_b^*	marginal dent depth
\mathbf{X}	LAGRANGIAN or material coordinates; initial position
\mathbf{x}	EULARIAN or spatial coordinates; current position
Z	BATDORF's parameter with $Z = L^2/(Rh)\sqrt{1-\nu^2}$

Symbol	Description
z_b	initial position of dimple apex in axial direction
α	ply angle; $\alpha = 0^\circ$ is parallel to cylinder axis
α_k	stiffness damping parameter
α_m	inertia damping parameter
β	axial half-wave length parameter with $\beta = m\pi/L$
γ_{xy}	shearing strain; $\gamma_{xy} = 2\varepsilon_{12} = \partial u/\partial y + \partial v/\partial x$
Δ_R	imperfection shape function
Δ_ζ	axial spacing between the apices of two dents
Δ_φ	circumferential spacing between the apices of two dents; angle
ϵ	linear strain tensor; $\varepsilon_{ij} = 1/2(\partial u_i/\partial x_j + \partial u_j/\partial x_i)$
$\bar{\epsilon}$	strains in the reference surface
$\bar{\epsilon}_x, \bar{\epsilon}_y, \bar{\gamma}_{xy}$	vector components of $\bar{\epsilon}$
η	hoop wave length parameter with $\eta = n/R$
$\ell\eta$	nonlinear strain increment
κ	negative curvatures of the reference surface
$\kappa_x, \kappa_y, \kappa_{xy}$	vector components of surface curvature κ with: $\kappa_x = -\partial^2 w/\partial x^2, \kappa_y = -\partial^2 w/\partial y^2, \kappa_{xy} = -2\partial^2 w/\partial x\partial y$
λ	eigenvalue
λ_{cr}	smallest eigenvalue
ν	POISSON'S ratio; $\nu = 0.3$ unless otherwise noted
ν_{12}	orthotropic POISSON'S ratio
ξ	perturbation amplitude, normalized
$\bar{\xi}$	imperfection amplitude, normalized
Π	potential energy
ρ	density
σ	CAUCHY stress tensor; $\mathbf{t} = \sigma \cdot \mathbf{n}$
$\sigma_{xx}, \sigma_{yy}, \tau_{xy}$	components of stress vector
$-\sigma_{cr}$	axial buckling stress

Symbol	Description
σ_{axial}	axial CAUCHY stress
σ_{hoop}	circumferential CAUCHY stress
φ	angle coordinate
φ_b	initial position of dimple apex in circumference
ϕ_x, ϕ_y	rotations about y -axis and x -axis, respectively

Coordinate Systems

Axes	Description
x, y, z	Cartesian coordinate system
r, φ, z	cylindrical coordinate system

Boundary Conditions

<i>Simply Supported</i> $w = \frac{\partial^2 w}{\partial x^2} = 0$		<i>Clamped</i> $w = \frac{\partial w}{\partial x} = 0$	
SS3	$\bar{v} = c, \quad N_x = 0$	CC3	$\bar{v} = c, \quad N_x = 0$
SS4	$\bar{v} = c, \quad \bar{u} = c$	CC4	$\bar{v} = c, \quad \bar{u} = c$

Abbreviations

CC3	clamped edges; constant edge loads
CC4	clamped edges; constant axial edge displacements
CFRP	carbon fibre reinforced plastic
DEVILS	European project “design and validation of imperfection tolerant laminated shells”
DOF	degrees of freedom; displacement and rotation components
FE	finite element
SSH	single-step HOUBOLT; implicit time-integration method
SS3	hinged edges; constant edge loads
SS4	hinged edges; constant axial edge displacements

Chapter 1

Introduction

Curved plates and shells are important structure elements of aircraft, vessels and vehicles. The accepted trend towards maximal travel speed at minimum energy input requires geometry optimization of structures like fuselages or panels regarding the weight, the physical limitations and the costs. Such optimized lightweight structures are therefore designed for heavy loadings with resulting safety margins as small as possible. Consequently, to prevent failure the critical states of stress and deformation as well as the maximum allowable loads have to be taken into account, what implies that all relevant measures are accurately known already in the design. In many cases the load carrying capacity of a shell structure is determined by their material and geometric stiffness that governs the deflections, the natural frequencies, and the static stability. Thin-walled structures are sensitive to instability phenomenon and have a tendency to respond with undesired dynamic amplitudes when being loaded by compressive membrane stresses beyond stability limits. When a state of static instability is reached the released amount of energy during the transition to a new stable state can result in disastrous structural responses. Therefore, accurate analysis concerning instability or buckling and reliable appointment of the critical loads is crucial for safe design of shell structures. The deformation pattern of the state after buckling may also to be of importance as it affects the integrity and the functionality of the over-all configuration.

Analytical solutions are available with which buckling loads can be calculated, though such analyses are restricted to basic and ideal shell ge-

ometries, load distributions, and boundary conditions. By consideration of geometric nonlinearity approximate solutions of sets of equations may also provide information about the post-buckling state of a basic shell; however, the efforts for the development of such codes appear to be unpleasant. In addition, such types of special-purpose programs can exclusively be used for buckling analyses of shells which are of the geometry, loading and boundary condition that were provided for. But due to the numerical procedures developed in recent decades, above all the Finite Element (FE) method, these obstacles regarding the limited adaptability could be eased rigorously. In mechanical engineering the FE method is commonly used and many commercial programs are available with partially sophisticated graphical user interfaces with integration into design software. Present FE software allows to perform enveloping buckling strength investigations also for complex geometries, material properties and boundary conditions. On the basis of structure models buckling loads can be calculated, and in consideration of large displacements and mass densities the buckling as well as the post-buckling behaviour of a shell structure can be reproduced, though with considerable computation effort. Anyway, a buckling analysis of an axially loaded, unstiffened cylindrical shell still can end in frustration after comparison of the analysis result with test data, in that despite elaborate calculation technique real shells may buckle already at loads less than a fifth of the values predicted in analysis [62].

Because of the extreme discrepancy between prediction and test results the buckling of axially-compressed thin-walled cylindrical shells attracted much more attention in the past than many other problems in structural mechanics. Real structures contain *imperfections*, i.e. irregularities in shape, material properties, boundary conditions, stress distribution, and so on. In classical buckling analysis however ideal conditions are considered, and FE models in general base on design drawings and therefore also approximate the structure without any deviations from nominal dimensions and geometries. The path-setting treatment of this problem has been published by (KOITER [54]) for cylindrical shells in order to define a sensitivity parameter that might allow for a classification of such shells with reference to their imperfection sensitivity. In these analyses the assumed shape of the geometric imperfection is based on the buckling pattern for the ideal cylinder, see also (BUDIANSKY & HUTCHINSON [20]), and many other references in the following years. Later (ARBOCZ [8]) has devoted a significant effort to the measurement of the real shape of test specimens, to the calculation of the buckling load of such geometrically imperfect structures and to the correlation

with related test results. His effort aims at the definition of quality criteria allowing for the assignment of knockdown factors to be applied to the theoretical buckling load values obtained for ideal shells.

The analyses to the dissertation on hand were performed subsequent to the activities contributing to the European project *DEVILS*¹ which focussed on the correlation of buckling loads of laminated test cylinders with analytical and numerical predictions, including the best available information of geometrical irregularities. Numerous FE calculations had been conducted until it was concluded that a satisfying and useful agreement between experienced and predicted buckling loads for such cylinders can be achieved if their measured imperfections are included in the analysis [60]. It was found that the consideration of imperfections requires the use of nonlinear FE analysis methods which take geometric nonlinearity into account. Further, to allow for description of all potentially critical deformation patterns for near isotropic cylinder shells a mesh size of the finite elements not wider than $0.5\sqrt{Rh}$ is recommended², based on the decay length of edge bending disturbances [81, 60]. The applied nonlinear buckling analysis method and the modeling of circular cylinders with four-node linear shell elements finally provided the basis for the FE analyses conducted for the studies described later in this thesis on cylinders having single dimple imperfections.

The effect of geometric imperfections and the crucial importance of their consideration in buckling analysis of cylindrical shells under axial load has been generally accepted for years. However, the parameters required for an application of *real* irregularities in a FE analysis are difficult to be specified. And measured values of real imperfections for the design of any new shell are hardly available. In the absence of such data alternatively *notional* patterns of initial deviations from the nominal shell geometry may be introduced to intentionally weaken the stiffness of a structure model. For instance, following KOITER's studies several commercial FE programs provide procedures with which buckling patterns that result for perfect shell geometry can be added to a shell model prior to an analysis. This method, in principle, allows to incorporate geometric imperfections also in an early design phase and without later expensive gauging of shell surfaces.

Classical buckling patterns of ideal cylinders may be described with harmonic displacement functions and differ basically in the number of waves

¹Brite-Euram project BE-7550 *DEVILS* "design and validation of imperfection tolerant laminated shells".

² R : nominal cylinder radius; h : shell wall thickness.

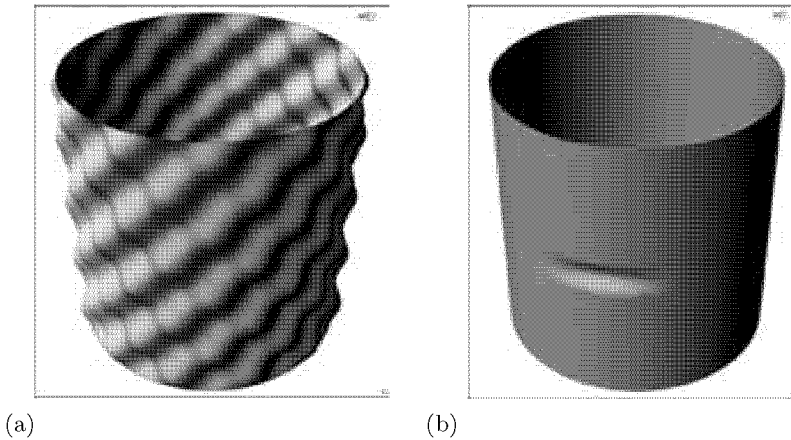


Figure 1.1: (a) Typical buckling pattern of an isotropic, unstiffened circular cylinder, and (b) cylinder having a single localized inward dimple.

in tangential and half-waves in axial direction, see Figure 1.1 (a). For safe shell design that imperfection shape is significant which yields the minimum buckling load. But, in general the wave numbers as well as the amplitude(s) of such buckling modes which contribute to the most damaging imperfection pattern are not known a priori. Thus, due to the lack of adequate imperfections parameters, shell structures still have to be designed by use of reduction factors to be applied to the analytical buckling loads for perfect shells. These factors recommended for shell design consider smallest empirical values and hence provide critical loads which appear to be rather conservative. For immobile cylinder structures underestimations of the effective load carrying capacity might be acceptable, in light-weight construction however surplus shell material runs counter to any effort to minimize transport energy consumption. Moreover, such instructions exist for steel and other isotropic shell materials but *not for laminated composite cylinders*, for instance. That is, in practice for a real composite cylinder without empirical data regarding irregularities and without sufficient analysis experience a serious prediction of the lowest buckling load to be expected appears hardly possible. Consequently, the safe usability of composite shells might be challenged though in aerospace these materials have become more and more important.

Similar to real shell surfaces the “mathematical” imperfections that resemble buckling patterns of ideal cylinders consist in a number of dimples

(Fig. 1.1 (a)), but these are evenly distributed over the entire shell surface and arranged side by side, alternately inwards and outwards. Thus, they reproduce localized irregularities like single *dents* (inward dimples) or *bulges* (outward dimples) of different amplitude inadequately. The stress and deformation states of a shell with randomized single dimples of various size are irregular and can not be deduced from the states which result for ideal-shell-buckling mode imperfections. The distribution of the stresses in and in the vicinity of any single dimple in a shell is hardly known as it results from changes in local shell curvatures and interferes with that of adjacent dimples as well as of any further curvature variations. On the occasion of the mentioned European project, nonlinear FE analyses of an axially loaded laminated carbon-fiber-reinforced plastic (CFRP) cylinder were performed applying its measured imperfection pattern as initial shell geometry that included a few relatively large discrete dents. Different from other analyses and shells, in this case the calculations result underestimates the experimental values notably. The extraordinary result provoked further analyses focusing on the damaging effect of *localized dimple imperfections*. Subsequent to the successful conclusion of the European project the relating investigations were continued within the scope of the present dissertation.

To investigate the particular influences of a single initial dimple on the instability behaviour of axially compressed cylinders systematically, and separate from any impact of other irregularities, discrete parametric dents or bulges were added to FE models of unstiffened circular cylinders of otherwise perfect geometry, see Figure 1.1 (b). The chosen imperfection shape, specified with single-periodic cosine functions, allowed for to vary the initial amplitude, the initial circumferential width as well as the initial axial height of the dimples independently of each other, and also irrespective of the buckling behaviour of the perfect shell. With regard to the absence of practical design recommendations for laminated composite cylinders the study on hand covers the analysis of isotropic as well as of laminated CFRP shells.

This thesis deals again with the structural stability of “simple” closed and unstiffened circular cylinders and the analysis thereof. Shell structures like fuselages in general consist of panels, frames, stringers, cut-outs, and other components of different sizes, geometries, and material properties. The choice of the rather “academic” cylinder shells for the further investigations bases on the extraordinary sensitivity of their buckling resistance to geometric imperfections under pure axial loading. That is, it was assumed that any potential improvement of the reliability

and accuracy of the buckling load prediction for such axially compressed cylinders will also advance the calculation of the load carrying capacity for more commonly used, general shell structures of arbitrary loading.

The finite element analyses of cylindrical shells having localized, parametric dimple imperfections aimed at finding answers to the following questions:

- Are there single, localized initial dimples (Fig. 1.1 (b)) which reduce the nominal axial buckling load of an unstiffened circular cylinder more than imperfections derived from classical buckling patterns for ideal shells (Fig. 1.1 (a))?
- Is there a *worst geometry* of such a single dimple imperfection? That is, are there initial aspect ratios of the dimple that damage the most?
- Is the effect of *inward* dimples (dents) on the axial cylinder stability the same as of *outward* dimples (bulges)?
- Is the instability behaviour the same for *isotropic* shells as for *laminated composite* shells (anisotropic) having such a localized dimple imperfection?
- Is there an important interaction between *two* initial dimples?

An objective of this thesis was to provide a tool which enables the FE analyst to define a notional single dent or bulge that reduces the axial stability of a cylindrical shell similarly to the most damaging imperfection to be expected for the real shell. Several parameter studies of the influences of the dimple size, shape, and amplitude on the load-carrying capacity of circular cylinders were conducted. The results of these studies served to answer the questions above. Additionally, the output data contains detailed information about the effects of local imperfections in FE buckling analyses which is helpful for the set-up of reliable reproductions of real geometric irregularities of cylinders as well as of general shell structures.

The dimple-parameter studies required a large amount of static and transient dynamic FE analyses. Most of the numerical calculations performed were nonlinear buckling analyses, i.e. nonlinear static analyses with intermediate linear eigenvalue extractions. To manage the large number of shells with different buckling loads and behaviour considered, the nonlinear buckling analysis was adapted for an adaptive load step

control which utilizes eigenvalues, calculated after a selected number of small loading steps, to determine the stability of pre-buckling states of stress and deformation. For a selection of cylinders and dimples additional nonlinear transient dynamic analyses were conducted with significant inertia damping introduced in order to research into the particular deformation processes of such shells under axial loading. Although the FE analyses discussed in this thesis are limited to axially compressed circular cylinders of linear-elastic shell material, on principle, the analysis methods used are applicable also for stability investigations of any other structure, load case and material behaviour. To support their potential applications for other buckling problems the linear and nonlinear static as well as the transient dynamic FE analysis methods are described in detail. As reference parameter settings for such calculations are hardly available, the full Chapter 3 is dedicated to the description of the nonlinear buckling analysis and the transient dynamic analysis as well as to related formulations and procedures (eg. Updated Lagrangian formulation, NEWTON-RAPHSON algorithm, implicit “single-step Houbolt” method). The reproduction of the algebraic basis of the eigenvalue problems involved and the origin of the so-called initial-stress or geometric stiffness matrices was prioritised; nevertheless, the explanations cover also the buckling analysis methods frequently addressed in the context of buckling, but whose application for axially-compressed imperfect cylinders appears less convenient (linear buckling analysis, explicit time integration, arc-length methods).

1.1 Shell Buckling in Brief

Buckling of shells is a vast subject whose comprehensive treatment requires entire books. Various specialized books and articles devoted to shell buckling exist [15], e.g. (TIMOSHENKO & GERE [76]), (BRUSH & ALMROTH [18]), or (BUSHNELL [21]). This section contains only summary of the relevant terminology and an explanation of basic instability phenomena and buckling analysis methods addressed in this thesis. More detailed descriptions of analytical and numerical methods used for the prediction of the load carrying capacity of circular cylinders follow in separate chapters.

1.1.1 On Instability Phenomena

The static stability or instability of a structure is a central feature of its equilibrium state. In general, *stable* equilibrium is referred to structures which, slightly displaced from their equilibrium position, eventually return to the initial position after removal of the disturbance; otherwise, disproportionate response denotes *unstable* equilibrium. Loading of shell structures over their stability limit results in sudden and accelerated increase of deflection. Instability phenomena are dynamic processes of large displacements and rotations; however, for analysis mostly the uncritical states prior to instability are focussed, following EULER's purely static equilibrium view of structures in their slightly deformed state [31].

Sequenced states of stress and deformation of a shell structure under changing load are often depicted by means of load-deformation curves which correspond to equilibrium paths. Characteristic runs of two types of instability failure are illustrated in Figure 1.2. The two graphs represent two different basic instability failure phenomena generally known in static analysis of perfect shell structures: (a) bifurcation buckling and (b) nonlinear collapse.

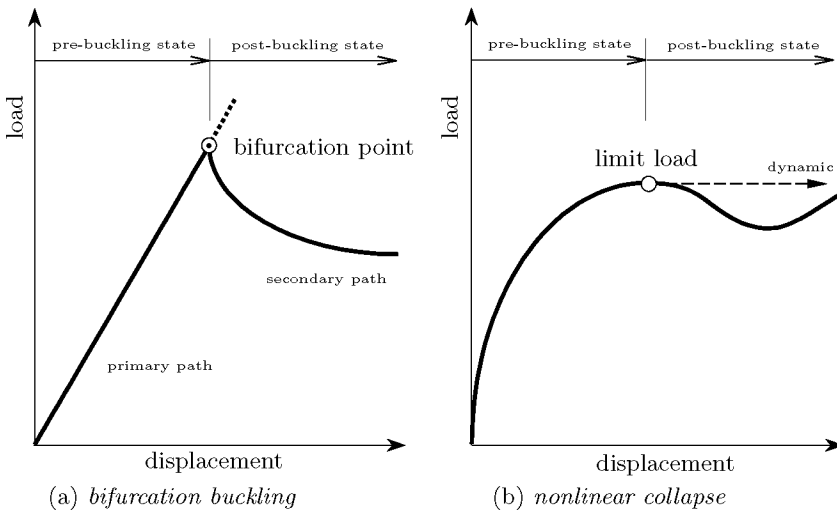


Figure 1.2: Characteristic load-deflections curves for (a) bifurcation buckling and (b) nonlinear collapse. Dashed arrow in (b) refers to sudden "snap-through" for load-controlled compression.

Bifurcation buckling refers to an analytical model where at the bifurcation point a further equilibrium path branches off from the primary equilibrium path with a different load-displacement characteristic. Thin, axially-compressed isotropic cylinders with perfect shell-geometry, for instance, first deform axisymmetrically along the primary path to a bifurcation point, see Figure 1.2 (a). Then, on the secondary path the deformation mode is non-axisymmetrical. The initial failure at the bifurcation point is characterized by a change from the initial axisymmetric to rapidly growing non-axisymmetrical deformations. The displacements prior to bifurcation buckling are assumed to be small, what allows to perform linear eigenvalue analyses to determine bifurcation points. Due to the nature of the mathematical formulations involved, bifurcation buckling is also commonly referred to as “linear buckling”.

Contrary to the linear primary paths for bifurcation buckling, that for *nonlinear collapse* is not straight-line, see Figure 1.2 (b): with increasing loading the deformation increments increase, and at the collapse or limit load the slope of the load-deflection curve is zero. With focus on the absence of forks along the equilibrium path this instability behaviour with nonlinear load-displacement characteristic is also called *limit-load buckling*. Further, nonlinear collapse is also generally known as “snap-through”, a label stemming from shallow arches and spherical caps under increasing, uniformly distributed lateral load: after having passed a certain limit load the caps and arcs suddenly snap towards a state which resembles the original structure in an inverted form [21]. The transition from axisymmetric to other axisymmetric patterns of some circular cylinders may also be mentioned as an example for nonlinear collapse. In this case the instability is connected with relatively large displacement amplitudes without a significant change of the shell pattern. Basically, limit-load buckling of shells requires analysis in consideration of geometric nonlinearity.

The definitions and terms describing structural instability phenomena are hardly unified. The expression “buckling”, for instance, is often used synonymously for bifurcation buckling, but may also cover all types of instability failure³. Bifurcation buckling is based on mathematical formulations of equilibrium which give theoretical buckling loads (bifurcation points) and respective buckling patterns; however, the displacement amplitudes of these buckling patterns as well as of the deflections after instability are not considered and any displacements prior to instabil-

³German language further distinguishes between “Beulen”, i.e. “buckling” of plates or shells, and “Knicken”, i.e. “buckling” of trusses.

ity are presumed to be small. Nonlinear collapse in turn refers to deformation process patterns which also cover considerable amplitudes of displacements already prior to instability. Based on observations this type of instability failure may also be called “buckling” as during tests after reaching the limit load visible dents or bulges emerge. On the other hand, any nonlinear collapse with deformation pattern after the instability, which differs from the patterns before the instability solely in displacement amplitude, may also be regarded as a matter of “large displacements”. Such definition confines “buckling” to transitions from the pre-buckling to a post-buckling state with a distinct change in the deflection mode and not only in a noticeable increase in amplitude; consequently, a shell having initial dents similar to those observable after the instability would flex but not “buckle”. However, in a less restrictive solution of the semantic dilemma the term “buckling”, or expressions like “nonlinear buckling” or “limit-load buckling”, could also be used for cases where at instability the lateral displacements are *suddenly accelerated*, ignoring whether the shell geometry prior and after instability resemble each other. Similarly, for the thesis on hand the buckling of axially compressed cylindrical shells was regarded as a dynamic process with rapid movements of the shell in radial direction when exceeding the stability limit, associated with a drop of the axial cylinder stiffness.

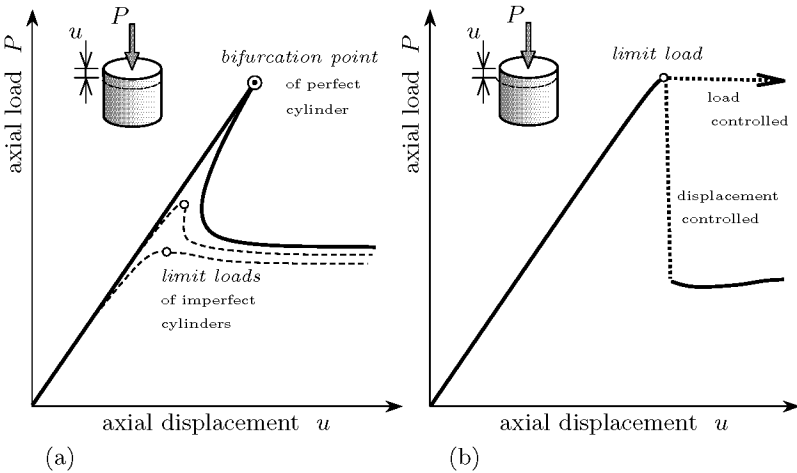


Figure 1.3: *Typical axial load-displacement curves for axially compressed cylinders: (a) theoretical, (b) experimental.*

Both equilibrium paths in Figure 1.2 display the process of compressive

load in dependence of displacements. In theory, for bifurcation buckling *radial* displacements are commonly used as abscissa as they refer to scaled amplitudes of harmonic deformation modes (eigenvectors, “buckling modes”) which are assumed to be zero prior to bifurcation buckling and non-zero positive or negative afterwards. But, for cylindrical shells in most cases the displacement direction considered in a graph is orthogonal to the shell normal and *parallel* to the load action direction. In Figure 1.3(a) a typical equilibrium path for bifurcation buckling of an axially compressed, thin isotropic cylinder shell with perfect geometry is shown. The *axial* load (axial compressive force) is plotted versus the *axial* edge displacement (end-shortening) as indicated in the graph. The primary equilibrium path is again straight up to the bifurcation point. The secondary path in turn intersects with the primary path in a small angle and first follows that line re-decreasing in load as well as in displacement. This progression of the theoretical secondary equilibrium path is a particular feature of perfect cylinders under axial loading and aggravates correct path-tracing in numerical analyses.

In engineering mechanics the definition for bifurcation buckling of thin-walled cylinders is based on the assumptions that the pre-buckling behaviour is linear, that the displacements prior to buckling are small, and hence that any *initial shell deformations* may be neglected. From this follows that in principle buckling loads of cylinders having geometric *imperfections* cannot be referred to bifurcation buckling. As the amplitudes of initial shell deformations increase continuously up to instability, pre-buckling deflections have to be taken into account, and depending on the deflection amplitudes the primary equilibrium path is nonlinear. The two dashed lines added to Figure 1.3(a) follow typical responses of cylinders with initial deformations of small and moderate amplitudes (upper and lower curve, resp.): the buckling loads are considerably reduced compared to the bifurcation point of the perfect shell; and at the maximum load the slope of the load-displacement curve is zero. Thus, the instability behaviour of imperfect shells are more of the nature of nonlinear collapse or limit-load buckling. Anyway, for initial deflections of small amplitudes that resemble theoretical buckling patterns of perfect shells, KOITER developed a theory which allows to approach the load-displacement curves of imperfect shells asymptotically to the primary and secondary paths for bifurcation buckling of respecting perfect shells.

In general, the progression of the axial load versus the axial displacement recorded during tests of cylinders differ from theoretical equilib-

rium paths as illustrated in Figure 1.3(a). At instability, a cylinder responds with rapid axial edge displacements in case of axial load as maintained loading parameter, whereas for displacement-controlled compression after instability the axial load drops down to the load level of the next stable equilibrium state. The almost horizontal and vertical dotted lines in Figure 1.3(b) idealize such behaviour of cylinders under load and displacement controlled axial compression, respectively.

The load-displacement curves in Figure 1.2 and 1.3 refer to the buckling of simple structures and single parts, in particular to the elastic buckling of axially-compressed, thin-walled unstiffened circular cylinders of medium length. In these cases the *buckling load* of the structure is simply the maximum load measured in compression tests or the smallest bifurcation point in calculations for perfect geometry. But in many practical cases the load-carrying behaviour is not as distinctive as shown in these graphs. For component assemblies like light-weight structures consisting of several shell members, for instance, the buckling of one component does not necessarily lead to the collapse of the entire structure as long as other, still stable components support an additional loading. In such situations a partial instability failure of a single structure part prior to the instability failure of the entire structure occurs. Consequently, for such cases regulations are needed which give information about what load level are to be classified as critical and assessed as the actual buckling load for the structure – the smallest value among the buckling loads for each single component or only the limit load at which the entire assembly collapses. Although adjustments of the definitions and the terminology hardly simplify instability analysis, an appropriate distinction between the instability phenomena involved is important in respect of their criticality and their treatment in the strength verification requirements of the structure to be investigated. In Figure 1.4 the further distinguishing between partial or *local buckling* and *total collapse* of a structure is explained by means of an load-displacement curve typical for stringer-stiffened shell panels. This kind of component assembly consisting in a cylindrically curved shell panel and frames is common practice, mainly in aeronautical engineering⁴. In this simplified example ideal connection between panel and frames is provided. The lower bend of the axial load-displacement curve refers to a local instability of the shell surface in between the two frames. After such local buckling the load-carrying portion of the shell surface is strongly reduced. But,

⁴See e.g. panels studied within the EC project *POSICOSS* “improved postbuckling simulation for design of fibre composite stiffened fuselage structures”.

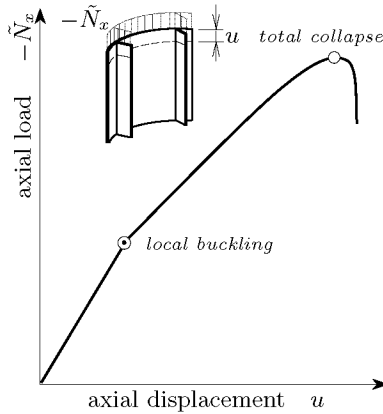


Figure 1.4: Typical axial load-displacement curve for an axially compressed stringer-stiffened panel. Axial shortening u versus axial compressive load per unit length $-\tilde{N}_x$.

depending on the load carrying capacity of the frames alone, additional loading can be supported up to the limit load of the entire panel structure. The structure finally collapses totally only at the curve peak due to failure of the frames. For commonly-used frames of isotropic material this limit load depends on the geometry of the frames and the material stiffness, but also on the yield stress of the frame material, for example. Such instability behaviour of frames and other stiffeners is analogous to the so-called *plastic buckling* of short columns where the ideal, classical (EULER) buckling load is higher than the yield point load [28]. Anyhow, although in general yielding, fracture and other material application limitations are important elements in an enveloping strength verification of a real structure, for this thesis only ideal-elastic material behaviour was considered for the analysed shells.

This dissertation deals solely with circular cylinders that have no additional component parts applied. But for FE models of axially compressed cylinders having a single, localized dimple imperfection yet particular forms of local instability could be observed: at loads smaller than the over-all stability limit of the entire cylinders, for some initial dimple sizes and geometries the shell strips of the cylinder that cover the dimples flattened and buckled similar to flat plates (see later). Therefore, in this

thesis the loss in axial instability of the cylinder locally within such shell strips is also referred to as “local buckling”, whereas “cylinder collapse” denotes the limit load of the entire cylinder.

The terms *pre-buckling* and *post-buckling* are often applied to address equilibrium states before and after an instability failure, respectively. For shell structures with occurrence of local buckling, in principle again additional specifications are needed since in such cases the pre-buckling states of the entire structures cover the states prior to total collapse as well as those before and after the local buckling. Hence, the post-buckling states of locally buckled components are likewise pre-buckling states of the entire structures. To avoid confusion hereinafter the term “pre-buckling” is always used in conjunction with over-all collapse. In general, structure analysis deals with the load-carrying behaviour prior to the collapse of a structure and the critical application limits. Likewise, the focus of this thesis is on the pre-buckling behaviour – of cylinders (having dimple imperfections). Nevertheless, the buckling and post-buckling behaviour of cylinders with or without imperfections was (and is) of importance for the applicability of the buckling analysis methods and the verification of the quality of the analysis results.

1.1.2 On Buckling Analyses

The pre-buckling and buckling behaviour involved and the shape of the equilibrium curve determine the applicability of the methods available to calculate the critical loads for a structure. For bifurcation buckling as depicted in Figure 1.2 (a) small pre-buckling deformations are assumed. Hence, for such cases the smallest, critical bifurcation point can be obtained by means of direct solution of linearised equilibrium equations and linear eigenvalue analyses. For limit-load buckling as illustrated in Figure 1.2 (b), however, nonlinear analysis methods are required which allow for large displacements and rotations.

The load-carrying capacity can be predicted *analytically* solely for a few basic geometries, boundary conditions and materials. But for ideal, thin-walled unstiffened isotropic circular cylinders of medium length under pure axial compression the classical axial buckling stress $-\sigma_{cr}$ in the shell surface is given by the common formula [62, 28, 25]:

$$-\sigma_{cr} = 0.605 \frac{E h}{R}$$

where R and h are the nominal cylinder radius and the wall thickness,

respectively; E is the YOUNG's modulus of the isotropic material with a POISSON's ratio of $\nu = 0.3$. Multiplied with the cross-sectional area ($2\pi R h$) a simple equation for the corresponding critical compressive axial load is obtained with

$$P_{cr} = 3.8 E h^2 .$$

These equations follow from bi-harmonic functions that solve the coupled partial differential equations for *hinged* cylinder edges and *infinitesimal displacements*. There are also similar close-form solutions of such DONNELL-type shell equations for axially compressed, thin-walled *laminated orthotropic composite cylinders*. But for such shells the buckling load is given in terms of the membrane, the bending and the extension-bending coupling stiffnesses of the material. In this dissertation derivations of these analytical solutions are presented; their application for the calculation of axial cylinder buckling loads will be called the "classical analysis" to draw a distinction from the numerical methods with finite elements. Such classical analysis is applicable exclusively for perfect cylinder geometry.

The *linear buckling analysis* is considered to be the standard reference for more elaborate FE calculations on shells and any other structures under static loading. It consists of the evaluation of an eigenvalue problem resulting in eigenvalues and related normalized buckling modes. The buckling load P_{cr} is obtained simply by multiplying the compressive load P by the smallest eigenvalue λ_{cr} . But, with such a linear buckling analysis the type of instability to be expected cannot be determined. In addition, deflection amplitudes are not taken into account.

During the loading towards the buckling load the geometry of a shell changes. This can be considered applying a LAGRANGE formulation that allows for large displacements and rotations. The applied loading has to be subdivided into sufficiently small load or displacement increments (steps). After a selected number of such increments *intermediate* linear eigenvalue extractions may be performed to determine the stability of the investigated pre-buckling state of stress and deformation [31, 80]. At buckling, the intermediate buckling load of the nonlinear pre-buckling state coincides with the buckling load [65, 17]. For the study on hand this nonlinear FE method with intermediary eigenvalue investigations was used as the principal analysis tool and is hereinafter called *nonlinear buckling analysis* [81]. This term as well as the method are hardly customary though standard NEWTON-RAPHSON procedures are used to solve the incremental nonlinear equilibrium-equation itera-

tively. Thus, the nonlinear FE methods, the numerical procedures and the eigenvalue problems involved will be explained in detail.

The standard NEWTON-RAPHSON procedures, used to solve the incremental nonlinear equilibrium equations iteratively, impose stepwise constant load parameter during the evaluation of the displacement field. Severe difficulties can be encountered with limit loads where the load-deformation curve becomes horizontal, see Figure 1.2 (b) [31]. To overcome these numerical problems RIKS [69], CRISFIELD [26], RAMM [66] and others developed the so-called *arc-length* methods which allow for level modification throughout the iterations by introducing an auxiliary equation which guides the solution to follow a certain path [46, 81]. These methods allow for equilibrium-path tracing at buckling loads also for highly nonlinear carrying behaviour, in particular for “snap-trough”. For buckling analyses of axially compressed cylinders of perfect geometry however they cannot be recommended because of the acute-angled run of the axial load-displacement curves typical for these shells (Fig. 1.3 (a)). In order to trace the abrupt turn of these curves at the bifurcation point very small arc-lengths and load steps are required.

Static FE analysis methods in general yield a buckling load and a respective buckling pattern, but they give neither information about the post-buckling load nor the the post-buckling pattern that can be observed during tests. In turn, the patterns resulting from classical analysis (see Fig. 1.1 (a)) in the majority of cases cannot be observed without technical aid due to the high velocity of shape changes within the transition from the pre-buckling state to a post-buckling state of equilibrium. This transition is characterized by severe dynamic movements of the shell in radial direction. In the meantime, FE software became available to reproduce this dynamic buckling process. If mass densities are specified for the shell elements then a *transient dynamic analysis* can be conducted in which each successive load or displacement increment is considered being a dynamic step of loading applied to the deformed structure. As the system remains always in a dynamic equilibrium this analysis method allows the continuation of the iterations throughout the sudden change of reaction forces and into the post-buckling states of equilibrium [58, 16, 81]. For the studies on hand with relatively slow compression velocities assumed (0.1 mm/s) the implicit “single-step HOUBOLT” operator for time-integration [23] was preferred to the more common explicit operators, but significant damping has to be assigned to control the dynamic shell motions at buckling and to keep the number of stable time steps as small as possible [61, 45].

In contrast to the classical analysis, with the FE analysis methods not only shells of perfect geometries but also such with *imperfections* can be investigated. However, any consideration of imperfections requires to take large displacements and rotations into account. That is, linear buckling analysis of a shell with imperfect geometry is *not* adequate, for such cases a nonlinear analysis (nonlinear buckling or transient dynamic analysis) is mandatory.

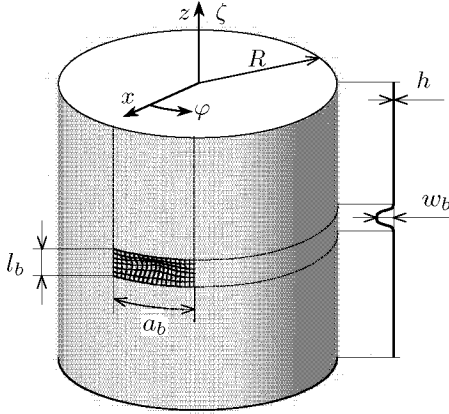
The imperative to always use nonlinear FE analyses dealing with geometric irregularities is a finding of the European project *DEVILS*⁵ on the analyses of laminated cylinders with measured imperfections and could be confirmed by the computations for the dissertation on hand.

1.2 Outline of the Thesis

Based on the positive experience with the static buckling and dynamic transient analyses of imperfect laminated CFRP cylinders within the scope the aforementioned Brite-Euram effort a large number of such FE analyses were conducted to investigate the pre-buckling behaviour of unstiffened isotropic as well as laminated composite cylinders having parametric dimple imperfections. Figure 1.5 displays the assumed pattern of a localized imperfection in the form of a single dimple within an otherwise perfect circular cylinder shell. The mathematical representation of the local variation of the shell radius $r(\varphi, \zeta)$ was included in a Fortran routine provided to define the initial position of the nodes of FE models. The chosen shape of a parametric dimple allowed to investigate the influence of its initial dimple amplitude w_b , its initial meridian height l_b , its initial circumferential width a_b , and its axial position systematically and independently of other geometric influencing variables. The dimple amplitude and its aspect ratio could be varied without any interaction or limitations and free from any pre-stresses.

The buckling behaviour of the unstiffened isotropic and laminated shells having such single dents or bulges was analysed solely by means of nonlinear FE methods, consistently taking large displacements and rotations into consideration. For the imperfection shapes and sizes considered no test results were available against which these numerical analysis results could have been benchmarked. Instead, they are supported by convinc-

⁵Brite-Euram project BE-7550 *DEVILS* “design and validation of imperfection tolerant laminated shells”.



$$r(\varphi, \zeta) = R - \frac{w_b}{4} \left\{ 1 - \cos\left(\frac{2\pi R}{a_b} \varphi\right) \right\} \left\{ 1 - \cos\left(\frac{2\pi}{l_b} \zeta\right) \right\} \quad \begin{array}{l} 0 \leq \varphi \leq a_b/R \\ 0 \leq \zeta \leq l_b \end{array}$$

$$r(\varphi, \zeta) = R \quad \textit{else}$$

Figure 1.5: Assumed shape of a single localized dimple imperfection. Initial amplitude w_b , initial circumferential width a_b , and initial axial height l_b are independent parameters.

ing results of such calculations for similar cylinders with perfect geometry and for laminated CFRP cylinders having measured imperfections. The results of the ideal circular cylindrical shells could be compared with values achieved with classical buckling analyses. And for the analysis results of the CFRP shells with measured imperfections finally test data was available for comparisons.

The nonlinear buckling and transient dynamic analyses of perfect unstiffened cylinders and such cylinders with measured imperfections applied, conducted within the scope of the project *DEVILS*, provided the basis for plausible analyses of such cylinders having a single localized dimple imperfection. The results of these reference calculations are discussed in Chapter 4 and Chapter 5. For the parameter studies containing a large number of imperfect shells with widely scattered buckling loads the *non-linear buckling analysis* was modified to provide an *automatic load step control* (Section 6.5).

The dissertation covered the buckling analyses of isotropic as well as of anisotropic laminated composite cylinders, of such shells with

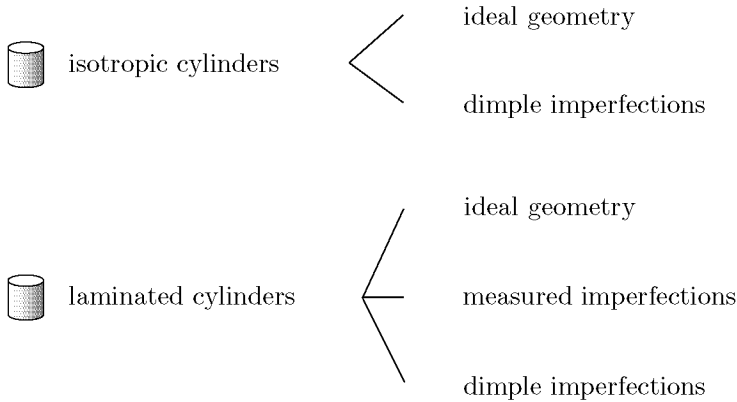


Figure 1.6: *Shell materials and geometries considered.*

ideal geometry, measured imperfections, and dimple imperfections, see Figure 1.6.

The isotropic cylinders considered are of aluminum and have nominal radii R between 187.5 mm and 1000 mm, lengths L between 150 mm and 1000 mm, and wall thicknesses h between 0.75 mm and 1,5 mm ($100 \leq R/h \leq 1000$; $0.4 \leq L/R \leq 5.1$).

The studies on the anisotropic carbon-fiber-reinforced plastic shells was focussed on *non-symmetrically*⁶ laminated cylinders with a nominal radius of $R = 250$ mm, a length of $L = 510$ mm, and with eight or ten layers of 0.125 mm stacked with different alignments.

As the buckling loads and the buckling behaviour of ideal laminated shells in general not only depend on the shell geometry but also on the laminate layout (see Section 4.2.2), also a dependency of material parameters on the sensitivity of the load-carrying capacity of such cylinders to single dimples was presumed. Thus, in order to investigate the effects of the nominal cylinder geometry (L , R , h) on the results due to variation of the dimple shape and size (w_b , l_b , a_b) alone, first a series of isotropic cylinders was analysed varying the initial dimple shape as well as the

⁶The stacking sequence of the laminate layers with different fiber orientation is not symmetrical with respect to the laminate middle surface what results in stretching-bending coupling.

nominal cylinder geometry systematically.

The investigations of the buckling behaviour of cylinders having single dimple imperfections was **limited to** thin-walled cylinders of medium length

- ⊖ with perfect circular edges
- ⊖ under pure axial compression,
- ⊖ to cylinders with either isotropic, linear elastic homogeneous shell material or ideal laminates of homogenous linear elastic layers,
- ⊖ to cylinders of constant shell thickness and
- ⊖ without stiffeners or cutouts between the two shell edges.

Although in the classical analysis of perfect cylinders simply supported cylinder edges are considered, for the FE analyses always clamped boundary conditions were applied. In majority of the cases infinitely stiff endplates were simulated causing uniform end-shortening. Anyway, alternatively analyses were conducted of shells with uniformly distributed edge loads but non-uniform edge displacements and the results illustrated in this thesis to point at the important differences, see Section 6.4.

For the isotropic as well as the laminated cylinders the influence of the initial amplitude w_b of a dimple with a given initial width a_b and a given initial height l_b on the buckling behaviour and the buckling loads was studied. Furthermore, for fixed initial amplitudes the initial circumferential width a_b and the initial meridian height l_b of the dimple were searched which give the minimum axial stability for a selected cylinder. The analysis results, i.e. the effect of these “worst” non-axisymmetric dents and bulges could then be compared with that of local axisymmetric dimples and that of enveloping imperfections in form of classical buckling patterns. Finally, for an isotropic reference cylinder having an initial dent the impact of a second identical initial dent was investigated for different relative positions.

In Figure 1.7 the analysis results for an axially compressed isotropic cylinder having a single inward or outward dimple of various initial amplitude are shown by way of example. The resulting buckling loads P_{cr} are normalized in respect to the classical buckling load for ideal geometry, $3.8Eh^2 = 599\text{ kN}$, and plotted against the initial dimple amplitude w_b , which in turn is normalized with reference to the wall thickness h .

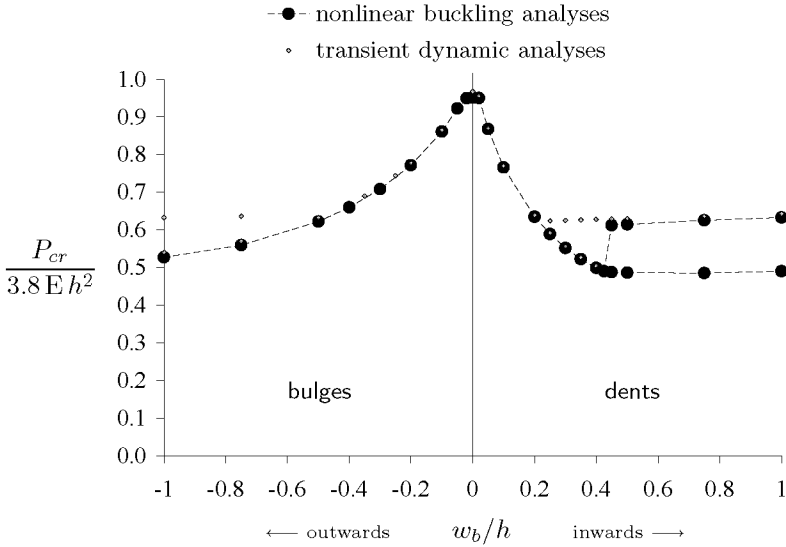


Figure 1.7: *FE Analysis results of an unstiffened aluminium cylinder having one inward or outward dimple at half the cylinder length. Buckling load P_{cr} , normalized in respect of the classical load, plotted against the initial amplitudes w_b , normalized with regard to the wall thickness h , for nonlinear analyses as indicated. Cylinder with nominal radius $R = 250$ mm, length $L = 510$ mm, and wall thickness $h = 1.5$ mm, dimples with initial height $l_b = 67$ mm and width $a_b = 181$ mm.*

The exemplifying cylinder is of nominal radius $R = 250$ mm, length $L = 510$ mm, and wall thickness $h = 1.5$ mm. The initial axial height $l_b = 67$ mm and the circumferential width $a_b = 181$ mm of the single dimple in turn correspond to the lengths and aspect ratio that resulted in the lowest axial cylinder stability for a given initial depth of $w_b/h = 0.1$. The right half for positive amplitude gives the results for dimples pointing inward (dents), the left half those for dimples pointing outward (bulges). The loads obtained by means of nonlinear buckling analyses are marked with bold dots and linked with dashed lines, the loads achieved with transient dynamic analyses are tagged with small gray rhombi.

Probably first the distribution of the bold dots, i.e. the nonlinear buckling analysis results, attracts attention as it is not symmetric in respect to the abscissa (zero amplitude = ideal shell). For inward dimples range

lower buckling loads resulted than for outward dimples of like absolute amplitude $|w_b|$, hence the reduction of the axial cylinder stability due to a single dimple is strongly influenced by the orientation of the dimple amplitude w_b . This asymmetry might be unexpected as in classical analysis the orientation of the radial displacement amplitude is irrelevant for the resulting axial buckling load. Furthermore, for dents initially deeper than a certain marginal depth w_b^*/h with nonlinear buckling analyses, for a given initial dent depth, more than one buckling load could be obtained (in Fig. 1.7: $w_b^*/h \approx 0.45$). Based on similar results for all cylinders having a dent⁷ considered, dents of deeper initial depth w_b/h than w_b^*/h were denoted as “deep dents”, such with smaller initial amplitude as “shallow dents”, see Chapter 6.6.1, page 275, and Chapter 6.6.4, page 347. In addition, the decrease of the axial stability with increasing initial depth w_b is largest for shallow dents; for deep dents with further increase in w_b the additional stability reduction is only small, or the buckling loads even increased again. Finally, a minimum buckling load can be spotted for a dent of initial depth of $w_b/h = 3/4$. For outward dimples, however, in contrast to inward dimples with nonlinear buckling analyses always only one buckling load could be obtained.

The extraordinary load-curves which resulted for static FE calculations of cylinders with inward dimples provoked further investigations by means of transient dynamic analyses of several selected shells. Particular attention was payed to the local changes in the hoop *curvatures* in and besides the dimples during the compression and buckling process. These curvatures were analysed via the circles given by the position of three adjacent nodes around the cylinder circumference.

From the results of the transient dynamic analyses exemplifying in Figure 1.7 (gray rhombi) for an isotropic cylinder having a dent or a bulge of various initial amplitude further particularities in the buckling behaviour of such shells can be taken. For shallow dents exceeding a certain initial depth two loads could be identified, in contrast to the static nonlinear buckling analyses which for shallow dents ($w_b < w_b^*$) gave only a single load close to the lower value obtained with transient dynamic analysis. But, for deep dents ($w_b > w_b^*$) the transient dynamic analyses gave only one buckling load whereas by means of the static nonlinear buckling analyses two loads were obtained. Finally, for outward dimples of initial elevation larger than a certain value, similar to some inward dimples, in addition to a first load a further higher buckling load was

⁷Applies for non-axisymmetric, localized dents of initial height small compared to the cylinder length.

found. Despite the additional complexity and variety in the distribution of the buckling loads for dimples of various initial amplitude, by means of such transient dynamic analyses and the tracing of the local decrease in shell curvature the observed differences between shallow dents and deep dents could be associated with the progression of local flattening of the shell strip over the dimple: in the case of shallow dents the flattening—and the associated local loss in axial geometric stiffness—is sudden and dynamic, in the case of deep dents however slow and smooth.

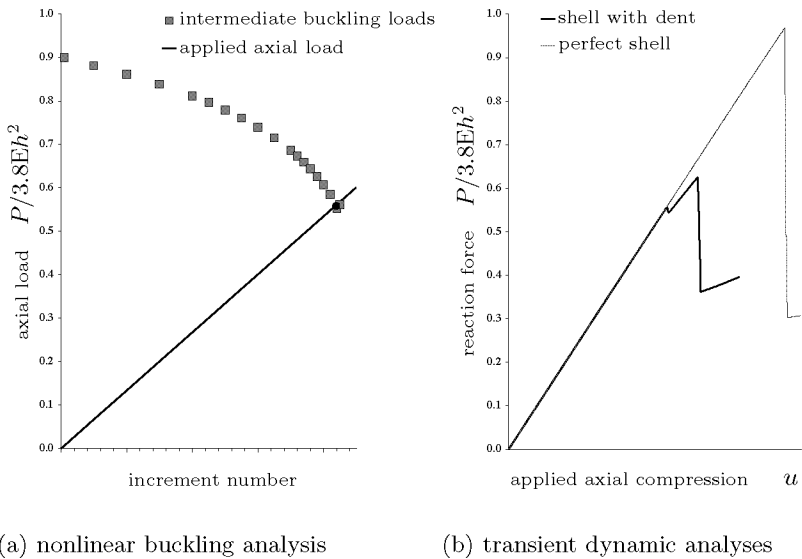


Figure 1.8: Analysis results for the isotropic cylinder in Fig. 1.7 above having a dent of initial depth $w_b/h = 0.3$. Nonlinear buckling analysis (a) with the applied loads and the buckling loads intermediately calculated at selected load increments (eigenvalues); black dot marks the point of their accord interpreted as the resulting nonlinear buckling load P_{cr} . Transient dynamic analysis (b) with the reaction forces due to the applied axial compression; thin line refers to results for the cylinder without imperfections.

By means of the isotropic shell already presented in Figure 1.7 but having an initial, shallow dent of initial depth $w_b/h = 0.3$ and again of initial axial height $l_b = 67\text{mm}$ and circumferential width $a_b = 181\text{mm}$ in Figure 1.8 the analysis results and the load levels to which in Figure 1.7 is referred to are demonstrated. In the left chart (a) the results of a nonlinear buckling analysis are reproduced, whereby the applied axial

loads (line) and the linear intermediate buckling loads (squares), all normalized, are plotted against the load increment number. After selected load increments, which in present case are of constant step size, linear buckling loads (square markers) were calculated per intermediate eigenvalue extraction to determine the stability of the investigated state of stress and deformation. At buckling the nonlinear state of equilibrium (line) coincides with the buckling load, thus the point of intersection (bold dot) was interpreted as the nonlinear buckling load P_{cr} used in Figure 1.7 for $w_b/h = 0.3$; consequently, for states of additional loading always intermediate buckling loads below the applied load resulted. In the right chart (b) the results of transient dynamic analyses are graphed for the shell with the initial dent as well for the cylinder of ideal geometry. The normalized reaction forces are plotted versus the applied axial end-shortening, using the identical ordinate scaling to that in (a). The curve of the results for the cylinder having the initial dent (bold line) follows linearly the straight load curve of the perfect shell (thin line) up to a load level where the curve forms a distinct zigzag course. This level is a first and local maximum in the equilibrium path of the imperfect shell and corresponds to the buckling load found with the static nonlinear buckling analysis, see bold dot in Fig. 1.7 (a). An observation of the altering hoop curvature in the dent apex showed that at this load the dent suddenly snaps inwards to form a flattened shell strip of quasi zero curvature and hence reduced geometric axial stiffness. This process will be referred to as “*local buckling*” at a load below the load of total “cylinder collapse”. In contrast to the static analysis, which was aborted due to “buckling”, the transient dynamic analysis could pass this local instability incident and the iterations continued with further axial compression up to the maximum of the load curve. At this limit load the entire cylinder started to collapse, and with increasing compression the reaction force dropped almost vertically towards a post-buckling state. The thin line shows the results obtained with the cylinder with perfect geometry for comparisons: in this case the curve is linear up to the cylinder collapse load which is about 50% higher than the limit load of the cylinder having the initial dent.

The FE analyses of cylinders having a initial dimple yielded particular deformation processes including different local buckling phenomena which were hardly known from unstiffened circular cylinders with neither perfect geometry nor with imperfections distributed over the entire shell surface. Nevertheless, by means of systematic parameter variation some interrelationships between the results and the nominal dimensions of the cylinder and the dimple could be derived. It will be shown that

the initial hoop curvature, given by the initial dimple depth and circumferential width, is the crucial factor for the difference between “shallow” and “deep” dents and hence for the process of the numerical buckling analyses. Furthermore, it was found that the cylinder length L is also decisive for the local deformation processes of the shell in and at the initial dimple (local buckling) observed. The items listed below are a selection of further **conclusions** drawn after the studies:

- ⊕ The design recommendations in standards and literature considered for thin-walled, unstiffened isotropic cylinders under axial compression seem to be conservative if the nominal cylinder length L as well as the radius R and the wall-thickness h are taken into account.
- ⊕ *Shallow dents* with an initial amplitude smaller than a certain marginal depth w_b^*/h provoke a distinct *local buckling* with a sudden snapping inwards of the dent to form a local flattened shell strip of reduced geometric axial stiffness. *Deep dents* with an initial amplitude larger than w_b^*/h , in turn, result in a continuous flattening of the shell, if not initially flattened, without any dynamic local buckling incident prior to the total *cylinder collapse*.
- ⊕ Localized, shallow dents of particular initial circumferential width a_b and axial height l_b reduce the buckling load as much as *axisymmetric* inward dimples of identical initial amplitude.
- ⊕ Localized, non-axisymmetric bulges impair the load carrying capacity less than localized dents of the same absolute initial amplitude $|w_b|$, initial width a_b and initial height l_b .
- ⊕ A non-axisymmetric, shallow dent of adequate initial width and height may be as damaging as an evenly distributed imperfection-pattern that is given by a classical buckling mode of initial amplitude w_{mn} that is half the initial amplitude w_b of the dent with $w_b = 2 \cdot w_{mn}$.
- ⊕ The difference between uniform edge loads and uniform edge displacements is important for cylinders having a single deep dent. For uniform edge loads after local loss in stability due to a flattened dimple the cylinder collapses directly after local buckling. The differences between clamped and hinged boundary conditions however are not of importance as regards the axial-stability reduction due to a single dimple at half the cylinder length.

- ⊕ For isotropic cylinders the initial axial *heights* of dents that reduced the buckling load the most for a preselected initial depth is close to the wavelength for classical axisymmetric buckling of a perfect cylinder $2l_c = 3.46\sqrt{Rh}$ and increases with increasing initial depth (see later, page 54). The initial *widths* of the “pessimum” dents resulted between two to three times the initial height.
- ⊕ The buckling load of a cylinder with single localized dent is only little different from that of a cylinder having *two dents* of identical size.
- ⊕ For the laminated cylinders accurate and general predictions of the minimum buckling loads and of critical dimple dimensions could not be derived on basis of the cylinder geometry alone as the buckling behaviour patterns of such shells depend strongly on the laminate stacking. However, there was no indication that any laminated cylinder with any non-axisymmetric dimple will result in a smaller buckling load than an isotropic cylinder of identical radius, length and wall thickness also having a non-axisymmetric dimple.

Thus, the questions asked on page 6 could be answered. Additional findings refer to “puzzles” that raised in the course of the investigations of cylinders with a single dimple due to the manifold buckling behaviour patterns observed. More details to these and further conclusions arrived at are described in the Chapter 7. The related analyses results will be discussed in Chapter 6.

Remarks on the structure of this thesis

In Figure 1.9 the content of this dissertation is depicted. The thread partially diverges from the common format for publications in science, *introduction – method – result – conclusion*, to emphasize the separation of the analysis of perfect cylinders from that of cylinders having imperfections. Hence, *Chapter 5* on cylinders with distributed imperfections commences with an “insertion” about theories and analysis methods for such shells which completes the content of Chapter 2 on shell calculus and the classical buckling analysis for perfect cylinders. In the last section of this chapter finally FE analysis results for laminated cylinders with distributed (measured) imperfections are described. In Chapter 4 on results for perfect cylinders and also in Chapter 6 on single dimple imperfections in separate sections first the results for isotropic shells

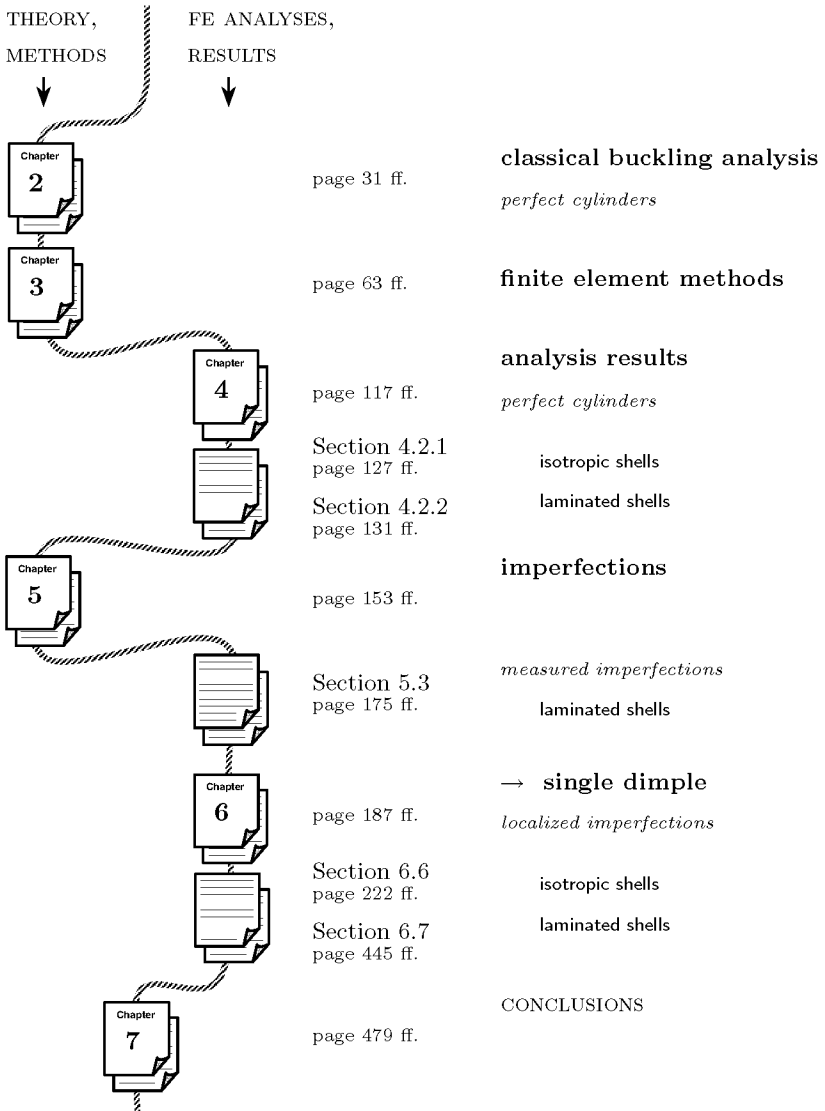


Figure 1.9: Thread of this thesis.

are reproduced, followed by those for laminated composite cylinders, see Figure 1.9 and the Contents listed on page ix.

Chapter 2 deals with DONNELL-type shell equations and their solutions for the buckling of axially compressed thin circular monocoque cylinders of medium length. The application of these formulas introduced for isotropic and laminated orthotropic cylinders corresponds to the so-called *classical buckling analysis* that is opposed to numerical buckling analysis by means of finite element models.

In *Chapter 3* the nonlinear finite element methods in general and their applications for the stability analysis of shells in particular are described in detail. The chapter covers the full description of the herein after called “nonlinear buckling analysis” as well as of the “transient dynamic analysis” of cylinder shells.

Chapter 4 is dedicated to the analysis results for several cylinders of *perfect initial geometry*. Results of nonlinear buckling analyses and transient dynamic analyses are discussed for isotropic cylinders, but above all for laminated CFRP cylinders, and compared with results of classical buckling analyses applying the closed-form solutions given in Chapter 2. These results are later used as reference base to the results for the imperfect cylinders.

In *Chapter 5* the analysis of cylinders having imperfections distributed over the entire shell surface is explained. The first two sections contain KOITER’s asymptotic theory, useful for small imperfections amplitudes, and more general analytical solutions for investigations with harmonic deformation patterns prior as well as after buckling. In the last section nonlinear buckling analysis and transient dynamic analysis results are discussed achieved for laminated CFRP cylinders with their measured imperfection patterns applied.

Chapter 6 contains the major part of this thesis as analysis results and the instability behaviour patterns of cylinders having single initial dimples are discussed. First sections deal with the above mentioned definition of the chosen parametric dimple, with the FE modeling of the shells, and with the establishment of a nonlinear buckling analysis with adaptive load step control. The 6th section describes the buckling of *isotropic* shells with an initial dimple, partitioned into a subsection on inward dimples and one on outward dimples. In further subsections critical widths and heights of dimples, minimal load-carrying capacities, stress distributions, cylinders having two identical inward dimples, and

finally the influence of boundary conditions and FE-model modifications are discussed. The 7th and last section is dedicated to *laminated composite* cylinders having a single dimple. Partitioned into three subsections again first the influence of the dimple amplitude is detailed, followed by the description of critical dimple sizes and minimum buckling loads to be expected for laminated cylinders having a dimple.

The thesis is concluded by *Chapter 7* which summarizes the findings.

Finally, in the Appendices A, B, and C surveys of the *nonlinear continuum mechanics*, of the bending and buckling of *plates*, and of the initial stress stiffness matrix used in nonlinear FE analysis are given, respectively. These items were appended to simplify cross-references by use of a consistent terminology.

Chapter 2

Classical Buckling Analysis of Axially Compressed Cylinders

In this chapter the differential equations are introduced used to analytically describe the states of deformation and stress of thin, circular cylinders. The shell theory considered bases on the KIRCHHOFF thin-plate theory and on DONNELL's approximations for thin shallow shells. Finally, closed-form solutions of the set of equilibrium and compatibility equations are given for thin orthotropic and laminated circular cylinders under pure axial compression.

The application of these formulas corresponds to the hereinafter called “classical buckling analysis” for simply-supported, thin mid-long cylinders of perfect initial geometry. These analytical formulations provide the basis for comparisons with numerical buckling analysis results for ideal cylinders as well as for the later study of cylinders having imperfections.

2.1 Shell Theory for Thin Circular Cylinders

Shells, like plates, are structure elements where one of the dimensions, the wall thickness, is considerably smaller than the other two. The local behaviour is assumed to be two-dimensional under plane stress and the wall thickness constant during loading. Basically, shells are curved structures whereas plates are initially flat. Due to the initial curvature in shells the effects of the loading in the middle surface and bending moments are stronger coupled than in flat plates since already very small lateral deflections provoke strains.

In the classical linear plate theory for small displacements in-plane loads are ignored or treated separately as a membrane problem. It is assumed therefore that stretching of the middle surface is exclusively related to external membrane forces and may be neglected in case of pure plate bending. But, considering large deflections of plates, as for shells the influence of bending on the membrane forces has to be considered. In Appendix B the governing equations for pure plate bending, for plates under combined in-plane and lateral loading, but also for plates with large deflections are given which account for compatibility between the strains and the deflection fields. For the set-up of the shell equations the formulations for plates with large lateral deflections can be adopted. On this account, the derivation of the relevant shell equations in this chapter follows that in Appendix B for plates.

The shell theory may be used for the analysis of the stresses and the deformations in thin shells considering different basic geometries, boundary conditions and load cases. The buckling analysis of axially compressed circular cylinders is only one of possible applications.

2.1.1 Kinematic Relations

This thesis deals with thin-walled, unstiffened cylindrical shells. As a first permissible simplification therefore only simply curved shells, i.e. shells solely curved about the cylinder axis are considered in the shell calculus reproduced herein. Further, the shell wall thickness h is assumed being essentially smaller than the cylinder radius R and remaining constant during loading. Finally, the transverse shear stress is considered to be negligible small.

Different variants of derivations of the general kinematic relations for cylinder shells may be found. In (DOYLE [31]), for instance, first the deformations and strains are specified in cylindrical coordinates, then linearised and finally converted to Cartesian coordinates. The subsequent explanations follow this approach. In a cylindrical coordinate

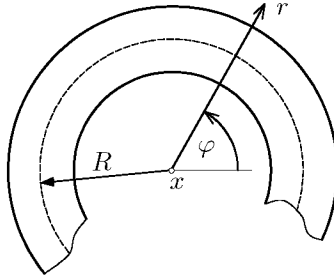


Figure 2.1: *Cylindrical coordinates for curved shell segment.*

system (r, φ, x) the components of the displacements in the (r, φ) -plane of a curved shell are denoted by u_r and u_φ , see Figure 2.1. The strains *in this plane* are related to these displacements by

$$\begin{aligned} \varepsilon_r &= \frac{\partial u_r}{\partial r} \quad , \\ \varepsilon_\varphi &= \frac{u_r}{r} + \frac{1}{r} \frac{\partial u_\varphi}{\partial \varphi} \quad , \\ \gamma_{r\varphi} &= \frac{1}{r} \frac{\partial u_r}{\partial \varphi} + \frac{\partial u_\varphi}{\partial r} - \frac{u_\varphi}{r} \quad . \end{aligned} \quad (2.1)$$

For thick shells the circumferential strain ε_φ is nonlinearly distributed. But for thin shallow shells these strains may be replaced with an approximate set [31]. Expanding the displacements in a TAYLOR series about the middle surface ($r = R$) gives such an approximated deformation of the shell in cylindrical coordinates:

$$\begin{aligned} u_x(r, \varphi, x) &\approx \bar{u}_x(\varphi, x) - \xi \frac{\partial \bar{u}_r}{\partial x} \quad , \\ u_\varphi(r, \varphi, x) &\approx \bar{u}_\varphi(\varphi, x) - \xi \left(\frac{1}{R} \frac{\partial \bar{u}_r}{\partial \varphi} - \frac{\bar{u}_\varphi}{R} \right) \quad , \\ u_r(r, \varphi, x) &\approx \bar{u}_r(\varphi, x) \quad , \end{aligned} \quad (2.2)$$

using the variable $\xi = r - R$. The items with a bar, \bar{u}_x , \bar{u}_φ , and \bar{u}_r , denote the displacements of the middle surface. The first equation allows

to provide for bending about the cylinder axis. The following strains result from derivation of expressions above:

$$\begin{aligned}\varepsilon_x &= \frac{\partial \bar{u}_x}{\partial x} - \xi \frac{\partial^2 \bar{u}_r}{\partial x^2} , \\ \varepsilon_\varphi &= \frac{1}{R} \frac{\partial \bar{u}_\varphi}{\partial \varphi} + \frac{\bar{u}_r}{R} - \frac{\xi}{R^2} \left(\frac{\partial^2 \bar{u}_r}{\partial \varphi^2} - \frac{\partial \bar{u}_\varphi}{\partial \varphi} \right) , \\ \gamma_{\varphi x} &= \frac{1}{R} \frac{\partial \bar{u}_x}{\partial \varphi} + \frac{\partial \bar{u}_\varphi}{\partial x} - \frac{\xi}{R} \left(2 \frac{\partial^2 \bar{u}_r}{\partial x \partial \varphi} - \frac{\partial \bar{u}_\varphi}{\partial x} \right) .\end{aligned}\quad (2.3)$$

At this state, it is beneficial to convert these expressions to a more usual form in a Cartesian coordinate system [31]. In Figure 2.2 the cylindrical

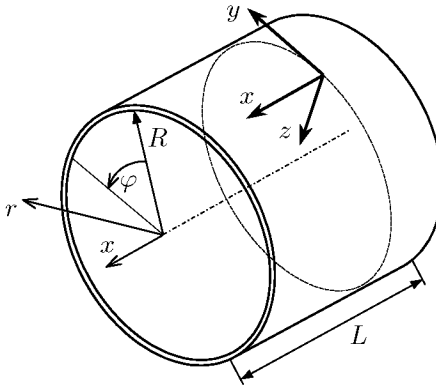


Figure 2.2: *Cartesian coordinates for cylindrical shells.*

coordinate system and a Cartesian coordinate system with $y = R \cdot \varphi$ in circumferential direction and x in axial direction is defined. The normal z with its origin in the reference surface¹ is pointed inwards, thus in opposite to the cylinder radius. The displacements u , v and w are oriented in x , y and z direction, respectively. Hence, with

$$\begin{aligned}R \cdot \varphi &\longrightarrow y \\ r &\longrightarrow -z \\ u_x &\longrightarrow u \\ u_\varphi &\longrightarrow -v \\ u_r &\longrightarrow -w\end{aligned}$$

¹The reference surface is not necessarily the middle surface.

the approximate displacements become

$$\begin{aligned} u(x, y, z) &\approx \bar{u}(x, y) - z \frac{\partial \bar{w}}{\partial x} \ , \\ v(x, y, z) &\approx \bar{v}(x, y) - z \left(\frac{\partial \bar{w}}{\partial y} + \frac{\bar{v}}{R} \right) \ , \\ w(x, y, z) &\approx \bar{w}(x, y) \ , \end{aligned} \quad (2.4)$$

and the strains are obtained accordingly

$$\begin{aligned} \varepsilon_x &= \frac{\partial \bar{u}}{\partial x} - z \frac{\partial^2 \bar{w}}{\partial x^2} \ , \\ \varepsilon_y &= \frac{\partial \bar{v}}{\partial y} - \frac{\bar{w}}{R} - z \left(\frac{\partial^2 \bar{w}}{\partial y^2} + \frac{1}{R} \frac{\partial \bar{v}}{\partial y} \right) \ , \\ \gamma_{xy} &= \frac{\partial \bar{u}}{\partial y} + \frac{\partial \bar{v}}{\partial x} - z \left(2 \frac{\partial^2 \bar{w}}{\partial x \partial y} + \frac{1}{R} \frac{\partial \bar{v}}{\partial x} \right) \ . \end{aligned} \quad (2.5)$$

Again, the letters with a bar, \bar{u} , \bar{v} , and \bar{w} , denote displacements in the reference surface in x , y , and z direction, respectively.

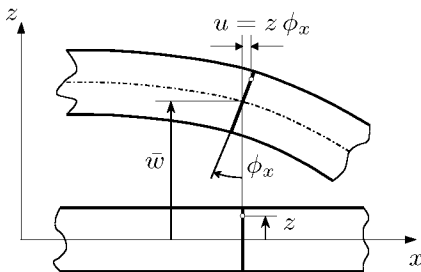


Figure 2.3: *Displacement in x direction due to rotation ϕ_x*

The relations above were derived under the assumption that the normals of the reference surface remain straight and normal to this surface and that the transverse normal stress is negligible small (KIRCHHOFF hypothesis, see Eq. (B.14)) [15, 31]. Therefore, the derivatives of the lateral displacement \bar{w} coincide with the negative rotations ϕ_x and ϕ_y as shown in Figure 2.3, describing the slope of the middle surface normal to its initial direction. According to the KIRCHHOFF thin-plate theory it applies:

$$\phi_x = -\frac{\partial \bar{w}}{\partial x} \ , \quad \phi_y = -\frac{\partial \bar{w}}{\partial y} \ . \quad (2.6)$$

That is, a vector perpendicular to the undeformed middle surface is also perpendicular to the deformed middle surface. The terms \bar{v}/R in Equation (2.4) for $v(x, y, z)$ and \bar{w}/R in Equation (2.5) for ε_y may be interpreted as a compensation of the initial, stress and strain-free “cylindrical bending” of the shell, given by $1/R$ which is to be added to the rotation ϕ_y and curvature $\partial^2 \bar{w}/\partial y^2$. Economizing the use of accents and indices, by use of the approximation $w(x, y, z) \approx \bar{w}$ in the subsequent expressions the bar over the letter w denoting lateral displacements is omitted.

In literature different expressions for the strains and curvatures in shells than those in (2.5) may be found. In (MARKUŠ [78]) a survey of some frequently mentioned shell theories (e.g. DONNELL, TIMOSHENKO, SANDERS, FLÜGGE) is given with concise lists of different contributions to the strains and curvatures. The expressions in (2.5) correspond to those in REISSNER’s theory [31, 78]. But, the probably simplest shell theory is based on DONNELL’s approximations [73, 78] which is also adopted for the “classical buckling analysis” of cylindrical shells presented herein. Under DONNELL’s kinematic assumptions [29] for thin, shallow shells with large R/h ratios the second terms in brackets with derivatives of the tangential displacement ($\partial \bar{v}/\partial x$, $\partial \bar{v}/\partial y$) are neglected. In this case, the strain distribution over the shell thickness h for thin cylindrical shells and small displacements may be written in vector form as

$$\begin{Bmatrix} \varepsilon_x \\ \varepsilon_y \\ \gamma_{xy} \end{Bmatrix} = \begin{Bmatrix} \frac{\partial \bar{u}}{\partial x} \\ \frac{\partial \bar{v}}{\partial y} - \frac{w}{R} \\ \frac{\partial \bar{u}}{\partial y} + \frac{\partial \bar{v}}{\partial x} \end{Bmatrix} + z \begin{Bmatrix} -\frac{\partial^2 w}{\partial x^2} \\ -\frac{\partial^2 w}{\partial y^2} \\ -2\frac{\partial^2 w}{\partial x \partial y} \end{Bmatrix} \quad (2.7)$$

or abbreviated:

$$\boldsymbol{\epsilon} = \bar{\boldsymbol{\epsilon}} + z \boldsymbol{\kappa}$$

The vector $\bar{\boldsymbol{\epsilon}}$ includes the strain distribution in the reference surface and the vector $\boldsymbol{\kappa}$ the *negative* curvature of this surface [40]. Note that these equations imply small displacements, sufficient thin and constant wall thickness ($h \ll R$), and an infinitely large transverse shear stiffness.

To specify the governing equations of shells with *large lateral displacements* the relations of a bent plate may be used by considering the influence of the initial curvatures to the displacements and stretches. Thus, following the strain expressions for plates with large deflections in

(B.28) and (B.29) of Section B.2.1, the components of the strain in the reference surface are given by

$$\bar{\epsilon} = \begin{Bmatrix} \bar{\epsilon}_x \\ \bar{\epsilon}_y \\ \bar{\gamma}_{xy} \end{Bmatrix} = \begin{Bmatrix} \frac{\partial \bar{u}}{\partial x} + \frac{1}{2} \left(\frac{\partial w}{\partial x} \right)^2 \\ \frac{\partial \bar{v}}{\partial y} - \frac{w}{R} + \frac{1}{2} \left(\frac{\partial w}{\partial y} \right)^2 \\ \frac{\partial \bar{u}}{\partial y} + \frac{\partial \bar{v}}{\partial x} + \frac{\partial w}{\partial x} \frac{\partial w}{\partial y} \end{Bmatrix} \quad (2.8)$$

Note the presence of additional square terms in derivatives of the lateral deflection w .

By differentiating the expression in (2.8) and elimination of \bar{u} and \bar{v} the *compatibility condition* is obtained, which has to hold between the components of strains:

$$\frac{\partial^2 \bar{\epsilon}_x}{\partial y^2} + \frac{\partial^2 \bar{\epsilon}_y}{\partial x^2} - \frac{\partial^2 \bar{\gamma}_{xy}}{\partial x \partial y} = \left(\frac{\partial^2 w}{\partial x \partial y} \right)^2 - \frac{\partial^2 w}{\partial x^2} \left(\frac{\partial^2 w}{\partial y^2} + \frac{1}{R} \right) \quad (2.9)$$

This differential equation differs from the compatibility equation for plates (B.32) on page 524 only in the term $+1/R$.

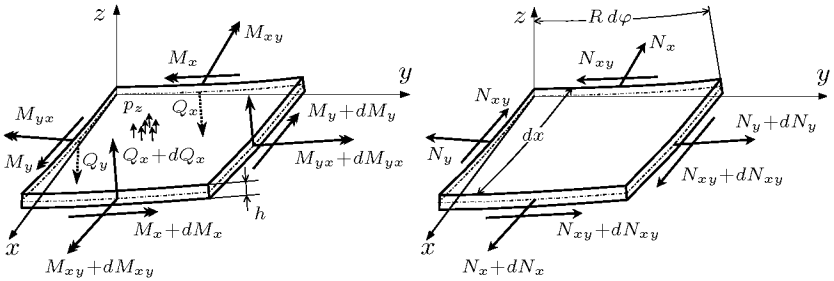


Figure 2.4: Segment of a cylindrical shell

For the stress resultants shown in Figure 2.4, i.e. the membrane forces and the bending and twisting forces the same definitions as for plates are valid (see Section B.2):

$$\begin{aligned} N_x &= \int_{-h/2}^{h/2} \sigma_{xx} dz, & N_y &= \int_{-h/2}^{h/2} \sigma_{yy} dz, \\ N_{xy} &= \int_{-h/2}^{h/2} \tau_{xy} dz = N_{yx}, \end{aligned} \quad (2.10)$$

for the membrane forces *per unit length*, and

$$\begin{aligned} M_x &= \int_{-h/2}^{h/2} \sigma_{xx} z \, dz, & M_y &= \int_{-h/2}^{h/2} \sigma_{yy} z \, dz, \\ M_{yx} &= \int_{-h/2}^{h/2} \tau_{xy} z \, dz = -M_{xy}, \end{aligned} \quad (2.11)$$

for the bending moments and the twisting moments, respectively, again per unit length. They are all functions of the coordinates x and y and correspond to the strains in the reference surface $\bar{\epsilon}$ and the curvatures κ .

Projection of the forces in Figure 2.4 in the x and the y -direction yields the following two equilibrium equations for constant wall thickness:

$$\begin{aligned} \frac{\partial N_x}{\partial x} + \frac{\partial N_{xy}}{\partial y} &= 0 \\ \frac{\partial N_y}{\partial y} + \frac{\partial N_{xy}}{\partial x} &= 0 \end{aligned} \quad (2.12)$$

whereby body forces and terms of inertia were ignored. Distributions of lateral forces Q_y in the second equation are also ignored due to the hypothesis that the analysed shells are shallow [15]. The general spacial differential equilibrium equation for a deformable body can be written as

$$\operatorname{div} \boldsymbol{\sigma} + \mathbf{b} = \rho \ddot{\mathbf{u}}$$

with the CAUCHY stresses $\boldsymbol{\sigma}$, the body forces \mathbf{b} , the density ρ and the velocities $\dot{\mathbf{u}}$, see Section A.4 on page 504. For the classical buckling analysis terms of inertia after $\rho \ddot{\mathbf{u}}$ and body forces as due to gravity are ignored, and the two equations (2.12) follow from $\operatorname{div} \boldsymbol{\sigma} = 0$ in the (x, y) -plane. These equations are identical with the equilibrium conditions for flat plates under in-plane load [40], again ignoring inertia and volume forces, see Section B.2.1.

The projection of all forces on the z -axis and the balance of the moments taken into account gives a third equilibrium equation (see Section B.2 for details):

$$\begin{aligned} \frac{\partial^2 M_x}{\partial x^2} + 2 \frac{\partial^2 M_{yx}}{\partial x \partial y} + \frac{\partial^2 M_y}{\partial y^2} &= \\ - \left[p_z + N_x \frac{\partial^2 w}{\partial x^2} + 2N_{xy} \frac{\partial^2 w}{\partial x \partial y} + N_y \left(\frac{\partial^2 w}{\partial y^2} + \frac{1}{R} \right) \right] \end{aligned} \quad (2.13)$$

The lateral load $+p_z$ as well as the displacement $+w$ are inward looking. An advantage of the DONNELL-type shell equations above is the possibility of recourse to the AIRY *stress function*. By introducing such a stress function $\mathcal{F}(x, y)$ the concurrent solution of the two equilibrium equations in (2.12) and the compatibility equation (2.9) may be simplified, since the number of unknown functions is reduced from three (\bar{u} , \bar{v} , w) to two (w , \mathcal{F}) [76, 73]. However, with the stress functions $\mathcal{F}(x, y)$ in the differential equations the boundary conditions to be fulfilled for the displacements in the reference surface can only be specified indirectly in terms of the membrane stresses.

With the definitions

$$N_x = \frac{\partial^2 \mathcal{F}}{\partial y^2} \quad , \quad N_y = \frac{\partial^2 \mathcal{F}}{\partial x^2} \quad , \quad N_{xy} = -\frac{\partial^2 \mathcal{F}}{\partial x \partial y} \quad (2.14)$$

the two equations in (2.12) are identically satisfied [76, 40]. The strain field resulting from the stress function, in turn, has to satisfy the compatibility condition (2.9).

Prior to define this strain field the constitutive law for the particular shell is to be introduced.

2.1.2 Constitutive Laws

The main equations for the linear-elastic stress-strain relationships used in this section are introduced in Section A.5, especially for general orthotropic materials as well as for transversally isotropic materials like laminated composites. The elasticity relations, which combine the membrane forces per unit length with the strains in the reference surface, for homogeneous **orthotropic material** and constant wall thickness h may be written in matrix form as:

$$\begin{Bmatrix} N_x \\ N_y \\ N_{xy} \end{Bmatrix} = \begin{bmatrix} A_{11} & A_{12} & 0 \\ A_{12} & A_{22} & 0 \\ 0 & 0 & A_{33} \end{bmatrix} \begin{Bmatrix} \bar{\varepsilon}_x \\ \bar{\varepsilon}_y \\ \bar{\gamma}_{xy} \end{Bmatrix} \quad (2.15)$$

or abbreviated: $\mathbf{N} = \mathbf{A} \bar{\boldsymbol{\varepsilon}}$.

The membrane compliance matrix, i.e. the inverse of \mathbf{A} , is frequently

denoted with a lower case letter such as “**a**” which contains

$$\mathbf{a} = \begin{bmatrix} \frac{1}{E_x h} & -\frac{\nu_{xy}}{E_y h} & 0 \\ -\frac{\nu_{xy}}{E_y h} & \frac{1}{E_y h} & 0 \\ 0 & 0 & \frac{1}{G_{xy} h} \end{bmatrix} = \mathbf{A}^{-1} \quad (2.16)$$

Consequently, the strains may be described in terms of membrane forces per unit length as

$$\bar{\boldsymbol{\epsilon}} = \mathbf{a} \mathbf{N} \quad ,$$

or in terms of the stress function $\mathcal{F}(x, y)$:

$$\begin{Bmatrix} \bar{\epsilon}_x \\ \bar{\epsilon}_y \\ \bar{\gamma}_{xy} \end{Bmatrix} = \begin{bmatrix} a_{11} & a_{12} & 0 \\ a_{12} & a_{22} & 0 \\ 0 & 0 & a_{33} \end{bmatrix} \begin{Bmatrix} \frac{\partial^2 \mathcal{F}}{\partial y^2} \\ \frac{\partial^2 \mathcal{F}}{\partial x^2} \\ -\frac{\partial^2 \mathcal{F}}{\partial x \partial y} \end{Bmatrix} \quad (2.17)$$

Similarly to the membrane stiffness the bending stiffness, i.e. the elasticity relation between moments and the change of curvature, may be set up in matrix form as:

$$\begin{Bmatrix} M_x \\ M_y \\ M_{yx} \end{Bmatrix} = \begin{bmatrix} D_{11} & D_{12} & 0 \\ D_{12} & D_{22} & 0 \\ 0 & 0 & D_{33} \end{bmatrix} \begin{Bmatrix} \kappa_x \\ \kappa_y \\ \kappa_{xy} \end{Bmatrix} \quad (2.18)$$

or in abbreviated form: $\mathbf{M} = \mathbf{D} \boldsymbol{\kappa}$.

The components of the symmetric bending stiffness matrix \mathbf{D} are the following:

$$\mathbf{D} = \begin{bmatrix} \frac{E_x h^3}{12(1-\nu_{xy}\nu_{yx})} & \frac{\nu_{xy}E_x h^3}{12(1-\nu_{xy}\nu_{yx})} & 0 \\ \frac{\nu_{xy}E_x h^3}{12(1-\nu_{xy}\nu_{yx})} & \frac{E_y h^3}{12(1-\nu_{xy}\nu_{yx})} & 0 \\ 0 & 0 & \frac{G_{xy} h^3}{12} \end{bmatrix} \quad (2.19)$$

In the formulations above, the axes of orthotropy are presumed to be parallel to the Cartesian coordinates of the cylindrical shell. Furthermore,

it is assumed that the membrane forces act centrally in the middle surface of the shell; that is, coupling effects between extension and bending are therefore neglected.

In the analysis of structures with general **laminated composite shells**, it may not be acted on the assumption above that the interdependence of membrane stretching ($\bar{\boldsymbol{\epsilon}}$, \mathbf{N}) and plate bending ($\boldsymbol{\kappa}$, \mathbf{M}) is negligible. In fact, the linear relation of the stress resultants and strains or curvatures in (2.15) and (2.18) have to be augmented with a coupling matrix \mathbf{B} , such that

$$\mathbf{N} = \mathbf{A} \bar{\boldsymbol{\epsilon}} + \mathbf{B} \boldsymbol{\kappa} \qquad \mathbf{M} = \mathbf{B}^T \bar{\boldsymbol{\epsilon}} + \mathbf{D} \boldsymbol{\kappa} \qquad (2.20)$$

The membrane stiffness matrix \mathbf{A} , the bending stiffness matrix \mathbf{D} , as well as the extension-bending coupling matrix \mathbf{B} may be determined from the classical lamination theory:

In a single ply the stress-strain relation is

$$\boldsymbol{\sigma}_k = \bar{\mathbf{Q}}_k \boldsymbol{\epsilon}_k \qquad (2.21)$$

where the stresses $\boldsymbol{\sigma}_k$ and the resulting strains $\boldsymbol{\epsilon}_k = (\bar{\boldsymbol{\epsilon}} + z \boldsymbol{\kappa})_k$ are related to the reference coordinate system (x, y) of the shell (see Section A.5) [40]. Insertion of (2.21) into the integrals to the resultants in (2.10) and (2.11) yields the common definition for the matrices \mathbf{A} , \mathbf{B} , and \mathbf{D} of a laminate consisting of N_{ply} layers:

$$\begin{aligned} \mathbf{A} &= \sum_{k=1}^{N_{ply}} \bar{\mathbf{Q}}_k (z_k - z_{k-1}) , \\ \mathbf{B} &= \frac{1}{2} \sum_{k=1}^{N_{ply}} \bar{\mathbf{Q}}_k (z_k^2 - z_{k-1}^2) , \\ \mathbf{D} &= \frac{1}{3} \sum_{k=1}^{N_{ply}} \bar{\mathbf{Q}}_k (z_k^3 - z_{k-1}^3) . \end{aligned} \qquad (2.22)$$

In Figure 2.5 the definition of the coordinates in a laminate and the corresponding orientation of the layer stacking, the ply numbering respectively, is shown. Note that the orientation of the stacking sequence is of prime importance for non-symmetric laminates where the layers with a given fibre orientation are not arranged symmetrically with respect to the middle surface of the laminated shell ($\rightarrow \mathbf{B} \neq 0$, see Fig. 2.5).

In the special case where only one ply forms the laminate and the fibres are oriented parallel/normal to the general structure coordinates

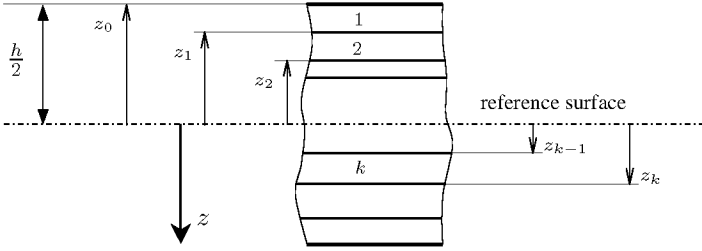


Figure 2.5: Definition of stacking sequences and coordinates in laminates

(x, y) , the membrane stiffness \mathbf{A} and the bending stiffness \mathbf{D} above correlate with the matrices introduced in the context of the relations for orthotropic materials (2.15) and (2.18), respectively.

In the compatibility condition in the form of Equation (2.9) and the equilibrium Equation (2.13) which have to be solved concurrently already include components in terms of the lateral displacements w and the membrane forces per unit length \mathbf{N} , but also such in terms of strains $\bar{\epsilon}$ and moments per unit length \mathbf{M} which have to be replaced. The transformation procedure used herein to obtain formulations of the compatibility and the equilibrium equation solely in terms of w and \mathbf{N} or \mathcal{F} follows that of (GEIER & SINGH [41]) and (GEIER, MEYER-PIENING & ZIMMERMANN [40]).

The first of the two matrix equations (2.20) is solved for the strains at the reference surface, that is:

$$\bar{\epsilon} = \mathbf{A}^{-1}(\mathbf{N} - \mathbf{B}\kappa) \quad (2.23)$$

This result is substituted in the second equation of (2.20) to obtain a semi-inverted form of the constitutive law as

$$\mathbf{M} = \mathbf{B}\mathbf{A}^{-1}\mathbf{N} + (\mathbf{D} - \mathbf{B}\mathbf{A}^{-1}\mathbf{B})\kappa \quad (2.24)$$

With the flexibility matrix

$$\mathbf{a} = \mathbf{A}^{-1} \quad , \quad (2.25)$$

the eccentricity matrix

$$\mathbf{b} = \mathbf{A}^{-1}\mathbf{B} \quad , \quad (2.26)$$

which is not symmetric ($\mathbf{b}^T \neq \mathbf{b}$),

and the *modified bending stiffness matrix*

$$\tilde{\mathbf{D}} = \mathbf{D} - \mathbf{B}^T \mathbf{A}^{-1} \mathbf{B} \quad , \quad (2.27)$$

the semi-inverted constitutive law may be written more concisely as [41, 40]

$$\begin{aligned} \bar{\boldsymbol{\epsilon}} &= \mathbf{a}\mathbf{N} - \mathbf{b}\boldsymbol{\kappa} \\ \mathbf{M} &= \mathbf{b}^T \mathbf{N} + \tilde{\mathbf{D}}\boldsymbol{\kappa} \end{aligned} \quad (2.28)$$

2.1.3 Systems of Differential Equations

The compatibility condition (2.9) and the equilibrium equation (2.13) may be transformed using the suitable constitutive law in Section above together with the definition of the curvatures $\boldsymbol{\kappa}$.

For cylindrical shells with **orthotropic** material and without eccentricities, with $\bar{\boldsymbol{\epsilon}} = \mathbf{a}\mathbf{N}$ inserted in (2.9) and $\mathbf{M} = \mathbf{D}\boldsymbol{\kappa}$ in (2.13) the strains and moments are substituted. Subsequently, the curvatures $\boldsymbol{\kappa}$ are replaced by derivatives of the lateral displacement w and the membrane forces per unit length \mathbf{N} by derivatives of the stress function \mathcal{F} according to the definitions in (2.7) and (2.14) respectively. The compatibility and the equilibrium equations for thin shallow cylindrical shells with orthotropic material, without eccentricities and with constant wall thickness finally become the following form:

$$\begin{aligned} a_{22} \frac{\partial^4 \mathcal{F}}{\partial x^4} + (2a_{12} + a_{33}) \frac{\partial^4 \mathcal{F}}{\partial x^2 \partial y^2} + a_{11} \frac{\partial^4 \mathcal{F}}{\partial y^4} = \\ \left(\frac{\partial^2 w}{\partial x \partial y} \right)^2 - \frac{\partial^2 w}{\partial x^2} \left(\frac{\partial^2 w}{\partial y^2} + \frac{1}{R} \right) \end{aligned} \quad (2.29)$$

$$\begin{aligned} D_{11} \frac{\partial^4 w}{\partial x^4} + 2(D_{12} + 2D_{33}) \frac{\partial^4 w}{\partial x^2 \partial y^2} + D_{22} \frac{\partial^4 w}{\partial y^4} = \\ p_z + \frac{\partial^2 \mathcal{F}}{\partial y^2} \frac{\partial^2 w}{\partial x^2} - 2 \frac{\partial^2 \mathcal{F}}{\partial x \partial y} \frac{\partial^2 w}{\partial x \partial y} + \frac{\partial^2 \mathcal{F}}{\partial x^2} \left[\frac{\partial^2 w}{\partial y^2} + \frac{1}{R} \right] \end{aligned} \quad (2.30)$$

A similar system of two partial differential equations may be obtained for thin **laminated** cylindrical shells using the semi-inverted constitutive law in Equation (2.28), $\bar{\boldsymbol{\epsilon}} = \mathbf{a}\mathbf{N} - \mathbf{b}\boldsymbol{\kappa}$; $\mathbf{M} = \mathbf{b}^T\mathbf{N} + \tilde{\mathbf{D}}\boldsymbol{\kappa}$. With the matrix components of the abbreviations \mathbf{a} , \mathbf{b} , and $\tilde{\mathbf{D}}$ introduced in (2.25) to (2.27) the system of differential equations may be written as

$$\begin{aligned}
 & a_{22} \frac{\partial^4 \mathcal{F}}{\partial x^4} + (2a_{12} + a_{33}) \frac{\partial^4 \mathcal{F}}{\partial x^2 \partial y^2} + a_{11} \frac{\partial^4 \mathcal{F}}{\partial y^4} - 2a_{23} \frac{\partial^4 \mathcal{F}}{\partial x^3 \partial y} - 2a_{13} \frac{\partial^4 \mathcal{F}}{\partial x \partial y^3} \\
 & + b_{21} \frac{\partial^4 w}{\partial x^4} + (b_{11} + b_{22} - 2b_{33}) \frac{\partial^4 w}{\partial x^2 \partial y^2} + b_{12} \frac{\partial^4 w}{\partial y^4} \\
 & + (2b_{23} - b_{31}) \frac{\partial^4 w}{\partial x^3 \partial y} + (2b_{13} - b_{32}) \frac{\partial^4 w}{\partial x \partial y^3} \\
 & + \frac{1}{R} \frac{\partial^2 w}{\partial x^2} - \left(\frac{\partial^2 w}{\partial x \partial y} \right)^2 + \frac{\partial^2 w}{\partial x^2} \frac{\partial^2 w}{\partial y^2} = 0
 \end{aligned} \tag{2.31}$$

$$\begin{aligned}
 & \tilde{D}_{11} \frac{\partial^4 w}{\partial x^4} + 2 \left(\tilde{D}_{12} + 2\tilde{D}_{33} \right) \frac{\partial^4 w}{\partial x^2 \partial y^2} + \tilde{D}_{22} \frac{\partial^4 w}{\partial y^4} \\
 & + 4\tilde{D}_{13} \frac{\partial^4 w}{\partial x^3 \partial y} + 4\tilde{D}_{23} \frac{\partial^4 w}{\partial x \partial y^3} \\
 & - b_{21} \frac{\partial^4 \mathcal{F}}{\partial x^4} - (b_{11} + b_{22} - 2b_{33}) \frac{\partial^4 \mathcal{F}}{\partial x^2 \partial y^2} - b_{12} \frac{\partial^4 \mathcal{F}}{\partial y^4} \\
 & - (2b_{23} - b_{31}) \frac{\partial^4 \mathcal{F}}{\partial x^3 \partial y} - (2b_{13} - b_{32}) \frac{\partial^4 \mathcal{F}}{\partial x \partial y^3} \\
 & - \frac{\partial^2 \mathcal{F}}{\partial y^2} \frac{\partial^2 w}{\partial x^2} + 2 \frac{\partial^2 \mathcal{F}}{\partial x \partial y} \frac{\partial^2 w}{\partial x \partial y} - \frac{\partial^2 \mathcal{F}}{\partial x^2} \left[\frac{\partial^2 w}{\partial y^2} + \frac{1}{R} \right] = p_z
 \end{aligned} \tag{2.32}$$

The system of the two coupled fourth-order differential equations (2.29) and (2.30) was derived by (DONNELL [29]) accordingly for isotropic shell material [15]. The nonlinear equations above form the basis for the analysis of orthotropic and laminated cylindrical shells under axial compression, bending, torsion as well as under external pressure. Approximate solutions with simultaneous consideration of eight boundary conditions may be found by the use of energy methods and approaches for the functions $w(x, y)$ and $\mathcal{F}(x, y)$ (see Section 2.3). For close-form solutions further approximations and simplifications of the set of equations are conducted.

2.2 Buckling of Perfect Cylinders – the Classical Solutions

The method to attain formulas which specify the buckling load of cylindrical shells is in principle mechanical similar to that for EULER column buckling or for buckling of flat plates as shown in Section B.3. The classical solution consists in solving the appropriate system of partial differential equations as introduced in Section 2.1.3 for orthotropic and laminated shells and arbitrary loading, but which is to be simplified to more convenient forms according to permissible assumptions. But, instead of deducing the finally used linearized equations directly, in the following the nonlinear DONNELL-type equations above are first adapted for their use in an incremental or perturbation analysis and then linearized [15].

The state of deformation and stress in a shell may be separated in a fundamental (pre-buckling) state and in stresses due to a “perturbation” associated with only incremental deflections. That is, the effect of small deformation increments starting from the initial state, denoted with w_0 and \mathcal{F}_0 , is examined [15]. The letters w and \mathcal{F} without index now indicate the small deflection and stress *increments*. The deflections and the derivatives of the stress function are modified accordingly to

$$\begin{aligned} w &\longrightarrow w_0 + w \quad , & \frac{\partial^2 \mathcal{F}}{\partial x^2} &\longrightarrow \tilde{N}_y + \frac{\partial^2 \mathcal{F}}{\partial x^2} \quad , \\ \frac{\partial^2 \mathcal{F}}{\partial y^2} &\longrightarrow \tilde{N}_x + \frac{\partial^2 \mathcal{F}}{\partial y^2} \quad , & \frac{\partial^2 \mathcal{F}}{\partial x \partial y} &\longrightarrow -\tilde{N}_{xy} + \frac{\partial^2 \mathcal{F}}{\partial x \partial y} \end{aligned}$$

where \tilde{N}_x , \tilde{N}_y and \tilde{N}_{xy} are the membrane forces per unit length of the initial state and correspond to the derivatives of \mathcal{F}_0 . That followed, in the coupled fourth-order differential compatibility and equilibrium equations w and the derivations of \mathcal{F} are replaced by one of the four expressions above. The next derivation steps are demonstrated by means of the shorter equations for orthotropic shells (2.29) and (2.30). Neglecting higher-order terms and considering the lateral load p_z as constant, after the transformations the compatibility equation becomes [15]:

$$\begin{aligned} a_{22} \frac{\partial^4 \mathcal{F}}{\partial x^4} + (2a_{12} + a_{33}) \frac{\partial^4 \mathcal{F}}{\partial x^2 \partial y^2} + a_{11} \frac{\partial^4 \mathcal{F}}{\partial y^4} = & \\ 2 \frac{\partial^2 w_0}{\partial x \partial y} \frac{\partial^2 w}{\partial x \partial y} - \frac{\partial^2 w_0}{\partial x^2} \frac{\partial^2 w}{\partial y^2} - \frac{\partial^2 w}{\partial x^2} \frac{\partial^2 w_0}{\partial y^2} - \frac{\partial^2 w}{\partial x^2} \frac{1}{R} & \end{aligned} \quad (2.33)$$

In a similar manner the modified equilibrium equation is obtained [15]:

$$\begin{aligned}
 D_{11} \frac{\partial^4 w}{\partial x^4} + 2(D_{12} + 2D_{33}) \frac{\partial^4 w}{\partial x^2 \partial y^2} + D_{22} \frac{\partial^4 w}{\partial y^4} = \\
 \tilde{N}_x \frac{\partial^2 w}{\partial x^2} + \frac{\partial^2 \mathcal{F}}{\partial y^2} \frac{\partial^2 w_0}{\partial x^2} + 2\tilde{N}_{xy} \frac{\partial^2 w}{\partial x \partial y} - 2 \frac{\partial^2 \mathcal{F}}{\partial x \partial y} \frac{\partial^2 w_0}{\partial x \partial y} \\
 + \tilde{N}_y \frac{\partial^2 w}{\partial y^2} + \frac{\partial^2 \mathcal{F}}{\partial x^2} \frac{\partial^2 w_0}{\partial y^2} + \frac{1}{R} \frac{\partial^2 \mathcal{F}}{\partial x^2}
 \end{aligned} \quad (2.34)$$

Finally, assuming that the initial state is a membrane state for which the shell is a perfect circular cylinder the initial deflection w_0 will be neglected (no initial imperfections) [15]. That is:

$$\frac{\partial^2 w_0}{\partial x^2} = 0, \quad \frac{\partial^2 w_0}{\partial y^2} = 0, \quad \frac{\partial^2 w_0}{\partial x \partial y} = 0.$$

This reduces the pair of differential equations (2.29) and (2.30) to the linearized expressions for compatibility and equilibrium in terms of the incremental w and \mathcal{F} and the stresses of the fundamental state:

$$a_{22} \frac{\partial^4 \mathcal{F}}{\partial x^4} + (2a_{12} + a_{33}) \frac{\partial^4 \mathcal{F}}{\partial x^2 \partial y^2} + a_{11} \frac{\partial^4 \mathcal{F}}{\partial y^4} = - \frac{\partial^2 w}{\partial x^2} \frac{1}{R} \quad (2.35)$$

$$\begin{aligned}
 D_{11} \frac{\partial^4 w}{\partial x^4} + 2(D_{12} + 2D_{33}) \frac{\partial^4 w}{\partial x^2 \partial y^2} + D_{22} \frac{\partial^4 w}{\partial y^4} = \\
 \tilde{N}_x \frac{\partial^2 w}{\partial x^2} + 2\tilde{N}_{xy} \frac{\partial^2 w}{\partial x \partial y} + \tilde{N}_y \frac{\partial^2 w}{\partial y^2} + \frac{1}{R} \frac{\partial^2 \mathcal{F}}{\partial x^2}
 \end{aligned} \quad (2.36)$$

These *linearized DONNELL-type equations for shallow shells with small deformations* will be used later for circular cylinders in this form, but for isotropic shells a compact equation including both the equilibrium and the compatibility expressions was deduced.

For isotropic shell material and using the LAPLACE-Operator² ∇^2 and D for the isotropic bending stiffness $D = Eh^3/12(1 - \nu^2)$ the system of two differential equations above can be rewritten in abbreviated form as [15]

$$\begin{aligned}
 \frac{1}{Eh} \nabla^4 \mathcal{F} = - \frac{\partial^2 w}{\partial x^2} \frac{1}{R} \\
 D \nabla^4 w = \tilde{N}_x \frac{\partial^2 w}{\partial x^2} + 2\tilde{N}_{xy} \frac{\partial^2 w}{\partial x \partial y} + \tilde{N}_y \frac{\partial^2 w}{\partial y^2} + \frac{1}{R} \frac{\partial^2 \mathcal{F}}{\partial x^2}
 \end{aligned} \quad (2.37)$$

² $\nabla^2 w = \partial^2 w / \partial x^2 + \partial^2 w / \partial y^2$. $\nabla^4 = (\nabla^2)^2$.

After double differentiation of the first expression with respect to x and division with R it follows that

$$\nabla^4 \frac{\partial^2 \mathcal{F}}{\partial x^2} \frac{1}{R} = -\frac{\partial^4 w}{\partial x^4} \frac{Eh}{R^2}$$

The last term of the second row in (2.37) may be replaced according to the right side of the expression above. By this means for the two fourth-order differential equations a single eighth-order differential equation is obtained:

$$D \nabla^8 w - \nabla^4 \left(\tilde{N}_x \frac{\partial^2 w}{\partial x^2} + 2\tilde{N}_{xy} \frac{\partial^2 w}{\partial x \partial y} + \tilde{N}_y \frac{\partial^2 w}{\partial y^2} \right) - \frac{Eh}{R^2} \frac{\partial^4 w}{\partial x^4} = 0 \quad (2.38)$$

This differential equation is the *linearized* DONNELL equation for *shallow shells* in the common form [29, 15]. After solving the incremental displacements w with (2.38), considering the membrane forces per unit length \tilde{N}_x , \tilde{N}_{xy} , \tilde{N}_y as constant, the stress function \mathcal{F} is solved from the first row in (2.37). Afterwards the strains are solved by means of the constitutive equations from which the displacements in the reference surface may be calculated [15].

The linearized DONNELL-type equations base on the assumptions that the constant wall thickness h is essentially smaller than the radius R , that the transversally shear stiffness is infinitely large, that the initial geometry is perfect (no initial curvature other than $1/R$) [15], and that the deflections are small in comparison to the wall thickness. Nevertheless, in cases pre-buckling curvature changes are negligible small DONNELL's shell theory may be used to calculate bifurcation loads.

Nonlinear DONNELL-type equations were frequently used for the investigation of the buckling and post-buckling behaviour of isotropic, orthotropic as well as of laminated cylindrical shells. Due to the approximations and simplicity of DONNELL's shell theory doubts have been cast on the accuracy of the involved equations [73]. Thus, (HOFF [47]), (MEYER-PIENING [59]), (SHEINMAN & GOLDFELD [73]) and others performed tests und calculations with other, more accurate shell theories including nonlinear terms in u and v for comparisons of the buckling loads with their solutions of DONNELL-type equations. They found that for thin, shallow cylindrical shells unless the square terms in derivatives of the deflection w (nonlinear strain components) are small against unity and the wavelike post-buckling patterns contain a sufficient number of circumferential waves good results may be obtained with the DONNELL-type equations also for relatively large deflections [59].

2.2.1 Boundary Conditions

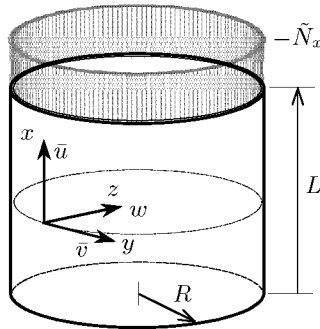


Figure 2.6: *Axially compressed circular cylinder.*

The set of DONNELL's differential equations is of eighth order, thus eight boundary conditions related to displacements and stresses in the reference surface are needed to define the eigenvalue problem. At the two cylinder edges at $x = 0$ or $x = L$ one of the following four fundamental combinations of four boundary conditions has to be hold:

<i>Simply Supported</i>		<i>Clamped</i>	
$w = \frac{\partial^2 w}{\partial x^2} = 0$		$w = \frac{\partial w}{\partial x} = 0$	
SS1	$N_{xy} = 0, \quad N_x = 0$	CC1	$N_{xy} = 0, \quad N_x = 0$
SS2	$N_{xy} = 0, \quad \bar{u} = c$	CC2	$N_{xy} = 0, \quad \bar{u} = c$
SS3	$\bar{v} = c, \quad N_x = 0$	CC3	$\bar{v} = c, \quad N_x = 0$
SS4	$\bar{v} = c, \quad \bar{u} = c$	CC4	$\bar{v} = c, \quad \bar{u} = c$

Table 2.1: *Notations for boundary conditions. c is a constant.*

Similar notations for the conditions of hinge support (SS i) and fixed support (CC i) to those in Table 2.1 were applied by (HOFF et al. [48]) and many other authors, e.g. (SHEINMAN & SIMITSES [74]) and (ARBOCZ & BABCOCK, JR. [6]). The membrane forces per unit length N_x and N_{xy} in

Table 2.1 due to displacements are equal to $\partial^2 \mathcal{F} / \partial y^2$ and $\partial^2 \mathcal{F} / \partial x \partial y$ respectively. The constant \mathbf{c} is zero or a value unvarying around the cylinder edge considered. In case of a immobile fixation the displacements are zero and $\mathbf{c} = 0$. For displacement controlled compressions, for instance, the constant \mathbf{c} equals the nonzero loading parameter ($\mathbf{c} = \bar{u} = \Delta L$).

The DONNELL-type equations are formulated in terms of the lateral displacement w and derivatives of the stress function \mathcal{F} . The boundary conditions which refer to the axial and tangential displacements in the reference surface $\bar{u}(x, y)$ and $\bar{v}(x, y)$ have to be reformulated in terms of $w(x, y)$ and $\mathcal{F}(x, y)$. This is disadvantageous, since thereby \bar{u} and \bar{v} are replaced by their derivatives. For example, for the axial displacement $\bar{u}(x, y)$ at the loaded edge ($x = L$) it applies [59]:

$$\bar{u}(L, y) = \bar{u}(0, y) + \int_0^L \left\{ a_{11} \frac{\partial^2 \mathcal{F}}{\partial y^2} + a_{12} \frac{\partial^2 \mathcal{F}}{\partial x^2} - \frac{1}{2} \left(\frac{\partial w}{\partial x} \right)^2 \right\} dx \quad (2.39)$$

using the strain expression for $\bar{\varepsilon}_x$ in (2.8). Constant axial displacement would additionally require that $\partial \bar{u} / \partial y = 0$. Consequently, the boundary conditions in \bar{u} as well as \bar{v} become much more complex and difficult to fulfill than in formulations which deal with functions for $\bar{u}(x, y)$ and $\bar{v}(x, y)$ together with that for $w(x, y)$.

For axially compressed cylinders in classic analysis the compressive axial membrane load per unit length of the fundamental state at the loaded end is given by the applied total compressive force P :

$$-\tilde{N}_x = \frac{P}{2\pi R} \quad (2.40)$$

Buckling under torsion or lateral load is not taken into consideration³ in the following; hence, the surface load p_z and the circumferential as well as the shear membrane loads per unit length of the fundamental state \tilde{N}_y and \tilde{N}_{xy} are set to zero:

$$\tilde{N}_y = 0 ; \quad \tilde{N}_{xy} = 0 ; \quad p_z = 0 .$$

In classical buckling analysis of cylinders under axial load the boundary conditions SS3 are considered, since in this case close-form solutions are available. Both the radial and tangential displacements w and \bar{v} are

³The solutions to these load cases are neither uninteresting nor trivial, but the imperfection sensitivity of cylinders under axial load is more pronounced, see Section 5.

constraint and the membrane load per unit length $-\tilde{N}_x$, constant around the edge, is the loading parameter. The axial displacement \bar{u} follows from the deformation state and potentially vary around the cylinder end. In practice, however, for compression tests the cylinder ends are fixed in rigid endplates and the axial displacement is the loading parameter. Thus, in tests more the fourth type of boundary conditions CC4 and SS4 are realized with constant axial displacement but potentially varying axial membrane stresses around the edges. Again the radial and the tangential displacements are both fixed. The first two types of boundary conditions SS1, CC1, SS2, and CC2 with unconstrained circumferential displacement \bar{v} are unlikely to be realized in practice. In comparison to results for the third and fourth boundary condition sets, for these more “academic” conditions also very low buckling loads were obtained [48].

In this thesis the classical analysis solutions of the DONNELL-type equations refer to the boundary conditions SS3 for simply supported cylinders. For the numerical buckling analyses however in general the boundary conditions CC4 for clamped edges were applied, simulating test conditions with rigid and plane-parallel endplates.

2.2.2 Orthotropic Cylindrical Shells

The DONNELL-type equations may be used to calculate the axial buckling load of centrally loaded, orthotropic monocoque cylinders of perfect geometry. With the aforementioned assumptions that $p_z = 0$, $\tilde{N}_y = 0$ and $\tilde{N}_{xy} = 0$ as well as that the pre-buckling state is linear (small strains and rotations), the compatibility and equilibrium Equation (2.35) and (2.36) can be rewritten as

$$a_{22} \frac{\partial^4 \mathcal{F}}{\partial x^4} + (2a_{12} + a_{33}) \frac{\partial^4 \mathcal{F}}{\partial x^2 \partial y^2} + a_{11} \frac{\partial^4 \mathcal{F}}{\partial y^4} + \frac{\partial^2 w}{\partial x^2} \frac{1}{R} = 0 \quad (2.41)$$

$$D_{11} \frac{\partial^4 w}{\partial x^4} + 2(D_{12} + 2D_{33}) \frac{\partial^4 w}{\partial x^2 \partial y^2} + D_{22} \frac{\partial^4 w}{\partial y^4} - \tilde{N}_x \frac{\partial^2 w}{\partial x^2} - \frac{\partial^2 \mathcal{F}}{\partial x^2} \frac{1}{R} = 0 \quad (2.42)$$

Of these linearized system of partial differential equations close-form solutions exist for *hinged* cylinder edges, i.e. for the simply supported boundary conditions SS3 (see Table 2.1, Section 2.2.1). For $x = 0$ and $x = L$ these conditions are:

$$w = 0, \quad \bar{v} = 0, \quad \frac{\partial^2 w}{\partial x^2} = 0, \quad N_x = \frac{\partial^2 \mathcal{F}}{\partial y^2} = 0 \quad (2.43)$$

The following bi-harmonic functions $w(x, y)$ and $\mathcal{F}(x, y)$ for the lateral deflection and the stress function fulfill these conditions SS3:

$$\begin{aligned} w(x, y) &= w_{mn} \sin \frac{m \pi x}{L} \cos \frac{n y}{R} \\ \mathcal{F}(x, y) &= f_{mn} \sin \frac{m \pi x}{L} \cos \frac{n y}{R} \end{aligned} \quad (2.44)$$

Note that m is the number of axial *half-waves* whereas n is the number of *complete waves* in circumference direction of a buckling mode [40]. With the abbreviations

$$\beta = \frac{m \pi}{L} \quad \text{and} \quad \eta = \frac{n}{R} \quad (2.45)$$

the compatibility equation gives

$$f_{mn} = \frac{w_{mn}}{R} \frac{\beta^2}{a_{11}\eta^4 + (2a_{12} + a_{33})\beta^2\eta^2 + a_{22}\beta^4} \quad (2.46)$$

Substitution of the functions $\mathcal{F}(x, y)$ and $w(x, y)$ in the equilibrium equation (2.42) yields

$$\left\{ \frac{\beta^2}{R} f_{mn} + w_{mn} \left(\tilde{N}_x \beta^2 + D_{11}\beta^4 + D_{22}\eta^4 + 2(D_{12} + 2D_{33})\beta^2\eta^2 \right) \right\} \sin \beta x \cos \eta y = 0 \quad (2.47)$$

After the replacement of f_{mn} by (2.46) the coefficient w_{mn} may be factored out, and since at least one coefficient w_{mn} has to be different from zero, the expression in the braces in (2.47) has to be zero.

Finally a single equation for the theoretical buckling load of cylindrical shells with orthotropic material and hinged edges is obtained:

$$\begin{aligned} -\tilde{N}_x &= \frac{D_{11}\beta^4 + 2(D_{12} + 2D_{33})\beta^2\eta^2 + D_{22}\eta^4}{\beta^2} \\ &+ \frac{1}{R^2} \frac{\beta^2}{a_{11}\eta^4 + (2a_{12} + a_{33})\beta^2\eta^2 + a_{22}\beta^4} \end{aligned} \quad (2.48)$$

The load per unit length considered as the axial buckling load is the smallest absolute value of $-\tilde{N}_x$ which may be found for any combination of m and n :

$$-N_{cr} = \min(|\tilde{N}_x|) \quad (2.49)$$

For **isotropic cylinders** subjected to axial compression the formula (2.48) may be rewritten in shorter form as

$$-N_{cr} = \min \left(\frac{E h^3}{12(1-\nu^2)} \frac{(\beta^2 + \eta^2)^2}{\beta^2} + \frac{E h}{R^2} \frac{\beta^2}{(\beta^2 + \eta^2)^2} \right) \quad (2.50)$$

In this case, for cylinders of intermediate length a close estimate of the smallest buckling load may be obtained directly by analytical minimization of $|N_{cr}|$ with respect to the quantity $(\beta^2 + \eta^2)^2/\beta^2$ in (2.50) [18]. Differentiation leads to the result that $|N_{cr}|$ is a minimum for

$$\frac{(\beta^2 + \eta^2)^2}{\beta^2} = \frac{2\sqrt{3(1-\nu^2)}}{h R} \quad (2.51)$$

Introduction in (2.50) and with $\sigma_{cl} = N_{cr}/h$ for isotropic cylinders with hinged edges a memorable formula for the theoretical buckling stress may be deduced:

$$-\sigma_{cl} = \frac{1}{\sqrt{3(1-\nu^2)}} \frac{E h}{R} ; \quad \text{for } \nu = 0.3 : -\sigma_{cl} = 0.605 \frac{E h}{R} \quad (2.52)$$

Multiplication of the buckling stress by the cutting area $2\pi R h$ finally gives the corresponding axial buckling load:

$$P_{cl} = \frac{2\pi}{\sqrt{3(1-\nu^2)}} E h^2 ; \quad \text{for } \nu = 0.3 : P_{cl} = 3.8 E h^2 \quad (2.53)$$

Different to the Introduction the bucking stress as well as the buckling load were labeled with a suffix “cl” instead of “cr” since P_{cl} will denote the “classical buckling loads” in opposition to buckling loads that result for numerical analyses.

From equation (2.51) it may be seen that cylindrical shells subjected to axial compression is a case for which a large number of instability modes, i.e. critical combinations of m and n , correspond to a single buckling load. In particular, (2.52) is the solution for axisymmetric ($n = 0$) as well as for asymmetric modes [18]. The large number of possible buckling modes with an identical or almost identical associated buckling load causes isotropic cylinders to be very sensitive to dimple imperfections as analysed herein.

Obviously the critical stress in (2.52) depends on the YOUNG’s modulus E , the wall thickness h , and the cylinder radius R , but not on the cylinder

length L . However, upper and lower bounds for the length L of cylinders exist to which (2.52) is applicable. (BATDORF [12]) introduced the widely known parameter Z with

$$Z = \frac{L^2}{Rh} \sqrt{1 - \nu^2} \quad (2.54)$$

which serves as a single measure for the relative thickness and length of isotropic cylinders instead of two (L/R , and R/h) and indicates the range over which the Equation (2.52) yields good approximations of the axial buckling load of an isotropic cylinder. DONNELL's theory for shallow shells implies that the wall thickness is sufficiently small ($R/h > 100$) and that the half-wavelength of buckling is short compared to the curvature radius R ($1/n^2 \ll 1$) [15, 59]. To very long cylinders which buckle rather like a column the formula (2.52) is inapplicable, since with DONNELL's theory only the buckling of profile faces may be considered – EULER loads for columns cannot be predicted [15].

The expression (2.52) for the critical stress is valid if $\sigma_{x\ cr}$ is significantly lower than the compressive yield stress of the material at hand. In technical standards (e.g. DIN 18800 part 4) some modified expressions may be found which takes yielding, different imperfections and the influence of the cylinder length into account.

Finally, as the cylinder radius R approaches infinity and Z zero, the buckling load expression (2.50) becomes that of a infinitely wide rectangular plate, see also Section B.3.

Axisymmetric Buckling ($n = 0$)

With axisymmetric buckling the circumferential wave-number n is zero, and thus the buckling loads depend only on the number of axial half-waves. Omitting the terms relating to n in (2.48) the equation for the buckling loads of axial compressed orthotropic cylinders becomes

$$-N_{cr} = \min \left(D_{11} \beta^2 + \frac{1}{R^2} \frac{1}{a_{22} \beta^2} \right) \quad (2.55)$$

Assuming that the axial wavelength parameter β is a continuous variable, an analytical minimisation as for isotropic cylinder in (2.50) may be performed [40]. Differentiation of (2.55) with respect to β^2 leads to the following condition for a minimal $|N_{cr}|$:

$$\beta = \sqrt[4]{\frac{1}{R^2 D_{11} a_{22}}} \quad (2.56)$$

Insertion of (2.56) into (2.55) yields the searched estimate of the axisymmetric buckling load per unit length as

$$-N_{cr} = \frac{2}{R} \sqrt{\frac{D_{11}}{a_{22}}} \quad (2.57)$$

A replacement of D_{11} and a_{22} by the corresponding expressions for isotropic materials and with $\sigma_{cr} = N_{cr}/h$ the common simpler formula (2.52) is obtained. In case of axisymmetric buckling the load $-N_{cr}$ is not a bifurcation point as for bifurcation buckling a transition from an axisymmetric to a non-axisymmetric deformation pattern is assumed.

With $\beta = m\pi/L$ and (2.56), the length of half-waves into which the shell buckles is

$$l_c = \frac{L}{m} = \pi \sqrt{R \sqrt{D_{11} a_{11}}} \quad (2.58)$$

or again in particular for isotropic shells:

$$l_c = \frac{\pi}{\sqrt[4]{12(1-\nu^2)}} \sqrt{R h} \quad \text{or for } \nu = 0.3 : \quad l_c = 1.73 \sqrt{R h} \quad (2.59)$$

Example: The axial half-wave length of an isotropic cylinder with radius $R = 250$ mm and wall-thickness $h = 1.5$ mm is: $l_c = 33$ mm, independent of the cylinder length L .

2.2.3 Laminated Cylindrical Shells

To obtain the classical solution of the DONNELL-type equations for the axial buckling load of perfect laminated shells, the same procedure as for orthotropic shells in Section 2.2.2 is followed.

In addition to the simplifying assumptions that the pre-buckling deformations are negligible small and the condition for pure axial loading, for the classic analysis the laminates are supposed to be strictly orthotropic; thus the terms D_{13} , D_{23} , D_{31} , D_{32} , B_{13} , B_{23} , B_{31} , and B_{32} are set to zero [40]. Consequently, the set of differential equations, (2.31) and (2.32), becomes:

$$\begin{aligned} a_{22} \frac{\partial^4 \mathcal{F}}{\partial x^4} + (2a_{12} + a_{33}) \frac{\partial^4 \mathcal{F}}{\partial x^2 \partial y^2} + a_{11} \frac{\partial^4 \mathcal{F}}{\partial y^4} + \frac{1}{R} \frac{\partial^2 w}{\partial x^2} \\ + b_{21} \frac{\partial^4 w}{\partial x^4} + (b_{11} + b_{22} - 2b_{33}) \frac{\partial^4 w}{\partial x^2 \partial y^2} + b_{12} \frac{\partial^4 w}{\partial y^4} = 0 \end{aligned} \quad (2.60)$$

$$\begin{aligned}
\tilde{D}_{11} \frac{\partial^4 w}{\partial x^4} + 2 \left(\tilde{D}_{12} + 2\tilde{D}_{33} \right) \frac{\partial^4 w}{\partial x^2 \partial y^2} + \tilde{D}_{22} \frac{\partial^4 w}{\partial y^4} \\
- b_{21} \frac{\partial^4 \mathcal{F}}{\partial x^4} - (b_{11} + b_{22} - 2b_{33}) \frac{\partial^4 \mathcal{F}}{\partial x^2 \partial y^2} - b_{12} \frac{\partial^4 \mathcal{F}}{\partial y^4} \\
- \tilde{N}_x \frac{\partial^2 w}{\partial x^2} - \frac{1}{R} \frac{\partial^2 \mathcal{F}}{\partial x^2} = 0
\end{aligned} \tag{2.61}$$

Close-form solutions exist again for hinged cylinder edges (boundary conditions SS3) with

$$w = 0, \quad \bar{v} = 0, \quad \frac{\partial^2 w}{\partial x^2} = 0, \quad N_x = 0 \quad \text{at } x = 0 \text{ and } x = L$$

with the buckling modes

$$\begin{aligned}
w(x, y) &= w_{mn} \sin \beta x \cos \eta y \\
\mathcal{F}(x, y) &= f_{mn} \sin \beta x \cos \eta y
\end{aligned}$$

where β and η are the already introduced axial and circumferential wave-length parameters with

$$\beta = \frac{m\pi}{L} \quad \text{and} \quad \eta = \frac{n}{R}$$

For pure axial compression, following the same calculation steps than in Section 2.2.2 and the condition for non-trivial solutions evaluated yields the bifurcation loads [40]

$$\begin{aligned}
-N_x = \frac{1}{\beta^2} \left\{ \tilde{D}_{11} \beta^4 + 2(\tilde{D}_{12} + 2\tilde{D}_{33}) \beta^2 \eta^2 + \tilde{D}_{22} \eta^4 \right. \\
\left. + \frac{\left[b_{21} \beta^4 + (b_{11} + b_{22} - 2b_{33}) \beta^2 \eta^2 + b_{12} \eta^4 - \frac{\beta^2}{R} \right]^2}{a_{11} \eta^4 + (2a_{12} + a_{33}) \beta^2 \eta^2 + a_{22} \beta^4} \right\} \tag{2.62}
\end{aligned}$$

The axial buckling load again is the smallest absolute value of $|\tilde{N}_x|$ which may be found for any combination of m axial half-waves and n circumferential waves:

$$-N_{cr} = \min(|\tilde{N}_x|)$$

In contrast to isotropic cylinders for laminated cylinders only one buckling mode with a (m, n) -pair is typically associated with the lowest buckling load. But, the critical load $-N_{cr}$ may not be obtained directly by analytical minimization of $|\tilde{N}_x|$ as for isotropic material but has to be

found by use of Equation (2.62) for a sufficient number of combinations of m and n . Again, multiplication of the smallest $|\tilde{N}_x|$ by the circumference $2\pi R$ yields the “classical” buckling load P_{cl} for the laminated cylinder.

In the following, the number of axial half-waves and circumferential waves associated with the smallest $|\tilde{N}_x|$ and hence the buckling load P_{cl} are marked with m_c and n_c , respectively.

Again, as the cylinder radius R approaches infinity, expression (2.62) becomes an equation for infinitely wide rectangular laminated plates.

(GEIER, MEYER-PIENING & ZIMMERMANN [40]) defined the curvatures κ and the coupling matrix \mathbf{B} with different sign what finally results solely in a positive $+\beta^2/R$ in the numerator in the second line of Equation (2.62) above instead of the negative term.

Equation (2.62) for thin, axially loaded and simply supported laminated cylinders with perfect geometry bases on the classical lamination theory, on DONNELL’s shallow-shell theory as well as on the assumption that the laminate is strictly orthotropic [40]. Thus, the accuracy of the results is subject to restrictions which relate to the cylinder geometry (L , R/h) and additionally which concern the shell material parameters given by the ply properties, the ply angles and the layer stacking. The range of the geometry parameter L^2/Rh (e.g.) over which (2.62) yields good results for arbitrary laminates was probably not yet investigated. But according to the shallow shell theory at least analysis results with n between 1 and 4 should be questioned. (MEYER-PIENING et al. [60]) calculated the axial buckling load of a series of CFRP composite cylinders with $R/h = 200$ and $L/R \approx 2$ by means of Equation (2.62) and also with the aid of a code which considers deep shell theory and anisotropic material (full matrices \mathbf{A} , \mathbf{B} , \mathbf{D}). The axial buckling loads obtained with (2.62) are slightly above those resulted for the more accurate method with differences below eight percent. (SHEINMAN & GOLDFELD [73]) in turn analysed laminated cylinders with $R/h = 100$ and $L/R = 2$ and observed significant discrepancies between DONNELL-type equation results and such achieved with more accurate shell theories, in dependence of the ply-angles and the boundary conditions.

Axisymmetric Buckling of Laminated Shells

The solution for axisymmetric buckling of laminated shells may be deduced from Equation (2.62). As for orthotropic shells the circumferential wave-number n and η are zero, and thus the buckling loads depend only on the number of axial half-waves m . The terms relating to η deleted in (2.62) the equation for the buckling loads $-N_{cr}$ may be minimized analytically if β is assumed to be continuous. The minimum is found for the axial half-wavelength

$$l_c = \frac{L}{m} = \pi \sqrt{R \sqrt{\tilde{D}_{11} a_{22} + b_{21}^2}} \quad (2.63)$$

which differs from l_c for orthotropic shells in (2.58) mainly in the additional eccentricity term b_{21}^2 [40]. The lowest buckling load per unit length for axisymmetric modes finally is

$$-N_{cr} = \frac{2}{R a_{22}} \left(\sqrt{\tilde{D}_{11} a_{22} + b_{21}^2} - b_{21} \right). \quad (2.64)$$

As aforementioned for the orthotropic shells, in case of axisymmetric buckling $-N_{cr}$ does not correspond to a bifurcation point. Note that the additive term b_{21} in (2.64) may be positive or negative depending on the stacking sequence of the laminate. The absolute values of the square root and of b_{21} are of the same order of magnitude. The sign of the eccentricity term b_{21} is determined by the expression $(a_{21} B_{11} + a_{22} B_{21})$, and since B_{12} and B_{11} typically have different signs, the sign of b_{21} is basically opposite to the sign of B_{11} . Consequently, if axially stiff layers are predominantly located at the outer side of the cylindrical shell (i.e. negative z_k ; see Figure 2.5) B_{11} will be negative and b_{21} positive, which gives low buckling loads if the buckling mode is axisymmetric (see Section 4.2.2) [40].

2.3 Approximate Solutions

In the previous sections the close-form solutions of the DONNELL-type shell equations for axial buckling of circular cylinders with simply supported boundary conditions were presented which could be found by direct integration. For more accurate shell theories with extended expressions for curvatures or for other boundary conditions, for instance, only approximative solutions and functions for the stress and displacement

fields may be found. In this Section briefly the concepts of the RALEIGH-RITZ method and the GALERKIN procedure are described which are frequently used for approximative solutions of differential equations.

The **RALEIGH-RITZ method** is a widely used approximate solution technique for differential equations. The method is based on variational principles, provided by the principles of virtual displacements (see Section A.4) or the minimal potential energy [67]. The dependent unknowns, e.g. the displacement \bar{u} , are approximated by finite FOURIER series of the form

$$\bar{u}(x) \approx \sum_{i=1}^{N_{ui}} \hat{u}_i X_i(x) + X_0 \quad (2.65)$$

with the unknown FOURIER coefficients \hat{u}_i and the number of retained terms N_{ui} . The *approximation functions* X_i should satisfy the homogeneous form of the specified essential boundary conditions and they should be linearly independent (orthogonal) and complete [67]. The function X_0 has to satisfy the inhomogeneous specified geometric boundary conditions. In the already presented case of cylinders with simply supported edges the deformations $\bar{u}(x, y)$, $\bar{v}(x, y)$, and $w(x, y)$ may be approximated, separating the variables, by the following double FOURIER series

$$\begin{aligned} \bar{u}(x, y) &\approx \frac{L}{R} \sum_{m=1}^{N_u} \sum_{n=1}^{N_u} \hat{u}_{mn} \cos \frac{m \pi x}{L} \cos \frac{n y}{R} \quad , \\ \bar{v}(x, y) &\approx \frac{L}{R} \sum_{m=1}^{N_v} \sum_{n=1}^{N_v} \hat{v}_{mn} \sin \frac{m \pi x}{L} \sin \frac{n y}{R} \quad , \\ w(x, y) &\approx \sum_{m=1}^{N_w} \sum_{n=1}^{N_w} \hat{w}_{mn} \sin \frac{m \pi x}{L} \cos \frac{n y}{R} \quad , \end{aligned} \quad (2.66)$$

where again m and n are the axial half-wave and the complete circumferential wave numbers, respectively. With the RALEIGH-RITZ method an approximate solution is obtained by requiring the *total potential energy* Π to be stationary with respect to all unknown coefficients \hat{u}_{mn} , \hat{v}_{mn} , and \hat{w}_{mn} [82], that is

$$\delta \Pi = \frac{\partial \Pi}{\partial \hat{u}_{mn}} = \frac{\partial \Pi}{\partial \hat{v}_{mn}} = \frac{\partial \Pi}{\partial \hat{w}_{mn}} = 0 \quad . \quad (2.67)$$

The change in the potential energy caused by a uniform axial compressive load P may be written as

$$\Pi = U_B + U_M + V_P \quad (2.68)$$

where the bending and membrane strain energy, U_B and U_M , and the load potential V_P for an axial compressive membrane stress $-\tilde{N}_x$ are given as [82]

$$\begin{aligned} U_B &= \frac{1}{2} \int_0^{2\pi R} \int_0^L (M_x \kappa_x + 2 M_{xy} \kappa_{xy} + M_y \kappa_y) dx dy \quad , \\ U_M &= \frac{1}{2} \int_0^{2\pi R} \int_0^L (N_x \bar{\varepsilon}_x + 2 N_{xy} \bar{\gamma}_{xy} + N_y \bar{\varepsilon}_y) dx dy \quad , \\ V_P &= - \int_0^{2\pi R} \int_0^L \tilde{N}_x \left(\frac{\partial \bar{u}}{\partial x} \right) dx dy \quad . \end{aligned} \quad (2.69)$$

The membrane and stress resultants are related to strains and changes in curvature through the constitutive equations (see Section 2.1.2), and the strain-displacements relations in turn, associated with the deformation components, are given by the kinematic equations as introduced in Section 2.1.1. Consequently, the forces and moments are first expressed in terms of displacements and subsequently substituted by the derivatives of the harmonic functions (2.66). The set of the coefficients to be determined are finally obtained by solving the system of equation derived from (2.67).

Another common and widely used method to generate approximate solutions of differential equations is the **GALERKIN procedure**. Analogous to the RALEIGH-RITZ method a function, e.g. $u(x)$, is approximated by truncated FOURIER series of the form

$$u(x) \approx \sum_{i=1}^{N_{ui}} \hat{u}_i X_i(x) + X_0 \quad (2.70)$$

whereby again X_0 have to satisfy possible inhomogeneous boundary conditions and the other functions X_i the homogenous boundary conditions. Although u fulfills the boundary conditions for arbitrary \hat{u}_i , inserted into the differential equation in the domain in the majority of the cases a residual (balance error) will result. To minimize this residual in the domain A the integral of the residual function r , weighted with some *weight functions* ψ_i , has to vanish over the domain A . Such methods are therefore also known under the term “weighted-residual methods”. With a linear differential operator \mathcal{L} a general differential equation may be written as

$$\mathcal{L}(u) = f \quad \in A \quad (2.71)$$

with the given force term f . Then, with (2.70) the residual function is

given by

$$r(\hat{u}_i, X_i, f) = \mathcal{L} \left(\sum_{i=1}^{N_{ui}} \hat{u}_i X_i(x) + X_0 \right) - f \neq 0 \quad (2.72)$$

With the N_{ui} linearly independent weight functions ψ_i the approximation for $u(x)$ is found for

$$\int_A r(\hat{u}_i, X_i, f) \psi_i dx \equiv 0 \quad i = 1, 2, \dots, N_{ui} \quad (2.73)$$

The weight functions ψ_i correspond to the approximation functions X_i in (2.65). Thus, the GALERKIN method is a generalization of the RALEIGH-RITZ method.

(I. SHEINMAN & Y. GOLDFELD [73]) for instance applied the GALERKIN procedure on the buckling analysis of axially compressed cylinders. They used the following truncated series for an approximation of the lateral displacements $w(x, y)$ and the stress function $\mathcal{F}(x, y)$:

$$w(x, y) = \sum_{i=0}^{2N_w} \hat{w}_i(x) Y_i(y), \quad \mathcal{F}(x, y) = \sum_{i=0}^{2N_F} \hat{f}_i(x) Y_i(y) \quad (2.74)$$

where $2N_w$ and $2N_F$ are the numbers of retained terms in the series, and

$$Y_i(y) = \begin{cases} \cos(iny) & i = 0, 1, 2, 3, \dots, N_\ell \\ \sin(iny) & i = N_\ell + 1, \dots, 2N_\ell \end{cases} \quad (2.75)$$

with the circumferential wave number n and N_ℓ standing for N_w or N_F as appropriate [73]. The set of partial differential equations (of compatibility and equilibrium) is reduced to a set of ordinary ones by separation of the variables with the functions in (2.74). Then, the balance error, caused by these truncated form of the series, is minimized if the following two integrals vanish:

$$\begin{aligned} \int_0^{2\pi R} [\text{compatibility eq.}] Y_i(y) dy &= 0 & i = 0, 1, \dots, 2N_F \\ \int_0^{2\pi R} [\text{equilibrium eq.}] Y_i(y) dy &= 0 & i = 0, 1, \dots, 2N_w \end{aligned} \quad (2.76)$$

A central difference scheme was then used to reduce the ordinary differential equations to an algebraic system of equations which was solved numerically [73].

The calculation of buckling loads with these approximative methods requires the complex definition of equation systems. Afterwards, the in most case vast number of unknown coefficients involved has to be handled with the aid of computers. Despite these obstacles several reliable special-purpose programs for buckling analyses of cylindrical shells were developed, also for moderately thick shells and clamped boundary conditions. However, for each shell geometry and set of boundary conditions a different system of equations has to be worked out. In addition, analytical or variational solutions to the differential equations may not be developed when complex geometries, arbitrary boundary conditions or nonlinearities are involved [67]. The also numerical *finite element method* is a generalization of the classical RALEIGH-RITZ and the weighted-residual methods which may be used for the solution of differential and integral equations without the mentioned restrictions. Thus, when a set of differential equations may only be solved approximately and only with help of numerical procedures for integrations and systems equations it seems nowadays obvious to apply the finite element method right from the beginning. Apart from the costs now the exercise of one of the commercial programs for finite element analyses on modern computers, applicable for arbitrary geometries and boundary conditions, is no doubt more attractive than the demanding (re-)development of an own code which is applicable solely for one single buckling problem.

Chapter 3

Buckling Analyses with Finite Elements

The analysis of continuous structures is difficult since closed-form solutions of stress and strain distributions in continua are available only for a few basic geometries and boundary conditions. Non-uniform structures might theoretically be subdivided into small simple structural elements, but their number and the number of the junctions would be large. The basic idea behind the *finite element method* is to overcome this problem by dividing the real structure into elements of simple geometries interconnected only at a finite number of nodal points. Only at these nodes some forces are introduced which represent the distributed stresses acting on the element edges. With such a discretization, the problem is reduced to a manageable assemblage of structural elements which are also analysable by numerical procedures [84]. In mechanical engineering this tool is very commonly used and a fundamental part of a CAE¹ environment. Many commercial Finite Element (FE) programs are available with partially sophisticated graphical user interfaces with integration into CAD² software.

The *linear* FE method is the most frequent employed technological aid for stress analysis in early design phases of complex structures. In textbooks on fundamental continuum mechanics the basic expressions and equations of the linear method may be found; and also in the engineering

¹Computed Aided Engineering

²Computed Aided Design

education the linear FE method and the corresponding formulations have become an essential part. The advantages of linear analysis is fairly obvious: simple direct solutions may be obtained with no need for costly load incrementation and iterative schemes. Furthermore, solutions for various load cases may be superimposed and the number of material constants required to describe the constitutive behaviour is kept to a minimum [46]. In cases where strains and rotations of a continuum may be assumed to remain infinitesimally small a linear structural analysis in general yields reliable results. However, the significant shift in design requirements in recent years for high-performance and efficient components in modern industries (e.g. in aerospace) has made more sophisticated analyses a necessity with geometric and physical *nonlinearities* taken into account. The assessment of existing structures containing irregularities or unforeseen loadings, the determination of structural instabilities and failures, and the simulation of material processing and manufacturing may also be mentioned as possible applications of the FE method which may require a nonlinear analysis [46]. But the *nonlinear* FE method implies iterative procedures and incrementation of the loading. This load incrementation for a nonlinear analysis requires some a priori knowledge of the analysis result and the progression of the calculation. Furthermore, end-users of nonlinear FE programs defining input parameters and selecting particular, optional codes are often confronted with terms and definitions referring to numerical mathematics and nonlinear continuum mechanics. Thus, such programs—otherwise more regarded as “black-boxes”—demand some basic knowledge about the formulations and procedures it contains. That is, in contrast to linear stress analysis where for the analyst the emphasis of his work is basically placed on the generation of the geometry and element assembly, for nonlinear analyses the specification of the loadings as well as of appropriate input values is most demanding.

The mostly applied FE method for structural *stability* investigations consist of a linear static stress analysis with subsequent linear eigenvalue extraction, although the scheme of this linear analysis method may be traced back to a nonlinear FE formulation. A nonlinear, more general form of this method with eigenvalue extractions was used for the shell models discussed later which considers large displacements and rotations for the pre-buckling states of stress and deformation. This herein named *nonlinear buckling analysis* is, in contrast to the so-called *linear buckling analysis*, not a standard option in commercial FE programs; hence, possible reproduction of the results discussed in this book need some information about the numerics involved in programs which base on nonlinear FE formulations.

In this chapter the Total and Updated Lagrangian nonlinear FE formulations are reproduced, which are of importance for the nonlinear buckling analysis well as the more common linear buckling analysis. Further, the transient dynamic analysis method is described which was used for simulations of cylinder compression accounting for inertia and quasi-static loading. These formulations are detailed *not* specifically for buckling analyses but generally for any possible FE application. Their derivations and the consistently used notation follow the works of several authors, such as (BATHE [14]), (RAMM [65]), or (Doyle [31]). Further, for the common linear as well as the less known nonlinear buckling analysis the derivation of the particular eigenvalue system involved and the content of the stress stiffness matrices are explained. Finally, the application of these three types of FE schemes to numerical buckling analysis of cylindrical shells is detailed.

3.1 Basic Concept of the Finite Element Method

The finite element method is a generalization of the classical variational and weighted-residual methods introduced in Section 2.3. Basically, a given domain or structure is seen as an assemblage of simple geometric shapes, called finite elements, for which it is possible to systematically generate the approximation (or interpolation) functions needed in the analytical solution of differential equations by a variational or weighted-residual method. The finite element method is as a piecewise or element-wise application of these approximation techniques [67]. (REDDY, [67]) states seven major steps in the finite element analysis of a typical problem:

1. Discretization of the domain into a set of finite elements (*mesh generation*).
2. Weak or virtual work formulation of the differential equation over a typical finite element.
3. Development of the finite element model of the problem using its weak form. The finite element model consists of a set of algebraic equations among the unknown parameters of the element.
4. Assembly of finite elements to obtain the global system (i.e. for the total structure resp. problem).

5. Imposing of boundary conditions and loading.
6. Solution of system equations.
7. Post-computation of solution and quantities of interest.

Mathematically, the discretization of structures with finite elements denotes a replacing of the integrals over the particular region V with a sum over the N_{el} number of elements of the integrals over the domain of each element $V^{(e)}$. For instance, the virtual work expression (A.28) in Section A.4 becomes

$$\delta W = \sum_{e=1}^{N_{el}} \int_{V^{(e)}} \mathbf{r}^{(e)} \cdot \delta \mathbf{u} \, dV = 0 \quad (3.1)$$

with \mathbf{r} denoting the residual force vector and $\delta \mathbf{u}$ virtual displacement vector. Since the information on displacements are only utilized at a certain number of nodal points, for stresses and strains approximation functions are necessary to compute the displacement field in-between these points. For a general finite *volume* element at each node n three displacements ($u_1^{(n)}, u_2^{(n)}, u_3^{(n)}$) in the Cartesian coordinate directions are possible. The displacement vector \mathbf{u} and the vector $\tilde{\mathbf{u}}$ including the nodal degrees of freedom, i.e. the displacements of the N nodes of a single element may then be given by

$$\begin{aligned} \tilde{\mathbf{u}}^T &= \{u_1^{(1)}, u_2^{(1)}, u_3^{(1)}, u_1^{(2)}, u_2^{(2)}, u_3^{(2)}, \dots, u_1^{(N)}, u_2^{(N)}, u_3^{(N)}\} \quad \text{and} \\ \mathbf{u}^T &= \{u_1, u_2, u_3\} \end{aligned} \quad (3.2)$$

The displacement vector \mathbf{u} is to be calculated by use of the relation

$$\mathbf{u} = \mathbf{H} \tilde{\mathbf{u}} \quad (3.3)$$

introducing the matrix \mathbf{H} which contains the interpolation or *shape functions*. The functions in \mathbf{H} are locally defined and depend on the element *type*. The vector $\tilde{\mathbf{u}}$ containing the nodal degrees of freedom may in addition to the translations also include rotations (e.g. thick shell elements).

3.2 Static Linear Formulation

With the aid of a short derivation of a general three-dimensional finite element for the familiar linear case, the notations and expressions used in present thesis are introduced in this section for the later descriptions of the nonlinear FE formulations in the subsequent sections.

The constitution of the relevant matrices and vectors of the numerical equation system in general bases on the principle of virtual displacements (Section A.4). In the linear case the displacement gradients are assumed to be infinitesimal small; thus, possible influences of rigid body motions, i.e. translations and rotations without any change in geometry, on the stress and strain tensors are neglected. With the virtual displacement vector $\delta \mathbf{u}$, the (CAUCHY) stress vector $\{\sigma_{ij}\}$

$$\{\sigma_{ij}\}^T = \{\sigma_{11}, \sigma_{22}, \sigma_{33}, \sigma_{12}, \sigma_{23}, \sigma_{31}\}$$

and the virtual linear (ALMANZI) strain vector $\{\delta \varepsilon_{ij}\}$

$$\{\delta \varepsilon_{ij}\}^T = \{\delta \varepsilon_{11}, \delta \varepsilon_{22}, \delta \varepsilon_{33}, 2\delta \varepsilon_{12}, 2\delta \varepsilon_{23}, 2\delta \varepsilon_{31}\}$$

the virtual work *per element* of a domain may then be written in vector form:

$$\int_V \{\delta \varepsilon_{ij}\}^T \{\sigma_{ij}\} dV = \int_V \delta \mathbf{u}^T \mathbf{b} dV - \int_{A_\sigma} \delta \mathbf{u}^T \mathbf{t} dA_\sigma \quad (3.4)$$

The body of volume V is potentially loaded by body forces \mathbf{b} and forces \mathbf{t} at the fraction of its boundary surface A_σ . To get the virtual work of the entire domain, according to (3.1), the integrals above have to be replaced by the sum over the number of finite elements of the integrals over the domain of each element. For a better readability of the formulas, in the following the summation signs and the corresponding superscript indices (e) are omitted, i.e. the expressions consider only one single element.

In accordance with equation A.37 of Section A.5 the stress-strain relation is given by

$$\{\sigma_{ij}\} = \mathbf{C} \{\varepsilon_{ij}\} \quad (3.5)$$

with the material matrix \mathbf{C} . This constitutive relation enables to replace the stresses in (3.4). The virtual work expression in terms of strains and displacements then is

$$\int_V \{\delta \varepsilon_{ij}\}^T \mathbf{C} \{\varepsilon_{ij}\} dV = \int_V \delta \mathbf{u}^T \mathbf{b} dV - \int_{A_\sigma} \delta \mathbf{u}^T \mathbf{t} dA_\sigma \quad (3.6)$$

The relation between the linear strains ε_{ij} and the displacements u_i in \mathbf{u} is given by expression (A.18)

$$\varepsilon_{ij} = \frac{1}{2} \left[\frac{\partial u_i}{\partial x_j} + \frac{\partial u_j}{\partial x_i} \right]$$

In turn, as initially mentioned, the displacements \mathbf{u} are connected with the nodal point degrees of freedom $\tilde{\mathbf{u}}$ by

$$\mathbf{u} = \mathbf{H} \tilde{\mathbf{u}} .$$

The relation between the virtual displacements $\delta \mathbf{u}$ and the virtual nodal point displacements may be expressed accordingly by

$$\delta \mathbf{u} = \mathbf{H} \delta \tilde{\mathbf{u}} . \quad (3.7)$$

By spatial derivation of the local shape functions in \mathbf{H} with respect to the coordinates \mathbf{x} a matrix \mathcal{B} may be specified with which the important, direct relation between the strains and the nodal point displacements is given by

$$\{\varepsilon_{ij}\} = \mathcal{B} \tilde{\mathbf{u}} \quad (3.8)$$

and accordingly for the virtual vectors

$$\{\delta \varepsilon_{ij}\} = \mathcal{B} \delta \tilde{\mathbf{u}} . \quad (3.9)$$

The matrix \mathcal{B} has to embrace the constellation of the spatial derivatives in the strain definition. The dependency of \mathcal{B} on the element size, shape and the position of the nodes always enforces to calculate this matrix separately for each element.

With the matrices \mathbf{H} and \mathcal{B} the discretization of the virtual work expression (3.6) may be completed by replacing the strains, the virtual displacements and virtual strains by terms of the nodal point displacements using the relations (3.7) to (3.9). This gives:

$$\int_V \delta \tilde{\mathbf{u}}^T \mathcal{B}^T \mathbf{C} \mathcal{B} \tilde{\mathbf{u}} dV = \int_V \delta \tilde{\mathbf{u}}^T \mathbf{H}^T \mathbf{b} dV + \int_{A_\sigma} \delta \tilde{\mathbf{u}}^T \mathbf{H}^T \mathbf{t} dA_\sigma$$

The nodal point displacements vectors $\delta \tilde{\mathbf{u}}$ and $\tilde{\mathbf{u}}$ are constant within the integrals and may therefore be separated; viz

$$\delta \tilde{\mathbf{u}}^T \left[\int_V \mathcal{B}^T \mathbf{C} \mathcal{B} dV \right] \tilde{\mathbf{u}} = \delta \tilde{\mathbf{u}}^T \int_V \mathbf{H}^T \mathbf{b} dV + \delta \tilde{\mathbf{u}}^T \int_{A_\sigma} \mathbf{H}^T \mathbf{t} dA_\sigma \quad (3.10)$$

Furthermore, the virtual nodal displacement vector $\delta\tilde{\mathbf{u}}$ may be eliminated, since all terms are multiplied by the same vector.

Finally, released from the virtual displacements $\delta\tilde{\mathbf{u}}$, the virtual work equation (3.10) above provides the common numerical system of equations:

$$\mathbf{K} \tilde{\mathbf{u}} = \mathbf{p} \quad (3.11)$$

introducing the system stiffness matrix \mathbf{K} and the force vector \mathbf{p} with:

$$\begin{aligned} \mathbf{K} &= \sum_{e=1}^{N_{el}} \int_{V^{(e)}} \mathbf{B}^{(e)T} \mathbf{C}^{(e)} \mathbf{B}^{(e)} dV \\ \mathbf{p} &= \sum_{e=1}^{N_{el}} \int_{V^{(e)}} \mathbf{H}^{(e)T} \mathbf{b}^{(e)} dV + \sum_{e=1}^{N_{el}} \int_{A_{\sigma}^{(e)}} \mathbf{H}^{(e)T} \mathbf{t}^{(e)} dA_{\sigma} \end{aligned} \quad (3.12)$$

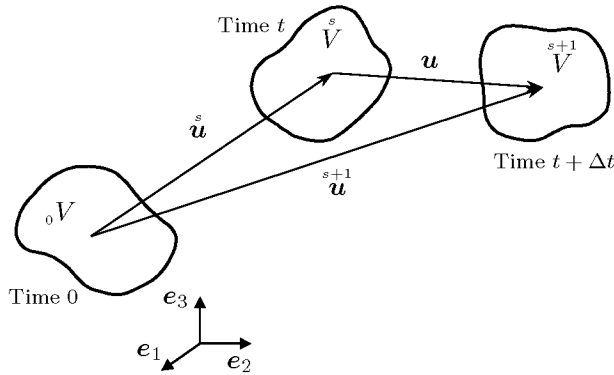
In the main equation system $\mathbf{K} \tilde{\mathbf{u}} = \mathbf{p}$ the label $\tilde{\mathbf{u}}$ stands for the unknown nodal point displacements of the entire model whereas in the preceding equations $\tilde{\mathbf{u}}$ denotes only the nodal displacements of a single element. According to this and (3.1), the definitions in (3.12) indicate the assembly of all elements of the model.

To receive the numerical system of equation the integrals in (3.12) have to be processed using suitable numerical integration techniques, for instance the GAUSS quadrature. The numerical integration methods are not discussed herein. For details attention is invited to the literature on FE methods, e.g. Ref. [84], [14], [52], or [53].

3.3 Static Nonlinear Formulations

In a nonlinear FE analysis possible changes of the stiffness matrix during the deformation process are considered, i.e. in contrast to the linear case the matrix \mathbf{K} in Equation (3.11) is not independent of the unknown displacements $\tilde{\mathbf{u}}$. Therefore, the now nonlinear equilibrium equation at a given load level cannot be solved directly. To overcome this problem the given load level is divided into a number of load steps or increments. The searched total displacements are then approximated by a chain of displacement increments which are obtained by solving the linearized equilibrium equation step-wise. The derivation of these linearized equilibrium equations results similar to the linear FE formulation in Section 3.2 from the use of the principle of virtual displacements described in Section A.4.

Many nonlinear FE programs are based on some form of LAGRANGIAN description of equilibrium [46]. A further formulation effective for the dealing of structures that undergo relatively large rotations but small strains is the *corotational* scheme [31]. In this method a local coordinate system is defined which moves with each element, and relatively to this coordinate system the element behaves linearly. Thus, the nonlinearities (rotations) of the problem are managed with the description of the moving (rotating) coordinates [31]. But, since the corotational scheme was not implemented in the codes mainly used for the FE analyses discussed herein this method is not further addressed. Instead, the Total Lagrangian and the Updated Lagrangian formulations are used and explained. In a **Total Lagrange** formulation the integrals in the virtual work expression are calculated with respect to the initial, undeformed configuration of the structure at time = 0. In an **Updated Lagrange** formulation the last known deformed configuration at time = t is alternatively taken as an initial state, and during the calculation proceeds, the reference state is continually updated. Since the Updated Lagrangian formulation may be understood as a variant of the Total Lagrangian formulation in the following this basis variant is primarily described. Like the linear FE formulation above the two formulations of nonlinear FE analysis are reproduced in detail to introduce the particular stiffness matrices, the force and the displacement vectors, and their different components. These matrices and vectors, all denoted in consistent notation, will later be used to describe the derivation to the system equations for buckling analyses with finite element models.

Figure 3.1: *Incremental decomposition of displacement*

3.3.1 Total Lagrangian Formulation

In the nonlinear scheme the virtual work expressions of equilibrium are nonlinear as regards the displacements \mathbf{u} . In Figure 3.1 an arbitrary body is shown which is displaced and distorted during a deformation process from its undeformed state at time = 0 to a new, yet *unknown* configuration at time $t + \Delta t$. Following the principle of dividing the nonlinear deformation process into small increments at time t the body is situated in a state for which the equilibrium equation is already evaluated. At this state, the solution for displacements, which satisfy the equilibrium equation at a time step Δt later, have to be found. To linearize the nonlinear equilibrium expression with respect to the initial configuration, the virtual work equation (A.33) in Section A.4 is transformed into a 1st order TAYLOR series approximation in time [46], viz:

$$\int_{{}_0V} {}_0\mathbf{r} \cdot \delta \mathbf{u}_0 dV \Big|_{t+\Delta t} = \int_{{}_0V} {}_0\mathbf{r} \cdot \delta \mathbf{u}_0 dV \Big|_t + \frac{D}{Dt} \left(\int_{{}_0V} {}_0\mathbf{r} \cdot \delta \mathbf{u}_0 dV \right)_t \Delta t = 0 \quad (3.13)$$

The terms in right side of the expression above are known at time t and linear with regard to Δt . In principle, only the derivative $D()/Dt$ of the virtual work expression (A.35) has to be defined to receive the searched incremental formulation. A desired deviation in time would lead to an inclusion of velocities $\dot{\mathbf{u}}$ in the virtual work expression. To avoid this, finite increments in displacements are considered with $\Delta \mathbf{u} = \dot{\mathbf{u}} \Delta t$ which

in turn provoke increments of the 2nd PIOLA-KIRCHHOFF stress ΔS .

Since the formulations presented in this section consider static and not dynamic problems, the time is introduced only as a parameter which controls the process of deformation. In static nonlinear FE analyses “ t ” is only regarded as “pseudo time” and is only useable as an orientation help. Inertia loads are not considered. Consequently, similar to the loading and the displacement the considered time span is divided into s time increments. To emphasize the difference in the numerical system, in the subsequent formulations “time” and therefore also the label t are replaced by terms of the increment number s .

For the description of the incremental formulations a special index notation is introduced: *indices down left* of a label mark the increment number of the reference state³ and *indices at the head* of a label mark the current increment. Thus, the coordinates of the body in Figure 3.1 at step s with known state and at step $s + 1$ with yet unknown state are

$$\begin{aligned} \overset{s}{\mathbf{x}} &= \mathbf{X} + \overset{s}{\mathbf{u}} & \text{and} \\ \overset{s+1}{\mathbf{x}} &= \mathbf{X} + \overset{s+1}{\mathbf{u}} \end{aligned} \quad (3.14)$$

respectively, introducing the corresponding *total displacements* $\overset{s}{\mathbf{u}}$ and $\overset{s+1}{\mathbf{u}}$ [14].

In order to abbreviate the formulations the increments in displacements, strains and stresses are labeled without a greek capital letter Δ often used in this context. Thus, without any index a *displacement increment* is defined by (see Fig. 3.1)

$$\mathbf{u} = \overset{s+1}{\mathbf{x}} - \overset{s}{\mathbf{x}} \quad (3.15)$$

and consequently, the total displacements in (3.14) are given by

$$\overset{s+1}{\mathbf{u}} = \overset{s}{\mathbf{u}} + \mathbf{u} \quad (3.16)$$

In the present formulation it is assumed that the state is known at increment s (i.e. at “real” time t) and the basic unknown is the displacement increment \mathbf{u} . The incremental decomposition of displacements (3.16) may be used to decompose the GREEN-LAGRANGE strains similarly [31]. Following (A.15) in Section A.2, the strain tensor at increment s is given by

$${}_{\circ}\overset{s}{\mathbf{E}} = \frac{1}{2} \left[\left(\frac{\partial \overset{s}{\mathbf{u}}}{\partial \mathbf{X}} \right) + \left(\frac{\partial \overset{s}{\mathbf{u}}}{\partial \mathbf{X}} \right)^T + \left(\frac{\partial \overset{s}{\mathbf{u}}}{\partial \mathbf{X}} \right)^T \cdot \left(\frac{\partial \overset{s}{\mathbf{u}}}{\partial \mathbf{X}} \right) \right] \quad (3.17)$$

³exception: the material coordinates ${}_{\circ}\mathbf{x} \equiv \mathbf{X}$; see (A.1) in Section A.1.

And accordingly at increment $s + 1$ replacing $\overset{s+1}{\mathbf{u}}$ by $(\overset{s}{\mathbf{u}} + \mathbf{u})$

$$\begin{aligned} \overset{s+1}{\mathbf{E}} &= \frac{1}{2} \left[\left(\frac{\partial \overset{s+1}{\mathbf{u}}}{\partial \mathbf{X}} \right) + \left(\frac{\partial \overset{s+1}{\mathbf{u}}}{\partial \mathbf{X}} \right)^T + \left(\frac{\partial \overset{s+1}{\mathbf{u}}}{\partial \mathbf{X}} \right)^T \cdot \left(\frac{\partial \overset{s+1}{\mathbf{u}}}{\partial \mathbf{X}} \right) \right] \\ &= \frac{1}{2} \left[\left(\frac{\partial \overset{s}{\mathbf{u}}}{\partial \mathbf{X}} + \frac{\partial \mathbf{u}}{\partial \mathbf{X}} \right) + \left(\frac{\partial \overset{s}{\mathbf{u}}}{\partial \mathbf{X}} + \frac{\partial \mathbf{u}}{\partial \mathbf{X}} \right)^T \right. \\ &\quad \left. + \left(\frac{\partial \overset{s}{\mathbf{u}}}{\partial \mathbf{X}} + \frac{\partial \mathbf{u}}{\partial \mathbf{X}} \right)^T \cdot \left(\frac{\partial \overset{s}{\mathbf{u}}}{\partial \mathbf{X}} + \frac{\partial \mathbf{u}}{\partial \mathbf{X}} \right) \right] \end{aligned} \quad (3.18)$$

After multiplication and rearrangement the decomposed strain relation may be rewritten in abbreviated form as

$$\overset{s+1}{\mathbf{E}} = \overset{s}{\mathbf{E}} + \overset{s}{\mathbf{E}} + \overset{s}{\boldsymbol{\eta}} \quad (3.19)$$

introducing the *linear strain increments* $\overset{s}{\mathbf{E}}$ and the *nonlinear strain increments* $\overset{s}{\boldsymbol{\eta}}$, respectively, by

$$\begin{aligned} \overset{s}{\mathbf{E}} &= \frac{1}{2} \left[\left(\frac{\partial \mathbf{u}}{\partial \mathbf{X}} \right) + \left(\frac{\partial \mathbf{u}}{\partial \mathbf{X}} \right)^T + \left(\frac{\partial \overset{s}{\mathbf{u}}}{\partial \mathbf{X}} \right)^T \cdot \left(\frac{\partial \mathbf{u}}{\partial \mathbf{X}} \right) + \left(\frac{\partial \mathbf{u}}{\partial \mathbf{X}} \right)^T \cdot \left(\frac{\partial \overset{s}{\mathbf{u}}}{\partial \mathbf{X}} \right) \right] \\ \overset{s}{\boldsymbol{\eta}} &= \frac{1}{2} \left[\left(\frac{\partial \mathbf{u}}{\partial \mathbf{X}} \right)^T \cdot \left(\frac{\partial \mathbf{u}}{\partial \mathbf{X}} \right) \right] \end{aligned} \quad (3.20)$$

It must be pointed out that $\overset{s}{\mathbf{E}}$ is an increment of strain from the current state but referenced to the initial configuration. $\overset{s}{\mathbf{E}}$ is linear in \mathbf{u} but contains also components of the current total displacements $\overset{s}{\mathbf{u}}$. The *nonlinear* term $\overset{s}{\boldsymbol{\eta}}$ finally contains only unknown displacements increments \mathbf{u} [31, 14].

As described in Section A.5, the constitutive relation between the 2nd PIOLA-KIRCHHOFF stress tensor $\overset{s}{\mathbf{S}}$ and the GREEN-LAGRANGE strain tensor $\overset{s}{\mathbf{E}}$ at increment s with respect to the initial state is given by

$$\overset{s}{\mathbf{S}} = \overset{s}{\mathbf{C}} : \overset{s}{\mathbf{E}} \quad (3.21)$$

with the (linear-elastic) material tensor $\overset{s}{\mathbf{C}}$. The corresponding constitutive relation at step $s + 1$ is obtained after expansion by the strain

increments of (3.20) as

$$\begin{aligned}
 {}_0\mathbf{S}^{s+1} &= {}_0\mathbf{C} : {}_0\mathbf{E}^{s+1} \\
 &= {}_0\mathbf{C} : {}_0\overset{s}{\mathbf{E}} + {}_0\mathbf{C} : \left({}_0\mathbf{E} + {}_0\boldsymbol{\eta} \right) \\
 &= {}_0\overset{s}{\mathbf{S}} + {}_0\mathbf{S}
 \end{aligned} \tag{3.22}$$

Thus, the stresses to be specified are the current stresses ${}_0\overset{s}{\mathbf{S}}$ plus a stress increment ${}_0\mathbf{S}$ [31].

With the defined stress and strain increments the nonlinear virtual work equilibrium expression may be decomposed into already calculated terms and a searched, incremental term of change. Considering expression (A.35) in Section A.4, the virtual work at increment $s+1$ may be written as

$$\begin{aligned}
 \int_{{}_0V} {}_0\overset{s+1}{\mathbf{S}} : \delta_{{}_0}\overset{s+1}{\mathbf{E}} \, {}_0dV &= \int_{{}_0V} {}_0\overset{s+1}{\mathbf{b}} \cdot \delta\mathbf{u} \, {}_0dV + \int_{{}_0A_\sigma} {}_0\overset{s+1}{\mathbf{t}} \cdot \delta\mathbf{u} \, {}_0dA_\sigma \\
 \delta_{{}_0}U^{s+1} &= \delta_{{}_0}W_{ex}^{s+1}
 \end{aligned} \tag{3.23}$$

The body forces ${}_0\overset{s+1}{\mathbf{b}}$ and surface loads ${}_0\overset{s+1}{\mathbf{t}}$ at step $s+1$ in the integrals of the virtual external work $\delta_{{}_0}W_{ex}^{s+1}$ are assumed to be conservative and to contain known values. Thus, only the virtual strain energy $\delta_{{}_0}U^{s+1}$ includes unknown real values and is to be incrementally decomposed: the virtual strain $\delta_{{}_0}\overset{s+1}{\mathbf{E}}$ is, according to (3.19), given by

$$\delta_{{}_0}\overset{s+1}{\mathbf{E}} = \delta_{{}_0}\overset{s}{\mathbf{E}} + \delta({}_0\mathbf{E} + {}_0\boldsymbol{\eta}) = 0 + \delta({}_0\mathbf{E} + {}_0\boldsymbol{\eta}) \tag{3.24}$$

respecting that a variation of the real, given strains ${}_0\overset{s}{\mathbf{E}}$ vanishes. Now, the subdivided stress and strain expressions in (3.22) and (3.24) may be inserted in the left hand side, i.e. the virtual strain energy term of (3.23), which yields

$$\begin{aligned}
 \int_{{}_0V} \left({}_0\overset{s}{\mathbf{S}} + {}_0\mathbf{S} \right) : \delta({}_0\mathbf{E} + {}_0\boldsymbol{\eta}) \, {}_0dV &= \delta_{{}_0}W_{ex}^{s+1} \\
 \text{and expanded:} \\
 \int_{{}_0V} {}_0\overset{s}{\mathbf{S}} : \delta_{{}_0}\overset{s}{\mathbf{E}} \, {}_0dV + \int_{{}_0V} {}_0\overset{s}{\mathbf{S}} : \delta_{{}_0}\boldsymbol{\eta} \, {}_0dV & \\
 + \int_{{}_0V} {}_0\mathbf{S} : \delta_{{}_0}\overset{s}{\mathbf{E}} \, {}_0dV + \int_{{}_0V} {}_0\mathbf{S} : \delta_{{}_0}\boldsymbol{\eta} \, {}_0dV &= \delta_{{}_0}W_{ex}^{s+1}
 \end{aligned} \tag{3.25}$$

This lengthy expression is slightly simplified by introducing an important approximation which subserves a linearization: the nonlinear strain increments ${}_0\boldsymbol{\eta}$ are considered to be small compared to the linear strain increments ${}_0\mathbf{E}$, thus the last integral in (3.25), including the pair of ${}_0\boldsymbol{\eta}$ and the stress increment ${}_0\mathbf{S}$, is neglected:

$${}_0\boldsymbol{\eta} \ll {}_0\mathbf{E} \quad \rightarrow \quad \int_{{}_0V} {}_0\mathbf{S} : \delta {}_0\boldsymbol{\eta} \, dV \approx 0 \quad (3.26)$$

Assuming that the constitutive relation (A.36) in Section A.5 with the linear-elastic material tensor ${}_0\mathbf{C}$ is also valid for terms of increments, the stress increment may be replaced by this expression involving a strain increment:

$${}_0\mathbf{S} \approx {}_0\mathbf{C} : {}_0\mathbf{E} \quad (3.27)$$

The virtual work expression may then be written as

$$\begin{aligned} \int_{{}_0V} {}_0\overset{s}{\mathbf{S}} : \delta {}_0\mathbf{E} \, dV + \int_{{}_0V} {}_0\overset{s}{\mathbf{S}} : \delta {}_0\boldsymbol{\eta} \, dV \\ + \int_{{}_0V} {}_0\mathbf{C} : {}_0\mathbf{E} : \delta {}_0\mathbf{E} \, dV = \delta {}_0\overset{s+1}{W}_{ex} \end{aligned} \quad (3.28)$$

which may further be rearranged to

$$\begin{aligned} \int_{{}_0V} {}_0\overset{s}{\mathbf{S}} : \delta {}_0\boldsymbol{\eta} \, dV + \int_{{}_0V} {}_0\mathbf{C} : {}_0\mathbf{E} : \delta {}_0\mathbf{E} \, dV = \\ \delta {}_0\overset{s+1}{W}_{ex} - \int_{{}_0V} {}_0\overset{s}{\mathbf{S}} : \delta {}_0\mathbf{E} \, dV \end{aligned} \quad (3.29)$$

This is the virtual work equation in terms of displacement increments \mathbf{u} at the left hand side, whereas at the right hand side essentially there are terms of load increments.

For the derivation of the nonlinear Finite Element formulation the expression above is to be converted similarly to the linear static FE method in Section 3.2. Again, the relevant steps of the discretization are demonstrated for an isoparametric, three-dimensional element as a general example. In so-called *isoparametric* elements the nodal point coordinates specify the spatial configuration of the element by means of the same approximation (*shape functions* \mathbf{H}) as the displacement field and the nodal point degrees of freedom are related. Therefore, the material coordinate vector of the initial configuration \mathbf{X} may be expressed in terms of the nodal point coordinates by

$$\mathbf{X} = \mathbf{H} \, {}_0\bar{\mathbf{x}} \quad (3.30)$$

As aforementioned, the displacement field vectors \mathbf{u} and $\delta\mathbf{u}$ are connected with the nodal point degrees of freedom vectors

$$\mathbf{u} = \mathbf{H} \tilde{\mathbf{u}} \quad \text{resp.} \quad \delta\mathbf{u} = \mathbf{H} \delta\tilde{\mathbf{u}}, \quad (3.31)$$

see Equation (3.3).

In accordance with Equations (3.20) the linear virtual strain increment $\delta_0\mathbf{E}$ and the nonlinear virtual strain increment $\delta_0\boldsymbol{\eta}$ are

$$\begin{aligned} \delta_0\mathbf{E} &= \frac{1}{2} \left[\left(\frac{\partial\delta\mathbf{u}}{\partial\mathbf{X}} \right) + \left(\frac{\partial\delta\mathbf{u}}{\partial\mathbf{X}} \right)^T + \left(\frac{\partial\dot{\mathbf{u}}}{\partial\mathbf{X}} \right)^T \cdot \left(\frac{\partial\delta\mathbf{u}}{\partial\mathbf{X}} \right) + \left(\frac{\partial\delta\mathbf{u}}{\partial\mathbf{X}} \right)^T \cdot \left(\frac{\partial\dot{\mathbf{u}}}{\partial\mathbf{X}} \right) \right] \\ \delta_0\boldsymbol{\eta} &= \frac{1}{2} \left[\left(\frac{\partial\delta\mathbf{u}}{\partial\mathbf{X}} \right)^T \cdot \left(\frac{\partial\mathbf{u}}{\partial\mathbf{X}} \right) + \left(\frac{\partial\mathbf{u}}{\partial\mathbf{X}} \right)^T \cdot \left(\frac{\partial\delta\mathbf{u}}{\partial\mathbf{X}} \right) \right] \end{aligned} \quad (3.32)$$

Again due to the chain rule, the nonlinear virtual strain expression $\delta_0\boldsymbol{\eta}$ contains derivatives of the unknown (real) displacements increments \mathbf{u} ; and similar to the strain increment the linear virtual strain term $\delta_0\mathbf{E}$ includes components of the current total displacements $\dot{\mathbf{u}}$.

Corresponding to the derivatives of the displacements with respect to the coordinates \mathbf{X} the derivatives of shape functions \mathbf{H} are positioned in special matrices, which specify the relations between the (virtual) strain increments and the (virtual) nodal point degrees of freedom (see Eqs.(3.20) and (3.32)). That is,

$${}_0\mathbf{E} \Rightarrow {}_0\overset{s}{\mathcal{B}}_l \tilde{\mathbf{u}} \quad \text{resp.} \quad \delta_0\mathbf{E} \Rightarrow {}_0\overset{s}{\mathcal{B}}_l \delta\tilde{\mathbf{u}} \quad (3.33)$$

As already mentioned, the ${}_0\mathcal{B}$ -matrices depend on the element geometry and the position of the nodes and have to be specified separately for each element of the model. The matrix ${}_0\overset{s}{\mathcal{B}}_l$ may be split into a matrix, e.g. ${}_0\overset{s}{\mathcal{B}}_{l0}$, which refers to the small strain part in ${}_0\mathbf{E}$ and a matrix, e.g. ${}_0\overset{s}{\mathcal{B}}_{lu}$, which considers the *initial displacement* part, hence

$${}_0\overset{s}{\mathcal{B}}_l = {}_0\overset{s}{\mathcal{B}}_{l0} + {}_0\overset{s}{\mathcal{B}}_{lu} \quad (3.34)$$

The first matrix, ${}_0\overset{s}{\mathcal{B}}_{l0}$, corresponds to the matrix \mathcal{B} of the linear FE formulation (see Section 3.2) but with derivatives which refer to the material coordinates instead of to the spatial ones.

The second integral in (3.29) may be transformed by arranging the components of the tensors into matrices:

$$\int_{\mathcal{V}} \mathbf{C} : \mathbf{E} : \delta \mathbf{E} dV \Rightarrow \int_{\mathcal{V}} \delta \tilde{\mathbf{u}}^T \mathbf{B}_l^s \mathbf{C} \mathbf{B}_l^s \tilde{\mathbf{u}} dV \quad (3.35)$$

In order to replace the tensorial scalar product into corresponding products of vectors and matrices the displacement derivatives are rearranged into vectors and matrices. The stresses are placed into a specifically shaped stress matrix [14, 27], all with respect to the constellations of the components given by the definition of the nonlinear strain increment $\delta \boldsymbol{\eta}$. Thus

$$\int_{\mathcal{V}} \mathbf{S} : \delta \boldsymbol{\eta} dV \Rightarrow \int_{\mathcal{V}} \left\{ \frac{\partial \delta u_i}{\partial x_j} \right\}^T \mathbf{S} \left\{ \frac{\partial u_i}{\partial x_j} \right\} dV \quad (3.36)$$

The vectors with the derivatives of the (virtual) displacements, in turn, are replaced by terms of the (virtual) nodal point displacement vector:

$$\left\{ \frac{\partial u_i}{\partial x_j} \right\} = \mathbf{B}_{nl}^s \tilde{\mathbf{u}} \quad \text{resp.} \quad \left\{ \frac{\partial \delta u_i}{\partial x_j} \right\} = \mathbf{B}_{nl}^s \delta \tilde{\mathbf{u}} \quad (3.37)$$

With the new matrices the integral may be expressed in matrix form as

$$\int_{\mathcal{V}} \left\{ \frac{\partial \delta u_i}{\partial x_j} \right\}^T \mathbf{S} \left\{ \frac{\partial u_i}{\partial x_j} \right\} dV \Rightarrow \int_{\mathcal{V}} \delta \tilde{\mathbf{u}}^T \mathbf{B}_{nl}^s \mathbf{S} \mathbf{B}_{nl}^s \tilde{\mathbf{u}} dV \quad (3.38)$$

The index “*nl*” is appended to point out the nonlinearity which rules the matrices in (3.38).

The stress components placed into a vector \mathbf{S} , together with the already introduced strain-displacement transformation matrix \mathbf{B}_l^s the last integral in (3.29) may finally also be rewritten in matrix form as

$$\int_{\mathcal{V}} \mathbf{S} : \delta \mathbf{E} dV \Rightarrow \int_{\mathcal{V}} \delta \tilde{\mathbf{u}}^T \mathbf{B}_l^s \{ \mathbf{S}_{ij}^s \} dV \quad (3.39)$$

The virtual external work terms in (3.23) are transformed in the same manner than it was demonstrated for the linear case (Eqs. (3.4) to (3.10)). Consequently, in matrix form the virtual work at increment $s + 1$ is given by

$$\delta_0 W_{ex}^{s+1} = \int_{\mathcal{V}} \delta \tilde{\mathbf{u}}^T \mathbf{H}^T \mathbf{b}^{s+1} dV + \int_{A_\sigma} \delta \tilde{\mathbf{u}}^T \mathbf{H}^T \mathbf{t}^{s+1} dA_\sigma \quad (3.40)$$

In conclusion, the total virtual work at increment s may be expressed in matrix form by

$$\begin{aligned} \delta \tilde{\mathbf{u}}^T \int_{\circ V} \circ \mathbf{B}_{nl}^{\circ s T} \circ \mathbf{S}^{\circ s} \circ \mathbf{B}_{nl}^{\circ s} \circ dV \tilde{\mathbf{u}} + \delta \tilde{\mathbf{u}}^T \int_{\circ V} \circ \mathbf{B}_l^{\circ s T} \circ \mathbf{C}^{\circ s} \circ \mathbf{B}_l^{\circ s} \circ dV \tilde{\mathbf{u}} = \\ \delta \tilde{\mathbf{u}}^T \int_{\circ V} \mathbf{H}^T \circ \mathbf{b}^{\circ s+1} \circ dV + \delta \tilde{\mathbf{u}}^T \int_{\circ A_\sigma} \mathbf{H}^T \circ \mathbf{t}^{\circ s+1} \circ dA_\sigma \quad (3.41) \\ - \delta \tilde{\mathbf{u}}^T \int_{\circ V} \circ \mathbf{B}_l^{\circ s T} \{ \circ S_{ij}^{\circ s} \} \circ dV \end{aligned}$$

According to (3.10) the virtual displacements $\delta \tilde{\mathbf{u}}$ are separated and may subsequently be eliminated. As desired, the strain energy expression are now written in terms of the known configuration at increment s . At this step, the integrals are to be evaluated for step $s+1$ considering the given external work expressions.

In accordance with the linear FE formulation the numerical system of equation in the **Total Lagrangian formulation** is given in short form by

$$\left[\circ \mathbf{K}_{nl}^{\circ s} + \circ \mathbf{K}_l^{\circ s} \right] \tilde{\mathbf{u}} = \mathbf{p}^{\circ s+1} - \circ \mathbf{f}^{\circ s} \quad (3.42)$$

with (for one element)

$$\circ \mathbf{K}_l^{\circ s} = \int_{\circ V} \circ \mathbf{B}_l^{\circ s T} \circ \mathbf{C}^{\circ s} \circ \mathbf{B}_l^{\circ s} \circ dV \quad (3.43)$$

$$\circ \mathbf{K}_{nl}^{\circ s} = \int_{\circ V} \circ \mathbf{B}_{nl}^{\circ s T} \circ \mathbf{S}^{\circ s} \circ \mathbf{B}_{nl}^{\circ s} \circ dV \quad (3.44)$$

$$\circ \mathbf{f}^{\circ s} = \int_{\circ V} \circ \mathbf{B}_l^{\circ s T} \{ \circ S_{ij}^{\circ s} \} \circ dV \quad (3.45)$$

$$\mathbf{p}^{\circ s+1} = \int_{\circ V} \mathbf{H}^T \circ \mathbf{b}^{\circ s+1} \circ dV + \int_{\circ A_\sigma} \mathbf{H}^T \circ \mathbf{t}^{\circ s+1} \circ dA_\sigma \quad (3.46)$$

where $\circ \mathbf{K}_l^{\circ s}$ and $\circ \mathbf{K}_{nl}^{\circ s}$ are the linear stiffness and the nonlinear stiffness matrices, respectively, and $\circ \mathbf{f}^{\circ s}$ and $\mathbf{p}^{\circ s+1}$ denote the internal resisting force and the external force vectors, respectively.

These are the formulas for the numerical system of equation for one single element. For the assembly of all elements of the model ("mesh") the matrices and vectors of the elements are accordingly added up. Again, to

avoid an “overdose” of indices in the formulations the element identifier and the sum label were omitted (see Eq. (3.12)).

3.3.2 Updated Lagrangian Formulation

In the previous formulation all kinematic variables are referred to the initial unloaded configuration. In accordance with the considerations on nonlinear continuum mechanics in Appendix A, where in a LAGRANGIAN description all behaviour is expressed with respect to the initial coordinates, the relations presented above correspond to the so-called *Total Lagrange* formulation. The equilibrium equations at step $s + 1$ are approximatively solved by referring all variables to an already calculated and thus known configuration which is in equilibrium. In addition to the initially undeformed configuration also the states between increment 0 and s are already known and could consequently be used as reference. Hence, the so-called *Updated Lagrange* formulation bases on the same methods as the Total Lagrange formulation uses, but in the Updated Lagrange formulation all kinematic variables refer to the configuration at increment s . The coordinate system remains unchanged, only new coordinate or position vectors provide with the displacement vectors. In the following, with the derivation steps already shown for the preceding Total Lagrange formulation, the relevant differences to the Updated Lagrange formulation are described herein.

Now the coordinates of the unknown state $s + 1$ are

$$\mathbf{x}^{s+1} = \mathbf{x}^s + \mathbf{u} \quad (3.47)$$

According to the notation introduced with Equation (3.14) the reference coordinates are given by: ${}_s\mathbf{x}$.

Consequently, the unknown *total displacements* \mathbf{u}^{s+1} are defined by

$$\mathbf{u}^{s+1} \equiv \mathbf{u} \quad (3.48)$$

which simplifies the incremental decomposition of the GREEN-LAGRANGE strain tensor significantly. Namely, the strain tensor at increment $s + 1$ in present case is given by

$${}_s\mathbf{E}^{s+1} = \frac{1}{2} \left[\left(\frac{\partial \mathbf{u}}{\partial {}_s\mathbf{x}} \right) + \left(\frac{\partial \mathbf{u}}{\partial {}_s\mathbf{x}} \right)^T + \left(\frac{\partial \mathbf{u}}{\partial {}_s\mathbf{x}} \right)^T \cdot \left(\frac{\partial \mathbf{u}}{\partial {}_s\mathbf{x}} \right) \right] \quad (3.49)$$

or in abbreviated form

$${}_s\mathbf{E}^{s+1} = {}_s\mathbf{E} + {}_s\boldsymbol{\eta} \quad (3.50)$$

In contrast to the Total Lagrangian formulation (see Eqs. (3.18) to (3.20)) the *linear* strain increment ${}_s\mathbf{E}$ does not include components of already known total displacements ${}^s\mathbf{u}$. The *nonlinear* term ${}_s\boldsymbol{\eta}$ in turn contains only unknown displacement increments \mathbf{u} .

The incremental decomposition of the GREEN-LAGRANGE stresses (see Eq. 3.22) yields in this case:

$${}_s\mathbf{S}^{s+1} = \boldsymbol{\sigma} + {}_s\mathbf{S} \quad (3.51)$$

whereby the already known stresses are identical to CAUCHY stresses $\boldsymbol{\sigma}$ due to the fact that it applies: ${}_s\mathbf{S} \equiv \boldsymbol{\sigma}$.

With these relations the virtual work expression (resp. the virtual strain energy part) in (3.25) for the Updated Lagrangian formulation may be written in expanded form as

$$\begin{aligned} \int_{{}_sV} \boldsymbol{\sigma} : \delta {}_s\mathbf{E} {}_s dV + \int_{{}_sV} \boldsymbol{\sigma} : \delta {}_s\boldsymbol{\eta} {}_s dV \\ + \int_{{}_sV} {}_s\mathbf{S} : \delta {}_s\mathbf{E} {}_s dV + \int_{{}_sV} {}_s\mathbf{S} : \delta {}_s\boldsymbol{\eta} {}_s dV = \delta {}_s W_{ex}^{s+1} \end{aligned} \quad (3.52)$$

Similar to the Total Lagrangian formulation the term with product of the stress increment and the nonlinear strain increment is neglected. Consequently, the approximation in this case is the following:

$${}_s\boldsymbol{\eta} \ll {}_s\mathbf{E} \quad \rightarrow \quad \int_{{}_sV} {}_s\mathbf{S} : \delta {}_s\boldsymbol{\eta} {}_0 dV \approx 0 \quad (3.53)$$

Again, the stress increment can be expressed in terms of strains using the following constitutive relation:

$${}_s\mathbf{S} \approx {}_s\mathbf{C} : {}_s\mathbf{E} \quad (3.54)$$

The virtual work expression in terms of displacements on the one side and in terms of loads of the other side (see Eq. (3.29)) is consequently given by

$$\begin{aligned} \int_{{}_sV} \boldsymbol{\sigma} : \delta {}_s\boldsymbol{\eta} {}_s dV + \int_{{}_sV} {}_s\mathbf{C} : {}_s\mathbf{E} : \delta {}_s\mathbf{E} {}_s dV = \\ \delta {}_s W_{ex}^{s+1} - \int_{{}_sV} \boldsymbol{\sigma} : \delta {}_s\mathbf{E} {}_s dV \end{aligned} \quad (3.55)$$

The needed steps of discretization may be conducted accordingly to the Total Lagrangian formulation. Thus, for a general three-dimensional isoparametric element, the reference coordinates ${}_s\mathbf{x}$ are expressed in terms of the corresponding nodal point coordinates ${}_s\tilde{\mathbf{x}}$ by

$${}_s\mathbf{x} = \mathbf{H} {}_s\tilde{\mathbf{x}} \quad (3.56)$$

with the shape functions in \mathbf{H} (see Eq. (3.3)). The relations between the (virtual) displacement fields and the (virtual) nodal point degrees of freedom are identical to those of the Total Lagrangian formulation:

$$\mathbf{u} = \mathbf{H} \tilde{\mathbf{u}} \quad \text{resp.} \quad \delta\mathbf{u} = \mathbf{H} \delta\tilde{\mathbf{u}} \quad (3.57)$$

The derivatives of the shape functions \mathbf{H} with respect to the coordinates ${}_s\mathbf{x}$ are positioned in matrices accordingly to the displacement derivatives in the strain increment expressions. Thus, with (3.50) and with

$$\delta_s \mathbf{E} = \frac{1}{2} \left[\left(\frac{\partial \delta \mathbf{u}}{\partial {}_s \mathbf{x}} \right) + \left(\frac{\partial \delta \mathbf{u}}{\partial {}_s \mathbf{x}} \right)^T \right] \quad (3.58)$$

the following transformations are introduced:

$${}_s \mathbf{E} \Rightarrow {}_s \mathbf{B}_l \tilde{\mathbf{u}} \quad \text{resp.} \quad \delta_s \mathbf{E} \Rightarrow {}_s \mathbf{B}_l \delta \tilde{\mathbf{u}} \quad (3.59)$$

As already mentioned, in contrast to the Total Lagrangian formulation, in the Updated Lagrangian formulation the (virtual) linear strain increments do not include any terms of initial displacements (see Eq. (3.34)).

Similar to the Total Lagrangian formulation, in consequence of the chain rule the nonlinear strain increments are given by

$$\delta_s \boldsymbol{\eta} = \frac{1}{2} \left[\left(\frac{\partial \delta \mathbf{u}}{\partial {}_s \mathbf{x}} \right)^T \cdot \left(\frac{\partial \mathbf{u}}{\partial {}_s \mathbf{x}} \right) + \left(\frac{\partial \mathbf{u}}{\partial {}_s \mathbf{x}} \right)^T \cdot \left(\frac{\partial \delta \mathbf{u}}{\partial {}_s \mathbf{x}} \right) \right] \quad (3.60)$$

In accordance with Eqs. (3.36) to (3.38) in the Total Lagrangian formulation, for the discretization of the first integral of the virtual work in (3.55) the derivatives of the (virtual) displacements are expressed in terms of nodal point displacements as

$$\left\{ \frac{\partial u_i}{\partial {}_s x_j} \right\} = {}_s \mathbf{B}_{nl} \tilde{\mathbf{u}} \quad \text{and} \quad \left\{ \frac{\partial \delta u_i}{\partial {}_s x_j} \right\} = {}_s \mathbf{B}_{nl} \delta \tilde{\mathbf{u}} \quad (3.61)$$

Consequently the transformation is given by

$$\int_{sV} \boldsymbol{\sigma} : \delta_s \boldsymbol{\eta}_s dV \Rightarrow \int_{sV} {}_s \mathbf{B}_{nl}^s T [\sigma_{ij}]_s {}_s \mathbf{B}_{nl}^s dV \quad (3.62)$$

All transformation matrices are now specified (see Eqs. (3.39) to (3.41)), thus the entire virtual work equation may be expressed in terms of nodal point displacements. Finally, after elimination of the virtual displacements $\delta \tilde{\mathbf{u}}$, the relevant **Updated Lagrangian** numerical equations system at increment s may be written in abbreviated form as

$$\left[{}_s \mathbf{K}_l + {}_s \mathbf{K}_{nl} \right] \tilde{\mathbf{u}} = {}_s \mathbf{p}^{s+1} - {}_s \mathbf{f} \quad (3.63)$$

with (for one element)

$${}_s \mathbf{K}_l = \int_{sV} {}_s \mathbf{B}_l^s T {}_s \mathbf{C}_s {}_s \mathbf{B}_l^s dV \quad (3.64)$$

$${}_s \mathbf{K}_{nl} = \int_{sV} {}_s \mathbf{B}_{nl}^s T [\sigma_{ij}]_s {}_s \mathbf{B}_{nl}^s dV \quad (3.65)$$

$${}_s \mathbf{f} = \int_{sV} {}_s \mathbf{B}_l^s T \{ \sigma_{ij} \}_s dV \quad (3.66)$$

$${}_s \mathbf{p}^{s+1} = \int_{sV} \mathbf{H}^T {}_s \mathbf{b}^{s+1} dV + \delta \tilde{\mathbf{u}}^T \int_{sA_\sigma} \mathbf{H}^T {}_s \mathbf{t}^{s+1} dA_\sigma \quad (3.67)$$

where again ${}_0 \mathbf{K}_l$ and ${}_0 \mathbf{K}_{nl}$ mark the linear stiffness and the nonlinear stiffness matrices, respectively, and ${}_0 \mathbf{f}$ and ${}_0 \mathbf{p}^{s+1}$ are the internal resisting force and the external force vectors, respectively.

For a direct comparison, the matrix and vectors definitions are listed similarly to the definitions in the Total Lagrangian formulation; see Eqs. (3.42) to (3.46).

Note that in both Lagrangian formulations the stiffness matrices \mathbf{K}_{nl} contain a particular *matrix* with *stress* components, whereas the internal force vectors \mathbf{f} include a *vector* with *stress* components.

Theoretically, the only difference between the Total and the Updated Lagrangian formulation is the choice of the reference state for the variables. Thus, for correct constitutive matrices both formulations should yield identical results. But in the Total Lagrangian formulation the linear incremental strains ${}_0 \mathbf{E}$ include an “initial displacement effect” which

provoke a more complex strain-displacement matrix ${}_0\mathbf{B}_l^s$ than in the Updated Lagrangian formulation (Eq. (3.20) vs. Eq. (3.49)) [14].

3.3.3 Solutions of the Nonlinear FE Equations

Problems of structural mechanics at which the strains and also the rigid body motions are assumed to be small may be solved using the linear Finite Element method of approximation and discretization. In Section 3.2 a derivation of the *static linear* FE formulation is described which concludes with the numerical linear system of equations

$$\mathbf{K} \tilde{\mathbf{u}} = \mathbf{p} \quad .$$

In this common equation \mathbf{K} stands for the overall stiffness matrix, thus for the stiffness matrix including the stiffness matrices of all finite elements involved in the model. Further, $\tilde{\mathbf{u}}$ represents the vector with *unknown* discrete displacements or nodal point degrees of freedom at all nodes of the model. The vector \mathbf{p} finally includes the *given* external forces acting at the nodes. See also (3.11) and (3.12). The “sparse” stiffness matrix in present linear case is always positive definite⁴ and the searched displacements may be found by inversion of the stiffness matrix using an adequate numerical solver of linear equation systems (e.g. GAUSS elimination algorithm [14]).

In the analyses cases presented in this thesis the strains are assumed to remain small, but the displacements and rotations are expected to become large. Despite the assumed linear elasticity, in such geometric nonlinear problems the stiffness matrix depends on the unknown nodal displacements $\tilde{\mathbf{u}}$. Thus, the searched vector $\tilde{\mathbf{u}}$ may not be specified directly for a given load, i.e. force vector \mathbf{p} , as it may be done in linear case. Consequently, all nonlinear problems are numerically solved in an incremental-iterative way using a sort of linearization applied at each load step. The Total and Updated Lagrangian formulations of incremental equilibrium described in Section 3.3 yield the appropriate numerical system of equations.

To linearize the virtual work expressions of equilibrium at increment $s + 1$ where the displacement field is yet unknown about the already known state s , the expression was transformed into a 1st order Taylor series approximation. Based on this, the virtual equilibrium equation

⁴if all rigid body motions of the model are restrained.

was incrementally decomposed and linearised. The resulting approximative, incremental equilibrium relations were finally discretized to FE equilibrium expressions like (3.42) or (3.63). In abbreviated form these equation systems may be written as

$$\left[{}_e\mathbf{K}_{nl} + {}_e\mathbf{K}_l \right] \tilde{\mathbf{u}} = \mathbf{p}^{s+1} - {}_e\mathbf{f} \quad (3.68)$$

with $\ell = 0$ for the Total Lagrangian formulation (see Eq. (3.42)) and with $\ell = s$ for the Updated Lagrangian formulation (see Eq. (3.63)).

The linear or stiffness matrix ${}_e\mathbf{K}_l$ and the nonlinear stiffness matrix ${}_e\mathbf{K}_{nl}$ together form the so-called *tangent stiffness matrix* ${}_e\mathbf{K}_T$, that is

$${}_e\mathbf{K}_T = {}_e\mathbf{K}_l + {}_e\mathbf{K}_{nl} \quad (3.69)$$

This yields a further abbreviation of the governing discretized equilibrium equation system as

$${}_e\mathbf{K}_T \tilde{\mathbf{u}} = \mathbf{p}^{s+1} - {}_e\mathbf{f} \quad (3.70)$$

The external forces \mathbf{p}^{s+1} associated with the external work in general depend also on the shape of the modeled body, but in the presented cases the forces may be assumed to be conservative and thus independent of the deformation.

Equation (3.70) may be used to evaluate an increment in the displacements which then can be used to ascertain approximations for the displacements, strains and stresses at step $s + 1$. With

$$\mathbf{u}^{s+1} = \tilde{\mathbf{u}} + \mathbf{u} \quad (3.71)$$

the approximative displacements at step $s + 1$ are specified. Subsequently, the strains and stresses are calculated following the hereunto adequate relations (see Section 3.3). With the approximations for the displacements, strains and stresses it is possible to verify how much the internal work differ from the external work. Exact equilibrium would require that

$${}_e\mathbf{r}^{s+1} = \mathbf{p}^{s+1} - {}_e\mathbf{f}^{s+1} = 0 \quad (3.72)$$

But in numerical solutions the internal resisting forces ${}_e\mathbf{f}^{s+1}$, which stem from the element stresses, in general are not equal to the applied load \mathbf{p}^{s+1} .

The equilibrium error as a result of the linearizations may be quantified by the *out-of-balance* or *residual force* vector ${}_{\ell}\mathbf{r}^{s+1}$. Since the resisting forces ${}_{\ell}\mathbf{f}^{s+1}$ depend nonlinearly on the nodal point displacements $\tilde{\mathbf{u}}$ the equilibrium error ${}_{\ell}\mathbf{r}^{s+1}$ has to be minimized *iteratively*. In a purely incremental method the external loads are applied as a sequence of load steps or increments, which are small enough that the reaction of the structure within a load step is approximatively linear. In such methods without corrective iteration steps the equilibrium errors of each increment would be added with the consequence that the solution would drift away from the true equilibrium path [46]. Thus, the incremental solution is to be combined with a iteration scheme within each increment. The most commonly used iteration schemes to minimize the residual forces at any increment are some kinds of the *NEWTON-RAPHSON algorithm* [14, 65, 46].

Newton-Raphson Algorithm

The NEWTON-RAPHSON formulas are basically identical for both LAGRANGIAN formulations. Thus, in the following the index ℓ which marks the reference configuration is omitted.

If in an iterative solution the approximative displacements $\tilde{\mathbf{u}}_i^{s+1}$ to the exact total displacements \mathbf{u}^{s+1} of increment $s+1$ is specified, an improvement may be received by use of the 1st order TAYLOR series expansion for the residual forces [14]:

$$\mathbf{r}(\tilde{\mathbf{u}}_{i+1}^{s+1}) = \mathbf{r}(\tilde{\mathbf{u}}_i^{s+1}) + \left[\frac{\partial \mathbf{r}}{\partial \tilde{\mathbf{u}}} \right]_{\tilde{\mathbf{u}}_i^{s+1}} \tilde{\mathbf{u}}_i \quad . \quad (3.73)$$

By insertion of (3.72) into (3.73) it may be written [14]

$$\left[\frac{\partial \mathbf{f}}{\partial \tilde{\mathbf{u}}} \right]_{\tilde{\mathbf{u}}_i^{s+1}} \tilde{\mathbf{u}}_i = \mathbf{p}^{s+1} - \mathbf{f}_i^{s+1} \quad (3.74)$$

whereby the external loads are assumed to be independent of the displacements. The derivative in (3.74) is the *tangent stiffness matrix* at iteration step i , thus

$$\left[\frac{\partial \mathbf{f}}{\partial \tilde{\mathbf{u}}} \right]_{\tilde{\mathbf{u}}_i^{s+1}} = \mathbf{K}_{Ti}^{s+1} \quad (3.75)$$

The tangent stiffness matrix $\mathbf{K}_{T_i}^{s+1}$ is presumed not to be singular. Consequently, (3.74) may be written as

$$\mathbf{K}_{T_i}^{s+1} \tilde{\mathbf{u}}_i = \mathbf{p}^{s+1} - \mathbf{f}_i^{s+1} . \quad (3.76)$$

Since the 1st order TAYLOR series expansion is truncated after the linear term Equation (3.73) is only an approximation. Hence, the corrective or iterative displacement increment $\tilde{\mathbf{u}}_i$, evaluated with (3.76), is used to compute the next improvement of the total displacements with

$$\mathbf{u}_{i+1}^{s+1} = \mathbf{u}_i^{s+1} + \tilde{\mathbf{u}}_i . \quad (3.77)$$

The relations (3.76) and (3.77) represent the NEWTON-RAPHSON solution of Equation (3.72) [14, 46].

The start conditions of the iterations ($i = 0$) of a load increment $s + 1$ are the values of the solution of the prior load increment s . These are

$$\mathbf{K}_{T0}^{s+1} = \mathbf{K}_T^s , \quad \mathbf{f}_0^{s+1} = \mathbf{f}^s , \quad \mathbf{u}_0^{s+1} = \mathbf{u}^s . \quad (3.78)$$

Consequently, (3.70) corresponds to (3.76) at the beginning of the iteration to find a solution for increment $s + 1$.

The iterations are continued until a useful convergence criterion is fulfilled. A possible criterion is for instance

$$\frac{\|\mathbf{r}(\tilde{\mathbf{u}}_i)^{s+1}\|}{\|\mathbf{p}^{s+1}\|} < \vartheta \quad (3.79)$$

where ϑ is a convergence tolerance for the norm of the residual force vector [14, 46, 65].

The disadvantage of this *full* NEWTON-RAPHSON method is the fact that for the evaluation of the corrective displacements in (3.76) the tangent stiffness matrix has to be established and inverted during each iteration. Thus, in a *modified* NEWTON-RAPHSON method the tangent stiffness is not updated after each iteration step i but only after each load increment s . This variant is less expensive than the full NEWTON-RAPHSON method but it requires more iterations and may cause more convergence problems in case of fast changes in the structure-stiffness.

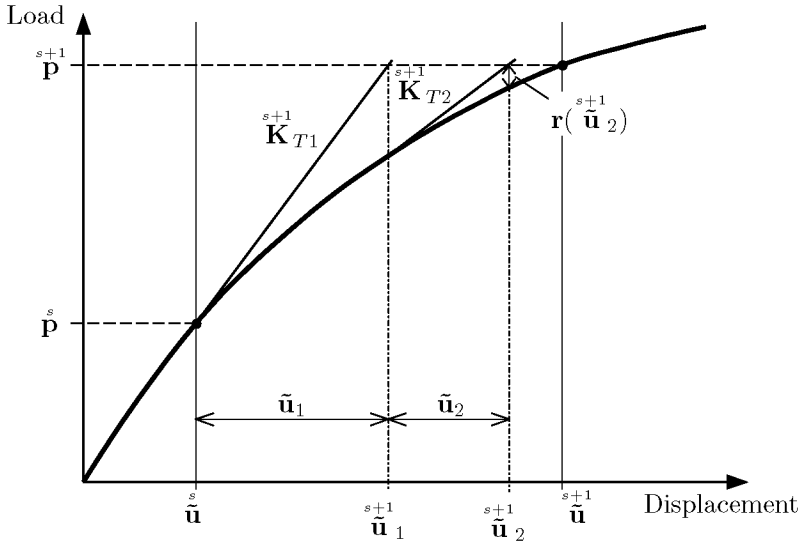


Figure 3.2: Full NEWTON-RAPHSON method

1. Iteration counter $i = 0$.
Estimation of the displacements $\tilde{\mathbf{u}}_0^{s+1}$ with the aid of the values of the last converged load step s : $\tilde{\mathbf{u}}_0^{s+1} = \tilde{\mathbf{u}}^s$.
2. Evaluation of the resisting forces $\tilde{\mathbf{f}}_i^{s+1}$ using the displacements $\tilde{\mathbf{u}}_i^{s+1}$.
3. Calculation of the residual forces: $\mathbf{r}(\tilde{\mathbf{u}}_i^{s+1}) = \tilde{\mathbf{p}}^{s+1} - \tilde{\mathbf{f}}_i^{s+1}$
4. Convergence check: (e.g.) continuation if $\|\mathbf{r}(\tilde{\mathbf{u}}_i^{s+1})\| > \vartheta \|\tilde{\mathbf{p}}^{s+1}\|$ where ϑ is an input convergence tolerance, otherwise termination of iteration and change to next increment $s + 2$.
5. Update of the tangent stiffness matrix \mathbf{K}_{Ti}^{s+1} .
6. Evaluation of the corrective displacements

$$\tilde{\mathbf{u}}_i = [\mathbf{K}_{Ti}^{s+1}]^{-1} \mathbf{r}(\tilde{\mathbf{u}}_i^{s+1})$$
7. Update of the estimated displacements with

$$\tilde{\mathbf{u}}_{i+1}^{s+1} = \tilde{\mathbf{u}}_i^{s+1} + \tilde{\mathbf{u}}_i$$
8. $i = i + 1$. **Go to 2.**

Table 3.1: Scheme of the Full NEWTON-RAPHSON method for the current increment $s + 1$. see Figure 3.2 [46].

Arc-length methods

The standard implemented NEWTON-RAPHSON procedures impose step-wise constant load parameters during the evaluation of the displacement field. In Section 3.5.2 *constraint methods* are presented which allow for load level modification throughout the iterations by introducing an auxiliary equation which guides the solution to follow a certain path.

3.4 Transient Dynamic Formulations

Engineering applications in which structures are subjected to time-varying loads such as impact, impulse or contact loading require transient dynamic analyses. In such dynamic problems it is usual to integrate the governing semi-discrete equations of motion using a time stepping algorithm. These so-called direct integration schemes may be classified as either *explicit* or *implicit* [46]. In this section the formulations and their derivations are again reproduced for their general application with any FE model, i.e. not specifically for shell structures under axial compression. Transient dynamic analyses of axially compressed cylinders are discussed only later in Section 3.5.3.

By D'ALAMBERT's principle, the external loads can be considered by combining the inertia and the applied loads as [31]

$$\rho \mathbf{p} \Rightarrow \rho \mathbf{p} - \rho \ddot{\mathbf{u}} - \eta \dot{\mathbf{u}} \quad (3.80)$$

with the acceleration vector $\ddot{\mathbf{u}}$, the velocity vector $\dot{\mathbf{u}}$, the density ρ and the damping ratio η introduced. Consequently, for the discretization a similar treatment as used for the body forces in Section 3.2 may be done. With $\mathbf{u} = \mathbf{H} \tilde{\mathbf{u}}$ as relation between nodal displacements and displacement field (see Equation 3.12), the virtual work of the inertia terms leads to

$$\begin{aligned} \int_{\circ V} (\rho \ddot{\mathbf{u}} + \eta \dot{\mathbf{u}}) \delta \mathbf{u} \circ dV &\Rightarrow \mathcal{M} \ddot{\mathbf{u}} = \int_{\circ V} \rho \mathbf{H}^T \mathbf{H} \circ dV \ddot{\mathbf{u}} \\ &+ \mathcal{C} \dot{\mathbf{u}} = \int_{\circ V} \eta \mathbf{H}^T \mathbf{H} \circ dV \dot{\mathbf{u}} \end{aligned} \quad (3.81)$$

where \mathcal{M} is called the element mass matrix and \mathcal{C} is called the element damping matrix [31]. Both matrices may be specified from the

undeformed configuration and have the same matrix form. Mass conservation during deformation demands that the mass matrix remains constant (see Equation A.10). All element matrices assembled, the mass and the damping matrices exhibit about the same symmetric and banded structure as the stiffness matrix. As a result, the equations of motion of the entire modeled structure may be expressed as

$$\mathcal{M} \ddot{\mathbf{u}} + \mathcal{C} \dot{\mathbf{u}} + \mathbf{f}(\tilde{\mathbf{u}}) = \mathbf{p} \quad (3.82)$$

whereby \mathcal{M} and \mathcal{C} are the structural mass and damping matrix, respectively, and $\ddot{\mathbf{u}}$ and $\dot{\mathbf{u}}$ are the nodal acceleration vector and nodal velocity vector. The vector \mathbf{p} includes the externally applied forces without the inertia contributions, and the vector $\mathbf{f}(\tilde{\mathbf{u}})$ contains the internal forces [80]. If linearity is assumed with respect to displacements, the internal force has the form

$$\mathbf{f}(\tilde{\mathbf{u}}) = \mathbf{K} \tilde{\mathbf{u}} \quad (3.83)$$

and the equation of motion may then also be written in the common form as

$$\mathcal{M} \ddot{\mathbf{u}} + \mathcal{C} \dot{\mathbf{u}} + \mathbf{K} \tilde{\mathbf{u}} = \mathbf{p} \quad (3.84)$$

Viscous damping assumed, the damping matrix is conveniently given by a combination of the mass and the stiffness matrix; that is:

$$\mathcal{C} = \alpha_m \mathcal{M} + \alpha_k \mathbf{K} \quad (3.85)$$

with the constants α_m and α_k . This proportional so-called RAYLEIGH damping is an approximation. For structures composed of different materials the relation is not suitable. Since real damping may have sources of many kinds, generally the two coefficients α_m and α_k have to be chosen by the program user to best represent the real structure on the basis of empirical studies and of experience [80, 31]. If α_k is different from zero the damping matrix depends on the deformations state like the stiffness matrix. Thus, for the general nonlinear case the term $(\mathcal{C} \dot{\mathbf{u}})$ in Equation (3.82) should be considered as a contribution to the internal force vector $\mathbf{f}(\tilde{\mathbf{u}}, \dot{\mathbf{u}})$ [46]. However, to simplify matters in the following the damping matrix is assumed to remain constant.

The direct time integration methods to solve the differential equation system (3.82) base on the principle to satisfy the static equilibrium, which now considers also inertia and damping, not for all time t but at certain discrete time steps. The displacements, the velocities and the accelerations may then vary within these time steps, i.e. within each time

interval [14]. Consequently, the solution methods for static calculation may also be used for the direct time integration effectively.

If the solution for the time span T is to be found, then T is divided into S constant time intervals Δt as $\Delta t = T/S$. Then, the solution is typically considered at time stations [46, 14]

$${}^s t \quad \text{and} \quad {}^{s+1} t = {}^s t + \Delta t \quad . \quad (3.86)$$

With this and in accordance with Section 3.3 the equation of motion (3.82) is rewritten for increment $s + 1$ to

$$\mathcal{M} \overset{s+1}{\ddot{\mathbf{u}}} + \mathcal{C} \overset{s+1}{\dot{\mathbf{u}}} + \mathbf{f}(\overset{s+1}{\mathbf{u}}) = \overset{s+1}{\mathbf{p}} \quad . \quad (3.87)$$

For a complete definition of an initial value problem the initial conditions for the displacements and velocities have to be specified. The time integration schemes for nonlinear problems do not differ for either the Total or the Updated Lagrange formulations, thus the index which marks the reference increment is omitted again.

The choice of the direct time integration method for the calculation of the chronology of the motion $\tilde{\mathbf{u}}(t)$ depend on the particular problem. Basically, with the explicit and the implicit integration schemes two different approaches are available.

3.4.1 Explicit Methods

In analysis cases where high frequencies dominate the solution (e.g. due to impact) or where the wave propagation is of interest, in general very small time intervals are necessary to simulate the process. The time integration then may be conducted most efficiently with the aid of explicit methods.

In principle, the equations of motion as a system of ordinary differential equations considered, any form of finite differences may be used to express the accelerations and velocities by displacements approximatively [14]. But, in most structural problems the *central difference operator* is used where the accelerations $\overset{s}{\ddot{\mathbf{u}}}$ and the velocities $\overset{s}{\dot{\mathbf{u}}}$ at time t are approximated by

$$\overset{s}{\ddot{\mathbf{u}}} = \frac{\overset{s+1}{\tilde{\mathbf{u}}} - 2\overset{s}{\tilde{\mathbf{u}}} + \overset{s-1}{\tilde{\mathbf{u}}}}{\Delta t^2} \quad \text{and} \quad \overset{s}{\dot{\mathbf{u}}} = \frac{\overset{s+1}{\tilde{\mathbf{u}}} - \overset{s-1}{\tilde{\mathbf{u}}}}{2\Delta t} \quad . \quad (3.88)$$

The solution for the displacements at time t^{s+1} is found by considering the differential equation of motion (3.87) at time t^s , that is:

$$\mathcal{M} \ddot{\mathbf{u}}^s + \mathcal{C} \dot{\mathbf{u}}^s + \mathbf{f}^s = \mathbf{p}^s . \quad (3.89)$$

Insertion of (3.88) in (3.89) yields [14, 80]:

$$\begin{aligned} \left(\frac{1}{\Delta t^2} \mathcal{M} + \frac{1}{2\Delta t} \mathcal{C} \right) \ddot{\mathbf{u}}^{s+1} &= \mathbf{p}^s - \mathbf{f}^s \\ &+ \frac{2}{\Delta t^2} \mathcal{M} \dot{\mathbf{u}}^s - \left(\frac{1}{\Delta t^2} \mathcal{M} - \frac{1}{2\Delta t} \mathcal{C} \right) \ddot{\mathbf{u}}^{s-1} . \end{aligned} \quad (3.90)$$

If $\ddot{\mathbf{u}}^{s-1}$ and $\dot{\mathbf{u}}^s$ are known the searched value of $\ddot{\mathbf{u}}^{s+1}$ may be readily be calculated with a triangular decomposition (see Equation 3.114) of the left bracket term. If \mathcal{M} and \mathcal{C} are available in diagonal form (“lumped mass”), then the inversion is trivial and in the right side of (3.90) only vectorial multiplications are necessary.

Note that in this explicit scheme the displacements (degrees of freedom) are evaluated as a function from known values of two preceding time steps and that no inversion of the (effective) tangent stiffness matrix is necessary. The term containing all nonlinearities is the internal resisting force vector \mathbf{f}^s in the right side of (3.90), which is calculated and assembled in accordance with Section 3.3 [80, 46].

The initial values have to be defined adequately since the vector $\ddot{\mathbf{u}}^{-1}$ is specified by use of the initial conditions $\dot{\mathbf{u}}^0$ and $\ddot{\mathbf{u}}^0$:

$$\ddot{\mathbf{u}}^{-1} = \ddot{\mathbf{u}}^0 - \Delta t \dot{\mathbf{u}}^0 + \frac{\Delta t^2}{2} \ddot{\mathbf{u}}^0 \quad (3.91)$$

where the initial accelerations are given by

$$\ddot{\mathbf{u}}^0 = \mathcal{M} \left(-\mathcal{C} \dot{\mathbf{u}}^0 - \mathbf{f}^0 + \mathbf{p}^0 \right) . \quad (3.92)$$

With this *explicit* scheme also very large systems may be computed with small time efforts per increment, but the central difference operator is *only conditionally stable*. The time interval length is limited by the expression

$$\Delta t \leq \frac{2}{\omega_{max}} \quad (3.93)$$

where ω_{max} is the highest frequency of the finite element model [46]. This very severe time interval limit, required for numerical stability, ensures accuracy in practically all modes of vibration. It can be shown that the highest system eigenfrequency is less than the highest eigenfrequency of the individual finite elements. This allows an easier estimation of the critical time intervals which will be conservative. Particularly for nonlinear problems such approximate expressions are often employed [46]. The most common form is [46, 80]

$$\Delta t \leq \xi \frac{L_{min}}{c_d} \quad (3.94)$$

where L_{min} is the smallest distance between any two nodes and c_d is the current, effective dilatational wave speed of the material with

$$c_d = \sqrt{\frac{E(1-\nu)}{\rho(1+\nu)(1-2\nu)}}$$

whereby in turn E is the bulk modulus, ν the POISSON ratio and ρ the density. ξ is a coefficient dependent on the type of element used. Note that an increase of the density leads to larger critical time intervals, whereas an increase of the stiffness has the opposite effect.

3.4.2 Implicit Methods

The probably best known direct time integration algorithm in structural mechanics is the implicit NEWMARK method. “Implicit”, since the approximations of the velocities and displacements at the time t^{s+1} depend not only on the known accelerations of the time t^s but also on the yet unknown accelerations to be calculated [80]. That is:

$$\begin{aligned} \dot{\mathbf{u}}^{s+1} &= \dot{\mathbf{u}}^s + \Delta t [(1-\gamma) \ddot{\mathbf{u}}^s + \gamma \ddot{\mathbf{u}}^{s+1}] \\ \mathbf{u}^{s+1} &= \mathbf{u}^s + \Delta t \dot{\mathbf{u}}^s + \frac{\Delta t^2}{2} [(1-2\beta) \ddot{\mathbf{u}}^s + 2\beta \ddot{\mathbf{u}}^{s+1}] \end{aligned} \quad (3.95)$$

The initially free parameter γ and β control the accuracy and stability of the method. For constant average acceleration with *unconditional stability* the NEWMARK method includes $\gamma = 1/2$ and $\beta = 1/4$.

The unknown accelerations may now be specified with the equation of motion in (3.87) and the approximations for the velocities and the

displacements. The resulting nonlinear system of equation can then be solved for the unknown accelerations using a NEWTON-RAPHSON scheme. But alternatively the approximations in (3.95) may be rearranged in a way that the accelerations and the velocities depend only on the unknown nodal displacements [80, 31]:

$$\begin{aligned}\ddot{\mathbf{u}}^{s+1} &= \frac{4}{\Delta t^2} (\mathring{\mathbf{u}}^{s+1} - \mathring{\mathbf{u}}^s) - \frac{4}{\Delta t} \dot{\mathbf{u}}^s - \ddot{\mathbf{u}}^s \\ \dot{\mathbf{u}}^{s+1} &= \frac{2}{\Delta t} (\mathring{\mathbf{u}}^{s+1} - \mathring{\mathbf{u}}^s) - \dot{\mathbf{u}}^s \\ \mathbf{u}^{s+1} &= \mathring{\mathbf{u}}^s + \tilde{\mathbf{u}}\end{aligned}\quad (3.96)$$

Insertion of these expressions in the equation of motion (3.87) again gives the following nonlinear system of equation for the yet unknown displacements:

$$\begin{aligned}\mathbf{r}(\mathring{\mathbf{u}}^{s+1}) &= \mathcal{M} \left[\frac{4}{\Delta t^2} (\mathring{\mathbf{u}}^{s+1} - \mathring{\mathbf{u}}^s) - \frac{4}{\Delta t} \dot{\mathbf{u}}^s - \ddot{\mathbf{u}}^s \right] \\ &+ \mathcal{C} \left[\frac{2}{\Delta t} (\mathring{\mathbf{u}}^{s+1} - \mathring{\mathbf{u}}^s) - \dot{\mathbf{u}}^s \right] + \mathbf{f}^{s+1} - \mathbf{p}^{s+1} = 0\end{aligned}\quad (3.97)$$

With the aid of the NEWTON-RAPHSON algorithm the displacements at time t^{s+1} may be evaluated. According to Section 3.3.3 the residual force vector $\mathbf{r}(\mathring{\mathbf{u}}^{s+1})$ is approximated as

$$\mathbf{r}(\mathring{\mathbf{u}}_{i+1}^{s+1}) = \mathbf{r}(\mathring{\mathbf{u}}_i^{s+1}) + \left[\frac{\partial \mathbf{r}}{\partial \mathring{\mathbf{u}}} \right]_{\mathring{\mathbf{u}}_i^{s+1}} \tilde{\mathbf{u}}_i \quad (3.98)$$

where i is the iteration number and $\tilde{\mathbf{u}}_i$ an iterative displacement increment. With the tangent stiffness matrix

$$\left[\frac{\partial \mathbf{f}}{\partial \mathring{\mathbf{u}}} \right]_{\mathring{\mathbf{u}}_i^{s+1}} = \mathbf{K}_{Ti}^{s+1} \quad (3.99)$$

the insertion of (3.97) for the residual forces into (3.98) yields the following expression

$$\begin{aligned}\left[\frac{4}{\Delta t^2} \mathcal{M} + \frac{2}{\Delta t} \mathcal{C} + \mathbf{K}_{Ti}^{s+1} \right] \tilde{\mathbf{u}}_i &= \mathbf{p}^{s+1} - \mathbf{f}_i^{s+1} \\ &- \mathcal{M} \left[\frac{4}{\Delta t^2} (\mathring{\mathbf{u}}_i^{s+1} - \mathring{\mathbf{u}}^s) - \frac{4}{\Delta t} \dot{\mathbf{u}}^s - \ddot{\mathbf{u}}^s \right] - \mathcal{C} \left[\frac{2}{\Delta t} (\mathring{\mathbf{u}}_i^{s+1} - \mathring{\mathbf{u}}^s) - \dot{\mathbf{u}}^s \right]\end{aligned}\quad (3.100)$$

With two definitions this lengthy formula may be brought into a form similar to the iterative algorithm for static problems (see Section 3.3.3): the effective stiffness matrix $\overset{s+1}{\mathbf{K}}_i$ is given by

$$\overset{s+1}{\mathbf{K}}_i = \frac{4}{\Delta t^2} \mathcal{M} + \frac{2}{\Delta t} \mathbf{C} + \overset{s+1}{\mathbf{K}}_{Ti} \quad (3.101)$$

and the effective residual load vector $\mathbf{r}(\overset{s+1}{\mathbf{u}}_i)$ is

$$\mathbf{r}(\overset{s+1}{\mathbf{u}}_i) = \overset{s+1}{\mathbf{p}} - \overset{s+1}{\mathbf{f}}_i - \mathcal{M} \left[\frac{4}{\Delta t^2} (\overset{s+1}{\mathbf{u}}_i - \overset{s}{\mathbf{u}}) - \frac{4}{\Delta t} \overset{s}{\dot{\mathbf{u}}} - \overset{s}{\ddot{\mathbf{u}}} \right] - \mathbf{C} \left[\frac{2}{\Delta t} (\overset{s+1}{\mathbf{u}}_i - \overset{s}{\mathbf{u}}) - \overset{s}{\dot{\mathbf{u}}} \right] \quad (3.102)$$

With these expressions again the corrective displacements at iteration i and the updated displacements may be evaluated:

$$\tilde{\mathbf{u}}_i = [\overset{s+1}{\mathbf{K}}_i]^{-1} \mathbf{r}(\overset{s+1}{\mathbf{u}}_i) \quad , \text{ resp.} \quad \overset{s+1}{\mathbf{u}}_{i+1} = \overset{s+1}{\mathbf{u}}_i + \tilde{\mathbf{u}}_i \quad (3.103)$$

This procedure is repeated until the appropriate norm of the residual force satisfies a given convergence criterion (see Section 3.3.3) [80, 31, 46].

Neglecting mass and damping, the formulations above become identical to the scheme for the iterative solution of static problems. Thus, the statics might be considered to be a special case of the dynamics. But this also means indirectly that in each iteration a triangular decomposition of the stiffness matrix is required. Consequently, per time step the implicit method is more expensive than the explicit method. The implicit NEWMARK method is unconditionally stable. The explicit method is also second-order accurate but not unconditionally stable. Hence, the disadvantage of a larger effort than the explicit scheme may be compensated by possible larger time intervals $\Delta t = T/S$ and thereby by a lower number of time steps S for a given time span T compared with explicit time integrations. Consequently, in general a use of the explicit method may only be recommended for structures of high specific material stiffness E/ρ if the analysed deformation process is short-time, thus for *crash* analyses for instance; for slow processes and long periods to be investigated however the number of time steps might be too discouraging.

Since lower eigenmodes are significantly better approximated by the spatial finite element discretisation than the higher ones, it would be beneficial to filter out higher frequencies during the direct time integration. With implicit methods the nullification of high-frequency modes is permissible, since these methods are preferably used for problems where

the lower frequencies are important for the response of the system. In the NEWMARK method this would demand that $\gamma > 0.5$, but unfortunately this would lead to a loss of accuracy [80]. Therefore, modifications of the implicit scheme above have been proposed which retain the second-order accuracy but with annihilation of higher frequencies. The so-called *numerical dissipation* is useful to control disturbing oscillations in the solution which stem from high-frequency modes [23]. One of the earliest algorithms to include numerical dissipation is the HOUBOLT method. This algorithm has the additional advantage of asymptotic annihilation in which the high-frequency response is nearly nullified in one time step [23]. The HOUBOLT method has been introduced in numerous commercial finite element programs (e.g. MARC[®]), but there are two noticeable disadvantages to this scheme: First, it is composed in linear multi-step form and thereby inherits difficulties in the starting condition and time interval changing. Second, the algorithm requires smaller time intervals than the standard NEWMARK method to minimize unavoidable low-frequency dissipation [23].

The HOUBOLT operator is based on cubic curve fitting through three previous steps and the current time step. This results in the expressions for the velocities and the accelerations as follows:

$$\begin{aligned} \dot{\mathbf{u}}^{s+1} &= \frac{\frac{11}{6} \mathbf{u}^{s+1} - 3 \mathbf{u}^s + \frac{3}{2} \mathbf{u}^{s-1} - \frac{1}{3} \mathbf{u}^{s-2}}{\Delta t} && \text{and} \\ \ddot{\mathbf{u}}^{s+1} &= \frac{2 \mathbf{u}^{s+1} - 5 \mathbf{u}^s + 4 \mathbf{u}^{s-1} - \mathbf{u}^{s-2}}{\Delta t^2} && \text{, respectively.} \end{aligned} \quad (3.104)$$

As already mentioned, the calculation of the displacement field at time t^{s+1} requires knowledge of the displacements at time t^s , t^{s-1} and, additionally, t^{s-2} , which leads to complicated specifications of the start conditions. Furthermore, variations of the time interval throughout a transient dynamic analysis is not possible.

In 1994 (CHUNG and HULBERT [23]) presented a single-step variant of the HOUBOLT algorithm. The so-called implicit **single-step Houbolt method** (SSH-method) is asymptotically annihilating high-frequency responses, but without the mentioned disadvantages of the multi-step form. Moreover, the method is stable and, with adequately sized time intervals, sufficiently accurate. In general form the equilibrium equation

of the single step scheme may be written as [23]

$$\begin{aligned} \alpha_{m1} \mathcal{M} \ddot{\mathbf{u}}^{s+1} + \alpha_{c1} \mathcal{C} \dot{\mathbf{u}}^{s+1} + \alpha_{k1} \mathbf{K} \mathbf{u}^{s+1} \\ + \alpha_m \mathcal{M} \dot{\mathbf{u}}^s + \alpha_c \mathcal{C} \dot{\mathbf{u}}^s + \alpha_k \mathbf{K} \mathbf{u}^s = \alpha_{f1} \mathbf{p}^{s+1} + \alpha_f \mathbf{p}^s . \end{aligned} \quad (3.105)$$

The velocities and accelerations at time t^{s+1} are approximated by

$$\begin{aligned} \ddot{\mathbf{u}}^{s+1} &= \ddot{\mathbf{u}}^s + \Delta t \dot{\ddot{\mathbf{u}}}^s + \beta_1 \Delta t^2 \ddot{\ddot{\mathbf{u}}}^s + \beta_2 \Delta t^2 \dot{\ddot{\mathbf{u}}}^{s+1} \\ \dot{\mathbf{u}}^{s+1} &= \dot{\mathbf{u}}^s + \gamma_1 \Delta t \dot{\dot{\mathbf{u}}}^s + \gamma_2 \Delta t \dot{\dot{\mathbf{u}}}^{s+1} . \end{aligned} \quad (3.106)$$

Note that the equilibrium equation includes terms corresponding to the beginning of the increment. Such an accumulation of unknown parameters in the three equations above is unwelcome and therefore to be reduced. Without loss of generality, the parameter α_{m1} may be set to 1. Asymptotic annihilation requires that

$$\alpha_k = 0 , \quad \beta_1 = \gamma_1 , \quad \beta_2 = \gamma_1 + \gamma_2 . \quad (3.107)$$

Further, second-order accuracy demands that

$$\begin{aligned} \alpha_m = -\frac{1}{2} , \quad \alpha_{k1} = \frac{1}{2\beta_2} , \quad \alpha_{f1} = \alpha_{k1} , \quad \alpha_f = \alpha_k , \\ \alpha_c = -\frac{2\beta_1 + \beta_2}{4\beta_2^2} , \quad \alpha_{c1} = \frac{2\beta_1 + 3\beta_2}{4\beta_2^2} . \end{aligned} \quad (3.108)$$

In this way, the number of unknown parameters has been reduced to two, γ_1 and γ_2 . According to the investigations of (CHUNG and HULBERT [23]) these two parameters should either be set to $\gamma_1 = -1/2$ and $\gamma_2 = 3/2$ to minimize the velocity error, or to $\gamma_1 = 0$ and $\gamma_2 = 1/2$ to avoid velocity overshoot⁵.

In 1999 MSC.Software introduced the SSH-method into the program MARC[®]. In accordance with the NEWMARK algorithm (Equations 3.101 to 3.103) and with specifications by MSC.Software [61] an iterative procedure for nonlinear dynamic transient analyses could be deduced as follows:

an effective stiffness matrix is given by:

$$\hat{\mathbf{K}}_i^{s+1} = \frac{2}{\Delta t^2} \mathcal{M} + \frac{\gamma_2(5\gamma_1 + 3\gamma_2)}{2(\gamma_1 + \gamma_2)\Delta t} \mathcal{C} + \mathbf{K}_{Ti}^{s+1} , \quad (3.109)$$

⁵In MARC[®] the default values are $\gamma_1 = -1/2$ and $\gamma_2 = 3/2$.

and a corresponding effective residual load vector may be defined as:

$$\mathbf{r}(\tilde{\mathbf{u}}_i^{s+1}) = \mathbf{p}^{s+1} - \mathbf{f}_i^{s+1} - \mathcal{M} \left[2(\gamma_1 + \gamma_2) \tilde{\mathbf{u}}_i^{s+1} - (\gamma_1 + \gamma_2) \tilde{\mathbf{u}}_i^s \right] + \mathbf{c} \left[\frac{5\gamma_1 + 3\gamma_2}{2(\gamma_1 + \gamma_2)} \tilde{\mathbf{u}}_i^{s+1} + \frac{3\gamma_1 + \gamma_2}{2(\gamma_1 + \gamma_2)} \tilde{\mathbf{u}}_i^s \right], \quad (3.110)$$

with the corresponding unknown accelerations and velocities

$$\begin{aligned} \tilde{\mathbf{u}}_i^{s+1} &= \frac{1}{\Delta t^2(\gamma_1 + \gamma_2)} \left(\tilde{\mathbf{u}}_i - \Delta t \tilde{\mathbf{u}}_i^s - \gamma_1 \Delta t^2 \tilde{\mathbf{u}}_i^s \right) \\ \tilde{\mathbf{u}}_i^{s+1} &= \tilde{\mathbf{u}}_i^s + \gamma_1 \Delta t \tilde{\mathbf{u}}_i^s + \frac{\gamma_2}{\Delta t(\gamma_1 + \gamma_2)} \left(\tilde{\mathbf{u}}_i - \Delta t \tilde{\mathbf{u}}_i^s - \gamma_1 \Delta t^2 \tilde{\mathbf{u}}_i^s \right). \end{aligned} \quad (3.111)$$

Again, the nodal displacements $\tilde{\mathbf{u}}_{i+1}^{s+1}$ are iteratively adjusted by addition of corrective displacement increments $\tilde{\mathbf{u}}_i$ until the appropriate norm of the residual force satisfies a given convergence criterion (see Section 3.3.3).

3.5 Buckling Analyses

One way to evaluate the maximum load a structure may carry before structural instability with the static finite element method is the execution of an incremental calculation by use of nonlinear LAGRANGIAN formulations. In accordance with the notation in Section 3.3.3 the linearized equilibrium condition for any loading increment s may be written as

$${}_{\ell} \mathbf{K}_{T_i} \tilde{\mathbf{u}}_i = \mathbf{p}_i^s - \mathbf{f}_i^s = \mathbf{r}(\tilde{\mathbf{u}}_i^s) \approx 0. \quad (3.112)$$

With an iterative process (e.g. NEWTON-RAPHSON, see Section 3.3.3) it is attempted to minimize the difference between the applied external forces \mathbf{p}_i^s and the internal forces \mathbf{f}_i^s . Convergence achieved after i iterations a set of additional displacement increments $\tilde{\mathbf{u}}_i$ is found which yields the total displacement vector $\tilde{\mathbf{u}}_i^s$ that corresponds to the given load level \mathbf{p}_i^s , and the residual force vector $\mathbf{r}(\tilde{\mathbf{u}}_i^s)$ (almost) vanishes. That is, the equilibrium condition of the deformed state at a load step s is approximately fulfilled. A structure tends to fail if the displacements for small additional load increments already become relatively large, what is an indication that the effective stiffness of the structure becomes small. Numerically this means that the determinant of the tangent stiffness

matrix ${}^s\mathbf{K}_T$ becomes smaller and smaller until, at collapse, the tangent stiffness matrix is singular, i.e. its determinant is zero. In the vicinity of the collapse load also convergence problems in the incremental solution of the equilibrium iterations may occur (see Section 3.3.3) [14]. Thus, in order to verify the condition of the system regarding critical points in load-displacement curves the determinant of the stiffness matrix is investigated as an accompanying measure.

For every load step s the iterative-incremental solution methods a triangular decomposition of the tangent stiffness matrix is necessary to solve the linear system of equation. For the decomposition of regular symmetrical matrices mainly two methods are available [17, 14]:

- the $\mathbf{L}^T\mathbf{D}\mathbf{L}$ decomposition. It applies that

$${}^s\mathbf{K}_T = \mathbf{L}^T\mathbf{D}\mathbf{L} \quad (3.113)$$

where \mathbf{L} is an upper triangular matrix with $L_{ii} = 1$, and \mathbf{D} is a diagonal matrix.

- decomposition after CHOLESKY. In this method the matrix is decomposed as follows:

$${}^s\mathbf{K}_T = \tilde{\mathbf{L}}^T\tilde{\mathbf{L}} \quad (3.114)$$

where $\tilde{\mathbf{L}}$ is an upper triangular matrix.

In both methods the determinant of the stiffness matrix may easily be calculated as a “byproduct” of the decomposition process. For a matrix with n_{dof} diagonal elements it follows that

$$\det {}^s\mathbf{K}_T = \det \mathbf{D} = \prod_{i=1}^{n_{dof}} D_{ii} \quad \text{in the } \mathbf{L}^T\mathbf{D}\mathbf{L} \text{ decomposition and}$$

$$\det {}^s\mathbf{K}_T = (\det \tilde{\mathbf{L}})^2 = \prod_{i=1}^{n_{dof}} \tilde{L}_{ii}^2 \quad \text{in the CHOLESKY decomposition [17].}$$

(3.115)

A state of equilibrium is *stable* if the stiffness matrix is *positive definite*. This is the case if its determinant is positive, i.e. if all D_{ii} are positive or all \tilde{L}_{ii} are real, respectively. A *singular* stiffness matrix means that the state of equilibrium is *indifferent*. In this case the determinant is zero which signifies that at least one D_{ii} or one \tilde{L}_{ii} is zero. At least one

D_{ii} being negative or at least one \tilde{L}_{ii} being imaginary finally denotes that the stiffness matrix is *indefinite* and that the equilibrium state is unstable [17, 80].

The determinant of ${}_{\epsilon}\overset{s}{\mathbf{K}}_T$ may be a very large number and care must be taken that the computer number limits are not exceeded. Thus, often only the appearance of negative D_{ii} or imaginary \tilde{L}_{ii} is used as indicator for the existence of an instability point.

However, $\det {}_{\epsilon}\overset{s}{\mathbf{K}}_T > 0$ is a necessary but not a sufficient condition for the stability of the investigated state of equilibrium [17], since an even number of negative D_{ii} or imaginary \tilde{L}_{ii} , respectively, yields also a positive determinant, although the stiffness matrix is non-positive definite and the respective state unstable [17, 14, 46, 80, 56].

In MARC[®] a very small or negative “singularity ratio” indicates an unstable state of equilibrium. This ratio is defined as the smallest ratio between ${}_{\epsilon}\overset{s}{K}_{ii}^{(i)}$ and ${}_{\epsilon}\overset{s}{K}_{ii}^{(i-1)}$, where ${}_{\epsilon}\overset{s}{K}_{ii}$ is the diagonal term of the i th degree of freedom. The diagonal terms are computed during a so called CROUT algorithm which may be used to decompose the stiffness matrix in an upper and a lower diagonal matrix [61, 64, 72].

In general, commercial FE programs stop the calculations when the stiffness matrix is (or seems to be) indefinite, which in linear analyses is mostly caused by undesired rigid body motions of the model. For non-linear analyses, numerical methods exist with which systems of equations may be solved despite an indefinite system matrix, but the usefulness of such results for engineers has to be questioned.

3.5.1 Linear Buckling Analysis

Due to the large numerical efforts of nonlinear incremental finite element calculations methods are preferred with which instability loads may be specified directly with the effort of only one load step. This applies particularly for perfect, elastic structures whose deformations are very small prior to buckling.

The direct methods for static instability investigations with finite elements base on the (EULER) assumption that the load-carrying capacity is reached if beside the fundamental equilibrium state at least one adjoining state of equilibrium with identical loading exists. Thus, with infinitesimal displacements as a disturbance it may be specified if an

equilibrium state is indifferent. With $s = F$ for the fundamental state and $s = N$ for its neighbouring state the states of deformations in the instability calculations coincide with the incremental states of displacements in a nonlinear finite element analysis [65, 17]. In accordance with the notation in Section 3.3.3 the linearized equilibrium equation for the adjacent state may therefore be written as (see Eq. 3.70)

$${}_{\ell}\mathbf{K}_T^F \tilde{\mathbf{u}} = \mathbf{p}^N - {}_{\ell}\mathbf{f}^F . \quad (3.116)$$

For infinitesimally proximate displacement states this is an exact equilibrium condition. Since the applied forces are identical for both states it applies that

$$\mathbf{p}^N = \mathbf{p}^F . \quad (3.117)$$

Furthermore, due to the condition that the fundamental state is in equilibrium the residual forces of the fundamental state vanish:

$${}_{\ell}\mathbf{r}^F = \mathbf{p}^F - {}_{\ell}\mathbf{f}^F = \mathbf{0} . \quad (3.118)$$

Consequently, with (3.116) a criterion for an indifferent state of equilibrium is given by

$${}_{\ell}\mathbf{K}_T^F \tilde{\mathbf{u}}_s = \mathbf{0} \quad (3.119)$$

where $\tilde{\mathbf{u}}_s$ stands for the infinitesimal displacements from the fundamental state to the adjacent state. This vector indicates the initial buckling mode, i.e. the shape of deformations at beginning of the post-buckling state (see later) [17]. There are only nontrivial solutions for $\tilde{\mathbf{u}}_s$ if the determinant of the tangent stiffness matrix vanishes

$$\det {}_{\ell}\mathbf{K}_T^F = 0 . \quad (3.120)$$

In literature for stability analyses it is usual to introduce proportional loading where the external load distribution is given by the loads \mathbf{p}^s and a scalar load multiplier λ ($\rightarrow \lambda \mathbf{p}^s$) [65, 17, 14, 31, 56, 80]. If the parameters of the fundamental state are expanded in a power series with reference to this multiplier λ together with the homogeneous equation (3.119), the following eigenvalue problem is obtained:

$$[\mathbf{K}_a + \lambda \mathbf{K}_b + \lambda^2 \mathbf{K}_c + \dots] \tilde{\mathbf{u}}_s = \mathbf{0} \quad (3.121)$$

with the *eigenvalues* λ , the independent matrices \mathbf{K}_a to \mathbf{K}_c and the *eigenvector* $\tilde{\mathbf{u}}_s$. The smallest eigenvalue leads to the critical load $\lambda_{cr} \mathbf{p}^s$

[65]. But this nonlinear eigenvalue problem may only be solved iteratively. Thus, the eigenvalue problem is reduced to the special linear case:

$$\left[\mathbf{K}_a + \lambda \mathbf{K}_b \right] \tilde{\mathbf{u}}_s = \mathbf{0} . \quad (3.122)$$

Any initial displacements of the fundamental state ignored the linearized eigenvalue problem in (3.122) may be redefined with the load parameter λ and the components of the tangent stiffness matrix introduced in Section 3.3 as

$$\left[{}^0\mathbf{K}_l + \lambda {}^1\mathbf{K}_{nl} \right] \tilde{\mathbf{u}}_s = \mathbf{0} . \quad (3.123)$$

Thereby ${}^0\mathbf{K}_l$ is the linear elastic stiffness matrix in a total Lagrangian formulation or in an Updated Lagrangian formulation at the first load increment (see Eqs. (3.43) and (3.64)), and ${}^1\mathbf{K}_{nl}$ is the nonlinear stiffness matrix after a first increment linearly calculated for the load level \mathbf{p}^1 (see Eqs. (3.44) and (3.65)). A linear relationship between the fundamental state and the external loads presumed, the buckling load is estimated with

$$\mathbf{p}_{cr} = \lambda_{cr} \mathbf{p}^1 \quad (3.124)$$

where λ_{cr} is the smallest eigenvalue. With $\lambda = \lambda_{cr}$ in (3.123) the corresponding eigenvector $\tilde{\mathbf{u}}_s$ is obtained which describes the *linear buckling mode*. The smallest eigenvalue is positive if the components of \mathbf{p}^1 cause compressive stresses.

This method of calculation is called *linear eigenanalysis* or **linear buckling analysis**. Nevertheless, the procedure corresponds to the 2nd order theory where *linearized* kinematical equations are used but the equilibrium is considered at a *deformed* configuration.

The linear material stiffness matrix ${}^0\mathbf{K}_l$ is identical to the system stiffness matrix \mathbf{K} of a linear finite element analysis for small displacements (see Section 3.2) and is therefore built accordingly. The nonlinear stress stiffness matrix ${}^1\mathbf{K}_{nl}$ in contrast has to be generated especially for the eigenvalue analysis, since in linear finite element analyses this contribution to the tangent stiffness matrix is not “automatically” generated as it is in a nonlinear analysis.

Nonlinear Stiffness Matrix

The nonlinear stiffness matrix⁶ \mathbf{K}_{nl} is commonly called either **geometric stiffness matrix** or **initial stress stiffness matrix**. The components of the matrix depend on the applied loads, in case of plates or shells basically on membrane forces. In Appendix C the content and the derivation of the nonlinear stiffness matrix is explained in more detail on basis of a plate element. According to Section 3.3.2 in an Updated Lagrangian formulation the transformation from the tensorial form of the corresponding virtual expression for a general, three-dimensional element may be written as

$$\int_{sV} \boldsymbol{\sigma} : \delta_s \boldsymbol{\eta}_s dV \Rightarrow \int_{sV} {}_s \mathbf{B}_{nl}^T [\sigma_{ij}]_s {}_s \mathbf{B}_{nl} dV = {}_s \mathbf{K}_{nl}$$

or, in vector/matrix notation for a plate element with the membrane forces $\{N_{ij}\} = \{\sigma_{ij}\}$:

$$\int_{sA} \{\delta_s \eta_{ij}\}^T \{N_{ij}\}_s dA = \int_{sA} \delta \tilde{\mathbf{u}}_w^T {}_s \mathbf{B}_w^T \begin{bmatrix} {}_s N_{xx} & {}_s N_{xy} \\ {}_s N_{xy} & {}_s N_{yy} \end{bmatrix} {}_s \mathbf{B}_w \tilde{\mathbf{u}}_w dA$$

where the matrices ${}_s \mathbf{B}_w$ rule the description of the derivatives of the (virtual) lateral displacements w (∂w), i.e. as in present case of the slopes in terms of the corresponding nodal degrees of freedom $\tilde{\mathbf{u}}_w$ with:

$$\left\{ \frac{\partial w}{\partial_s x_i} \right\} = {}_s \mathbf{B}_w \tilde{\mathbf{u}}_w \quad \text{resp.} \quad \left\{ \frac{\partial \delta w}{\partial_s x_i} \right\} = {}_s \mathbf{B}_w \delta \tilde{\mathbf{u}}_w$$

A central feature of the nonlinear stiffness matrix is the fact that for the generation of \mathbf{K}_{nl} a precedent static analysis is necessary where the reaction of the structure due to a given loading is calculated. Consequently: *the nonlinear stiffness matrix of an unloaded structure is zero*. Furthermore, in a finite element analysis the deflections and thus also the slopes, i.e. the *geometric* variables from which actually stem the nonlinearity on hand, are members of the a priori unknown nodal degrees of freedom vector $\tilde{\mathbf{u}}$ (see Appendix C). Therefore, the author considers the label “initial stress stiffness matrix” as more plausible.

⁶In literature the symbol for the nonlinear stiffness matrix is often tagged with a ‘G’ or ‘g’ instead of the ‘nl’.

Extraction of Eigenvalues and Eigenvectors

The extraction of eigenvalues and eigenvectors of a system is also required for the calculation of natural frequencies of vibration. The structural eigenvalue problem has therefore received considerable attention since the wider spread of the finite element method, and much work has been devoted to develop eigenvalue extraction methods, especially for the often very large but usually narrow-band system matrices involved in finite element models [45]. Mathematically, the solution of the generalized eigenproblem is of interest:

$$\mathbf{A} \mathbf{u}_\delta = \lambda \mathbf{\Xi} \mathbf{u}_\delta \quad (3.125)$$

where in the case presented above the matrices \mathbf{A} and $\mathbf{\Xi}$ would represent the in general indefinite nonlinear stiffness matrix \mathbf{K}_{nl} and the linear stiffness matrix \mathbf{K}_l [14]. There exist N_{dof} eigenvalues

$$0 \leq \lambda_1 \leq \lambda_2 \leq \dots \leq \lambda_{N_{dof}} \quad (3.126)$$

and corresponding N_{dof} eigenvectors $\mathbf{u}_{\delta i}$ which fulfill Equation (3.125). But in most cases only very few (the smallest) eigenvalues are requested. If $\mathbf{\Xi}$ is an identity matrix \mathbf{I} , then the generalized eigenproblem (3.125) reduces to a standard eigenproblem. The solution for the eigenpairs $(\lambda_i, \mathbf{u}_{\delta i})$ of interest may also be written as

$$\mathbf{A} \mathbf{U}_\delta = \mathbf{\Xi} \mathbf{U}_\delta \mathbf{\Lambda} \quad (3.127)$$

with the matrix \mathbf{U}_δ , whose columns are equal to the requested eigenvectors $\mathbf{u}_{\delta i}$, and the diagonal matrix $\mathbf{\Lambda}$ containing the eigenvalues λ_i . Important and useful predicates of the eigenvectors are that it applies:

$$\begin{aligned} \mathbf{U}_\delta^T \mathbf{A} \mathbf{U}_\delta &= \mathbf{\Lambda} \\ \mathbf{U}_\delta^T \mathbf{\Xi} \mathbf{U}_\delta &= \mathbf{I} \end{aligned} \quad (3.128)$$

A first and common technique used to calculate eigenvectors is the *inverse vector iteration method*⁷, which also enables to evaluate the corresponding eigenvalues simultaneously. Inverse iteration is applied to several important iteration procedures, including the *subspace iteration* [14, 45, 72]. In this solution a starting iteration vector \mathbf{x}_1 is assumed

⁷also referred to as “inverse power sweep”.

with $\mathbf{y}_1 = \Xi \mathbf{x}_1$ and then in each iteration step $k = 1, 2, \dots$ the equations

$$\begin{aligned} \mathcal{A} \tilde{\mathbf{x}}_{k+1} &= \mathbf{y}_k \\ \tilde{\mathbf{y}}_{k+1} &= \Xi \tilde{\mathbf{x}}_{k+1} \\ \tilde{\lambda}_{k+1} = \tilde{\lambda}(\mathbf{x}_{k+1}) &= \frac{\tilde{\mathbf{x}}_{k+1}^T \mathbf{y}_k}{\tilde{\mathbf{x}}_{k+1}^T \tilde{\mathbf{y}}_{k+1}} \\ \mathbf{y}_{k+1} &= \frac{\tilde{\mathbf{y}}_{k+1}}{\sqrt{\tilde{\mathbf{x}}_{k+1}^T \tilde{\mathbf{y}}_{k+1}}} \end{aligned} \quad (3.129)$$

are evaluated [14]. If $\mathbf{y}_1^T \mathbf{u}_{\delta 1} \neq 0$ then:

$$\mathbf{y}_{k+1} \longrightarrow \Xi \mathbf{u}_{\delta 1} \quad \text{and} \quad \tilde{\lambda}(\mathbf{x}_{k+1}) \longrightarrow \lambda_1 \quad \text{for} \quad k \longrightarrow \infty \quad (3.130)$$

Denoting the current approximation to λ_1 by $\tilde{\lambda}_{k+1}$ convergence is reached when

$$\frac{\tilde{\lambda}_{k+1} - \tilde{\lambda}_k}{\tilde{\lambda}_{k+1}} \leq \psi \quad (3.131)$$

A useful value for ψ is 10^{-5} .

There is a so-called forward iteration which is complementary to the inverse iteration in that this method yields the eigenvector corresponding to the largest eigenvalue [14].

A further, very important and more effective method to extract eigenpairs is the *Householder-QR* scheme, where first with so-called HOUSEHOLDER transformations the matrix \mathcal{A} is reduced to tri-diagonal form; then, with QR iterations the eigenvalues are obtained using the factorization of the now tri-diagonal matrix \mathcal{A} into \mathbf{QR} , where \mathbf{Q} is an orthonormal matrix and \mathbf{R} an upper triangular matrix, that is:

$$\mathcal{A} = \mathbf{QR} \quad \text{and} \quad \mathbf{RQ} = \mathbf{Q}^T \mathcal{A} \mathbf{Q}; \quad (3.132)$$

with $\mathcal{A}_1 = \mathcal{A}$ for iteration steps $k = 1, 2, \dots$ it is

$$\begin{aligned} \mathcal{A}_k &= \mathbf{Q}_k \mathbf{R}_k & \text{and subsequent:} \\ \mathcal{A}_{k+1} &= \mathbf{R}_k \mathbf{Q}_k \end{aligned} \quad (3.133)$$

where

$$\mathcal{A}_{k+1} \longrightarrow \Lambda \quad \text{and} \quad \mathbf{Q}_1 \dots \mathbf{Q}_{k-1} \mathbf{Q}_k \longrightarrow \mathbf{U}_\delta \quad \text{for} \quad k \longrightarrow \infty \quad (3.134)$$

Finally, by use of inverse iteration the required eigenvectors of the tri-diagonal matrix are calculated and transformed in order to obtain the

eigenvectors of \mathcal{A} . Since this method is restricted to standard eigenproblems, if the generalized eigenproblem $\mathcal{A}\mathbf{u}_\delta = \lambda \mathbf{\Xi} \mathbf{u}_\delta$ is considered, it has priority to be transformed into the standard form $\mathcal{A}\mathbf{u}_\delta = \lambda \mathbf{u}_\delta$ [14, 45].

For large FE models these procedures are computationally very expensive. Therefore, in the last decades efficient procedures have been developed, in which the eigenproblem is first transformed into smaller matrix systems whose eigenpairs are then computed with standard methods as mentioned above. In the so-called *subspace iteration method* first a small set of base vectors is created, defining a “subspace”, which is then transformed by simultaneous inverse power iteration into the space containing the lowest few eigenvectors of the overall system [45, 14]. But the method reputed occasionally to be the most efficient one for large FE models is the LANCZOS eigensolver: equation (3.125) may be rewritten as

$$\frac{1}{\lambda} \mathbf{\Xi} \mathbf{u}_\delta = \mathbf{\Xi} \mathcal{A}^{-1} \mathbf{\Xi} \mathbf{u}_\delta \quad (3.135)$$

With the transformation

$$\mathbf{u}_\delta = \mathbf{V} \hat{\mathbf{u}}_\delta \quad (3.136)$$

and a multiplication by \mathbf{V} on both sides, Equation (3.135) becomes

$$\frac{1}{\lambda} \mathbf{V}^T \mathbf{\Xi} \mathbf{V} \hat{\mathbf{u}}_\delta = \mathbf{V}^T \mathbf{\Xi} \mathcal{A}^{-1} \mathbf{\Xi} \mathbf{V} \hat{\mathbf{u}}_\delta \quad (3.137)$$

with $\hat{\mathbf{u}}_\delta$ denoting the eigenvector of the reduced matrix system. The LANCZOS algorithm results in a transformation such that

$$\begin{aligned} \mathbf{V}^T \mathbf{\Xi} \mathbf{V} &= \mathbf{I} \\ \mathbf{V}^T \mathbf{\Xi} \mathcal{A}^{-1} \mathbf{\Xi} \mathbf{V} &= \mathbf{T}_q \end{aligned} \quad (3.138)$$

with the symmetric tri-diagonal matrix \mathbf{T}_q of order q and the identity matrix \mathbf{I} . The matrix \mathbf{V} contains a sequence of vectors \mathbf{v}_i with $\mathbf{V} = [\mathbf{v}_1, \mathbf{v}_2, \dots, \mathbf{v}_q]$. The original eigenproblem (3.135) is reduced to the following new eigenvalue problem:

$$\frac{1}{\lambda} \hat{\mathbf{u}}_\delta = \mathbf{T}_q \hat{\mathbf{u}}_\delta \quad (3.139)$$

that is, the eigenvalues of \mathbf{T}_q are the reciprocals of $\mathcal{A}\mathbf{u}_\delta = \lambda \mathbf{\Xi} \mathbf{u}_\delta$ and the eigenvectors of the two problems are related as given in (3.136). The reduced eigenproblem may be computed with (e.g.) the HOUSEHOLDER-QR method [61, 45, 14]. Unfortunately, the LANCZOS algorithm is accompanied by some numerical problems: in the solution of large systems

the required orthogonality of the base vectors \mathbf{v}_i may not be fulfilled [72, 14]. The practical use of the LANCZOS method lies in that if q is smaller than the number of degrees of freedom of the total model, the eigenvalues of \mathbf{T}_q may give good approximations to the smallest eigenvalues of the problem (3.125). However, the actual accuracy with which the smallest eigenvalues of (3.125) are approximated as well as whether a required eigenvalue has been missed completely is unknown. Thus, the method has to be combined with a corrective, iterative scheme, and eigenvalue error bounds checks have to be computed [14]. Consequently, the use of the LANCZOS method needs some experience, in contrast to the slower inverse vector iteration method for instance.

3.5.2 Nonlinear Buckling Analysis

A linear buckling analysis according to Equation (3.123) which bases on a simple linear stress analysis with subsequent linear eigenvalue extraction yields only useful results if the pre-buckling behaviour of a structure is linear as well. Thus, basically only bifurcation points may be estimated accurately. Despite this restriction the linear buckling analysis has become the standard reference for more elaborated instability investigations. In practice structures are typically FE-modeled and investigated with perfect geometries and boundary conditions where the state of stress at the fundamental state is mainly governed by membrane stresses and the pre-buckling deformations are assumed to be negligible. In these cases the effort for (additional) nonlinear finite element calculations is normally not indicated. But, the pre-buckling behaviour of many thin-walled structures includes large pre-buckling displacements in the range of the shell wall thickness and above, or their state of stress is dominated by bending stresses. The consideration of geometric imperfections in a FE model is an example where nonlinear collapse has to be expected as failure type. For the calculation of the limit loads of such structures alternative methods to the linear buckling analysis have to be applied.

In order to consider the initial displacements it seems to be obvious to introduce the corresponding component of the tangent stiffness matrix \mathbf{K}_T into the calculations, although there is no mathematical foundation how the tangent stiffness matrix is to be split for a given problem [56]. In the Total Lagrangian formulation the linear stiffness matrix ${}_0\mathbf{K}_l^s$ (Eq. (3.43)) may be divided in a common linear material stiffness ma-

trix ${}^s_0\mathbf{K}_{l0}$ and an initial-displacement stiffness matrix ${}^s_0\mathbf{K}_{lu}$ which stems from the initial displacement part in the incremental GREEN-LAGRANGE strains (see Eq. (3.34) in Section 3.3). That is,

$${}^s_0\mathbf{K}_l = {}^s_0\mathbf{K}_{l0} + {}^s_0\mathbf{K}_{lu} \quad (3.140)$$

With this matrix the instability analysis above is expanded to a deformed configuration at increment s as basis for eigenvalue analyses. This deformed fundamental state may be specified with a linear or a nonlinear static analysis. A direct extrapolation of the linear buckling analysis according to (3.123) in a Total Lagrange formulation yields the following eigenvalue problem [65, 17]:

$$\left[{}^0_0\mathbf{K}_{l0} + {}^s_0\mathbf{K}_{lu} + \lambda {}^s_0\mathbf{K}_{nl} \right] \tilde{\mathbf{u}}_s = 0 . \quad (3.141)$$

Since both the initial-displacement stiffness matrix ${}^s_0\mathbf{K}_{lu}$ and the initial stress stiffness matrix ${}^s_0\mathbf{K}_{nl}$ depend on the relating state of deformation, in (RAMM [65]) it is argued that the different handling of these two matrices in (3.141) is not justifiable but should rather be added to one matrix, that is:

$$\left[{}^0_0\mathbf{K}_{l0} + \lambda ({}^s_0\mathbf{K}_{lu} + {}^s_0\mathbf{K}_{nl}) \right] \tilde{\mathbf{u}}_s = 0 . \quad (3.142)$$

The formulations in the expressions (3.141) and (3.142) base on the assumption that the reached load level in the fundamental state is changed by the multiplier λ where at buckling it applies that $\lambda = 1$. Alternatively to these linear amplifications of parameters of the fundamental state also incremental values of an already reached equilibrium state can be altered to estimate critical loads [65, 17]. That is, the eigenvalue problem may be modified in a way that only an increment of load is computed with $\lambda = 0$ at buckling. A TAYLOR series expansion of the tangent stiffness matrix ${}^s_\ell\mathbf{K}_T$ about the load parameter up to the linear term yields the following new eigenvalue problem:

$$\left[{}^s_\ell\mathbf{K}_T + \lambda {}^s_\ell\Delta\mathbf{K}_T \right] \tilde{\mathbf{u}}_s = 0 \quad (3.143)$$

with the increment of the tangent stiffness matrix

$${}^s_\ell\Delta\mathbf{K}_T = {}^{s+1}_\ell\mathbf{K}_T - {}^s_\ell\mathbf{K}_T . \quad (3.144)$$

In this notation the eigenvalue problem in a Total Lagrange formulation ($\ell = 0$) and in an Updated Lagrange formulation ($\ell = s$) is identical. For a better survey the matrices of the two neighboured equilibrium states in (3.144) are decomposed [17] in accordance with (3.69) and (3.63) to:

$$\begin{aligned} {}_e\Delta\mathbf{K}_T &= [{}_\ell\overset{s+1}{\mathbf{K}}_l + {}_\ell\overset{s+1}{\mathbf{K}}_{nl}] - [{}_\ell\overset{s}{\mathbf{K}}_l + {}_\ell\overset{s}{\mathbf{K}}_{nl}] \\ &= [{}_\ell\overset{s+1}{\mathbf{K}}_l - {}_\ell\overset{s}{\mathbf{K}}_l] + [{}_\ell\overset{s+1}{\mathbf{K}}_{nl} - {}_\ell\overset{s}{\mathbf{K}}_{nl}] \\ &= {}_e\Delta\mathbf{K}_l + {}_e\Delta\mathbf{K}_{nl} \end{aligned} \quad (3.145)$$

Expanded the eigenvalue problem becomes the new form

$$\left[{}_\ell\overset{s}{\mathbf{K}}_l + {}_\ell\overset{s}{\mathbf{K}}_{nl} + \lambda ({}_e\Delta\mathbf{K}_l + {}_e\Delta\mathbf{K}_{nl}) \right] \tilde{\mathbf{u}}_s = 0. \quad (3.146)$$

An analysis with (3.146) after the first load step \mathbf{p} yields the same results as with (3.142), since in this case the *incremental stiffness matrices* ${}_e\Delta\mathbf{K}_l$ and ${}_e\Delta\mathbf{K}_{nl}$ coincide with the *total stiffness matrices* ${}_\ell\overset{s}{\mathbf{K}}_l$ and ${}_\ell\overset{s}{\mathbf{K}}_{nl}$ [17]. Such buckling analyses at advanced load states cause variations which depend on the size of the load increments, but these disappear at the critical point since singularity is only indicated by the tangent stiffness matrix and not by the incremental stiffness matrices. Therefore, the incremental linear stiffness matrix may be omitted without causing considerable changes in the resulting critical load estimations. Finally, the eigenvalue problem to be solved for increment $s + 1$ may be expressed as

$$\left[{}_\ell\overset{s}{\mathbf{K}}_l + {}_\ell\overset{s}{\mathbf{K}}_{nl} + \lambda {}_e\Delta\mathbf{K}_{nl} \right] \tilde{\mathbf{u}}_s = 0 \quad (3.147)$$

with the incremental geometric or stress stiffness matrix ${}_e\Delta\mathbf{K}_{nl}$ with reference at the undeformed state (Total Lagrange: $\ell = 0$) or at the current state (Updated Lagrange: $\ell = s$). Accordingly, the estimated buckling load at increment $s + 1$ is calculated with

$$\mathbf{p}_{cr}^{s+1} = \mathbf{p}^s + \lambda_{cr}^{s+1} \Delta\mathbf{p}^{s+1} \quad (3.148)$$

where λ_{cr}^{s+1} is the smallest eigenvalue and $\Delta\mathbf{p}^{s+1}$ the load increment at increment $s + 1$. Again, with $\lambda = \lambda_{cr}^{s+1}$ in Equation (3.147) the eigenvector $\tilde{\mathbf{u}}_s^{s+1}$ is found which describes the corresponding buckling mode. For positive eigenvalues the members of the load and load-increment vectors are oriented to cause compressive stresses.

In the following, this type of incremental instability investigation is called **nonlinear buckling analysis**. This name might provoke some “semantic”

discussions, since in fact the method consists of *linear* eigenvalue calculations at prior *nonlinearly* computed equilibrium states. The nonlinear buckling analysis bases on a nonlinear static finite element calculation (with NEWTON-RAPHSON iterations) where after a selected number of load increments, as an additional accompanying measure, a linear eigenvalue investigation is performed to determine how many times the corresponding load increment (disturbance) could be added to the actual state of stress and deformation to obtain a singular tangent stiffness matrix. At buckling, the corresponding eigenvalue is zero which means that the nonlinear pre-buckling state of stress coincides with the buckling stress. The choice of the final step size and the density of the increments with eigenvalue extractions should be judged on the basis of the permissible final extrapolation towards the instability.

In contrast to the continuous monitoring of the determinant of the tangent stiffness matrix during loading, the eigenvalue extractions do not only indicate whether the structure is still stable, but yield also actual estimations of the buckling load for the corresponding state of deformation and stress. That is, with the difference between the current load level and the corresponding estimated buckling load an additional quantity is available which indicates the respective reserve of the loading capacity up to buckling.

For the cases presented within this thesis the nonlinear buckling analysis described above was mainly performed using the finite element program MARC[®] by MSC.Software Corporation. The necessary numeric functions are adequately integrated already since a fairly long time. In this commercial program the user has the choice between a Total Lagrange and an Updated Lagrange variant to consider possible large displacements and rotations. In this regard, comparative calculations with ABAQUS[®] and corresponding settings yield identical results as those with the Updated Lagrange variant in MARC[®] (see Figure 3.3). Results with the Total Lagrange variant in MARC[®] however could not be reproduced.

The buckling analyses of cylinders discussed in this thesis were conducted with MARC[®] and its implemented Updated Lagrange scheme, mainly because of its high flexibility as regards the intervention options via (Fortran) user-subroutines and the dealing with negative eigenvalues.

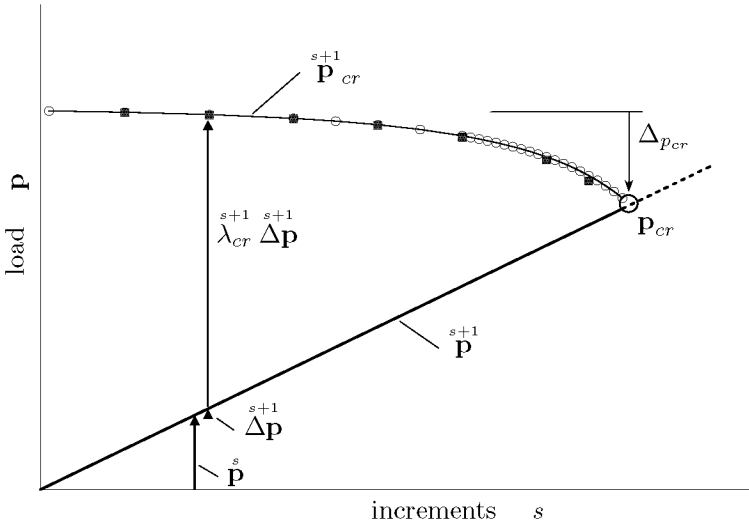


Figure 3.3: Nonlinear buckling analysis: *nonlinear equilibrium states (bold line) and corresponding linear buckling loads (markers), which each correspond to a linear extrapolation from a nonlinear equilibrium state. Circles refer to a calculation with MARC[®], quadrats to one with ABAQUS[®]. Δp_{cr} denotes the reduction of the buckling load by consideration of nonlinear pre-buckling states.*

Arc-Length Methods

The nonlinear buckling analysis allows in both the Total and the Updated Lagrange procedure to consider non-proportional loads and material nonlinearities in the loading history. Though these numerical tools also enable to determine limit loads on highly nonlinear load-deflection curves, the tracing of this equilibrium curve beyond a limit load into the post-buckling range cause problems.

The common method for the solution of nonlinear problems, explained in Section 3.3.3 (NEWTON-RAPHSON method), is a combination of a load stepping and an iterative procedure. Reaching a limit load where an equilibrium path becomes horizontal (point A_{cr} in Figure 3.4) difficulties with convergence are experienced since the iterative procedure imposes stepwise constant load parameter during the evaluation of the displacement field; hence, the solution tends to “jump” (“snap-through”) to point A_{∞} [46]. For the ascending branch of a equilibrium curve, load control is generally the most efficient method, but alternatively displace-

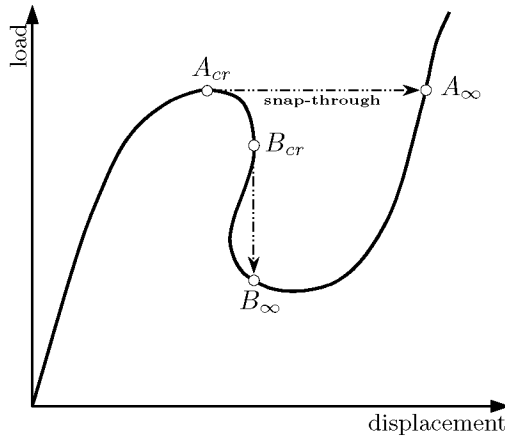


Figure 3.4: *Dynamic response under load control and displacement control*

ment control may be adopted. In such an analysis case similar convergence difficulties occur when point B_{cr} in Figure 3.4 is reached and the solution tends to jump down to point B_{∞} .

RIKS [69], CRISFIELD [26], RAMM [66] and others introduced the *arc-length* methods to overcome these difficulties. The essence of these methods is that in the iterative procedure the load parameter becomes a variable just like the displacement variables; these $n_{dof} + 1$ unknowns are solved using n_{dof} equilibrium equations and one additional constraint equation [31]. This auxiliary equation constrains the iterative displacements to follow a specified path towards a converged solution [46]. Generally, for the i th iteration within increment s , this constraint may be written as [46]

$$\tilde{\mathbf{u}}^T \tilde{\mathbf{u}} + (\Delta\lambda)^2 \mathbf{p}^T \mathbf{p} = \dot{\ell}^2 \quad (3.149)$$

where $\tilde{\mathbf{u}}$ is the incremental displacement vector and \mathbf{p} is the fixed applied load vector. $\Delta\lambda$ is an increment of the “load-level parameter” λ which multiplies \mathbf{p} while $\dot{\ell}$ fixes the “arc-length” of the increment in $n_{dof} + 1$ dimensional space [27, 26, 46]. Direct application of the constraint Equation (3.149) destroys the symmetry and the banded structure of the n_{dof} governing equilibrium equations, which may be redefined with the $n_{dof} + 1$ unknowns ($\tilde{\mathbf{u}}^s$ and λ) according to Equation 3.112 as

$$\mathbf{r}(\tilde{\mathbf{u}}_i^s, \lambda_i) = \lambda_i \mathbf{p} - \mathbf{f}_i \approx 0 \quad (3.150)$$

whereby again \mathbf{r} is the residual load vector and \mathbf{f}_i^s the internal force vector. The mentioned difficulty may be overcome with the following approach for the iterative displacements $\tilde{\mathbf{u}}_i$ (see Section 3.3.3):

$$\tilde{\mathbf{u}}_i = [\mathbf{K}_{T_i}^s]^{-1} \mathbf{r}(\tilde{\mathbf{u}}_i, \lambda) + \Delta\lambda_i [\mathbf{K}_{T_i}^s]^{-1} \mathbf{p} . \quad (3.151)$$

Thus, the iterative variation of the load level $\Delta\lambda_i$ within an increment is expressed as a function of the corresponding displacement change $\tilde{\mathbf{u}}_i$. Equation (3.151) is fundamental to all constrained methods which are similarly formulated and differ only in the evaluation of $\Delta\lambda_i$. This depends on the nature of the constraining surface adopted [46]. A discussion of some of the arc-length methods may be found in (CRISFIELD [27]) and a survey is given in (HINTON, Ed. et al. [46]) and in (WRIGGERS [80]).

Dealing with snap-through problems, for the descending branch of the equilibrium curve the sign of the load increment is specified by means of the sign of the determinant of the tangent stiffness matrix [46].

The success of the methods depend on the suitable choice of the initial load level and the arc-lengths. In order to estimate an adequate parameter setting the program user needs some precognition of the carrying behaviour of the modeled structure on hand, or the values have to be found by trial and error. For subsequent arc-lengths the one used in the first increment may be adopted (“constant arc-length method”). Alternatively, they are reduced or increased at the start of a new load increment depending on the number of desired and the number of required iterations in the previous increment. Additionally, such a solution enables automations of the load increment arrangement [46].

3.5.3 Transient Dynamic Analysis

The convergence difficulties with the NEWTON-RAPHSON iterations for static analysis when dealing with nonlinear collapse may also be avoided by considering inertia effects. Shortly after reaching the limit point of a load-deflection curve the true, dynamic response follows about the dashed lines in Figure 3.4 which denote ideal cases of either constant force or displacement. The solid static line would maintain equilibrium in accordance with the static equilibrium formulations but would be unstable. The attempt to investigate the structural behaviour involving dynamic “snap-throughs” with static computer program must fail

due to the absence of additional forces in the static equilibrium equations necessary for balance during “snapping” along the dashed lines in Figure 3.4. As the system remains always in a dynamic equilibrium, the analyses with dynamic computer programs, which consider these missing inertia forces, allow the iteration throughout the sudden change of reaction loads into the post-buckling states of equilibrium.

The usability of the dynamic transient FE analysis for buckling phenomena had already been demonstrated in (BISAGNI [16]) exercising ABAQUS[®]/Explicit, (ALMROTH et al. [2]) and in (KRÖPLIN and DINKLER [58]). Impressive results of an application of an explicit code in LS-DYNA[®] are presented in (REID et al. [68]), simulating the indenting and buckling of aluminium beverage cans, but with high *impact* velocities up to 3810 m/s, compared with velocities in the order of only 1 mm/s used for the buckling analyses of the cylinders discussed in this book.

Since controlling shell edge load leads to disastrous deformations at buckling, the post-buckling investigations in general will be limited to shell shortening as the loading parameter.

At buckling condition, the buckling pattern develops and the shell is accelerated to exhibit dynamic deflections into the post-buckling state. In case of perfect cylinders with controlled end-shortening the drop of the axial reaction force is almost vertical. Thus, the load increments, i.e. the time steps respectively, have to be sufficiently small. Applying damping may help to increase the step size in this critical range. For transient dynamic FE analysis structural damping is in general introduced as a linear combination of the mass matrix and/or the stiffness matrix (RAYLEIGH damping, see Section 3.4). The higher the damping parameter the longer the time steps may be chosen at a pre-selected constant compression velocity. If the number of steps is too restricted real loading durations of buckling tests may not be adequately modelled. Further, realistic damping parameters are difficult to define and are probably too low to guarantee dynamic equilibrium during the mentioned critical stage with a given (higher) compression velocity and (smaller) number of time steps. Therefore a compromise between these parameters has to be found by trial for each analysis case, see example below.

The implicit single-step Houbolt method (SSH-method, see Section 3.4) is unconditionally stable. Therefore, the number of time steps needed to guarantee equilibrium is significantly smaller than needed using an explicit operator (only conditionally stable). It should be noted that in dynamic analyses the material parameters depend on each other.

The dilatational wave speed of the material, $\sim \sqrt{E/\rho}$, demands that the ratio of the YOUNG's modulus to the density has to be taken into account regarding the definition of their units⁸. In the condition equation (3.94) for stability in explicit operators, the wave speed is the denominator. Therefore, ignoring real densities and stiffness, an increase of the density reduces the minimal stable time step.

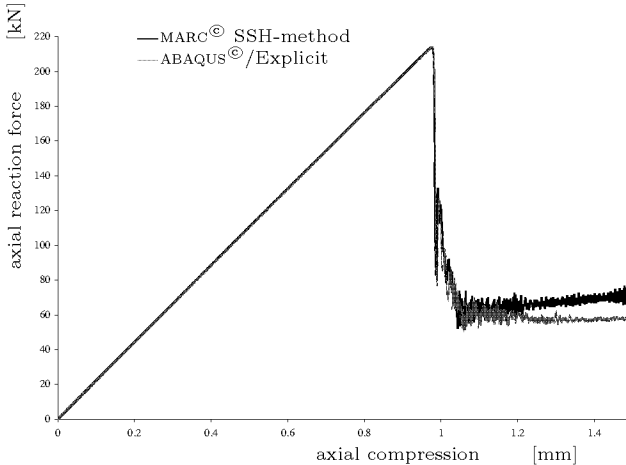


Figure 3.5: *Dynamic FE analysis results of an axially compressed ideal CFRP cylinder without damping but with scaled up density (factor 1000). Constant compression velocity: 0.3 mm/s. Comparison of calculations with MARC[®] (implicit SSH-method) and with ABAQUS[®]/Explicit.*

The number of time steps required for the transient dynamic analysis of the cylinders presented herein with real densities are in the range of 5000, whereas comparative tests using ABAQUS[®]/Explicit needed about 10 million time steps. In Figure 3.5 the result of a dynamic transient analysis of an axially compressed ideal CFRP cylinder is shown which was conducted with ABAQUS[®]/Explicit with its central difference operator implemented (see Section 3.4). The density used was increased with a factor of 1000 and the compression velocity was set to 0.3 mm/s. With the greater mass, the application of damping was not necessary. The result shows good agreement with the result yielded by the use of the SSH-method with equal density and velocity and likewise zero damping matrix. Since the -per step- faster matrix system handling of the explicit

⁸That is, if the material parameters are not given in Pa, kg, s and m (strongly recommended!) but in MPa, s, kg and mm, the density has to be specified in tons per mm³ instead of kg/m².

operator of ABAQUS[®]/Explicit was not able to reduce the analysis duration to the range of the implicit operator of MARC[®], the use of explicit operators is not recommended as long as the shell structure is not an object of a crash analysis. Anyway, the criteria for the choice of one of the implicit or explicit time integration methods are also dependent on the available FE program due to different complexities implemented.

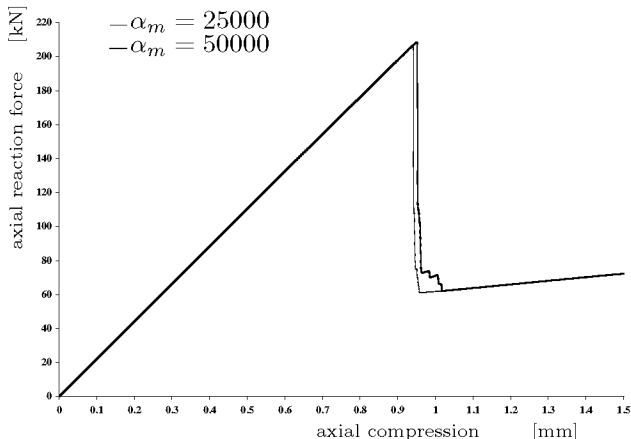


Figure 3.6: *Dynamic FE analysis results of an axially compressed ideal CFRP cylinder for two different damping parameters.*

Since the SSH-method suppresses high-frequency oscillations (numerical damping), no additional structural damping is necessary and thus the damping parameter α_k in

$$\mathbf{C} = \alpha_m \mathbf{M} + \alpha_k \mathbf{K}$$

for the damping matrix \mathbf{C} may be set to zero. With only one damping parameter (α_m) the search of an adequate parameter-set is much simplified. Figure 3.6 shows the effects of increasing the damping parameter α_m (pure inertia damping) from 25000 to 50000. The axial compression of a cylinder leads to an linearly distributed velocity field within the cylinder shell. The velocities of the nodes is zero at the bottom edge and increase up to the loaded edge with the given value. Consequently, with damping small additional axial forces are generated which should be minimized. The stiff composite cylinder in Figure 3.6 is almost not affected by increasing the damping, but for other specimens this may influence the value of axial shortening where the change from one post-buckling mode to a next one occurs. Therefore, it is recommended to use the smallest damping parameters possible for successful

iterations throughout the collapse with the selected compression velocity and number of time steps.

Chapter 4

Buckling Analysis Results for Ideal Cylinders

The instability behaviour of axially compressed thin isotropic cylinders with perfect shell geometries is a prime example of bifurcation buckling (see Introduction, Section 1.1). Such cylinders first deform axisymmetrically along a pre-buckling equilibrium path to a bifurcation point. Then, on the post-buckling path the shell deformation is non-axisymmetrical. With increasing compression further bifurcation points in succession on the equilibrium path may be specified, which correspond to the particular change from a buckling pattern to another. The eigenvectors, calculated during linear buckling analyses, represent the initial buckling modes, i.e. the shell patterns immediately after buckling (see Section 3.5, Equation (3.123)).

Severe dynamic movements of the shell in radial direction characterize the transition from the pre-buckling state to a post-buckling state of equilibrium. During such displacements the initial buckling pattern transforms rapidly into a stable post-buckling pattern. Static FE analysis methods in general result in a buckling load and a respective buckling pattern, but they give neither information about the post-buckling load nor the post-buckling patterns that can be observed during tests. In turn, the patterns resulting from classic analyses, in the majority of

cases, cannot be observed without technical aid due to the high velocity of shape changes within the transition. With high-speed movies it is possible to visualize the initial buckling patterns, but such investigations require complex optical equipment.

For perfect, simply supported and hinged cylinders close-form solutions of partial differential equation systems are available which yield the number of deflection waves in axial and circumferential direction for a respective buckling load (see Section 2.2). However, for isotropic cylindrical shells under axial load many combinations of wave numbers exist with almost identical corresponding membrane stresses. Thus, though the numerically calculated buckling load may directly be compared with the solution of an analytical approach, the comparison of the buckling patterns is often not reliable, since the shape represented by the eigenvector relating to the lowest eigenvalue is not necessarily identical to the pattern described by the combination of wave numbers with the lowest compressive membrane stresses. In practice, this fact and the frequent absence of possibilities to compare with buckling shapes observed during tests may provoke uncertainty about the quality of numerical solutions; mainly considering that a FE buckling analysis of a structure for which a simple formula exists is only useful as a benchmark test prior to instability investigations of structures of which analytical approaches are either very complicated or unavailable.

This chapter deals with the numerical buckling analysis of axially compressed ideal-elastic isotropic and laminated circular monocoque cylinders with perfect shell geometry. The results of the static linear and nonlinear buckling analyses as well as the results of transient dynamic analyses of such cylinders are described and compared with analytical solutions and with test results. The aim is to introduce the buckling behaviour of the cylinders with perfect geometry for later comparison with the shells with initial geometric imperfections. It is necessary to dwell on the analysis of perfect cylinders since the buckling behaviour of these cylinders also influence that of cylinders with imperfect shell geometry and the imperfection sensitivity. Moreover, the author used the analysis of the ideal shells as basis of comparison and thus adjusted the input parameters to the perfect cylinders for all his FE calculations to this thesis, thus also for the imperfect shells.

4.1 The Cylinders and their Modeling

4.1.1 Isotropic Shells

Based on the dimensions of CFRP cylinders analysed during an European project the author “invented” a set of unstiffened isotropic cylinders with a YOUNG’s modulus E of 70000 MPa (aluminium alloy) and radii R from 100 to 1000 mm, lengths L from 150 to 1000 mm and shell thicknesses h from 0.75 to 1.5 mm. As customary, the POISSON’s ratio was set to 0.3. The specifications of these cylindrical shells are given in Table 4.1.

The last specimen in the table stems from investigations from DLR Braunschweig in the late sixties with cylindrical shells made of Hostaphan (Mylar). This cylinder was selected for calibrations of the dynamic calculations, since of this specimen high-speed movies are available which were recorded during axial buckling tests. Results of transient dynamic analyses are given in Section 4.3.

4.1.2 Laminated Shells

In the late nineties, DLR and ETH Zurich, together with EMPA in Dübendorf, had co-operated within a Brite-Euram project¹ to study the buckling behaviour of laminated composite cylinders, to be investigated for their use as shell for a new helicopter tail structure (Eurocopter). The contribution of the author to the project consisted in linear and nonlinear finite element analyses of these laminated cylinders under axial compression and combined axial and torsion loading. The summary of the related analyses and tests are published in (MEYER-PIENING et al. [60]). Since the FE calculations of axially compressed cylinders presented herein base on the experiences with the investigations of the CFRP composite cylinders the analyses of these specimens are explained more detailed.

The inner radius of the CFRP cylinders investigated within the project DEVILS is 250 mm, their length L is 510 mm, and their shell wall thickness h is 1.25 mm. For the calculations the inner radius was accepted as their mean cylinder radius R . The laminates consist of 10 layers of

¹Brite-Euram project BE-7550 *DEVILS* “design and validation of imperfection tolerant laminated shells”.

$$Z = \frac{L^2}{R^2 h} \sqrt{1 - \nu^2}$$

R [mm]	h [mm]	L [mm]	E [MPa]	\sqrt{Rh} [mm]	$\frac{R}{h}$	$\frac{L}{R}$	Z	FE model mesh			
								number of elements			nodes
								axial	circ.	total	
187.5	0.75	510	70000	11.9	250	2.72	1764	86	198	17028	17226
250	0.75	510	70000	13.7	333	2.04	1323	74	229	16946	17175
375	0.75	510	70000	16.8	500	1.36	882	60	280	16800	17080
500	0.75	510	70000	19.4	667	1.02	662	52	324	16848	17172
750	0.75	510	70000	23.7	1000	0.68	441	43	397	17071	17468
1000	0.75	510	70000	27.4	1333	0.51	331	37	458	16946	17404
100	1	510	70000	10.0	100	5.10	2481	102	125	12750	12875
187.5	1	510	70000	13.7	188	2.72	1323	74	172	12728	12900
250	1	510	70000	15.8	250	2.04	992	64	198	12672	12870
375	1	510	70000	19.4	375	1.36	662	52	243	12636	12879
500	1	510	70000	22.4	500	1.02	496	45	280	12600	12880
750	1	510	70000	27.4	750	0.68	331	37	344	12728	13072
1000	1	510	70000	31.6	1000	0.51	248	32	397	12704	13101
187.5	1.5	510	70000	16.8	125	2.72	882	60	140	8400	8540
250	1.5	510	70000	19.4	167	2.04	662	52	162	8424	8586
187.5	1	382.5	70000	13.7	188	2.04	744	55	172	9460	9632
250	1	382.5	70000	15.8	250	1.53	558	48	198	9504	9702
375	1	382.5	70000	19.4	375	1.02	372	39	243	9477	9720
500	1	382.5	70000	22.4	500	0.77	279	34	280	9520	9800
750	1	382.5	70000	27.4	750	0.51	186	27	344	9288	9632
1000	1	382.5	70000	31.6	1000	0.38	140	24	397	9528	9925
250	1.5	255	70000	19.4	167	1.02	165	26	162	4212	4374
250	1.5	382.5	70000	19.4	167	1.53	372	39	162	6318	6480
250	1.5	510	70000	19.4	167	2.04	662	52	162	8424	8586
250	1.5	765	70000	19.4	167	3.06	1489	79	162	12798	12960
250	1.5	1000	70000	19.4	167	4.00	2544	103	162	16686	16848
375	1	150	70000	19.4	375	0.40	57	15	243	3645	3888
375	1	200	70000	19.4	375	0.53	102	20	243	4860	5103
375	1	255	70000	19.4	375	0.68	165	26	243	6318	6561
375	1	300	70000	19.4	375	0.80	229	30	243	7290	7533
375	1	382.5	70000	19.4	375	1.02	372	39	243	9477	9720
375	1	450	70000	19.4	375	1.20	515	46	243	11178	11421
375	1	510	70000	19.4	375	1.36	662	52	243	12636	12879
375	1	600	70000	19.4	375	1.60	916	61	243	14823	15066
375	1	765	70000	19.4	375	2.04	1489	79	243	19197	19440
375	1	1000	70000	19.4	375	2.67	2544	103	243	25029	25272
500	0.75	255	70000	19.4	667	0.51	165	26	324	8424	8748
500	0.75	382.5	70000	19.4	667	0.77	372	39	324	12636	12960
500	0.75	510	70000	19.4	667	1.02	662	52	324	16848	17172
500	0.75	765	70000	19.4	667	1.53	1489	79	324	25596	25920
100	0.254	200	5500	5.0	400	2.00	1526	60	180	10800	10980

Table 4.1: Dimensions, material stiffness and the number of elements in axial and circumferential direction of divers analysed unstiffened, linear-elastic isotropic cylinders.

unidirectional carbon/epoxy prepregs with the following ply properties which were measured with small specimens:

$$E_1 = 123550 \text{ MPa} \quad \nu_{12} = 0.32$$

$$E_2 = 8708 \text{ MPa} \quad G_{12} = 5695 \text{ MPa}$$

Each ply has the thickness 0.125 mm [40]. The laminate stacking sequences of some of the DEVILS specimens labeled with Z28, Z30, Z32 and Z33 are contained in Figure 4.1.

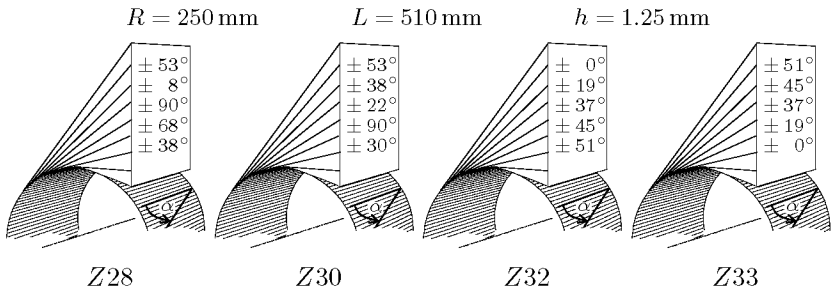


Figure 4.1: Identification of the DEVILS cylinders with their stacking sequences.

For a physical explanation of the effect observed on the non-symmetrically laminated DEVILS cylinders above, (GEIER, MEYER-PIENING & ZIMMERMANN [40]) introduced cylinders with the same dimensions and ply properties than the specimens above but with four axially stiff layers near one shell surface and four $\pm\alpha$ layers next to the other. The stacking of two the types of the so created additional cylinder shells are given in Figure 4.2. For the investigation of laminated cylinders having single dimple imperfections the author added some shells to the set from Ref. [40] to get more cylinders with stackings as shown in Figure 4.2 with ply-angles α between zero and 90 degrees.

To analyse the influence of the stretching-bending coupling for $\alpha = 60^\circ$ two 8-ply laminates were introduced with stacking sequences which are symmetric referring to the middle surface of the shell:

$$Z0.60s: \quad [0^\circ_2, +60^\circ, -60^\circ_2, +60^\circ, 0^\circ_2]$$

$$Z60.0s: \quad [+60^\circ, -60^\circ, 0^\circ_4, -60^\circ, +60^\circ]$$

They may be compared with the non-symmetric laminates Z0.60 and Z60.0, see Fig. 4.2.

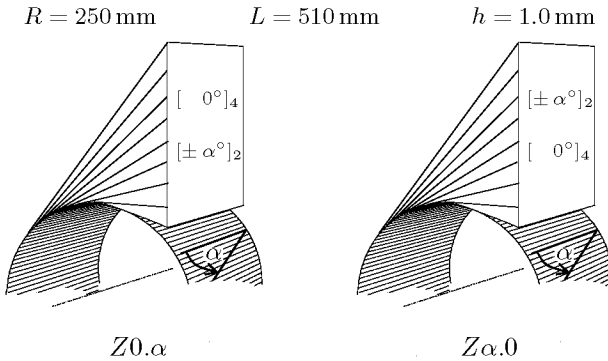


Figure 4.2: Identification of the eight-layered cylinder shells $Z0.\alpha$ and $Z\alpha.0$ with a with their stacking sequences referring to the fibre orientation angle α .

Note that the stacking sequences are given from outer to inner ply, 0° being axially oriented (see Fig. 2.5). Stacking sequences meant for manufacturing instruction should be given inverse since during the fabrication of cylindrical laminates in general the first ply is placed at the inner side. Moreover, the layer stacking sequences above are designed for academic use only; the practical application of these eccentric laminates is not advisable.

Finally, (I. SHEINMAN and Y. GOLDFELD [73]) investigated analytically the buckling behaviour of angle-ply ($\pm\alpha$) graphite/epoxy cylindrical shells with a radius $R = 1.27$ m, a length $L = 2.54$ m, a thickness $h = 12.7$ mm ($R/h = 100$), and with properties of the 2-ply laminates as follows:

$$E_1 = 140400 \text{ MPa} \quad \nu_{12} = 0.26$$

$$E_2 = 9730 \text{ MPa} \quad G_{12} = 4110 \text{ MPa}$$

The two researchers conducted buckling analyses of these shells on the basis of three different shell theories: alternatively to DONNELL's theory as herein presented (see Section 2.1.1) also one of SANDER and one of TIMOSHENKO [78]. They used formulations in terms of the AIRY stress function \mathcal{F} and the lateral displacement w , but also in terms of the three displacement components \bar{u} , \bar{v} and w , see Section 2.1. The author used their presented findings on some discrepancies between these formulations for different boundary conditions for comparisons with linear and nonlinear FE analyses of these cylinders with clamped and hinged edges.

4.1.3 Type and Number of Elements

The FE analyses were mainly conducted with help of MARC[®]. Parametric investigations led to the choice of the four-node bilinear, thick (MINDLIN type) shell element No. 75 for the formation of the model. The four-node Discrete KIRCHHOFF elements offered in MARC[®] yielded similar results, but they were implemented into the program code in a late phase of the studies. Moreover, element No. 75 is still the default shell element in MARC[®]. Therefore, the models were continuously generated with this older thick shell element.

The number of nodes and elements has to be selected to allow for adequate description of all potentially critical modes. On the basis of the decay length of edge bending disturbances, an element mesh size not wider than $0.5\sqrt{Rh}$ is recommended. Consequently, for the DEVILS specimens 60 shell elements in axial direction and 180 in circumferential direction were used. In Figure 4.3 the influence of number of almost

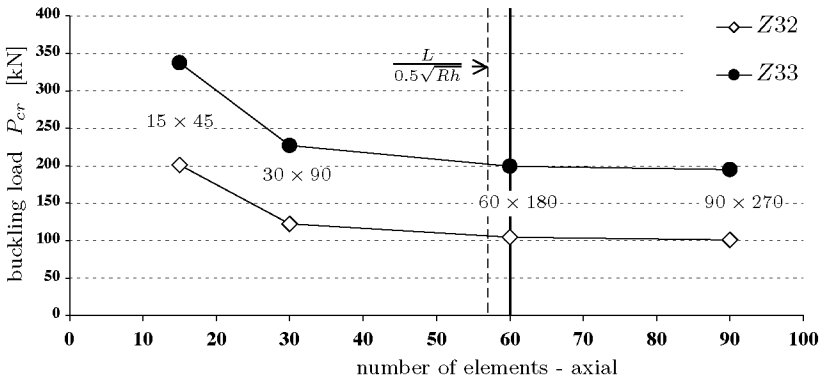


Figure 4.3: Linear buckling loads of cylinder Z32 and Z33 for different numbers of elements in axial direction.

square elements on the linear buckling load is plotted. It can be seen that a further refinement of the element mesh would hardly justify the superproportional increase of the computation costs involved. The used 60×180 -model contained 10980 nodes and thus about 66000 degrees of freedom, a matrix system size which still may be managed by modern computers with acceptable computation times.

The element edge lengths of the isotropic shells introduced in Section 4.1.1

were also specified² by the formula $0.5\sqrt{Rh}$. The so generated number of elements and nodes are listed in Table 4.1 on page 120.

4.1.4 Boundary Conditions

Both edges of the cylinders were considered to be either clamped or hinged. The boundary conditions on both cylinder ends were modeled with aid of additional nodes on the cylinder axis whose degrees of freedom were joint with the nodes on one edge. In this way infinitely rigid, plane parallel endplates were simulated and the axial force attached to the auxiliary center node was uniformly distributed on the edge nodes.

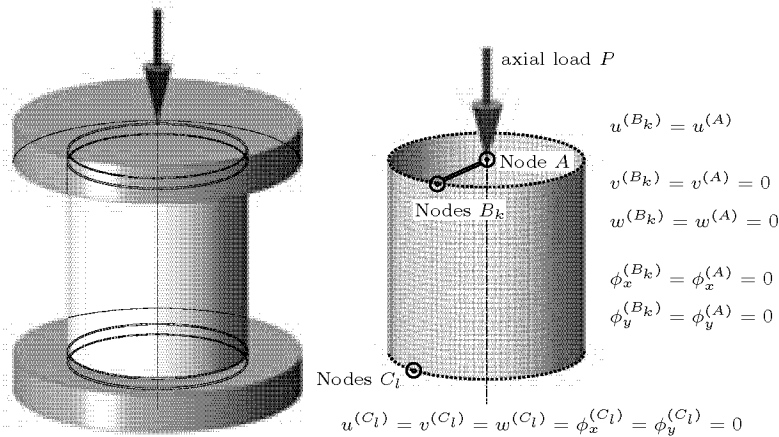


Figure 4.4: Modeling of clamped edges with tied nodes.

Figure 4.4 demonstrates the simulation of clamped cylinder edges: the k nodes B_k of the loaded edge are linked with an additional node A on the center line on which the loading is applied. For the fixation of the bottom edge the l nodes C_l are linked with a further node on the centre line which gives the total reaction force. The axial compressive load P was applied at the centre node A .

For clamped edges the translational degrees of freedom (DOF) u , v , w and the rotational DOF ϕ_x , ϕ_y of the central node on one end, and of all DOF except the translation in axial direction u of the central node

²Exception: Mylar cylinder with a 60×180 -mesh.

on the loaded end are set to zero (see Figure 4.4). For hinged edges only the translational DOF were fixed, the rotations ϕ_x, ϕ_y are left free.

The configuration for clamped edges served to simulate the boundary conditions CC4 in the classical analysis and was applied for comparisons with test results, see Section 2.2.1 on page 48. The set-up for hinged edges in turn corresponds to the boundary conditions SS4. Unless otherwise noted for the finite element analyses always the clamped boundary conditions CC4 were applied.

The close-form solution in the classical analysis was derived for the simply-supported boundary conditions SS3, see Section 2.2.1. These conditions as well as the clamped conditions CC3, with applied constant membrane stresses \tilde{N}_x around a cylinder edge, are simulated by means of the simpler direct application of equal point forces distributed over the edge nodes. These point loads act centrally on the shell, i.e. on the middle surface of the elements which was considered as reference for shell stretching and bending. With this configuration no virtual rigid endplates are present and thus the axial edge displacements are not necessarily constant. For the analysis of perfect cylinders the two conditions SS3 and CC3 were not applied. During the DEVILS project good comparisons between test results and FE analysis results, all with conditions CC4, was considered more important than the match with the classical analysis. Additionally, it was observed that for *perfect* cylinders under axial load the differences between the buckling loads calculated with conditions CC3 and those obtained with CC4 are negligible small.

4.2 Static FE Analysis Results

As a basic principle it is highly recommended to conduct a linear static stress analysis prior to any buckling calculation. In this way, possible modelling mistakes, e.g. wrong material properties or boundary conditions, may be detected more likely. This guideline does apply all the more if eccentric laminates are used as shell material, since in this case the effective direction of the element normal and the element x-axis has to be checked very carefully³ for correct numerical representation. The experience confirms the benefit of the verification of stress fields prior to linear or nonlinear buckling analyses in any case.

³Specifications in the program manuals are correct in most cases, but exceptions are not impossible...

The *linear buckling analysis*, as described in Section 3.5, is considered to be the standard buckling analysis method for more expensive numerical simulations of shells under compressive loading. This procedure consists of the evaluation of an eigenvalue problem resulting in eigenvalues and related normalised mode shapes. In the present cases the *linear buckling load* P_{cr} is computed as

$$P_{cr} = \lambda_{cr} P$$

where P is the compressive load applied to the above-mentioned center node and λ_{cr} is the smallest eigenvalue⁴, see Section 3.5.1, Eq. (3.124).

Singularity investigation of system matrices at buckling is also applied in the herein called *nonlinear buckling analysis*. This static analysis method, detailed in Section 3.5.2, considers a load-dependent pre-buckling deformation during loading up to the structural instability. After a selected number of small load or edge displacement increments a linear eigenvalue investigation is performed to determine the stability of the investigated pre-buckling state of stress and deformation. The at preselected increments conducted eigenvalue calculation yields a buckling load at increment $s + 1$ with

$$P_{cr}^{s+1} = P^s + \lambda_{cr}^{s+1} \Delta P^s$$

where P^s is the applied load at the preceding increment s , λ_{cr}^{s+1} is the smallest eigenvalue and ΔP^s the load increment at increment $s + 1$, see Section 3.5.2, Eq. (3.148).

In MARC[®] large displacements and rotations were considered by means of the Updated Lagrange formulation implemented. The eigenvalues and eigenvectors were all calculated with the *inverse vector iteration* code in MARC[®] as shortly described in Section 3.5. For the convergence parameter ϑ_λ (see Eq. 3.131) a value of 10^{-4} was selected for nonlinear buckling analysis and 10^{-5} for the purely linear variant. The maximal number of iteration steps had to be raised to 10000.

The probably faster LANCZOS eigensolver implemented in MARC[®] could not be used alternatively for the nonlinear buckling analysis without temporary problems while extracting the eigenvalues in the possibly range from zero to some hundreds. Further, in MARC[®] a combination of the Total Lagrange formulation with incremental eigenvalue extractions seemed not to be foreseen.

⁴The extraction of more than only one eigenvalue may be beneficial since the first value found by the solver is not necessarily the smallest.

4.2.1 Results for the Isotropic Cylinders

In Table 4.2 the analysis results of the isotropic cylinders presented in Section 4.1.1 are listed. For comparison in the last column the buckling loads P_{cl} are plotted which were calculated with the formula from classical analysis for axial buckling of perfect isotropic circular cylinders as

$$P_{cl} = \frac{2\pi}{\sqrt{3(1-\nu^2)}} E h^2 \quad ,$$

$$P_{cl} = 3.8 E h^2 \quad \text{for } \nu = 0.3 \quad .$$

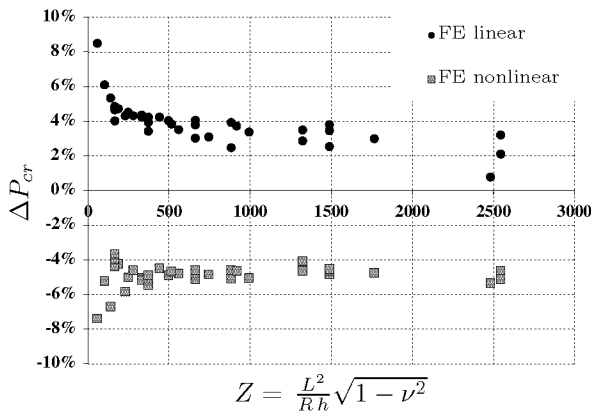


Figure 4.5: Deviations of FE linear and nonlinear buckling analysis results from classical analysis results P_{cl} versus BATDORF's parameter Z for the isotropic cylinders. Numerical results for clamped, classical analysis results for hinged cylinder edges.

Figure 4.5 presents the deviations of the numerical buckling analysis results from the values estimated with the equation above in dependence of BATDORF's parameter Z ; the error values are given in percentages of the FE analysis results. For cylinders with $Z > 100$ or $L/R > 0.75$ the linear buckling analyses (FE) yielded 4% to 5% higher buckling loads than the classical analysis, whereas the nonlinear analyses (FE) led to about 5% lower buckling loads. The deviations of the shorter cylinders with less than 10% may also be considered as small since dealing with FE analysis results. The analytical approach for axially compressed circular cylinders bases on close-form solutions of the equilibrium and

$$Z = \frac{L^2}{R h} \sqrt{1 - \nu^2}$$

R [mm]	h [mm]	L [mm]	E [MPa]	$\frac{R}{h}$	$\frac{L}{R}$	Z	FE analyses		analytic $= 3.8 E h^2$ P_{cl} [kN]
							linear P_{Cr} [kN]	nonlinear P_{Cr} [kN]	
187.5	0.75	510	70000	250	2.72	1764	154.3	142.9	149.7
250	0.75	510	70000	333	2.04	1323	155.1	143.8	149.7
375	0.75	510	70000	500	1.36	882	155.8	143.1	149.7
500	0.75	510	70000	667	1.02	662	156.0	143.1	149.7
750	0.75	510	70000	1000	0.68	441	156.3	143.3	149.7
1000	0.75	510	70000	1333	0.51	331	156.5	142.5	149.7
100	1	510	70000	100	5.10	2481	268.2	252.6	266.1
187.5	1	510	70000	188	2.72	1323	274.0	254.3	266.1
250	1	510	70000	250	2.04	992	275.4	253.3	266.1
375	1	510	70000	375	1.36	662	276.6	253.9	266.1
500	1	510	70000	500	1.02	496	277.3	253.7	266.1
750	1	510	70000	750	0.68	331	277.9	253.0	266.1
1000	1	510	70000	1000	0.51	248	278.7	253.4	266.1
187.5	1.5	510	70000	125	2.72	882	613.9	569.7	598.7
250	1.5	510	70000	167	2.04	662	617.4	569.5	598.7
187.5	1	382.5	70000	188	2.04	744	274.6	253.8	266.1
250	1	382.5	70000	250	1.53	558	275.8	253.9	266.1
375	1	382.5	70000	375	1.02	372	277.0	253.2	266.1
500	1	382.5	70000	500	0.77	279	278.1	254.4	266.1
750	1	382.5	70000	750	0.51	186	279.3	255.3	266.1
1000	1	382.5	70000	1000	0.38	140	281.1	249.4	266.1
250	1.5	255	70000	167	1.02	165	623.8	573.6	598.7
250	1.5	382.5	70000	167	1.53	372	619.9	567.7	598.7
250	1.5	510	70000	167	2.04	662	617.4	569.5	598.7
250	1.5	765	70000	167	3.06	1489	614.3	571.2	598.7
250	1.5	1000	70000	167	4.00	2544	611.6	569.6	598.7
375	1	150	70000	375	0.40	57	290.8	247.8	266.1
375	1	200	70000	375	0.53	102	283.4	252.9	266.1
375	1	255	70000	375	0.68	165	279.1	256.0	266.1
375	1	300	70000	375	0.80	229	278.1	251.4	266.1
375	1	382.5	70000	375	1.02	372	277.0	253.2	266.1
375	1	450	70000	375	1.20	515	276.7	254.2	266.1
375	1	510	70000	375	1.36	662	276.6	253.9	266.1
375	1	600	70000	375	1.60	916	276.4	254.3	266.1
375	1	765	70000	375	2.04	1489	275.6	254.3	266.1
375	1	1000	70000	375	2.67	2544	274.9	254.4	266.1
500	0.75	255	70000	667	0.51	165	157.3	144.4	149.7
500	0.75	382.5	70000	667	0.77	372	156.3	142.7	149.7
500	0.75	510	70000	667	1.02	662	156.0	143.1	149.7
500	0.75	765	70000	667	1.53	1489	155.6	143.2	149.7
100	0.25	200	5500	400	2.00	1526	1.4	1.3	1.3

Table 4.2: Static buckling analyses results of axially compressed unstiffened, linear-elastic isotropic cylinders with their dimensions and material stiffness.

compatibility equations for simply supported edges and considers neither the length nor the radius of the shell. Anyway, the results for shells with ideal geometry are close to the more complex numerical analysis results with clamped cylinder edges assumed. Consequently, for linear-elastic cylinders without imperfections and hence with linear pre-buckling state the effort of a nonlinear buckling analysis may hardly be justified if no further computations of the structure with changed conditions are conducted.

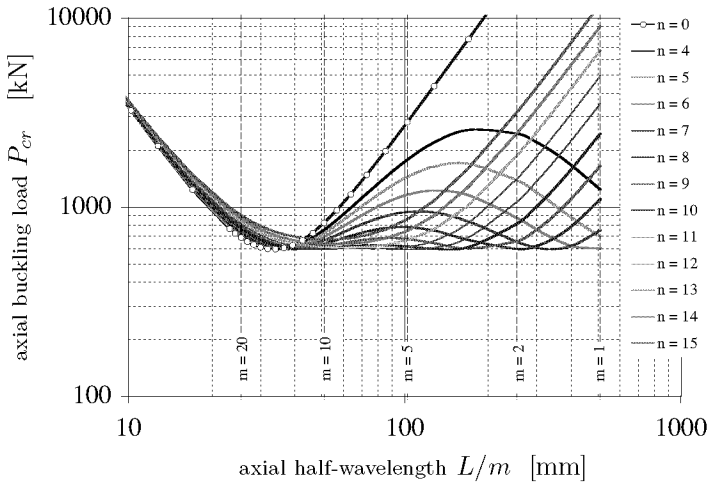


Figure 4.6: *Buckling loads of a classical analysis for the aluminium cylinder with $R = 250$ mm, $L = 510$ mm and $h = 1.5$ mm. Results for different axial half-wave numbers m and circumferential wave numbers n .*

Many combinations of wave numbers result with only very little difference between the corresponding buckling loads. In Figure 4.6 the analysis result for some axial half-wave numbers m and circumferential wave numbers n are plotted. Only values for integer wave numbers n and m are relevant, but for a better visualisation continuous lines are drawn. Anyway, none of the combinations of m and n can be identified as the minimal buckling load, all minima are almost identical with loads of about 600 kN.

In Figure 4.7 a selection of linear buckling modes (eigenmodes) of the isotropic cylinders is shown. Characteristic that they all have modes with a relatively high number of circumferential and axial waves or half-waves. The patterns shown in Figure 4.7 at each case relate to the

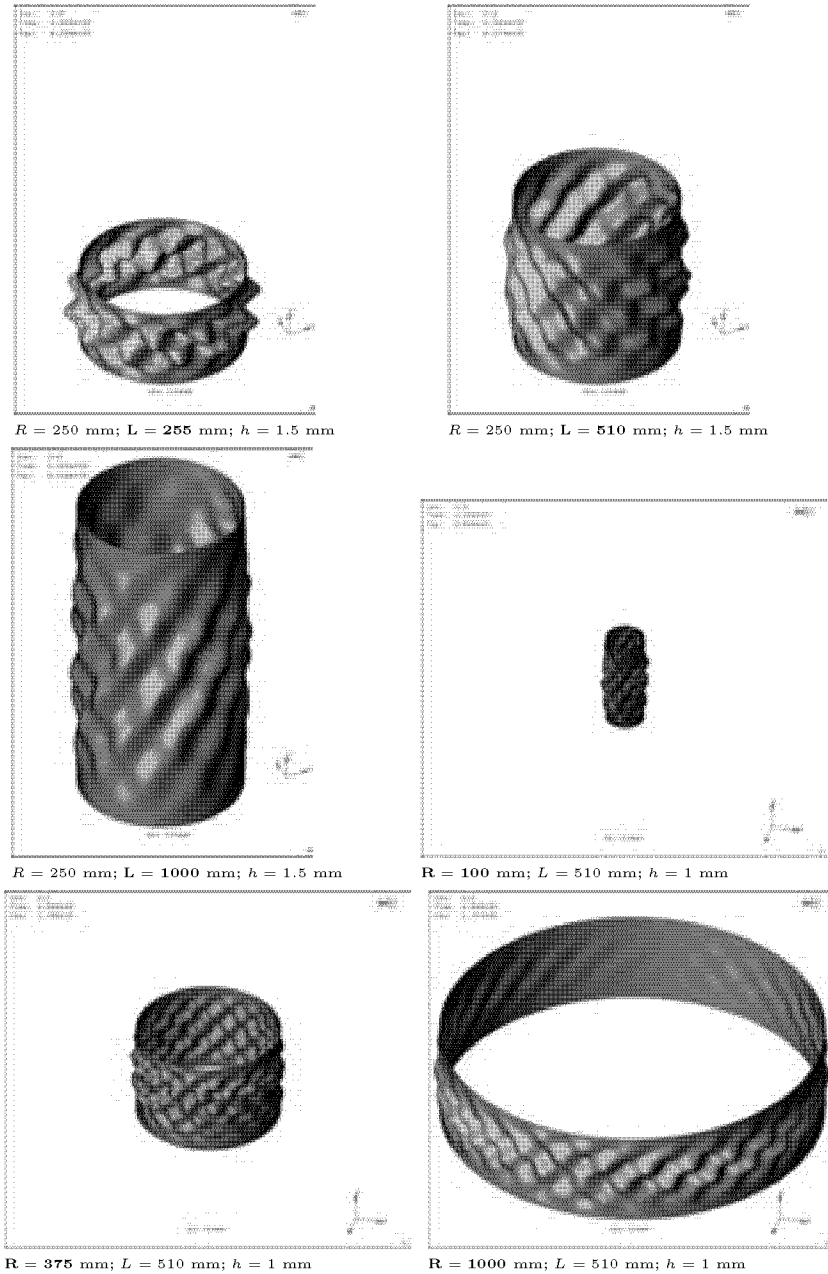


Figure 4.7: Linear buckling modes of some isotropic cylinders with a Young modulus of $E = 70$ GPa and a Poisson ratio of $\nu = 0.3$.

smallest value of six buckling loads requested. Any symmetry in these high-frequency buckling pattern is occasional since in contrast to the analytical approach no harmonic or bi-harmonic functions are involved in FE solutions. As initially mentioned, the buckling modes of elastic circular cylinders linearly calculated with eigenvalue analyses represent the initial buckling modes which in general may not be observed during tests without technical aid. Moreover, in contrast to these eigenmodes, the visible stable post-buckling patterns will consist of waves with low frequencies.

4.2.2 Results for the Laminated Cylinders

Throughout the DEVILS project it was discovered that cylinders with identical dimensions, identical membrane and bending stiffness (identical ply directions) but reversed stacking sequence (resulting in merely opposing sign in the coupling stiffness matrix for the shell) experienced a strikingly different buckling behaviour. When the predominantly axially stiff layers were arranged at the outside of the cylinder (Z32) the shell buckled at nearly half the load value compared to the shell which had the stacking sequence reversed and the more axially oriented fibers positioned at the inside (Z33). With the analytical solution presented in Section 2.2.3 and with the finite element method this effect could be reproduced [60, 81].

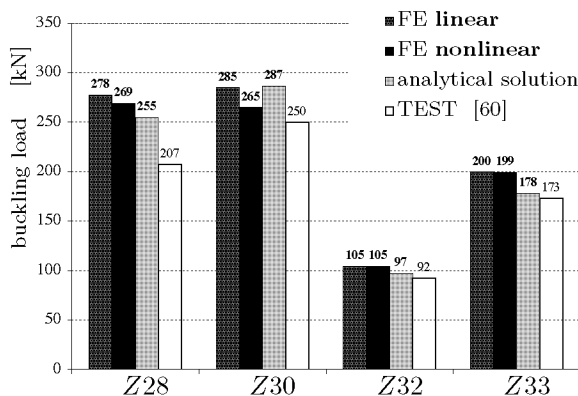


Figure 4.8: FE buckling analysis results of the DEVILS cylinders with ideal geometry.

The results of the static FE analyses and of the analytical method achieved for the four DEVILS cylinders with ideal geometry are graphed in Figure 4.8. Except for cylinder Z30, the analytical solution gives lower buckling loads than a linear as well as a nonlinear static FE analysis. But this close-form solution of differential equations refers to simply supported edges whereas the FE analyses refer to clamped edges. Attention should also be paid to the discrepancy between the test buckling loads and the calculated values in Figure 4.8 for the cylinders Z28 and Z30. The efforts to obtain a better agreement between numerical analysis and testing by inclusion of imperfections are subject of a later chapter.

The stacking sequence of cylinder Z30 is a result of an optimisation of the fibre orientation of the five double plies regarding the buckling resistance; therefore, cylinder Z30 is the “optimum”, the specimen with the highest buckling load among the cylinders considered within the test campaign. Shell Z32 in turn was designed as “pessimum”, i.e. the one with the lowest buckling load. The stacking of Z33 finally was obtained by reversing the order of plies of cylinder Z32. Figure 4.8 manifests that cylinder Z32 has significantly lower buckling loads than Z33. In the diagrams in Figure 4.9 and 4.10 the buckling loads for

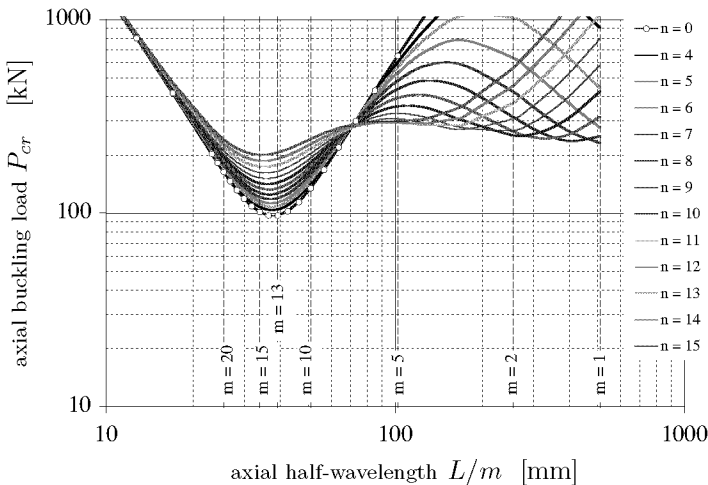


Figure 4.9: Results of the classical analysis: Z32.

various circumferential wave numbers n as function of the axial half-wavelength L/m are shown for the two cylinders Z32 and Z33. Again, although only loads for integer wave numbers n are relevant continuous

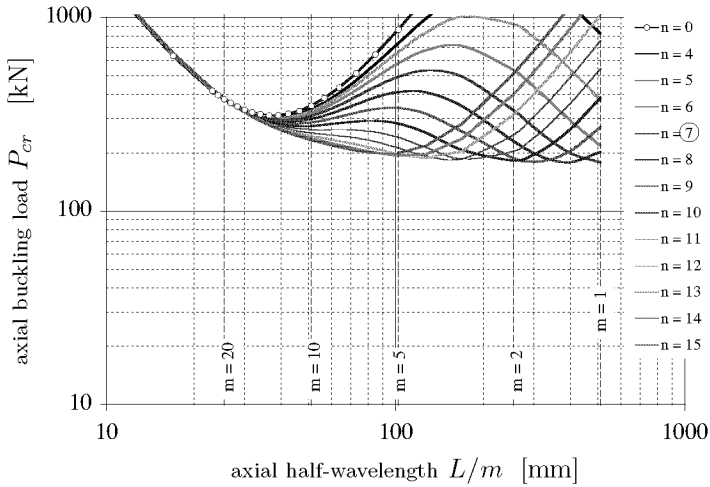


Figure 4.10: *Results of the classical analysis: cylinder Z33.*

lines were drawn for a better visualisation. With cylinder *Z32* a group of low buckling loads at the left side, i.e. at small axial half-wavelengths strike. The corresponding mode shapes are long in the circumferential direction and short in the axial direction, the lower curve refers to $n = 0$, that is for axisymmetric buckling as depicted in Figure 4.11 For shell *Z33* no such group of mode shape close to $n = 0$ with low buckling load may be detected. On contrary, the critical loads of axially short modes are shifted up to values higher than those of axially longer and circumferential shorter mode shapes [40]. The buckling loads and modes of the two cylinders, calculated with the analytical method, are

$$Z32: \quad P_{cr} = 97.3 \text{ kN}; \quad m_c = 13; \quad n_c = 0;$$

$$Z33: \quad P_{cr} = 178.0 \text{ kN}; \quad m_c = 1; \quad n_c = 7.$$

In Figure 4.11 the results of linear buckling analyses are plotted. In fact, in case of cylinder *Z32* the buckling pattern is of axisymmetric shape, matching Moiré pictures obtained during testing, and also confirming the result of the classical analytical method discussed above. But the irritating spiral buckling pattern of cylinder *Z33* (Fig. 4.11, right) could neither be measured nor described by classical analytical solutions. The post-buckling pattern observed during the tests of specimen *Z32* consisted of one row of eight large dimples ($m = 1, n = 8$), the post-buckling mode of *Z33* of two staggered rows of nine large buckles ($m = 2, n = 9$).

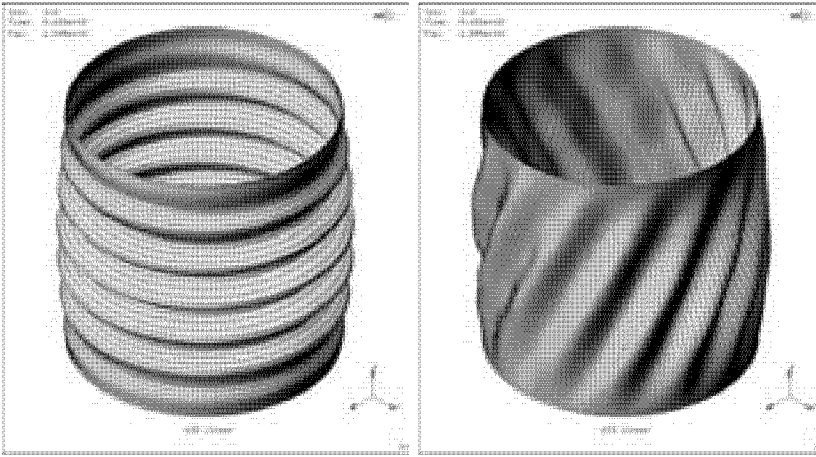


Figure 4.11: *Buckling modes of cylinder Z32 (left) and Z33 (right). Results of linear buckling analyses.*

(GEIER, MEYER-PIENING & ZIMMERMANN [40]) give a mechanical explanation of the behaviour observed of cylinders with opposite stacking sequences. If axially stiff layers are predominantly located at the outer side of the cylindrical shell the component b_{21} of the eccentricity matrix is positive, and hence the buckling load is low if the buckling mode is axisymmetric (see Section 2.2.3, Eq. 2.64):

$$P_{cr} = 2\pi R N_{cr} = \frac{4\pi}{a_{22}} \left(\sqrt{\tilde{D}_{11} a_{22} + b_{21}^2} - b_{21} \right).$$

Consequently, for cylinder Z32 with the axially stiff layers at the outer side of the shell the eccentricity term results $b_{21} = +0.3046$ mm, and for Z33 with reversed stacking $b_{21} = -0.3046$ mm, and for both laminates the value of the root expression in the formula above is 0.5799. The corresponding axisymmetric buckling load finally is $P_{cr} = 96.8$ kN for Z32 and $P_{cr} = 311.9$ kN for Z33. These loads are somewhat smaller than the axisymmetric buckling loads calculated for discrete axial half-wave numbers. Note that non-axisymmetric modes of Z33 are connected with lower loads ($P_{cr} = 178$ kN) [40].

A physical interpretation presented by (GEIER, MEYER-PIENING & ZIMMERMANN [40]) bases on the consideration of the POISSON's ratio effect: consider an axially compressed cylinder $Z0.\alpha$ or $Z\alpha.0$ which is caused to expand due to the POISSON's ratio effect, and assume a super-

imposed infinitesimal axisymmetric buckling load deformation. Then, in the regions which buckle outward the compressive strain gets smaller near the outer surface and increases near the inner surface. In right side

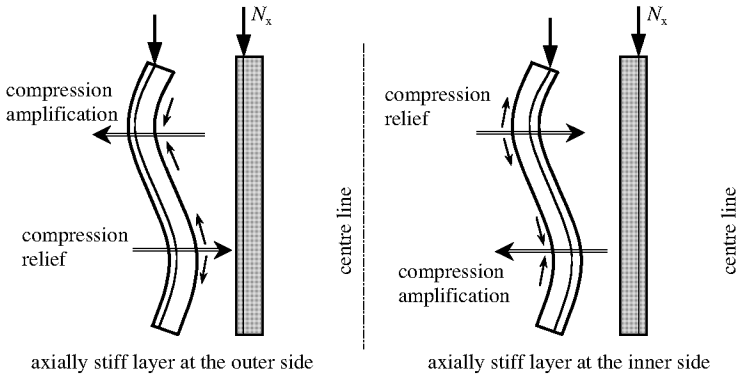


Figure 4.12: *Compression relief and amplification due to bending* [40].

of Figure 4.12 the inner layer is axially stiff with nearly zero POISSON's ratio, while the outer layer has $\pm\alpha$ orientation with high POISSON's ratio. At the buckle bulging outward the outer layer tends to shrink radially and thus to oppose the buckling deformation. At the inward buckle, due to the increase of compressive strain, the outer ply tends to expand radially. This again opposes the buckling deformation [40]. In the left side of Figure 4.12 again the stacking sequence is reversed, the eccentricity is opposite. The axially stiff layer is now placed at the outer side and the $\pm\alpha$ layer is placed next to inner surface. In the parts moving outward at bucking, again caused by the POISSON's ratio effect, the inner ply tends to grow radially. In the parts moving inwards it tends to shrink; hence, buckling deformation is increased which leads to a low buckling load [40].

The linear FE buckling analysis results of the two cylinders Z0.45 and Z45.0 in Figure 4.13 illustrate the different behaviour of cylinders with 0° -plies near one surface and $\pm\alpha$ layers near the other. The first cylinder (left) has the stacking sequence $[0^\circ_4, (+45^\circ, -45^\circ)_2]$, the stacking of the second cylinder (right), $[(-45^\circ, +45^\circ)_2, 0^\circ_4]$, is reversed compared to the first laminate. The first cylinder Z0.45 (left) with axial stiff layers at the outer side of the shell again buckles axisymmetrically ($n_c = 0$) with a buckling load of 70 kN, which is significantly lower than the buckling load of cylinder Z45.0 (right) with 107 kN and with its axial stiff

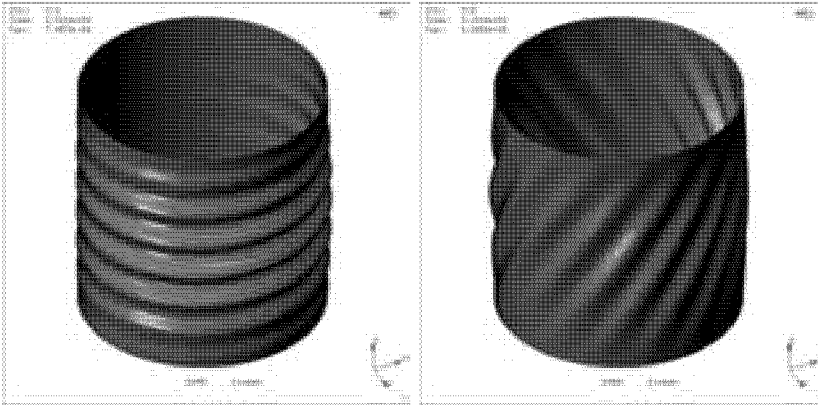


Figure 4.13: Linear buckling modes of cylinder Z0.45 (left) and Z45.0 (right) with laminates $[0^{\circ}_4, (+45^{\circ}, -45^{\circ})_2]$ and $[(-45^{\circ}, +45^{\circ})_2, 0^{\circ}_4]$ respectively.

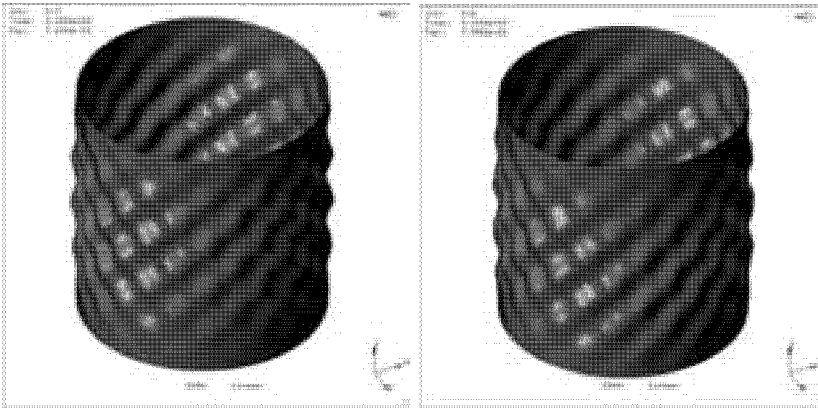


Figure 4.14: Linear buckling modes of cylinder Z0.90 (left) and Z90.0 (right) with laminates $[0^{\circ}_4, 90^{\circ}_4]$ and $[90^{\circ}_4, 0^{\circ}_4]$ respectively.

layers at the inner layer. Similar to cylinder Z33, latter buckles non-axisymmetrically. The results of the FE linear buckling analysis of the cylinder Z0.90 and Z90.0 in Figure 4.14 manifest a remarkable difference to the two cylinders Z45.0 and Z0.45 above. With their opposite stacking sequences $[0^\circ_4, 90^\circ_4]$ (left) and $[90^\circ_4, 0^\circ_4]$ (right) they are also eccentrically laminated and have the same dimensions and ply properties, but $\pm\alpha$ layers with high POISSON's ratio are missing. Hence, both cylinders buckle non-axisymmetrically at almost equal buckling loads (76 and 75 kN).

The presence of ply packages with high POISSON's ratio and their position influence strongly the buckling loads and modes. In Table 4.3

label	stacking	axisymmetric buckling Eq. (2.64)				Eq. (2.62)			
		b_{21}	a_{22}	\tilde{D}_{11}	$\sqrt{^*}$	P_{cl}	P_{cl}	m_c	n_c
		[mm]	[mm/N]	[Nmm]	[mm]	[kN]	[kN]		
Z0.00	0°_8	0.0000	1.15	10371	1.09	119.4	73.6	5	14
Z0.10	$0^\circ_4, (\pm 10^\circ)_2$	0.0467	1.13	10027	1.07	113.2	89.5	5	14
Z0.15	$0^\circ_4, (\pm 15^\circ)_2$	0.1007	1.10	9583	1.03	106.2	105.4	7	13
Z0.20	$0^\circ_4, (\pm 20^\circ)_2$	0.1656	1.05	8925	0.98	97.7	98.0	10	0
Z0.30	$0^\circ_4, (\pm 30^\circ)_2$	0.2729	0.85	7016	0.82	80.8	81.1	11	0
Z0.35	$0^\circ_4, (\pm 35^\circ)_2$	0.2898	0.85	5948	0.77	74.6	74.6	12	0
Z0.45	$0^\circ_4, (\pm 45^\circ)_2$	0.2465	0.47	4179	0.50	69.9	70.2	14	0
Z0.55	$0^\circ_4, (\pm 55^\circ)_2$	0.1607	0.30	3153	0.35	78.0	78.1	17	0
Z0.60	$0^\circ_4, (\pm 60^\circ)_2$	0.1201	0.25	2863	0.29	87.1	87.1	19	0
Z0.70	$0^\circ_4, (\pm 70^\circ)_2$	0.0573	0.25	2551	0.26	113.2	113.3	22	0
Z0.75	$0^\circ_4, (\pm 75^\circ)_2$	0.0359	0.17	2477	0.21	127.5	107.8	12	15
Z0.90	$0^\circ_4, 90^\circ_4$	0.0092	0.15	2406	0.19	151.5	73.2	10	15
Z0.00	0°_8	0.0000	1.15	10371	1.09	119.4	73.6	5	14
Z10.0	$(\mp 10^\circ)_2, 0^\circ_4$	-0.0467	1.13	10027	1.07	123.5	78.3	5	14
Z20.0	$(\mp 20^\circ)_2, 0^\circ_4$	-0.1656	1.05	8925	0.98	137.3	91.2	5	15
Z30.0	$(\mp 30^\circ)_2, 0^\circ_4$	-0.2729	0.85	7016	0.82	161.8	104.7	5	15
Z35.0	$(\mp 35^\circ)_2, 0^\circ_4$	-0.2898	1.13	5948	0.87	176.7	108.3	5	15
Z45.0	$(\mp 45^\circ)_2, 0^\circ_4$	-0.2465	0.47	4179	0.50	203.2	107.4	6	16
Z55.0	$(\mp 55^\circ)_2, 0^\circ_4$	-0.1607	0.30	3153	0.35	212.1	99.4	7	16
Z60.0	$(\mp 60^\circ)_2, 0^\circ_4$	-0.1201	0.25	2863	0.29	208.1	94.5	8	16
Z75.0	$(\mp 75^\circ)_2, 0^\circ_4$	-0.0359	0.17	2477	0.21	180.7	80.1	9	15
Z90.0	$90^\circ_4, 0^\circ_4$	-0.0092	0.15	2406	0.19	166.8	73.2	9	14

$$\sqrt{^*} = \sqrt{\tilde{D}_{11}a_{22} + b_{21}^2}$$

Table 4.3: Terms of eccentricity b_{21} , compliance a_{22} and modified bending stiffness \tilde{D}_{11} and the resulting buckling loads of axisymmetric and non-axisymmetric buckling for the cylinders Z0. α and Z α .0. In the upper block the cylinders with axially stiff layers at the outer side, in the lower block those with axially stiff layers at the inner side of the laminate.

the results are listed of the application of the formulas, referring to the close-form solutions for non-axisymmetric and axisymmetric buckling

as presented in Section 2.2.3, on the the cylinders $Z0.\alpha$ and $Z\alpha.0$ with stackings $[0^{\circ}_4, (\pm\alpha)_2]$ and vice versa for different ply angles α . The buckling loads correspond also to the lines in Figure 4.15. From the cylinders in the upper block with their axially stiff layers at the outer side of the shell only the six specimens with magnitudes of the eccentricity term b_{21} that are sized enough in comparison with the magnitude of the root expression in Equation (2.64) buckle axisymmetrically. For the others the classical analytical solution for non-axisymmetric buckling with 13 to 15 circumferential waves n_c yields the lower buckling loads. In Figure 4.16 the cylinders and the corresponding loads in Table 4.3 are plotted in function of b_{21} to demonstrate the theoretical limits for axisymmetric buckling. Values for $n_c = 0$ are available for laminates $Z0.\alpha$ with α between 16° and 70° (high POISSON's ratio). For negative b_{21} in any case non-axisymmetric buckling (line with diamonds) gives lowest buckling loads. From Table 4.3 may further be taken that the number of axial half-waves m_c arises with decreasing circumferential flexibility a_{22} and axial bending stiffness \bar{D}_{11} . In Figure 4.15 the FE analysis results of the cylinders $Z0.\alpha$ and $Z\alpha.0$ are plotted. It can be seen that for cylindrical shells with $\alpha = \pm 45^{\circ}$ the difference between the buckling loads of the cylinders with stiff layer at the outer side (i.e. axisymmetric buckling, low buckling load) and the cylinder with stiff layer at the inner side is maximal and almost vanish for $\alpha = 0^{\circ}$ and $\alpha = 90^{\circ}$.

The buckling modes of cylinder $Z0.20$ and of $Z0.70$ resulting from linear FE analyses are not axisymmetric ($n_c \neq 0$) as predicted with the classical analysis but have some spiral shapes similar to cylinder $Z33$ with different helix angles. This discrepancy might stem from the impossibility to describe spiral patterns with the bi-harmonic functions in the shell calculus without a phase shift along the cylinder axis considered. This shortcoming might also explain the exceptionally lower buckling loads for $\alpha = 15^{\circ}$ and $\alpha = 75^{\circ}$ in Figure 4.15 of numerical analyses compared with the values of classical analyses.

The buckling behaviour of the two cylinders $Z0.60s$ and $Z60.0s$ with symmetric stackings as

$$\begin{aligned} Z0.60s: & \quad [0^{\circ}_2, +60^{\circ}, -60^{\circ}_2, +60^{\circ}, 0^{\circ}_2] \\ Z60.0s: & \quad [+60^{\circ}, -60^{\circ}, 0^{\circ}_4, -60^{\circ}, +60^{\circ}] \end{aligned}$$

is different: the first cylinder with axially stiff layers positioned next to the shell surfaces buckles non-axisymmetrically, whereas the second specimen with its axially stiff layers at the middle surface of the shell buckles axisymmetrically. In Table 4.5 the results of the analytical and numerical methods according to Section 2.2.3 and 3.5 for these cylinders

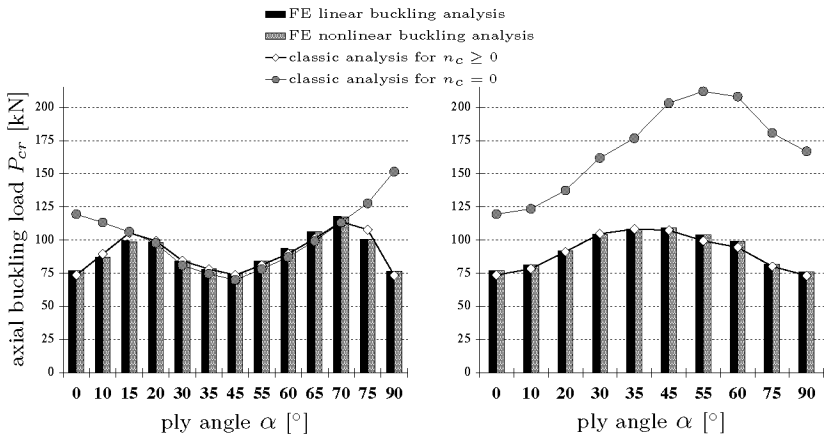


Figure 4.15: FE analysis results of the cylinders $Z0.\alpha$ (left) and $Z\alpha.0$ (right) with laminates $[0^4, (+\alpha, -\alpha)_2]$ and reverse in function of the ply angle α . The lines with diamonds mark analytical solutions according to Section 2.2.3, the circles such solutions especially for axisymmetric buckling.

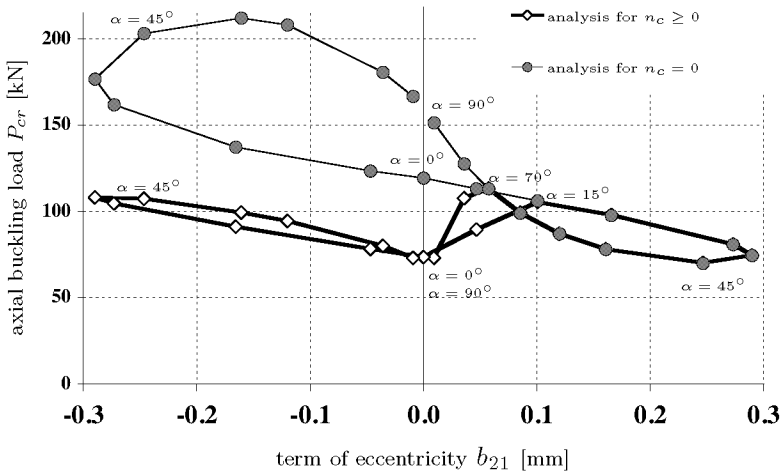


Figure 4.16: Buckling loads of the cylinders $Z0.\alpha$ and $Z\alpha.0$ in function of the eccentricity term b_{21} . The lines with diamonds denote classical analytical solutions, those with circlets solutions for axisymmetric buckling.

are listed. Due to the symmetry of their stackings the coupling stiffness for both laminates are zero ($\mathbf{B} = 0$). Thus, the eccentricity term b_{21} is also zero and the formula (2.62) for the buckling load in Section 2.2 for laminated cylindrical shells may be shortened to obtain the shape of the formula for orthotropic cylinder shell material (2.48). This is also valid for the buckling loads of axisymmetric buckling which are then given by

$$P_{cl} = 4\pi\sqrt{\frac{D_{11}}{a_{22}}}$$

Hence, the buckling pattern is governed by the relation of the axial bending stiffness to the circumferential flexibility. The replacement of the term of axial bending stiffness D_{11} by the term D_{22} (circumferential bending stiffness) and of the circumferential compliance term a_{22} by a_{11} (axial flexibility) in expression above yield an approximation for the buckling loads of checkerboard buckling with higher values for m_c and n_c . In Table 4.4 both root expressions including D_{11}/a_{22} and D_{22}/a_{11}

	axisymmetric buckling, Eq. (2.57)					Equation (2.48)		
	a_{22}	D_{11}	$\sqrt{\frac{D_{11}}{a_{22}}}$	$\sqrt{\frac{D_{22}}{a_{11}}}$	P_{cl}	P_{cl}	m_c	n_c
	[mm/N]	[Nmm]	[N]	[N]	[kN]	[kN]		
Z0.60s	$2.5 \cdot 10^{-5}$	9262	19268	9822	242.1	120.3	2	10
Z60.0s	$2.5 \cdot 10^{-5}$	2611	10231	19479	128.6	128.6	20	0

Table 4.4: Values of some relevant terms for axisymmetric buckling of cylinder Z0.60s and Z60.0s.

are given for the two cylinders. The compliance a_{22} is identical for both cylinder (and also for the “eccentric” Z0.60 and Z60.0). In the case of the second cylinder Z60.0s with the stiff layers at the mid-surface of the laminate the axial bending stiffness D_{11} is only 2611 Nmm and thus the root expression for axisymmetric buckling with 10 kN is smaller than the expression for non-axisymmetric buckling with 19 kN and thus the cylinder will buckle with $n_c = 0$. The axial bending stiffness of the first shell, Z0.60s, with the axially stiff layers at the periphery of the shell is significantly higher ($D_{11} = 9262$ Nmm) than that of its counterpart and the value of the root expression $\sqrt{D_{22}/a_{11}}$ is smaller than the value of the root expression $\sqrt{D_{11}/a_{22}}$ in the equation for axisymmetric buckling loads above. This indicates that the number of wave in circumference n_c for Z0.60s will be different from zero. In Table 4.5 finally the FE static analysis results for these cylinders are given for comparison with the

	analytic	FE linear	FE nonlinear
	P_{cl}	P_{cl}	P_{cl}
	[kN]	[kN]	[kN]
Z0.60s	120.3	117.0	116.9
Z60.0s	128.6	132.8	132.7

Table 4.5: Resulting buckling loads of the shells with symmetric stacking Z0.60s and Z60.0s.

analytical method. For both specimens with ideal geometry the difference between linear and nonlinear buckling analysis is negligible small. Compared with the analytic values both FE results are somewhat higher in case of the second cylinder with axisymmetric buckling, whereas the numerical solutions are noticeable smaller than the analytical solution in case of the first laminate. The analytical approach yield a buckling pattern with $m_c = 10$ and $n_c = 2$ whereas with linear FE calculation a spiral pattern similar to that of Z33 (see Fig. 4.11) or Z45.0 (see Fig. 4.13) may be obtained. The discrepancy might stem from a bad consideration of internal shear forces in the analytical method, especially in the case at hand with angle-ply of $\pm\alpha = 60^\circ$ close together with $\alpha = 0^\circ$ -plies.

Control calculations confirmed the assumption that the difference between hinged and clamped supports of axially compressed cylinder of sufficient length L regarding the buckling load is not important for linear buckling analyses. In Figure 4.17 the analysis results of the 2-ply CFRP cylindrical shells, taken from (SHEINMAN and GOLDFELD [73]), for different angle-ply and boundary conditions are plotted. The upper figure refers to simply supported boundary conditions, i.e. to the boundary conditions SS4 in case of the FE analyses and to the conditions SS3 for the w - \mathcal{F} DONNELL-type formulation according to Section 2.1.3 as well as for the \bar{u} - \bar{v} - w formulation (other, more accurate shell theories). The lower chart shows the solutions for clamped cylinder edges, i.e. for CC4 and for CC3 respectively. In both charts the maximum buckling occurs at angle-ply with $\alpha = 60^\circ$. There is only little difference between the linear FE buckling analysis results (lines with squares) as well as for the solution of the DONNELL-type equations (thick lines) for both sets of boundary conditions. The gap between the results of the nonlinear and linear FE analyses again are greatest at angle-ply with $\alpha = 60^\circ$ and for hinged respectively simply supported edges. In the

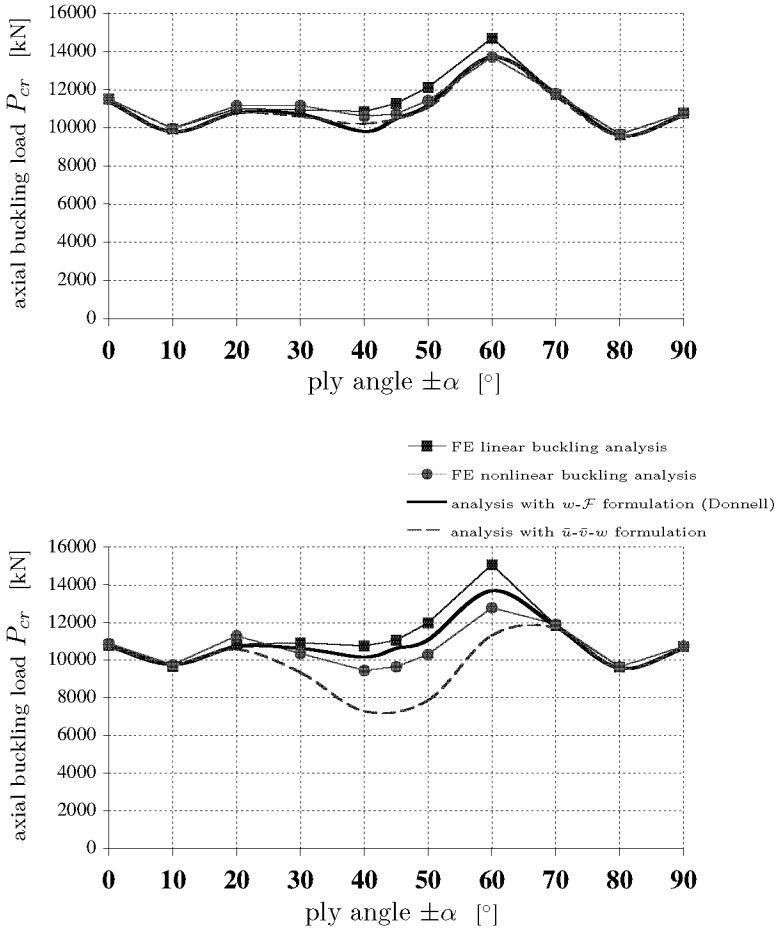


Figure 4.17: Static buckling analysis results of the 2-ply CFRP cylinder with radius $R = 1.27$ m, $L = 2.54$ m, and $h = 12,7$ mm. Buckling load vs angle-ply ($\pm\alpha$) with clamped edges (top) and simply supported edges (bottom).

upper chart the discrepancy between the solutions for the $\bar{u}\text{-}\bar{v}\text{-}w$ formulation and the other methods for $30^\circ \leq \alpha \leq 60^\circ$ strikes. (SHEINMAN and GOLDFELD [73]) report that, possibly due to internal shear forces caused by the laminate stacking, the $w\text{-}\mathcal{F}$ formulation just missed the lowest eigenvalue; the second eigenvalues of the $\bar{u}\text{-}\bar{v}\text{-}w$ formulation were close to the first values of the $w\text{-}\mathcal{F}$ calculation. In the $w\text{-}\mathcal{F}$ formulation the boundary conditions are to be defined in terms of w and \mathcal{F} , with the consequence that the conditions in \bar{u} and \bar{v} are not fully satisfied. However, the FE analysis results in the most cases are closer to the $w\text{-}\mathcal{F}$ solutions than to the $\bar{u}\text{-}\bar{v}\text{-}w$ solutions with direct definition of the edge displacements. This might provide an indication that the lower $\bar{u}\text{-}\bar{v}\text{-}w$ solutions for simply-supported boundary conditions stem more from internal shear forces than from the different formulation of the boundary conditions. The linear buckling analysis yielded always higher buckling loads than the nonlinear analysis as well as the $w\text{-}\mathcal{F}$ formulation.

Finally, except the 2-ply CFRP cylindrical shells with simply supported boundary conditions, the differences between the buckling loads achieved with the numerical linear and nonlinear buckling analyses, as well as between these numerical calculations and the rather simple analytical approaches, are marginal for the presented laminated cylinders. However, as long as no test results are available it is advisable to compare FE analysis results with results of a suitable analytical approach with the compatible set of boundary conditions (and vice versa).

4.3 Transient Dynamic Analysis Results

In the a previous section it was reported that the DEVILS cylinder Z33 according to the static FE buckling analysis has a spiral buckling pattern (see Figure 4.11), a mode which, in contrast to the axisymmetric shape of specimen Z32, could not be observed during tests and not confirmed by an analytical approach either. The transition from the pre-buckling state to a post-buckling state of equilibrium with the corresponding dynamic shell movements can hardly be reproduced with static numerical analysis methods. Thus, if there was not the time exposure it would be obvious to use FE codes with direct time integration for a dynamic analysis of the dynamic buckling phenomenon right from the start. But to date the performance of the computers available and the complex input settings in most cases discourage the analyst from such a transient dynamic analysis, all the more for the buckling load of ideal cylinders

the unequally faster prediction with an analytical approach yield equal or even better results. Nevertheless, the important differences between static buckling patterns and observed post-buckling patterns was a motivation to investigate the dynamic transition including the post-buckling behaviour.

When DLR Braunschweig (former DFVLR) was performing experiments in the late sixties with circular cylinders made of Hostaphan (Mylar) the experimenters became interested in the dynamic behaviour of the shell wall during buckling. With high-speed movies [35, 36] it became visible that, in the case of elastic shell material and axial loading, the initial buckling pattern was not similar to the post-buckling pattern that can be detected after the shell came to a rest. Based on the high-speed movies of the Mylar cylinder, dynamic transient FE analyses with quasi static loading, as introduced in Section 3.4, were performed, basically to calibrate the dynamic calculations, as for other cylinders, e.g. the above-mentioned DEVILS cylinders, no high-speed pictures are available.

The investigated isotropic cylinder, matching the above mentioned high-speed movies, has a diameter of 200 mm, a length of 200 mm, a wall thickness of 0.254 mm and a YOUNG's modulus of about 5500 MPa (in axial direction). The assigned mass density was 1400 kg/m³.

Again, the used FE program was MARC[®] and 10800 thick rectangular shell elements (element No. 75) formed the model. For numerical time integration the implicit single-step Houbolt method (SSH-method, see Section 3.4) was selected. The damping matrix was introduced as 50000 times the mass matrix (pure inertia damping). The constant compression velocity was set to 0.1 mm/s, and the selected smallest time step for an axial displacement increment was 0.001 seconds.

The results of such calculations are given in Figure 4.18 for ideal geometry and with stiffness properties as indicated in the figure. These curves are compared with the curve reproduced from the movie taken during the test. It was possible to arrange the output of successive deformation states as to create a simulated movie and the results proved to be rather similar to what had been discovered in the high-speed movies. The instability started from a zone near the edge(s) which are laterally constraint by rigid endplates. The first buckle then multiplies, travels throughout the shell, increases in size and settles towards the center of the shell in two staggered rows of buckles. This pattern was then recorded as first stable post-buckling pattern, see Figure 4.19.

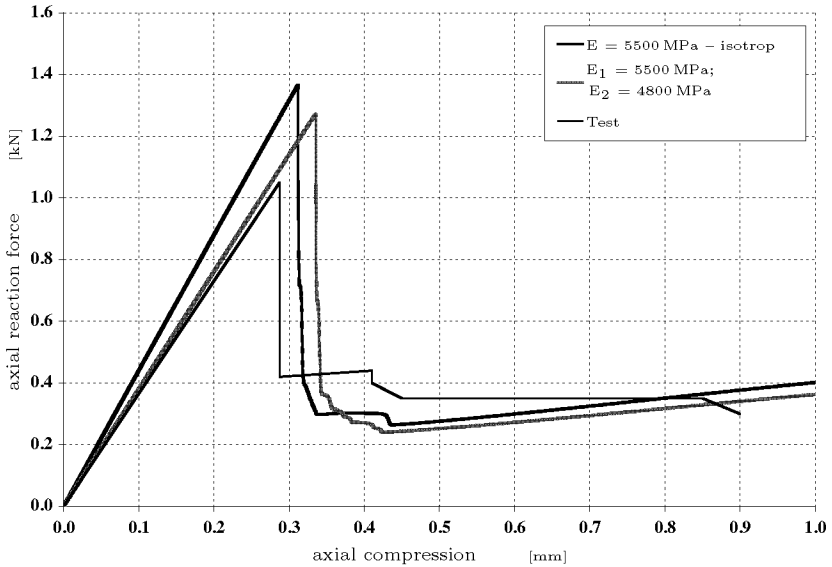


Figure 4.18: Results of transient dynamic calculations (SSH-method) for a Hostaphan cylinder with isotropic material and for somewhat orthotropic properties, compared with a corresponding curve found in a high-speed movie. The damping matrix was estimated to be 50000 times the mass matrix.

Noteworthy that the cylinder in the test, in contrast to that in the calculations, was not of ideal geometry⁵.

The obtained results were considered satisfying (see Figure 4.20) and, thus, stimulated further investigations with this software in order to study the buckling behaviour of the laminate DEVILS cylinders. Above all, the noticeable differences between the static buckling and stable post-buckling patterns of two specimens Z32 and Z33 were investigated.

As in the case for the Hostaphan cylinder the dynamic analyses of the CFRP cylinders was also conducted with help of the SSH-method implemented in MARC[®]. In this case the assigned mass density was 1600 kg/m³. Again, the compression velocity was 0.1 mm/s, but the damping matrix was now introduced as 25000 times the mass matrix. Other parameters remained equal to the static analyses. The large factor to the damping matrix was found by trying and was a practical compromise considering the material values, the chosen compression velocity

⁵At this stage of the studies imperfections were not considered in the calculations.

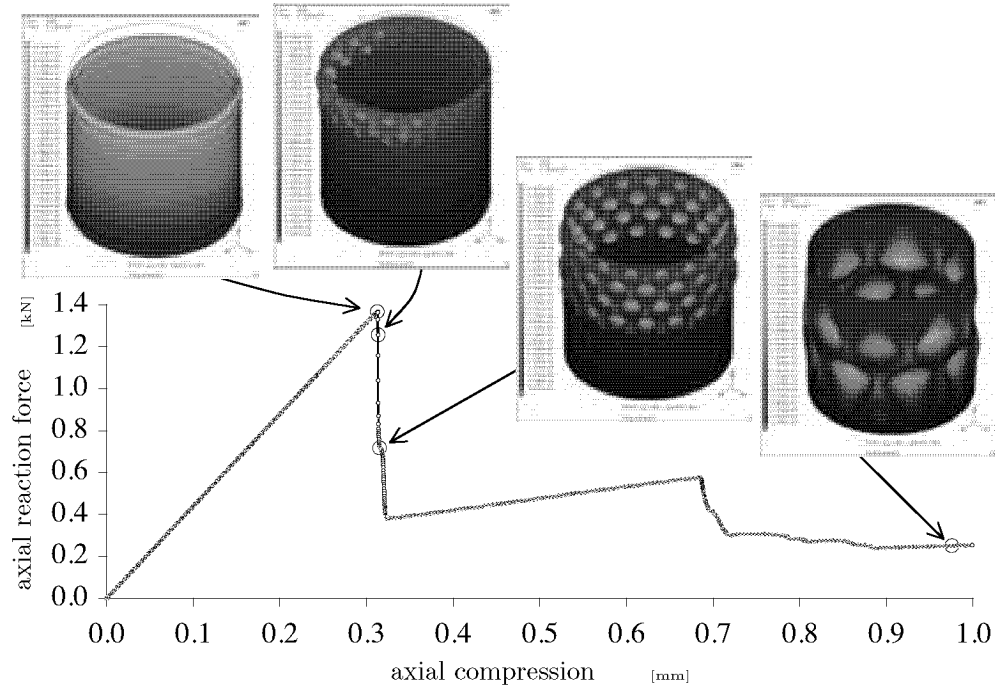


Figure 4.19: Results of a transient dynamic FE analysis of the isotropic “Mylar” cylinder, but with higher damping introduced: damping matrix $60000 \times$ mass matrix. The deformations plotted in the included pictures are automatically scaled up referring the particular largest value.

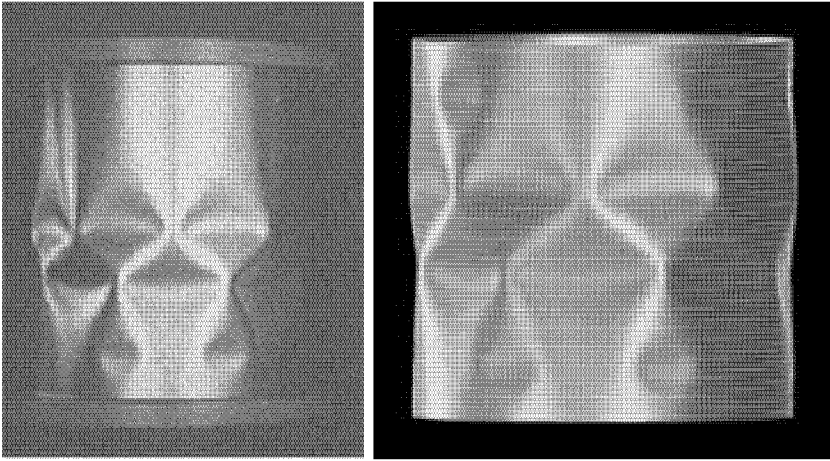


Figure 4.20: *Selected picture of a high-speed movie with post-buckling pattern of the Hostaphan cylinder (left) and the corresponding pattern of a FE simulation with the SSH-method (right).*

and the number of increments.

The results of such an analysis for cylinder *Z32* with perfect cylinder geometry is plotted in Figure 4.21. The constant reaction force at buckling for about 0.1 mm of compression is special in this case. The axisymmetric deformation pattern, known from static analysis and tests, is already developed prior to reaching the buckling load. This load is identical to the value achieved by nonlinear buckling analyses (105 kN). The change to the first post-buckling state starts with non-axisymmetric waves on the top and in the valleys of the middle axisymmetric waves. The post-buckling pattern is clearly different to the pattern achieved by other analyses.

In Figure 4.22 the results of a dynamic analysis for cylinder *Z33* with ideal geometry are shown and the improved buckling resistance compared with cylinder *Z32* can be seen. In this case the collapse is significant, manifested by the sharp angle at buckling and the vertical downfall of the load vs. axial deflection curve. The buckling load is slightly higher compared with the results in Figure 4.8 (207 kN). The deformation pattern very close and prior to buckling is similar to the mode resulting from a linear buckling analysis (Fig. 4.11). When compression is increased this shape is quickly replaced by small buckles starting at one edge. After

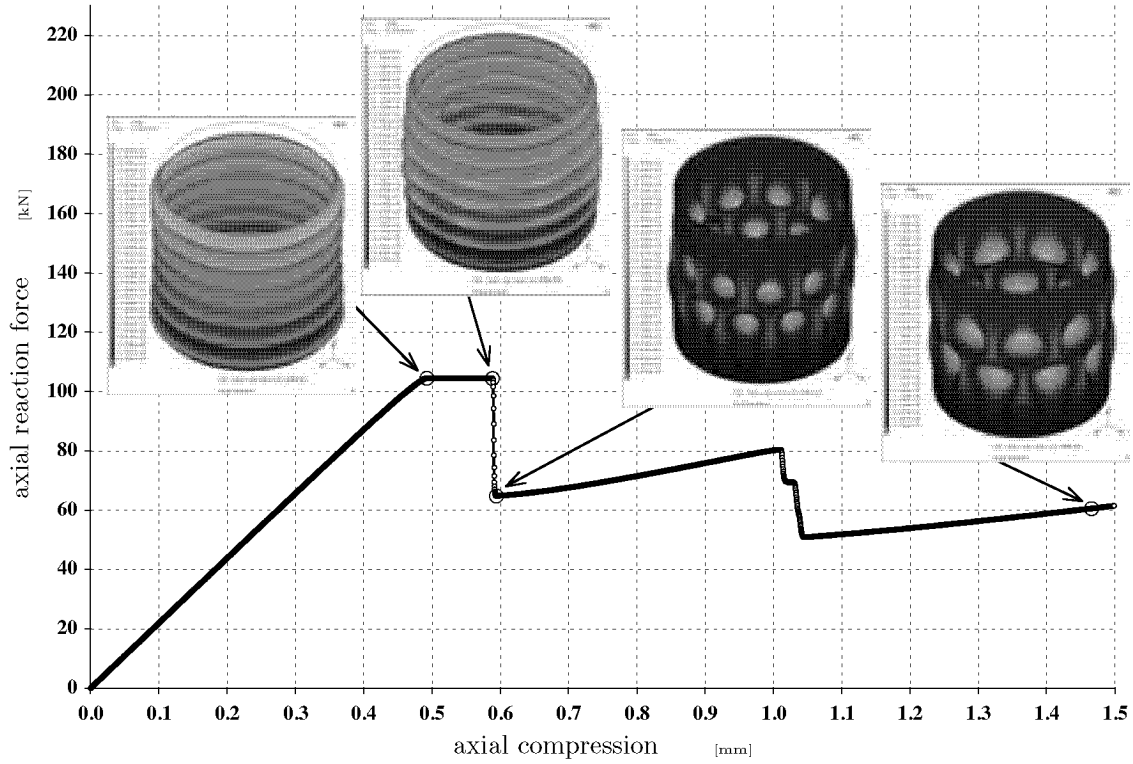


Figure 4.21: *Dynamic FE analysis result of cylinder Z32 with ideal geometry. The plotted patterns are automatically scaled.*

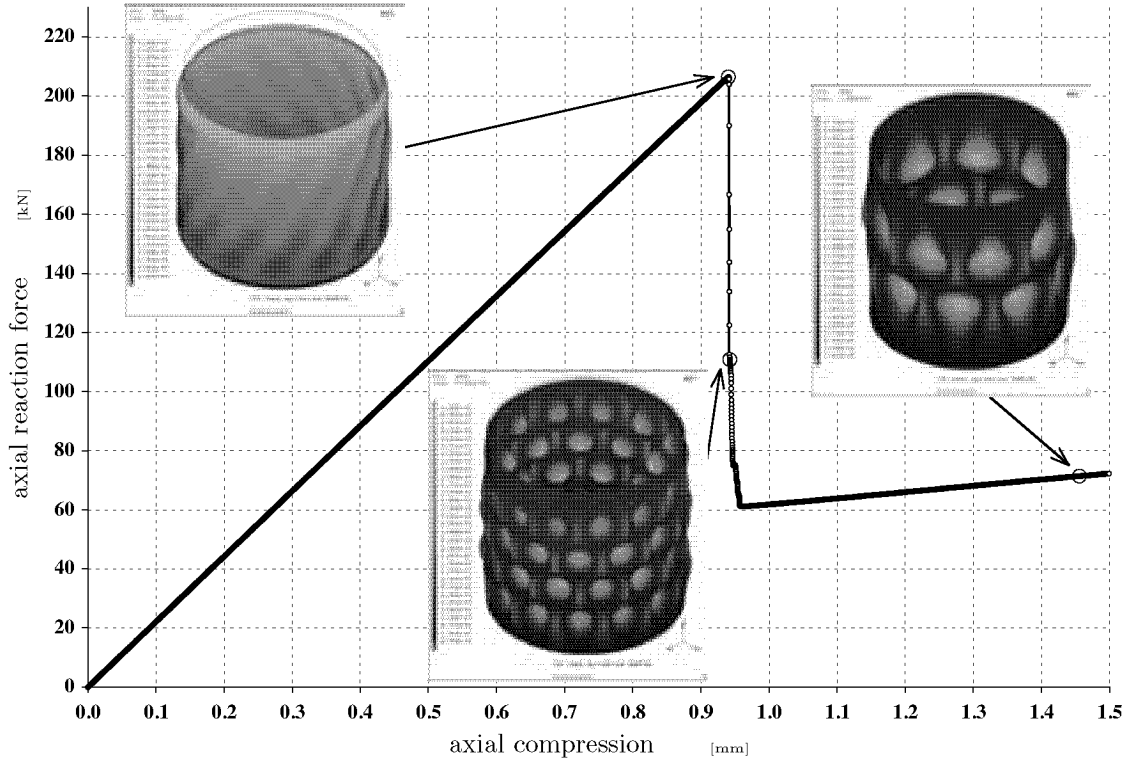


Figure 4.22: *Dynamic FE analysis result of cylinder Z33 with ideal geometry.*

having filled up the entire surface, the buckles increase and get reduced in number until the state of a first stable post-buckling pattern with two staggered rows of larger buckles is attained. Actually, this deformation pattern ($m = 2$, $n = 8$) was observed during tests.

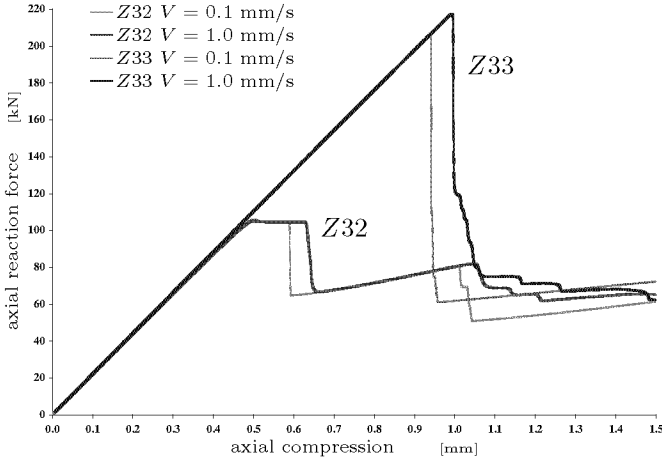


Figure 4.23: *Dynamic FE analysis results of cylinder Z33 and Z32 with ideal geometry for a compression velocity of 0.1 mm/s and for a velocity of 1.0 mm/s.*

The chosen compression velocity of 0.1 mm/s leads to almost identical buckling loads than those achieved by nonlinear static analysis. Possible over-shoots and additional axial forces through damping are small and may be neglected. The real velocity was about 0.1 mm per minute, i.e. circa 60 times lower than in the FE simulations – a value which would require exorbitant damping or computation time. Figure 4.23 manifests the change of the velocity to 1.0 mm/s: over-shoots are then noticeable for both specimens. The slower the compression velocity the closer the resulting collapse load becomes to the corresponding static nonlinear buckling load. With too high velocities arbitrary loads above the static result may be found. Therefore, a dynamic transient analysis must not substitute a static, nonlinear buckling analysis for the specification of a collapse load.

In the charts presented above including dynamic analysis results the resulting axial reaction force are plotted in dependency of the given axial compression ΔL , i.e. the axial displacement u of the loaded edge nodes. The resulting forces are also frequently presented versus the lateral displacements w according to the searched amplitudes of the harmonic func-

tions $w(x, y)$ used to describe the displacement field analytically. But in FE buckling analysis of ideal circular cylinders the significance of the so-called modal displacement values is low. In the post-processing of the FE method the result extraction of displacements is conducted at discrete points; thus, the identification of the set of amplitudes for harmonic functions (e.g. FOURIER series) would require the data extraction for all nodes of the model. Since during buckling tests, in contrast to the lateral shell movements, the axial displacement may easily be recorded without touching the shell, axial load - axial displacement curves as shown above may be found more significant for direct comparisons between FE simulations and tests. In Figure 4.24 the axial reaction forces, achieved from

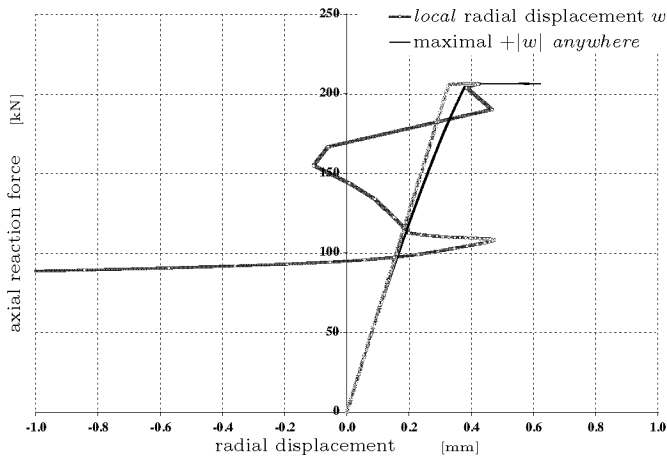


Figure 4.24: Resulting load-deflection curve of cylinder Z33 with ideal geometry. Axial reaction force vs. radial displacement w . The marked gray line refer to one node at half the cylinder length, the black lines to the maximal lateral displacement (absolute) at any node of the model.

a dynamic transient analysis of cylinder Z33, are plotted alternatively against the lateral displacement. The gray line refer to displacements at one node placed at half the cylinder length, whereas the black lines represent the maximum absolute values among all nodes of the cylinder model. It may be seen that prior to buckling the values for the selected single node are smaller than the values at some point else. The nodes with the maximal positive w are placed close to the edges where the expansion, caused by the POISSON effect, is disabled which in turn leads to the characteristic abating axisymmetric bulges at the edges, see Figure 4.22. Close after buckling the single node moves somewhat pe-

cularly in- and outwards, whereas the movement for maximal w -values is pointed inwards and the relating nodes are now placed somewhere in the midfield of the element mesh (the black line for negative w is not shown).

Chapter 5

Buckling of Cylinders with Distributed Imperfections

In the previous chapters the classical solutions and the linear and nonlinear finite elements methods used to specify the load carrying capacity of axially compressed, thin-walled isotropic or laminated, unstiffened circular cylindrical shells were described. Further, analysis results for such shells were discussed. In these calculations it was assumed that the shell geometry prior to loading at each case is that of an ideal circular cylinder, and that they are under uniformly distributed axial load. That is, possible imperfections like cut-outs, radial deviations of the shell middle surface from the nominal radius, wall-thickness variations, local material defects, eccentric edge loading, and so on, have been ignored.

But during tests or even in operation such cylindrical shells may buckle or collapse at much lower loads than predicted in analysis. In addition, test results of equally dimensioned cylinders under pure axial compression may be widely scattered (see Figure 5.4). The main reason why many shells fail at a much smaller load than the classical critical load may be assigned to the combined effect of nonlinearity and imperfections. (VON CÁRMÁN, DUNN, and TSIEN [77]) could demonstrate by approximate nonlinear analysis that, after reaching the critical state, the load can rapidly decrease at increasing deflection, what means that the stiffness

of the structure is reduced. They also demonstrated that even small disturbances may cause the shell to “jump” from a pre-buckling to a post-buckling state at which the load carrying capacity is much reduced [15].

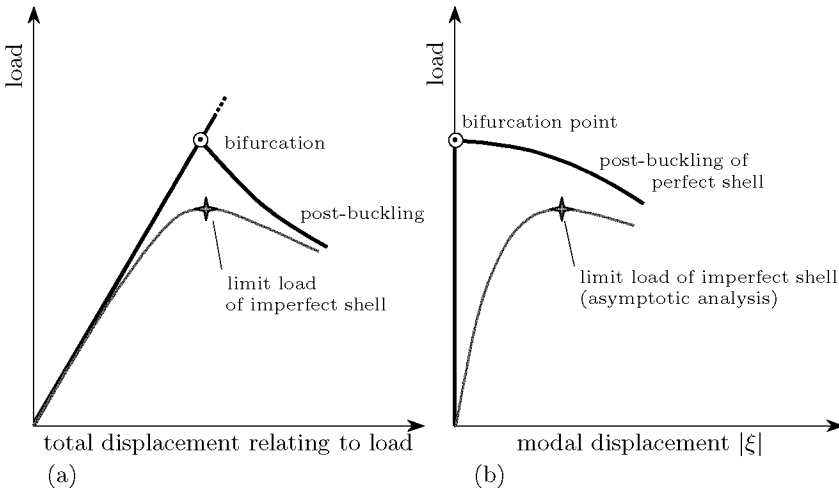
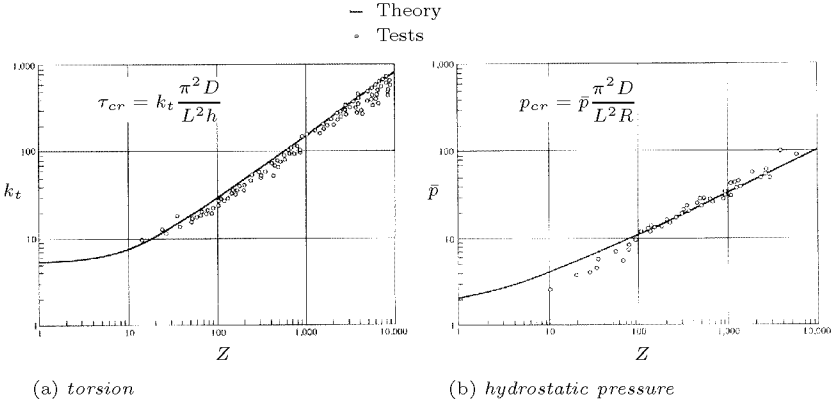


Figure 5.1: *Load-deflection curves with limit and bifurcation points. (a) general nonlinear analysis, (b) asymptotic analysis. From (BUSHNELL [21]).*

In the classical analysis of perfect cylindrical shells, see Section 2.2, it is assumed that the pre-buckling state is a membrane state and that deflections prior to buckling have negligible effect. Consequently, the amplitudes of the harmonic functions which describe the deflection and the membrane stress field in analysis remain zero. Figure 5.1 depicts typical load-deflection curves of (a) a general nonlinear analysis and of (b) an asymptotic analysis for a thin isotropic cylinder under axial compression, see Introduction Section 1.1. For perfect cylinder geometry prior to buckling the axial cylinder or “spring” stiffness is constant and thus the axial-load/compression curve in Figure 5.1(a) is a straight line. Having passed the bifurcation point the cylinder buckles and with continuous cylinder end-shortening the axial load decreases, indicating that the axial cylinder stiffness degrades. In Figure 5.1(b) the pre-buckling state is represented by the thick vertical line following the axis of ordinates. At the bifurcation point solutions of the equilibrium equations exist with non-zero modal amplitudes (radial displacements), denoted with ξ , and the shell ceases to be stable. The bold line in the figure, referring to a

post-buckling path, runs downwards with increasing ξ , what indicates that the load carrying capacity in the post-buckling state of the initially perfect shell at hand is reduced. (KOITER [54]) developed a general theory of stability that describes the immediate post-buckling behaviour asymptotically. He introduced the concept of a multidimensional space whose coordinates are the load and the amplitude of various possible post-buckling modes [15]. The curves in Figure 5.1(b) relate to only one mode with amplitude ξ . In KOITER's asymptotic theory the vertical line for the pre-buckling state together with the post-buckling path may be approached asymptotically by a polynomial expansion. This enables to describe the effect of small deflections in the post-buckling state as well as the effect of initial imperfections. The measures of the polynomial coefficients also indicate the sensitivity of a structure to initial deflections, to evenly distributed imperfections respectively. The thin line in Figure 5.1(b) corresponds to such a polynomial approach for an imperfect shell. The reduced buckling load of the imperfect shell compared with the bifurcation load of the perfect shell is marked with a star. Important for the buckling analysis of imperfect structures is to know, how imperfection sensitive the shell is and, above all, how much the critical load is reduced depending on the expected initial imperfection amplitude(s) in comparison to the classical load of the counterpart with perfect geometry.

Cylindrical shells subjected to external pressure or torsion are not as imperfection-sensitive as axially compressed cylinders are. That is, the difference between theoretical buckling pressure or torsion and test results is considerably smaller than the deviations of theoretical from experimental axial buckling loads; and in addition, the test results of cylinders under external pressure and torsion have a much smaller scatter bandwidth than those for axially compressed cylinders, see Figure 5.2. In Section 4.2.1 it was shown for the case of isotropic shell material that in the classical theory of cylindrical shells under pure axial compression the axisymmetric and many double periodic buckling modes (m and n) are associated with the same or almost the same buckling load. Cylinders under external pressure or under torsion, however, typically buckle in one half-wave in axial direction and thus the buckling mode referring to the appropriate lowest bifurcation load in these cases is determined solely by the number of waves along the circumference [18]. The interaction of the many modes with the same axial buckling loads contributes to the high imperfection sensitivity of cylindrical shells. Very small amplitudes of initial deflections composed of any of the critical buckling modes reduce the load carrying capacity due to interaction between the initial



$$Z = \frac{L^2}{Rh} \sqrt{1 - \nu^2}$$

$$D = \frac{E h^3}{12(1 - \nu^2)}$$

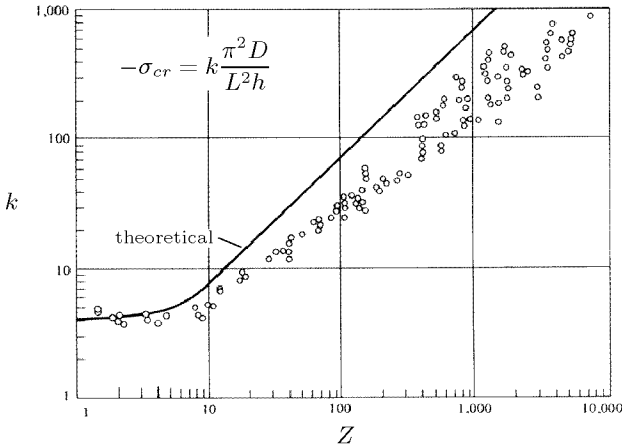


Figure 5.2: Comparison of theoretical and experimental buckling values for isotropic cylinders subjected to torsion, hydrostatic pressure, or axial compression. From (BRUSH & ALMROTH [18]).

deflection mode and the post-buckling deflection mode of the perfect shell.

Even very carefully manufactured cylinder with therefore minor dimension deviations may locally buckle at an average axial stress considerably below the theoretical, classical bifurcation stress of (see Section 2.2) [21]:

$$-\sigma_{cl} = \bar{C} \frac{Eh}{R} = \frac{1}{\sqrt{3(1-\nu^2)}} \frac{Eh}{R} ; \quad (5.1)$$

$$\bar{C} = 0.605 \quad \text{for} \quad \nu = 0.3 .$$

From this formula follows by multiplication with the cut area $2\pi Rh$ that the theoretical buckling load is given by

$$P_{cl} = 3.8 Eh^2 \quad ;$$

thus, the critical axial load is assumed to be independent of the nominal cylinder radius R and length L . But already (DONNELL & WAN [30]) and also (WEINGARTEN et al. [79]) demonstrated the increasing discrepancy between tests and theory with increasing radius/wall-thickness ratio R/h [21, 5]. This trend may be explained by the decreasing stiffening effect of the shell curvature $1/R$ with increasing radius R in comparison to flat plates. Therefore, the influence of initial imperfections, which are unavoidable and dependent on the fabrication method, arises with increasing R/h ratio [30, 21]. Figure 5.3 reproduces curves for different R/h ratios proposed for safe shell design by (BATDORF et al. [13]). These curves were derived from test values as plotted in Figure 5.2(c) and demonstrate the larger buckling load reduction to be expected for larger R/h ratios.

On the basis of experimental data (WEINGARTEN et al. [79]) proposed a lower bound curve for the buckling coefficient \bar{C} in Equation 5.1 as

$$\bar{C} = 0.606 - 0.546 \left(1 - e^{-\frac{1}{16} \sqrt{\frac{R}{h}}} \right) \quad \forall \quad 0.5 < \frac{L}{R} < 5 \quad (5.2)$$

According to the test results for short cylinders with $L/R < 0.5$ the difference between theory and experiments is smaller. Thus, (WEINGARTEN et al. [79]) corrected their formula above to obtain a lower bound for all R/h and L/R tested:

$$\bar{C} = 0.606 - 0.546 \left(1 - e^{-\frac{1}{16} \sqrt{\frac{R}{h}}} \right) + 0.9 \left(\frac{R}{L} \right)^2 \frac{h}{R} \quad (5.3)$$

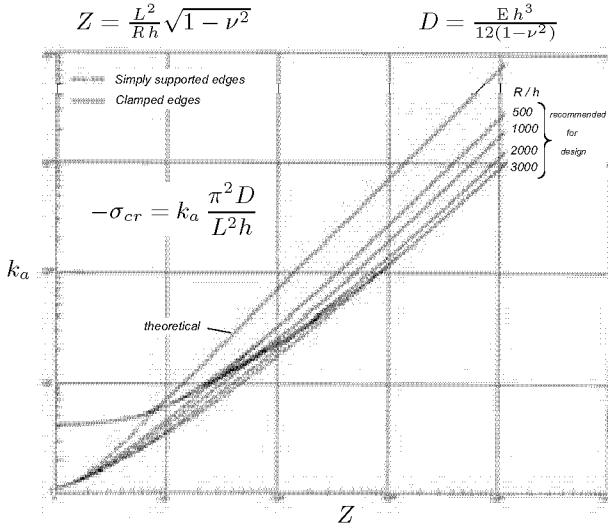


Figure 5.3: Buckling stress coefficients k for thin-walled cylinders under axial load. Theoretical values and recommended values for radius/wall-thickness ratios R/h as indicated. From (BATDORF et al. [13]).

for cylinders in the range $100 < R/h < 4000$ and $0.031 < L/R < 5$ [79, 25]. The important discrepancy between the theoretical buckling loads and the loads obtained from tests for axially compressed shallow cylinders of medium length induced many further researchers to ascertain reduced buckling loads for safe shell design, e.g. (GERARD & BECKER [42]) and (HARRIS et al. [71]). Their recommendations were used for design guidelines established by most industrial organizations like e.g. the National Aeronautics and Space Administration NASA or the German Institute for Standardization DIN [18]. In the NASA Space Vehicle Design Criteria, SP-8007 [62], for instance the following safe buckling loads for thin-walled isotropic monocoque cylinders are recommended:

$$\frac{P_{cr}}{P_{cl}} = 1 - 0.902 \left(1 - e^{-\frac{1}{16} \sqrt{\frac{R}{h}}} \right) \quad \forall \quad \frac{R}{h} < 1500 \quad (5.4)$$

whereby the ratio P_{cr}/P_{cl} has the meaning of a reduction or *knock-down factor* which should be multiplied with the classical buckling load P_{cl} to obtain the safe value. The formula (5.4) follows from the lower bound curve of WEINGARTEN et al. in Equation (5.2). In Figure 5.4 this curve is reproduced together with distributed test values. Thus, in accordance with test experiences and with the formula (5.4), the buckling of cylin-

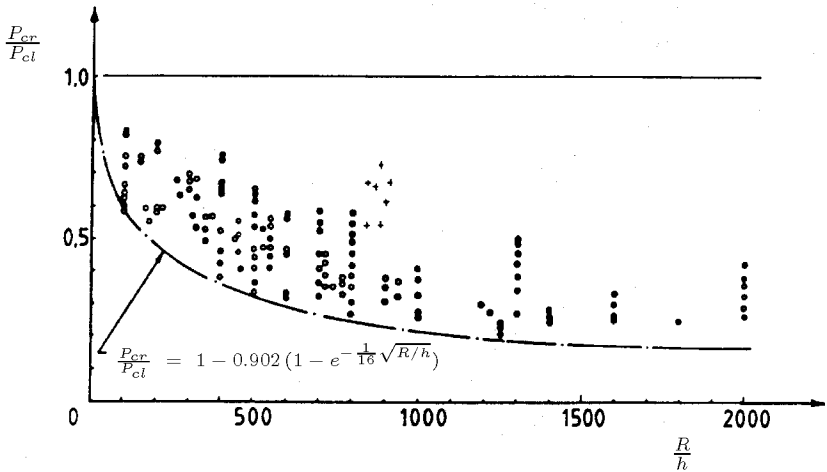


Figure 5.4: *Test data for isotropic cylinders under axial compression. From (ARBOCZ & HOL [8]).*

ders with larger R/h ratios has to be expected already at axial loads which are less than 20% of the theoretical value. The load curves above exemplify for the axial elastic buckling of thin-walled isotropic circular cylinders, but design guidelines are also available for the buckling of plates and panels, stiffened cylinders and consider also possible plasticity. The German standard DIN 18 800 part 4 for isotropic shell structures, for instance, deals with dimension tolerances (single dimples, eccentricities) as well as with the yield stresses, see Section 6.1 on page 191ff.

As shown in the previous sections, the estimated axial buckling loads of perfect cylinders obtained by the linear and nonlinear buckling analyses do not differ substantially; hence, the consideration of geometric nonlinearities in the pre-buckling state in the analysis of *perfect* shells in general may not reduce the difference between the calculated buckling loads and the loads obtained with experiments. To get FE analysis results closer to test values it might be obvious to apply initial deflections to the cylinder and to perform a linear or a nonlinear FE buckling analysis of the now imperfect cylindrical shell. In Figure 5.1(a) an example with nonlinear collapse of an imperfect shell is shown. In such a case pre-buckling deformations of the shell may not be assumed to remain small and hence a nonlinear buckling analysis would be advised. The main drawback of any buckling analysis under consideration of imperfections

is the fact that in most cases neither the sensitivity of the appropriate imperfection shape nor suitable initial deflection amplitudes are known a priori without measurement of the distortions of the real cylinder geometry to be analysed. Thus, in structural design mostly only the perfect shell is analysed and the resulting buckling load is reduced with a factor based on empiric data and standards as mentioned above.

This chapter describes the analytical treatment of the influence of geometric imperfections on the buckling load of axially compressed cylinders. The focus is on the imperfection patterns which are considered with the corresponding approaches. First KOITER's asymptotic post-buckling theory is introduced that yield an estimate of the buckling loads due to inclusion of buckling modes of the perfect shell as imperfection with very small initial deflection amplitudes. Applying initial radial deflections in form of series expansions to the deflection component of the perfect shell, substituting them into the nonlinear DONNELL equations, also larger imperfection amplitudes may be assumed. Such a nonlinear approach to a certain extent also allows for inclusion of measured and random imperfections. In this context the number and wave-lengths of interacting modes to be considered in the series representation of such imperfection shapes is of interest. All the imperfection patterns discussed in this chapter are distributed over the entire cylinder surface, hence also the pre-buckling state of stress and deformation of the entire cylinder is disturbed. This in contrast to localized imperfections, which are the main subject of this work but are very difficult to treat analytically, that is, without use of FE models. Nevertheless, most analytical results available for comparison with FE buckling analyses of imperfect shells refer to methods described in this chapter, achieved by several researchers in the last decades. Finally, linear and nonlinear buckling analysis as well as transient dynamic analysis results for laminated CFRP cylinders are presented, of which the measured real imperfect shell surfaces were directly considered for the set-up of their FE models. The author's experiences with these FE analyses during the project DEVILS may be regarded as basis for the subsequent investigations on cylinders with localized imperfections.

5.1 Asymptotic Post-Buckling Theory

In his famous and pioneering doctoral thesis (KOITER [54]) 1945 developed a theory which supplies evidence that the unavoidable existence of small structural imperfections are responsible for the mentioned gaps between classical and experimental buckling loads. Despite its importance this so-called *asymptotic post-buckling theory* received little attention until the early 1960's since KOITER's thesis was written in Dutch language [21]. But after a translation into English his theory was often applied to the buckling of stiffened and monocoque elastic and elastic-plastic shells [21, 19]. A large number of papers on KOITER's theory and the effect of imperfections on buckling was published, e.g. a compact representation of the asymptotic theory by (BUDIANSKY [19]), a survey or introduction by (BUDIANSKY & HUTCHINSON [20]), by (COHEN [24]), by (ALMROTH [1]), or by (ARBOCZ & HOL [8]), just to mention a few.

The earlier mentioned high imperfection sensitivity of axially compressed cylindrical shells may also be explained with the fact that the polynomial expansion of the potential energy Π contains a cubic term, that is [15]:

$$\Pi = c_0 + c_1\xi + c_2\xi^2 + c_3\xi^3 + \dots \quad (5.5)$$

where ξ is the amplitude of the dominant buckling mode associated with the lowest bifurcation load, and c_0 , c_1 , etc. are coefficients which depend on the axial load as well as the type and magnitude of the imperfections. The cubic term for shells is nonzero (in contrast to imperfection insensitive structures such as flat plates) and may be particularly large. In a classical, linear buckling analysis the potential energy expression is always quadratic; the cubic and higher order terms can only be considered by nonlinear analyses. A classical bifurcation buckling analysis represents a search for the load at which the equilibrium of a structure ceases to be stable and becomes neutral, but there is no information given about the stability of the structure. In order to specify whether or not the structure is stable *at* the bifurcation load, the determination of the characteristics of the post-buckling path in the neighbourhood of the bifurcation point is necessary [21]. For this purpose, in his general elastic post-buckling theory (KOITER [54]) assumed that the eigenvalue problem for the buckling load P_{cl} will yield a unique buckling mode and introduced an asymptotically exact expansion for the load P in terms of the normalized buckling modal amplitude ξ . That is, the equilibrium path of a perfect structure referring to P , resulting from the condition

$\partial\Pi/\partial\xi = 0$ (see Eq. (5.5)), can be described by the series expansion

$$\frac{P}{P_{cl}} = 1 + a\xi + b\xi^2 + \dots \quad (5.6)$$

whereby at the critical state $\xi = 0$. Depending on the vanishing or

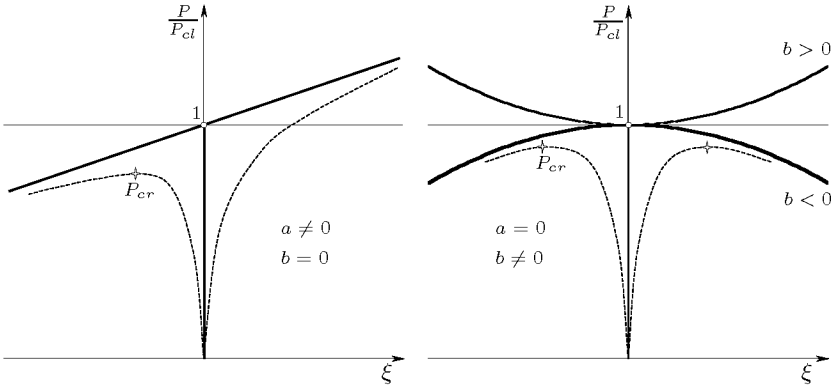


Figure 5.5: *Different types of elastic initial post-buckling behaviour. Nonsymmetric (left) and symmetric post-buckling (right). Solid lines represent perfect, dashed lines imperfect structures.*

nonvanishing of the coefficients a and b , and on the sign of b , some basic types of initial post-buckling behaviour can be distinguished [15]. In Figure 5.5 different types of elastic initial post-buckling behaviour of are shown. For the case at the left side, which is asymmetric with respect to the sign of ξ , a negative normalized *imperfection* amplitude $\bar{\xi}$ will convert bifurcation buckling into nonlinear collapse at a reduced load P_{cr} . For the symmetric case (e.g. axially compressed cylinder) at the right side of Figure 5.5 the factor a is zero and thus the initial relationship between the load and the buckling displacement amplitude is governed by the sign and the magnitude of b . If “KOITER’s b -factor” is negative the load-carrying capacity is reduced after buckling and the shell is imperfection sensitive, whereas a positive b would indicate that the structure retains some resistance for higher loads after bifurcation [21, 63].

A measure of the imperfection sensitivity of a structure may then be obtained by consideration of the effect of an initial, stress-free deviation of the shell middle surface from the perfect geometry in the shape of the buckling mode [21], as shown in Figure 5.6. Thus, if $a = 0$ the limit

load P_{cr} is related to the classical buckling load P_{cl} by the asymptotic formula of the form

$$\left(1 - \frac{P_{cr}}{P_{cl}}\right)^{3/2} = \frac{3\sqrt{3}}{2} \sqrt{-b} |\bar{\xi}| \frac{P_{cr}}{P_{cl}} \quad (5.7)$$

whereby $\bar{\xi}$ is the normalized amplitude of the initial imperfection, the buckling mode respectively [20]. With the imperfection amplitude Δ_R the perturbation amplitude would be given by $\bar{\xi} = \Delta_R/h$. As shown in Figure 5.7, more negative values of b are associated with greater sensitivity of the critical load P_{cr} to initial geometric imperfections.

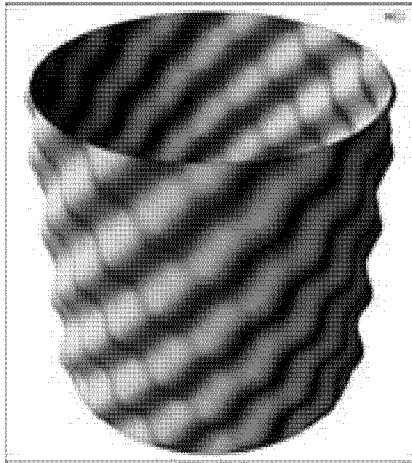


Figure 5.6: Possible buckling mode of an axially compressed isotropic cylinder.

In order to use curves like (5.7) to determine knock-down factors the imperfection sensitivity parameter b has to be calculated. To demonstrate the great complexities involved the fundamental equations to be solved for the determination of b are introduced in the following. The derivation follows the publication of (HUTCHINSON & FRAUENTHAL [50]) on eccentrically stiffened and barrelled shells and (ARBOCZ & HOL [8]) on anisotropic shells [21]. Some simplifications were done for the present case of purely axially compressed, isotropic circular monocoque cylinders.

Since the external loading and the boundary conditions are axisymmetric the *pre-buckling* solution will also be axisymmetric. Thus, neglecting terms including derivatives which refer to the circumference coordinate y ,

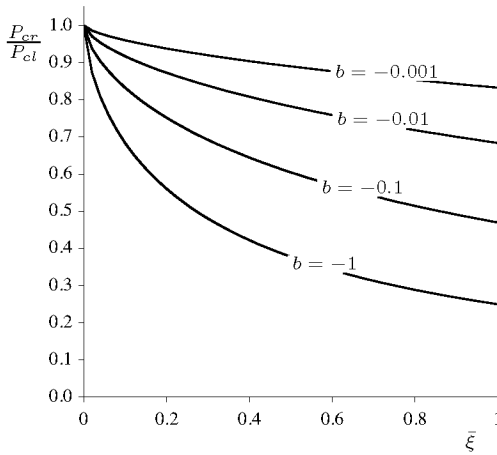


Figure 5.7: Imperfection sensitivity as a function of parameter b . The knock-down factors P_{cr}/P_{cl} are calculated according to the asymptotic formula (5.7).

the compatibility equation (see Section 2.2) for elastic isotropic materials becomes

$$\frac{\partial^4 \mathcal{F}_0}{\partial x^4} + \frac{E h}{R} \frac{\partial^2 w_0}{\partial x^2} = 0 \quad (5.8)$$

and the equilibrium equation is

$$\frac{\partial^4 w_0}{\partial x^4} - \frac{1}{R D} \frac{\partial^2 \mathcal{F}_0}{\partial x^2} = 0 \quad (5.9)$$

where \mathcal{F} is the AIRY stress function, w the displacement component in shell normal direction (positive inward) and D is the shell bending stiffness. The index '0' indicates the pre-buckling state (0th-order state). Although the pre-buckling behaviour is nonlinear, the two differential equations (5.8 and 5.9) are linear in w_0 and \mathcal{F}_0 . With the applied axial compressive force P the assumed

$$w_0 = h \tilde{w}_0(x, P) \quad \text{and} \quad \mathcal{F}_0 = -\frac{1}{2} y^2 \frac{P}{2\pi R} + f_0(x, P) \quad (5.10)$$

substituted into (5.8) and (5.9) and rearranged yields a fourth-order linear ordinary differential equation with constant coefficients which admits an exponential solution [8].

Assuming that P_{cl} is the axial load at which a non-axisymmetric bifurcation from the pre-buckling state occurs. Then, in accordance with

KOITER's theory an asymptotic perturbation expansion of the solution can be obtained which is valid in the vicinity of this bifurcation point. That is,

$$\begin{aligned}\frac{P}{P_{cl}} &= 1 + a\xi + b\xi^2 + \dots \\ w &= w_0 + \xi w_1 + \xi^2 w_2 + \dots \\ \mathcal{F} &= \mathcal{F}_0 + \xi \mathcal{F}_1 + \xi^2 \mathcal{F}_2 + \dots\end{aligned}\quad (5.11)$$

where w_1 is a unique buckling node, normalised with respect to the shell thickness h , and w_2 is orthogonal to w_1 in an appropriate sense [50, 8]. The terms \mathcal{F}_i of the AIRY stress function are associated with the corresponding terms of the normal displacement component w_i . With the amplitude of the buckling mode δ the normalized perturbation amplitude ξ may also be identified with $\xi = \delta/h$. For perfect shells the variation of P/P_{cl} with ξ in the neighbourhood of the bifurcation point (i.e. $P = P_{cl}$ and $\xi = 0$) is of interest. Near the bifurcation point P_{cl} the asymptotic expansion given in (5.11) is valid [8]. Hence, the pre-buckling solution is also expanded about the bifurcation load P_{cl} so that

$$\begin{aligned}w_0 &= w_0(x, P_{cl}) + (P - P_{cl}) \left[\frac{\partial w_0}{\partial P} \right]_{P_{cl}} + \frac{1}{2} (P - P_{cl})^2 \left[\frac{\partial^2 w_0}{\partial P^2} \right]_{P_{cl}} + \dots \\ \mathcal{F}_0 &= \mathcal{F}_0(x, P_{cl}) + (P - P_{cl}) \left[\frac{\partial \mathcal{F}_0}{\partial P} \right]_{P_{cl}} + \frac{1}{2} (P - P_{cl})^2 \left[\frac{\partial^2 \mathcal{F}_0}{\partial P^2} \right]_{P_{cl}} + \dots\end{aligned}\quad (5.12)$$

The problem for $[\partial w_0/\partial P]_{P_{cl}}$ and $[\partial \mathcal{F}_0/\partial P]_{P_{cl}}$ follows from the equations for \tilde{w}_0 and f_0 in (5.10). The load difference is expanded in similar way:

$$P - P_{cl} = a P_{cl} \xi + b P_{cl} \xi^2 + \dots \quad (5.13)$$

A formal substitution of the expansions in (5.11) together with (5.12) and (5.13) into the governing differential equations gives a sequence of equations corresponding to like powers of ξ and $(P - P_{cl})$ [50, 8, 24].

The classical buckling problem (1st-order state) is a linear eigenvalue problem stemming from the insertion of the expansions (5.11) into the governing differential equations. P_{cl} is assumed to be the load at which a non-axisymmetric bifurcation from the axisymmetric pre-buckling state occurs. Thus, after collection of all terms linear in ξ [21]:

$$\frac{\partial^4 \mathcal{F}_1}{\partial x^4} + 2 \frac{\partial^4 \mathcal{F}_1}{\partial x^2 \partial y^2} + \frac{\partial^4 \mathcal{F}_1}{\partial y^4} = -\frac{Eh}{R} \frac{\partial^2 w_1}{\partial x^2} - Eh^2 \frac{\partial^2 \tilde{w}_0}{\partial x^2} \frac{\partial^2 w_1}{\partial y^2}, \quad (5.14a)$$

$$\begin{aligned} \frac{\partial^4 w_1}{\partial x^4} + 2 \frac{\partial^4 w_1}{\partial x^2 \partial y^2} + \frac{\partial^4 w_1}{\partial y^4} = \\ \frac{1}{D} \left(\frac{\partial^2 \mathcal{F}_1}{\partial y^2} h \frac{\partial^2 \tilde{w}_0}{\partial x^2} + \frac{1}{R} \frac{\partial^2 \mathcal{F}_1}{\partial x^2} + \frac{\partial^2 f_0}{\partial x^2} \frac{\partial^2 w_1}{\partial y^2} - \frac{P_{cl}}{2\pi R} \frac{\partial^2 w_1}{\partial x^2} \right). \end{aligned} \quad (5.14b)$$

This system of differential equations permits separable solutions of the form

$$\begin{aligned} w_1(x, y) &= h \tilde{w}_1(x) \cos\left(\frac{ny}{R}\right), \\ \mathcal{F}_1(x, y) &= f_1(x) \cos\left(\frac{ny}{R}\right), \end{aligned} \quad (5.15)$$

where n again is the number of circumferential waves associated with the buckling mode (see Section 2.2) [8]. Substitution finally results in a set of homogenous differential equations with variable coefficients. Together with appropriate boundary conditions this equation system then forms a eigenvalue problem which is solved numerically [8, 21].

By insertion of the expansions (5.11) into the governing differential equations and collection of all terms quadratic in ξ the following second-order linear boundary value problem is obtained:

$$\begin{aligned} \frac{\partial^4 \mathcal{F}_2}{\partial x^4} + 2 \frac{\partial^4 \mathcal{F}_2}{\partial x^2 \partial y^2} + \frac{\partial^4 \mathcal{F}_2}{\partial y^4} = -\frac{Eh}{R} \frac{\partial^2 w_2}{\partial x^2} - Eh^2 \frac{\partial^2 \tilde{w}_0}{\partial x^2} \frac{\partial^2 w_2}{\partial y^2} \\ + \frac{1}{2} \frac{Eh^3}{R^2} n^2 \left\{ \tilde{w}_1 \frac{\partial^2 \tilde{w}_1}{\partial x^2} + \frac{\partial \tilde{w}_1}{\partial x} \frac{\partial \tilde{w}_1}{\partial x} \left(\tilde{w}_1 \frac{\partial^2 \tilde{w}_1}{\partial x^2} - \frac{\partial \tilde{w}_1}{\partial x} \frac{\partial \tilde{w}_1}{\partial x} \right) \cos\left(2\frac{ny}{R}\right) \right\}, \end{aligned} \quad (5.16a)$$

$$\begin{aligned} \frac{\partial^4 w_2}{\partial x^4} + 2 \frac{\partial^4 w_2}{\partial x^2 \partial y^2} + \frac{\partial^4 w_2}{\partial y^4} = \\ \frac{1}{D} \left(\frac{\partial^2 \mathcal{F}_2}{\partial y^2} h \frac{\partial^2 \tilde{w}_0}{\partial x^2} + \frac{1}{R} \frac{\partial^2 \mathcal{F}_2}{\partial x^2} + \frac{\partial^2 f_0}{\partial x^2} \frac{\partial^2 w_2}{\partial y^2} - \frac{P_{cl}}{2\pi R} \frac{\partial^2 w_2}{\partial x^2} \right) \\ - \frac{h}{2D} n^2 \left\{ \tilde{w}_1 \frac{\partial^2 f_1}{\partial x^2} + \frac{\partial \tilde{w}_1}{\partial x} \frac{\partial f_1}{\partial x} + \frac{\partial^2 \tilde{w}_1}{\partial x^2} f_1 \right. \\ \left. + \left(\tilde{w}_1 \frac{\partial^2 f_1}{\partial x^2} - \frac{\partial \tilde{w}_1}{\partial x} \frac{\partial f_1}{\partial x} + \frac{\partial^2 \tilde{w}_1}{\partial x^2} f_1 \right) \cos\left(2\frac{ny}{R}\right) \right\}. \end{aligned} \quad (5.16b)$$

These two equations again may be reduced to two systems of ordinary differential equations with separation of variables according to [50, 8]

$$\begin{aligned} w_2(x, y) &= h \tilde{w}_{21}(x) + h \tilde{w}_{22}(x) \cos\left(2\frac{ny}{R}\right), \\ \mathcal{F}_2(x, y) &= f_{21}(x) + f_{22}(x) \cos\left(2\frac{ny}{R}\right). \end{aligned} \quad (5.17)$$

These two ansatz functions substituted into (5.16) finally yields, after some manipulations, a system of inhomogeneous differential equations with variable coefficients. Together with the boundary conditions this problem has to be solved numerically.

Finally, by considering that the virtual work has to vanish for equilibrium, for perfect shells and $a = 0$ the following formula for b may be deduced [21, 8, 37, 39]:

$$b = \frac{1}{P_{cl}} \frac{I_{\mathcal{F}_2 w_{11}} + 2 I_{\mathcal{F}_1 w_{12}}}{I_{d\mathcal{F}_2 w_{11}} + 2 I_{\mathcal{F}_1 d w_{01}}} \quad (5.18)$$

with the four integrals over the entire middle shell surface

$$I_{\mathcal{F}_2 w_{11}} = \int_A \frac{\partial^2 \mathcal{F}_2}{\partial x^2} \left(\frac{\partial w_1}{\partial y} \right)^2 + \frac{\partial^2 \mathcal{F}_2}{\partial y^2} \left(\frac{\partial w_1}{\partial x} \right)^2 - 2 \frac{\partial^2 \mathcal{F}_2}{\partial x \partial y} \left(\frac{\partial w_1}{\partial x} \frac{\partial w_1}{\partial y} \right) dA \quad (5.19a)$$

$$I_{\mathcal{F}_1 w_{12}} = \int_A \frac{\partial^2 \mathcal{F}_1}{\partial x^2} \frac{\partial w_1}{\partial y} \frac{\partial w_2}{\partial y} + \frac{\partial^2 \mathcal{F}_1}{\partial y^2} \frac{\partial w_1}{\partial x} \frac{\partial w_2}{\partial x} - \frac{\partial^2 \mathcal{F}_1}{\partial x \partial y} \left(\frac{\partial w_1}{\partial x} \frac{\partial w_2}{\partial y} + \frac{\partial w_1}{\partial y} \frac{\partial w_2}{\partial x} \right) dA \quad (5.19b)$$

$$I_{d\mathcal{F}_2 w_{11}} = \int_A \frac{\partial^2}{\partial x^2} \left[\frac{\partial \mathcal{F}_0}{\partial P} \right]_{P_{cl}} \left(\frac{\partial w_1}{\partial y} \right)^2 + \frac{\partial^2}{\partial y^2} \left[\frac{\partial \mathcal{F}_0}{\partial P} \right]_{P_{cl}} \left(\frac{\partial w_1}{\partial x} \right)^2 - 2 \frac{\partial^2}{\partial x \partial y} \left[\frac{\partial \mathcal{F}_0}{\partial P} \right]_{P_{cl}} \left(\frac{\partial w_1}{\partial x} \frac{\partial w_1}{\partial y} \right) dA \quad (5.19c)$$

$$I_{\mathcal{F}_1 d w_{01}} = \int_A \frac{\partial^2 \mathcal{F}_1}{\partial x^2} \frac{\partial}{\partial y} \left[\frac{\partial w_0}{\partial P} \right]_{P_{cl}} \frac{\partial w_1}{\partial y} + \frac{\partial^2 \mathcal{F}_1}{\partial y^2} \frac{\partial}{\partial x} \left[\frac{\partial w_0}{\partial P} \right]_{P_{cl}} \frac{\partial w_1}{\partial x} - \frac{\partial^2 \mathcal{F}_1}{\partial x \partial y} \left(\frac{\partial}{\partial x} \left[\frac{\partial w_0}{\partial P} \right]_{P_{cl}} \frac{\partial w_1}{\partial y} + \frac{\partial}{\partial y} \left[\frac{\partial w_0}{\partial P} \right]_{P_{cl}} \frac{\partial w_1}{\partial x} \right) dA \quad (5.19d)$$

The complete solution for w_0 , w_1 , w_2 , \mathcal{F}_0 , \mathcal{F}_1 and \mathcal{F}_2 needed for the calculation of the formula (5.18) for parameter b above implies the prior (numerical) calculation of the coefficients \tilde{w}_0 , \tilde{w}_1 , \tilde{w}_{21} , \tilde{w}_{22} , f_0 , f_1 , f_{21} and f_{22} which form a large set of equation systems. Since here only the concept of the derivation of the solutions is of interest, a listing of such equations was abandoned, see e.g. (ARBOCZ & HOL [8]).

The formulation in (5.7) for the relation between the limit load of the imperfect structure to the bifurcation load of the perfect structure bases on the assumptions that (1) the pre-buckling state is linearized, that (2) pre-buckling deformations and (3) dead loads may be neglected, and

that (4) the imperfection shape considered is affine to the classical buckling mode [24]. Thus, (COHEN [24]) generalized above analysis to cases for which the preceding assumptions are not valid, and introduced an asymptotic formulation including nonlinear pre-buckling effects where the variation of $P(\xi, \bar{\xi})$ in the vicinity of the bifurcation point P_{cl} is given by the following expansion [8, 24]:

$$(P - P_{cl})\xi = a P_{cl} \xi^2 + b P_{cl} \xi^3 + \dots - \alpha P_{cl} \bar{\xi} - \beta (P - P_{cl}) \bar{\xi} + O(\xi, \bar{\xi}) \quad (5.20)$$

For $a = 0$ the corresponding asymptotic formula is given by [8]

$$\left(1 - \frac{P_{cr}}{P_{cl}}\right)^{3/2} = \frac{3}{2} \sqrt{-3 \alpha^2 b} \left[1 - \frac{\beta}{\alpha} \left(1 - \frac{P_{cr}}{P_{cl}}\right)\right] |\bar{\xi}| \quad (5.21)$$

The two additional imperfection form factors α and β have to be calculated with similar complexity to a and b [8]. In the case of a linear pre-buckling state $\alpha = \beta$, and for $\beta = 1$, i.e. for neglected pre-buckling deformations, the modified formula (5.21) coincides with KOITER's formula (5.7) [24].

In the last decades (HUTCHINSON & FRAUENTHAL [50]), (ARBOCZ & HOL [8]), (GEIER [39]) and other researchers developed numerical methods which may be used to calculate the “unattractive” various boundary-value problems and to evaluate b and the other parameters. Since such computer codes are programmed for particular shell geometries, load cases, materials and boundary conditions, an application of the procedures to an other stability problem mostly requires fundamental adaptations in the program code. Consequently, despite the great usefulness of such programs their spread in the structural design community is rather small. But in some commercial FE programs (e.g. MARC[®], ABAQUS[®]) options were introduced to consider normalized linear buckling modes to be added to the perfect structure for subsequent static FE calculations. This way, after a linear buckling analysis further (linear, or better: non-linear) static analyses with different amplitudes of the considered mode, the imperfection sensitivity of the modelled structure may be approximated by means of the resulting series of reduced buckling loads.

5.2 Nonlinear Analysis Approaches

The results of KOITER's general asymptotic theory described above are only valid for very small initial imperfections (i.e. for amplitudes up to about 30% of the shell thickness [55]) in the vicinity of the bifurcation point of the perfect shell. Thus, for larger imperfection amplitudes in the nonlinear approach an initial stress-free imperfections shape $\Delta_R(x, y)$ is introduced and a series expansion for the normal displacement increment w is assumed to be added to that of the perfect shell in the pre-buckling state [21]. This approach base on the nonlinear DONNELL-type equilibrium and compatibility equations for thin shells. In accordance with (HUTCHINSON [49]) the equations for an initially imperfect, axially compressed cylindrical shell become

$$\begin{aligned} \frac{\partial^4 w}{\partial x^4} + 2 \frac{\partial^4 w}{\partial x^2 \partial y^2} + \frac{\partial^4 w}{\partial y^4} = \frac{1}{D} \left[\frac{\partial^2 \mathcal{F}}{\partial y^2} \left(\frac{\partial^2 \Delta_R}{\partial x^2} + \frac{\partial^2 w}{\partial x^2} \right) \right. \\ \left. - 2 \frac{\partial^2 \mathcal{F}}{\partial x \partial y} \frac{\partial^2 \Delta_R}{\partial x \partial y} - 2 \frac{\partial^2 \mathcal{F}}{\partial x \partial y} \frac{\partial^2 w}{\partial x \partial y} + \frac{\partial^2 \mathcal{F}}{\partial x^2} \left(\frac{\partial^2 \Delta_R}{\partial y^2} + \frac{\partial^2 w}{\partial y^2} \right) + \frac{1}{R} \frac{\partial^2 \mathcal{F}}{\partial x^2} \right], \end{aligned} \quad (5.22a)$$

$$\begin{aligned} \frac{\partial^4 \mathcal{F}}{\partial x^4} + 2 \frac{\partial^4 \mathcal{F}}{\partial x^2 \partial y^2} + \frac{\partial^4 \mathcal{F}}{\partial y^4} = E h \left[\left(\frac{\partial^2 w}{\partial x \partial y} \right)^2 - \frac{\partial^2 w}{\partial y^2} \left(\frac{\partial^2 \Delta_R}{\partial x^2} + \frac{\partial^2 w}{\partial x^2} \right) \right. \\ \left. - \frac{\partial^2 w}{\partial x^2} \frac{\partial^2 \Delta_R}{\partial y^2} + 2 \frac{\partial^2 w}{\partial x \partial y} \frac{\partial^2 \Delta_R}{\partial x \partial y} + \frac{1}{R} \frac{\partial^2 w}{\partial x^2} \right]. \end{aligned} \quad (5.22b)$$

For a simply-supported perfect cylinder ($\Delta_R = 0$) under axial compressive load P the radial displacement and stress function may be written as

$$\begin{aligned} w(x, y) &= \frac{\nu}{E} \frac{P}{2\pi h} + w_0 \\ \mathcal{F}(x, y) &= -\frac{1}{2} y^2 \frac{P}{2\pi R} + f_0 \end{aligned} \quad (5.23)$$

where the first terms constitute the pre-buckling solution for the perfect shell. The classical buckling equations (see Section 2.2) may be obtained by substituting (5.23) in the DONNELL-type Equations (5.22) and then linearizing the resulting equations with respect to \mathcal{F} and w [49]. Such

equations for perfect cylinders were described in Section 2.2. The classical buckling load is associated with a set of critical buckling modes, including the axisymmetric mode $w = \cos(q_0 x/R)$ and the asymmetric mode $w = \cos(\frac{1}{2}q_0 x/R) \cos(\frac{1}{2}q_0 y/R)$ with square buckles¹. KOITER's general theory for cylindrical shells indicates that an imperfection in the form of the axisymmetric buckling mode (see Figure 5.8)

$$\Delta_R(x) = \bar{\xi} \cos\left(\frac{q_0 x}{R}\right) \quad \text{with: } q_0 = [12(1 - \nu^2)]^{1/4} \sqrt{\frac{R}{h}} \quad (5.24)$$

is the most degrading and is able to reduce the buckling load of an axially

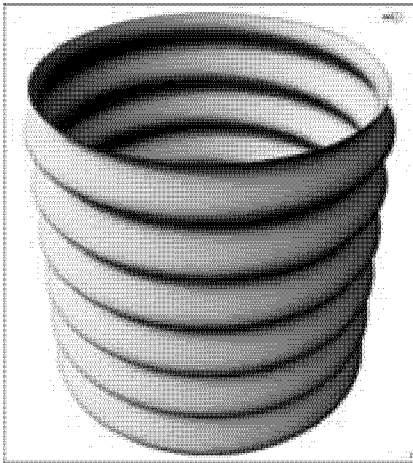


Figure 5.8: *Cylinder with axisymmetric imperfection.*

compressed shell to 1/2 or even 1/3 of the classical load for values of $\bar{\xi}$ only a small fraction of the shell thickness [55, 49]. In general, any radial imperfection pattern Δ_R may be represented by a double Fourier series in the axial and circumferential coordinates x and y . In (HUTCHINSON [49]) only two of such a series are considered for an isotropic shell, one axisymmetric and one asymmetric, each taken in the form of a linear buckling mode as given above; thus,

$$\Delta_R(x, y) = -\bar{\xi}_1 h \cos\left(\frac{q_0}{R} x\right) + \bar{\xi}_2 h \cos\left(\frac{1}{2} \frac{q_0}{R} x\right) \cos\left(\frac{1}{2} \frac{q_0}{R} y\right) \quad (5.25)$$

where $\bar{\xi}_1$ and $\bar{\xi}_2$ are the ratios of the imperfection amplitudes to the shell thickness. But, any equilibrium state can be written in the form of

¹In this formulation it is assumed that the cylinder is infinitely long; i.e. neither the cylinder length L nor any edge conditions are considered.

(5.23); thus, $w(x, y)$ is approximated by

$$\begin{aligned} w(x, y) = \frac{\nu}{E} \frac{P}{2\pi h} + \xi_1 h \cos\left(\frac{q_0}{R}x\right) + \xi_2 h \cos\left(\frac{1}{2}\frac{q_0}{R}x\right) \cos\left(\frac{1}{2}\frac{q_0}{R}y\right) \\ + \xi_3 h \sin\left(\frac{1}{2}\frac{q_0}{R}x\right) \cos\left(\frac{1}{2}\frac{q_0}{R}y\right) \end{aligned} \quad (5.26)$$

with ξ_1 , ξ_2 and ξ_3 standing for the undetermined ratios of the amplitudes of the radial deflection increment to the shell thickness. To specify these coefficients, (5.26) is inserted into the compatibility equation in (5.22), which is then solved exactly for \mathcal{F} in terms of w . The equilibrium equation in (5.22) is then solved approximatively by substitution therein of \mathcal{F} and w and then applying the GALERKIN procedure [49]. In (HUTCHINSON [49]) a solution for ξ_1 , ξ_2 and ξ_3 in (5.26) for an axially compressed isotropic cylinder with uniform internal pressure may be found. Since in this thesis only the axial and circumferential wavelengths of the considered initial imperfections shapes are of interest, the solution for the amplitudes are not considered.

5.2.1 Application of Measured Imperfections

(ARBOCZ & BABCOCK [6]) used a more general approach for application to cylinders with measured imperfections which do not necessarily resemble buckling modes of the perfect shell. For example, for axially compressed isotropic cylindrical shells they assume that the initial imperfection has the form

$$\begin{aligned} \Delta_R(x, y) = \bar{\xi}_1 h \cos\left(i\frac{2\pi}{L}x\right) + \bar{\xi}_2 h \cos\left(k\frac{2\pi}{L}x\right) \cos\left(l\frac{1}{R}y\right) \\ + \bar{\xi}_3 h \sin\left(k\frac{2\pi}{L}x\right) \cos\left(l\frac{1}{R}y\right) \end{aligned} \quad (5.27)$$

and approximate the incremental normal deflection w as

$$\begin{aligned} w(x, y) = \frac{\nu}{E} \frac{P}{2\pi h} + \xi_1 h \cos\left(i\frac{2\pi}{L}x\right) + \xi_2 h \cos\left(k\frac{2\pi}{L}x\right) \cos\left(l\frac{1}{R}y\right) \\ + \xi_3 h \sin\left(k\frac{2\pi}{L}x\right) \cos\left(l\frac{1}{R}y\right) \end{aligned} \quad (5.28)$$

The result of the nonlinear equations obtained for the undetermined normalized amplitudes ξ_1 , ξ_2 and ξ_3 in terms of a normalized load parameter

was then used to investigate the behaviour and the bifurcation or limit loads of different imperfection shapes, i.e. with the particular $\bar{\xi}_i$ either considered or not, depending on the geometrical parameters i , k and l (with $k = i/2$). Then, the combination of one axisymmetric and one asymmetric imperfection component which would yield the lowest buckling load was searched [6]. The imperfection surface shape $\Delta_R(x, y)$ in (5.27) is understood as a truncated representation of measured imperfection surfaces. (ARBOCZ & BABCOCK [6]) used a non-contact probe for complete imperfection surveys on different shells before as well as during the loading process up to the buckling load [10, 75]. In order to determine the dominant modal components of the imperfection surfaces the measured radial displacement fields were expanded in double FOURIER series. The resulting coefficients finally gave the information necessary to define the truncated imperfection representation $\Delta_R(x, y)$ in (5.27). The initial imperfections of the measured shells were predominantly composed of lower-order modes (a few axial and circumferential waves) [6]. It was found that the mode components which apparently contributed to the reduction of the buckling load were not necessarily predominant in the initial imperfections. The pairs ($\bar{\xi}_1 \neq 0, \bar{\xi}_2 \neq 0, \bar{\xi}_3 = 0$ OR $\bar{\xi}_1 \neq 0, \bar{\xi}_2 = 0, \bar{\xi}_3 \neq 0$) of most degrading modal components, as determined by the analysis, were composed of an axisymmetric imperfection with one wave in axial direction and an asymmetric imperfection with one half-wave in axial direction, see Figure 5.9. The most degrading shape of the asymmetric imperfection in turn was found to be determined by a coupling to a significant axisymmetric mode and by an equivalence between the asymmetric mode and a buckling mode with corresponding buckling load close to the classical value [6]. After all, the dominant part of the measured imperfections seemed to be adequately approximated by the truncated expansion (5.27) since the analytical results showed good agreement with the experimental values.

For later correlation studies between experimental buckling loads and analytical predictions based on measured imperfection shapes, (ARBOCZ & BABCOCK [7]) extended the representation (5.27) of the initial imperfec-

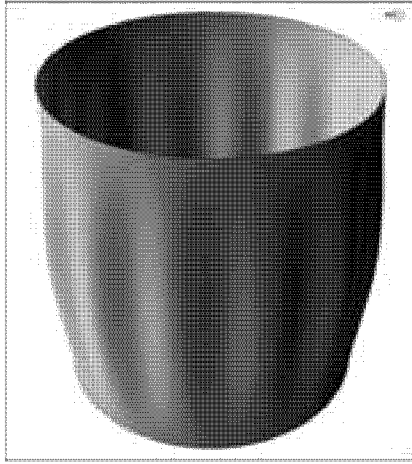


Figure 5.9: *Cylinder with imperfection composed of an axisymmetric imperfection with one wave in axial direction and an asymmetric imperfection with one half-wave in axial direction.*

tions to double FOURIER series as

$$\begin{aligned} \Delta_R(x, y) = & h \sum_{i=1}^{N_1} \bar{\xi}_{i0} \cos\left(i\frac{\pi}{L}x\right) + h \sum_{k=1}^{N_2} \sum_{l=1}^{N_2} \bar{\xi}_{kl} h \cos\left(k\frac{\pi}{L}x\right) \cos\left(l\frac{1}{R}y\right) \\ & + h \sum_{k=1}^{N_3} \sum_{l=1}^{N_3} \bar{\xi}'_{kl} h \sin\left(k\frac{\pi}{L}x\right) \cos\left(l\frac{1}{R}y\right) \end{aligned} \quad (5.29)$$

to investigate the influence of multiple imperfection modes. The number of modes considered in the analysis was (and is) limited by practical considerations (computation effort, disk space). Thus, only the modes which dominated the pre-buckling and buckling behaviour of a cylinder were identified. As mentioned above, it was shown that harmonic imperfection components dominate if they have significant initial amplitudes and correspond to modes of an eigenvalue close to the classical value [7, 10]. The increased complexity of these studies with consideration of up to twenty modes was honoured by an additional enhancement of the agreement between analyses and tests. Furthermore, it was concluded that suitable combinations of axisymmetric and asymmetric modes will always be more damaging than either a single axisymmetric (see KOI-

TER's theory) or a single asymmetric mode, presumed that realistic variation of the imperfection amplitudes is taken into account [7].

The application of artificial initial imperfections in form of buckling modes, or their combinations, as described above bases on the assumption that these are the possible imperfection shapes which reduce the buckling load most of all. Ignoring the real circumstances, for safe shell design the analyst is forced to presume the worst case and to consider knock-down factors of about 20%. In civil engineering such conservative design recommendations might be followed with perfect satisfaction, but in aerospace industry lightweight structures have to be dimensioned as close to the physical limits as possible. In most cases the real imperfection shape will differ from the harmonic eigenmodes relating to lowest buckling loads. Thus, in lightweight construction it would be beneficial to investigate the real imperfections and to derive appropriate enhanced, i.e. higher knock-down factors. Such investigations, i.e. the measurement of imperfections, and the subsequent analyses with the imperfect geometry considered may actually lead to buckling loads very close to test values, as it was shown, for instance, during the DEVILS project. But, measurements [75, 22, 6] of the particular imperfections is at least very complex, or impossible if in an early design state the structure is not yet available.

5.2.2 Application of Stochastic Imperfections

Real imperfections are random in nature; hence, some kind of stochastic analysis would be advisable as an alternative to measurements. The buckling of imperfection sensitive structures with small random initial imperfections was already studied by (AMAZIGO & BUDIANSKY [3]), (ROORDA [70]), (HANSEN [44]) and others. In absence of experimental evidence about the type of imperfections that occur in practice and in order to reduce the mathematical complexity of the problem, the researchers worked with some form of simplified imperfection distribution [9]. (ELISHAKOFF [33]) generalized the stochastic methods to consider experimentally measured initial imperfections and introduced a reliability function $R(\frac{P}{P_{cl}})$ with

$$R\left(\frac{P}{P_{cl}}\right) = Prob\left(\frac{P_{random}}{P_{cl}} \geq \frac{P}{P_{cl}}\right) . \quad (5.30)$$

The knowledge of this function permits the evaluation of the allowable load level P_a/P_{cl} (knock-down factor) for which the desired reliability is

achieved, for a whole group of similar shells produced by a given manufacturing process [9]. For the estimation of $R(\frac{P}{P_{cl}})$ statistical measures of the basic random variables representing the Fourier coefficients of the initial imperfections have to be evaluated. For this, a sufficiently detailed initial imperfection data bank, including the values of truncated double FOURIER representations similar to (5.29), of a sample of nominally identical shells is necessary [8, 22]. Thus, ARBOCZ, SINGER and others founded the *Initial Imperfection Data Bank* and began to collect data of characteristic, measured initial imperfections distributions of many cylinders manufactured by different processes [75, 5, 9]. The aim of this collection is to be able to offer probable imperfection distributions with corresponding higher knockdown factors depending on the manufacturing process and the shell geometry.

5.3 FE Analysis Results for Cylinders with Measured Imperfections

In Section 4.1 four laminated CFRP cylinders were introduced to demonstrate the buckling analysis of ideal cylindrical shells under axial compression. These cylinders were analysed during the Brite-Euram project “design and validation of imperfection-tolerant laminated shells” (DEVILS). A goal of this project was the analytical as well as the experimental investigation of the buckling behaviour of thin-walled CFRP cylinders under axial compression and combined axial and torsion loading. It was attempted to compose guidelines for the dimensioning as well as the analytical and numerical predictions of the buckling loads of such shells. Further, questing for design recommendations with improved knock-down factors for cylindrical composite shells manufactured with different methods, the imperfection sensitivity mainly to geometric imperfections was investigated with considerable effort.

Altogether nine cylindrical shells with an inner radius R of 250 mm, a shell thickness h of 1.25 mm, and a free length L of 510 mm were tested at DLR in Braunschweig and at EMPA in Dübendorf. The cylinders shells were manufactured from carbon-epoxy prepregs which in turn were produced by filament winding over a heated cylindrical mandrel. The prepregs were cut into suitable sizes and then assembled by placing them around a steel cylinder. After placing each layer, gaps between the fibres and gas bubbles were removed manually via a rubber roller. Finally, a tear-off fabric was added and was over-wound by a tensioned

layer of glass fibres. The laminate hardened at 140° for twelve hours. After removal of the glass fibre layer and the core the cylinder edges were trimmed. To determine the geometrical quality of the specimens, the internal and external surfaces of the cylinders were mapped [60]. In the ETH, prior to the test campaign, only the inner surface of the shells were measured in radial direction with aid of laser beam scanning. Due to minor misalignments of the cylinders on the measurement device, the results had to be adjusted analytically [60]. In contrast to the work of ARBOCZ and BABCOCK (Ref. [7]) described in Section 5.2.1, the mapped imperfection surfaces were not expanded in FOURIER series in order to represent and model the real imperfect shell by means of truncated series expansions with the dominant modal components for the subsequent nonlinear analysis. For the application of the imperfection shapes to finite element models the measured points could particularly be fitted and then the coordinates of the points were then considered as the position of the element nodes of the unloaded FE models.

The measurement provided 30 points in axial direction and 90 points in the circumference. Since the used element mesh has twice as much nodes as measured points available, additional points had to be generated by linear interpolation. Figure 5.10 shows the uncoiled imperfect geometries of cylinder Z30 and Z33 as included in the FE models. The deviations of specimen Z30 from nominal radius are small and indicate an elliptic form of the relatively smooth cylinder surface, whereas the surface of specimen Z33 has a slightly nose-shaped distortion near one edge - potentially a result of edge bonding and probably connected with an internal, unknown stress field. In addition, the measured surface of cylinder Z33 includes some deeper notches in a crinkly face of the "nose".

More detailed information on the test facilities, the results, and also on the five laminated shells not considered in this work, may be found in (MEYER-PIENING et al. [60]).

The considered initial imperfections in the FE models represent the deviations of the inner shell surfaces from the nominal radius, whereas possible local wall thickness variations are ignored, that is, the wall thickness h was assumed constant with a value of 1.25 mm over the entire surface. The numerical analysis methods that the author utilized for the buckling load predictions of the cylinders with their measured imperfection shapes applied were the same as for the computations of these shells with perfect geometry, see Section 4.2.2. For the cylinders under axial compression and combined axial and torsion loading linear and nonlinear buckling analyses (see Section 3.5) were performed. In addition, for some

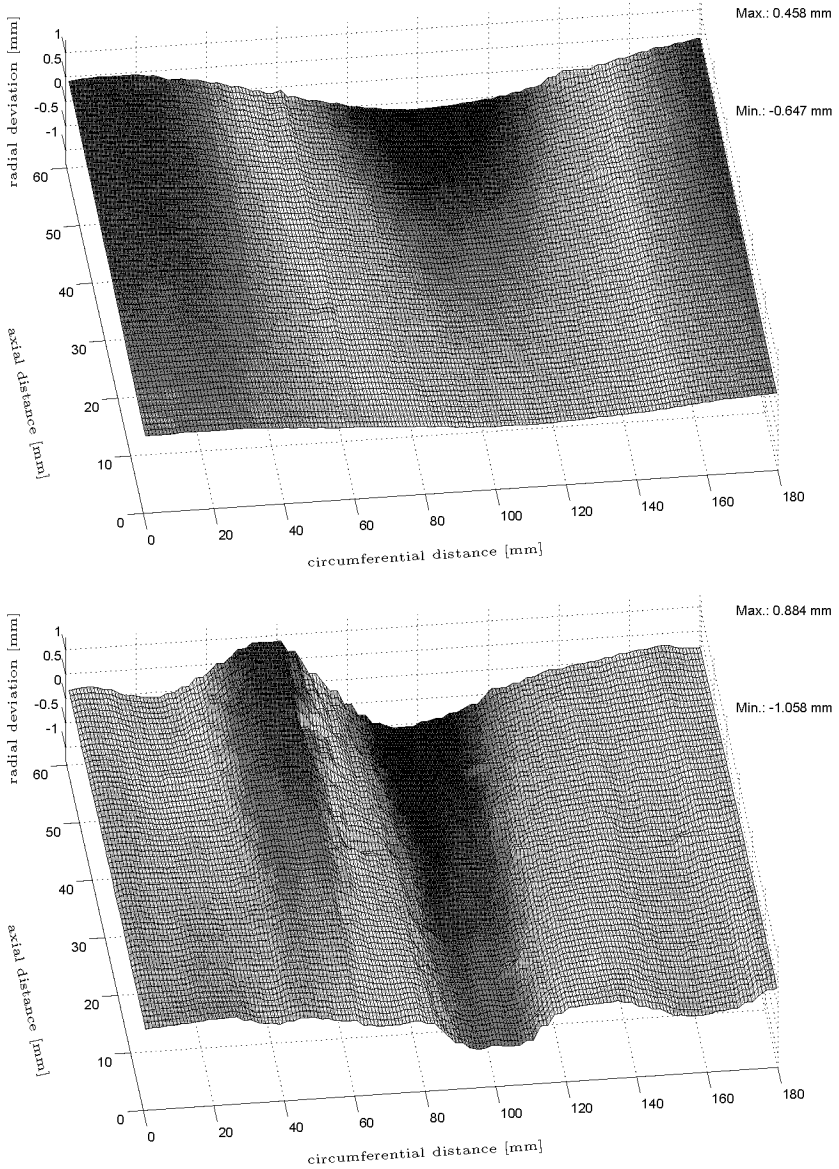


Figure 5.10: Imperfections of cylinder Z30 (top) and Z33 (bottom), measured prior to testing at the inner shell surfaces. Meshes with 61×180 points as used for FE models. Max./min. deviations from nominal radius (250 mm) rightmost.

selected cylinders the buckling behaviour under pure axial compression was investigated by means of transient dynamic analyses. These FE analyses, of which the results are shown in the following, were obtained with MARC[®], again with models consisting of 60×180 bilinear thick shell elements of type No. 75.

5.3.1 Buckling Analysis Results

The results of the FE buckling analyses may be found in Figure 5.11. The identification of the laminates:

Z28 : $[\pm 53^\circ, \pm 8^\circ, \pm 90^\circ, \pm 68^\circ, \pm 38^\circ]$; Z32 : $[\pm 0^\circ, \pm 19^\circ, \pm 37^\circ, \pm 45^\circ, \pm 51^\circ]$;

Z30 : $[\pm 53^\circ, \pm 38^\circ, \pm 22^\circ, \pm 90^\circ, \pm 30^\circ]$; Z33 : $[\pm 51^\circ, \pm 45^\circ, \pm 37^\circ, \pm 19^\circ, \pm 0^\circ]$;

(first angle-ply refer to the outside layers, see Fig. 4.1).

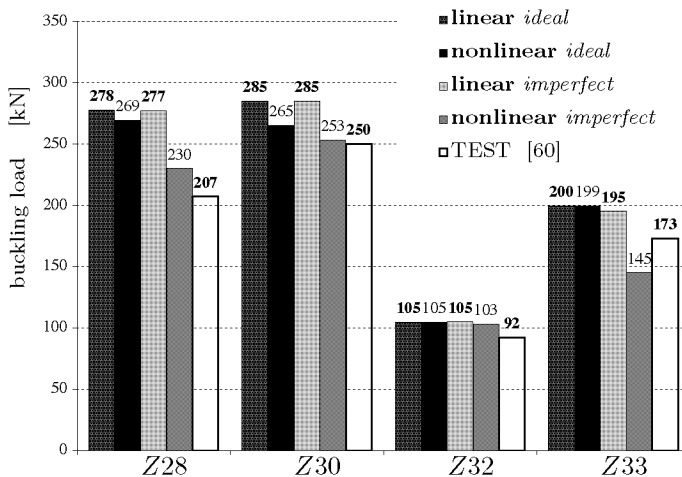


Figure 5.11: Linear and nonlinear static FE buckling analysis results of the DEVILS cylinders with ideal geometry and with applied measured imperfections. Test results enclosed for comparison.

nonlinear buckling analyses yielded little difference to the linear analysis results in the case of ideal geometry but had noticeable influence on the results of cylinders with imperfect geometry. This effect was minor in the case of Z32 with the low buckling loads. For Z33, the reduction of the

load-carrying capacity was overestimated after the real geometry was accounted for, potentially due to the fact that built-in stresses within the shell were ignored. The better conformance of cylinder Z30 with imperfect geometry with the test result might be explained with the smoother imperfection surface and the absence of deeper notches.

Since in general FE analysis results yield higher buckling loads than reached in tests, the analysis result of cylinder Z33 provoked further investigations including the influence of dents and notches on the load carrying capacity of cylindrical shells. Nevertheless, by introducing measured imperfections as initial geometry, important findings could be demonstrated: (i) laminated cylinders with maximised buckling resistance tend to be imperfection sensitive in buckling analyses, and (ii) considering imperfections in FE analyses nonlinear procedures are mandatory.

In Figure 5.12 the nonlinear buckling analysis results for cylinder Z28 and Z33 with perfect shell geometry and with measured imperfections, in both cases subject to combined torsion and axial loading, are plotted. For the combined loads the load ratio was maintained throughout the incremental calculation. The results, the almost-coincidence of the FE results for torsion loads larger than 4 kNm respectively, confirm the assumption that shells which are imperfection-sensitive under axial compression are not so sensitive to combined loads [60].

5.3.2 Transient Dynamic Analysis Results

The dynamic analyses were performed with MARC[®] and the implemented implicit single-step Houbolt operator (SSH-method) for numerical time integration (see Section 3.4). A suitable parameter set especially for dynamic analysis of the laminated cylinders was found by trial, dealing with the collapse of cylinder Z33 with ideal geometry. Hence, the compression velocity was again 0.1 mm/s and the damping matrix was introduced as 25 000 times the mass matrix considered a mass density of 1600 kg/m³. For the specimens with imperfections and hence reduced structural stiffness, less damping could be applied. Nevertheless, for accurate comparisons all other input parameter values than those relating to a geometric or stacking sequence variation were retained unchanged.

Figure 5.13 shows the results of a transient dynamic analysis for the cylinder Z32 with measured imperfections added to the cylinder geometry. The constant reaction force at buckling in the case of ideal geometry

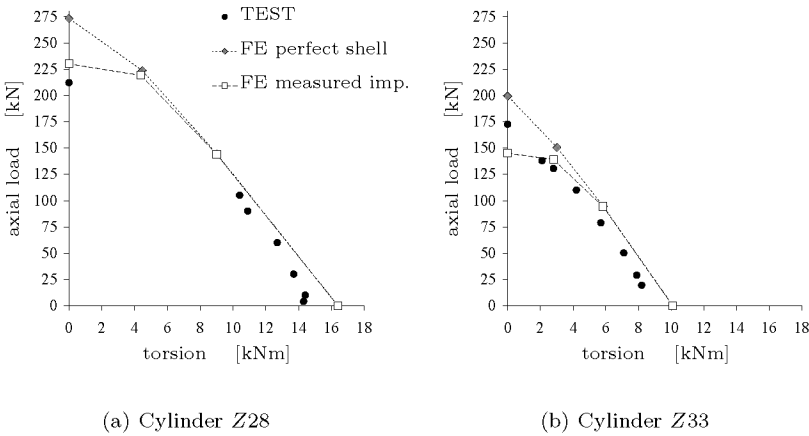


Figure 5.12: *Nonlinear FE buckling analysis and test results for two DEVILS composite cylinders under combined torsion and axial loading.*

(thin line, see Fig. 4.21) is replaced by a reduction of the global stiffness close to the buckling load, which is only slightly smaller than the value for the ideal cylinder geometry, but again almost identical to the value produced by a nonlinear static analysis (103 kN). The imperfections are to a certain extent similar to those of specimen Z33 (Fig. 5.10). The first included picture in Figure 5.13 with scaled-up deformations may give a hint of their small modulating effects. The final post-buckling pattern and the corresponding reaction force are identical to the case of ideal geometry. The first post-buckling pattern (third picture) in turn with only one row of buckles correlates with the pattern observed during tests at DLR ($m/n = 1/8$) [60].

The result of a transient dynamic analysis for the cylinder Z33 with applied measured imperfections is shown in Figure 5.14. In this case, the analytical buckling resistance is significantly reduced in comparison to the ideal cylinder Z33 (thin line, see Fig. 4.22). The buckling load is only $P_{cr} = 145$ kN, again identical to results achieved by static nonlinear analysis. The small dents in the imperfection surface (Fig. 5.10) can be well recognised in the first two pictures with scaled-up deformation plots. The fact that both the nonlinear buckling analysis and the nonlinear dynamic transient analysis yielded a lower collapse load than tests resulted (Fig. 5.11) may possibly be explained by the non-

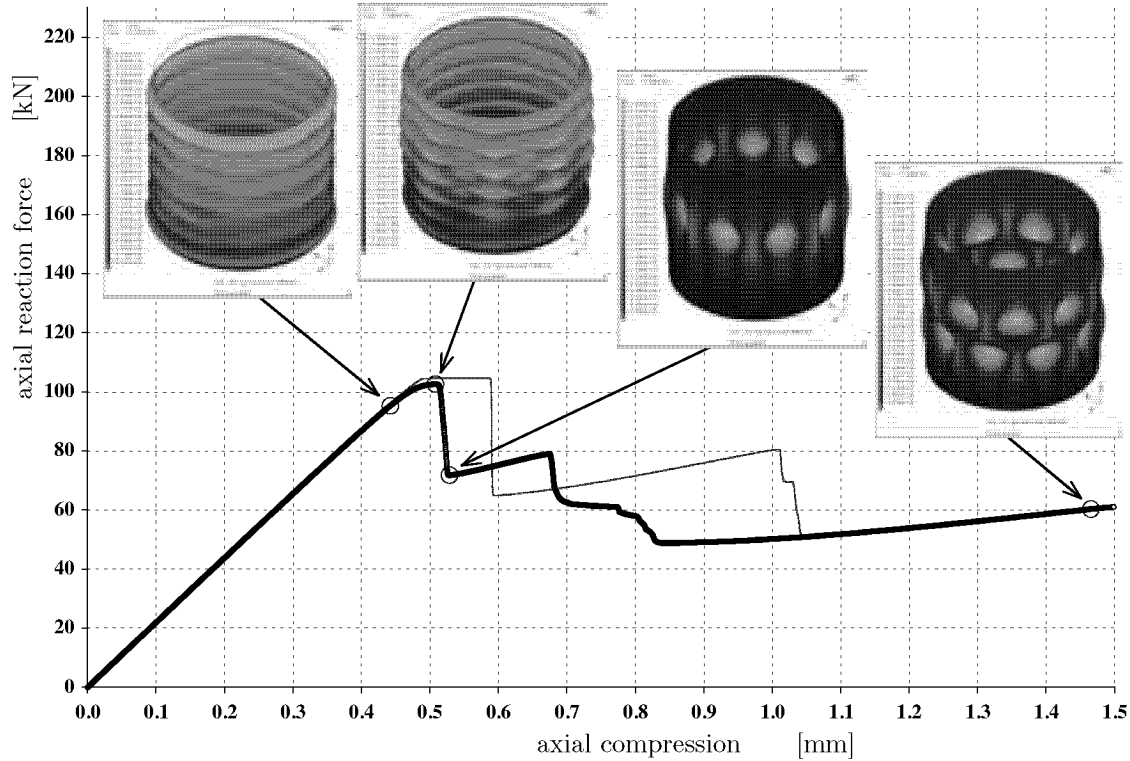


Figure 5.13: *Dynamic FE analysis result of cylinder Z32 with measured imperfections. Thin line represent analysis result with ideal geometry.*

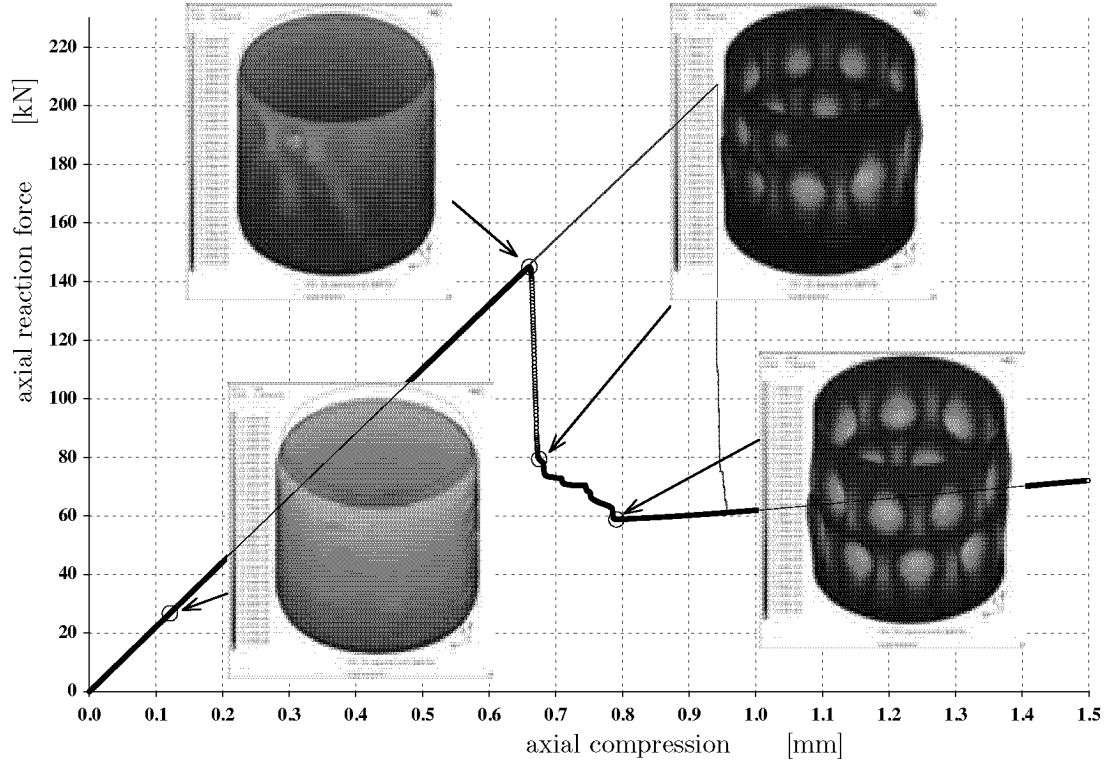


Figure 5.14: *Dynamic FE analysis result of cylinder Z33 with measured imperfections. Thin line represent analysis result with ideal geometry.*

consideration of potential pre-stresses. Again, the post-buckling pattern and the corresponding reaction force are identical to the case of ideal geometry.

That the dynamic transient FE method also enables satisfactory results is demonstrated in Figure 5.15 by means of cylinder Z30 with its measured imperfections (Fig. 5.10). The (thick) line, referring to the FE result, is almost congruent to the (thin) compression line stored during a test at DLR in Braunschweig. The lower thin line refers to decompression after collapse. This reversion of the endplate to its initial position, i.e. to the initial cylinder length, was not simulated. The almost perfect agreement of the FE simulation with the test in the pre-buckling state and at collapse can be viewed as fortunate coincidence since the FE analysis input parameters (velocity, damping), adopted from investigations on cylinder Z33, were not especially modified for this shell.

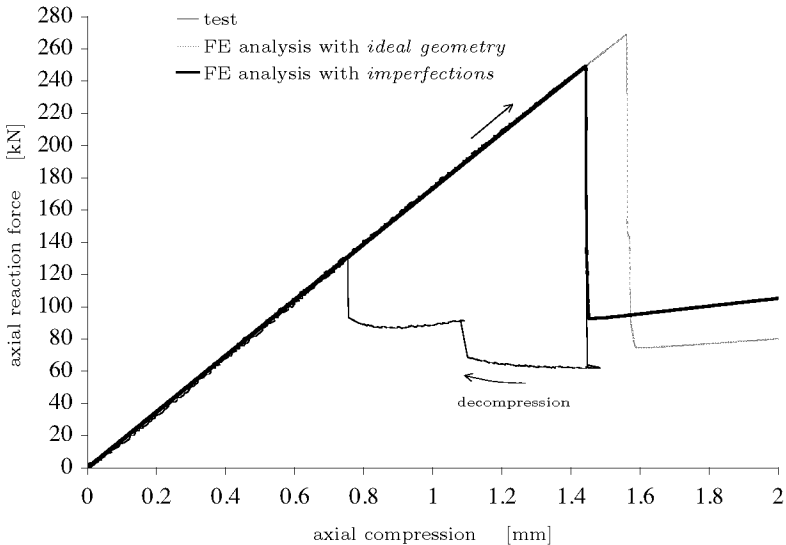


Figure 5.15: *Dynamic FE analysis result of cylinder Z30 with measured imperfections. Comparison with test (DLR): the compression line of the test fits with the FE simulation; decompression (bottom line) was not analysed.*

After the conclusion of the DEVILS project the question remained unanswered why the FE analyses of the CFRP cylinder Z33 with its measured imperfections considered yields considerably lower buckling loads than observed during tests (see Fig. 4.8 rightmost). In the comparison with

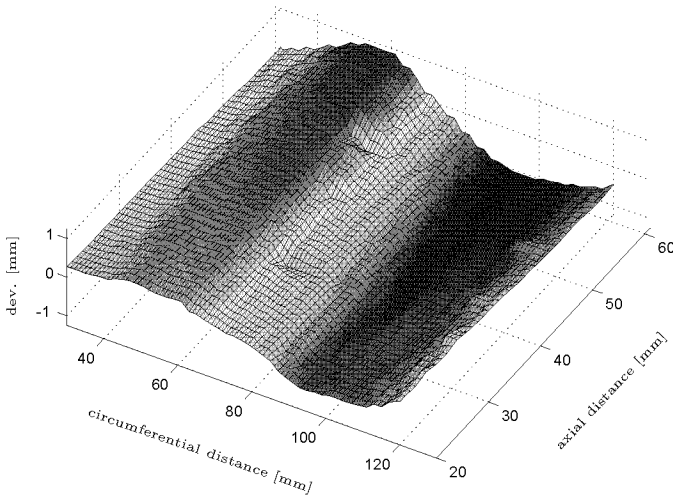


Figure 5.16: *Imperfections of cylinder Z33. Closer view to the deeper notches in a nose-shaped distortion in the inner surface of the specimen. See also Fig. 5.10.*

the imperfections of cylinder Z30, of which FE analyses as expected give higher buckling loads than the tests, the relatively large notches in the measured inner surface of specimen Z33 attract attention (see Fig. 5.10). A closer view to these single dents in the crinkled nose-shape deformation is given in Figure 5.16 with a different view angle. These distortions are potentially a result of edge bonding. Possible internal stress fields, coming from fabrication or test preparation, were unknown and could not be considered as pre-stresses in analyses. Furthermore, since the distortion measurement was only conducted for the inner cylinder surface possible local shell thickness variations are also ignored. Thus, having missed to collect more information about the condition of the shell before and during the tests it became hardly possible to identify the real origin of the underestimated buckling load after the conclusion of the test campaign. But, a nonlinear buckling analysis of Z33 with its imperfections and with fictitious pre-stresses yielded a slightly higher buckling load. For this investigation the pre-stress field was stored after a static FE stress analysis of the perfect cylinder of which only the edges are displaced from the stress-free position on a perfect circle to a corresponding measured position. This surely somewhat peculiar analysis case at least

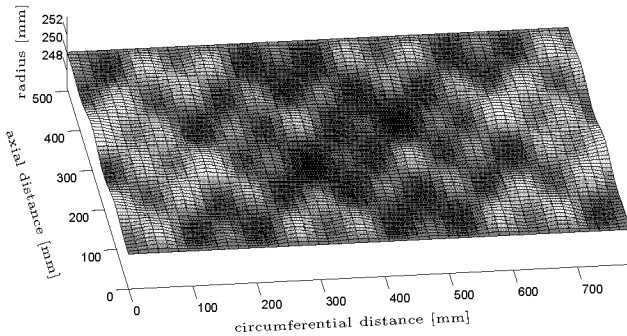
may give a hint that internal stresses due to edge bonding might increase the buckling resistance of a cylinder with such local imperfections. For a further study the deepest notches in the imperfection surface, shown in Figure 5.16, were replaced by manual linear interpolation according to the position of the nodes around the particular notch. A nonlinear buckling analysis of Z33 with the resulting imperfection surface effected a buckling load close to the test value. Thus, the difficulties with the underestimation of the buckling resistance with great probability are caused by these notches, or by the local connected curvatures and stress disturbances respectively, and not by the vaster nose-shaped deformation. But for all that (or just due to the open questions), the influence of the notches to the collapse load of the CFRP cylinders was a motivation to begin a new analysis endeavour for numerous circular cylinders which initially are of perfect geometry despite different single (one or two) dents or bulges. The related investigations and their results are subject of the succeeding chapters.

Chapter 6

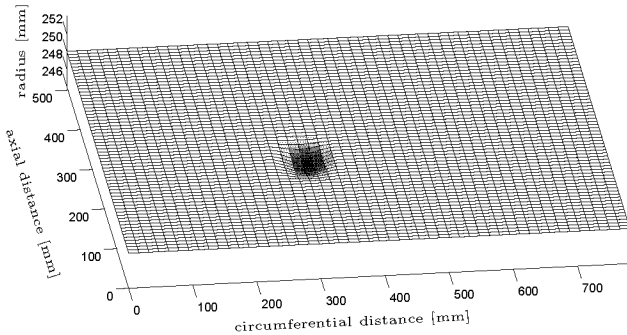
Buckling of Cylinders with Localized Imperfections

The imperfection shapes described in the previous sections are distributed over the entire cylinder shell surface. That is, the lateral deviation from the nominal cylinder radius may be different from zero at any point of the shell between the cylinder edges. Assumed that a shell will not be designed intentionally, for what reason ever, with a geometry similar to the classical buckling mode with short wavelengths, on average a cylindrical shell will have small initial imperfections with longer wavelengths. In addition to such overall geometrical disturbances *local* defects like dents, notches or bulges of different sizes and amplitudes have to be expected. The small notches measured in the inner surface of the laminated cylinder Z33 (see Figure 5.16), for example, are located in a long-wave overall imperfection. Cylinder shells may have large dimples for some design reason or, more likely, due to unsuitable manufacturing or some ungentle contact with other structures. For buckling analyses in the past imperfections as presented in the previous sections were described by use of a single bi-harmonic function with amplitude and two wavelengths, but also by means of a superposition of multiple buckling modes. In Figure 6.1(a) the uncoiled cylinder surface with an overall imperfection pattern composed of three superposed classical modes of equal amplitude is depicted. In the resulting interference pattern some

dents and bulges of small amplitude but also others of large amplitude can be found. Thus, by addition of multiple buckling modes localized dimples may be reproduced. The shell geometry around these dimples however differs also from that of a perfect circular cylinder, i.e. such distinct local imperfections are embedded in an overall imperfection surface. During cylinder compression the local deformation and stress field of each dimple interferes with that of the overall imperfection as well as with that of the adjacent dimples. Consequently, the influence of such small localized dents or bulges on the buckling resistance and behaviour of a cylinder shell may hardly be ascertained separately.



(a) *Distributed inward and outward dimples*



(b) *Single inward dimple (dent)*

Figure 6.1: *Local dimple imperfection in uncoiled cylinder surfaces with (a) other distributed inward and outward dimples of different amplitude, and (b) with otherwise perfect shell geometry.*

In order to investigate how much a single dent or bulge may reduce the

buckling load of the perfect cylinder alone, it is beneficial to work with a cylinder which has a single dimple imperfection but otherwise is of perfect shell geometry. Figure 6.1(b) shows such an exemplary cylinder surface (uncoiled) with a single dent. The dent was arranged to be at the location of one of the dents in the interference pattern in the plot (a) above. Such configurations with a dent or bulge embedded in an otherwise perfect cylinder shell enabled to investigate the exclusive influence of the initial size and geometry of dimple imperfections on the buckling resistance of cylinders. The author used finite element models of such shells, for the mentioned reason, to investigate the buckling behavior of axially compressed isotropic and laminated cylinders with single parametric initial dents or bulges, see Figure 6.2 below.

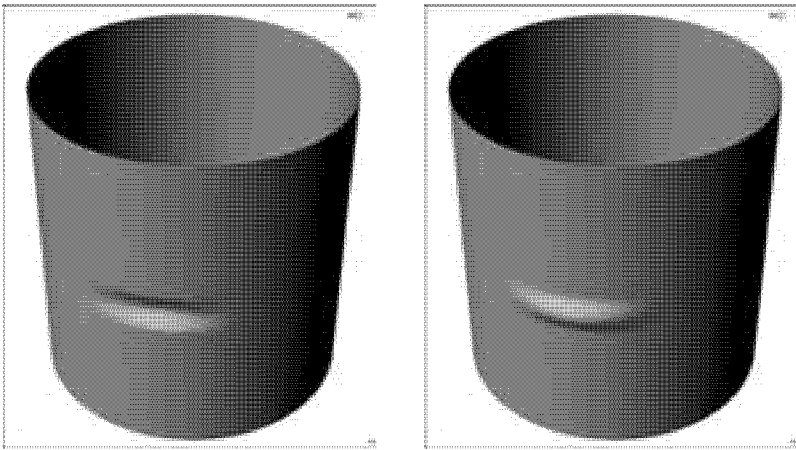


Figure 6.2: *Single, localized inward dimple ("dent", left) or outward dimple ("bulge", right) with its initial amplitude, its initial width, and its initial height as three free parameters.*

Real cylinders with intentionally introduced defects are not totally free from other imperfections; thus, reliable and reproducible buckling tests results of cylinders having a single dimple of small initial amplitude are difficult to achieve. A potential reduction of the cylinder buckling load could hardly be attributed to the intentional initial dimple if its amplitude is of the same order of magnitude than that of other, unavoidable stochastic imperfections. In addition, except for some special dimple shapes the buckling loads of such shells may be calculated with analytical or semi-analytical approaches only with daunting efforts, since

shell surfaces with a localized dimple require double FOURIER series with many terms for the descriptions of the initial cylinder geometry as well as for the description of the deformation and stress fields whilst loading, see Section 2.3 and 5.2. Consequently, the investigation on the buckling behaviour of cylinders with localized dents or bulges was restraint to buckling analyses and simulations with FE models. The confidence in having obtained reasonable analysis results base on the fact that the analysis methods as well as the modeling of the cylinders was adopted from the analyses of the cylinders with ideal geometry and of the laminated CFRP cylinders with measured imperfections considered of which test data was available. The applied analysis methods, i.e. the nonlinear buckling analysis and the transient dynamic analysis, and the mentioned analysis results were detailed in the previous sections.

Since the buckling behaviour of the shells was analysed exclusively by means of FE models, there was no need to consider neither of the configuration of the initial dimples nor of the geometry of the origin cylinder. It was therefore possible to apply dimples of which the initial amplitude, the initial height, as well as the initial width could be varied independently from each other. With these three free parameters their influence on the buckling load could be investigated separately for different cylinders. Further, dimple widths and heights causing minimal cylinder stability could be searched systematically and independently from the wavelengths of classical buckling modes.

This main section deals with the buckling analysis results for thin-walled cylinders of medium length having a single initial dimple and illustrates the particular deformation process of selected shells. After the description of the FE modeling and the analysis methods adopted for the parameter studies first the analysis results for *isotropic cylinders* with a dent or a bulge (\rightarrow Section 6.6) are detailed. Subsequently the results for *laminated CFRP cylinders* having a local dimple (\rightarrow Section 6.7) are described. For the isotropic cylinders this section contains also detailed representations of particular stress distributions and of shells having two dents at different locations.

6.1 Local Imperfections

The reduction of the load carrying capacity due to localized dimple imperfections of cylindrical *isotropic* structures is considered in the German standard DIN 18800 part 4. The standard was worked out for steel structures, but is also applicable for other similar isotropic materials. It provides safe buckling loads of isotropic cylinders in consideration of dimples, but also of eccentricities and other tolerances. The depth of a dimple imperfection w_b should not exceed 1 % of the length of a particular gauge, see Figure 6.3. The gauge length in meridian direction l_{mz}

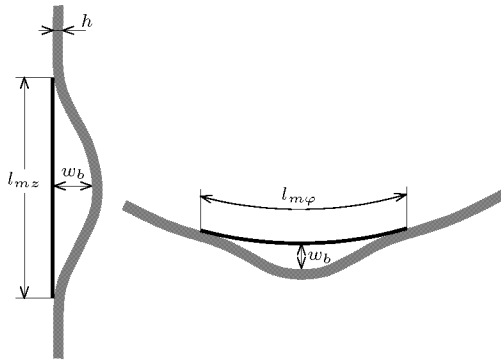


Figure 6.3: DIN 18800/4: gauge lengths l_{mz} and $l_{m\varphi}$ and initial depths w_b for possible dimples in steel cylinders.

is given by

$$l_{mz} = 4\sqrt{Rh}$$

and the length in circumferential direction $l_{m\varphi}$ by

$$l_{m\varphi} = \frac{2.3 R}{\sqrt{R/L\sqrt{R/h}}} \quad \text{but: } l_{m\varphi} \leq R$$

with the cylinder length L , the cylinder radius R , and the shell wall thickness h . Both gauge lengths may be limited to two meters and are derived from the approximate wave-lengths of the buckling patterns of axial compressed cylinders (l_{mz}) and cylinders under external pressure ($l_{m\varphi}$). The standard deals with the influences of the cylinder lengths and the thickness ratios but also of yielding stresses! Presuming sufficiently high yield stresses, for dimples with depths which exceed the

limit w_{bMAX} given above not more than twice a linear relation for a reduction factor is stated:

$$f_{red} = \kappa_{red} \left[1 - \frac{1}{3} \sqrt{\frac{\sigma_{0.2}}{\sigma_{cl}}} \left(\frac{w_b}{w_{bMAX}} - 1 \right) \right] \quad \text{for: } \sqrt{\frac{\sigma_{0.2}}{\sigma_{cl}}} < 1.5$$

$$f_{red} = \kappa_{red} \left(1.5 - 0.5 \frac{w_b}{w_{bMAX}} \right) \quad \text{for: } \sqrt{\frac{\sigma_{0.2}}{\sigma_{cl}}} \geq 1.5$$

That is, the factor f_{red} has to be applied to a classical buckling load which prior is to be reduced with a factor κ_{red} . This reduction factor in turn is only dependent on the relation between ideal buckling stress σ_{cl} and the yield stress $\sigma_{0.2}$:

$$\kappa_{red} = 1.233 - 0.933 \sqrt{\frac{\sigma_{0.2}}{\sigma_{cl}}} \quad \text{for: } 0.25 < \sqrt{\frac{\sigma_{0.2}}{\sigma_{cl}}} \leq 1.0$$

$$\kappa_{red} = 0.3 / \sqrt{\frac{\sigma_{0.2}}{\sigma_{cl}}}^3 \quad \text{for: } 1.0 < \sqrt{\frac{\sigma_{0.2}}{\sigma_{cl}}} \leq 1.5$$

The factor κ_{red} considers the influence of general, geometric and structural imperfections as well as that of non-elastic material behaviour.

EXAMPLE: For a steel cylinder with $R = 250$ mm, $h = 1$ mm, and $L = 510$ mm for example the gauge lengths l_{mx} and $l_{m\varphi}$ are about 63 and 207 mm, respectively; thus, the depth of an initial dimple should not exceed 0.63 mm, and the reduction factor for a initial depth of 1.2 mm is about 0.55. But this factor f_{red} reduces a buckling load which is already scaled down to circa 40 percent of the classical buckling stress (509 MPa) for a yield stress of 400 MPa. Finally, according to the standard the limit load for shells with high imperfection sensitivity like axially compressed cylinders is obtained by division of the reduced load with an additional security value. For the present example the final reduction factor to be applied to the classical buckling load would be $0.4 \times 0.55 / 1.22 = 0.18$.

But, since the influence of general imperfections, the impact of a single dimple, as well as the effects of non-elastic material behaviour are not considered separately, analysis results of cylinders with localized dimples embedded in otherwise unrealistic perfect shells may not be compared with the values recommended as permissible loads in this standard. Furthermore, the disadvantageous combination of geometry and material parameters in the formulations for recommended reductions of buckling loads impedes serious applications of this standard also for materials with different behaviour like fibre-reinforced composites or other synthetics.

For dents which are axisymmetric analytical solutions for the prediction of the reduced buckling loads were found, benefiting from the permissible reductions of the problem in this case (omission of derivatives with respect to the circumferential direction). Following KOITER's general asymptotic theory (see Section 5.1) at the end of the sixties (AMAZIGO & BUDIANSKY [3]) obtained an asymptotic formula for the buckling load of an infinitely long cylindrical shell under axial compression containing an axisymmetric imperfection in the form

$$\Delta_R(x) = -\bar{\xi} h e^{-\alpha x} . \quad (6.1)$$

The asymptotic formula valid only for small imperfections is given by

$$\left(1 - \frac{P_{cr}}{P_{cl}}\right)^{3/2} = \frac{3\sqrt{3(1-\nu^2)}}{2^{3/2}} |I_{\Delta}| \frac{P_{cr}}{P_{cl}} \quad \text{where:} \quad (6.2)$$

$$I_{\Delta} = \int_{-\infty}^{\infty} \frac{\Delta_R}{h} e^{i\tilde{x}} d\tilde{x} \quad \text{with:} \quad \tilde{x} = \frac{\pi x}{l_c}; \quad l_c = 1.73 \sqrt{R h} .$$

The length l_c is the half wavelength of the classical axisymmetric buckling mode for isotropic shell material with $\nu = 0.3$ (see Section 2.2.2) [3, 51, 21]. With the same asymptotic formula (6.2) thereupon (HUTCHINSON, TENNYSON & MUGGERIDGE [51]) performed analyses of cylinders having a single axisymmetrical dent or bulge in cosine form (see Fig. 6.4); that is:

$$\Delta_R(x) = -\frac{\bar{\xi} h}{2} \left\{ 1 - \cos\left(\frac{\pi}{l_x} x\right) \right\} \quad |x| \leq l_x \quad (6.3)$$

$$= 0 \quad |x| > l_x$$

Results can be obtained for various values of the wavelength ratio l_x/l_c . In case of $l_x = l_c$ for example the integral I_{Δ} in (6.2) becomes:

$$I_{\Delta} = \frac{\pi}{2} \bar{\xi}$$

Solutions for (6.3) are reproduced in Section 6.6.3, page 340 ff. Alternatively to the asymptotic theory they also conducted numerical calculations with such ring-shaped cosine dimples, considering nonlinear pre-buckling and deformation states as well as boundary effects. The analytical results could be compared with tests on epoxy-plastic cylindrical

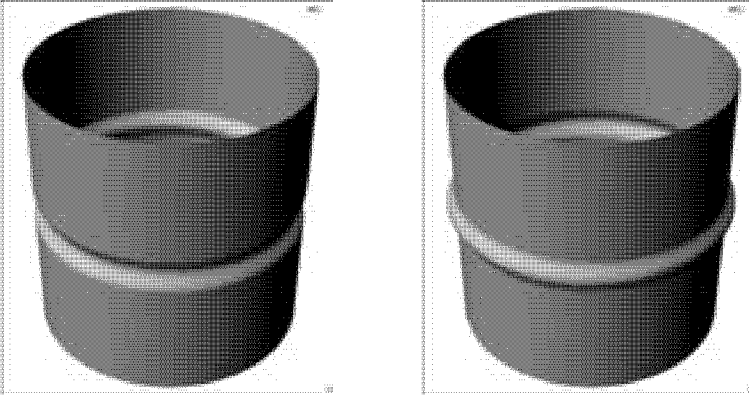


Figure 6.4: *Local, axisymmetrical dimple imperfections. Ring-shaped dent (left) and bulge (right).*

shells with such imperfections [51, 21]. It was found that the sensitivity to a ring dimple of critical height l_c is severe, but less so than that corresponding to imperfections extending the complete cylinder length in the shape of the axisymmetric bifurcation mode as described in the previous sections [51, 21].

In (EDLUND [32]) a study on longitudinal “flattened strip” imperfections which has been given an initial inward displacement is described (see Figure 6.5). A modification of KOITER’s asymptotic formula (5.7) is

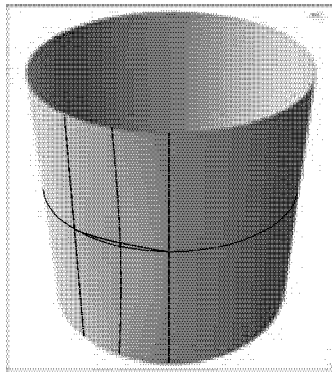


Figure 6.5: *Cylinder with a longitudinal “flattened strip” imperfection.*

proposed where the imperfection parameter $\bar{\xi}$ is replaced by a product

$R_2^0 K_1^0$ of the local radius of curvature R_2^0 in the plane at $x = L/2$ and the local curvature K_2^0 along the cylinder meridian, both in the middle of the imperfection. This approach for the analysis of local initial buckling is restricted again for small imperfection amplitudes, longer imperfection wave-lengths, and small $R_2^0 K_1^0$. A few tests gave a qualitative illustration of the plate-like behaviour of a strip with rather large values of K_1^0 and R_2^0 [32].

Both the axisymmetric dimple and the “flattened strip” imperfection are localized only either in axial or circumferential direction. But, a few reports of axial buckling tests of cylinders having dimple with limited dimensions in both directions could be found. (FOSTER [38]) for instance conducted tests of conical and cylindrical epoxy shells having a V-shaped dent approximated by two triangular facets of the so-called YOSHIMURA buckling pattern [83] for axial compression buckling. Analytically the defect was modelled by modifying an analogy approach where the cylindrical shell is considered as a space frame with the members of the frame aligned with the edges of the YOSHIMURA buckling pattern; the buckling analysis of the cylinder is then considered as the buckling analysis of the frame members [38] (see Figure 6.6). The size of

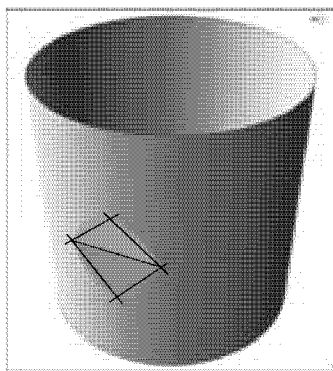


Figure 6.6: *Cylinder with a localized imperfection in the form of a V-shaped dent. Thin lines to indicate the space frame model for an analytical approach.*

the dimples was controlled by the size of the V-shaped notch cut into a mandril during the defect generation. Thus, the width of the dimple was always close to the length of the intersection line of the two flat faces. Subsequently (KRISHNAKUMAR & FOSTER [57]) extended the investigations on cylinders having such diamond-shaped dimples with tests of cylinders afflicted with multiple defects of that type. Finally, on the

basis of their test data they derived an empirical relation for the knock-down factors P_{cr}/P_{cl} considering the number N_n and the circumferential width θ (angle) of the dimples, see Section 6.6.6, with:

$$\frac{P_{cr}}{P_{cl}} = 0.92 e^{-0.173 N_n^{0.461} \theta^{0.187}}$$

In this formula the reduction of the buckling load depends only on the shell geometry and not on the shell material. However, the height of the V-shaped dent is not considered and its initial depth follows from its initial width.

(EDLUND [32]) reports on tests of axially compressed brass cylinder having a dent which is approximatively circular with diameter $a_b \approx 13\sqrt{Rh}$. When the amplitude of the initial dent w_b was successively increased from $w_b/h = 1.0$ to 7.0 the relative buckling load, the knock-down factor, was found to decrease from $P_{cr}/P_{cl} = 0.71$ to 0.18 [32]. Analytical predictions on basis of an asymptotic formulation, similar to the above-mentioned case with the flattened strip, with dents assumed in cosine profile both in axial and in circumferential direction yielded only good results for dent amplitudes up to $w_b = 2.5h$ [32].

The amplitudes and the dimensions in axial and in circumferential direction of the two localized imperfections described above were both not arbitrarily and independently varied. That is, due to its geometry of a V-shape the amplitude of the first local dent is interdependent on the given cylinder radius and the chosen dent width. And the meridian length of the second, circular dimple is identical to its width in circumferential direction.

6.2 Definition of a Localized Dimple with Free Parameters

As already mentioned, the purpose of the present thesis was to investigate the instability behaviour of localized dimples of variable width, variable meridian length and also of variable amplitude, whereby in contrast to the majority of the previously described dimple shapes these three measures were a priori assumed to be independent from each other. Therefore, following the shape of the axisymmetric dimples used by (HUTCHINSON, TENNYSON & MUGGERIDGE [51]) and the geometry of the dimples considered in the German standard DIN 18800, for the

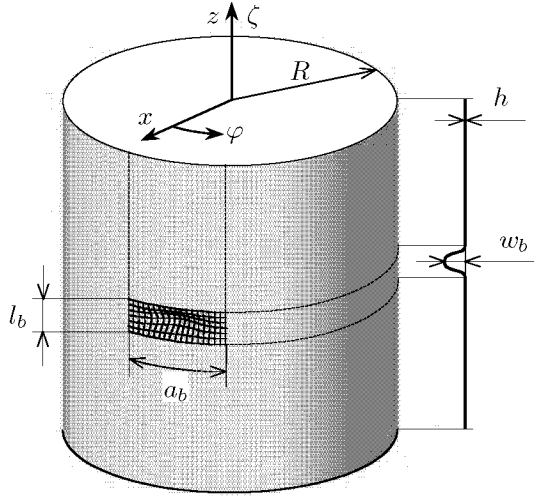


Figure 6.7: Assumed shape of a single dent

studies on effect of single initial dents or bulges parametrically the geometry of ideal cylindrical shells was modified by adding an imperfection of the shape

$$\Delta_R(\varphi, \zeta) = \frac{w_b}{4} \left\{ 1 - \cos\left(\frac{2\pi R}{a_b} \varphi\right) \right\} \left\{ 1 - \cos\left(\frac{2\pi}{l_b} \zeta\right) \right\} \quad \begin{array}{l} 0 \leq \varphi \leq a_b/R \\ 0 \leq \zeta \leq l_b \end{array}$$

$$\Delta_R(\varphi, \zeta) = 0 \quad \textit{else}$$
(6.4)

with the circumferential width a_b , the meridian height l_b and the amplitude w_b which may be arbitrarily varied, see Figure 6.7. The function Δ_R describes the local radial deviation from nominal cylinder radius R , thus the actual radius $r(\varphi, \zeta)$ is given by:

$$r(\varphi, \zeta) = R - \Delta_R . \quad (6.5)$$

Consequently, the amplitude w_b is defined *positive* for imperfections pointed *inwards*. Finally, the position of the dimple apex in the cylinder shell surface is determined by z_b in axial direction and by φ_b in circumference.

The amplitude w_b and the lengths l_b and a_b are like the nominal cylin-

der measurements R , L , and h *initial* dimensions, i.e. they describe the origin unloaded shell configuration. During compression the dimple geometry will change.

The choice of this modelling of actual dents or bulges defined by (6.4) bases on its simplicity for implementation. For comparison, also a dent with partial V-shape was applied whose geometry in axial direction is modelled with linear equations instead of the cosine in (6.4). In this case the harmonic description in circumference was retained unchanged and all dimensions are identical to the “double cosine”-dimple given by (6.4) for like parameters w_b , l_b and a_b . There are no buckling tests available of cylinders afflicted with arbitrarily dimensioned initial dimple imperfections as described above in (6.4) which could evidence the correctness of the analytical results presented later. But a few buckling analyses were conducted of an axially compressed isotropic cylinder with different large diamond shaped dents (see Fig. 6.6) for comparisons with the buckling test results of (KRISHNAKUMAR & FOSTER [57]), see above.

6.3 Limitations of the Investigation

The chosen imperfection geometry defined in (6.4) with the three dimple size parameters (w_b , l_b , a_b), the two position parameters (z_b , φ_b), the three cylinder quantities (R , L , h) as well as the material parameters would enable, in principle, to investigate an infinite number of dents and bulges applied in an infinite number of possible cylinders. As customary in cases where such complex parameter spaces are studied, in order to reduce the number of parameter combinations to be considered to a manageable amount, the parameter study at hand was restricted to a number of exemplary, middle-long thin cylinders and a search after initial dimple dimensions which result in extremal effect on the reduction of the axial buckling loads.

The investigation was limited on the one hand to isotropic shell material with different YOUNG moduli E and a POISSON's ratio $\nu = 0.3$, and on the other hand to laminated CFRP cylinders with different membrane, coupling and bending stiffness \mathbf{A} , \mathbf{B} , and \mathbf{D} , respectively. All the investigated cylinders are identical to those presented in Section 4.1 for the buckling analyses of perfect cylinders. Hence, for the investigation on the influences of the cylinder dimensions R , L , and h on the damaging effect of single dimples in isotropic cylinders the about forty thin,

middle-long shells listed in Table 4.1 on page 120 exemplified. And for the analysis of laminated cylinders the laminated CFRP shells taken from the DEVILS project ($Z28$, $Z30$, $Z32$, $Z33$) and the cylinders $Z0.\alpha$ and $Z\alpha.0$ with eccentric layer stacking and various ply angles α as well as the two symmetrically laminated shells $Z0.60s$ and $Z60.0s$ served. Again, these cylinders were introduced in Section 4.1.2 for the analyses of these shells having perfect geometry.

For cylinders afflicted with only one initial dimple the position on the circumference φ_b may a priori be ignored. The axial distance of the dimple apex from one cylinder edge z_b was set to $L/2$ for the determination of critical parameter combinations, since at half the cylinder length potential influences of the edge bearings are minimal.

Consequently, the problem to be analysed was reduced to two separate parameter studies with searches for critical dimple dimensions and dimple imperfection sensitivities with

- $\frac{P_{cr}}{P_{crit}} = f(R, L, h, w_b, l_b, a_b, E)$ for isotropic cylinders, and
- $\frac{P_{cr}}{P_{crit}} = f(w_b, l_b, a_b, \mathbf{A}, \mathbf{B}, \mathbf{D})$ for laminated cylinders.

For all buckling analyses it was presumed that the shells are stress-free in the unloaded state, i.e. possible pre-stresses or residual stress fields were excluded. It was further supposed that the resulting stresses in the cylinder shells under-run the yield point or ultimate strength of the chosen shell material. That is, the HOOKEAN law for linear elastic material was assumed to remain valid for all states of loading. Furthermore, initial material imperfections and shell thickness variations as well as local material damages like cracks or delaminations during loading were ignored. Hence, the material of the isotropic shells was supposed to be linear elastic and homogenous and that of the composite cylinders layer-wise likewise homogenous and linear elastic.

The analysed shells initially have the form of closed, circular cylinders. Apart from the determined dimple imperfections the cylindrical shells are free from further imperfections, and between the cylinder ends (at $x = 0$ and $x = L$) possible stiffeners were excluded as well as longitudinal cuts of the shell. Due to stress field rearrangements towards stiffeners or additional edges between the cylinder ends the buckling behaviour of the structure would become much more complex and the analysis of shell afflicted with a dimple would be dominated not by the dimple pattern but rather by the dimensions of the stiffeners and the type of boundary

conditions at the longitudinal edges.

Since axially compressed circular cylinders are more sensitive to geometric imperfections than cylinders under external pressure or torsion the investigations on the buckling behaviour of isotropic and laminated cylinders having parametric dents or bulges was restricted to cylindrical shells under pure axial compression.

Similar to the analysis of the shells without imperfections the cylinder shells were considered being clamped. The two circular edge planes remained parallel and even during loading, simulating infinitely stiff end-plates and causing uniform end-shortening (boundary conditions CC4). The influence of non-uniformly applied axial loads to the cylinder stability and local shell buckling was not considered for this work. But in order to accentuate the importance of the boundary conditions, alternatively buckling analyses were conducted of cylinders with uniform membrane forces applied to the edges (boundary conditions CC3), see Section 6.4.

Recapitulating, the conducted parameter study was limited to

- cylinders under pure axial compression;
- cylinders with either isotropic, linear elastic homogeneous shell material, or ideal laminates of homogenous linear elastic layers;
- cylinders with perfect circular edges;
- cylinders without stiffeners between the two shell edges; and
- cylinders with constant shell thickness.

6.4 FE Models and Boundary Conditions

The finite element models of the cylinders with imperfections were established with the same number and type of elements as the cylinders with perfect geometry. That is, independent from the shell material the cylinder models consist of almost square bilinear, MINDLIN-type shell elements with initial side lengths given by the formula $0.5\sqrt{Rh}$. The number of elements and nodes of the cylinder models for the calculations with single dimples were maintained from the perfect counterparts and may be found in Section 4.1.3 (isotropic shells: Table 4.1, p. 120).

Due to rearrangements in the displacement and stress fields during loading in the vicinity of the initial dimples stress concentrations have to be expected. Thus, a detailed static stress analysis at a particular load level

would probably require local mesh refinements. But since any modification of the stress field leads to changes in the corresponding initial stress stiffness matrix (see Section 3.5), the usage of locally refined meshes may not be recommended if local buckling as well as the collapse of the entire structure is analysed in the same calculation. Inadequately assembled triangle elements, for instance, may cause some inhomogeneities in the shear stress field. Such unintentional “intrinsic imperfections” finally can result in unexpected local buckling of a cylinder without geometric imperfections. Therefore, to ensure correct comparison with ideal cylinders the mesh of the cylinders having initial dimples should be identical to the mesh of the cylinder with ideal circular surface, as well as the analysis input parameters. However, departure from this recommendation is indicated if the geometry of a local imperfection in an otherwise perfect cylinder makes it impossible to built-up a homogeneously sized and shaped element mesh (e.g. circular cutouts).

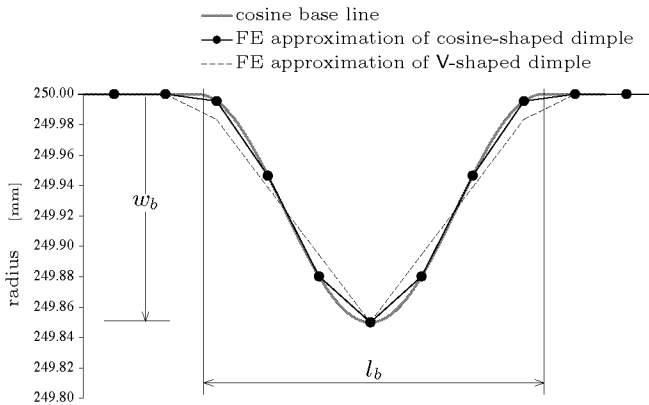


Figure 6.8: Radial and axial positions of nodes on the path over the apex of a dimple with amplitude $w_b = 0.15$ mm and meridian length $l_b = 67$ mm. Profiles of the cosine-shaped dimple according to the definition (6.4) and of the dimple with axial V-shape. FE approximations with a mesh size of 9.7 mm.

Obviously, the selected mesh size limits the minimal initial lateral measures of the dimples which may be described. That is, with mesh sizes specified by the length $0.5\sqrt{Rh}$ the dimple width a_b and height l_b have to be larger than the value \sqrt{Rh} . In Figure 6.8 the radial deviations

of an inward dimple from the nominal radius $R = 250$ mm depending on the axial position is compared with the discrete initial nodal positions of the FE modeling. In the example at hand the initial element length is $0.5\sqrt{R}h = 9.7$ mm and the meridian length of the dimple l_b is 66 mm. This results in the presented rather rough approximation with seven nodes involved in the description of the cosine line over the dimple apex. The dashed line with triangles refers to an alternative dent with identical l_b and w_b but having a V-shape in axial direction. As it will be shown later, the relatively small geometric differences between the approximations of the two dimple shapes are accompanied by resulting buckling loads which differ only a little.

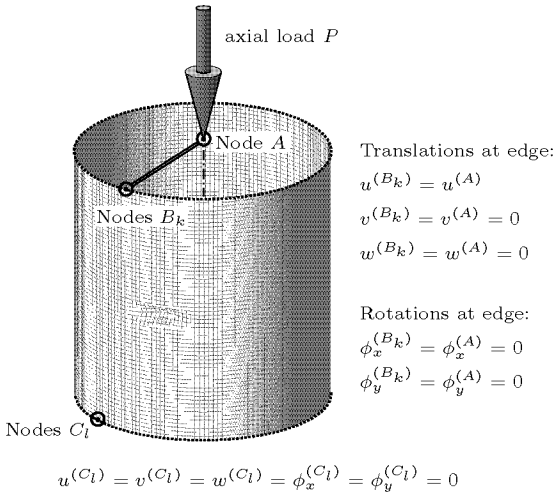


Figure 6.9: FE model with clamped edges simulated with tied nodes.

Again, as performed for the ideal cylinders (see Section 4.1.4), the boundary conditions on the shell edges were simulated with auxiliary nodes on the cylinder axis whose degrees of freedom (DOF) were joint with the nodes on an edge. Figure 6.9 illustrates the chosen modeling of clamped cylinder edges: the loading was applied on the additional node A on the axis which was linked with the k nodes B_k on the loaded edge in the form of a set of algebraic equations (listed in Fig. 6.9) which enforced the translations and rotations of the nodes B_k to follow those of the guiding node A . The specification of the boundary conditions for the l

nodes C_l on the unloaded edge was done in a similar way, i.e. with a further node of the center line.

For clamped edges only the axial displacement u of A is left moveable, the rotations ϕ_x and ϕ_y , and the lateral displacements v and w were disabled. For hinged edges only the translational DOF were considered in the set of algebraic equations representing the joints between the nodes, the rotations are left free.

Such a modeling of clamped or hinged cylinder edges with tied nodes ensures that the edge planes remain parallel and even during loading, what simulates rigid endplates and the analytical boundary conditions SS4 or CC4. The numerical analyses of cylinders with dimple imperfections base on the experiences with the numerical analysis of cylinders with measured imperfections for which the clamped boundary conditions CC4 were applied. Consequently, unless otherwise noted for the cylinders having single dents or bulges again always clamped edges (CC4) were simulated.

The direct application of the axial load not on a central node but uniformly distributed on the edge nodes causes potentially non-uniform axial edge displacements. Such a setting simulates the boundary conditions SS3 or CC3 in the shell calculus, see Section 2.2.1. Since the difference between uniform edge membrane forces (CC3) and uniform edge displacements (CC4) may result in considerable discrepancies in the cylinder stability, some comparable buckling analyses with a loading according to the boundary conditions set CC3 were conducted and reported in this thesis, see Section 6.6.7.

6.5 Adaptations to the Buckling Analyses

Since quasi no test results are available of cylinders which have single dimples with dimensions in the wide range considered, to guarantee plausible numerical simulation results the way of the modeling of the shell geometry and the boundary conditions as well as the analysis methods were adopted from the calculations performed during the Brite-Euram project DEVILS. For these analyses it was profited from the opportunity to compare buckling tests results with FE analysis results of cylinders with measured imperfections applied. Missing test data it would have been beneficial to have at least analytical formulations and their results for comparison. The shell geometries analysed are analogous to a

spherical cap with elastic foundation inserted in a perfect circular cylinder whose lateral extent in the cylinder shell and foundation parameter change continuously during loading. The development of an analytical approach for this problem would have been an honorable work, but the solution of the emerging large systems of equations would have required approximative numerical calculations anyway. Thus and because the Finite Element method implemented in commercial programs offers numerical solutions also for analyses with localized imperfections no efforts were made to deduce a new, special analytical formulation and relating codes. The investigation on the imperfect cylinders consisted in linear and mainly in nonlinear buckling analyses as well as in transient dynamic analyses with suitable finite shell element models, see Section 3.5. The supply of useful recommendations and parameters for such relatively sophisticated FE analyses might attract more attention by potential readers and program end-users than a list of series coefficients involved in the shell calculus¹.

The confidence in the buckling analysis results of the shells with dimple imperfections presented in the following may only be justified with the experience of working with the used analysis methods, shell elements and the manner of modeling of cylinders with only slightly different shell geometries. Consequently, the buckling analyses of cylinders afflicted with dimple imperfections were conducted solely with MARC[®]. Already during the project DEVILS it was found that basically a nonlinear buckling analysis is demanded if any imperfection is applied to the model to adequately account for geometric nonlinearities. Consequently, linear buckling analyses were performed only for a few cases (see Section 6.6.7). For the nonlinear buckling and the transient dynamic analyses large displacements and rotations were considered by use of the implemented Updated Lagrangian formulations.

6.5.1 Nonlinear Buckling Analysis with Adaptive Load Step Control

For linear buckling analyses with finite elements basically no knowledge about the bifurcation load level is needed to calculate the lowest eigenvalue and the respective eigenvector; viz, after the input of the unloaded geometry, material properties, and boundary conditions the values for

¹Though the author complains the anticipated loss of the senior scientists' know-how needed for the challenges associated with complex analytical formulations.

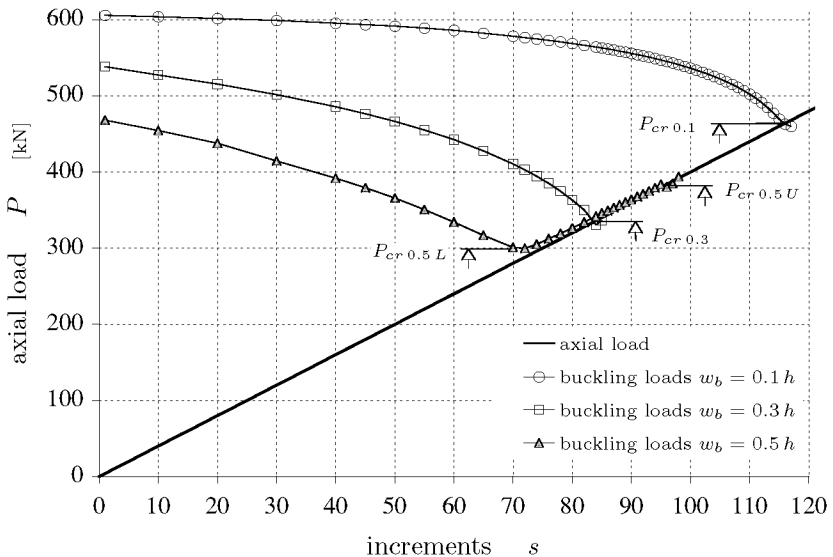


Figure 6.10: Results of nonlinear buckling analyses of an axially compressed aluminium cylinder having a single dent of different initial depths w_b . The lateral dent dimensions are $l_b = 67$ mm and $a_b = 181$ mm; the cylinder dimensions are $R = 250$ mm, $h = 1.5$ mm, and $L = 510$ mm. The thick line refers to the respective applied loads, the signs in the thin lines to buckling loads calculated at the corresponding increments.

the applied loads in principle may be chosen arbitrarily². But in any nonlinear buckling analysis the loading is to be applied in increments which have to be of sufficiently small step size. The schedule line of the loading and the increments at which an accompanying linear eigenvalue investigation is performed have to be pre-selected in a way that a permissible final extrapolation towards the instability yield a sufficiently accurate value for the buckling load. In Figure 6.10 the difficulties with the arrangement of the loading and the accompanying buckling load calculations is demonstrated. In the case at hand an isotropic cylinder was investigated which had one inward dimple with an initial depth w_b of $0.1h$, $0.3h$, or $0.5h$. The lateral dimple parameters l_b and a_b were set to 67 and 181 mm, respectively³. The buckling loads of the ideal cylinder

²However, values close to the classical, analytical buckling loads are recommended for good convergence.

³The values for l_b and a_b refer to the dimple with $w_b = 0.1h$ which causes maximal damage of this cylinder, see Section 6.6.3.

with a radius $R = 250$ mm, a shell thickness $h = 1.5$ mm, and a length $L = 510$ mm are 599 kN, analytically, and 570 kN resulting from a non-linear buckling analysis (see Table 4.2, p. 128). The markers in the lines plotted in Figure 6.10 denote the buckling loads which were computed via linear eigenvalue calculations at the corresponding increments. The horizontal distances of the markers indicate the increasing frequency of the buckling load predictions with increasing number of increments s . That is, e.g. between $s = 40$ and 70 after each fifth increment, and after $s = 85$ after each increment such eigenvalue calculations were performed, see Section 3.5.2. The shell with a dent having an initial depth $w_b = 0.1h$ (top line with circlets) results in buckling loads which form a curve that intersects the thick straight line with the total load between $s = 110$ and 120 in a way that allows an accurate specification of the searched nonlinear buckling load $P_{cr0.1} \approx 460$ kN. A dimple with an initial depth $w_b = 0.3h$ applied to the cylinder yield a considerably reduced nonlinear buckling load $P_{cr0.3}$ compared with $P_{cr0.1}$. In this case, the intersection of the line marking the computed buckling loads (middle line with squares) and the thick line is placed between $s = 80$ and 90 where only at each second increment a buckling load was calculated, and hence a permissible visual estimate of the buckling load $P_{cr0.3} \approx 355$ kN is less exact than that for $P_{cr0.1}$. Applying the analysis method to the cylinder with a dent of initial depth $w_b = 0.5h$, an irritating run of the curve chaining the resulting buckling loads (line with triangles) may be observed: at a first critical axial load level at which some local buckling occurs ($P_{cr0.5L} \approx 299$ kN), in Figure 6.10 at increment $s = 72$, the two curves referring the axial load and the estimated buckling loads approach each other but do not coincide. The buckling loads computed after this level increase with continuous load accumulation, indicating that further buckling loads predicted from the new state of stress and deformation point at the load level at which the entire cylinder will collapse ($P_{cr0.1U} \approx 392$ kN). Possible explanations for such particular buckling and nonlinear pre-buckling behaviour are given later. For both load levels, $P_{cr0.1L}$ and $P_{cr0.5U}$, the actual arrangement of the different eigenvalue extracting frequencies is not ideal for an accurate visual judgment for the results. Thus, in contrast to a linear buckling analysis, for a nonlinear buckling analysis some a priori-knowledge about the resulting buckling load(s) is necessary to be able to pre-select a small step size and a higher eigenvalue-extraction frequency only where needed. In the examples of Figure 6.10 the dimples applied reduce the buckling load down to only half the value of the ideal cylinder. Moreover, a linear buckling analysis of the cylinder having a dimple with $w_b = 0.3h$ yields

a buckling load which is more than 50% too high compared with the result of a nonlinear buckling analysis. Hence, missing better information on the resulting nonlinear buckling load prior to the calculations, in such cases analysis reruns have to be expected. Thus, this conventional type of a nonlinear buckling analysis is useful if only a small number of FE models is investigated and expensive reruns of such nonlinear analyses are justifiable. But for complex parameter studies with imperfections considered, which may lead to widely scattered buckling loads of possibly only 20% of that of the associated perfect cylinder, an analysis method with a need of several trial-and-error reruns to obtain the final result is surely not satisfying.

The nonlinear buckling analysis was therefore modified for an adaptive load step control which does not need any precognition of the result. In the modified method the loading step is continuously adjusted to the intermediate buckling-load prediction and is a proprietary development of a set of FORTRAN user-subroutines which intervene into the pre- and post-processing codes of MARC[®]. In Figure 6.11 the scheme of the nonlinear buckling analysis with adaptive load step control is diagrammed.

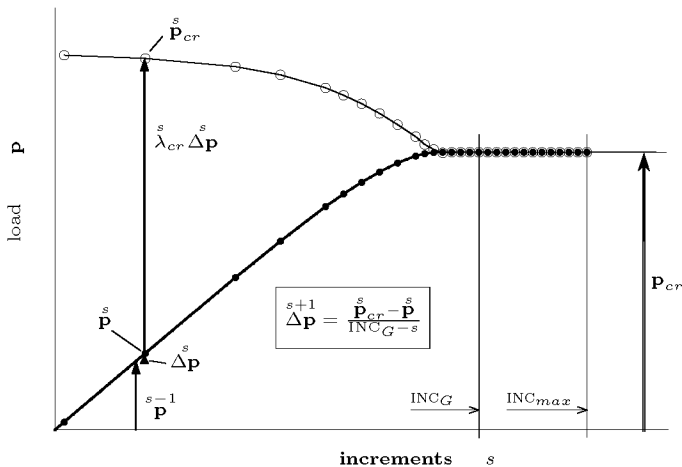


Figure 6.11: Nonlinear buckling analysis with adaptive load step control: *Nonlinear pre-buckling states of equilibrium and corresponding intermediate buckling loads.*

Basically, only the number of increments INC_G at which the buckling

load is to be reached and an adequate schedule of the increments with an eigenvalue extraction has to be pre-selected. But, in contrast to the conventional procedure the schedule is not sensitive to the final buckling load \mathbf{p}_{cr} . The first load increments, in principle, may be set arbitrarily. Then, after a first eigenvalue calculation the predicted buckling load according to the actual pre-buckling state, i.e. the applied total load \mathbf{p} , is calculated. With this information the subsequent load increments are computed by the ratio of the difference between the already reached total load \mathbf{p} and the current predicted buckling load \mathbf{p}_{cr} to the number of remaining increments before INC_G , that is:

$$\Delta \mathbf{p}^{s+1} = \frac{\mathbf{p}_{cr}^s - \mathbf{p}^s}{\text{INC}_G - s} \quad , \quad \text{with}$$

$$\mathbf{p}_{cr}^s = \mathbf{p}^{s-1} + \lambda_{cr}^s \Delta \mathbf{p}^s \quad .$$

The new load increment $\Delta \mathbf{p}^{s+1}$ is applied up to the next increment with eigenvalue extraction and a resulting buckling load prediction. Close to buckling the difference between the final buckling load and the applied total load becomes smaller and smaller until the eigenvalue approaches $\lambda_{cr} = 1$; this means that the applied load coincide with the final buckling load and thus the new load increment is zero. In cases with some nonlinear pre-buckling behaviour where the prior load increment may be oversized the eigenvalue is $\lambda_{cr} < 1$ which results in a negative new load increment, thus in a tensile load that corrects the loading towards a lower buckling load. After having reached the buckling condition the computation may continue; the load increments will not vanish totally but will be of relatively small positive or negative value. Consequently, the eigenvalue tend to zero since the applied loads at the actual and the preceding increments become almost identical and hence both nearly coincide with the buckling load. At this stage, the calculation may be aborted due to difficulties in the numerical eigenvalue extraction for zero load increments. However, intentionally the computation will end only when the maximal number of increments INC_{max} is reached or if the provided break condition is fulfilled, e.g. if the relative difference between the actual predicted buckling load and the actual applied total load undershoots a given value.

In Figure 6.12 (right) the results of such a nonlinear analysis with adaptive load step control are depicted. The resulting final buckling load is identical to the value yielded by the conventional method (left chart), but the adaptive method needs no visual judgement for the troublesome extrapolation to the final buckling load (larger circle in Fig.6.12, left

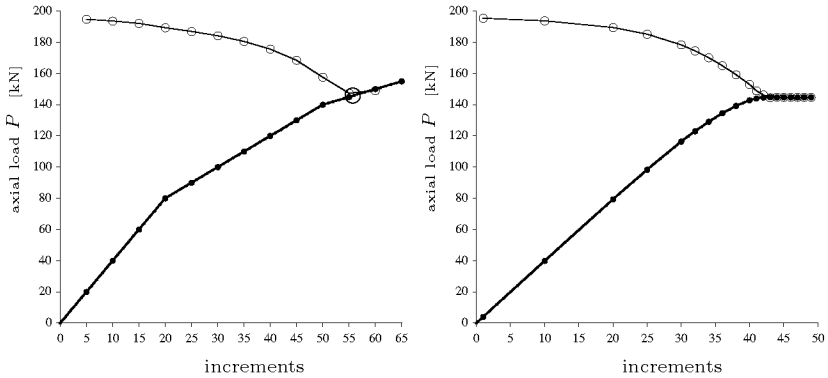


Figure 6.12: Applied axial loads and corresponding intermediately calculated buckling loads. Conventional method (left), and with adaptive axial load step control (right).

chart); in fact, the adaptive variant allows to identify the final buckling load adequately by picking up the last value in a list containing the chronology of the loads \mathbf{p}_{cr}^s and \mathbf{p}^s successively sampled during the computations. The two kinks of the thick axial-load line in the left chart at increment 20 and 50 stem from the change of the axial load-step size to allow for an accurate estimation of the final buckling load.

Note that the nonlinear run of the curves representing the applied loads in charts like those in Figure 6.12 do not refer to a nonlinear stiffness or pre-buckling behaviour. In contrast to the more familiar load-deflection curves the abscissa indicates the increment number s at which a particular axial load level is reached. Hence, the bends of the curves in Figure 6.12 stem from the variation of the load step size and not from the structural stiffness.

On the basis of the experience with this adaptive method provided for buckling analyses of imperfect cylinders, it is recommended to initiate new eigenvalue extractions at every load increment after about 80% of the expected number of increments prior to buckling INC_G , since nonlinearities caused by imperfections may lead to a significant reduction of the intermediate buckling loads with continuous increase of the applied load, which in turn results in an early conjunction of the upper and lower load curves in both charts of Fig. 6.12.

For the first analysis performed the number of increments for the pre-buckling state INC_G was set to 50, but later it was found that in cases

1. Increment 0 is a null step, i.e. zero loading: $\overset{0}{\mathbf{p}} = 0 \quad \overset{0}{\mathbf{u}} = 0$

First increment $s = 1$

Initial load step size is given by the fraction of an arbitrary load \mathbf{p}_A

$$\Delta \overset{1}{\mathbf{p}} = \frac{\mathbf{p}_A}{\text{INC}_G}$$

2. Calculation of the nodal displacements $\overset{s}{\mathbf{u}}$ with a NEWTON-RAPHSON algorithm.
The total applied loads needed thereby are given by $\overset{s}{\mathbf{p}} = \overset{s-1}{\mathbf{p}} + \Delta \overset{s}{\mathbf{p}}$
3. At some pre-selected increments an intermediate buckling load estimate is conducted. This gives the intermediate buckling load

$$\overset{s}{\mathbf{p}}_{cr} = \overset{s-1}{\mathbf{p}} + \lambda_{cr}^s \Delta \overset{s}{\mathbf{p}}$$

4. If at increment s a new buckling load was estimated according to 3. , then *update* the *load step size* for the next increments with:

$$\Delta \overset{s+1}{\mathbf{p}} = \frac{\overset{s}{\mathbf{p}}_{cr} - \overset{s}{\mathbf{p}}}{\text{INC}_G - s}$$

$$\text{if } s \geq \text{INC}_G \text{ then: } \Delta \overset{s+1}{\mathbf{p}} = \overset{s}{\mathbf{p}}_{cr} - \overset{s}{\mathbf{p}}$$

5. At buckling it applies

$$\overset{s}{\mathbf{p}}_{cr} \equiv \overset{s}{\mathbf{p}} \quad \Rightarrow \quad \Delta \overset{s+1}{\mathbf{p}} = 0$$

6. Termination of the NEWTON-RAPHSON calculations if

$$s \geq \text{INC}_{max} \quad \text{OR} \quad \frac{\overset{s}{\mathbf{p}}_{cr} - \overset{s}{\mathbf{p}}}{\overset{s}{\mathbf{p}}} < \psi$$

where INC_{max} is the maximal number of increments ($\text{INC}_{max} > \text{INC}_G$), and ψ is an input tolerance.

7. $s = s + 1$. **Go to** 2.

Recommended parameter setting:

- $\mathbf{p}_A \approx \mathbf{p}_{cr id}$ i.e. a value close to the classical or linear buckling load of the investigated cylinder without imperfections.
- $\text{INC}_G = 100$
- $\text{INC}_{max} = 250$
- $\psi = 10^{-6}$

Table 6.1: Scheme of the adaptive loading step control for the use in static nonlinear calculations, provided for complex parameter studies on imperfect cylinders. See also Fig. 6.11.

with considerable pre-buckling deformations it is beneficial to select $INC_G = 80$ to $INC_G = 100$ for smaller primary load steps.

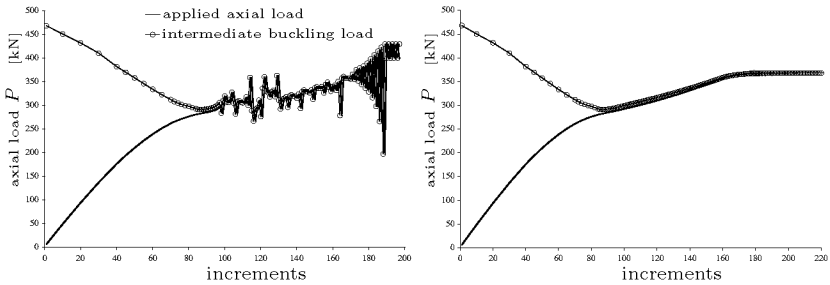


Figure 6.13: Results of nonlinear buckling analyses of an isotropic cylinder ($R = 250$ mm, $h = 1.5$ mm, $L = 510$ mm) with an inward single buckle of initial depth $w_b = h/2$. With (right) and without restricted load step size enlargement (left). See Fig. 6.10.

In Figure 6.13 the results of two nonlinear buckling analyses pursuant to Table 6.1 of the isotropic cylinder, already presented in Figure 6.10, with a single dent of of initial depth $w_b = h/2$ are plotted. In the left chart difficulties with an undesired zigzag course of the loads at increments after a local buckling are in evidence. This phenomenon due to unregulated alternating compressive and tensile load steps occurs if no additional provisions are made which prevent excessive over- or underestimations of the actual structural stability and the subsequent corrections. Thus, in order to obtain an unambiguously identifiable value also for the overall collapse load $P_{cr 0.5U}$ (see Fig. 6.10), a possible enlargement (absolute value) of each load step was restricted to 1% of the precedent step. The right chart in Figure 6.13 finally demonstrates the results of a nonlinear buckling analysis with this step-size change restriction: calculated with such a modification two resulting buckling loads may clearly be distinguished: a first load level at the local minimum of the curve with the buckling loads, denoting local buckling, and a second, higher load level at the conjunction of this curve with the curve of applied axial loads, marking cylinder collapse. The first critical load appears at about 80% of INC_G , the second need another about a hundred increments (depending on the load difference between local and cylinder buckling), thus with a $INC_G = 100$ suggested the maximal number of increments INC_{max} should be set to more than 250.

Although it would be possible to start the nonlinear FE calculations with an arbitrarily small initial load step size also set to ± 1 N, due to

the restriction of possible load step enlargements, as explained above, it is recommended to begin with a large value and to enable a stepwise reduction. Therefore, the initial load step should be set to

$$\Delta \mathbf{p}^1 = \frac{\mathbf{P}_A}{INC_G}$$

with a user-defined value \mathbf{p}_A close to the classical or linear buckling load of the investigated cylinder without imperfections.

Nonlinear buckling analyses with the herein proposed adaptive step-size control may also be performed with axial displacements instead of axial loads applied to cylinder edges. In Figure 6.14 the results of a buckling

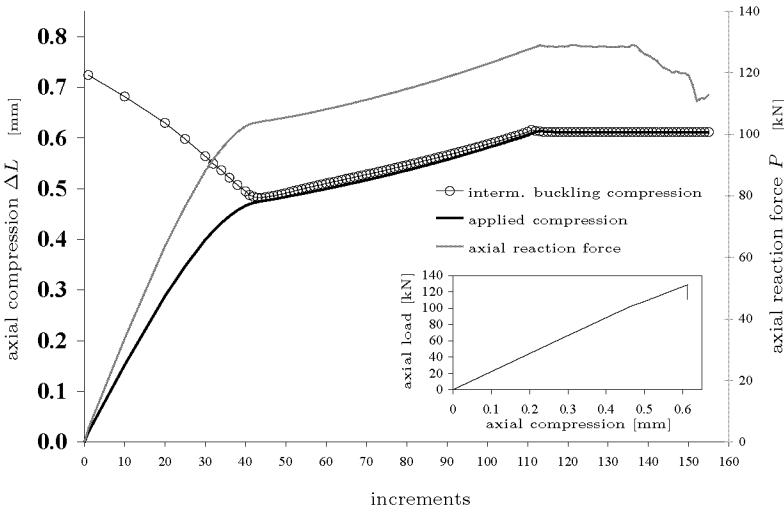


Figure 6.14: Results of a nonlinear buckling analysis for a laminated cylinder (Z33) with a single dent of initial depth $w_b/h = 0.5$ using adaptive displacement step control.

analysis with stepwise axial cylinder shortening of a laminated cylinder (Z33) having a deep initial dent is demonstrated. The aligned circlelets stand for intermediately predicted buckling compressions, which were used for the successive update of the applied compression step size. The thick black curve represents the progression of the accumulated applied cylinder end-shortening and the grey curve that of the corresponding total axial reaction force. Note the presence of a local buckling event at

increment 43 identifiable by the minimal value for the locally predicted buckling compressions. Noteworthy also the downfall of the reaction force after increment 136 at an almost constant cylinder length. This might be explained by multiple solutions for the shell displacement field for a given loading at collapse; however, in view of the post-buckling state these solutions have no scientific relevance. In the small graph included into Figure 6.14 the total axial reaction force at corresponding axial cylinder shortening is reproduced. Hardly visible a kink in this curve stemming from the mentioned local buckling event at about 100 kN.

An important disadvantage of the nonlinear buckling analysis described above consists in the numerous eigenvalue extractions which are conducted during a standard static nonlinear FE analysis as an optional, accompanying analysis measure. Compared with the solution of the main equation system (NEWTON-RAPHSON procedure) the solution of eigenvalue problems with large matrices is very time consuming and may even cause storage problems during the iterations. For these eigenvalue extractions the *inverse power sweep* procedure as implemented into MARC[©] was used (see Section 3.5.1). The dimensions of the cylinders which could be considered during the research work were therefore restricted by their number of degrees of freedom, their size of the system matrices respectively, and the CPU time needed for a nonlinear buckling analysis. The arc-length methods described shortly in Section 3.5.2 also account for possible large displacements and rotations but do not contain expensive accompanying eigenvalue extractions. This might be a reason why the arc-length methods are preferred by many FE analysts as the standard option for nonlinear buckling analyses also for large systems. The same specimen and dimple than shown in Figure 6.14 was calculated using an arc-length method with a linearized constraint equation⁴ for comparison. In Figure 6.15 the relating results are plotted in a load-axial displacement diagram similar to the small graph added to Figure 6.14. The maximum load and the kink, indicating local buckling, are identical to the calculation using the nonlinear buckling load with standard NEWTON-RAPHSON iterations and eigenvalue extractions. But with the arc-length method a solution path-tracing into the initial post-buckling state was possible. After a sharp inversion of the direction having passed the peak load level the curve follows the decline of the stiffness in terms of displacements and forces to re-increase up to a second peak. But, the sudden sharp inversion at the load maxima imposes difficulties in the definition of adequately small load step sizes,

⁴In MARC[©] denoted by “modified Riks-Ramm method”.

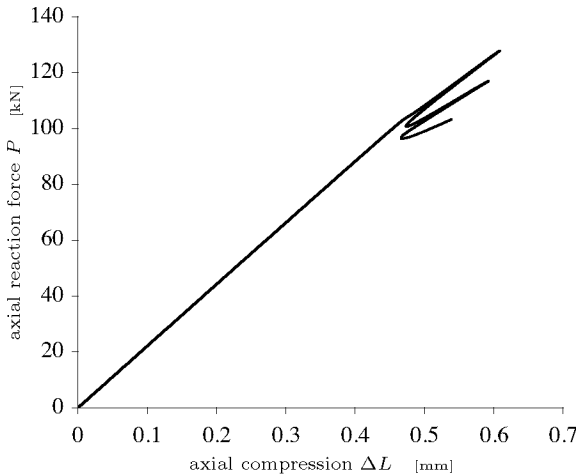


Figure 6.15: *Results of a nonlinear buckling analysis for a laminated cylinder (Z33) with a single dent of initial depth $w_0/h = 0.5$ using arc-length controlled iterations.*

since the loading automation implemented in the code refers to the prior step for the definition of the current step, and thus, since in the case at hand the only slightly nonlinear behaviour prior to the cylinder collapse does not indicate such severe nonlinearities, at and after buckling very small increments have to be pre-selected for the critical range of loading. This, in turn, leads to some reruns or, again, to a need of a good a priori-knowledge of the result if the number of increments should be retained in a reasonable range.

Nevertheless, despite the considerable additional time exposure the specially developed method with adaptive load step control was preferred for the hundreds of different shells and dimple imperfections to be analysed during the investigation. The benefit of the method to yield the searched nonlinear buckling load already after a first analysis run prevailed the mentioned disadvantage. And the minimisation of computation times was not subject of the investigation, anyway. Implementation of new, faster algorithms or improvements of the implemented LANCZOS method for its stable usage also in nonlinear buckling analyses with the Updated Lagrangian procedure might reduce the problem with the CPU time and storage space in the future, together with the further developments in computer engineering to be expected.

6.5.2 Transient Dynamic Analysis

Due to the relatively large computation time exposure transient dynamic analyses were conducted only for a limited number of shells and imperfections with some particular buckling behaviour. For the direct time integration in the transient dynamic analyses again the implicit single-step HOUBOLT operator (SSH-method) was used with input parameters which were adjusted to the result of a nonlinear buckling analysis and the analysis of the cylinders with perfect geometry. The successful usage of the SSH-method for axial buckling analyses of cylinders with measured imperfections was described in Section 5.3.2.

With the transient dynamic analysis it is possible to pass over the critical axial compression level where cylinder collapse occurs to reach the post-buckling states. The remaining stable load-carrying capacity of the collapsed cylinder was not of interest, but the simulation of the dynamic deflections of the shell close to and immediately after buckling enabled by this method was used for explanations of some particular buckling or pre-buckling behaviour. Namely, in contrast to the static nonlinear buckling analysis possible local buckling in the vicinity of an initial dimple prior to the total collapse of the cylinder may also be traced. Nevertheless, due to the efforts needed the transient dynamic analysis has to be understood as a complementary method to specify the load carrying capacity of a structure and not as the prime buckling analysis method that should be used at first. The application for a buckling analysis is possible but as long as only the critical load is of interest the conducting of a less complex (static) nonlinear (buckling) analysis will be sufficient and thus preferable. But, for the investigation of shells with dimple imperfections such dynamic analyses yielded results which were a welcome confirmation of the results obtained with the respective nonlinear buckling analysis.

Figure 6.16 depicts the result of such an analysis for a laminated CFRP cylinder (*Z33*) having a dent of initial depth $h/2$. The shell and the dent are both identical to those exemplifying in Figure 6.14, computed with a nonlinear buckling analysis, and those for Figure 6.15 analysed with an arc-length method. Such as for cylinder *Z33* with perfect shell the damping matrix was set to 25 000 times the mass matrix for a mass density of 1600 kg/m^3 and an axial compression velocity of 0.1 mm/s . Similar to the result of analysis with an arc-length method the collapse load and the kink in curve between $\Delta L = 0.4 \text{ mm}$ and 0.5 mm , stemming from some local buckling, are very close to the result of a nonlinear buck-

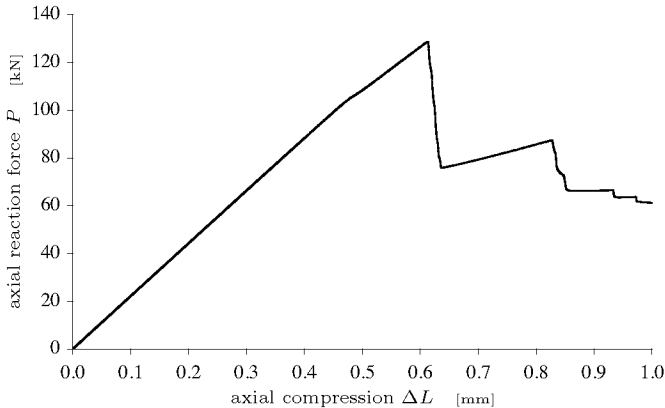


Figure 6.16: Results of a transient dynamic analysis for a laminated cylinder (Z33) with a single dent of initial depth $w_b/h = 0.5$ using the implicit SSH-method for time integration.

ling analysis, see Figure 6.14. But the dynamic analysis yields a more familiar run of the load-compression curve, quasi simulating a buckling test, than the arc-length method which represents a rather “academic” path-tracing of equilibrium states impossible to observe during tests.

Although the influences of dimples to the buckling loads observed may also be demonstrated by means of laminated shells, the different sensitivities to the variations of the dimple size parameters were mainly analysed with isotropic cylinders. The selected isotropic cylinders of interest were likewise calculated with a compression velocity of 0.1 mm/s; and considering aluminium as shell material with a YOUNG’s modulus of 70 000 MPa and a mass density of 2700 kg/m³, the damping matrix was introduced as 50 000 times the mass matrix, a value successfully taken from the dynamic analysis of the thin Mylar cylinder (see Section 4.3, Fig. 4.18). Again, other input parameters were adopted and selected on basis of a nonlinear buckling analysis.

The relatively large damping parameters α_m of 25 000 and 50 000 used for the shells described herein were assessed on the basis of dynamic transient analyses for the respective cylinders having perfect geometry, always using SI units (m, kg, s) and the selected compression velocity of 10^{-4} m/s (see Section 3.4).

6.5.3 Accompanying Data Collection

The result of any finite element analysis consists primarily in nodal displacements and forces. Other measures like stresses or strains are only computed if required during the post-processing phase of an increment or load step. A nonlinear buckling analysis as described herein required up to 200 increments, a transient dynamic analysis with the implicit single-step Houbolt method even 4000 or more. Hence, the extraction and recording of all displacement and stress fields, all vectors and scalars that might be of interest for the evaluation after the analysis, would clearly blast any storage capacity. For the analysis of the cylinders the evaluation of stress fields could therefore only be conducted during additional nonlinear static FE analysis with constant load steps. And for three-dimensional deformation plots in a dynamic analysis only each tenth increment, at most, was scheduled for the recording of all nodal displacements and coordinates required.

The continuous collection of scalars causes less storage space problems than that of field or matrix measures, e.g. stress distributions, and are basically preferred for the evaluation of FE analysis results. For the buckling analyses of axially compressed cylinders first of all the alteration of the axial force and the cylinder length are of interest. The eigenvalues calculated in some selected increments during a nonlinear buckling analysis may also be understood as scalars which are to be collected applying this method. Other useful quantities which were extracted continuously during transient dynamic analysis are the actual radius and the local curvature at the nodal point of the dimple apex, see Table 6.2 below. Further possible variables which may come to mind for the observation of different buckling effects are the strain and the kinetic energy, the eigenfrequencies, or the compliance of adjacent state of deformation. The monitoring of the latter was described by (WULLSCHLEGER & MEYER-PIENING [81]). But the additional information received by the observation of these quantities only confirm the indications already given by the states of deformation visualized in 3D graphics or in load-deflection diagrams.

In Section 3.5 it was explained that during the incremental nonlinear finite element analyses as conducted for the shells with dimples the volume integral of the stresses over a FE model yields the current internal forces at the state of increment which have to be equilibrated iteratively with the external forces (NEWTON-RAPHSON procedure). Additionally, the stresses are the main component of the current initial stress or geometric

stiffness matrix. For all calculations the Updated Lagrangian formulation was used, hence all kinematic variables referred to the last increment in equilibrium. Consequently, the resulting stresses are CAUCHY stresses σ , and accordingly all stresses presented within this thesis are CAUCHY stresses. The numerical integration over a shell surface in general is performed with the so-called GAUSSIAN quadrature, whereas for the integration through the shell thickness a NEWTON-COTES quadrature formula like the trapezoidal method or the SIMPSON's rule is preferred [61, 84, 14]. For a four-node bilinear shell element, see Figure 6.17, in

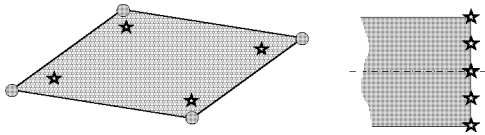


Figure 6.17: *Sampling points (stars) for numerical integration over finite shell elements. Points for the GAUSSIAN quadrature (left) and for the NEWTON-COTES quadrature (right, SIMPSON's rule).*

general four sampling or integration points (tagged with stars) are provided in a surface of a shell section; hence, for a shell with 10 sections or layers 40 scalars of a stress quantity have to be calculated after a load increment with requested data collection. The membrane force per unit length N_{ig} of an element i at a GAUSSIAN integration point g was calculated as the sum over the stress $\sigma_{\ell ig}$ of the shell sections (layers), multiplied by the shell thickness h and divided by the number of shell sections or laminate layers n_ℓ :

$$N = \int_{-h/2}^{h/2} \sigma \, dz \quad \longrightarrow \quad N_{ig} = \frac{h}{n_\ell} \sum_{\ell=1}^{n_\ell} \sigma_{\ell ig} \quad (6.6)$$

The number of integration points through the thickness may be specified by the program user or is given by the number of laminate layers, whereas the number of GAUSSIAN integration points in a surface is determined by the type of the used finite element. The effectively implemented integration schemes as well as the sequence of the integration points are specific to the program. Thus, for the output of stresses (or strains) the reading of particular program manuals is advised. In the majority of cases, the missing stress values between the integration points are

calculated by linear interpolation. The presentation of stresses in finite elements is then conducted by means of colour contour plots added to the FE model surfaces.

In the shell theory of circular cylinders in Chapter 2 a travelling Cartesian coordinate system was defined with the x -axes in direction of the cylinder axes, the y -axes in tangential direction, and the z -axes parallel to the radius towards the cylinder axes, see Figure 2.2, page 34. But the Cartesian coordinate system defined for the finite element models is substantially different: the z -axes is congruent with the cylinder axes and the x - as well as the y -axes are positioned at the centre of the lower circular cylinder edge. Thus, in order to guard against misunderstandings, the stresses and membrane forces per unit length resulting from the FE analyses in axial direction were labelled with a subscript “axial”, the components in tangential direction accordingly with “hoop”, and the shear loading finally with “shear”. That following, the membrane forces per unit length N_{axial} and N_{hoop} approximate the axial and hoop membrane forces per unit length N_x and N_y of the calculus, respectively. The shear membrane forces per unit length N_{xy} finally are approximated by the membrane forces N_{shear} . The membrane forces per unit length indicate the size of the corresponding membrane stresses, i.e. the respective component of the stresses in the reference surface of a shell.

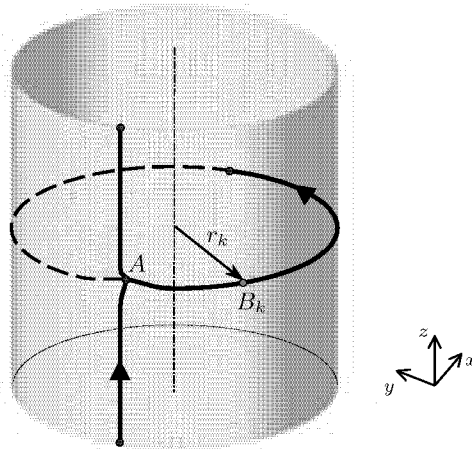


Figure 6.18: Horizontal and vertical paths over dimple apex, point A, for selective, disc-space saving, nodal or element data collection.

In order to enhance the amount of significant information recordable during an analysis, horizontal and vertical *paths*, see Figure 6.18, including the apex of a dimple imperfection, point *A*, were defined and introduced into specially developed or complemented FORTRAN user-subroutines which interfere into the post-processing codes of MARC[®], similar to the routines developed for the adaptive load step control described in Section 6.5.1. At each increment a row with the local values of one measure along such a path was written in a text file. The resulting data matrices with sizes up to 6000 rows (increments) and 400 columns (number of nodes or elements in a path) could be managed with programs like Excel[®] or Matlab[®] without notable problems. The quantities which were found to be useful for the evaluation and interpretation of the results and which were extracted for nodes and elements on the paths during the analyses were (1) the actual radius at the nodes, (2) the mean membrane forces per unit length at the particular elements, and (3) the local curvatures.

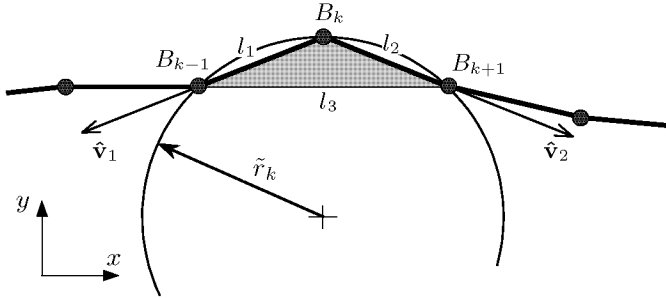
The radius r_k at a nodal point B_k of load increment s equals the distance of a node from the cylinder axis in the hoop plane of the path; that is:

$$r_k = \sqrt{\overset{s}{x}_k^2 + \overset{s}{y}_k^2} \quad (6.7)$$

where $\overset{s}{x}_k$ and $\overset{s}{y}_k$ are the coordinates of the Node at increment s with the cylinder axis at $x = y = 0$, see Figure 6.18. As mentioned above, this Cartesian coordinate system was used for the finite element models and differs from that used in the shell calculus with the x -axis parallel to the cylinder axis there.

For a high sampling rate, to reduce the memory requirements only one value per shell element of a path was stored. The so collected *mean* membrane forces per unit length \bar{N}_i of an element in a path were calculated as the sum over the average stress $\bar{\sigma}_{\ell i}$ of the shell sections (layers), multiplied by the shell thickness h and divided by the number of shell sections or laminate layers n_ℓ :

$$\bar{N}_i = \frac{h}{n_\ell} \sum_{\ell=1}^{n_\ell} \bar{\sigma}_{\ell i} = \frac{h}{n_\ell} \sum_{\ell=1}^{n_\ell} \left(\frac{1}{4} \sum_{g=1}^4 \sigma_{\ell i g} \right) . \quad (6.8)$$



Estimation of local curvatures on nodal paths

The curvature at a node B_k may be approximated by the inverse of the circumference radius of a triangle given by the positions of node B_k and the two adjacent nodes B_{k-1} and B_{k+1} (see Figure above):

1. *Coordinates of the three nodes involved:*

$$N_k: \quad \mathbf{x}_k = \{x_k, y_k, z_k\}, \quad N_{k-1}: \quad \mathbf{x}_{k-1} = \{x_{k-1}, y_{k-1}, z_{k-1}\}, \\ N_{k+1}: \quad \mathbf{x}_{k+1} = \{x_{k+1}, y_{k+1}, z_{k+1}\}, \quad \text{where } z_k = z_{k+1} = z_{k-1}.$$

2. *Definition of vector $\hat{\mathbf{v}}_1$ and $\hat{\mathbf{v}}_2$:*

$$\hat{\mathbf{v}}_1 = \mathbf{x}_k - \mathbf{x}_{k-1} \quad \text{and} \quad \hat{\mathbf{v}}_2 = \mathbf{x}_{k+1} - \mathbf{x}_k$$

3. *Side lengths of the triangle:*

$$l_1 = \|\mathbf{x}_k - \mathbf{x}_{k-1}\|; \quad l_2 = \|\mathbf{x}_{k+1} - \mathbf{x}_k\|; \quad l_3 = \|\mathbf{x}_{k+1} - \mathbf{x}_{k-1}\|.$$

4. *Area of the triangle:*

$$A_k = \sqrt{s(s-l_1)(s-l_2)(s-l_3)} \quad \text{with} \quad s = \frac{1}{2}(l_1 + l_2 + l_3)$$

5. *circumference radius of the triangle:*

if $A_k > 0$ then:

$$\tilde{r}_k = \frac{l_1 l_2 l_3}{4A_k}$$

else: $\tilde{r}_k = 10^{20}$

6. *The orientation of the local curvature* (inwards/outwards) was specified by the sign of the z -component of vector $\hat{\mathbf{v}}_3 = \hat{\mathbf{v}}_1 \times \hat{\mathbf{v}}_2$.

The orientation is defined so that in case of perfect shells the positive circumference radius \tilde{r}_k is equivalent to the nominal radius R of the cylinder: $\tilde{r}_k \equiv +R$.

7. *Approximated local curvature:* $\frac{1}{\tilde{r}_k}$

Table 6.2: Scheme of the calculation of local curvatures $1/\tilde{r}_k$ on basis of triangle circumferences.

Due to the curvature of the shell a circular cylinder may resist more axial load than a corresponding flat plate. Depending on imperfection geometry and state of loading and deformation the local shell radius may be or may become much larger than the nominal radius R of the cylinder (see flattened strip in Fig. 6.5 or the V-shaped dent according to a YOSHIMURA pattern in Fig. 6.6). This means that the respective curvature in circumferential direction becomes very small or zero. Because of such a partial flattening of the shell the stiffening effect of the shell curvature vanishes locally and a nonlinear instability of the shell region at the imperfection has to be expected prior to total collapse of the cylinder. Therefore, for a better understanding of the effects involved and the change of the local curvature during loading along the horizontal path through the dimples was calculated and recorded. The curvature at a node B_k was approximated by the inverse of the circumference radius \tilde{r}_k of the triangle given by the node B_k and the two adjacent nodes B_{k-1} and B_{k+1} . The process of the calculation for a node B_k is described in Table 6.2.

6.6 Isotropic Cylinders with Dimples

In the previous sections the tools, the models and the restraints of the investigations were described. In the following, buckling analysis results of thin-walled, axially compressed isotropic unstiffened cylinders of medium length which have one or two outward or inward dimples are presented.

For the analysis of cylinders with distributed imperfections as described in Chapter 5 mainly the influence of the imperfection amplitude(s) to the particular buckling load P_{cr} is of interest. The resulting normalized buckling load P_{cr}/P_{cl} indicates a reduction factor or knock-down factor that should be applied to the analytical, classical buckling load P_{cl} for safe shell design. Pursuant to this it was assumed that results of the variation of the initial depth or elevation w_b of the dimple imperfection and the relating reductions of the nonlinear buckling analysis results of the perfect cylinder $P_{cr\ id}$ could attract more attention than those of other influencing factors like the initial dimple width a_b or height l_b or the nominal cylinder dimensions R , L , or h . Consequently, the presentation of the analysis results of the variations of the initial dimple amplitude w_b , including its sign, precedes that of the other parameters studies.

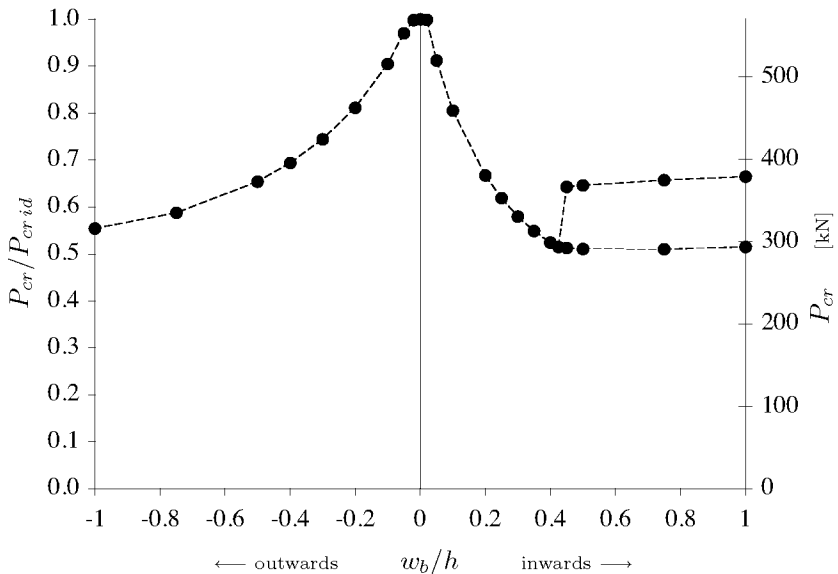


Figure 6.19: Nonlinear buckling analysis results of an aluminium cylinder having one inward or outward dimple at $L/2$ for various initial amplitudes w_b/h . Left ordinate: normalized buckling load with regard to the perfect cylinder; right ordinate: axial buckling load. Cylinder with $R = 250$ mm, $L = 510$ mm, and $h = 1.5$ mm, dimples with height $l_b = 67$ mm and width $a_b = 181$ mm.

Figure 6.19 represents the results of nonlinear buckling analyses for an isotropic cylinder with a single dent or bulge of different initial amplitude w_b/h . Positive w_b -values refer to inward dimples, negative to outward. The circumferential width and the meridian height of these dimples are always $a_b = 181$ mm and $l_b = 67$ mm respectively. The right ordinate in the diagram refers to the resulting axial buckling loads P_{cr} of the shells, whereas the left indicates the normalized buckling load $P_{cr}/P_{cr id}$. With a radius R of 250 mm, a length L of 510 mm, and a shell wall thickness h of 1.5 mm the nonlinear buckling load of this aluminium cylinder with perfect shell geometry, i.e. $w_b = 0$, is $P_{cr id} = 569.5$ kN (see Table 4.2, Section 4.2.1). It can be taken from Figure 6.19 that the curve for the sensitivity to the dimple imperfections is not symmetrical to $w_b/h = 0$: inward dimples within the given amplitude range reduce the load carrying capacity of the cylinder more than outward dimples with like width, length and amplitude.

The unequal sensitivity of axially compressed cylinders to dents compared with that to bulges can be explained by means of the dimples formed whilst the buckling of circular cylinders with *perfect* shell geometry as demonstrated in Section 4.3. Prior to instability thin perfect isotropic cylinders under axial compression expand due to the POISSON'S ratio effect, except at the edges where the increase in diameter in general is restrained. In this pre-buckling state of deformation and stress the small deflections are axisymmetrical and the potential energy is dominated by the share due to membrane action. In Section 4.3 the progression of the shell deformation is described by means of a Hostaphan cylinder (see Fig. 4.19). At buckling the shell starts to deform non-axisymmetrically into a first post-buckling pattern with many small, almost square buckles. With further axial compression this initial chess-board pattern changes to a diamond pattern which has ridges in the incline directions and furrows in the circumferential direction. This so-called YOSHIMURA pattern represents a quasi inextensible mapping of the shell surface, i.e. the combined length of all furrows in each cross section is approximately equal to the original cylinder circumference. Consequently, after the formation of the large and deep buckles for this pattern the membrane potential energy becomes negligible small and most of the potential energy is caused by bending at the ridges and the furrows [15]. From the contour-deformation plots in Figure 4.19 it can be learned that in the large post-buckling deformations the buckles tend to grow inward rather than outward: in contrast to an inward deflection, which may be accommodated with bending, an outward deflection of the buckles on the shell surface requires large membrane stretching.

However, in Figure 6.19 above all the splitting of the solution curve into two lines for dents with amplitudes larger than circa $w_b = 0.4 h$ strikes. These curves are typical for nonlinear buckling analysis results of cylinders with an *inward* dimple imperfection of a shape according to Section 6.2 and uniform axial edge displacements. In the next section peculiarities of the analysis results for such *dents* are specified by means of several isotropic cylinders. Afterwards some characteristics of *outward* dimples are presented within Section 6.6.2, page 296, considering similar cylinders.

6.6.1 Inward Dimples

The investigations into the instability behaviour of isotropic cylinders with single dents were performed mainly on basis of the cylinder with nominal radius $R = 250$ mm, length $L = 510$ mm, and shell wall thickness $h = 1.5$ mm, and with aluminium as shell material ($E = 70\,000$ MPa, $\nu = 0.3$). This cylinder was then used as *reference* for the analysis of effects due cylinder geometry variations.

Pure Variation of the Initial Dent Depth w_b

Although the initial meridian height l_b and circumferential width a_b of a dimple with a given initial depth w_b also influence the buckling behaviour of the shell, first the impact on the reduction of the axial stability and stiffness are discussed for dents with different initial depth but with given fixed initial width and height.

In the right half of Figure 6.19 the results of nonlinear buckling analyses of this cylinder with a single dent of various depth w_b/h can be seen. The initial width of the dent is always $a_b = 181$ mm, the initial meridian height always $l_b = 67$ mm. These values for a_b and l_b are the result of a search for the lateral dimensions of a dent with $w_b/h = 0.1$ that yielded the minimal buckling load for the reference cylinder on hand, see Section 6.6.3 on page 325 ff.

Figure 6.20 and 6.21 indicate how the points of the curve in Figure 6.19 were accomplished. Each small chart reproduce a result of a nonlinear buckling analysis with adaptive load step control as described in Section 6.5.1. The lower curve in these charts denotes the applied axial load, the upper the buckling loads calculated at selected increments. The left picture in Figure 6.20 refers to an analysis of the reference cylinder with a dent of depth $w_b/h = 0.3$: after circa 80 increments the eigenvalues were zero and the continuously increased axial force attained the nonlinear buckling load. This load $P_{cr} = 330$ kN is identical to the result of a conventional nonlinear buckling analysis for this shell tagged with $P_{cr0.3}$ in Figure 6.10. Together with the result of a nonlinear buckling analysis of this cylinder with perfect geometry $P_{cr id} = 570$ kN a normalized buckling load of $P_{cr}/P_{cr id} = 0.58$ is obtained. This single value is marked with a large circle in Figure 6.20 and 6.21 according to the initial dimple depth $w_b/h = 0.3$. The curve progressions of the loads in the right chart of Figure 6.20, resulting from a modified nonlinear

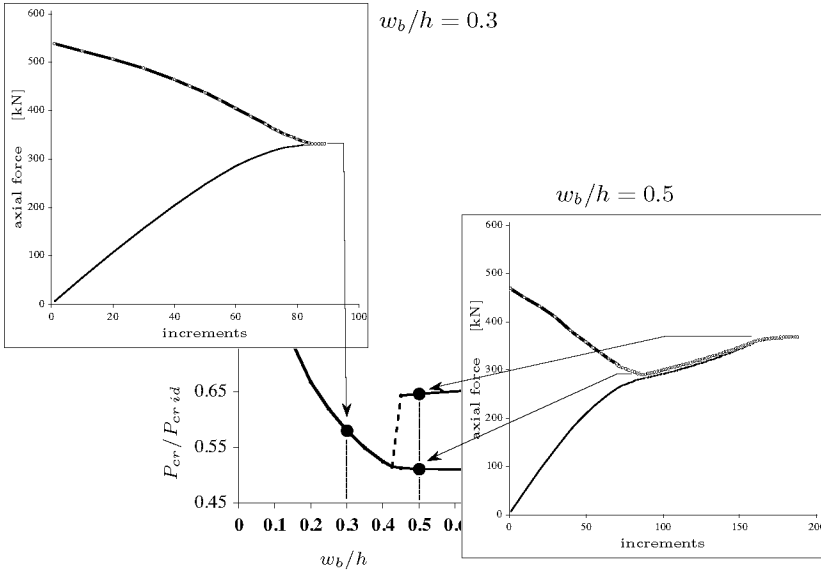


Figure 6.20: Results of nonlinear buckling analyses with adaptive load step control for an isotropic cylinder having an inward dimple of depth $w_b/h = 0.3$ or $w_b/h = 0.5$. The arrows demonstrate the relationship between the calculated buckling loads of such analyses and the corresponding points in the curve indicating the buckling load ratio $P_{cr}/P_{cr, id}$ vs the initial dimple depth w_b .

buckling analysis for a dent with an initial depth $w_b/h = 0.5$, is substantially different to that of the dent with $w_b/h = 0.3$: after 85 increments the upper curve approaches the lower curve but there is no contact. In this case a further increase of the axial load was possible until after additional about 100 increments finally the two curves coincided. Thus, two critical load levels can be recognized: a first lower load at the minimum of the upper buckling load curve with $P_{cr} = 291$ kN, and a second upper load at the intersection point with $P_{cr} = 368$ kN. This characteristic of a nonlinear buckling analysis for this dimple with $w_b/h = 0.5$ was already shown in Figure 6.10 where the lower load is denoted with $P_{cr, 0.5L}$ and the upper with $P_{cr, 0.5U}$. The normalized loads of the former is $P_{cr}/P_{cr, id} = 0.51$ and $P_{cr}/P_{cr, id} = 0.65$ of the latter. According to the initial depth $w_b/h = 0.5$ these two values are each marked with a large circle in Figure 6.20 and also in Figure 6.21.

The five small charts in Figure 6.21 depict the progression of the result-

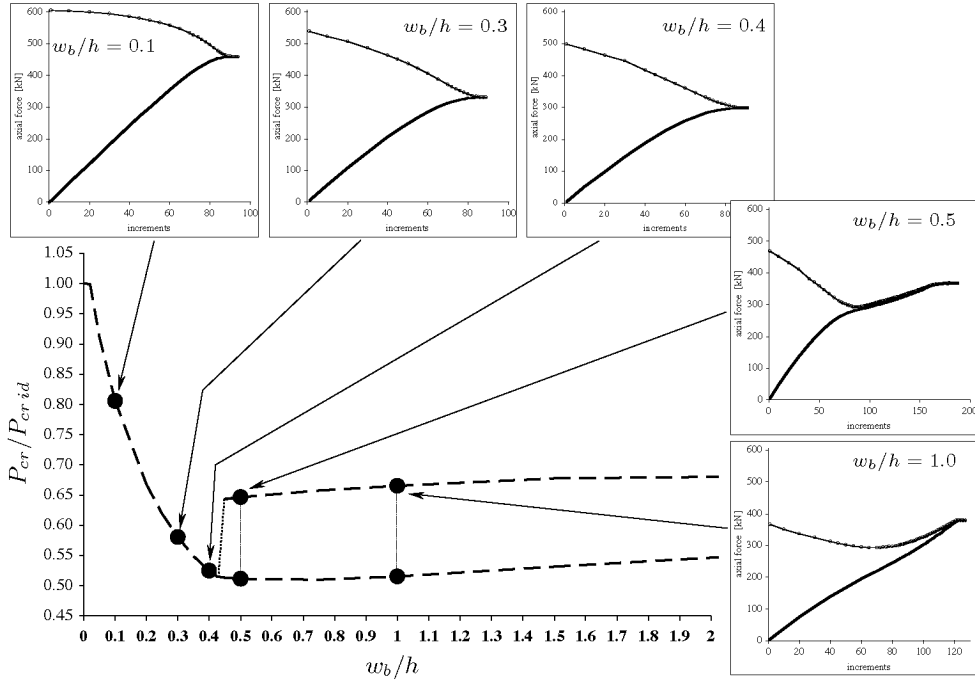


Figure 6.21: Plots indicating the resulting load curves of nonlinear buckling analyses with adaptive load step control and corresponding normalized buckling loads $P_{cr}/P_{cr,ld}$ for dents with selected initial depths w_b/h applied to an isotropic cylinder.

ing buckling load curves for different initial dent depths. The ordinates are each arranged in an axial-force range from 0 to 600 kN. The curves in the first three charts with $w_b/h = 0.1, 0.3,$ and 0.4 differ only in the decreasing first buckling load (first circle close to the ordinate) with increasing initial dimple depth w_b/h as well as in the decrease of the resulting nonlinear buckling load at the contact point of the curve. The lower of the two resulting critical loads of the cylinder with initial depth $w_b/h = 0.5$ and $w_b/h = 1$ are both close to the single nonlinear buckling load of the shell with $w_b/h = 0.4$. But compared with the dimple of initial depth $w_b/h = 0.5$ the specimen with $w_b/h = 1$, pictured in its result chart down right, yield a straighter lower force curve and a minimum point of the also concave upper curve which in this case is notably distant from the lower force curve.

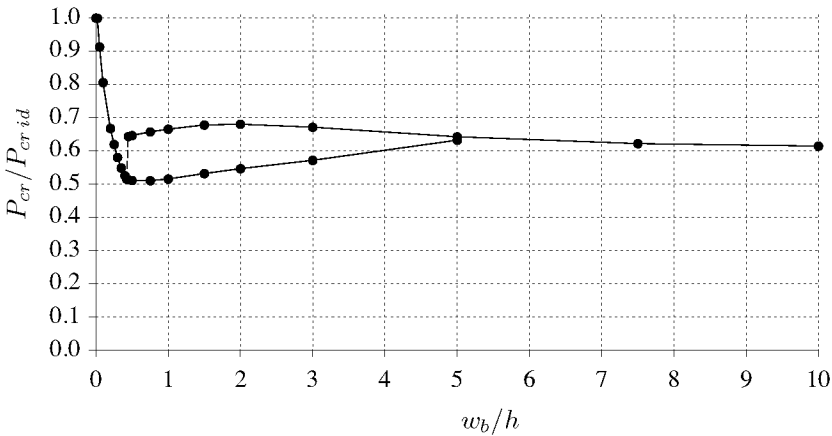


Figure 6.22: Normalized buckling loads of an isotropic cylinder having a deep inward dimple with initial depths up to $w_b/h = 10$. See Figure 6.19 for the range between $w_b/h = 0$ and 1.

From the lower dimple-sensitivity curve in Figure 6.21 at a depth of about $w_b/h = 0.75$ a minimal load-carrying capacity of the cylinder (“worst” dimple depth) of $P_{cr}/P_{cr id} = 0.51$ may be identified. In Figure 6.22 the nonlinear buckling analysis results for the isotropic cylinder having a dent with severe initial depths of up to ten times the shell wall thickness. It can be seen that the lower imperfection-sensitivity curve, corresponding to the lower critical load of the particular analysis result, for dent depths w_b/h more than 0.75 increases with growing dimple amplitude. The upper curve climaxes at $w_b/h = 2$ with a nor-

malized load of $P_{cr}/P_{cr id} = 0.68$. For approximatively $w_b/h = 5$ the two sensitivity curves coincide, indicating that the effect responsible for the branching in two curves vanishes for shells with very deep dents. The

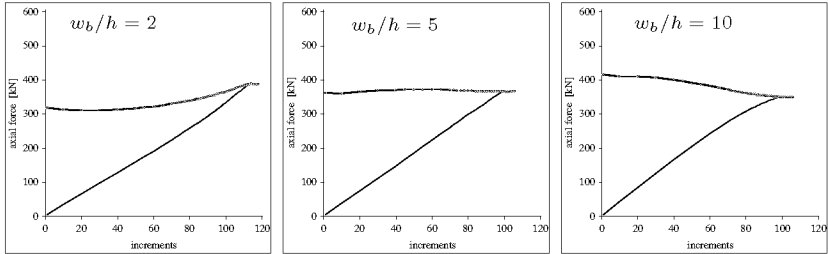


Figure 6.23: *Nonlinear buckling analysis results of the isotropic cylinder in Figure 6.21 having a single dent with an initial depth as indicated.*

curve progressions of the nonlinear buckling analysis results of the shell with $w_b/h = 2, 5,$ and 10 may be found in Figure 6.23. The pattern of the upper load curve in the left graph ($w_b/h = 2$) is similar to that of chart down right in Figure 6.21 ($w_b/h = 1$): the curve is concave and thus a minimum point different to the point where the curve touches the lower applied-force curve may be identified. The analysis of the shell with $w_b/h = 5$ yields a buckling-load curve which is almost horizontal, and the applied-force curve rises relatively straight. The right chart finally with the analysis result for $w_b/h = 10$ features load curves that resembles the curves from initial dent depths of less than $w_b/h = 0.425$ plotted in Figure 6.21.

The analysis of other cylinders with accordingly dimensioned dents yielded similar curve progressions in the resulting representations of the knock-down factor to those depicted in the figures above. The minimal buckling loads $P_{cr}/P_{cr id}$ obtained for the considered cylinders and conditions are analysis results for dents with initial depths less than $w_b/h = 1$. Thus, the buckling analyses for very large dimple amplitudes as shown in Figure 6.22 were limited to the reference cylinder on hand. As already mentioned, mainly the dimple imperfections which reduce the cylinder stability the most were of interest. Therefore, it was found that additional calculations to verify the quality of the nonlinear buckling analysis results of the cylinders with imperfection amplitudes of more than $w_b/h = 2$ are not indicated.

Smaller buckling loads for deeper dimples was expected, but the appear-

ance of a second, higher buckling load for a given initial dimple depth provoked several additional calculations. In Section 6.5.1 it was already mentioned that the first critical load refers to a local instability at the dimple imperfection, whereas the second corresponds to the total collapse of the cylinder. But, the observed differences in the load-curve progressions of the nonlinear buckling analysis results could not give any indication why the dent with $w_b/h = 0.4$ yields a single buckling load, whereas the only slightly deeper dent with $w_b/h = 0.45$ results in two buckling loads for otherwise identical dimple and shell geometry. The analysis results above could lead to the assumption that from a certain initial dent depth, due to deformations and growing curvatures, the load-carrying capacity of the cylinder is increased during loading which makes this “stability reserve” from the first, local buckling load to the upper, over-all collapse load and the typical concave buckling-load curves in the small charts above. According to the transient dynamic analysis results for these dents however, it is more the modified nonlinear buckling analysis method that is either terminated when the applied axial force reaches the lower buckling load or is continued up to the upper collapse load. That is, not the load carrying capacity or axial system stiffness of the cylinder is notably affected due to a little increase of w_b at the branching of the buckling loads in Figure 6.21, but the particular process of the nonlinear buckling analysis!

Figure 6.24 shows the resulting buckling loads P_{cr} of *transient dynamic analyses* again of a single dent applied to the reference cylinder with different initial depths w_b/h in the range from zero to one (see Section 6.5.2). It can be recognized that for initial-dent depths between $w_b/h = 0.2$ and 0.25 a branching in two loads developed: from this particular depth up to that of $w_b/h = 0.4$ in contrast to the static buckling analyses the dynamic analyses yielded two critical loads. In Figure 6.25(a) the provenience of the upper und lower buckling loads is demonstrated by means of the shell with $w_b/h = 0.3$ as an example. The line in the axial load-displacement diagram is almost straight between the origin and a cylinder end-shortening ΔL of about 1.02 mm. Afterwards, for an axial reaction force of $P = 333$ kN a first local maximum with a subsequent decline in force is evident. This force was considered as a lower buckling load and is very close to the single buckling load $P_{cr} = 330$ kN obtained with a nonlinear buckling analysis as reproduced in Figure 6.25(b). In the load-displacement diagram of the dynamic analysis, subsequent to the local climax and the local minimum the curve again increases for an axial compression of about $\Delta L = 0.1$ mm until a second maximum with a reaction force of 374 kN is reached. This load

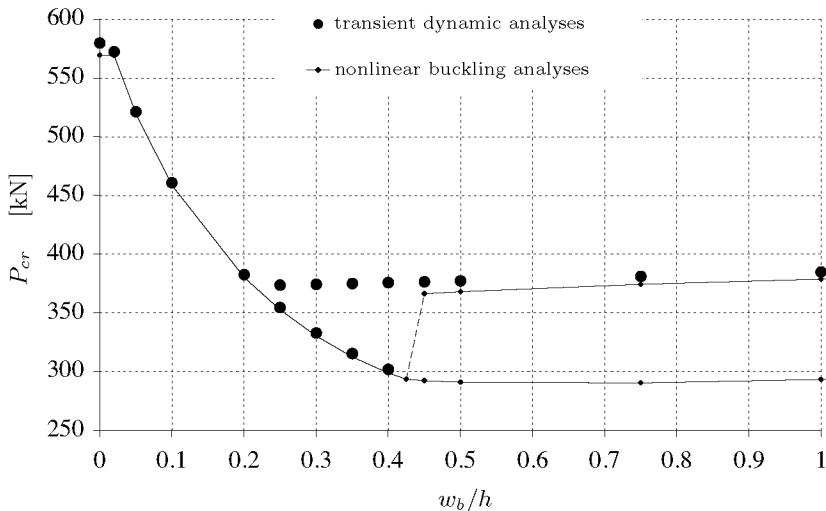


Figure 6.24: *Transient dynamic analysis results of an aluminium cylinder afflicted with a single dent of various initial depth w_b/h . Buckling loads obtained by nonlinear buckling analyses are indicated with thin lines for comparison.*

was denoted as upper buckling load and, according to the deep “plunge” after the second climax, signifies the load where the total collapse of the cylinder occurs. There is no correspondent in the nonlinear buckling analysis result in Figure 6.25(b) for this second, upper buckling load level, because the analysis was aborted after having reached the first, lower buckling load level with the distinct local maximum of the axial load-displacement curve in Figure 6.25(a).

The resulting (first) buckling loads achieved with transient dynamic analyses agree well with the corresponding nonlinear buckling analysis results for dents with initial amplitudes between $w_b/h = 0.02$ and 0.4 , whereas for the buckling load of the cylinder with perfect geometry and the upper collapse loads for dents with $w_b/h > 0.2$ the dynamic analysis, due to inertia forces, yielded somewhat higher loads (differences $< 5\%$). In Figure 6.26 the normalized buckling loads for the reference cylinder with a dent are again plotted versus the initial dent width w_b/h . In this case, due to the slightly higher $P_{cr id}$, the dynamic analyses for the declining, lower line gave somewhat smaller values than the nonlinear buckling analyses, and for the upper buckling load level they led to values that agree well with the values of the static analyses.

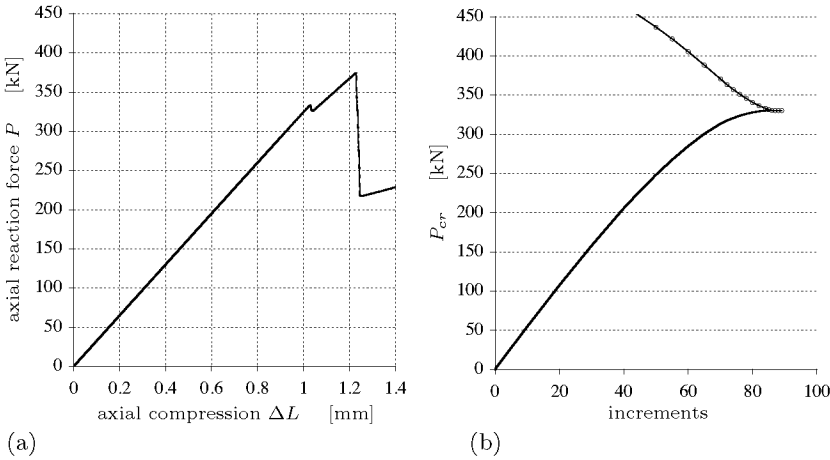


Figure 6.25: *Transient dynamic analysis result (a) of an axially compressed aluminium cylinder having a single dent with an initial depth of $w_b/h = 0.3$, and corresponding result of a nonlinear buckling analysis (b), see Fig. 6.20.*

Analogous to the nonlinear buckling analysis results in Figure 6.21, the plots reproducing the results of transient dynamic analyses are shown in Figure 6.27 exemplarily for five initial dent depths w_b/h and the resulting normalised buckling loads $P_{cr}/P_{cr id}$ are marked accordingly. The diagrams showing the buckling loads against the dimple amplitude in Figure 6.24, 6.26, and 6.27 can be divided into three parts: a first for $0 < w_b/h < 0.2$ with a heavily decreasing curve, a second for $0.2 < w_b/h < 0.4$ with two load levels, and finally a third for $0.4 < w_b/h$ with a single, almost horizontal load line. The first section meaning relatively shallow dents includes dynamic analysis results like that for $w_b/h = 0.1$ in the first chart of Figure 6.27. The progression of the load-displacement curve is analogous to one of a perfect shell being a straight line up to cylinder buckling. The second, probably most interesting section yields load-deformation curves with two distinct maxima like that for $w_b/h = 0.3$ in Figure 6.25(a), or with a saddle point and a climax for $w_b/h = 0.4$ as shown in the third sketch in Figure 6.27.

In both cases, between the origin and the first visible critical load the resulting curves are nearly straight lines. The initial curve gradient (for all shells and dents identical) may be used to define an axial cylinder stiffness or pressure spring stiffness k_s . For the given compression and resulting force values this ratio is about $k_s \approx 324 \text{ kN/mm}$. The curve

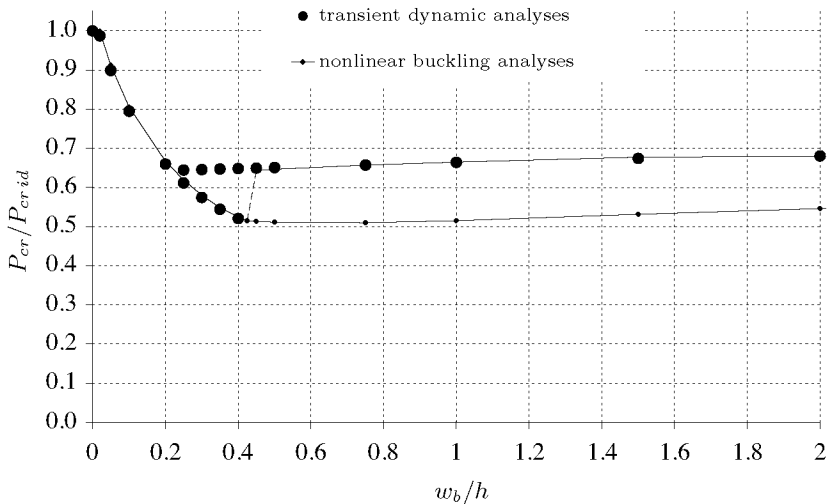


Figure 6.26: *Normalized buckling loads of transient dynamic analyses for an aluminium cylinder with a single dent of various initial depth w_b/h . Corresponding results of nonlinear buckling analyses are indicated with thin lines for comparison.*

following the zig-zag course with the local maximum and minimum obtained for the shell with $w_b/h = 0.3$ again is almost a straight line, but with a reduced gradient and thus smaller spring ratio: $k_s \approx 261$ kN/mm, what means that the axial geometric stiffness of the cylinder after local buckling is almost 20% weaker than the initial one. With increasing initial dimple depth w_b/h the characteristic of the local maximum in the load-displacement curves diminishes and is replaced by a saddle point (e.g. $w_b/h = 0.4$). In the third section of the $P_{cr}/P_{cr id}$ -diagram for $0.4 < w_b/h$ finally, a change of the curve gradient may not accurately be assigned to a value of axial compression. Consequently, the lower critical loads for such dents, ascertained by nonlinear buckling analyses, may not be specified with transient dynamic analyses alone.

In Figure 6.28 the results of a transient dynamic analysis for the same shell as in Figure 6.25 but with the axial compressive force P as loading parameter are depicted. Both the lower local buckling load at about 333 kN and the upper collapse load at circa 374 kN could be attained prior to the abort due to excessive displacements at total cylinder col-

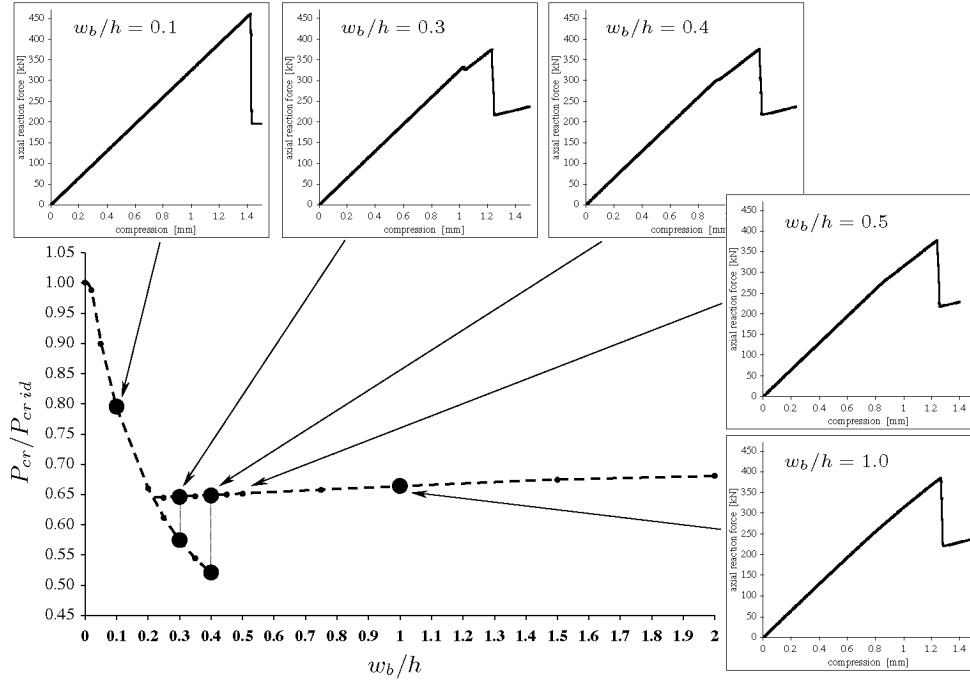


Figure 6.27: Plots indicating the resulting load curves of transient dynamic analyses and corresponding knock-down factors $P_{cr}/P_{cr, id}$ for dents with selected initial depths w_b/h applied to an aluminium cylinder.

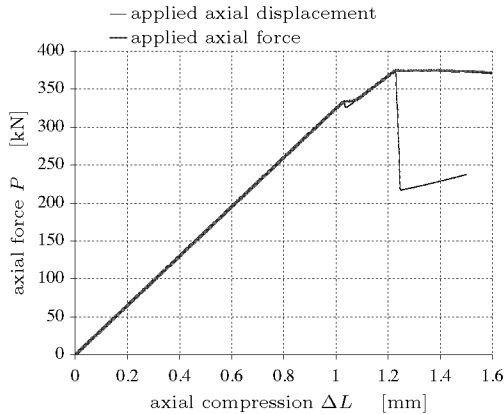


Figure 6.28: *Transient dynamic analysis results for an aluminium cylinder having a single dent with an initial depth of $w_b/h = 0.3$. Comparison between force-controlled (bold line) and displacement-controlled axial compression (thin line).*

lapse. Rigid plane-parallel endplates simulated⁵, after the sudden snapping inwards of the dent further increase of the load was possible since the over-all stability limit of the partially flattened cylinder was not yet reached.

In order to find possible explanations for the observed differences in the curve progressions of the transient dynamic and nonlinear buckling analysis results merely due to the variation of the dent amplitude shown in the charts of Figure 6.27 and 6.21, a few dents were calculated with more elaborateness with regard to the data recording as introduced in Section 6.5.3. For the investigation of the effects responsible for the different buckling behaviour mainly the particular alteration of the local curvatures gave valuable information. In Figure 6.29 the local radii r_k at nodal points along the horizontal path between the dimple apex and the opposite point are shown for the dent with an initial depth of $w_b/h = 0.3$ and an initial width of $a_b = 181$ mm applied to the reference cylinder for four different states of deformation corresponding to the given axial compression ΔL as indicated. The radius of the node at the dent apex may be found along the ordinate. The line — depicts the unloaded state ($\Delta L = 0$) of the hoop over the dimple apex (point A) where the original radius of the dimple apex is $r_A = 250.0 - 0.3 \cdot 1.5 = 249.55$ mm.

⁵Boundary conditions CC4: uniform edge displacements

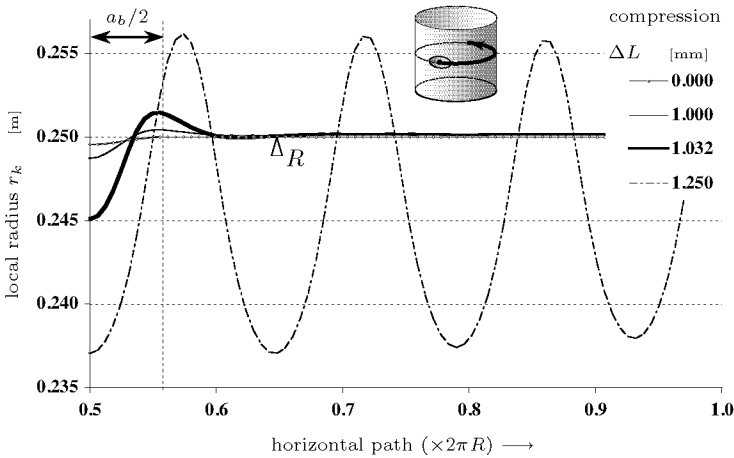


Figure 6.29: Radii r_k at nodal points along a horizontal path (CCW) for half the cylinder circumference starting at the apex of a dent with an initial depth of $w_b = 0.3h$ and an initial width of $a_b = 181$ mm.

With increasing loading the dent continuously deepens, but for a compression less than $\Delta L = 1.0$ mm the reduction of the apex radius r_A is less than 1 mm (thin line). After further loading, close to local buckling with an axial compression of about $\Delta L = 1.03$ mm (thick line, see Figure 6.25(a)), the dent moves quickly a few millimeter inwards. The dash-dotted, “sinusoidal” line finally represents the radii r_k of a configuration after total cylinder collapse for $\Delta L = 1.25$ mm. The continuous denting of the imperfection centre is accompanied by formation of growing lateral bulges at the sides of the initial dent, in Figure 6.29 marked with a vertical dotted line. The amplitudes of outward dimples formed whilst the loading process are smaller than the occurring depths of the buckles. This observation, confirmed by the buckling behaviour of other cylinders, can be explained with the potentially higher imposed circumferential stretching of the shell and thus higher membrane energy for the formation of a large bulge compared with that of a dent with similar dimensions. In the present example, after cylinder buckling (dash-dotted line) the outward deviation from the origin shell radius is about 6 mm, compared with that inwards of more than 15 mm.

Figure 6.30 reproduces the approximated circumferential curvatures $1/\tilde{r}_k$ at the nodes of the horizontal path between the dimple apex and its opposite point in the shell surface again for the dent with $w_b/h = 0.3$ and

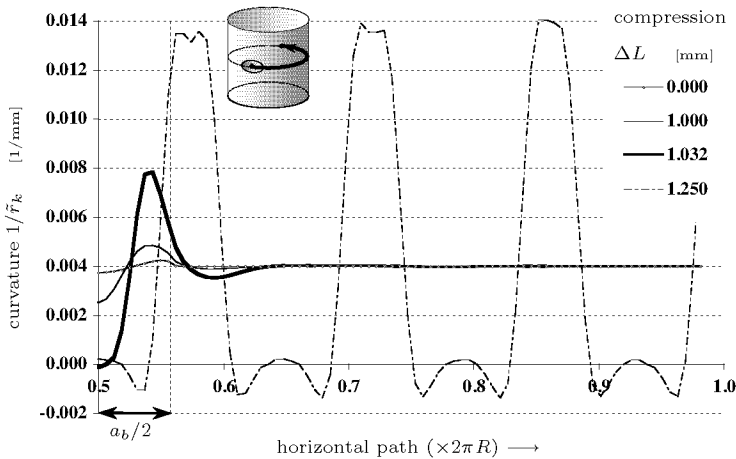


Figure 6.30: *Approximated circumferential curvatures $1/\tilde{r}_k$ at nodal points along a horizontal path for half the cylinder circumference starting at the apex of a dent with an initial depth of $w_b = 0.3h$ and an initial width of $a_b = 181$ mm.*

the four axial-compression levels already used for Figure 6.29. The local curvatures correspond to the particular run of the local radius r_k and were calculated by the procedure described in Section 6.5.3, page 221. The curvature of the unloaded perfect cylinder with a radius R of 250 mm is $1/\tilde{r}_k = 0.004$ $1/\text{mm}$. For comparisons with the radii r_k along the path the curves of the local curvatures $1/\tilde{r}_k$ are plotted with identical line-styles than the r_k -curves in Figure 6.29: the line --- stands for the initial pattern with a dent of $a_b = 181$ mm, the thin line for the shape close to local buckling (axial compression $\Delta L = 1$ mm), and the thick line for deformed shell at local buckling; the dash-dotted line finally corresponds to the state after cylinder buckling with a row of large buckles. The main attention was turned to the thick line which gives the approximated curvatures just at the local buckling with an axial compression of about $\Delta L = 1.03$ mm. The curvature at the dimple apex is about zero, what means that there the additional stiffening effect due to the shell curvature compared with a flat plate vanishes. As a consequence some local buckling occurs with the already mentioned reduction of the axial cylinder stiffness already prior to cylinder collapse. The local curvatures in Figure 6.30 cannot be derived by observing the curve progressions of the local radii in Figure 6.29 since the abscissa of the graph is the path

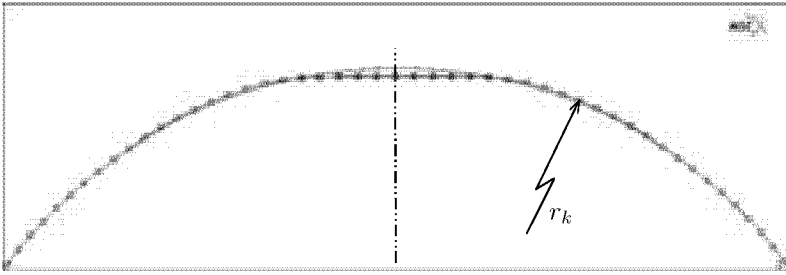


Figure 6.31: Deformed finite element model of the cylinder with the dent of initial depth of $w_b = 0.3h$ resulting for an axial compression of $\Delta L = 1.032$ mm. Displacements plotted without magnification. View from top to the node series of the horizontal path over the dimple apex. Thin line depicts a circle of radius $R = 250$ mm.

around the curved cylinder shell unwound to a straight line, and the amplitudes of the radii are plotted with large magnification. Figure 6.31 depicts a top view on the node series of the shell above for an axial compression of $\Delta L = 1.032$ mm with the dent in the middle. In this case the real spatial position of the element nodes are shown without magnification of the displacements. The radii resulting from these positions for the part at the right side of the dashed symmetry line correspond to the radii along the thick line in Figure 6.29 for the nodes from the dent apex to $0.64 \times 2\pi R$. In fact, at local buckling ($\Delta L = 1.03$ mm) the edges of the first three elements on both side of the symmetry line (dimple apex) are straight horizontal lines and thus there the local curvature is quasi zero. Accordingly, for the first nodes the thick line in Figure 6.30 indicates almost zero curvature $1/\tilde{r}_k$.

To clarify the influence of the local curvature on the local buckling behaviour at the dimple imperfection the continuous alteration of the approximated curvature $1/\tilde{r}_A$ at the dimple apex was plotted in dependence of the axial compression ΔL . In Figure 6.32 such a $1/\tilde{r}_A$ -curve is shown for the shell and the dent presented in Figure 6.30. The thick lines refer to the curvature, the thin line to the axial reaction force of the respective transient dynamic analysis results. Chart 6.32(b) focuses the range of the loading ΔL where local buckling develops. It can be seen that this local maximum of the thin axial-force curve at about $\Delta L = 0.3$ mm is located where after a dynamic fall of the curve standing for the dent apex-curvature reaches zero and travels to negative values. The values of $1/\tilde{r}_A$ close to zero for $\Delta L > 0.35$ mm with the some outliers imposed nu-

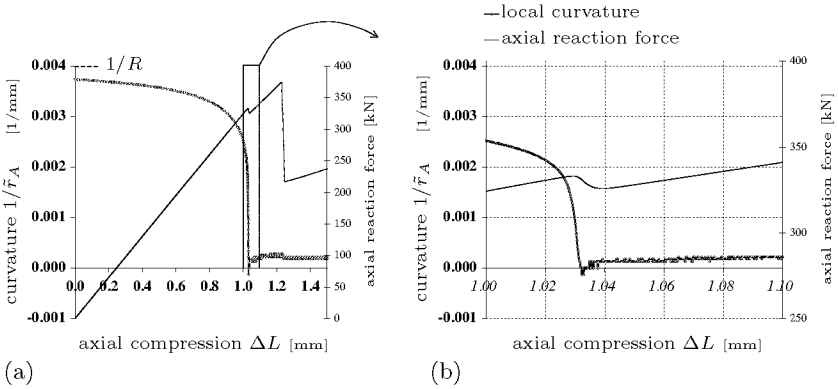


Figure 6.32: Alteration of the approximated curvature $1/\tilde{r}_A$ at the apex of a dent with an initial depth of $w_b/h = 0.3$. Chart (b) points out the framed part in chart (a) including the lower buckling load indicated by the local maximum of the thin axial-force line.

merical difficulties due to possible division by zero during the curvature calculation for quasi infinite local radii of curvature \tilde{r}_A (see page 221). The presented local curvatures are approximated values; thus, the small local curvatures resulting after buckling may be considered as $1/\tilde{r}_A \approx 0$.

Figure 6.33 depicts the curve progressions of the curvature at the apex of five exemplary initial dent depths w_b/h as indicated and presents the associated normalized buckling loads $P_{cr}/P_{cr id}$. The appropriate load curves of the transient dynamic analyses may be found in Figure 6.27. The amplification of the depth of the dent with $w_b/h = 0.1$ in the pre-buckling state is only small, but very close to the cylinder collapse the dimple suddenly increases and deepens so far that at the apex negative curvatures result. The local-curvature curves for the dimples with $w_b/h = 0.3$ and $w_b/h = 0.4$, which exhibit local buckling in a distinct way, have a continuous enlargement of the gradient and a drop to zero in case of $w_b/h = 0.3$ or to a value close to zero in case of $w_b/h = 0.4$ at local buckling. Former dent results in a local buckling that is linked with a local maximum in the load curve, latter in such that is associated with a saddle point in its load curve (see Fig. 6.27). The gradient of the curve resulting for the dent with $w_b/h = 0.5$ increases more harmonically, i.e. with a smoother edge than the three preceding curves; and, instead of following the trend towards zero, the curve gradient suddenly decreases with a small round edge. This edge is found about a value of

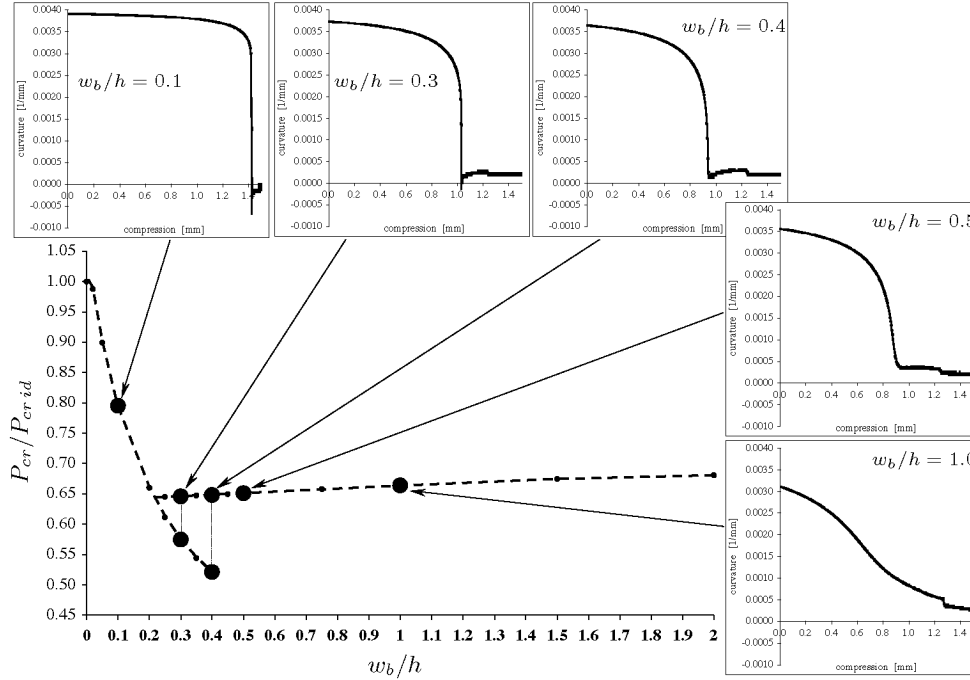


Figure 6.33: Plots reproducing the approximated circumferential curvature $1/\tilde{r}_A$ at the dimple-apex node resulting from transient dynamic analyses for cylinders having a single dent of initial depth w_b/h as indicated.

axial compression where with nonlinear buckling analyses a lower critical buckling compression may be determined ($\Delta L_{cr L} = 0.91$ mm). The curvature curve for $w_b/h = 1$ finally has an increase as well as a decrease in its gradient with a smaller alteration rate compared to the curves of the other shells. In this case, the local buckling compression found with nonlinear buckling analyses at $\Delta L_{cr L} = 0.92$ mm could not be confirmed, since at this critical axial compression no special feature of the curvature curve is identifiable which could be used for the ascertainment of a critical loading.

Although the differences in the alteration of the local curvature between the dimples with $w_b/h = 0.3, 0.4,$ and 0.5 are rather indistinct, the curves in the charts of Figure 6.33 gave indications that the distance covered by the dimple apex between the initial position and the flattened shell configuration is responsible for the obvious differences in the load curves shown in the graphs of Figure 6.27. In the following the influence of the deformation process of the shell around the initial dimple on the buckling behaviour, local or of the entire cylinder, is displayed in more details by means of the three exemplary dents with an initial depth of $w_b/h = 0.1,$ of $w_b/h = 0.3,$ and of $w_b/h = 0.5.$ The presented plots were extracted from results of nonlinear buckling analyses as well as from transient dynamic analyses. To facilitate comparisons, the graphical representations of buckling modes, stress fields, displacements, and curvatures of these three shells were included in succession consistently with identical order, graph styles and perspectives. Some results were already shown earlier in alternative graphs which can be consulted for comparisons. To prevent unnecessary repetitions some explanations on the content of the figures are anticipated.

The first set of charts, [Fig. 6.34](#), [Fig. 6.40](#), and [Fig. 6.49](#), always consists of a plot reproducing the result of a nonlinear buckling analysis with adaptive load step control (a), of a plot showing the deformations of the cylinder for an axial load close to a critical value (c), and of pictures of linear buckling modes for an axial load of $P = 40$ kN in (b) as well as for the axial load level given in (c). The lower curve in the load-diagram (a) again gives the run of the total axial force applied to the cylinder, the upper curve chains the buckling loads derived from the lowest eigenvalues which were calculated at selected axial load levels. The shaded deformation plot (c) depicts the scaled-up nodal displacements which were nonlinearly calculated with constant load steps. The buckling modes shown in plot (b) and (d) correspond to the eigenvectors linked with the lowest linear eigenvalues found at the selected load level.

The items of such eigenvectors represent values of nodal point displacements which have no significance in terms of real shell deformation at buckling; thus, on principle modal deflections may be displayed with any arbitrary magnification factor. To ensure direct comparison, the plots in (b) to (d) do not result from the analysis shown in chart (a) with at each case differently adopted load steps but from standard nonlinear buckling analyses with a constant step size of 4000 kN. The graph (a) was included as an orientation guide concerning the difference between the indicated axial load levels and the critical load(s).

The second illustration set, Fig. 6.35, Fig. 6.41, and Fig. 6.50, at each case includes the membrane stress distribution in axial direction N_{axial} (left, force per unit length) and in circumferential direction N_{hoop} (right) for a selected applied axial load. The contour plots were applied to the appropriate scaled-up deformation plots, the icon with the force-curve progressions are again included to mark the applied load compared to the buckling loads. The membrane forces per unit length equal to the stresses averaged over the shell normal times the shell wall thickness. The cylinder segment opposite to the dimple approximate the shell field of the shell without imperfection and hence the color there corresponds with the nominal membrane force per unit length of $P/(2\pi R)$ with the given, applied total axial load P . Note the variation of the membrane stresses close to the cylinder edges and the presence of considerable compressive hoop stresses resulting from the restraint of the tangential expansion due to the POISSON's ratio effect at the cylinder edges.

The third set, Fig. 6.36, Figs. 6.42, and Fig. 6.51, at each case presents the result of a transient dynamic analysis with the single-step HOUBOLT operator for time integration and input parameters for the aluminium cylinder as given in Section 6.5.2. The included deformation plots depict the resulting shell deflections for the applied axial compression as marked in the P - ΔL -diagram. The displacements are shown *without* magnification and the colors of the applied contour plots refer to absolute values of total-displacement vector lengths (in metres). The top color-map level (light gray) always indicates the maximum total displacement for the corresponding loading.

The fourth representation, Fig. 6.37, Fig. 6.43 and Fig. 6.46, as well as Fig. 6.52 and Fig. 6.55, by means of a lower surface plot always describes the variation of the local radius r_k along the horizontal path (CCW) between the dimple apex and its opposite point successively arranged for a critical section of axial compression ΔL . Each node of the resulting surface mesh reproduces the local radius for a given end-shortening ΔL

and a point in the horizontal path. Curves from the left to the right surface edge correspond to r_k -curves along the horizontal path for given ΔL -values similar to the four curves introduced in Figure 6.29. The curve along the left edge (bottom-up) at $0.5 \times 2\pi R$ is identical with the red line in the upper diagram showing the alteration of the radius at the dimple apex r_A for a section of axial compression ΔL , whereas the blue line equals with the curve along the right edge of the surface plot and represents the alteration of the radius at the point with $1 \times 2\pi R$ thus diagonally opposite to the dimple. The thin line in the upper diagram finally marks the axial reaction forces for the given values of end-shortening ΔL .

The fifth plot, Fig. 6.38, Fig. 6.44 and Fig. 6.47, as well as Fig. 6.53 and Fig. 6.56, at each case displays the progressions of the approximated circumferential curvatures $1/\tilde{r}_k$ along the horizontal path (CCW) between the dimple apex and its diagonally opposite point successively arranged for a critical section of axial compression ΔL , again in form of a surface plot. The settings of the x- and the y-axes as well as the view angle correspond to that of the preceding surface plot which depicts the progressions of the local radii as described above. The line \longleftrightarrow serves to indicate the upper edge of a plane with zero curvature $1/\tilde{r}_k = 0$. The curvature of the perfect cylinder in the unloaded state is $1/\tilde{r}_k = 4 \times 10^{-3} \text{ 1/mm}$.

The sixth and last plot, Fig. 6.39, Fig. 6.45 and Fig. 6.48, as well as Fig. 6.54 and Fig. 6.57, always shows, again by means of a surface plot, the progressions of the local radii r_k of nodal points along the *vertical* path over the dimple apex from one cylinder edge to the other, successively arranged for a critical section of axial compression ΔL . This section includes the same ΔL than the two preceding figures that present the radii and curvature along the horizontal path. The apex of the dimple is located at the middle of the path (long x-axis from left to right); therefore, the run of the curve from the bottom up in the furrow of the surface mesh at $0.5 \times L$ corresponds with the red line in the upper diagram of the always preceding page displaying the alteration of the radius at the dimple apex r_A for a given section of axial compression ΔL .

1. Inward Dimple with Initial Depth $w_b/h = 0.1$:

The nonlinear buckling analysis of the aluminium cylinder having a single, shallow inward dimple with an initial depth of $w_b/h = 0.1$ and initial lateral dimensions $a_b = 181 \text{ mm}$ and $l_b = 67 \text{ mm}$ yielded an axial buck-

ling load of $P_{cr} = 459$ kN. This critical load could be confirmed by a transient dynamic analysis which gave a maximum reaction force of $P_{cr} = 461$ kN for an applied cylinder end-shortening of $\Delta L_{cr} = 1.42$ mm.

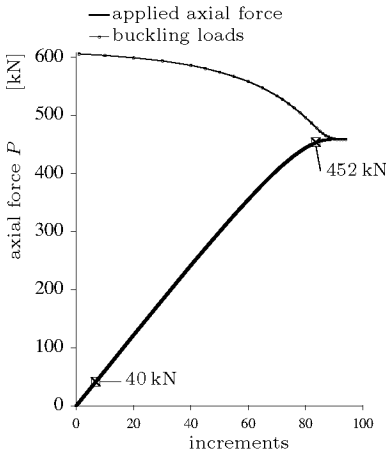
Figure 6.34(b) depicts the buckling mode calculated at an applied axial load of only $P = 40$ kN. Note the visible buckles also at the shell segment diagonally opposite to the dimple imperfection. This buckling pattern resembles the shape which results with a linear buckling load and is also similar to the modes of the cylinder without imperfection. But the buckling mode of the shell with the dent in Figure 6.34(d), resulting for an axial load of $P = 452$ kN just before cylinder collapse has only visible deformations close to the imperfection which build bulges in form of an 'X' with the initial dent in its centre. This pattern can also be recognized in the contour plot for the axial membrane forces per unit length N_{axial} in Figure 6.35 of the shell at hand calculated for an axial load of $P = 400$ kN. This compressive load corresponds to a nominal axial membrane force per unit length of $N_{axial} = -255$ N/mm. Despite the load difference of 52 kN the shape and position of the buckles in 6.34(d) may be derived from the variations of the contour colors, of the axial membrane stresses respectively. The maximal axial compressive force per unit length with $N_{axial} = -263$ N/mm is to be found at the apex of the initial dent. Due to the bulging of the shell around the imperfection developed at that load level, see Figure 6.34(c), left and right of the imperfection the axial membrane force is slightly reduced to $N_{axial} = -250$ N/mm. The distribution of the tangential membrane stress or membrane force per unit length N_{hoop} shown in the right contour plot of Figure 6.35 may be deduced from the bulging and denting of the shell indicated in the deformation plot in Figure 6.34(c): former leads to tensile stresses (white), latter to compressive stresses (red). The nominal tangential membrane force per unit length is $N_{hoop} = 0$ (lime-green).

Figure 6.36 reproduces the result of a transient dynamic analysis. The rising axial-force curve prior to buckling of the cylinder is a straight line. Shortly after collapse a quasi vertical fall of the axial reaction force manifests itself from a critical load of $P_{cr} = 461$ kN down to a first stable post-buckling load level of almost $P = 200$ kN. This curve in the P - ΔL -diagram with a sharp angle at buckling resemble the curve resulting for the Hostaphan cylinder with assumed perfect geometry in Figure 4.19, page 146. The included plots in Figure 6.36 show five selected states of deformation during and after cylinder buckling. The first displays that the depth of the applied dent just before collapse does increase only a little. The following dynamic decrease of the reaction force is associated with a rapid, considerable denting of the imperfection, see Figure 6.37, and a sudden axial widening of the dent, see Figure 6.39. The transaction responsible for the almost vertical force line first consists

of a settlement of new buckles at the left and the right of the deepened imperfection, afterwards on both sides of the initial dent successively further buckles develop in three rows until all the cylinder surface is covered by buckles. The first stable post-buckling state is reached when the rearrangement of the shell into three rows of nine dimples of equal size is accomplished. The step down of the axial reaction force between $\Delta L = 1.5$ and 1.6 mm stems from the rearrangement to the second post-buckling pattern with two rows of larger dimples, whereby the initial dent is squeezed outwards, see fifth plot in Figure 6.36.

The transformation process to the first post-buckling pattern is also displayed in Figure 6.37. The cylinder collapse, i.e. the decline of the force curve (thin line), commences after the accelerated inward displacement of the dent apex, visible by the first elbow along the red line in the upper chart or along the left boundary of the radius surface in the lower plot. The short re-rise of the red line after this plunge refers to an adjustment after an over-shoot inwards of the dimple apex during the local buckling. This sudden local buckling by snapping inwards of the dent initiates the immediately following propagation of new dents and bulges and hence also the total collapse of the cylinder. The snapping of the dimple apex to a position with negative curvature can be recognized by the sharp decline of the respective curvature-curve along the left surface edge in Figure 6.38, or in the first chart of Figure 6.33, page 240. The total cylinder collapse occurs instantaneously after the local buckling.

The successive formation of dimples for increasing cylinder compression around the cylinder (along the path from left to right) is also demonstrated with the transversely arranged lower ends of the valleys in the radius surface. The positions of these ends indicate at what axial compression (left short y-axis) the associated dimples emerge. Towards the end of the transformation the “wave-front” reaches the point across from the apex of the imperfection. Occasionally placed on a bulge, this point moves outwards what is shown with the runs of the right boundary of the radius surface and of the blue line in the graph above. Finally the rearrangement in nine buckles around the cylinder is completed, the radial shell movements almost vanish and hence the local radii as well as the axial reaction force remain quasi constant.



(a) Nonlinear buckling analysis result

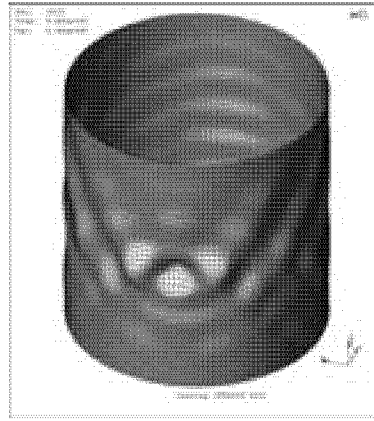
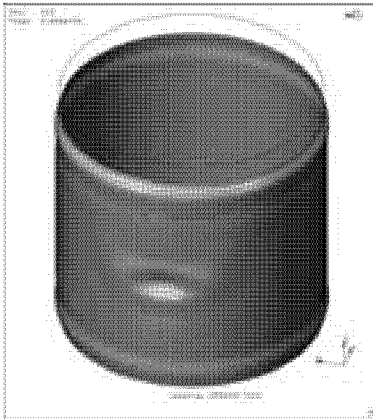
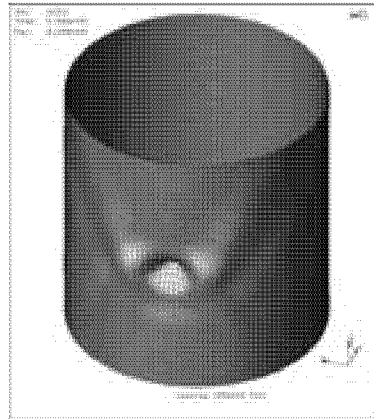
(b) Buckling mode at $P = 40$ kN(c) Displacements at $P = 452$ kN(d) Buckling mode at $P = 452$ kN

Figure 6.34: Results of a nonlinear buckling analysis with adaptive load step control (a) for the cylinder having a dent of initial depth $w_i/h = 0.1$ and selected buckling modes (eigenvectors) calculated for an applied axial load of $P = 40$ kN (b) and $P = 452$ kN (d). Chart (c) displays the scaled-up cylinder deformations which lead to the buckling mode in (d).

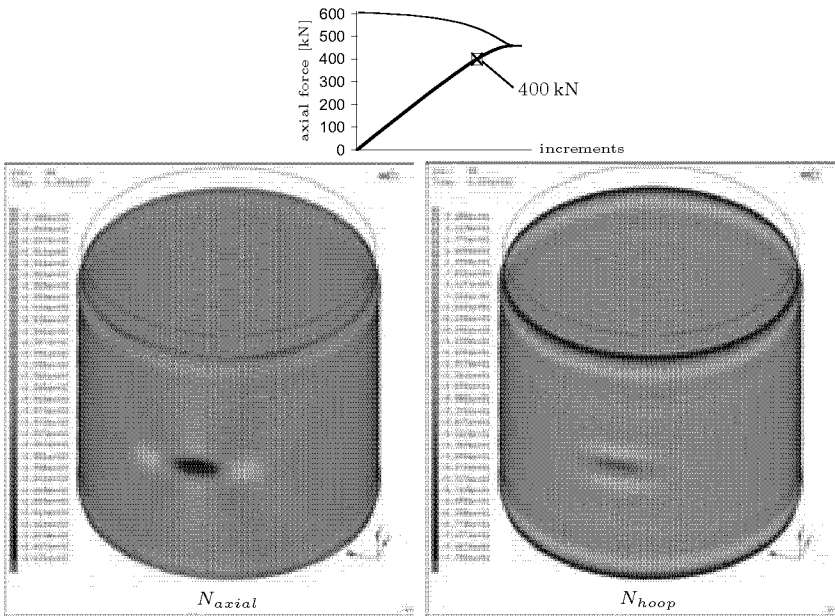


Figure 6.35: Axial membrane forces per unit length N_{axial} and circumferential membrane forces per unit length N_{hoop} of the cylinder with a dent of initial depth $w_0/h = 0.1$ at an applied axial load of 400 kN. Values in color maps are given in N/mm. Result of a nonlinear static analysis.

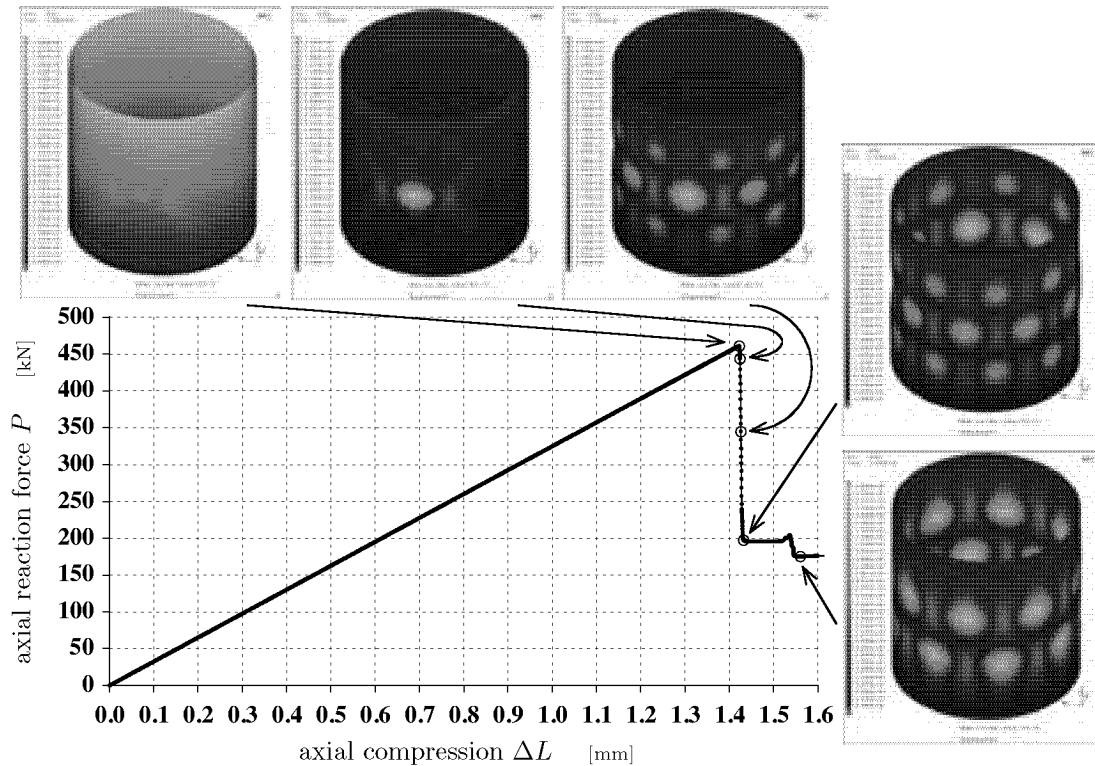


Figure 6.36: Result of a transient dynamic analysis for the isotropic cylinder having an inward dimple of initial depth $w_b/h = 0.1$. The deformations in the pictures are displayed without magnification, the contour color maps refer to total-displacement vector lengths in metres.

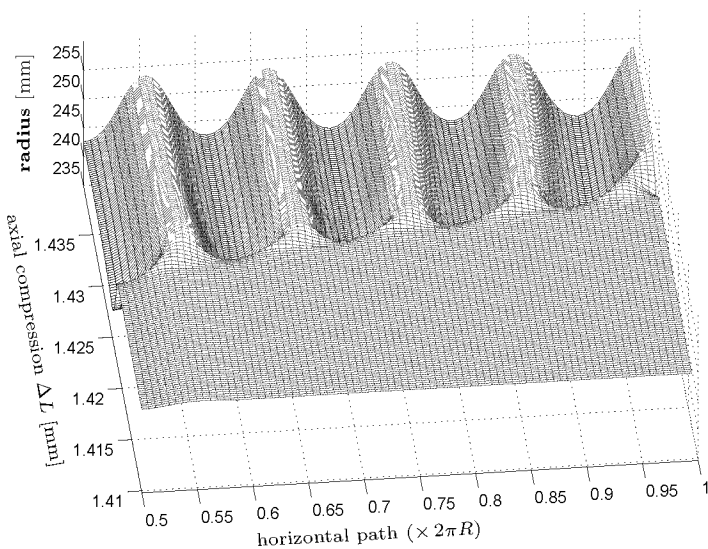
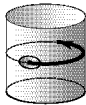
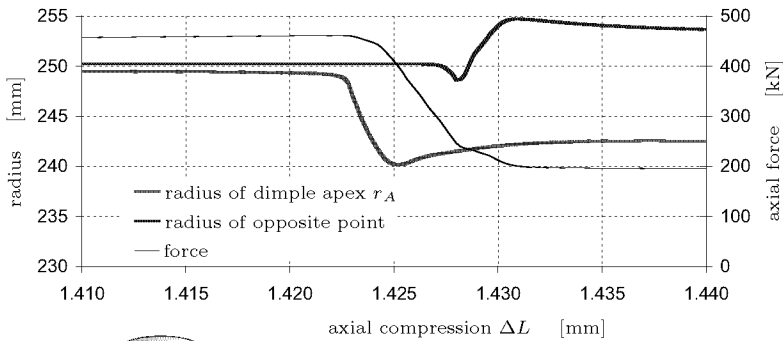


Figure 6.37: *Sequenced progressions of the local radii r_k along the horizontal path between the dimple apex and its opposite point (lower surface plot) for a dent of initial depth $w_b/h = 0.1$. The progression of the left edge of the radius surface matches with the red line, that of the right surface edge with the blue line in the upper diagram. The thin black line follows the axial reaction force.*

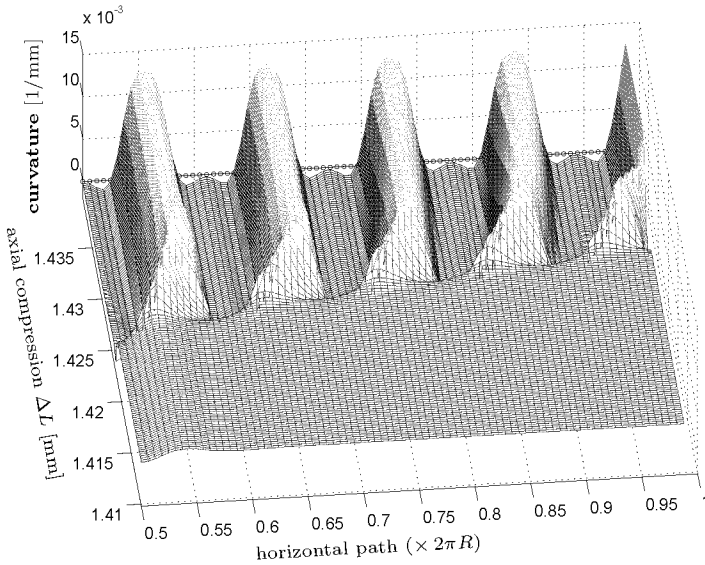


Figure 6.38: *Sequenced progressions of the local curvatures $1/\tilde{r}_k$ along the horizontal path between the dimple apex and its opposite point for a dent of initial depth $w_b/h = 0.1$.*

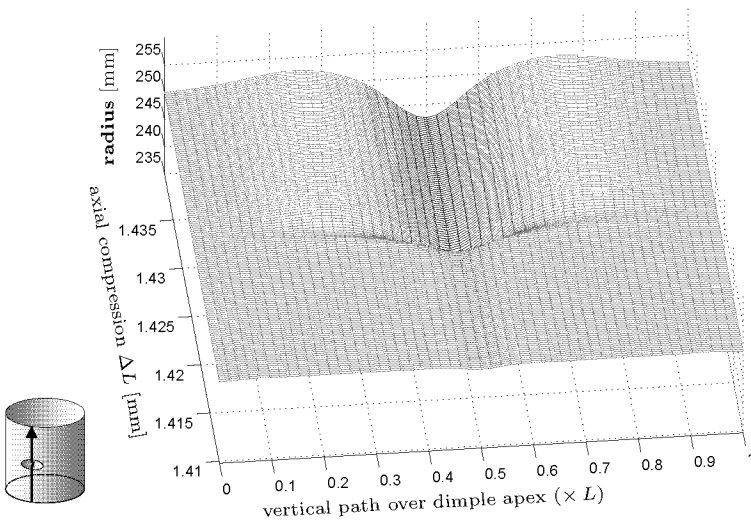


Figure 6.39: *Sequenced progressions of the local radii along the vertical path over the dimple apex at $L/2$ for a dent of initial depth $w_b/h = 0.1$.*

2. Inward Dimple with Initial Depth $w_b/h = 0.3$:

The nonlinear buckling analysis of the aluminium cylinder having an inward dimple with an initial depth of $w_b/h = 0.3$ and initial lateral dimensions $a_b = 181$ mm and $l_b = 67$ mm yielded an axial buckling load of $P_{cr} = 330$ kN, whereas the transient dynamic analysis resulted in a lower critical reaction force, with $P_{crL} = 333$ kN close to the static value above, as well as in an upper, maximum reaction force $P_{crU} = 374$ kN, see also Figure 6.25. These forces correspond to applied compressions of $\Delta L_{crL} = 1.03$ mm for the lower, and $\Delta L_{crU} = 1.23$ mm for the upper load.

Figure 6.40 reproduces the results of nonlinear buckling analyses for the shell at hand. In plot (b) the buckling mode calculated at an axial load of $P = 40$ kN is shown, which has buckles only in the front half of the cylinder shell that contains the initial dent. This shape differs substantially from that in Figure 6.34(b) of the antecedent dent of initial depth $w_b/h = 0.1$ for the identical load that has visible dimples distributed throughout the entire cylinder surface. The dimples of the eigenmode given in plot (d) for an applied load of $P = 328$ kN, hence close to buckling are even more concentrated within the immediate vicinity of the deepened dimple imperfection. This estimated buckling pattern correlates modally with the shape of the dimples formed in the cylinder shell at the load of $P = 328$ kN as presented in the deformation plot (c).

According to the nonlinear buckling analysis with adaptive load step control buckling with accelerated increase of the amplitudes of the imperfection is expected. On the behaviour after this local buckling and hence on the collapse of the cylinder no indication is available. In contrast to the deformations of the cylinder with the dent of initial depth $w_b/h = 0.1$ near its total collapse (see 6.34(c)), the dent with $w_b/h = 0.3$ immediately prior to local buckling results in deformations as displayed in plot 6.40(c) with a deeper indentation of the initial dimple, although with an applied axial force of $P = 328$ kN the cylinder with the initial dent at hand is less loaded than the shallower dent ($P = 452$ kN). Further, the bulging of the shell at hand in (c) around the imperfection is dominated more distinctly by the two outward dimples beside the initial dent than the previous shell with a flattish ring-formed bulge around the dent as indicated in 6.34(c).

Notably wider differences between the shell having a dent with initial depth $w_b/h = 0.1$ and that with $w_b/h = 0.3$ can be seen in the the membrane stress distributions in the cylinder charged with an axial force close to the (local) buckling loads. In the left color contour plot of Figure 6.41 the membrane forces per unit length N_{axial} of the shell at hand, calculated for an axial load of $P = 328$ kN, are displayed. The nominal axial membrane force per unit length of this compressive

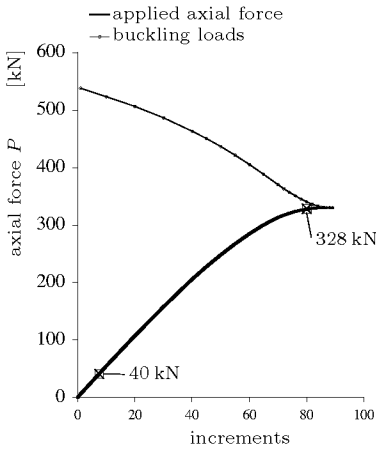
load is $N_{axial} = -209$ N/mm. First, the two dark spots beside the dimple apex strike which refer to maximal compressive membrane forces of about $N_{axial} = -230$ N/mm. Compared to the dent with $w_b/h = 0.1$, depicted in Figure 6.41, the concentration of compressive axial stresses at the apex is split into two peaks at the edge of the dimple. On the two bulges on the left and the right of the dimple the axial compressive membrane force is diminished to a minimum value of about $N_{axial} = -189$ N/mm. Despite the lower applied load the maximum deviations from the nominal value with ± 20 N/mm absolute or ± 10 % relative are about three times higher than the deviations calculated for the dent with $w_b/h = 0.1$ (about ± 3 %). In addition to the spots with extremal values at the dent and the bulges a bright yellow, vertical strip from the bottom-up stands out with weakened axial membrane stresses, flanked by red $\rangle \langle$ -formed shell parts with elevated stresses. The pattern of the contribution of the tangential membrane force per unit length N_{hoop} is similar to that of the shell with $w_b/h = 0.1$, but with the deeper denting the compressive stress concentrated at the dimple apex is considerably higher (max. -95 N/mm). Again, the slight bulging above and below the dent leads to notable tensile tangential stresses. The deviations from zero of the hoop force per unit length N_{hoop} are more than twice higher than those for the dent of initial depth $w_b/h = 0.1$.

The transient dynamic analysis of the cylinder with a dent of initial depth $w_b/h = 0.3$ resulted in a progression of the axial reaction force with a first, lower critical load and a second, higher load of instability, as already mentioned. In Figure 6.42 the results are presented by means of two sub-figures: the first shows the pre-buckling state up to the distinct local maximum in the force curve indicating the first critical load, the second focuses on the subsequent buckling load with total collapse of the cylinder and the first stable post-buckling state. From the first two contour-deformation plots included in Subfigure 6.42 A can be taken that just prior to the first local maximum in the force curve the dimple is indented only for less than 1.5 mm. But this critical load reached, the dent vertex rapidly moves inwards for some seven millimeters until a visible local minimum in the curve is attained, see 3rd and 4th plots. That following, with further end-shortening the continuous deepening of the dimple is decelerated. In Subfigure 6.42 B can be seen that during the continuous compression from the first, local buckling load to the load where the entire cylinder shell starts to buckle the further denting of the initial dimple is marginal. The over-all buckling is initiated by the accelerated formation of two new buckles beside the initial dent and its lateral bulges, see second deformation plot. The that following drop of the axial reaction force with two little cusps (delayed shell motions) is guided by the step-wise formation of new buckles around the cylinder in one row at $L/2$, until the entire cylinder circumference is filled with seven large and deep dimples, see 4th and 5th plot. This is the first

stable post-buckling pattern which differs substantially from that of the previous dent of $w_b/h = 0.1$ in Figure 6.36.

The deformation process of the shell whilst the local and the over-all buckling was also displayed in the plots which demonstrate the alteration of the radius and the curvature at special points or along paths in the cylinder surface with increasing loading. Figure 6.43 reproduces the resulting progressions of the radii r_k at nodal points along the horizontal path from the dent apex half around the cylinder, sequenced bottom-up for increasing end-shortening. Following the alteration left boundary of the radius surface or the red line in the diagram above, i.e. the radius of the dimple apex r_A , it can be seen that the local force maximum (thin line) is situated at a ΔL where the radius of the dimple starts to shrink rapidly. The sudden denting of the imperfection during the local buckling at hand is combined with a widening of the dimple in circumferential as well as in axial direction, see Figure 6.45. The movement inwards of the dimple vertex leads to a local flattening of the shell. This can be recognized at the run of the left boundary of the curvature surface in Figure 6.44 which displays the alteration of the local curvatures $1/\tilde{r}_k$ along the middle hoop for subsequent load levels according to the local radii in Figure 6.43. Compared with the previous shallower dent of $w_b/h = 0.1$ the indentation of the initial dimple during buckling is smaller and less abrupt and no notable “snap-through”, i.e. snapping to negative circumferential curvatures occurs.

In Figures 6.46 to 6.48 the process of continuous formation and propagation of buckles around the cylinder during the buckling of the cylinder after further compression is described. The initial dent only deepens a little after the local buckling and also its height and width only alter marginally.



(a) Nonlinear buckling analysis result

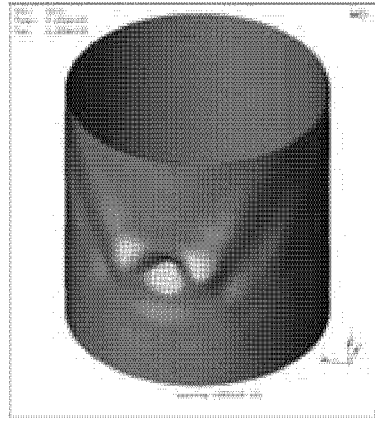
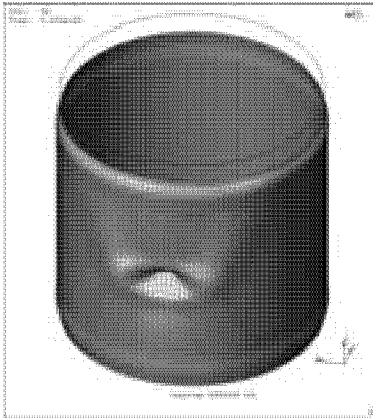
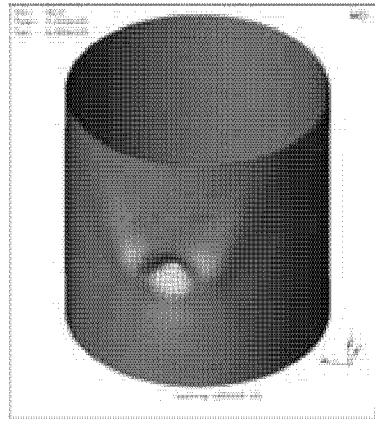
(b) Buckling mode at $P = 40$ kN(c) Displacements at $P = 328$ kN(d) Buckling mode at $P = 328$ kN

Figure 6.40: Results of a nonlinear buckling analysis with adaptive load step control (a) for the cylinder having a dent of initial depth $w_i/h = 0.3$ and selected buckling modes (eigenvectors) calculated for an applied axial load of $P = 40$ kN (b) and $P = 328$ kN (d). Chart (c) displays the scaled-up cylinder deformations which lead to the buckling mode in (d).

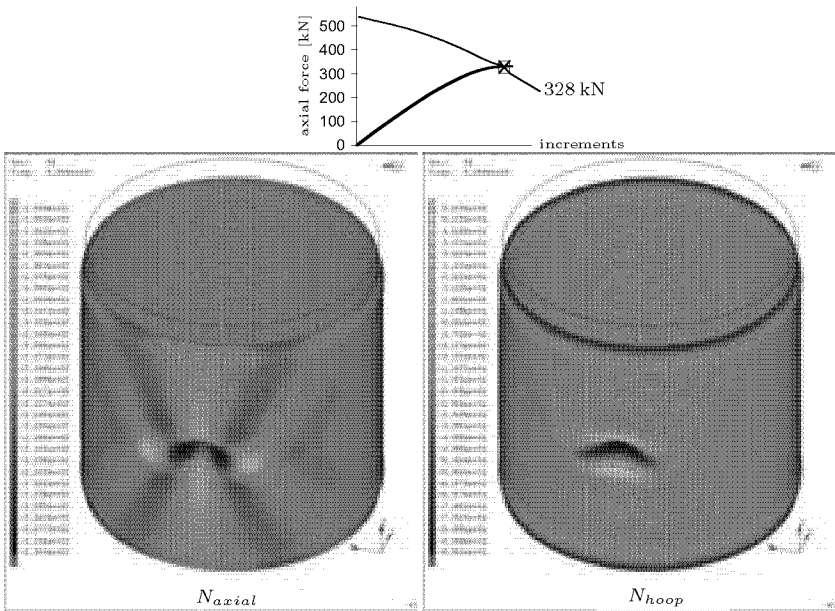


Figure 6.41: Axial membrane force per unit length N_{axial} and circumferential membrane forces per unit length N_{hoop} of the cylinder with a dent of initial depth $w_b/h = 0.3$ at an applied axial load of 328 kN. Values in color maps are given in N/mm. Result of a nonlinear static analysis.

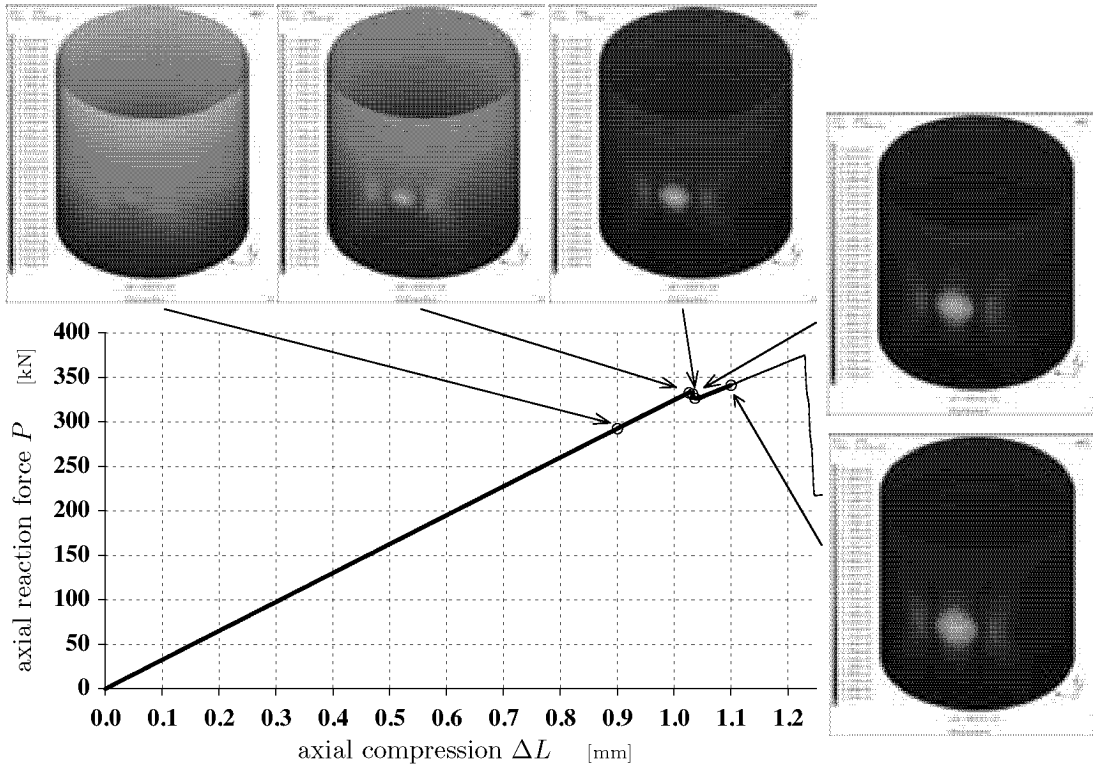


Figure 6.42 A: Result of a transient dynamic analysis for the isotropic cylinder having an inward dimple of initial depth $w_b/h = 0.3$. First part with the local buckling. The deformations are displayed without magnification, the contour color maps refer to total-displacement vector lengths in metres.

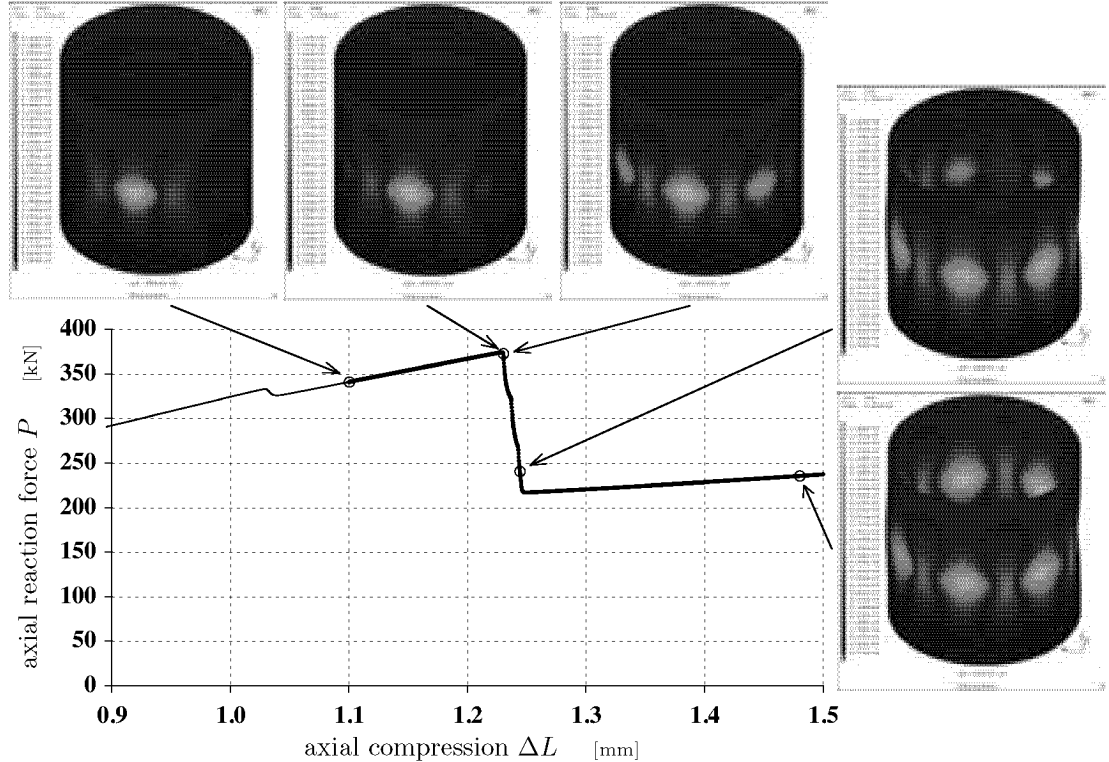


Figure 6.42 B: Continuation to previous figure. Second part with cylinder collapse.

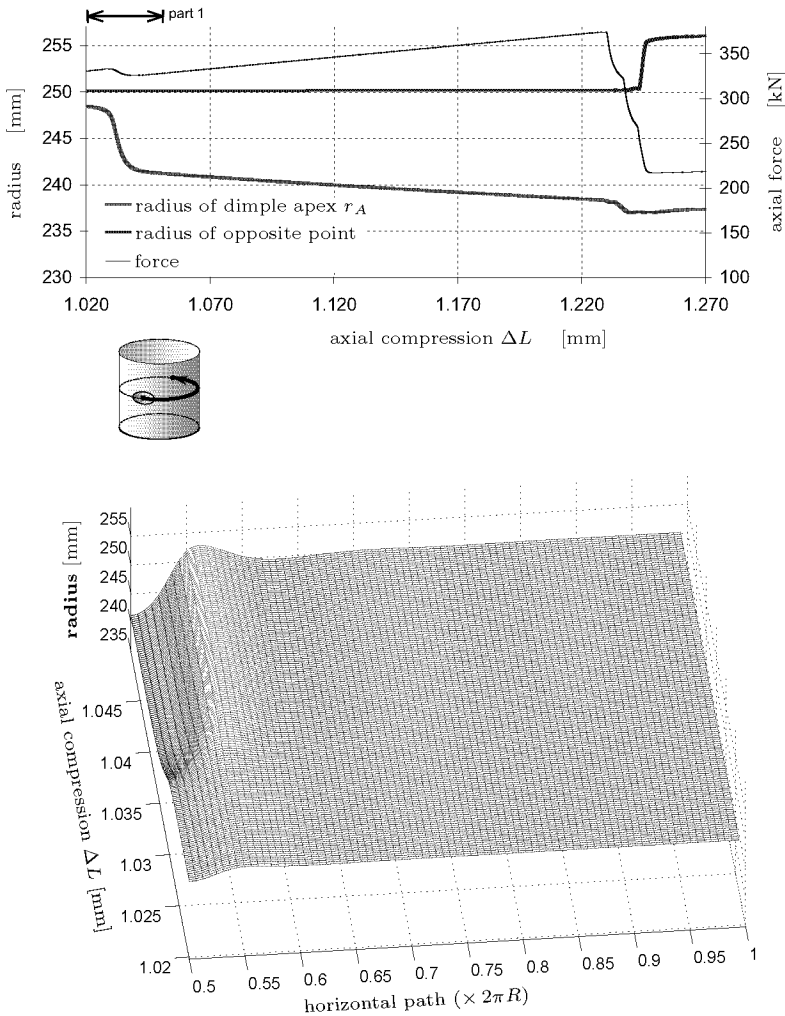


Figure 6.43: *Sequenced progressions of the local radii r_k along the horizontal path between the dimple apex and its opposite point (lower surface plot) for a dent of initial depth $w_b/h = 0.3$. Part 1 as indicated in the upper chart including local buckling. The progression of the left edge of the resulting surface matches with the red line in the upper diagram, that of the right edge with the blue line. The thin black line follows the axial reaction forces.*

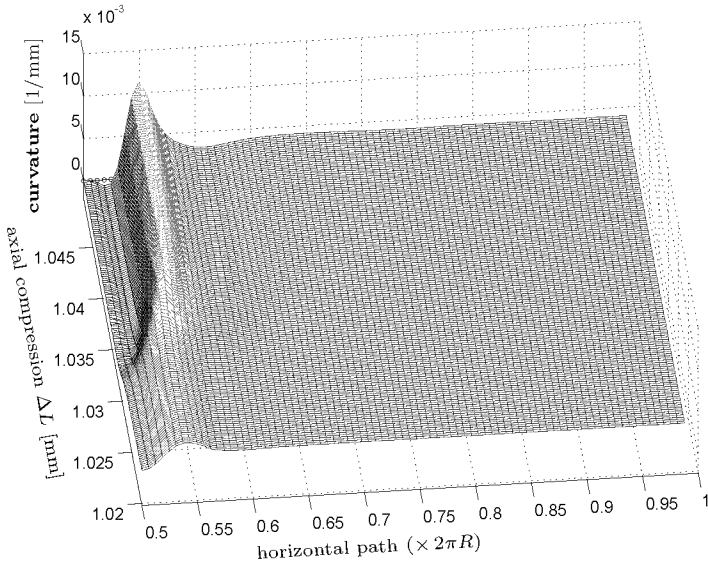


Figure 6.44: Sequenced progressions of the local curvatures $1/\tilde{r}_k$ along the horizontal path as given in Fig. 6.43 for a dent with $w_b/h = 0.3$. 1st part.

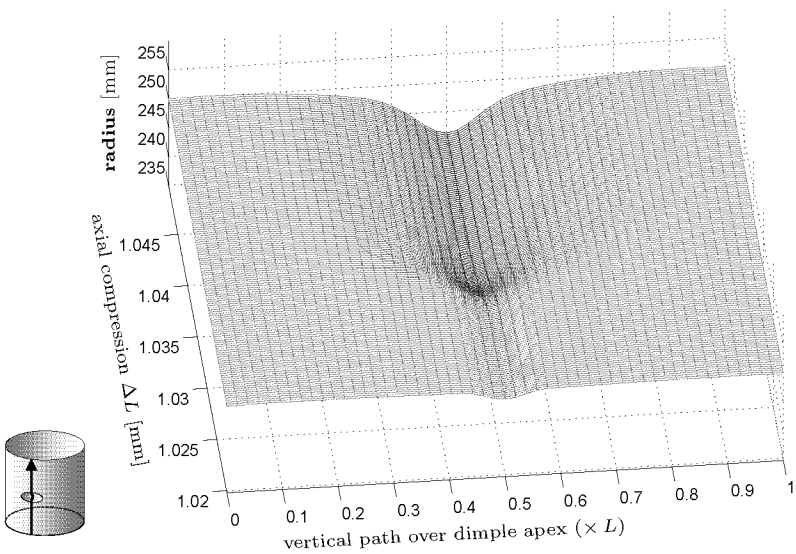


Figure 6.45: Sequenced progressions of the local radii along the vertical path over the dimple apex at $L/2$ for a dent with $w_b/h = 0.3$. 1st part.

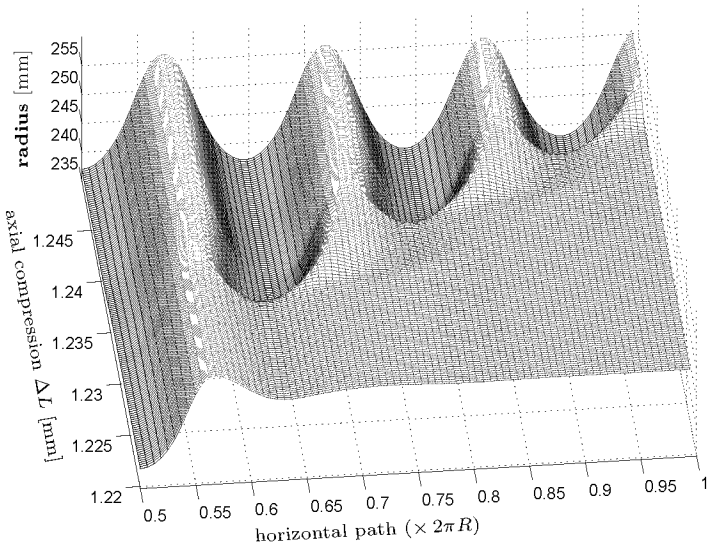
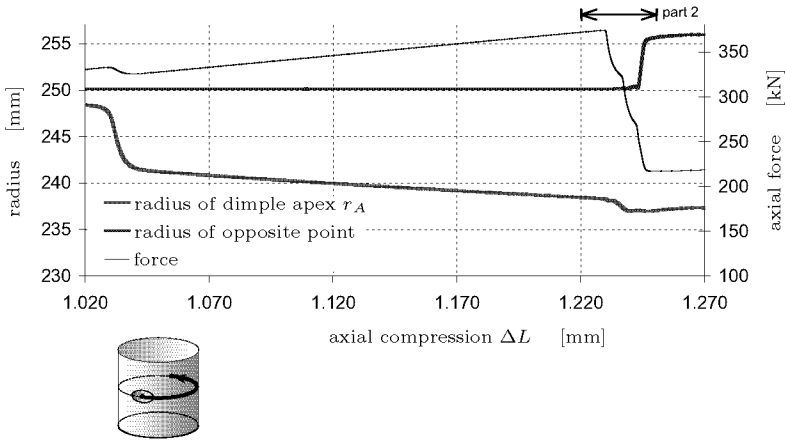


Figure 6.46: *Sequenced progressions of the local radii r_k along the horizontal path between the dimple apex and its opposite point (lower surface plot) for a dent of initial depth $w_b/h = 0.3$. Part 2 including cylinder collapse as indicated in the upper chart (see Fig. 6.43, p. 258).*

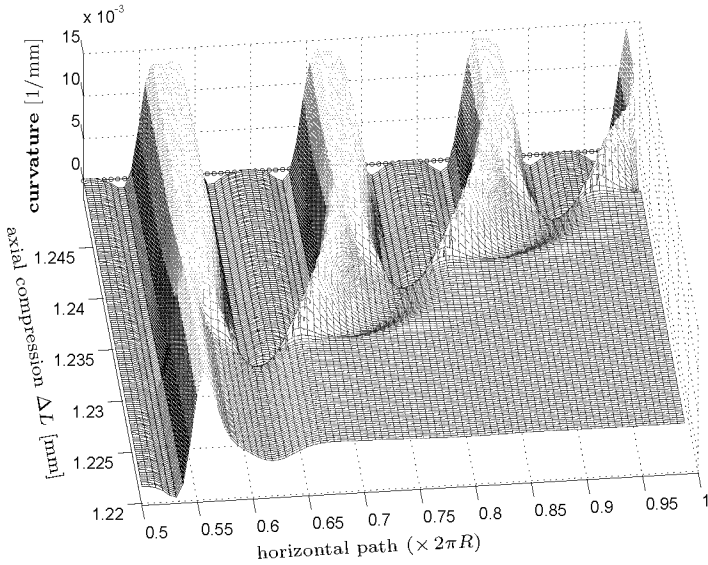


Figure 6.47: *Sequenced progressions of the local curvatures $1/\tilde{r}_k$ along the horizontal path for the dent with $w_b/h = 0.3$. 2nd part, see Fig. 6.44, p. 259.*

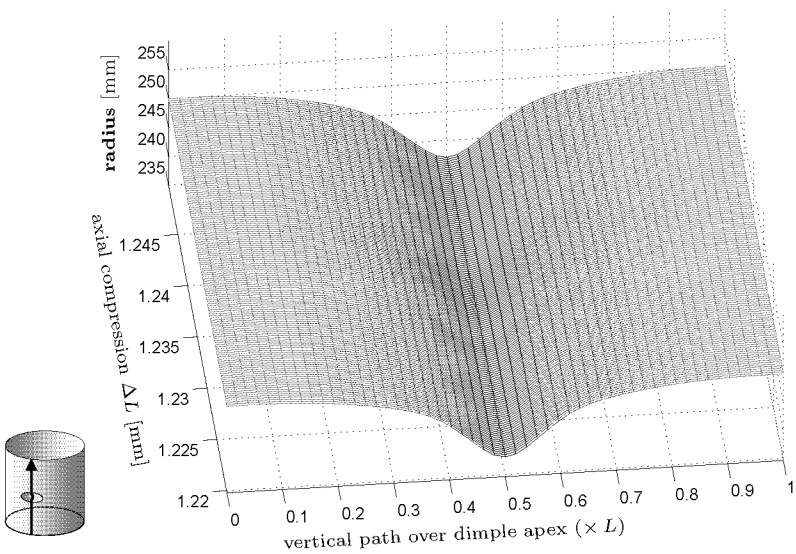


Figure 6.48: *Sequenced progressions of the local radii along the vertical path for the dent with $w_b/h = 0.3$. 2nd part, see Fig. 6.45, p. 259.*

3. Inward Dimple with Initial Depth $w_b/h = 0.5$:

The nonlinear buckling analyses of the aluminium cylinder having an inward dimple with an initial depth of $w_b/h = 0.5$ and initial lateral dimensions $a_b = 181$ mm and $b_b = 67$ mm yielded an axial buckling load of $P_{cr} = 368$ kN (P_{crU}). Additionally, according to a minimum value of buckling loads calculated in between the nonlinear static analysis, a lower critical load of $P_{cr} = 291$ kN could be determined (P_{crL}). The upper load P_{crU} for cylinder collapse could be confirmed with a transient dynamic analysis which yielded a maximum reaction force of $P_{cr} = 377$ kN, whereas for the lower load in the force curve of the dynamic analysis only a slight bend could be attributed to. The lower critical load was found at compressions of about $\Delta L_{crL} \approx 0.9$ mm, and the total cylinder collapse occurs at an end-shortening of $\Delta L_{crU} = 1.24$ mm.

In Figure 6.49 the results of nonlinear buckling analyses for the initial dent at hand are displayed. The buckling mode in plot (b) resulted for an applied compressive load of only $P = 40$ kN has additional dimples only in the vicinity of the original dent, similar to the results for the dent with $w_b/h = 0.3$ and an identical axial force but more pronounced, see Figure 6.40(b), and in contrast to the dent with $w_b = 0.1h$, see Figure 6.34(b). Mainly the buckling mode depicted in plot (d), calculated at an applied axial force of $P = 288$ kN thus close to P_{crL} , attracted attention. This mode does not correspond in position and lateral extents of the dimples to the pattern of the deformed cylinder as shown in plot (c) resulting for this given load level, but includes an inward and an outward dimple at the flanks of the initial dent. The middle node of the sine which these two buckles form is located at the apex of the origin dent. This peculiar eigenmode on hand is a consequence of the membrane forces distribution resulting for this state of deformation at the given axial load of $P = 288$ kN as reproduced in Figure 6.50: both the axial membrane forces per unit length N_{axial} and the hoop membrane forces per unit length N_{hoop} have two separate peaks of compressive load at the flanks of the deepened dent. Simulating the axial compression of longer cylinder with like radius and wall thickness afflicted with deep dents of like lateral extents, in fact such asymmetric local buckling shapes could be observed, see pages 283 ff for a 50 % longer cylinder as an example.

In the left contour-deformation plot of Figure 6.50 the axial membrane forces per unit length N_{axial} are shown which again result for an axial compressive load of $P = 288$ kN. The nominal axial membrane force per unit length corresponding to this load is $N_{axial} = -183$ N/mm. The maximum compressive axial membrane force in the above mentioned dark spots beside the dent is about $N_{axial} = -254$ N/mm. In-between these spots a vertical bright colored strip with diminished axial stresses can be seen with a minimum axial membrane force per unit length of $N_{axial} = -112$ N/mm placed at the dent apex. These extremal devia-

tions from the nominal value of the axial membrane force per unit length with ± 71 N/mm or $\pm 33\%$ are again about three times higher than that of the previously presented dent with $w_b/h = 0.3$ despite the lower applied force. Similar to the two shallower dimple imperfections, further spots with minor axial compressive stresses are to be found on the vertex of the two bulges beside the dent formed during the cylinder loading. Furthermore, again two red $\rangle\langle$ -formed shell parts with elevated stresses can be recognized which flank the bright colored strip of reduced axial stress. The contribution of the hoop membrane force per unit length N_{hoop} shown in the right contour plot of Figure 6.50 with the two separate spots of maximum compressive stress at the dimple flanks (min. $N_{hoop} = -106$ N/mm) differs clearly from that of the two precedent, initially shallower dents with a single peak at the dimple apex. Above and below the dimple hardly visible bulges are formed on which notable tensile hoop stresses emerge (max. $N_{hoop} = 73$ N/mm).

In Figure 6.51 the results of a transient dynamic analysis is shown. Between an applied axial compression of $\Delta L = 0.85$ and 0.9 mm a bend of the reaction-force curve can be seen which indicates some weakening of the axial cylinder stiffness. This loading is near the lower critical end-shortening $\Delta L_{cr L}$ or load $P_{cr L}$ determined by a nonlinear buckling analysis, see Figure 6.49. By means of the dynamic analysis no such exact value of axial force can be specified in this case with a smooth transition from the initial curve gradient to the other. The first and the second contour-deformation plots in Figure 6.51, which depict shell configurations just before and after the visible force-curve bend, differ only marginally, solely an accelerated denting of the dimple can be detected. Afterwards, with continuous axial cylinder compression further shell deformation is again decelerated (see 3rd plot) until up to maximum reaction force close to the cylinder collapse. The over-all buckling (4th to 6th plot) is initiated by the formation of two new buckles beside the bulges which flank the initial dent. During the quasi vertical drop of the axial reaction force then further buckles propagate around the cylinder. The first stable post-buckling pattern finally consists of seven large dimples in one row, alike the cylinder with the dent of initial depth $w_b/h = 0.3$ in Figure 6.42.

The absence of a really striking change of the shell configuration at the load level where the axial stiffness decreases is also demonstrated with the sequenced curve progressions of Figures 6.52 to 6.54. From the red line in the upper chart of Figure 6.52 can be taken that the weakening of the cylinder resistance is accompanied merely by a slight short-term acceleration of the continuous dent deepening. That is, being already relatively deep prior to loading, the dent whilst axial compression is deformed in a way that it approaches a shape of a flattened dimple more gently than the precedent shells. In Figure 6.53 the vanishing

curvatures in the dent centre manifest the slow flattening of the shell.

For the sake of completeness, in Figure 6.55 to 6.57 also the alteration of the subsequent deformation states including those for the total collapse is reproduced. The shape of the widened and deepened initial dimple alters only a little during the total collapse of the cylinder. Again similar to the other shells in succession continuously new buckles are formed which settle beside the already existing dimples.

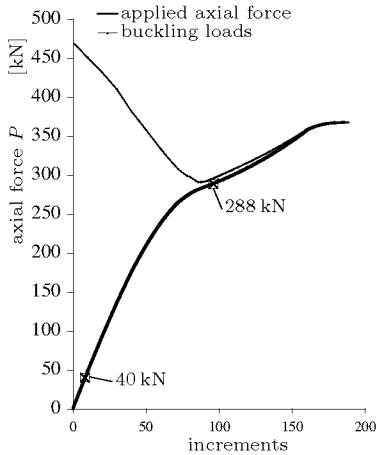
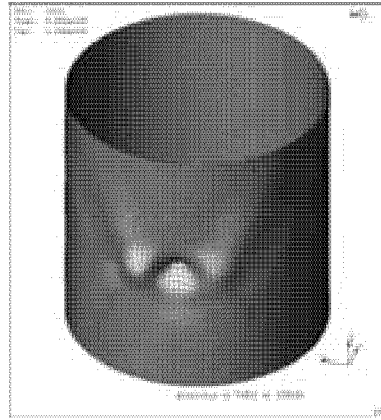
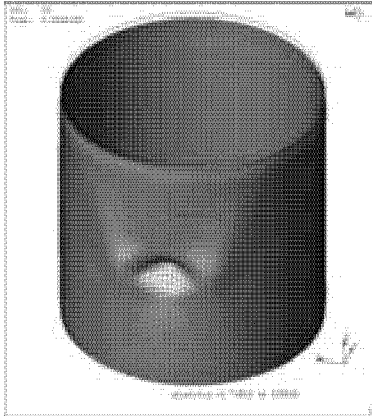
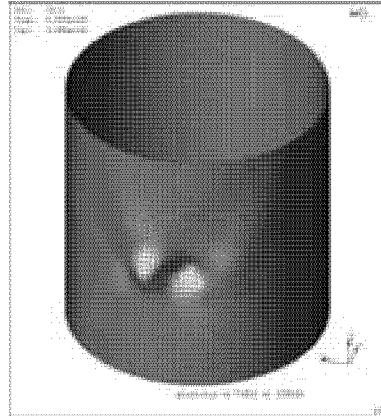
(a) *Nonlinear buckling analysis result*(b) *Buckling mode at $P = 40$ kN*(c) *Displacements at $P = 288$ kN*(d) *Buckling mode at $P = 288$ kN*

Figure 6.49: Results of a nonlinear buckling analysis with adaptive load step control (a) for the cylinder having a dent of initial depth $w_b/h = 0.5$ and selected buckling modes (eigenvectors) calculated for an applied axial load of $P = 40$ kN (b) and $P = 288$ kN (d). Chart (c) displays the scaled-up cylinder deformations which lead to the buckling mode in (d).

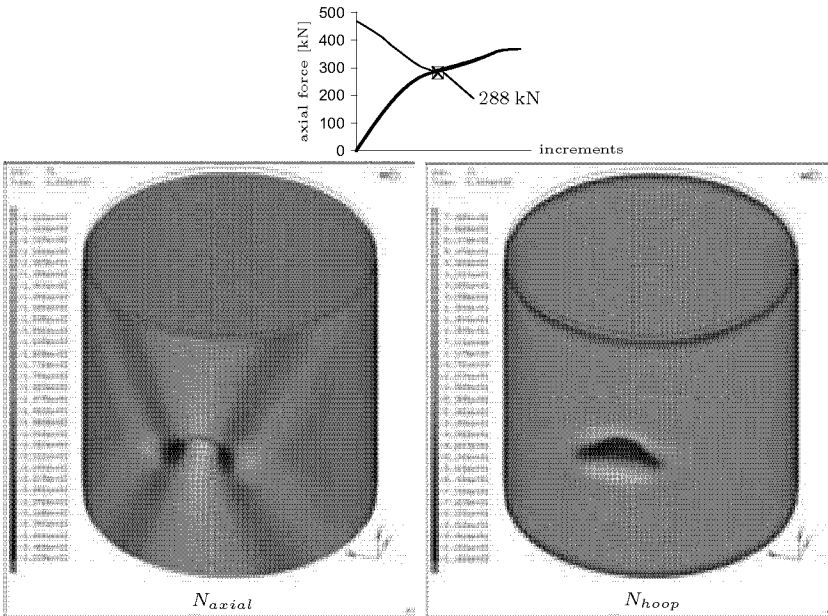


Figure 6.50: Axial membrane forces per unit length N_{axial} and circumferential membrane force per unit length N_{hoop} of the cylinder with a dent of initial depth $w_b = h/2$ at an applied axial load of 288 kN. Values in color maps are given in N/mm. Result of a nonlinear static analysis.

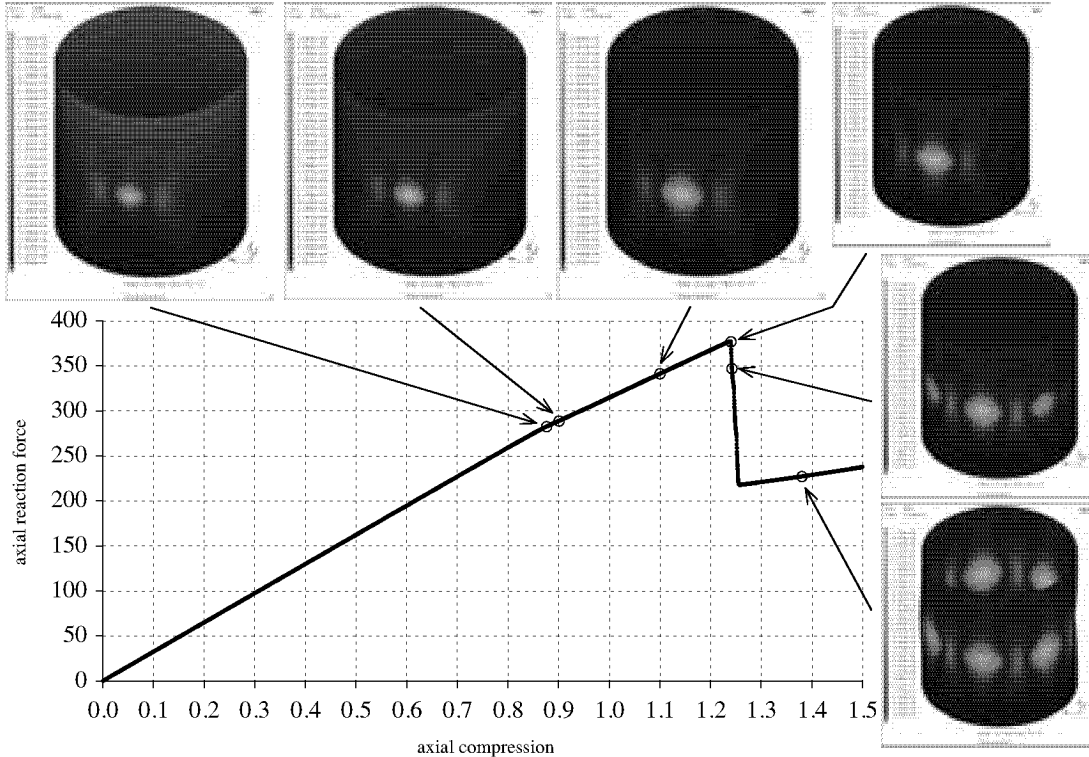


Figure 6.51: Result of a transient dynamic analysis for the isotropic cylinder having an inward dimple of initial depth $w_b/h = 0.5$. The deformations in the pictures are displayed without magnification, the contour color maps refer to total-displacement vector lengths in metres.

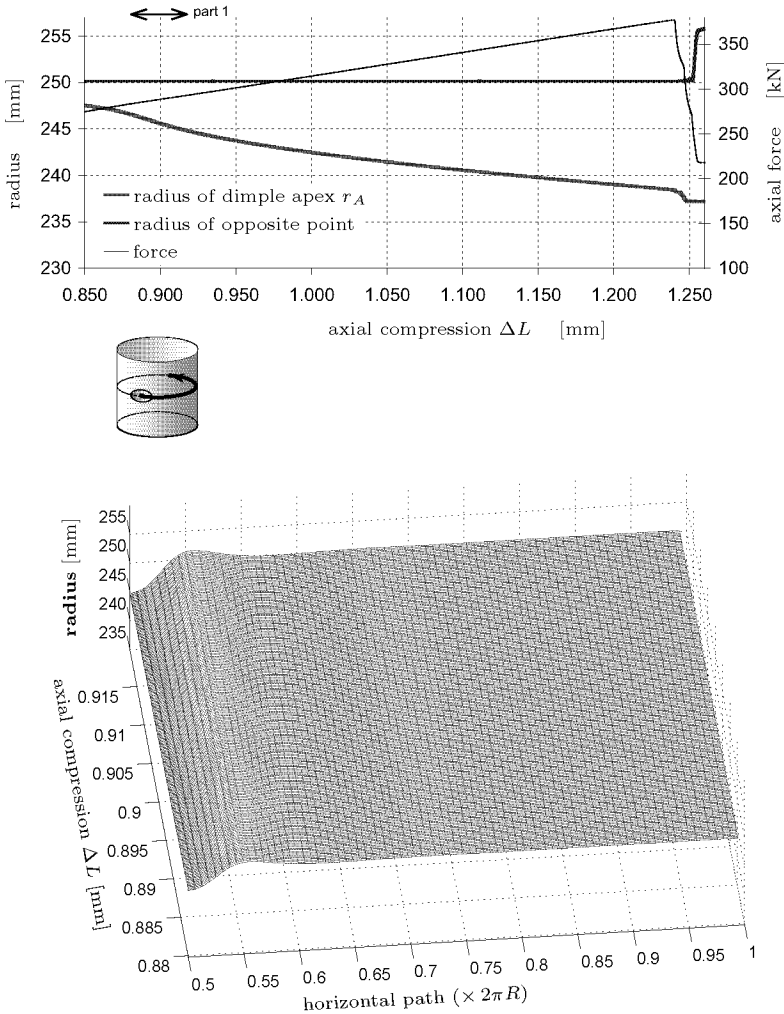


Figure 6.52: Sequenced progressions of the local radii r_k along the horizontal path between the dimple apex and its opposite point (lower surface plot) for a dent of initial depth $w_b/h = 0.5$. 1st part including local instability at about $\Delta L = 0.9$ mm. The progression of the left edge of the resulting surface matches with the red line in the upper diagram, that of the right edge with the blue line. The thin black line follows the axial reaction forces.

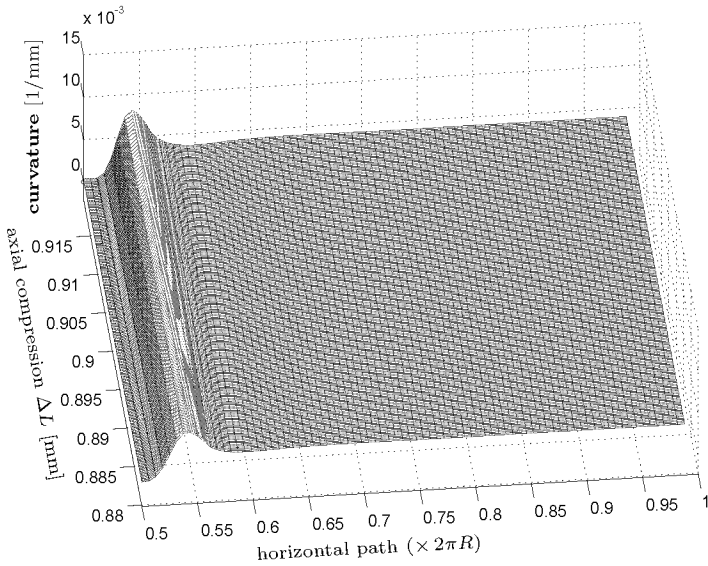


Figure 6.53: *Sequenced progressions of the local curvatures $1/\tilde{r}_k$ along the horizontal path as given in Fig. 6.52 for a dent with $w_b/h = 0.5$. 1st part.*

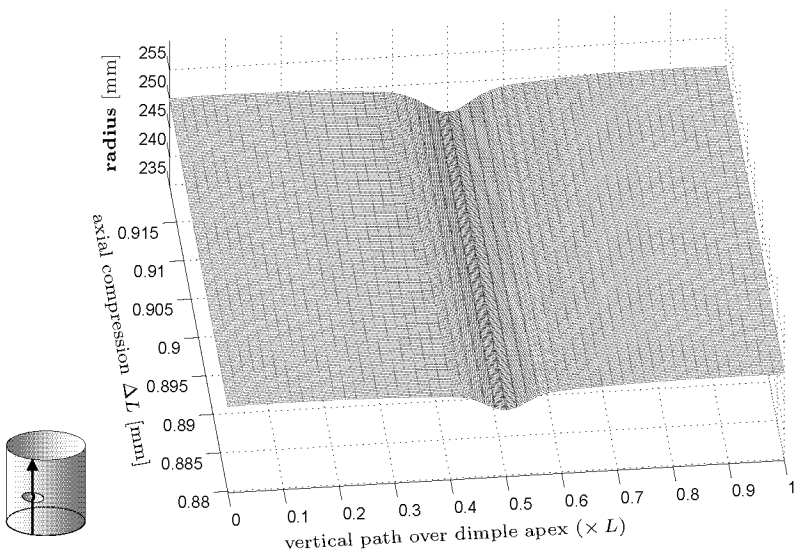


Figure 6.54: *Sequenced progressions of the local radii along the vertical path over the dimple apex at $L/2$ for a dent with $w_b/h = 0.5$. 1st part.*

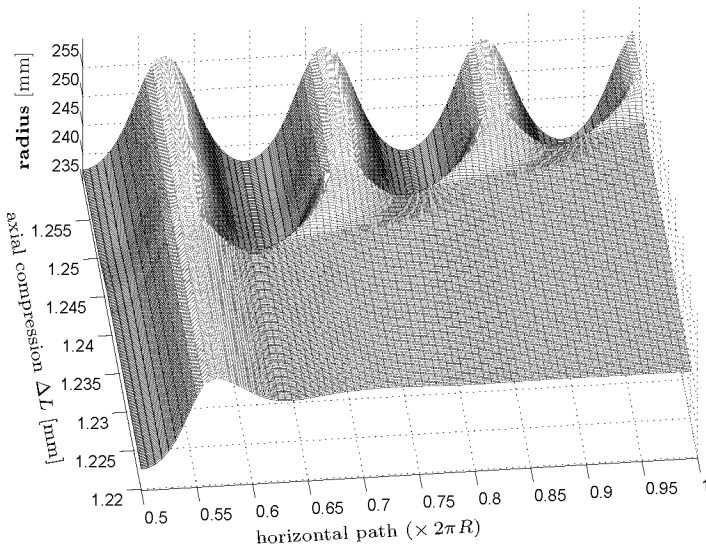
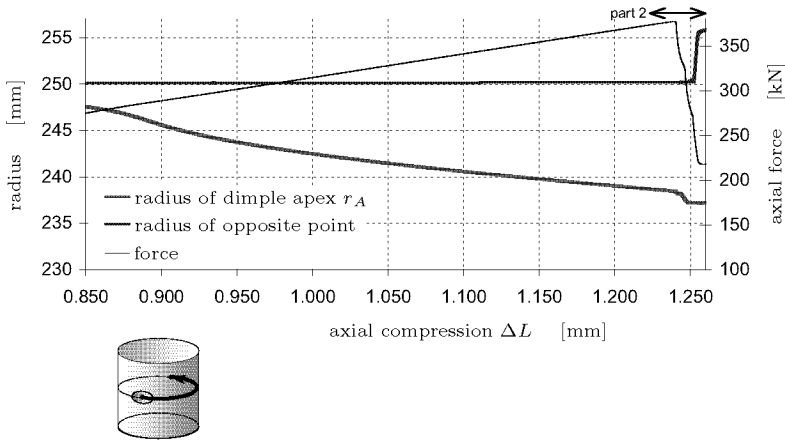


Figure 6.55: *Sequenced progressions of the local radii r_k along the horizontal path between the dimple apex and its opposite point (lower surface plot) for a dent of initial depth $w_b/h = 0.5$. Part 2 including cylinder collapse as indicated in the upper chart (see Fig. 6.52, p. 268).*

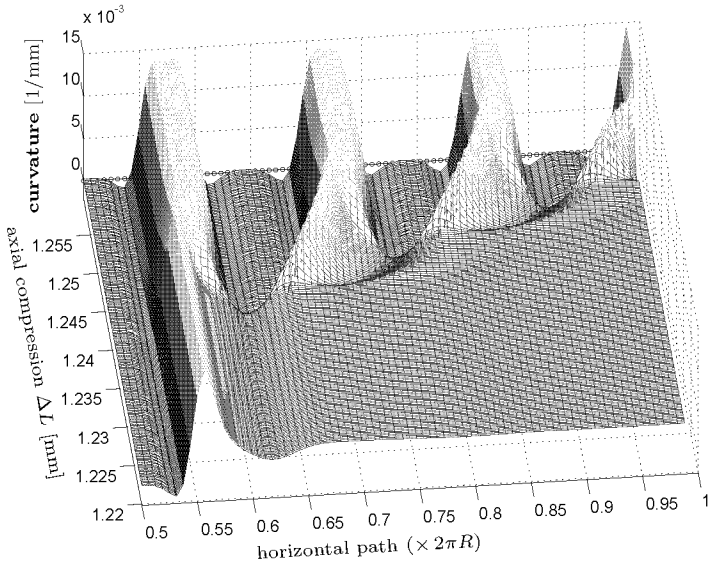


Figure 6.56: *Sequenced progressions of the local curvatures $1/\tilde{r}_k$ along the horizontal path for the dent with $w_b/h = 0.5$. 2nd part, see Fig. 6.53, p. 269.*

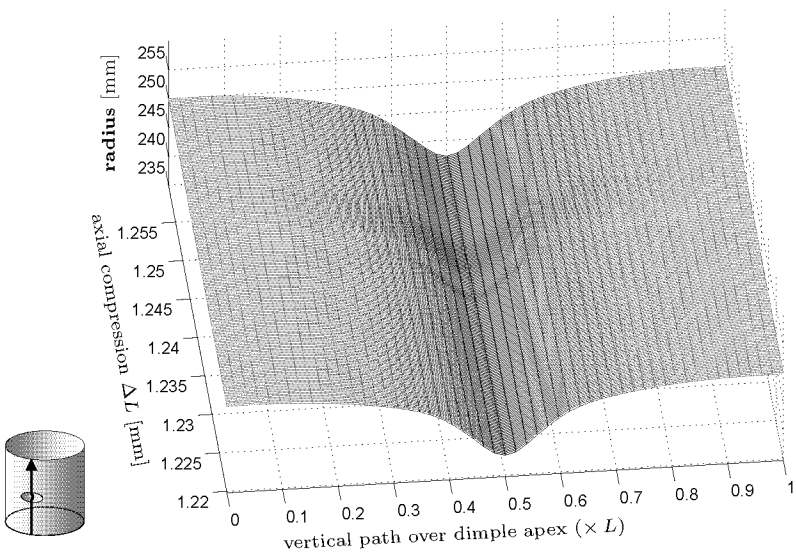


Figure 6.57: *Sequenced progressions of the local radii along the vertical path for the dent with $w_b/h = 0.5$. 2nd part, see Fig. 6.54, p. 269.*

The runs of the forces, local radii, and local circumferential curvatures presented in the figures above served to find an explanation for the different load-displacement curves. Whilst axial loading the cylinders having an initial inward dimple are continuously deformed in a way that the depth as well as lateral size of the dimple are increased. This deformation process with a deepening of the dent centre and some bulging at the dent edges leads to a shape of a dimple with considerably smaller circumferential curvature than the unloaded ideal cylinder. Therefore, the so developed partially flattened shell strip loses in geometric stiffness and thus also the axial cylinder (spring) stiffness decreases. The contour plots for the axial membrane-stress distributions indicate that due to the initial dent and the successively resulting deformations always a stress rearrangement proceeds in a way that the shell above and below the initial dimple is relieved, whereas the shell segments sideways of the dimple have to sustain growing additional loading. The more or less deepened and widened dimple with further compression leads to an axial-stress relief in the dimple and a rearrangement of the stress towards the lateral bulges, where in turn the curvature and hence the geometric stiffness is increased due to the bulging. Rigid end plates provided⁶, additional axial loading can be applied to the partially flattened cylinder. The over-all collapse of the cylinder then occurs when the stability limit of the shell with the new configuration is reached.

The type of nonlinearity of the state prior to the cylinder collapse depends on the distance between the initial amplitude w_b of the dent and the depth of the deflected dimple which forms a flattened strip. The depth of the dimple without circumferential curvature is about 8 mm. That is, for a deep dent of initial depth $w_b/h = 5$ almost no movement of the dimple apex is necessary to flatten the cylinder partially.

In Figure 6.58 above-presented diagrams including the alterations of (a) the axial reaction force P , of (b) the radius r_A and (c) the circumferential curvature \tilde{r}_A at the dimple centre of the three dents with initial depths $w_b/h = 0.1$, $w_b/h = 0.3$, and $w_b/h = 0.5$ were put on top of each other to enable quantitative comparisons. The dent with an initial depth of $w_b/h = 0.1$ (blue lines) applied to the aluminium cylinder is relatively shallow. Hence, similar to a perfect cylinder prior to instability the loading of the shell is dominated by membrane stress. During compression, in this state the dimple is deepened only marginally and also the local membrane stresses deviate only a little from the nominal values. Consequently, for small axial loads the buckling mode consists

⁶Boundary conditions CC4 or SS4

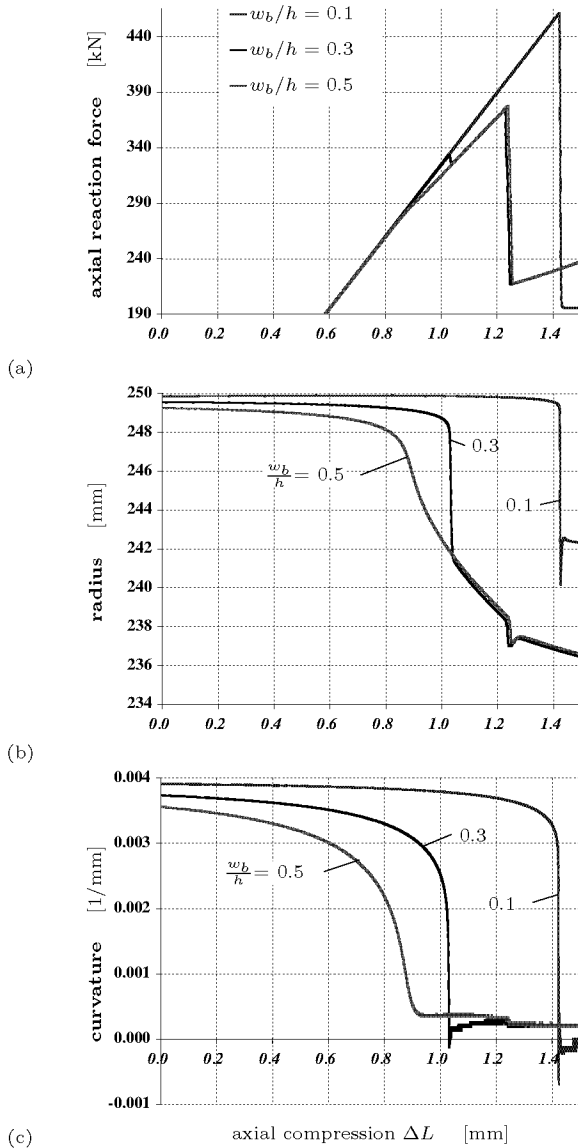


Figure 6.58: Comparisons of the alteration of (a) the axial reaction force P , (b) of the radius of the dimple apex r_A , and (c) of the approximated curvature at the dimple apex $1/\bar{r}_A$ for the cylinder having one of the three selected dents of initial depth as indicated. Results of transient dynamic analyses.

of buckles distributed over the entire cylinder surface. Close to collapse then the denting of the dimple is accelerated and suddenly the dent apex quickly moves about 8mm inwards. The dimple centre thereby overshoots the above-mentioned position for a buckle shape with vanishing circumferential curvature. The new configuration of the shell after this local snapping inwards including the deep and wide buckle is not stable at the current load level. That is, the current state of stress and deformation exceeds the stability limit of the partially flattened shell, and therefore instantaneously after the “local buckling”, i.e. the snapping of the initial dimple, the cylinder collapses totally. The dimple of initial depth $w_b/h = 0.3$ (black lines) results in a zigzag-shaped axial load-displacement curve with a distinct local maximum referring to “local buckling”. Compared with the shallower dent of initial depth $w_b/h = 0.1$ above, during loading more bending of the shell around the dimple is initiated and local buckling occurs already after about 1.03mm of axial compression. At this load the dimple centre suddenly and rapidly moves inwards to a radius of about 242mm which corresponds approximately to the radius of a shell strip centre with zero circumferential curvature. Consequently, the axial stiffness is decreased, but at this lower load level the state of deformation and stress of the cylinder with a flattened strip the stability limit of the entire cylinder is not reached yet⁷. Therefore, with a visible lower gradient of the axial-force curve further axial compression of about 0.1mm can be applied up to the total cylinder collapse. The relatively deep dimple with an initial depth of $w_b/h = 0.5$ (red lines) finally results in a curved axial load-displacement curve without a clear local maximum point prior to the over-all buckling of the cylinder. From the beginning of axial loading the dimple deepens continuously until at an end-shortening of about 0.9mm the radial displacement of the dimple apex is only slightly accelerated to reach a local radius which again belongs to a flattened shell strip. After this slow flattening further compression is possible since at the current load the state of stress and deformation under-runs the stability limit of the partially flattened cylinder. The weakened axial cylinder stiffness is again identical to that of the dent of initial depth $w_b/h = 0.3$ after local instability. The buckling behaviour of the cylinder with a dent of initial depth $w_b/h = 0.5$ differs solely from that of the shell with a dent of initial depth $w_b/h = 0.3$ in the lack of a sudden snapping inwards. Instead of a short and rapid flattening of the cylinder shell the dimple deepens and flattens continuously.

⁷Rigid endplates provided.

New Definitions

Introductory, the buckling phenomenon was classified into either “bifurcation buckling” or “nonlinear collapse”. Former term means a sudden, fundamental change of the structure pattern, whereas the latter refers to a sudden increase of the amplitude(s) of the deformation shape at buckling. In connection with thin cylinders under axial loading “bifurcation buckling” refers to an analytical model where at the critical load the axisymmetrical pre-buckling pattern is immediately replaced by a non-axisymmetrically pattern with many small formed buckles. Consequently, this type of buckling may only be attributed to cylinders with perfect shell geometry. Cylinders having imperfections will buckle in a way which can be related to “nonlinear collapse” which more generally denotes an acceleration of shell deformations at a limit load. However, problems are provoked in the description of the buckling behaviour of cylinders which have a single dimple. Normally “buckling” is simply associated with a sudden appearance of small visible buckles in an initially ideal-looking shell surface. Thus, if dealing with cylinders having one or more visible buckles already in the initial state, the question may arise “can a buckled shell buckle?”. The semantic troubles joint with this question were managed considering the initial dimples as small spherical caps which are elastically supported in a cylinder, and which have their own deformation and possible buckling behaviour. In the preceding pages it was shown that some initial dents resulted in a particular local instability due to a sudden partial flattening of the shell in the initial dent, e.g. the dent of initial depth $w_b/h = 0.3$ on page 254 ff. Under the boundary conditions on hand and for some initial dent depths after this first critical load additional axial loading up to the over-all collapse of the cylinder could be applied. The subsequent consistent terminology was introduced for a clear and simpler distinction between these two buckling events in further explanations and descriptions, see Figure 6.60.

Cylinder collapse denotes the over-all buckling of the cylinder at the maximum load $P_{cr U}$ in an axial load-displacement curve, associated with a rapid propagation of further dents beside the initial dimple.

Local buckling represents the dynamic radial displacement inwards of the dent apex to form a shape of a flattened shell strip at a load $P_{cr L}$ below the cylinder collapse load, associated with a loss of axial geometric stiffness.

The term “local buckling” is also used in connection with the instability

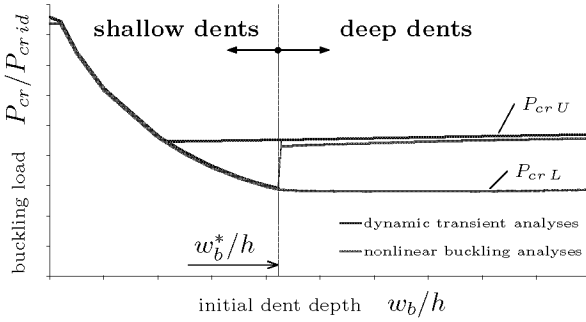


Figure 6.59: Differentiation between *shallow* and *deep* dents.

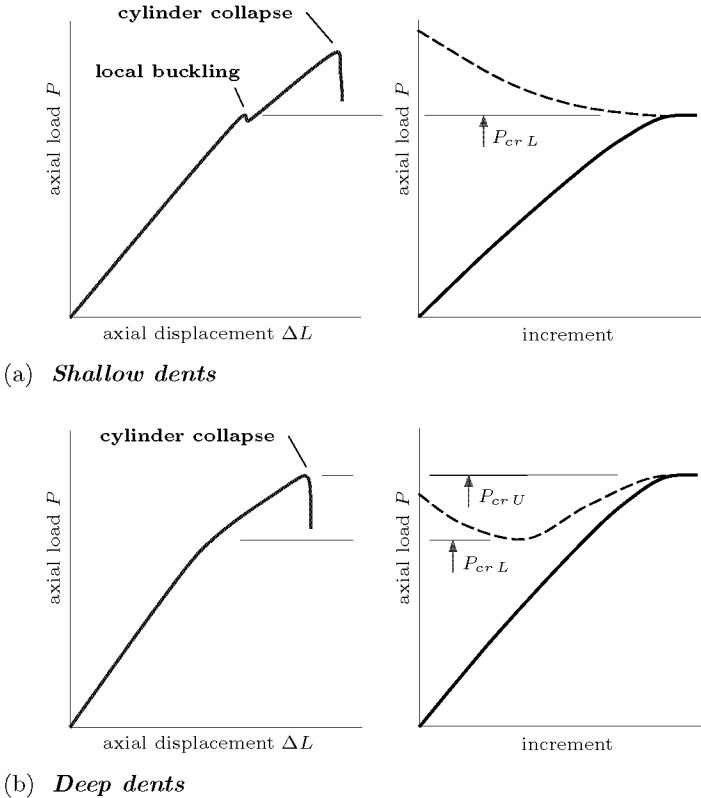


Figure 6.60: Typical curve progressions for shallow and deep dents. Left charts for dynamic transient analysis results, right charts for nonlinear buckling analysis results. Dashed lines denote buckling loads, continuous lines axial loads.

behaviour of beams having cross sections that consist of L-profiles. In such cases local buckling refers to the collapse of a single profile face at a load different to the EULER load at which the entire beam buckles like a column. The buckling in a shell between stringer-stiffeners of a panel (see Introduction Section 1.1) before collapse of the entire structure may also be mentioned as an example for “local buckling”.

The kind of local buckling in a cylinder with a dent depends on its initial depth w_b . For initial depths smaller than a certain **marginal depth** w_b^* , see Figure 6.59, the *local buckling* consists of a sudden snapping inwards of the dimple with a possible local maximum in the axial load-displacement curve at a load P_{crL} below the cylinder collapse load P_{crU} . For initially deeper dents with $w_b > w_b^*$, in contrast, the radial displacement of the apex prior to the cylinder collapse is smaller and less dynamic. During axial loading the shell is continuously flattened locally and the axial cylinder stiffness slowly decreased. In case of the reference cylinder the marginal was about $w_b^*/h = 0.45$, see Figure 6.20 and 6.24. In the following, depending on the local buckling behaviour, and therefore on the initial dent depth w_b/h , the inward dimples will be called either shallow dents or deep dents, see Figure 6.60:

Shallow dents are initial inward dimples of initial depths $w_b \leq w_b^*$ which led to pronounced local buckling caused by sudden dynamic radial displacement of the dent apex to a position for vanishing circumferential shell curvature. Nonlinear buckling analyses were aborted at the local buckling load P_{crL} , see Figure 6.60(a). In case of very small initial dent depths w_b the cylinder collapse occurred immediately after dynamic local buckling (e.g. reference cylinder with dent of $w_b/h = 0.1$). For deeper depths w_b the cylinder collapse resulted at a load above the local buckling and with dynamic transient analyses axial load-displacement curves were obtained with a zig-zag course (P_{crL} = local maximum, e.g. reference cylinder with dent of $w_b/h = 0.3$).

Deep dents are initial inward dimples of initial depths $w_b > w_b^*$ which led to an initial or slow loss of the local geometric stiffness caused by initial dent apex positions with vanishing circumferential shell curvature or by continuous arrangement of the dent apex to such positions. The only slow or initial partial shell flattening allowed for achievement of the cylinder collapse load P_{crU} also with nonlinear buckling analyses, see Figure 6.60(b). Nonlinear buckling analyses also yielded a lower buckling load P_{crL} identified by the minimum value within the series of buckling loads which were obtained by eigenvalue extractions after selected loading increments. Dynamic transient analyses in contrast yielded axial

load-displacement curves solely with a bend or smooth kink which made it impossible to ascertain a lower buckling load $P_{cr L}$ with these analyses (e.g. reference shell with $w_b/h = 0.5$).

The distinction between shallow and deep dents proposed above is only suitable for cylinders with uniform edge displacements, i.e. for boundary conditions CC4 or SS4 which simulate rigid and plane-parallel endplates. Due to their minor axial stiffness the flattened shell strips are stress released and their contribution to the resistance to axial buckling is decreased. But these boundary conditions provide that the curved shell remaining to the left and the right of the flattened strip may absorb the share of the additional axial loading until cylinder collapse occurs. It will be shown later (Section 6.6.7) that for shells with uniform axial edge loads applied (conditions CC3 or SS3), however, uncontrolled axial displacement of the edge over the dent resulted what provoked local buckling of the flattened shell with directly following cylinder collapse. That is, under these boundary conditions the lower (local) buckling load is about the upper (cylinder collapse) load, $P_{cr L} \approx P_{cr U}$, not only for shallow dents but also for deep dents.

Uniform edge displacements provided, in case of deep dents the lateral displacement of the dent apex forming a flattened shell strip evolved slowly without a dynamic snapping inwards. Consequently, in principle the lower load $P_{cr L}$ ascertained with nonlinear buckling analyses cannot be attributed to “buckling” in the mentioned sense but is rather a result of large displacements and rotations. Nevertheless, since the loads $P_{cr L}$ resulted close to the loads at which local buckling in evidence has to be expected for shells with uniform axial edge loads, the expression “buckling load” for $P_{cr L}$ was found acceptable also for deep dents in shells with uniform edge displacements.

Minimum buckling loads $P_{cr MIN}$ are the lowest local buckling load $P_{cr L}$ obtained with nonlinear buckling analyses of a cylinder having a single dent of given initial width a_b and height l_b , see Figure 6.61. The minimum buckling load $P_{cr MIN}$ depends on the cylinder dimensions and on the initial dent height and width.

Further distinctions of cases would have been possible, for instance between shallow dents with the cylinder collapse directly following the local buckling and shallow dents with local buckling at loads notably below the cylinder collapse load. But additional terms or abbreviations derived from these differentiations could hardly help the analyses and were therefore not considered.

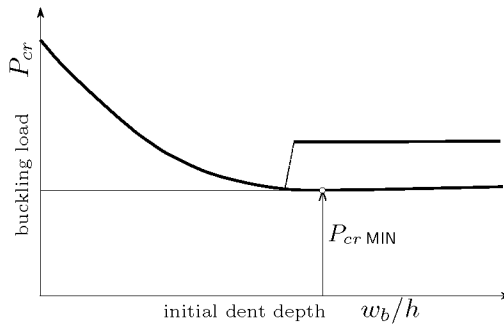


Figure 6.61: *Specification of the minimum buckling load $P_{cr \text{ MIN}}$ resulted from a series of nonlinear buckling analyses of a cylinder with a single dent.*

Influence of the Cylinder Dimensions R and h

After the investigation of the effect of a single dimple on the buckling behaviour of the aluminium cylinder with a radius of $R = 250$ mm, a length of $L = 510$ mm, and a shell wall thickness of $h = 1.5$ mm, the reduction of the stability due to different dimples was also calculated for some further aluminum cylinders with other lengths, radii and wall thicknesses. The selected shells are included in the list of the isotropic cylinders with ideal shell geometry presented in Section 4.2.1, page 127.

The initial circumferential width and the initial meridian height of all the dents presented above with $a_b = 181$ mm and $l_b = 67$ mm respectively resulted from a systematic search for the pair of initial lateral dimensions (a_b, l_b) of the shallow dent with initial depth $w_b/h = 0.1$ that leads to minimum stability of the above-mentioned reference cylinder. These calculations with fixed initial dimple amplitude w_b but varied initial dimple width a_b and height l_b for a number of isotropic cylinders are detailed in Section 6.6.3, page 325. It will be shown that for a shallow dent the “worst” initial dent height l_b was close to the classical axial wave-length for axisymmetric buckling⁸ of (perfect) isotropic cylinders $2l_c \approx 3.46\sqrt{Rh}$. The “worst” initial dent width a_b is about 2.5 to 3 times the height l_b , depending on the cylinder length L . Consequently, for isotropic cylinders with like products $R \cdot h$ and length L , the lateral dimensions a_b and l_b of the dent for minimal cylinder stability are identical. After the determination of these lateral initial lengths a_b and l_b , sets of shells were built by applying dents with the specified a_b and l_b fixed

⁸See Section 2.2.2.

but the initial dimple depth w_b/h varied, and then again the buckling loads were calculated systematically. For cylinders with identical factors $R \cdot h$ and length not only the dimensions a_b and w_b are equal but for like *normalized* initial dent depths w_b/h the *normalized* local buckling loads $P_{cr U}/P_{cr id}$ are also congruent. In Figure 6.62 this agreement is

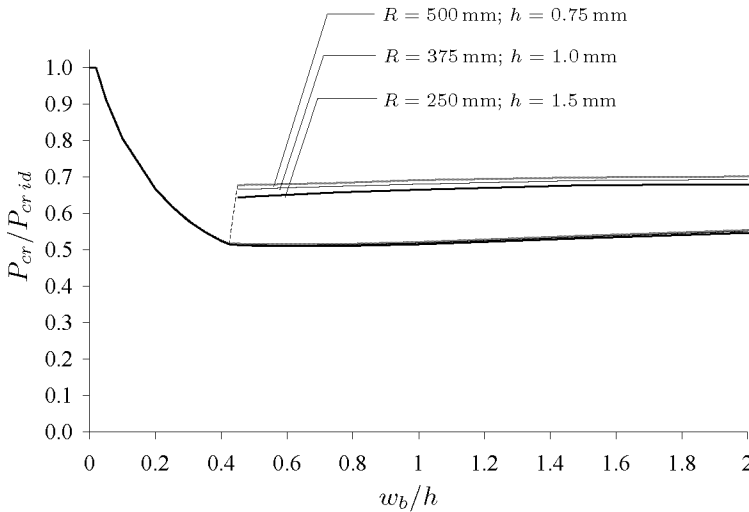


Figure 6.62: *Normalized buckling loads of three isotropic cylinders having a single dent of various normalized initial depth w_b/h . Cylinder radius R and shell wall thickness h as indicated for constant factor $R \cdot h$. Cylinder length: $L = 510$ mm; initial lateral dent dimensions: $a_b = 181$ mm, $l_b = 67$ mm.*

demonstrated by means of the buckling loads $P_{cr}/P_{cr id}$ of three cylinders with a length of $L = 510$ mm having a dent of different normalized initial depth w_b/h . Their radii and the wall thicknesses indicated in the figure were selected so that $R \cdot h = 375 \text{ mm}^2$. For these shells the initial lateral dimensions resulted in $a_b = 181$ mm and $l_b = 67$ mm, minimizing the cylinder stability for $w_b/h = 0.1$. The buckling loads normalized in respect of the limit load of the perfect cylinder $P_{cr id}$, resulting from non-linear buckling analyses as detailed above, in fact nearly coincide for the local buckling loads $P_{cr L}$ in cases of shallow dents ($w_b/h < 0.45$) as well as for the lower buckling loads $P_{cr L}$ in cases of deep dents. But obviously the upper loads $P_{cr U}$ referring to the cylinder collapse are higher for the cylinders with longer radius R . This might stem from their larger cylin-

der circumference and the therefore relatively wider shell surface range without notable stress deviations at like a_b and decay length for equal \sqrt{Rh} resulting in the states of deformation with an already flattened dimple.

Influence of the Cylinder Length L

The cylinder length L notably influences the reduction of the critical loads of a cylinder due to a dent of given dimensions. Figure 6.63 reproduces the normalized buckling loads $P_{cr}/P_{cr id}$ for cylinders with a radius of $R = 250$ mm, a shell wall thickness of $h = 1.5$ mm, and lengths between $L = 255$ and 765 mm. The initial meridian height l_b and circumferential width a_b of the dents added to these cylinders, specified for minimal cylinder stability at a fixed initial dimple depth, also depend on the cylinder length L , see Section 6.6.3. The initial dimple length l_b for $L = 255$ mm resulted in 65 mm, for $L = 765$ mm in 69 mm, and the initial dimple width a_b resulted in 176 mm and 183 mm respectively. The differences in the initial dent dimensions are still negligible. The minimum buckling loads $P_{cr MIN}$ of a given cylinder with various initial dimple amplitudes decreases with increasing cylinder length L ; that is, the imperfection sensitivity of longer cylinders is higher compared to that of shells with otherwise identical dimensions. This effect may be explained with the comparatively larger lateral displacements at the dimples of longer cylinder shells placed at $L/2$. With a longer distance from the cylinder edges during axial loading the dimple tip is displaced inwards with less shell bending resistance, and therefore local buckling occurs for lower axial loads. The three shells in Figure 6.63 were created by initial shortening or elongation of the reference cylinder by 255 mm. Obviously, the alteration rate of the minimum buckling loads $P_{cr MIN}/P_{cr id}$ varying L for longer cylinder is notably smaller than that for shorter shells. The reference cylinder with $L = 510$ mm yields a minimum $P_{cr MIN}/P_{cr id}$ of about 0.52, that of the 50% longer shell with $L = 765$ mm such of 0.47, thus a difference of circa 0.05. A further doubling the length of the longer shell to a length of $L = 1430$ mm (not pictured) yielded a minimum normalized buckling load of about 0.41, hence again a difference of 0.06, but here for a 200% longer cylinder. That is, further initial increase of the length L of an already “long” cylinder affects the reduction of the minimum buckling load only little.

In Figure 6.63 the vertical distances between the lower and the upper normalized buckling loads, i.e. between the local buckling load

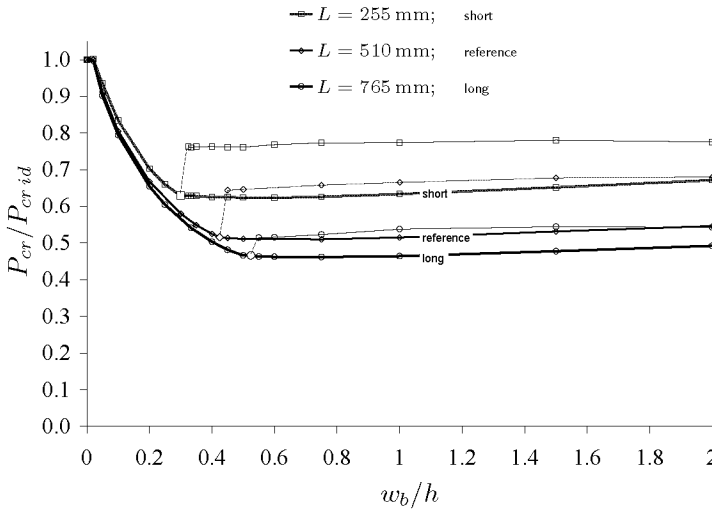


Figure 6.63: Influence of the cylinder length L on the normalized buckling load of an isotropic cylinder with a single dent of various initial depth. Cylinder radius $R = 250$ mm, shell wall thickness $h = 1.5$ mm. Mean initial dimple dimensions $a_b = 180$ mm and $l_b = 68$ mm.

$P_{crL}/P_{cr,id}$ and the cylinder collapse load $P_{crU}/P_{cr,id}$, for deep dents is about 0.15 for the reference cylinder with a length of $L = 510$ mm and also for the 50% shorter shell with $L = 255$ mm. But, in case of the longer cylinder with $L = 765$ mm these differences are only about half as large. These buckling loads were obtained with nonlinear buckling analyses with adaptive load step control. In Figure 6.64 also the normalized buckling loads $P_{cr}/P_{cr,id}$ resulting of transient dynamic analyses for the initially elongated cylinder with $L = 765$ mm, accordingly with dents of different initial depths w_b/h , are displayed. See Figure 6.24, page 231, for comparisons with the results for the reference cylinder of length $L = 510$ mm. The minimum normalized buckling load of about $P_{crU}/P_{cr,id} \approx 0.47$ obtained by nonlinear buckling analyses were confirmed by the dynamic transient analysis for the dent of initial depth $w_b/h = 0.5$. But the dynamic analyses yielded maximum buckling loads which built a quasi straight horizontal chain of bold dots at buckling loads $P_{crU}/P_{cr,id}$ of about 0.6; thus, the cylinder collapse loads resulted for the transient dynamic analyses are substantially higher compared

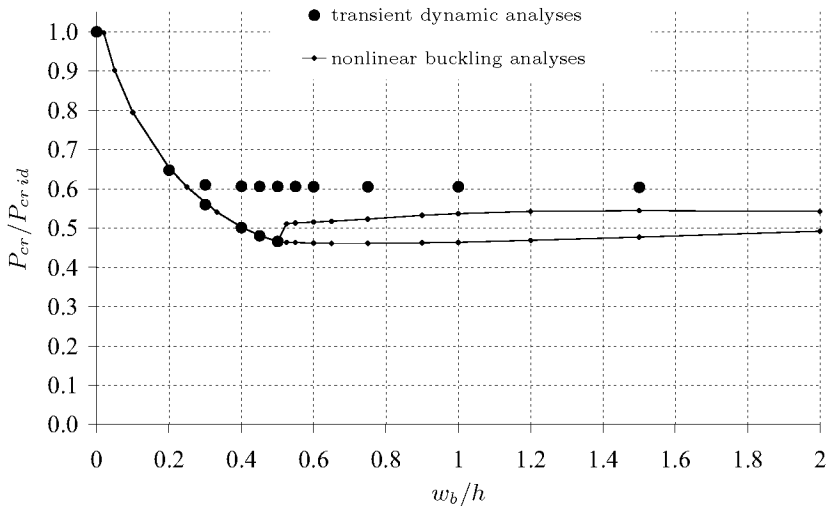


Figure 6.64: Comparison between buckling loads $P_{cr}/P_{cr id}$ resulting for transient dynamic and nonlinear buckling analyses for an aluminium cylinder of length $L = 765$ mm with a single dent of various initial depth w_b/h . Cylinder radius $R = 250$ mm and wall thickness $h = 1.5$ mm correspond to those of the shorter reference cylinder.

with the maximum buckling loads obtained by means of modified nonlinear buckling analyses. And, in contrast to the nonlinear buckling analysis results, the mentioned distances between the lowest and the topmost buckling loads of the dynamic analysis results for the cylinder of initial length $L = 765$ mm are similar in size to those of the cylinder of length $L = 510$ mm, see also Figure 6.63 and 6.24.

Figure 6.65 demonstrates the alteration of the reaction force with increasing cylinder end-shortening ΔL resulting for a transient dynamic analysis of the cylinder of length $L = 765$ mm having a dent of initial depth $w_b/h = 1$, as an example to explain the origin of the different critical load levels. The lateral initial dimple dimensions were again $a_b = 183$ mm and $l_b = 69$ mm, the other cylinder dimensions again that of the reference cylinder. The fifth chart in Figure 6.27, page 234, depicts the corresponding load-displacement curve for the reference cylinder with $L = 510$ mm having also a dent with an initial depth of $w_b/h = 1$ with respective lateral dimensions. Similar to the behaviour of the reference cylinder with the dent of initial depth $w_b/h = 0.5$ presented in pages

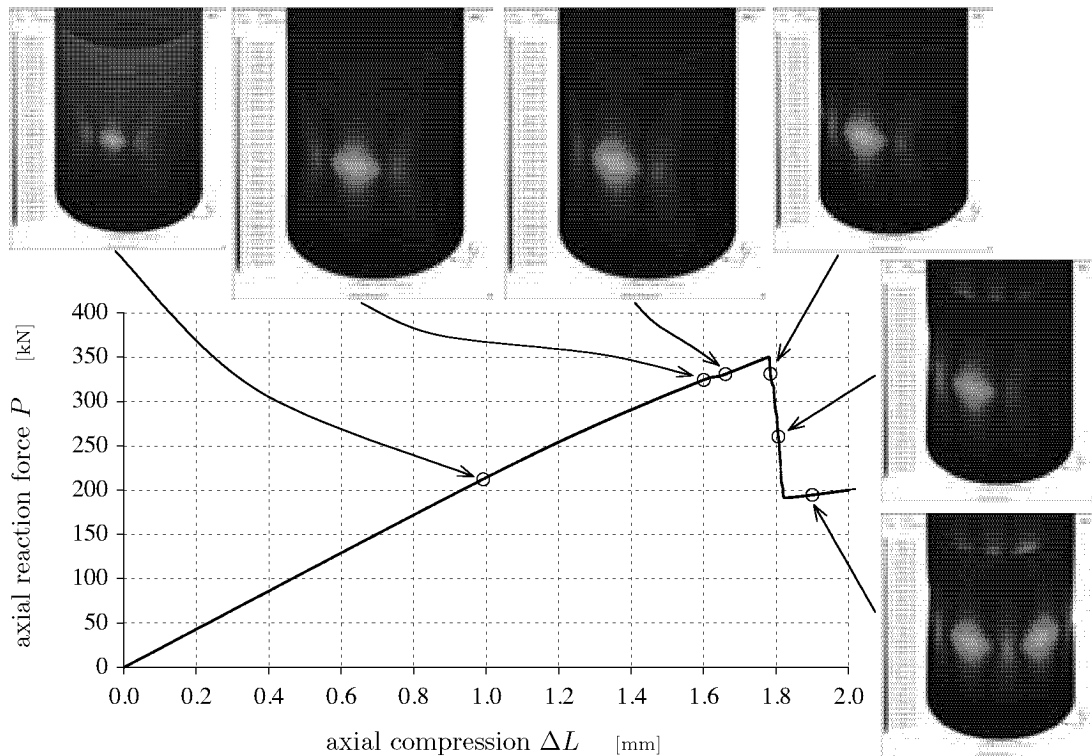


Figure 6.65: Result of a transient dynamic analysis for the reference cylinder elongated to a length of $L = 765$ mm, having an inward dimple of initial depth $w_b/h = 1$. The deformations in the pictures are displayed without magnification, the contour color maps refer to total-displacement vector lengths in metres.

267 ff, up to an applied compression of about $\Delta L = 1.6$ mm the dimple apex was continuously displaced inwards to slowly flatten the cylinder shell partially, what led to a continuous decrease in axial cylinder stiffness and hence to the first bend in the P - ΔL -curve in Figure 6.65 (1st and 2nd deformation plots). BUT, after some further compression to $\Delta L = 1.66$ mm the apex of the deepened and flattened dent was *shifted laterally* (3rd plot). This striking second, local buckling incident is responsible for the zig-zag in the load-displacement curve prior to the cylinder collapse load. There is no local maximum point in the axial load-displacement curve for an adequate specification of a critical load, but roughly this buckling phenomenon occurred at an axial reaction force of about $P = 328$ kN. Normalized with the collapse load of the ideal cylinder of length $L = 765$ mm, $P_{cr} = 579$ kN, this value yields a normalized buckling load of $P_{cr}/P_{cr id} \approx 0.57$. During this local buckling or shell-

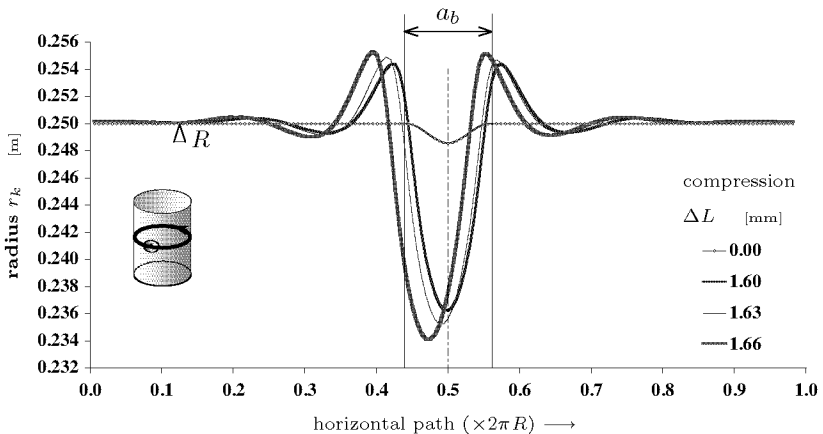


Figure 6.66: Radii r_k at nodal points along a horizontal path (CCW) over the apex of a dent with an initial depth of $w_b = h$ and an initial width of $a_b = 183$ mm. Results for the cylinder with length $L = 765$ mm, radius $R = 250$ mm and wall thickness $h = 1.5$ mm.

shape transformation process no elements or nodes were shifted, but the radius r_k of several nodes involved were increased or decreased. In Figure 6.66 the local radii along the horizontal path around the cylinder over the dent are shown for the initial configuration (dotted line), and for patterns resulting for axial compressions prior (blue line) and after this local buckling process (bold red) as indicated. Initially and before the transformation, thus $\Delta L < 0.6$ mm, the dimple apex is located at

0.5 times the circumference. After the transformation the apex is arranged at the middle of the left flank of the origin dent, i.e. displaced to the left (CW) by a fourth of the initial dent wave-length, hence by $a_b/4$. Furthermore, during the rearrangement the dimple is deepened by about further 2 mm.

After reaching the peak level of the reaction force at $P_{cr} = 350$ kN for an applied compression of about $\Delta L_{cr} = 1.78$ mm, the cylinder collapse was initiated by the sudden deepening of one further dimple beside the shifted origin dent. That following further buckles settled beside the first one in a row until the entire cylinder circumference is filled with six large buckles. Thus, in contrast to the shorter reference cylinder with such dents, during cylinder collapse dimples emerge not on both side of the initial dent but only on that side to which the dent priorly was displaced, cf Figure 6.42 or 6.51. The collapse load $P_{cr} = 350$ kN gives a normalized buckling load of $P_{cr}/P_{cr id} = 0.6$, in Figure 6.64 for $w_b/h = 1$ accordingly marked with a bold dot.

The transformation process at about $P = 328$ kN described above for the dynamic analysis results corresponds to a transition from one local buckling mode to a next one. Concerning the instability behaviour of the entire cylinder these two patterns may also be called “pre-buckling shapes” since they occur prior to the total collapse of the cylinder. In Figure 6.67 the results of a nonlinear buckling analysis with adaptive load step control are reproduced for the cylinder with length $L = 765$ mm having a dent of initial depth $w_b/h = 1$, thus for the shell also shown in Figure 6.65. Graph (a) reproduces the alterations of the applied axial force and the intermediately calculated buckling loads with increasing number of load increments. These curves are similar to that of the shorter reference cylinder with the respective dent, see fifth chart in Figure 6.21. The deformation plot in Figure 6.67 (c) shows the scaled-up displacements of the shell resulting for an applied axial force of 220 kN, again large rotations and displacements considered. The plots (b) and (d) display the buckling modes to the smallest eigenvalues calculated at axial loads of $P = 40$ kN and $P = 220$ kN, respectively. The state of stress and deformation at $P = 220$ kN yielded the lowest buckling load within the upper dotted line in graph (a) ($\rightarrow P_{cr L}$). Apart from the displacements amplitudes the first buckling mode in (b) with one deepened dent flanked by two small bulges is similar to the deformation pattern in (c). But, the second buckling mode (d), calculated for a load of $P = 220$ kN, is substantially different: instead of one deep single dent two large inward and outward dimples are arranged on the left and the

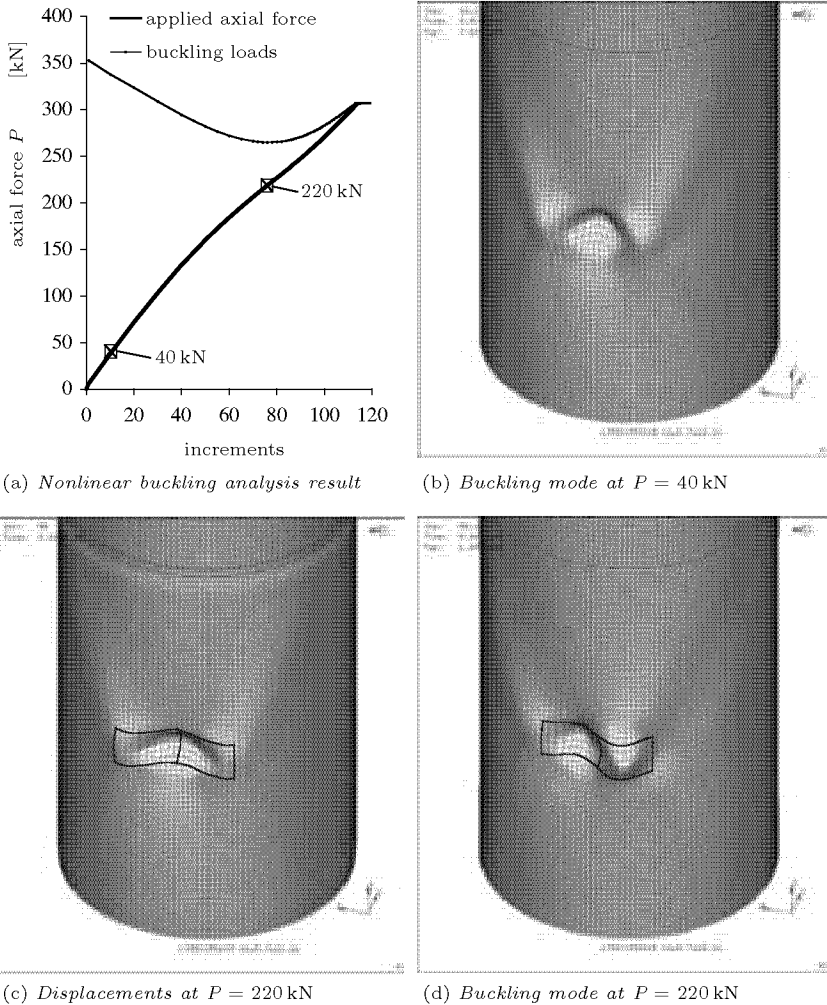


Figure 6.67: Results of a nonlinear buckling analysis with adaptive load step control (a) for the cylinder of length $L = 765$ mm having a dent of initial depth $w_b/h = 1.0$ and selected buckling modes calculated for an applied axial load of $P = 40$ kN (b) and $P = 220$ kN (d). Chart (c) displays the scaled-up cylinder deformations which lead to the buckling mode in (d). The bold lines in the FE mesh indicate the initial edges and position of the dent.

right of the initial vertex of the applied dent. The thick lines in the FE mesh added to the plots (c) and (d) indicate the initial edges of the dent with an initial width $a_b = 183\text{mm}$ and an initial height $l_b = 69\text{mm}$. It can be seen that the vertices of the two main buckles in plot (d) are arranged in the middle of the half of the framed shell segment, hence at $a_b/4$ from the initial apex of the applied dent. This position of the inward dimple apex is identical to that of the dent apex displaced laterally after the local buckling incident as reproduced in Figure 6.65 for the results of a transient dynamic analysis. Consequently, this process was interpreted as dynamic reconfiguration or “jump” from a pattern like the buckling mode in plot (b) of Figure 6.67 to a pattern which resembles the lateral inward dimple of the buckling mode in plot (d). Nonlinear buckling analyses of this cylinder having this dent yielded an upper buckling load of only $P_{cr}/P_{cr id} = 0.54$. The small gap between this factor and the normalized load $P_{cr}/P_{cr id} \approx 0.57$ at the lateral shift of the dimple resulting from a dynamic analysis led to the assumption that the nonlinear buckling analyses with adaptive load step control were aborted when reaching the load at which this second local instability phenomenon occurs. Consequently, this process was regarded as “local buckling” and not simply as a matter of large displacements.

Prior to this local buckling, due to the deformation process described above, the shell is already partially flattened. This leads to stress rearrangements with elevated compressive membrane stresses at the lateral dimple flanks and to reduced stresses at the centre of the dent. The membrane stress (membrane forces per unit length) fields resulting for such deformation states of the shell in Figure 6.67 with $L = 765\text{mm}$ are similar to that of reference cylinder with $L = 510\text{mm}$ having a dent of initial depth $w_b/h = 0.5$ as displayed in the contour-deformation plots of Figure 6.50, page 266, for an axial load of $P = 288\text{kN}$. The deformations in the plots of Figure 6.50 are pictured with scaled-up displacements, thus the real shape of a partially flattened strip at the dimple is not visible. According to these nonlinear static analyses results two concentrations of *compressive* membrane stresses are placed at the flanks of the flattened dimple for the axial forces N_{axial} as well as for the hoop membrane forces N_{hoop} per unit length. The antisymmetric buckling mode with an inward and an outward dimple in Figure 6.67 (d) is a result of this particular, combined axial and tangential compressive loading of the plate-like shell strip.

The buckling mode or eigenvector of the reference cylinder calculated at an axial load of $P = 288\text{kN}$ presented in Figure 6.49, page 265, is

also of the type with two lateral buckles alike the mode of the longer cylinder in Figure 6.67 (b). However, for all considered dents applied to the reference cylinder of length $L = 510$ mm the transient dynamic analysis yielded deformation and buckling processes without the lateral travel of the previously flattened dimple prior to the cylinder collapse as it was observed for the 50 % longer cylinder, see Figure 6.51. Missing this local buckling incident the choice of the geometry parameters for the reference cylinder was “a bit unlucky”, since for a representation of the general instability behaviour of cylinders with dents this shell was obviously too short. Probably the ratio of the initial dent width to the cylinder length (boundary effects), a_b/L , plays an decisive role for the appearance of this local buckling behaviour in the numerical simulation of axially compressed cylinders afflicted with deep dents. For dents with a shorter initial circumferential width a_b applied to the reference cylinder of length $L = 510$ mm also local buckling with lateral dimple-apex shift could be observed. The 50 % longer cylinder, in turn, having a dent with a notably elongated initial width a_b was not affected by this phenomenon.

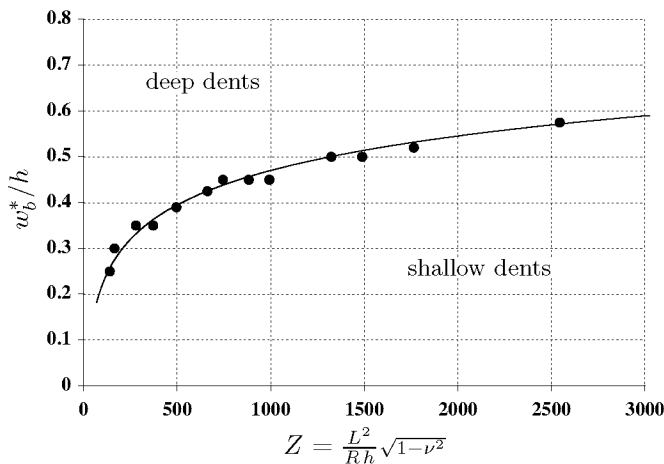


Figure 6.68: *Maximum initial dent depths for shallow dents w_b^*/h versus Batdorf's cylinder parameter Z . Results of nonlinear buckling analyses for some isotropic cylinders having a dent with lateral dimensions specified for $w_b/h = 0.1$.*

From Figure 6.63 can be taken that for shorter cylinders the marginal dent depth w_b^*/h , which separates shallow from deep dents, is shifted towards smaller initial depths w_b/h . The normalized dent amplitudes w_b^*/h are marked with circlets. The alteration of the normalized buckling

loads with increasing normalized initial dent depth w_b/h was calculated at selected points for several cylinders with diverse lengths, radii, and shell thicknesses and dents with initial lateral dimensions always determined for a given initial amplitude. In Figure 6.68 the marginal initial dent depths w_b^*/h are plotted in dependency of BATDORF's parameter Z which relates the square of the cylinder length to the factor $R \cdot h$. By means of these resulting dent depths a trend line could be added for a rough estimate of the maximum initial amplitude w_b^*/h for shallow dents, i.e. for dents which cause distinct local buckling prior to cylinder collapse, see also Fig. 6.71.

Influence of Initial Dimple Width a_b and Height l_b

The effect of the initial dimple depth on the buckling loads is coupled with the influence of the initial lateral dimensions of the dimple. Both the circumferential width a_b and the meridian height l_b for minimal cylinder stability increase with increasing initial dimple depth w_b . And, for deep dents with sized initial dent width and height the lower buckling load P_{crL} denoting local buckling decreases.

In Figure 6.69 the results of nonlinear buckling analyses are displayed for the reference cylinder having a dent with various normalized initial depths w_b/h . The black lines follow the normalized buckling loads resulting for dents with a fixed initial width of $a_b = 181$ mm and a fixed height of $l_b = 67$ mm. These two lateral dimensions, as already mentioned, correspond to the extents of a shallow dent with an initial depth of $w_b/h = 0.1$ which yielded the lowest buckling load, see Section 6.6.3. A similar minimum search for a dent of initial depth $w_b/h = 0.5$ resulted in an initial height of $l_b = 82$ mm and an initial width of $a_b = 283$ mm. That is, the deep dent yielded a 24% longer initial height l_b and a 32% larger initial width a_b compared to the shallow dent. By variation of the initial amplitude w_b/h of the dent with this sized pair of lateral dimensions a further set of cylindrical shells was formed and again nonlinear buckling analyses were performed. The resulting critical loads for these shells are reproduced in Figure 6.69, plotted with bold gray dots and lines. The dark lines and diamonds refer to buckling loads obtained with the reference cylinder having a dent with a 9% longer initial width, $a_b = 196$ mm, and a 13% longer initial height, $l_b = 75$ mm compared with the lengths to the shallow dent. The local buckling loads P_{crL} as well as the minimum buckling load P_{crMIN}/P_{crid} of the shell with the wider dents are lower than the values for the smaller dents. The normalized minimum buckling

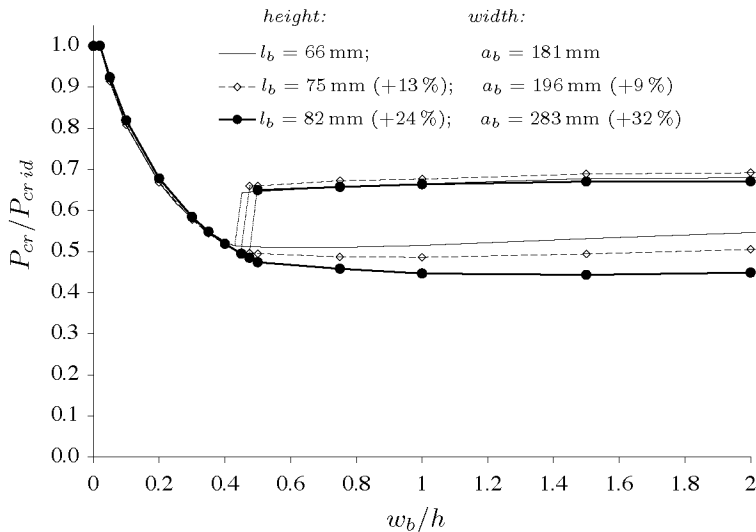


Figure 6.69: Normalized buckling loads $P_{cr}/P_{cr id}$ of the reference cylinder with a single dent of various initial depth w_b/h . Comparison between nonlinear buckling analysis results for dents with lateral dimensions as indicated.

load found for the smaller dents is $P_{cr \text{ MIN}}/P_{cr id} = 0.51$, whereas that of the larger dent is $P_{cr \text{ MIN}}/P_{cr id} = 0.49$ (−5%) for the medium size and $P_{cr \text{ MIN}}/P_{cr id} = 0.44$ (−13%) for the big size. The first minimum value resulted at an initial depth of about $w_b/h = 0.75$, the last at about $w_b/h = 1.5$; thus, by increasing the initial lateral dimple lengths a_b and l_b the “worst” dent is shifted to a larger initial amplitude.

Note that having lateral dimensions which led to minimal cylinder stability for a shallow dent of initial depth $w_b/h = 0.1$, for amplitudes $w_b/h < w_b^/h$ the smaller dents in fact resulted in slightly lower buckling loads than the wider dents.*

In case of the reference cylinder with its length of $L = 510$ mm the differences between the cylinder collapse load $P_{cr U}$ resulting for the two sets of dimple dimensions are negligibly small within the range of initial dent depths presented in Figure 6.69. But, the cylinder collapse loads resulting for longer cylinders in contrast are considerably raised when increasing the initial lateral lengths of the applied dent. Figure 6.70 displays the normalized buckling loads $P_{cr}/P_{cr id}$ resulting for the cylinder

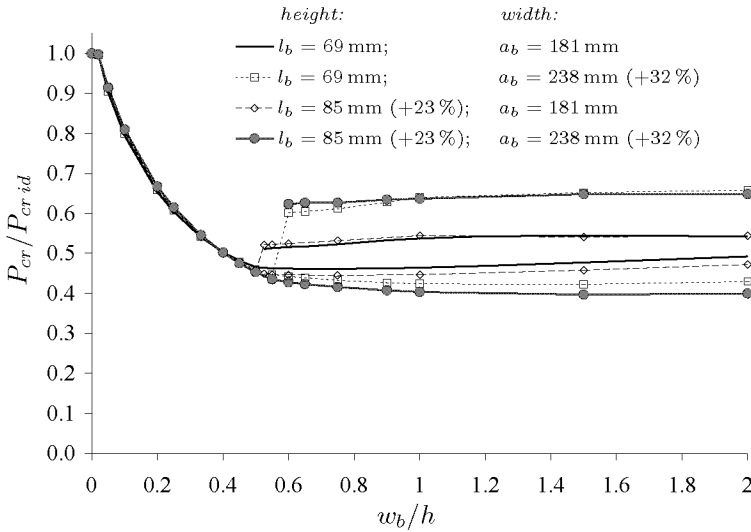


Figure 6.70: Normalized buckling loads $P_{cr}/P_{cr,id}$ of the reference cylinder initially elongated by 50%, to $L = 765$ mm ($R = 250$ mm, $h = 1.5$ mm), with a single dent of different initial depth w_b/h . Comparison between sets of dents with initial widths a_b and lengths l_b as indicated; reference dent with $l_b = 69$ mm and $a_b = 181$ mm.

with a length of $L = 765$ mm having a dent of different initial width a_b and meridian height l_b again in dependency of the normalized initial depth w_b/h of the dent. The cylinder length is 50% longer than that of the reference cylinder whereas the radius with $R = 250$ mm and the wall thickness with $h = 1.5$ mm are identical. The instability behaviour of this cylinder having dimples of initial width $a_b = 181$ mm and initial height $l_b = 69$ mm resulting for nonlinear buckling analyses as well as for transient dynamic analyses were detailed in the previous subsection, see Figures 6.64 to 6.67. It could be shown that these dimple and cylinder parameter combinations lead to aborts of the nonlinear buckling analyses at loads below the cylinder collapse load due to a second local buckling incident, and thus to underestimations of the cylinder stability ignoring the notable gaps between the second buckling loads and the cylinder collapse loads found for this cylinder length⁹. The bold gray dots indicate the results for dents with an initial width of $a_b = 238$ mm and

⁹Rigid endplates provided.

an initial height of $l_b = 85$ mm, that is for dents initially widened and elongated by 32% and 23% respectively. The thin lines with squares and rhombi chain the resulting buckling loads for dents with an either widened initial width a_b or an elongated meridian height l_b , see legend included. As for the reference cylinder the sized dent diminishes the lower buckling load P_{crL} by about 14%. But in case of the longer cylinder at hand the second buckling loads are drastically elevated for large initial depths. The effect of the single elongation of the initial meridian height l_b to the buckling loads is rather small, whereas the expansion of the initial dent width a_b seems to be responsible for the important differences in the buckling loads. As already mentioned in the previous section, for notably increased ratios of the dimple width to the cylinder length, a_b/L , the collapse load of the longer cylinder was reached with modified nonlinear buckling analyses since in this case the second local buckling did not occur. The cylinder collapse loads of the shell with $L = 765$ mm having dents of initial width $a_b = 181$ mm resulting for the dynamic analyses, plotted in Figure 6.64, page 283, yielded buckling loads $P_{cr}/P_{cr id}$ close to 0.6. Therefore, the effective distances between the cylinder collapse loads for $a_b = 181$ mm and for $a_b = 238$ mm are essentially smaller.

Initially wider dents gave deeper marginal initial dent depths w_b^*/h for distinct local buckling. In Figure 6.71 depths w_b^*/h obtained for dents with initial heights and widths specified for $w_b/h = 0.1$ are marked with bold dots, the deeper depths w_b^*/h which resulted for dents initially widened by 32% are labelled with circlets, see Figure 6.68. But, according to these three shells of different BATDORF parameter Z for such wider dents the marginal depth w_b^*/h can be roughly estimated with a vertical shift of about 0.05 from the trend line included for the w_b^*/h of initially smaller dents.

Finally, as already mentioned, the minimum buckling loads $P_{cr MIN}$ of wider dents resulted at deeper initial depths compared with the smaller dent dimensioned for minimal buckling loads due to a dent of initial depth $w_b/h = 0.1$, see Figure 6.69. Further elongations of the initial dent width a_b yielded still lower minimum buckling loads $P_{cr MIN}/P_{cr id}$ with the values for ring-shaped dents as lower bound. For example, ring-shaped dents of initial meridian height $l_b = 64$ mm and varied initial depths w_b/h , applied to the reference cylinder with a length of $L = 510$ mm, resulted in the low normalized loads $P_{cr}/P_{cr id}$ reproduced in Figure 6.72 (bold line). According to these nonlinear buckling analysis results the minimum load carrying capacity of the shell with such a local

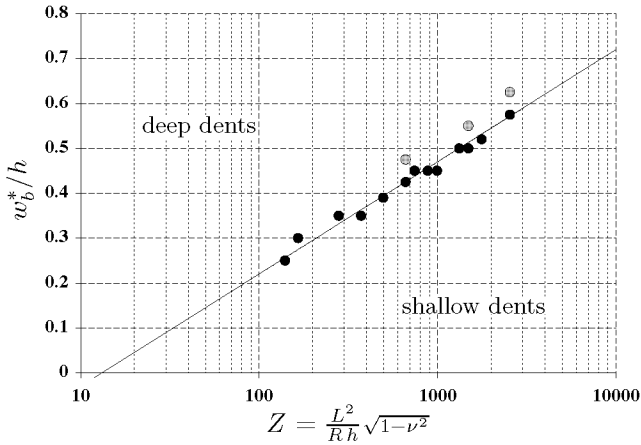


Figure 6.71: Maximum initial dent depths for shallow dents w_b^*/h versus Batdorf's cylinder parameter Z . Results of nonlinear buckling analyses for some isotropic cylinders having a dent with lateral dimensions specified for $w_b/h = 0.1$ (bold dots) or for a dent with a 32% longer initial width a_b and a 24% longer initial height l_b (circlets).

axisymmetric dent is only about 30% of the buckling load resulting for the cylinder with perfect geometry, whereas the localized dent with the elongated initial width and height reduces the minimal stability limit to about 44% (small gray dots), the dent with the smaller initial lateral dimensions to about 51% (small black dots) of the perfect cylinder. Note that for initial dimple depths between $w_b/h = 0.1$ and 0.4 the localized dents yielded slightly lower buckling loads than the ring-shaped dent; that is, shallow dents with short initial width were more damaging than wide or ring-shaped dents, see also Section 6.6.3.

Influence of the isotropic material parameters E and ν

For the isotropic cylinder having a small single dent nonlinear buckling analyses were performed with a YOUNG's modulus of $E = 7000$ MPa, thus with an elasticity only 10% of that of aluminium. The normalized buckling loads which resulted for a few dent depths were almost identical to that obtained for the reference aluminium cylinder with the corresponding dimple. Consequently, the influence of the YOUNG's modulus

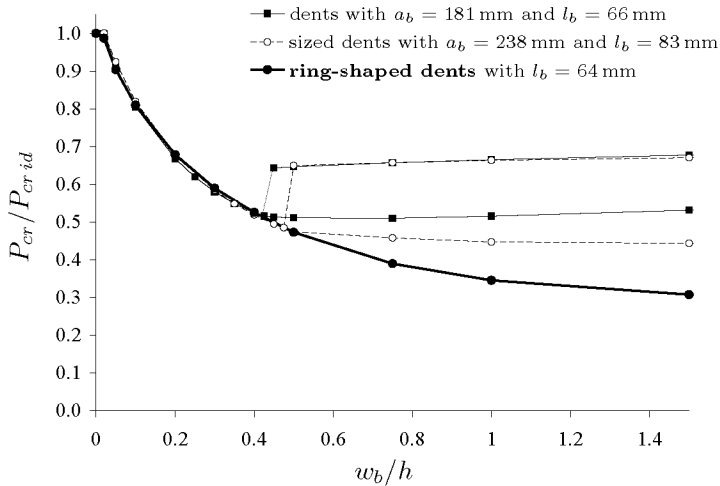


Figure 6.72: Normalized buckling loads $P_{cr}/P_{cr id}$ for the reference cylinder ($L = 510$ mm) with a single dent of different initial depth w_b/h . Comparison between results for a ring-shaped dent (bold line) and dents with initial circumferential widths a_b as indicated.

E on the buckling behaviour of isotropic cylinders with a single dimple imperfection can be neglected.

Isotropic cylinders under axial compression increase in radius because of the POISSON'S ratio effect. At the edges in general the change of the diameter is restrained, what leads to some shell bulging and stress elevations close to the cylinder ends. For a short-term investigation of the influence of these effects on the stability of the reference cylinder with a single dent, the POISSON'S ratio ν of the cylinder shell material was set to zero and nonlinear buckling analyses were performed for perfect shell geometry and for dents of various initial dent depth. The buckling load resulting for the perfect cylinder with $\nu = 0$ was about 4% higher than with $\nu = 0.3$. But the buckling loads for the shell having a dent resulted about 6% lower without transverse strain compared to the corresponding shell with standard material, probably since with $\nu = 0$ the positive effect of the circumference expansion against the continuous deepening of the dimple was missing.

6.6.2 Outward Dimples

As for isotropic cylinders with an inward dimple, the analysis of isotropic cylinders having a single outward dimple (bulge) was made mainly by means of a the reference aluminium cylinder with a radius $R = 250$ mm, a length $L = 510$ mm, and a shell thickness $h = 1.5$ mm. The yielded results were then again used for comparisons with other shells.

The inward dimples applied to the reference cylinder and used to describe the effects of dimple depth variations had an initial meridian height l_b and an initial circumferential width a_b which yielded the minimal cylinder stability for a shallow dent of initial depth $w_b/h = 0.1$. As demonstrated in the previous section, in fact shallow dents of this initial width and height resulted in lower critical loads than wider dents or axisymmetrical dimples. In Section 6.6.3 it will be shown that for outward dimples short initial circumferential widths a_b always resulted in higher buckling loads than a ring-shaped bulge of similar height. That is, for a given meridian height l_b and initial elevation w_b no initial circumferential width with $a_b < 2\pi R$ could be found that yield a lesser axial buckling load of the aluminium reference cylinder, neither for small initial amplitudes $-w_b$. Thus, an investigation limited into bulges which lead to the minimum cylinder stability would probably require exclusive finite element calculations of cylinders with a ring-shaped dimple. Nevertheless, this thesis focuses the impact of localized dimple imperfections, i.e. with limited initial dimensions in all directions. Consequently, the initial heights l_b and widths a_b specified for the inward dimples were also applied to the outward dimples to investigate the reduction of the cylinder buckling loads due to a single, relatively small bulge in dependency of its initial elevation w_b .

Pure Variation of the Initial Bulge Elevation $-w_b$

In Figure 6.19, page 223, the buckling loads for the reference cylinder with a single dent of various normalized initial depth as well as for the shell with a single bulge of different initial normalized elevation w_b/h (left half) is depicted. As mentioned above, with an initial width $a_b = 181$ mm and an initial height $l_b = 67$ mm the lateral dimensions of the bulges are identical to those of the dents shown in this figure. Figure 6.73 again reproduces these nonlinear buckling analysis results for the reference cylinder having a single bulge also for initial elevations up to $w_b/h = -10$. Rightmost of the chart the normalized buckling

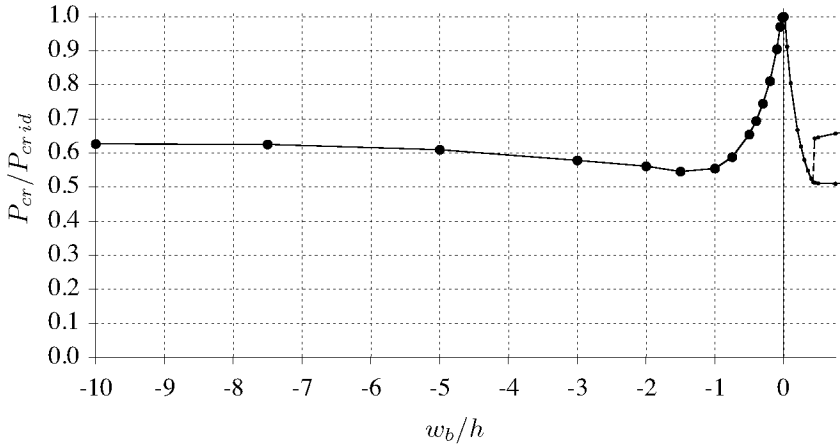


Figure 6.73: *Normalized buckling loads of an aluminium cylinder having an outward dimple with initial amplitudes up to $w_b/h = -10$. Cylinder with $R = 250$ mm, $L = 510$ mm, and $h = 1.5$ mm. The initial width and the initial height of the bulge are always $a_b = 181$ mm and $b_b = 67$ mm respectively.*

loads $P_{cr}/P_{cr id}$ of the corresponding inward dimples with depths up to $w_b/h = 0.75$ are plotted for comparison. Thus, above all for absolute dimple amplitudes $|w_b|$ of about the wall thickness h outward dimples caused considerably higher buckling loads than dents with like lateral dimensions. However, for large amplitudes the difference tends to diminish: the normalized buckling loads of bulges seem to converge with growing elevation towards about the same value than that of the deep dents displayed in Figure 6.22, page 228. For the shell and the dimple size on hand the normalized minimum buckling load of the bulges is about $P_{cr}/P_{cr id} = 0.55$ for an initial amplitude close to $w_b/h = -1.5$, compared with the lower minimum of $P_{cr MIN}/P_{cr id} = 0.51$ of the dents at an initial depth of only $w_b/h = 0.75$. Hence, the sensitivity of the cylinder to bulges is notably lower than that to dents as regards the initial amplitude as well as the minimum buckling load of the most damaging dimples.

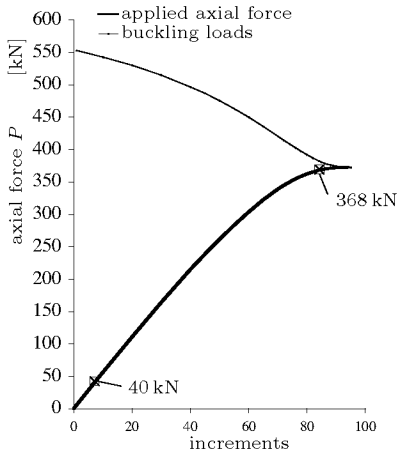
The nonlinear buckling analyses with adaptive load step control of isotropic cylinders having a single bulge caused less troubles to realize feasible results compared to the analyses of deeper dents: the bulges with moderate initial elevations yielded always only one single buckling load. That is, the intermediate buckling loads calculated within a nonlinear

static analysis decreased steadily and finally coincided directly with the applied total loads. Loads ascertainable at the minimum value of a concave chain of buckling loads could not be found for bulges, in contrast to deep dents as described in Section 6.5, or in Figure 6.20, page 226, for a dent of initial depth $w_b/h = 0.5$.

In Figure 6.74 as an example the results of nonlinear buckling analyses for the bulge with an initial elevation of $w_b/h = -0.5$ are shown. The set-up of this page corresponds to that of Figures 6.34, 6.40, and 6.49, see also the explanations on page 241 ff. Chart 6.74(a) depicts the applied axial force resulting for a nonlinear buckling analysis with adapted load increments (thick line) which finally correlates with the linear buckling loads computed after selected load steps. This conjoint value yields the nonlinear buckling load $P_{cr} = 373 \text{ kN}$ and the ratio $P_{cr}/P_{cr \text{ id}} = 0.65$. Plot (c) illustrates the scaled-up deformations of the shell resulting for an applied axial load of $P = 368 \text{ kN}$ close to buckling. Again, the dimple climax is originally located at $L/2$. Whilst axial compression this nodal point is only little displaced, whereas the upper and the lower flanks of the bulge form two new inward dimples. Similar to the initial single dents, besides the initial bulge and the two dents the shell is slightly bulged. In Figure 6.75 the formation of the two dimples above and below the bulge is demonstrated by means of the radii of the nodal points along the axial path including the bulge climax for an axial force of $P = 368 \text{ kN}$ in comparison with the origin radii. The apex of the applied bulge remains almost immobile during loading, since a radial displacement outwards would cause a circumferential shell stretching in addition to the expansion due to the POISSON'S ratio effect. The shell with its initial concave curvatures at the upper and lower bulge flanks is rather bend inwards about the quasi fixed bulge climax, forming the two inward dimples.

Figure 6.74(b) and (d) display the linear buckling modes calculated for states of stress and deformation at a small force of $P = 40 \text{ kN}$ and at a force with $P = 368 \text{ kN}$ close to instability. In both cases the horizontal arc over the bulge apex at $L/2$ serves as a swivelling axis for the shell segment which above buckles inwards and outwards below. That is, according to these eigenvectors at buckling one of the two formed dents is put over to be converted into a bulge.

In the two color contour plots of Figure 6.76 membrane stress distributions in the reference cylinder again having an bulge of initial elevation $w_b/h = -0.5$ are shown for an axial load of $P = 368 \text{ kN}$. Thus, the plots give the state of membrane stress which lead to the eigenmodes in



(a) Nonlinear buckling analysis result

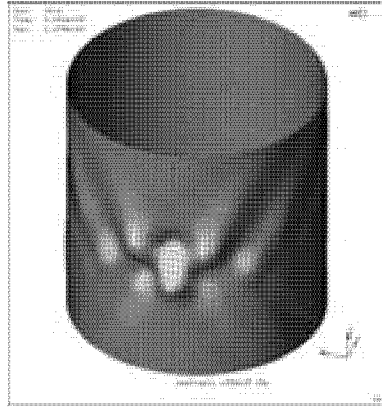
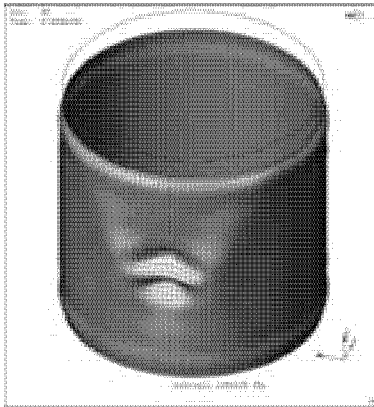
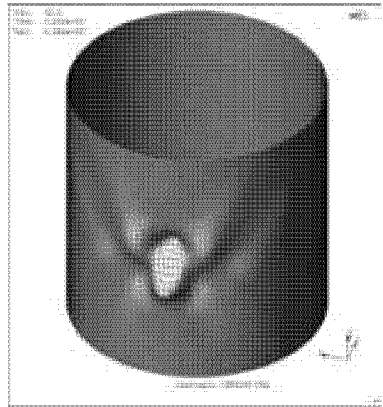
(b) Buckling mode at $P = 40$ kN(c) Displacements at $P = 368$ kN(d) Buckling mode at $P = 368$ kN

Figure 6.74: Results of a nonlinear buckling analysis with adaptive load step control (a) for the cylinder having a bulge of initial elevation $w_b/h = -0.5$ and selected buckling modes (eigenvectors) calculated for an applied axial load of $P = 40$ kN (b) and $P = 368$ kN (d). Chart (c) displays the scaled-up cylinder deformations which lead to the buckling mode in (d).

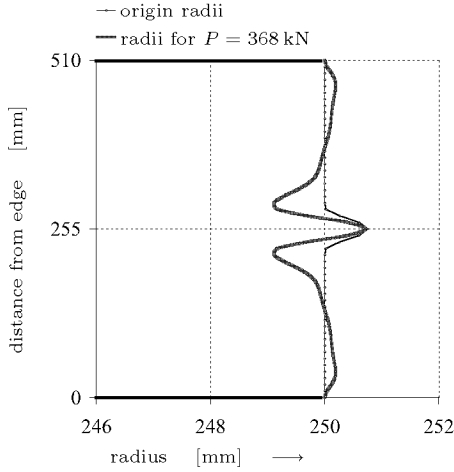


Figure 6.75: *Local radii along the vertical path from the bottom up over the apex of an outward dimple with an initial elevation $w_b/h = -0.5$. Initial configuration (black) and calculated deformed state for an applied axial force of $P = 368$ kN (red).*

6.74(d). The nominal axial membrane stress to this compressive force is $N_{axial} = 234$ N/mm. The variations of the axial membrane stress within the deformed shell are displayed in the left plot. Similar to the shells with a single inward dimple (e.g. Fig. 6.41), the vertical strip over the dimple apexes is released, at the peak of the applied bulge the axial membrane stress is diminished by 34 N/mm or 14% of the nominal value. At the two lateral ends of the two formed dents, but also at the cylinder edges, concentrations of elevated compressive membrane stresses can be recognized. However, the maximum compressive membrane stress N_{axial} at these spots is only 11 N/mm or 5% over the nominal value. That is, the local relief due to stress rearrangement at the bulge tip is about three times larger than the local additional loading at the buckle flanks and shell edges. Again as for cylinders with a single dent but with higher extremal values, on bulges notable tensile hoop membrane stresses N_{hoop} emerge, visualized in the right plot of Figure 6.76 with a bright strip. And, in turn, on the inward dimples dark dots can be seen which refer to high compressive membrane stresses in circumferential direction.

To complete the calculations, transient dynamic analyses were also conducted for the isotropic cylinder with single outward dimples of identical

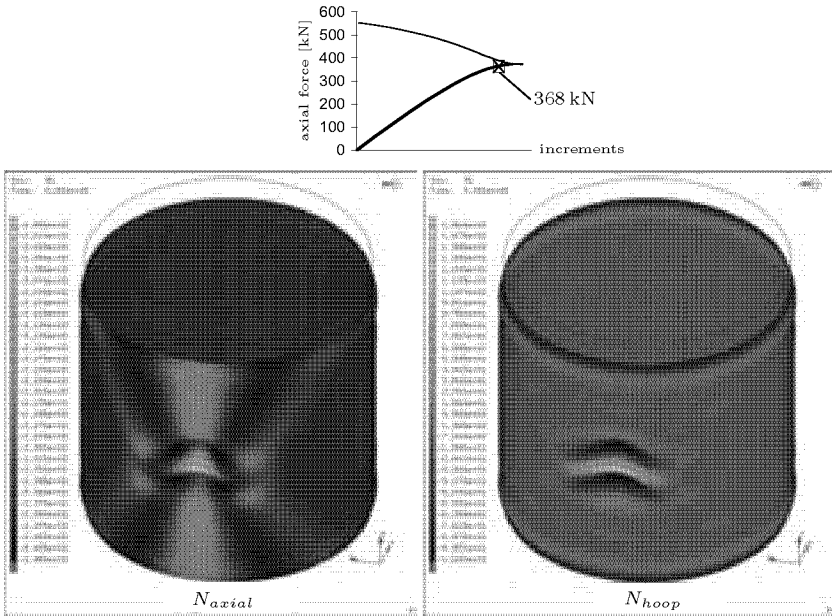


Figure 6.76: Axial membrane stress N_{axial} and circumferential membrane stress N_{hoop} of the cylinder with a bulge of initial elevation $w_b/h = -0.5$ at an applied axial load of 368 kN. Values in color maps are given in N/mm. Result of a nonlinear static analysis.

initial lateral dimensions to those of the dents detailed in the previous section. In Figure 6.77 the normalized buckling loads $P_{cr}/P_{cr id}$ are reproduced for the reference cylinder having bulges with different initial elevations w_b/h , an initial width of $a_b = 181$ mm and an initial height of $l_b = 67$ mm. The results of the transient dynamic analyses are marked with big dots, those of nonlinear buckling analyses with adaptive load step control as given in Figure 6.73, page 297, are chained with a thin line. Obviously, for initial elevations larger than $w_b/h = -0.5$ the top buckling loads obtained by transient dynamic analyses could not be reached with nonlinear buckling analyses. These topmost axial forces correspond to the cylinder collapse loads. Similar to the corresponding dents with initial depths of more than $w_b/h = 0.2$, see Figure 6.24, nonlinear buckling analyses with bulges were aborted when reaching a load level where some local buckling occurs and the force-axial displacement curve of a transient dynamic analysis has a more or less distinct zigzag course. The axial reaction forces to the local maxima in such

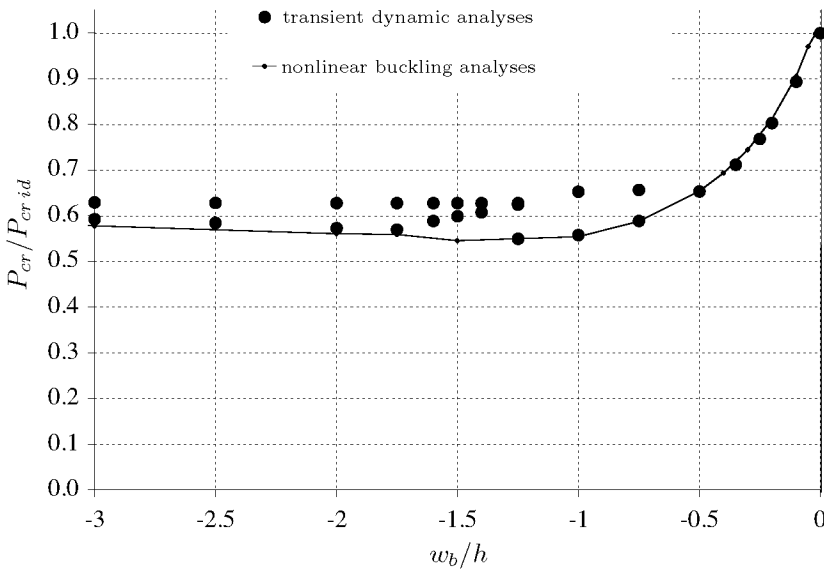


Figure 6.77: *Transient dynamic analysis results of the reference cylinder having a single bulge of various initial elevation w_b/h . Buckling loads obtained by nonlinear buckling analyses are chained with a thin line for comparison.*

load curves yielded the bottom dots or buckling loads in Figure 6.77. In Figure 6.78 typical axial load-displacement curves and the respective normalized buckling loads are shown for some selected initial bulge amplitudes. These transient dynamic analyses results serve to point at the origin of the dots in Figure 6.77. The lower red dots with dashed circlets for initial bulge elevations from $w_b/h = -0.4$ to -0.6 are ignored in Figure 6.77 because they refer to loads merely located about a bend in the load curves missing a distinct local maximum value that could be used to determine a precise amount of axial loading for some local buckling.

Two different kinds of *local buckling processes* in the vicinity of the initial bulge could be distinguished which may occur prior to total cylinder collapse and which are associated with a bend or a local maximum in the axial load-displacement curves:

- (I) Snapping inwards of one of the formed dents above and below the initial bulge and arising of the other (bright red dots). The new shape resembles the buckling mode in Figure 6.74(d).

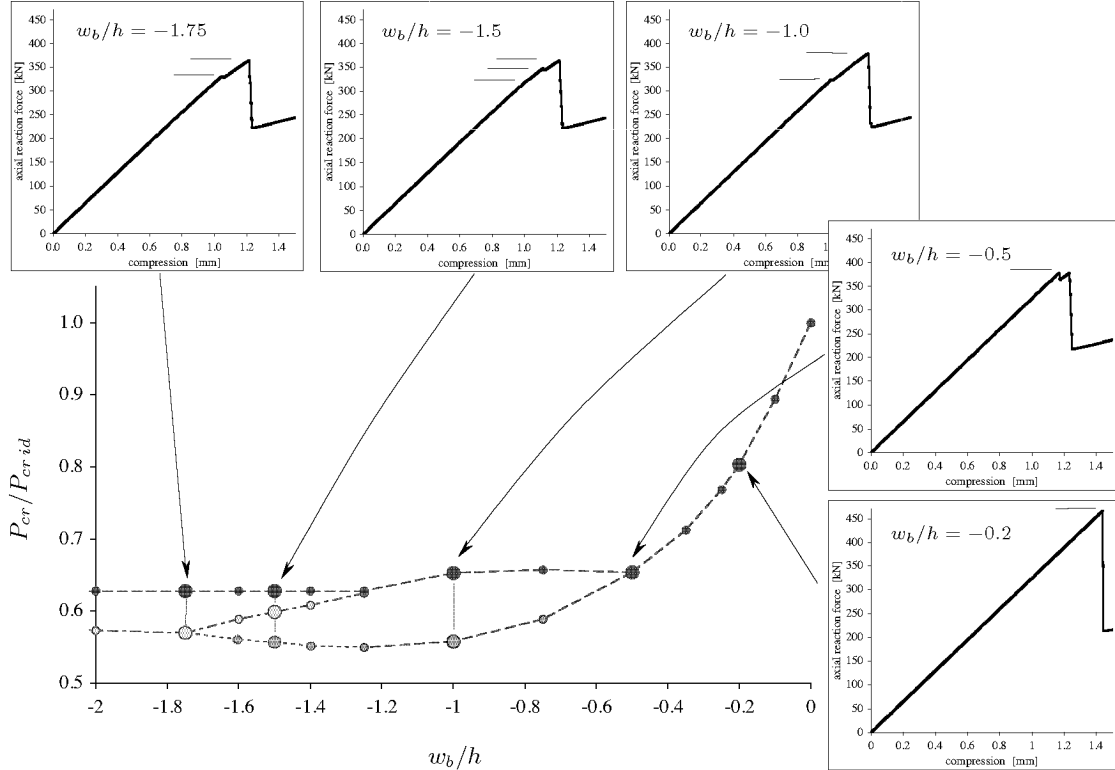


Figure 6.78: Resulting axial load-displacement curves of transient dynamic analyses and corresponding normalized buckling loads $P_{cr}/P_{cr, id}$ for bulges with selected initial elevations $-w_b/h$ applied to the reference cylinder.

- (II) Dynamic lateral shifting of the apex of one of the growing dents above or below the initial bulge, followed by a deepening of the accordingly staggered opposite dent (yellow dots).

In order to demonstrate these two different local-buckling-mode changes observed, in the following the axial-compression process with respective deformation states of the cylinder with one of the bulges in Figure 6.78 are demonstrated by means of selected contour-deformation plots extracted from the transient dynamic analyses results. These analyses were again conducted with the single-step Houbolt operator for time integration and input parameters as given in Section 6.5.2. As already mentioned, during cylinder compression up to the cylinder collapse the origin bulge apex is almost unmovable and the formed dimples may emerge everywhere in the shell around the initial bulge. Thus, the alteration of the local radii at the nodes along the preselected horizontal or vertical path over the bulge climax as introduced in Section 6.5.3 in general were not informative for the analysis of different critical local movements of the cylinder shell.

Similar to the selected inward dimples in the previous Section 6.6.1, the deformation plots included in the Figures 6.79 to 6.82 and 6.85 give the resulting shell deflections for the applied axial compression as flagged in the P - ΔL -diagram. The displacements are shown again without magnification and the colors of the applied contour plots refer to absolute values of total-displacement vector lengths (in metres). The top color-map level (light gray) always indicates the maximum total displacement for the corresponding loading.

1. Outward Dimple with Initial Elevation $w_b/h = -0.2$:

Figure 6.79 depicts the transient dynamic analysis results for the reference cylinder having a relatively flat bulge with an initial elevation $w_b/h = -0.2$. The P - ΔL -curve is a straight line up to the single climax for total cylinder collapse at an axial reaction force of $P_{cr} = 466$ kN resulting for an applied axial compression of $\Delta L_{cr} = 1.44$ mm. This buckling load is very close to the result of a nonlinear buckling analysis with $P_{cr} = 462$ kN.

According to the sequence of deformation plots included, prior to cylinder collapse the shell consists of two almost identical inward dimples emerged below and above the origin bulge (1st plot). The buckling is locally initiated by a sudden snapping inwards of the upper dent (2nd plot) followed by the arise of the opposite dent. This action immediately starts the settlement of new dimples in two staggered rows beside

the formed inward respectively outward buckles (3rd plot). The ring including the apex of the initial bulge separates these two rows and splits the deforming cylinder into two symmetric halves. Finally the collapse process is terminated and the first stable post-buckling state reached when the buckles in the two rows fill the entire cylinder circumference (4th plot).

The behaviour of the shell and imperfection on hand can be compared with the corresponding shallow dent of initial depth $w_b/h = 0.1$, which at cylinder collapse also at first snaps inwards, followed by a rapid settlement of buckles in staggered rows around the cylinder, see Figure 6.36.

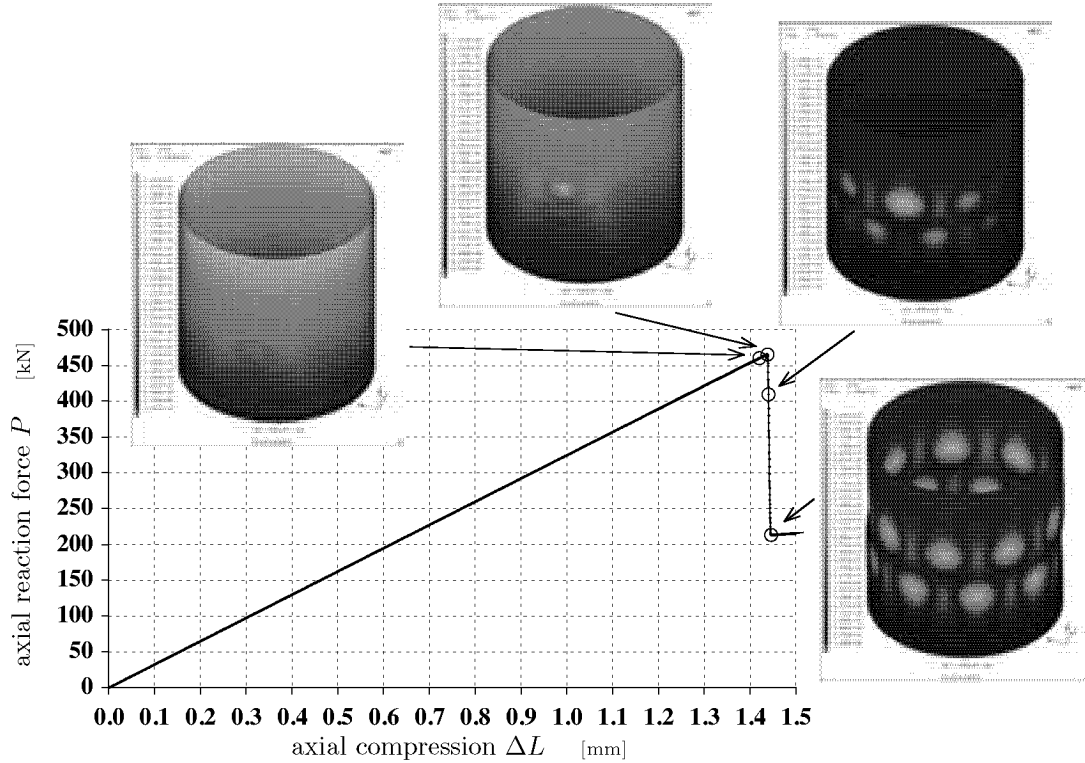


Figure 6.79: Result of a transient dynamic analysis for the isotropic cylinder having an outward dimple of initial elevation $w_b/h = -0.2$. The deformations in the pictures are displayed without magnification, the contour color maps refer to total-displacement vector lengths in metres.

2. Outward Dimple with Initial Elevation $w_b/h = -0.5$:

The transient dynamic analysis results for the reference cylinder having a bulge with an initial elevation $w_b/h = -0.5$ are reproduced in Figure 6.80. The P - ΔL -curve once again is straight-line up to the first peak at an axial reaction force of $P_{cr} = 378$ kN for an applied axial compression of $\Delta L_{cr} = 1.17$ mm. This force confirmed the value yielded with a nonlinear buckling analysis of $P_{cr} = 373$ kN.

The first two included plots give information about the local deformation process responsible for the loss of axial cylinder stability: at local buckling the dent which emerged above the initial bulge suddenly snaps inwards, increases and flattens the shell, whereas the dent below accordingly arises and disappears. This process fits with type (I) of local buckling defined above. The so emerged large dent acts alike the applied single inward dimple of initial depth $w_b/h = 0.3$ presented in Section 6.6.1, see e.g. Figure 6.42, page 256. The dent apex rapidly moves to a position where the hoop curvature quasi vanishes and the dimple forms a flattened shell strip. Accordingly the axial cylinder stiffness is reduced.

However, the new geometry with rearranged stresses allows further axial loading of the cylinder, until at an end-shortening of $\Delta L_{cr} = 1.23$ mm the cylinder collapses totally. The resulting axial reaction force is $P_{cr} = 378$ kN, thus a value almost identical to the first peak. The cylinder buckling begins with the formation of buckles beside the big dent formed during local buckling (3rd plot), then further dimples emerge which settle around the cylinder side by side (4th plot). The first stable post-buckling pattern, finally arranged with a single row of buckles, resembles the pattern resulting for the dents of initial depth $w_b/h = 0.3$ in Fig. 6.42 or $w_b/h = 0.5$ in Fig. 6.51. But the apex of the dimple which emerged at last and opposite to the initial bulge is located at $L/2$, i.e. at half the cylinder length, in contrast to the first buckle that is eccentrically formed prior to buckling above the origin bulge. Consequently, the row of buckles around the cylinder in the post-buckling pattern at hand is slightly skew.

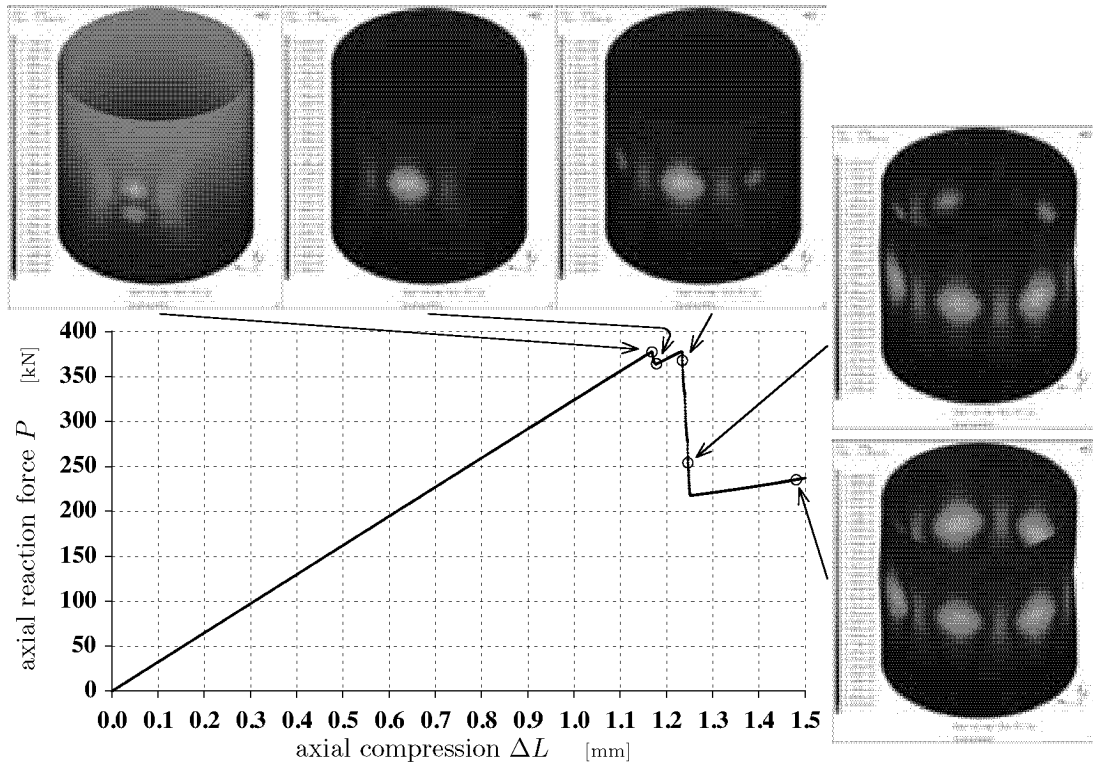


Figure 6.80: Result of a transient dynamic analysis for the isotropic cylinder having an outward dimple of initial elevation $w_b/h = -0.5$. The deformations in the pictures are displayed without magnification, the contour color maps refer to total-displacement vector lengths in metres.

3. Outward Dimple with Initial Elevation $w_b/h = -1.0$:

The force-axial compression curve resulting for a dynamic transient analysis of the reference cylinder with an outward dimple of initial elevation $w_b = -h$ is shown in Figure 6.81 A and 6.81 B. The first figure includes deformation plots which demonstrate the local buckling of the shell around the bulge, the second one plots which give the total cylinder collapse for continued cylinder compression. The resulting axial force for the local instability is $P_{crL} = 324$ kN, that for the cylinder collapse $P_{crL} = 378$ kN. Nonlinear buckling analyses yielded only one buckling load of $P_{cr} = 316$ kN, which is slightly below the force P_{crL} obtained with the transient dynamic analysis at local buckling. The nonlinear buckling analysis with adaptive load step control were again aborted when reaching the local buckling load, ignoring any remaining axial buckling resistance of the cylinder with simulated rigid endplates.

Prior to local buckling two similar dents emerge above and below the applied bulge, see first plot in Figure 6.81 A. At an applied axial compression of about $\Delta L_{crL} = 1.0$ mm the upper dent suddenly snaps inwards whereas the lower arises and almost vanishes. This local instability led to a zigzag course of the P - ΔL -curve with a distinct local maximum that enabled accurate determination of the critical axial reaction force P_{crL} . This local buckling behaviour is similar to that of the previous bulge of initial elevation $w_b/h = -0.5$ or the dent of initial depth $w_b/h = 0.3$ detailed in Section 6.6.1. The upper dent then deepens, increases and its apex reaches a position of considerably reduced local circumferential curvature. Therefore, the axial cylinder stiffness is suddenly reduced what leads to the load curve progression on hand with a zigzag course and a reduction of the ascending slope.

At the axial load level immediately after the local buckling the state of strain and stress of the cylinder with the wide, flattened dent is below the stability limit of the deformed cylinder. Thus an additional end-shortening of about $\Delta L = 0.22$ mm could be applied until the total collapse of the cylinder was reached. From the deformation plots in Figure 6.81 B can be taken that whilst further loading, prior to cylinder collapse, the deep dent above the origin bulge is continuously displaced to one side of the meridian line over the bulge vertex, whereas the hardly visible, shallow dent below the bulge is displaced to the opposite side. The radial displacement of the bulge apex during axial cylinder compression again remains very small in comparison to the amplitudes of the emerged buckles. At an applied axial compression of about $\Delta L_{crU} = 1.23$ mm the cylinder collapse is initiated by the formation of a new dimple beside the large dent, followed by the re-amplification of the smaller, but also staggered dent below the origin bulge. Afterwards, beside the now increased lower dent new buckles are formed side by side in a slightly skew row around the cylinder. The dimples settled around

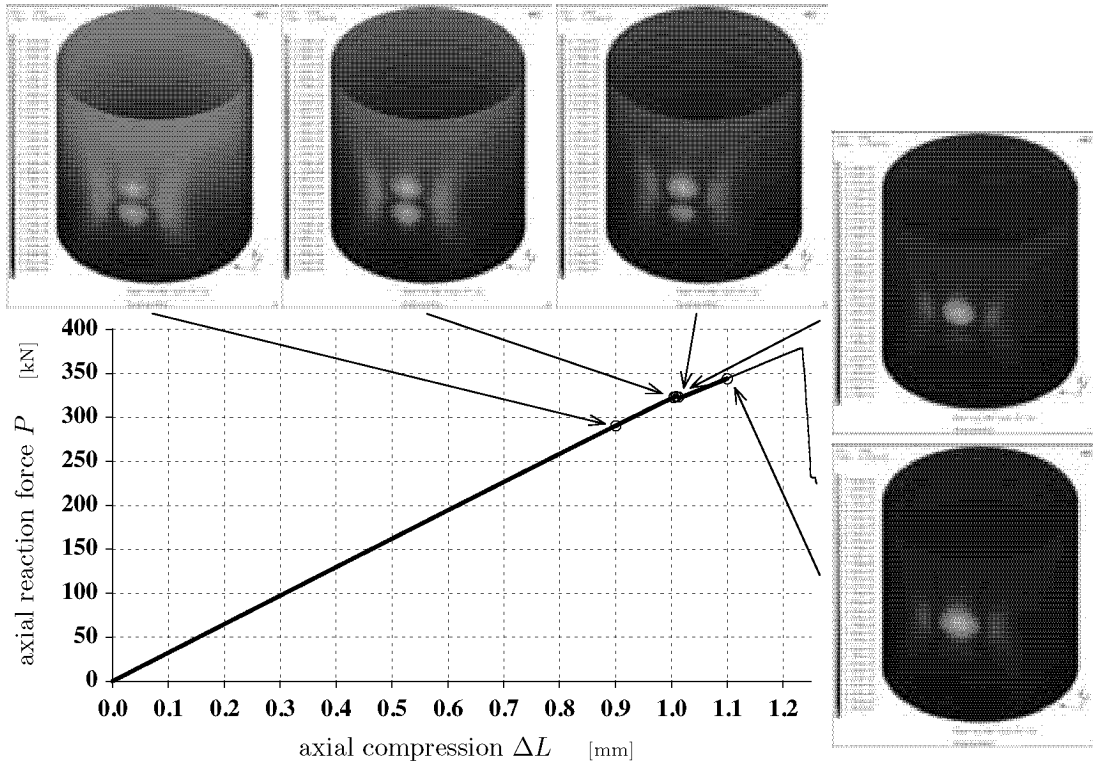


Figure 6.81 A: Result of a transient dynamic analysis for the isotropic cylinder having an outward dimple of initial elevation $w_b/h = -1$. First part with a local instability. The deformations are displayed without magnification, the contour color maps refer to total-displacement vector lengths in metres.

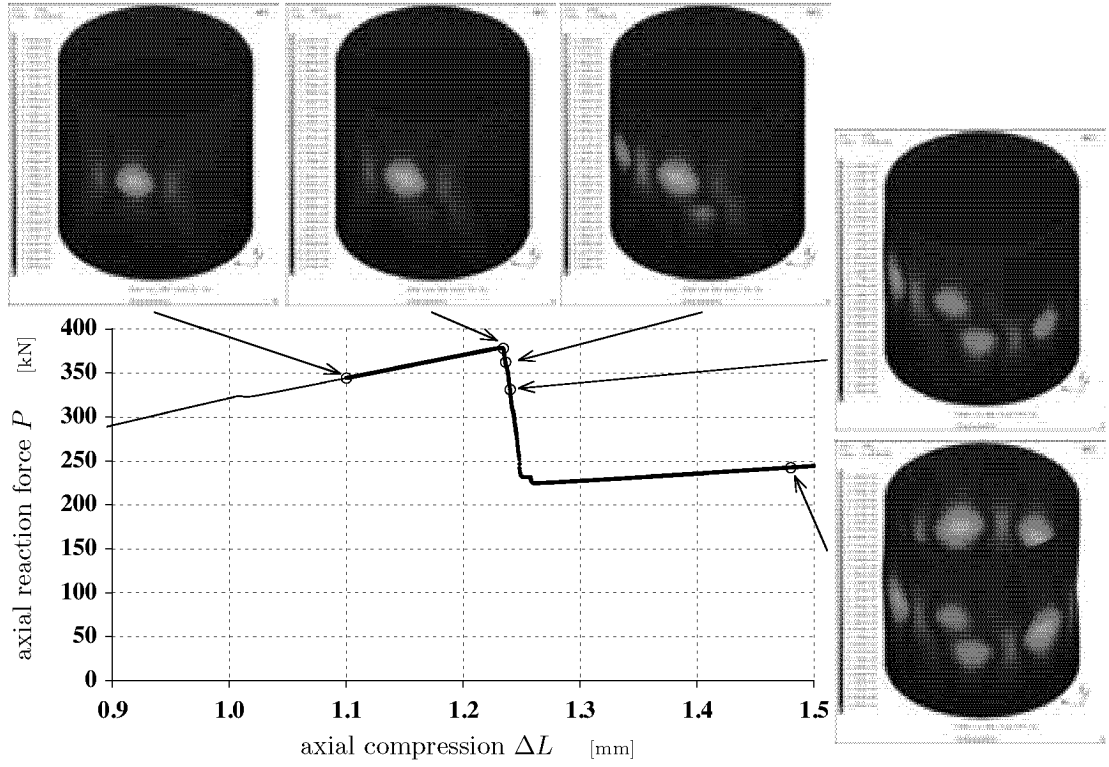


Figure 6.81 B: Continuation to previous figure. Transient dynamic analysis results for a bulge of initial elevation $w_b/h = -1$. Second part with cylinder collapse.

the cylinder in one direction beside the dent above the origin bulge, together with the dimples which settled in the other direction beside the dent below the bulge, finally fill the entire circumference in one spiral row. Then, above and below the initial bulge two staggered dents of almost identical size have come to a rest. This first stable post-buckling pattern with further compression is modified in a way that the apex of the increasing buckles in the row on the right and the left of the origin bulge are axially displaced to the circumference at $L/2$.

Similar to the local buckling behaviour of the previous bulge of half initial elevation $w_b/h = -0.5$, the deformation process which leads to the zigzag course of the P - ΔL -curve and which is shown in Figure 6.81 A for the local buckling corresponds to kind (I) of the two mode replacement-incidents described on page 304. The that following successive deformation process prior to the cylinder collapse and consisting in a lateral displacement of the dent apex above the origin bulge correspond to kind (II).

4. Outward Dimple with Initial Elevation $w_b/h = -1.5$:

The results of a transient dynamic analysis for the reference cylinder having an outward dimple of initial elevation $w_b/h = -1.5$ are depicted in Figure 6.82, again separated in two parts for local buckling and for cylinder collapse. For the bulge on hand, in Figure 6.78, page 303, three different critical load levels are marked. In Figure 6.83 a close-up view of the axial load-compression curve resulting for the transient dynamic analysis shows the peaks or bends which led to the specification of these three particular load levels. The first local buckling incident occurred between an applied axial compression of $\Delta L_{cr} = 1.0$ and 1.02 mm, or at a resulting axial reaction force of about $P_{cr} \approx 323$ kN. The shape of the bend in the P - ΔL -curve found at this load level allowed only a rough estimate of this critical axial reaction force. However, the buckling load obtained with a nonlinear buckling analysis of $P_{cr} = 311$ kN is close to the critical load range of the transient dynamic analysis result. The static analysis with adaptive load step control was again aborted due to the local buckling. The local maximum, i.e. the first lower peak in the P - ΔL -curve of the transient dynamic analysis at an applied axial compression of $\Delta L_{cr L} = 1.11$ mm enabled an accurate determination of a further local buckling load with $P_{cr L} = 347$ kN. Cylinder collapse finally occurred at the maximum reaction force of $P_{cr U} = 364$ kN resulting for an applied end-shortening of $\Delta L_{cr U} = 1.21$ mm.

The first two deformation plots included in Figure 6.82 A reproduce the deformation process responsible for the first local buckling and the bend in the P - ΔL -curve. Similar to the local buckling behaviour of the two

previous bulges again during axial compression above and below the initial bulge dents continuously emerge and deepen. Reaching the critical load the upper dent increases in amplitude whereas the lower dimple decreases. In Figure 6.84 this transformation process is demonstrated by means of the alteration of the radii at the nodal points along the vertical path over the bulge vertex placed at $0.5L$ resulting for axial compressions between $\Delta L = 1$ and 1.3 mm. This process again corresponds to the local buckling of kind (I) described in page 304. The local instability led to a small reduction of the slope of the P - ΔL -curve, i.e. to a slight decrease in axial cylinder stiffness due to the shell-flattening in the upper dent, but for the initial bulge amplitude on hand no zigzag course with an intermediate fall of the reaction force occurred.

The second local buckling incident at about $\Delta L = 1.11$ mm, however, caused such a curve progression with a distinct local maximum. According to the third to the sixth deformation plots in Figure 6.82, this critical load reached, the larger upper dent suddenly is displaced towards the left side of the vertical path over the bulge vertex. The lower dent is also displaced but in opposite direction and re-increases in size. At the end of this local buckling-event the lower staggered dent is also flattened and as large as the upper; the apexes of the two dents are placed in a line tilted about the origin bulge tip. This local deformation process corresponds to kind (II) of local buckling defined above. Due the now wider range with flattened strips and hence of reduced geometric stiffness the axial cylinder stiffness is once again slightly diminished, but the rearranged state is still below the stability limit of the deformed cylinder.

After further compression finally the peak load followed by the total cylinder collapse is reached. The down-fall of the reaction force displayed in Figure 6.82 B is associated with the settlement of new buckles around the cylinder in a row beside the upper dent as well as in a row beside the lower dent. The first stable post-buckling shape is attained when the two rows of formed buckles is united to one hoop of large buckles, which then travel to the centre of the cylinder surface. This pattern resembles the post-buckling pattern of the previous bulge with $w_b/h = -1$ in Figure 6.81 B.

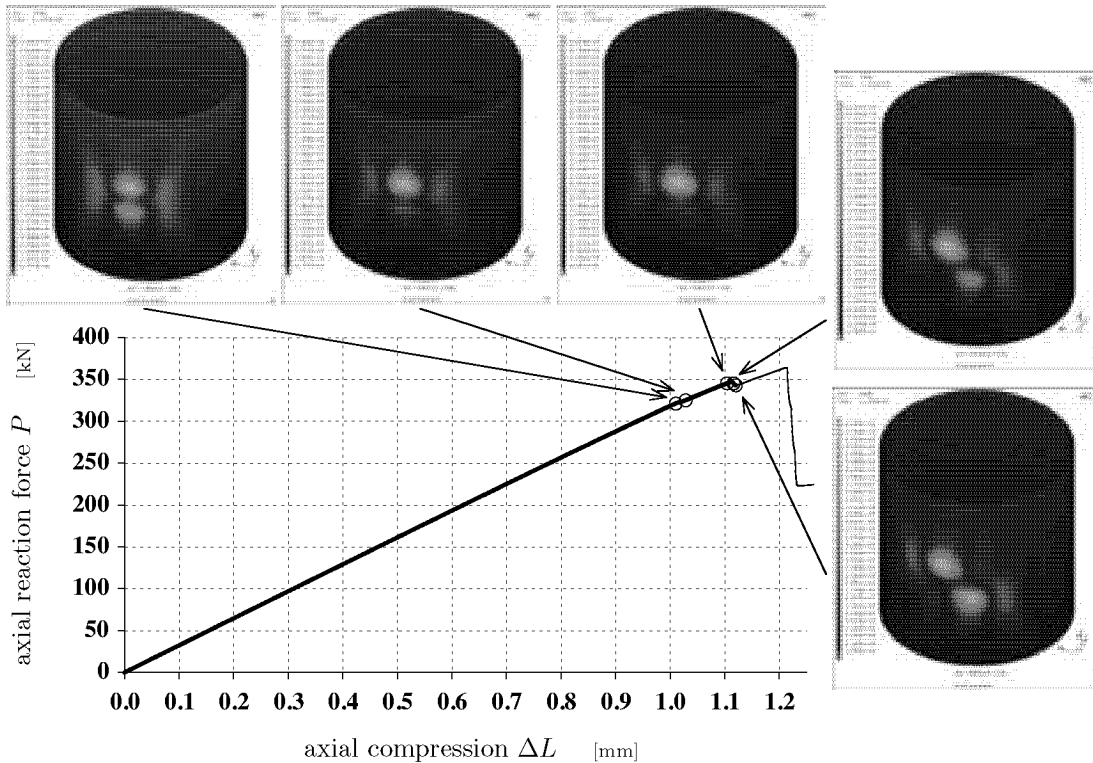


Figure 6.82 A: Result of a transient dynamic analysis for the isotropic cylinder having an outward dimple of initial elevation $w_b/h = -1.5$. First part with two local instabilities. The deformations are displayed without magnification, the contour color maps refer to total-displacement vector lengths in metres.

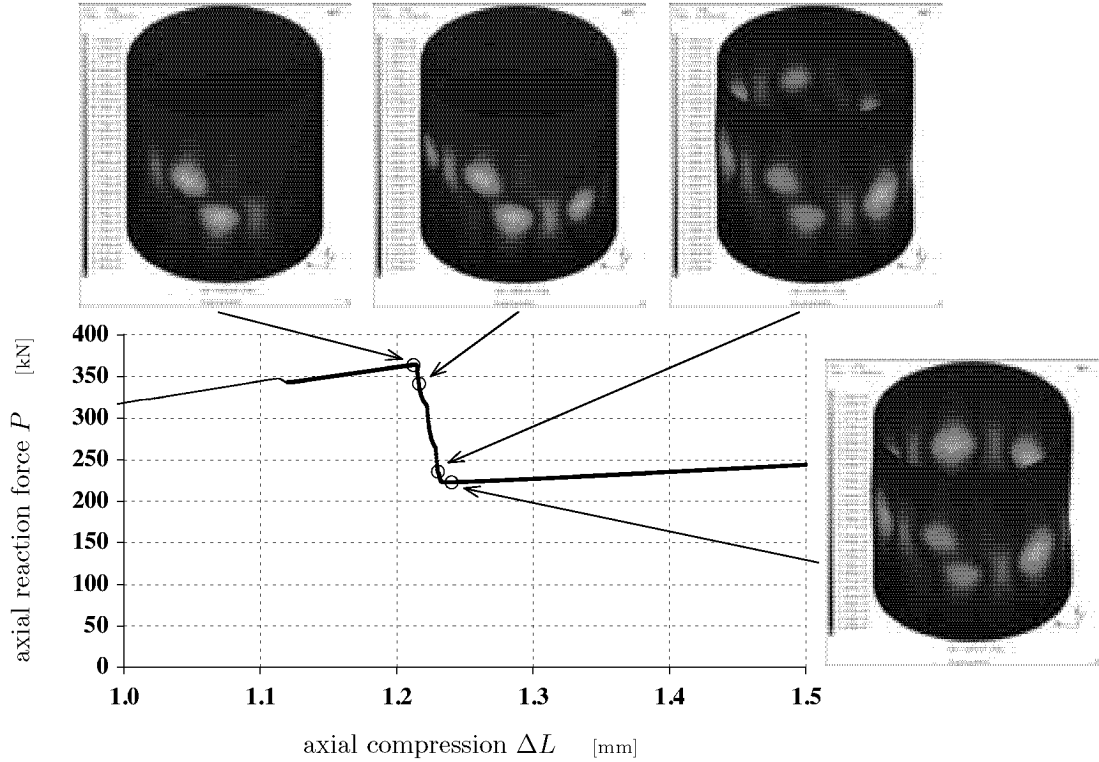


Figure 6.82 B: Continuation to previous figure. Transient dynamic analysis results for a bulge of initial elevation $w_b/h = -1.5$. Second part with cylinder collapse.

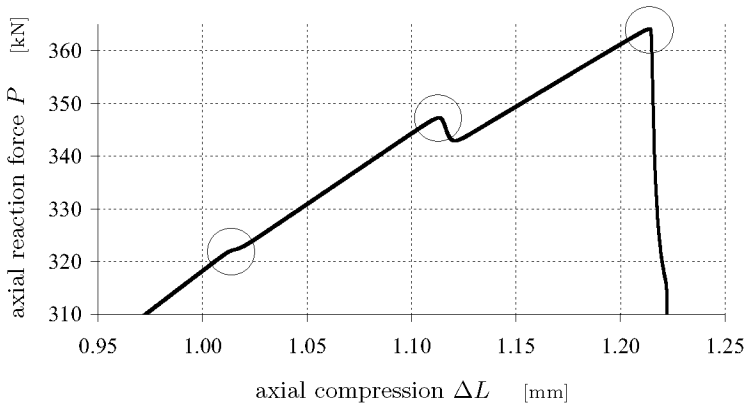


Figure 6.83: Close-up view of the axial force-compression curve resulting for a transient dynamic analysis of the bulge of initial elevation $w_b/h = -1.5$ applied to the reference cylinder. The bend (1st circle) and the first local maximum (2nd circle) in the P - ΔL -curve indicate twice local buckling, the top peak (3rd circle) refers to the cylinder collapse.

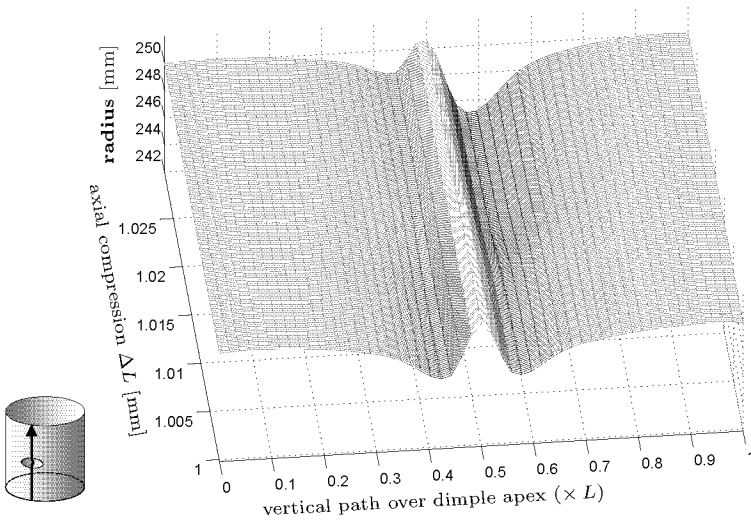


Figure 6.84: Sequenced progressions of the local radii along the vertical path for the bulge with $w_b/h = -1.5$. Local instability with a replacement of the deformation mode prior to cylinder collapse according to the 1st and the 2nd deformation plot in Fig. 6.82 A.

5. Outward Dimple with Initial Elevation $w_b/h = -1.75$:

The results of a transient dynamic analysis for the reference cylinder having a bulge with an initial elevation of $w_b/h = -1.75$ are displayed in Figure 6.85. The axial force-displacement curve has one local maximum stemming from local buckling and a climax indicating total collapse of the cylinder. The local buckling occurred for an axial compression of about $\Delta L_{crL} = 1.04$ mm where with a first resulting axial reaction force of $P_{crL} = 330$ kN a first peak is reached. The analysis yielded a maximum axial force of $P_{crU} = 364$ kN for an applied end-shortening of $\Delta L_{crU} = 1.21$ mm. Again only the lower buckling load P_{crL} could be confirmed by nonlinear buckling analyses, resulting in a critical load of $P_{crL} = 315$ kN, since the static analyses were aborted due to local buckling.

Whilst compression prior to local buckling again two deep dents of similar size are formed which deepen continuously. The first three deformation plots included in Figure 6.85 show that during the local buckling the two dents above and below are displaced aside from the meridian over the bulge tip. The upper, slightly deeper dimple moves counter-clockwise, the lower clockwise. After this process, which corresponds to the kind (II) of local buckling defined in page 304, the axial cylinder stiffness is reduced, probably since the staggered dents mean a widening of the range of partially flattened shell segments with reduced geometric stiffness.

However, due to load rearrangements, with the axial load level after local buckling the stability limit of the locally deformed cylinder is not reached yet enabling further axial compression. The cylinder collapse finally is initiated by the formation of new buckles in a row around the half cylinder circumference beside the upper dent and another beside the lower dent, similar to the collapse of the cylinder with a bulge of initial depth $w_b/h = -1.5$. That is, the deformation process to the first stable post-buckling pattern is accomplished when the two rows are filled with dimples and joint to a single ring.

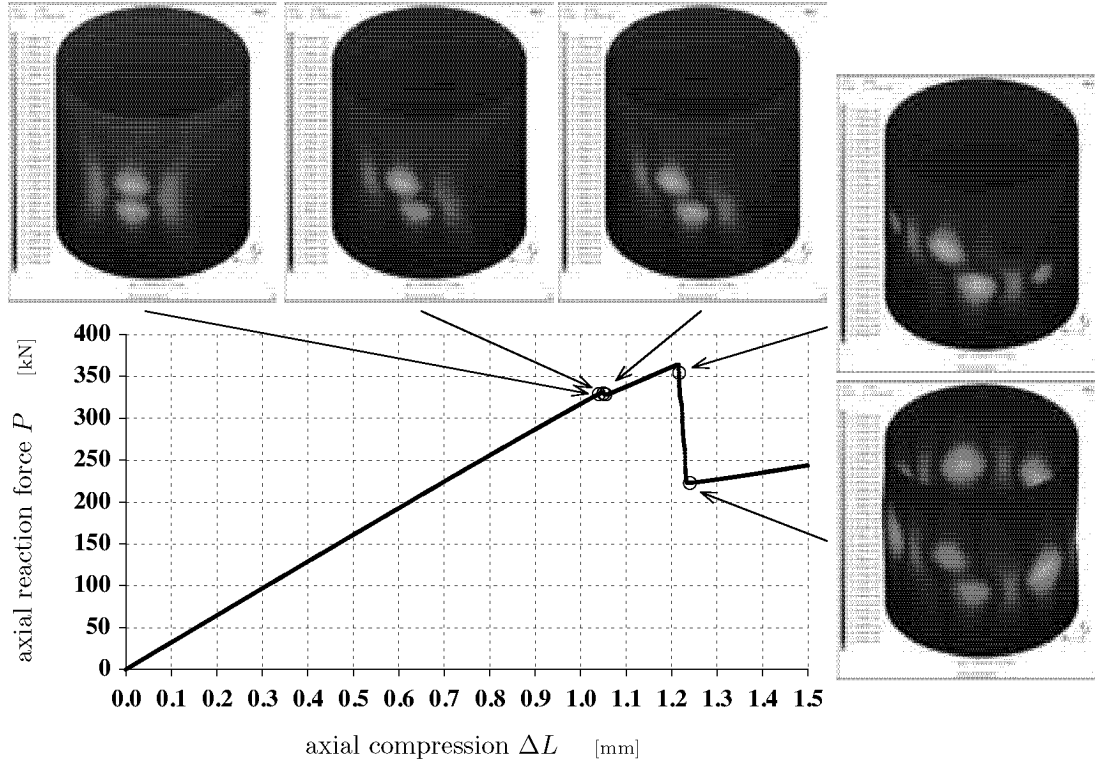


Figure 6.85: Result of a transient dynamic analysis for the isotropic cylinder having an outward dimple of initial elevation $w_b/h = -1.75$. The deformations in the pictures are displayed without magnification, the contour color maps refer to total-displacement vector lengths in metres.

According to the analysis results above two typical buckling modes are involved in the local instability behaviour of isotropic cylinder shells having an initial outward dimple. In the shaded deformation plots of Figure 6.86 these patterns are shown by means of the eigenvectors close to local buckling calculated during nonlinear buckling analyses of the reference cylinder with a bulge of initial elevation (a) $w_b/h = -0.5$ and (b) $w_b/h = -1.75$. The two particular local buckling processes introduced

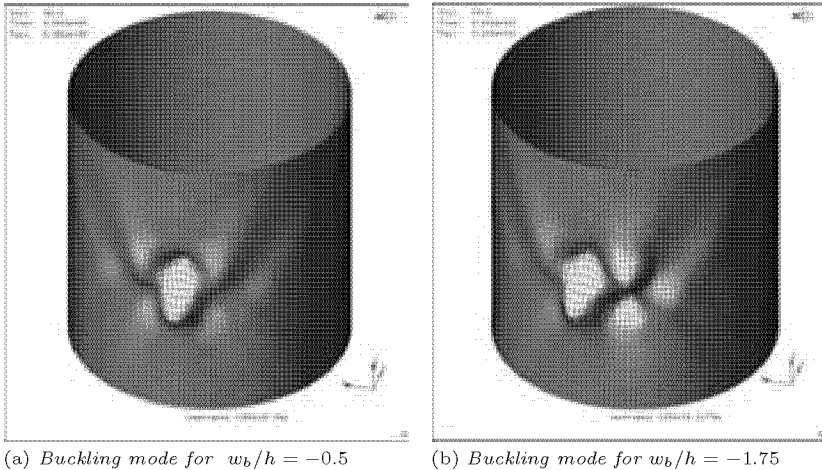


Figure 6.86: *Buckling mode (eigenvector) to the lowest eigenvalue calculated at applied forces close to local buckling of the reference cylinder afflicted with an outward dimple of initial elevation $w_b/h = -0.5$ and -1.75 as indicated.*

in page 304 which were observed in the dynamic transient analysis results above finally end in patterns similar to one of these two buckling modes. Process type (I) leads to a deep inward dimple above the initial bulge according to the buckling mode in 6.86(a). And type (II) ends with a deep dimple again above the initial bulge but laterally shifted in one direction and another below the initial bulge, shifted in opposite direction, similar to the buckling shape in plot (b). During axial loading above and below the initial bulge always an inward dimple is formed. The local buckling behaviour is guided by the manner the depth and the location of the apex of these dents change. Hence the local buckling behaviour of cylinders with an initial bulge resembles that of the cylinder with an initial dent.

The upper inward dimple in Figure 6.86(a) is similar to the dimple of the buckling mode of the cylinder with an dent of initial depth $w_b/h = 0.3$

in Figure 6.40(d), page 6.40. And in fact, the corresponding deformation process above the bulge of initial amplitude $w_b/h = -0.5$ resulting for a dynamic analysis and reproduced in Figure 6.80, page 308, is analogous to that at the dent with $w_b/h = 0.3$, see Figure 6.42 in page 256: the dent is only slightly deepened until at a critical load the dent suddenly snaps inwards to form a flattened shell strip. The upper and the lower pair of inward and outward dimples in Figure 6.86(b), in turn, correspond to the two adjacent dimples in the buckling mode for the cylinder having a deep dent, for instance with an initial depth of $w_b/h = 0.5$ as displayed in Figure 6.40(d), page 254. Also in this case an analogy can be found between the local buckling behaviours resulting for transient dynamic analyses for the cylinder afflicted with a bulge of initial amplitude $w_b/h = -1.75$, see upper cylinder halves in Figure 6.85, and for the longer cylinder with $L = 765$ mm having a dent of initial depth $w_b/h = +1$ shown in Figure 6.65, page 284: prior to this local buckling incident the dents are already deepened and hence similar to a flattened horizontal strip with two peaks of combined axial-tangential compressive loading; the dent apex then suddenly travels laterally towards one of these peaks.

Simultaneous increase in depth of both dents above and below the bulge requires increasing bending about the tangent at the bulge vertex. Thus, this tangent acts rather as a swiveling axes about which the two dimples are tilted in-, respectively outwards. Consequently, in the buckling modes of Figure 6.86 the dimple above the initial bulge is directed inwards, the dimple below outwards, or vice versa. These buckling modes are eigenvectors, hence the (normed) amplitudes are arbitrarily scalable, and the consequences for the formation of such shapes (e.g. strains) are ignored. In contrast to the eigenvectors, the transient dynamic analyses yields amplitudes of outward dimples which are considerably smaller compared to the amplitudes of the dents, since an immoderate local increase of the radius would lead to excessive tangential stretching. But as already mentioned, whilst axially compression and buckling of cylindrical shells rather the bending energy is increased than the strain energy.

Influence of the Cylinder Dimensions L , R , and h

As shown above, the modified nonlinear buckling analyses of the reference cylinder having an outward dimple yielded only one buckling load P_{cr} for some local buckling. Consequently, for bulges of large¹⁰ initial

¹⁰Reference cylinder: 'large' if $w_b/h > -0.5$; see Fig. 6.78, p. 303.

elevations with such static calculations the cylinder collapse load of the shell with rigid endplates simulated remains unknown. But, in contrast to the shells with an initial inward dimple, for the initial bulges the investigation on the influence of the cylinder radius R , the initial cylinder length L , and the shell wall thickness h on the nonlinear buckling analysis results could be limited to the alteration of the lower, local buckling load (P_{crL}).

As for the initial dents, cylinders with identical factor $R \cdot h$ having an initial bulge yielded identical *normalized* buckling loads $P_{cr}/P_{cr id}$ for like *normalized* initial dimple amplitudes w_b/h , see pages 279 ff and Figure 6.62.

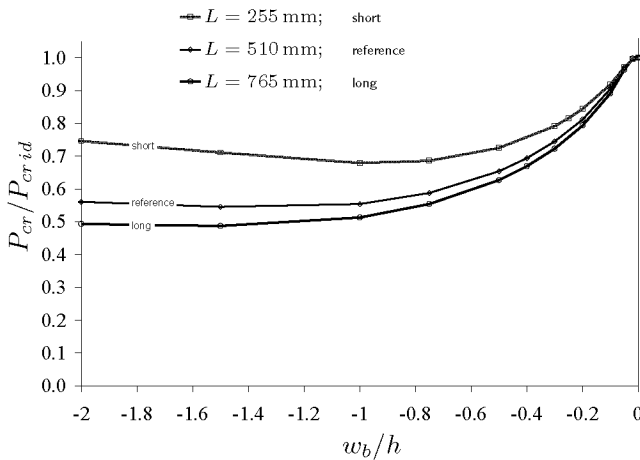


Figure 6.87: Influence of the cylinder length L on the normalized buckling load $P_{cr}/P_{cr id}$ of an isotropic cylinder with a single bulge of various initial elevation $-w_b/h$. Cylinder radius $R = 250$ mm, shell wall thickness $h = 1.5$ mm. Mean initial dimple dimensions $a_b = 180$ mm and $l_b = 68$ mm.

The influence of the cylinder length L on the buckling loads for initial bulges is similar to that for initial dents as detailed in page 281: the distance between the shell edges and the initial dimples at $L/2$ increases with growing initial cylinder length L ; thus, for like axial loading the radial displacements increase as well, and therefore lower buckling loads resulted for longer shells compared to the reference cylinder. In Figure 6.87 the nonlinear buckling analysis results for the reference cylinder with radius $R = 250$ mm, wall thickness $h = 1.5$ mm, and length $L = 510$ mm

are displayed together with the results for cylinders with like R and h but a longer length of $L = 765$ mm, or a smaller length of only $L = 255$ mm. Again, the difference between the normalized buckling loads $P_{cr}/P_{cr id}$ for the reference cylinder (middle curve) and for the 50% shorter cylinder (upper curve) is significantly larger than the difference between the loads of the reference cylinder and the 50% longer cylinder (lower curve).

For initial bulges, the distances between the cylinder collapse load and the local buckling load, see Figure 6.78 in page 303, of the cylinder with initial length $L = 765$ mm are of the same size as those of the reference cylinder, only the initial amplitudes of minimum buckling load are again slightly shifted. Accordingly, no notable difference in the local buckling behaviour of these cylinders in Figure 6.87 could be observed.

Influence of Dimple Width a_b and Height l_b

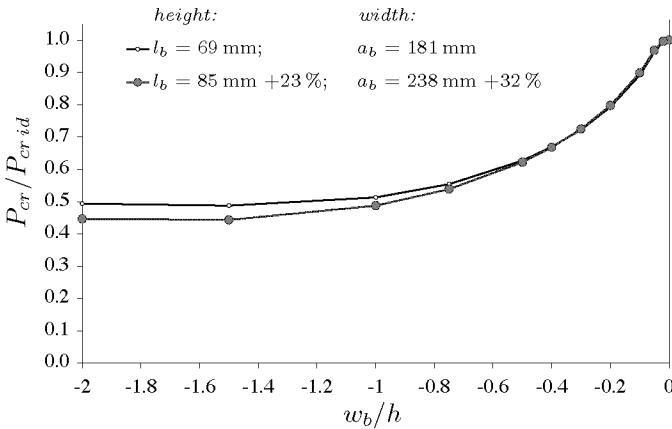


Figure 6.88: Resulting normalized buckling loads $P_{cr}/P_{cr id}$ for the elongated reference cylinder with $L = 765$ mm, $R = 250$ mm, $h = 1.5$ mm, having a single bulge of different initial elevation $-w_b/h$. Comparison between two sets of bulges with initial widths a_b and lengths l_b as indicated; reference dimple with $l_b = 69$ mm and $a_b = 181$ mm.

In Figure 6.88 the normalized buckling loads $P_{cr}/P_{cr id}$ of the cylinder with $L = 765$ mm, $R = 250$ mm, and $h = 1.5$ mm having a single bulge of various initial amplitude w_b/h and either of initial width

$a_b = 181$ mm and height $l_b = 69$ mm, or $a_b = 238$ mm and $l_b = 85$ mm, respectively. The former dimension pair corresponds to the initial circumferential width and meridian height of the inward dimple applied to the cylinder on hand which yielded the minimum nonlinear buckling analysis results for an initial depth of $w_b/h = 0.1$, see Section 6.6.3. The later pair contains the lengths a_b and l_b for an initially 23% longer and 32% wider bulge. Buckling loads resulting for the cylinder with $L = 765$ mm having a single inward dimple with these two sets of initial dimple dimensions are plotted in Figure 6.70, page 292. The effect of an increase of the initial width a_b and the initial height l_b for bulges is notably less important than that of dents, see page 290. Nonlinear buckling analyses of the sized bulge yielded a minimum local buckling load of $P_{cr} = 253$ kN for an initial elevation of $w_b/h = -1.5$, which is a value 9% below that for the bulge with the smaller lateral dimensions, $P_{cr} = 279$ kN. In comparison, the corresponding two sets of dents resulted in a difference between the smallest local buckling loads of about 14%, see Figure 6.70. The upper thin lines in Figure 6.89 show that the effect of a similar expansion of the initial bulge width a_b and height l_b in case of the reference cylinder with $L = 510$ mm is analogous to that of the longer cylinder in Figure 6.88.

The buckling loads in Figure 6.88 are results of nonlinear buckling analyses with adaptive load step control and refer to the loads at which first local buckling occurs. In contrast to the initial dents, as already mentioned, for initial bulges the nonlinear buckling analyses gave no further axial buckling loads beyond these loads which would indicate cylinder collapse. Consequently, only the impact of the bulge-size variations on the local buckling load is apparent. However, the cylinder collapse loads found with transient dynamic analyses for the shell having one of the bulges in the two sets of a_b and l_b confirmed the observation for dents: the differences in the loads $P_{cr}/P_{cr id}$ for like amplitudes w_b/h between the cylinder collapse load of the shells having a bulge with a initial width $a_b = 181$ mm and such with a sized bulge of $a_b = 238$ mm are much smaller compared to the differences between the lower local buckling loads.

As aforementioned, the initial width a_b and heights l_b of the bulges given above correspond to the origin lengths of the inward dimples with a given initial depth w_b (mostly $w_b/h = 0.1$) which yielded the lowest buckling load of the shell involved. According to the results detailed in Section 6.6.3, page 325 ff, shallow dents ($w_b \leq w_b^*$) with widths a_b of only 12% of the cylinder circumference $2\pi R$ tend to result in smaller

buckling loads than any ring-shaped dent, see Figure 6.72 on page 295. But by contrast, outward dimples with initial widths a_b smaller than the cylinder circumference always provoked higher buckling loads than ring-shaped bulges. Figure 6.89 depicts the normalized buckling loads

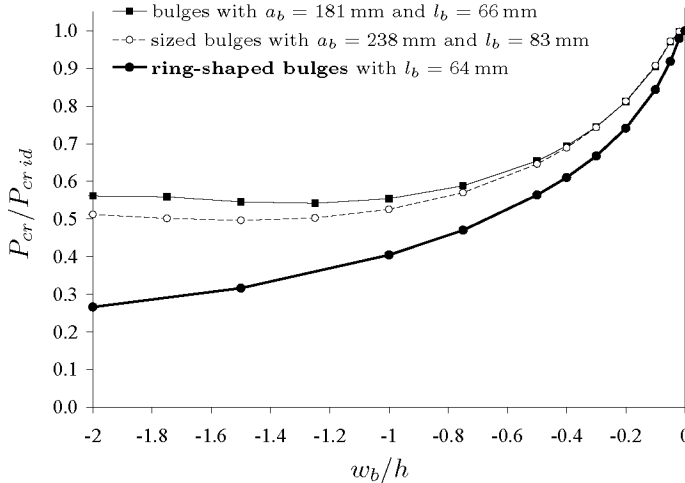


Figure 6.89: Normalized buckling loads $P_{cr}/P_{cr id}$ for the reference cylinder ($L = 510$ mm) with a single bulge of different initial elevation $-w_b/h$. Comparison between results for a ring-shaped bulge (bold line) and bulges with initial circumferential widths a_b as indicated.

$P_{cr}/P_{cr id}$ of the reference cylinder having a single bulge with initial elevations w_b/h between 0 and -2 and initial widths a_b and heights l_b as indicated. The critical loads along the bold line resulted for the cylinder with a single axisymmetric bulge. It can be seen that the buckling loads of the ring-shaped bulge are always below those of the dimples with an initial width of $a_b = 181$ mm as well as of $a_b = 238$ mm (compare with Fig. 6.72, page 295).

Influence of the isotropic material parameters E and ν

As explicated for inward dimples in Section 6.6.1, page 294 ff, the influence of the YOUNG'S modulus on the buckling analysis results of the isotropic cylinders having a single dent is negligible. According to a few analysis results, this applies also for isotropic cylinders with a single

bulge.

The behaviour of an isotropic cylinder with a POISSON'S ratio of $\nu = 0$ having a single bulge is analogous to such a cylinder having a single dent, see page 6.6.1 ff; and also the differences between the buckling loads resulting for $\nu = 0$ and $\nu = 0.3$ correspond to those for dents.

6.6.3 Lateral Dimensions of Dimples Provoking Minimal Cylinder Stability

In the previous sections the buckling behaviour and the critical loads of axially compressed isotropic cylindrical shells with a single inward or outward dimple depending on the initial amplitude w_b of the dimple were discussed. The initial meridian height l_b and the initial circumferential width a_b of these dents or bulges were considered given measures for the selected cylinder dimensions R , L , and h . This section deals with the results of scores of nonlinear buckling analyses which yielded these initial dimple widths and heights used for a number of isotropic cylinders of different length, radius and wall thickness.

The **initial height** $l_{\bar{b}}$ and the **initial width** $a_{\bar{b}}$ are defined herein as the meridian height l_b and the circumferential width a_b of a single dimple with a pre-selected amplitude w_b which resulted in the lowest buckling load P_{cr} of an axially compressed circular cylinder with this dimple and otherwise perfect geometry:

$$\text{initial height} \quad l_{\bar{b}}(w_b) := \min_{l_b} \{P_{cr}(l_b, a_b, w_b)\} \quad (6.9)$$

$$\text{initial width} \quad a_{\bar{b}}(w_b) := \min_{a_b} \{P_{cr}(l_b, a_b, w_b)\} \quad (6.10)$$

The initial dimple height l_b as well as the initial dimple width a_b are free parameters of a "double cosine-dimple" as defined in Section 6.2, page 196.

Without any numerical analysis which considers geometric nonlinearities the continuous radial displacements *during* the axial compression of a cylinder having a single dimple may not be quantified accurately. Further, there was no obvious indication given by the *initial* cylinder and dimple geometry for an analytical approach of the searched initial dent dimensions provoking minimal cylinder stability. The minimum searches were therefore performed by means of nonlinear buckling analyses varying iteratively either the initial dimple height l_b or the dimple width a_b for each preselected initial dimple amplitude w_b .

The dependence of initial dimple amplitude w_b and the cylinder dimensions L, R, h on the “pessimism lengths” $l_{\bar{b}}$ and $a_{\bar{b}}$ is different for inward and for outward dimples. Thus, again first the search for the $l_{\bar{b}}$ and the $a_{\bar{b}}$ of inward dimples is detailed. That of bulges will follow on page 326. In contrast to isotropic cylinders, the buckling behaviour of laminated cylinders depends strongly on the material parameters, and so for laminated cylinders the lengths $a_{\bar{b}}$ and $l_{\bar{b}}$ also vary not only with different cylinder dimensions and initial dimple amplitude but also with the laminate stacking; thus, the behaviour of single dimples in laminated cylinders is dealt with separately in Section 6.7, page 445.

According to the results the initial height $l_{\bar{b}}$ as well as the initial width $a_{\bar{b}}$ of a dimple in a cylinder are different from zero also for vanishing initial dimple amplitude. It was found that these dimple dimensions are correlated with the analytical wavelength of axisymmetric cylinder buckling $2l_c$. This wavelength may be understood as eigenvalue which is characteristic for an isotropic cylinder and which is independent of the buckle amplitude. Consequently, the initial dimple height $l_{\bar{b}}$ and width $a_{\bar{b}}$ may be interpreted as eigenvalues of a particular cylinder with a single cosine-shaped dimple of a particular initial amplitude.

Nonlinear buckling analyses of cylinders having dimples with initial depths w_b/h less than 0.05 resulted in buckling loads P_{cr} almost identical to those of the perfect cylinder $P_{cr id}$. Therefore, with load variations within the range of the those due to general numerical discrepancies accurate minimum searches for the initial dimple height $l_{\bar{b}}$ and width $a_{\bar{b}}$ were ruled out.

Isotropic Cylinders with Inward Dimples

In Figure 6.90 the results of nonlinear buckling analyses of the isotropic reference cylinder with $R = 250$ mm, $L = 510$ and $h = 1.5$ having an single inward dimple of fixed initial depth (a) $w_b/h = 0.1$ and (b) $w_b/h = 0.3$ with different initial meridian heights l_b and initial circumferential widths a_b are reproduced. The shaded surfaces represent the buckling loads of the shells normalized with respect to the perfect reference cylinder, $P_{cr}/P_{cr id}$, plotted over the matrix of the varied lateral dimple dimensions l_b and a_b . For a better visibility only values for dents with a height l_b smaller than a half of the cylinder length and a width a_b smaller than a half of the cylinder circumference are shown. The thick lines in the contour plots below these surfaces refer to lateral dent

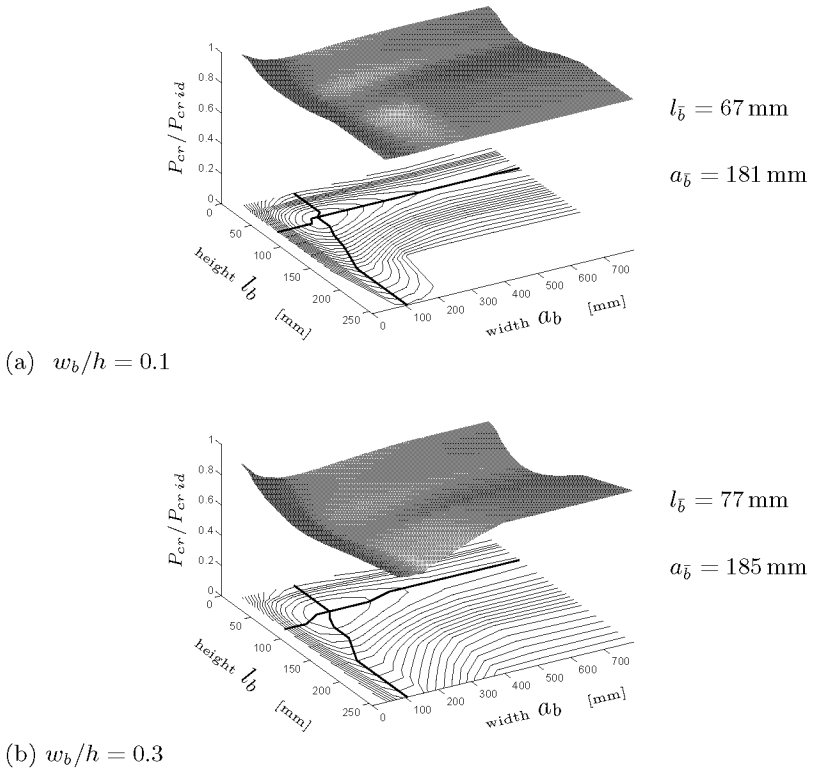


Figure 6.90: Normalized buckling loads $P_{cr}/P_{cr,isd}$ of the isotropic reference cylinder having a single dent of initial depth (a) $w_b/h = 0.1$ or (b) $w_b/h = 0.3$ with different lateral initial meridian heights l_b and initial circumferential widths a_b . Thick lines in the contour plots refer to l_b and a_b which give minimal buckling loads.

dimensions which give the largest impact to the axial cylinder stability. Their intersection points, in the minimum of the shaded surface, finally yield the searched values for the initial height $l_{\bar{b}}$ and width $a_{\bar{b}}$ of a single dent for the given cylinder dimensions and the given initial dimple depth w_b that results in the smallest buckling resistance.

To reduce the analysis effort not all combinations of the lateral dimple dimensions were calculated for all considered cylinders as it was done for the reference shell. The thick “minimum lines” in the contour plots of Figure 6.90 for varied widths a_b are quite straight. Thus, for each cylinder and each given initial depth w_b first the extremal value of the meridian height for an initially estimated extremal value of the width was iteratively searched. With the initial height $l_{\bar{b}}$ found this way, the extremal value for the length $a_{\bar{b}}$ was deduced. That is, any interdependence of the two lateral dimensions were neglected. This assumption is not totally correct, since the thick lines are neither perpendicular nor straight. Therefore, in cases with solutions for the “pessimum width” $l_{\bar{b}}$ far from the initially estimated value the search procedure was reiterated. This procedure was not very elaborate but nevertheless quite time-consuming, since to obtain the searched lengths $l_{\bar{b}}$ and $a_{\bar{b}}$ with good accuracy together more than twenty nonlinear buckling analyses were needed for each cylinder and each initial depth w_b considered.

In Figure 6.91 the dependency of the buckling load on the initial meridian dent height l_b for the reference cylinder having an single inward buckle with a given initial depth $w_b/h = 0.3$ and a fixed initial width $2\pi R/a_b = 8.0$ (8.4 in enclosed chart) is shown. The minimal buckling load may be found at l_b between 10 and 20 percent of the cylinder length L , which corresponds to 5 to 10 full waves in axial direction. In order to obtain accurate solutions for the searched extremal values, the investigated variable was split at each case to get ten to twenty sampling points with increments which close to the minimum are smaller than one percent of the cylinder length or of its circumference. The black circles in the curves of Figure 6.91 mark the buckling loads P_{cr} yielded for the dent with dimensions pursuant to the values at the sampling points. In the included close-up about the minimum value $l_{\bar{b}}$ the distances between these points are 1/10 or 1/20 of the number of full waves L/l_b in axial direction. In the case on hand, the meridian length referring to the minimum value was found at $l_{\bar{b}} = 77$ mm or $L/l_{\bar{b}} = 6.65$.

In search of the extremal values of the initial width of dents $a_{\bar{b}}$ it was proceeded similarly to those of the initial height $l_{\bar{b}}$. In Figure 6.92 the nonlinear buckling loads of the cylinder above having an inward dimple again

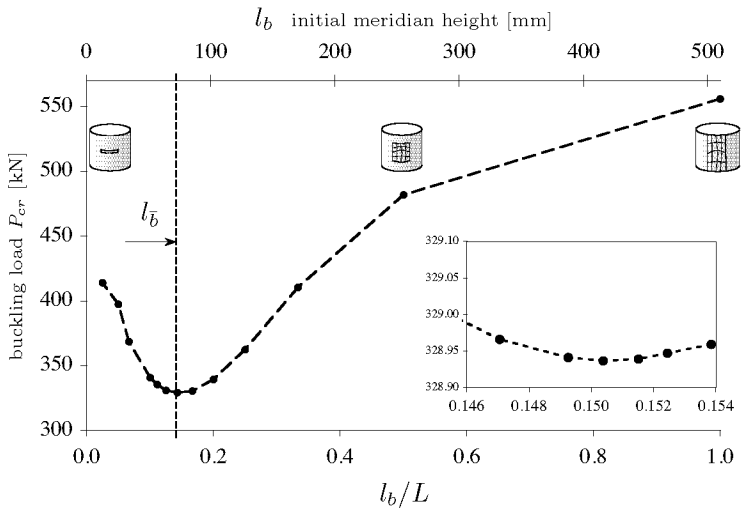


Figure 6.91: Buckling loads of an isotropic cylinder having a single dent with an initial depth of $w_b/h = 0.3$, a fixed initial width $2\pi R/a_b = 8.0$ (8.4 in included chart) and a variable initial height l_b .

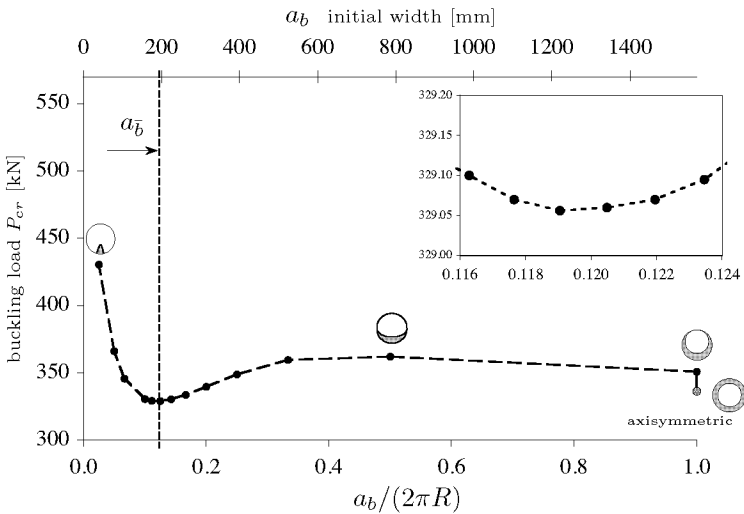


Figure 6.92: Buckling loads of the reference cylinder having a dent with a given initial depth $w_b/h = 0.3$, a given initial height $L/l_b = 7.0$ and a variable initial width a_b .

with a given initial depth $w_b/h = 0.3$, a given initial height $L/l_b = 7.0$, but variable initial widths a_b are reproduced. Worth mentioning that a dent with one full wave in circumference, i.e. with an initial width a_b equal to the cylinder circumference, is four percent less damaging than the axisymmetric, ring-shaped dimple. For clarification some icons, showing the particular cylinder plan views, are included. It is of vital importance that in cases with inward dents two minimal values may be identified: one minimal buckling load exists for an inward axisymmetric dent, marked with a gray circle, and another at about 10 percent of the cylinder circumference. For the latter minimum value at $a_{\bar{b}} = 184\text{ mm}$ or $2\pi R/a_b = 8.5$, again a close-up is included in Figure 6.92.

In Table 6.3 the resulting initial meridian heights $l_{\bar{b}}$ and the initial circumferential widths $a_{\bar{b}}$ of a single dent with an initial depth $w_b/h = 0.1$ are listed. Every table row refers to an isotropic cylinder with length L , radius R , and wall thickness h , whose buckling loads due to the applied dent with $w_b/h = 0.1$ and the indicated lengths $l_{\bar{b}}$ and $a_{\bar{b}}$ were reduced the most. The finite element modeling of these aluminium cylinders are listed in Table 4.1 in Section 4.1.1 on page 120. The respective buckling loads of the cylinders without any imperfection P_{crit} may be found in Table 4.2 in Section 4.2.1 on page 128. The shells cover a range of the radius/wall thickness ratio R/h from 100 to 1333 and a range of the length/radius ratio L/R from 0.38 to 5.1. BATDORF's geometry parameter Z in the seventh table column ranges between 57 and 2544 for a general POISSON's ratio of $\nu = 0.3$. From the table finally also the wavelengths $2l_c$ of the classical axisymmetrical buckling mode of the listed cylinders can be taken, see Section 2.2.2.

In the following first the resulting initial dent heights $l_{\bar{b}}$ in the table above and their predictions are commented. Subsequently the resulting initial dent widths $a_{\bar{b}}$ and their predictions will be discussed similarly.

Initial dent heights $l_{\bar{b}}$:

The resulting initial dent heights $l_{\bar{b}}$ provoking minimal buckling loads of the cylinders having a dent with initial depth $w_b/h = 0.1$ in Table 6.3 are almost equal to the analytical wavelength $2l_c$ for axisymmetrical buckling; that is: $l_{\bar{b}}/2l_c \approx 1.0$. However, for deeper initial dent depths w_b/h the dent-height/wavelength ratio $l_{\bar{b}}/2l_c$ is slightly higher. In Figure 6.93 the ratio $l_{\bar{b}}/2l_c$ versus the initial normalized dent depth w_b/h is plotted for some of the isotropic cylinders in Table 6.3 above. The thick trend line follows the results of an empirical formula for the

R [mm]	h [mm]	L [mm]	$\frac{R}{h}$	$\frac{L}{R}$	Z	$2l_c$ [mm]	initial dent height				initial dent width			
							l_b^* [mm]	$\frac{l_b^*}{2l_c}$	formula	l_b^* Δl_h	a_b^* [mm]	$\frac{a_b^*}{2l_c}$	formula	a_b^* Δa_h
187.5	0.75	510	250	2.72	1764	41.0	40	0.99	42	-2.7 %	113	2.76	111	1.88 %
250	0.75	510	333	2.04	1323	47.3	47	0.99	48	-2.6 %	129	2.72	127	1.11 %
375	0.75	510	500	1.36	882	58.0	58	1.00	59	-1.5 %	156	2.69	155	0.87 %
500	0.75	510	667	1.02	662	66.9	66	0.99	68	-2.5 %	181	2.70	178	1.50 %
750	0.75	510	1000	0.68	441	82.0	85	1.04	83	2.2 %	220	2.69	217	1.50 %
1000	0.75	510	1333	0.51	331	94.7	98	1.04	96	2.1 %	253	2.68	250	1.34 %
100	1	510	100	5.10	2481	34.6	34	0.99	35	-2.4 %	94	2.71	95	-1.29 %
187.5	1	510	188	2.72	1323	47.3	47	0.99	48	-2.6 %	127	2.68	127	-0.53 %
250	1	510	250	2.04	992	54.7	54	0.99	55	-2.2 %	150	2.74	146	2.37 %
375	1	510	375	1.36	662	66.9	66	0.99	68	-2.5 %	181	2.70	178	1.50 %
500	1	510	500	1.02	496	77.3	80	1.03	78	1.6 %	207	2.67	205	0.94 %
750	1	510	750	0.68	331	94.7	98	1.04	96	2.1 %	252	2.66	250	0.80 %
1000	1	510	1000	0.51	248	109.3	109	0.99	111	-2.2 %	286	2.61	288	-0.91 %
187.5	1.5	510	125	2.72	882	58.0	58	1.00	59	-1.5 %	155	2.67	155	0.21 %
250	1.5	510	167	2.04	662	66.9	67	1.00	68	-1.9 %	181	2.70	178	1.50 %
187.5	1	382.5	188	2.04	744	47.3	50	1.05	48	3.4 %	124	2.62	126	-1.56 %
250	1	382.5	250	1.53	558	54.7	55	1.00	55	-1.5 %	145	2.66	145	0.34 %
375	1	382.5	375	1.02	372	66.9	70	1.04	68	2.4 %	177	2.65	177	0.14 %
500	1	382.5	500	0.77	279	77.3	77	0.99	78	-2.5 %	203	2.62	204	-0.61 %
750	1	382.5	750	0.51	186	94.7	98	1.04	96	2.1 %	244	2.58	249	-2.06 %
1000	1	382.5	1000	0.38	140	109.3	106	0.97	111	-4.2 %	296	2.71	288	3.04 %
250	1.5	255	167	1.02	165	66.9	65	0.98	68	-3.8 %	176	2.64	176	0.16 %
250	1.5	382.5	167	1.53	372	66.9	70	1.04	68	2.4 %	176	2.64	177	-0.24 %
250	1.5	510	167	2.04	662	66.9	67	1.00	68	-1.9 %	181	2.70	178	1.50 %
250	1.5	765	167	3.06	1489	66.9	69	1.03	68	1.4 %	183	2.73	181	1.11 %
250	1.5	1000	167	4.00	2544	66.9	69	1.04	68	2.2 %	183	2.73	184	-0.83 %
375	1	150	375	0.40	57	66.9	68	1.02	68	0.4 %	162	2.43	176	-7.60 %
375	1	200	375	0.53	102	66.9	67	1.00	68	-1.9 %	175	2.61	176	-0.84 %
375	1	255	375	0.68	165	66.9	65	0.98	68	-3.8 %	177	2.65	176	0.53 %
375	1	300	375	0.80	229	66.9	67	1.00	68	-1.9 %	171	2.55	176	-3.23 %
375	1	382.5	375	1.02	372	66.9	70	1.04	68	2.4 %	177	2.65	177	0.14 %
375	1	450	375	1.20	515	66.9	66	0.99	68	-2.6 %	177	2.65	177	-0.13 %
375	1	510	375	1.36	662	66.9	66	0.99	68	-2.5 %	181	2.70	178	1.50 %
375	1	600	375	1.60	916	66.9	70	1.04	68	2.7 %	178	2.67	179	-0.13 %
375	1	765	375	2.04	1489	66.9	69	1.03	68	1.4 %	184	2.75	181	1.90 %
375	1	1000	375	2.67	2544	66.9	69	1.03	68	1.5 %	183	2.73	184	-0.83 %
500	0.75	255	667	0.51	165	66.9	65	0.98	68	-3.8 %	176	2.64	176	0.16 %
500	0.75	382.5	667	0.77	372	66.9	70	1.04	68	2.4 %	178	2.67	177	0.90 %
500	0.75	510	667	1.02	662	66.9	66	0.99	68	-2.5 %	181	2.70	178	1.50 %
500	0.75	765	667	1.53	1489	66.9	69	1.03	68	1.4 %	184	2.74	181	1.70 %

see Figure 6.7, page 197;

$$Z = \frac{L^2}{Rh} \sqrt{1 - \nu^2} ; \quad 2l_c = \frac{2\pi}{[12(1-\nu^2)]^{1/4}} \sqrt{Rh} \approx 3.46\sqrt{Rh} \quad (\nu = 0.3)$$

Table 6.3: Lateral initial lengths a_b^* and l_b^* of a single inward dimple of initial depth $w_b/h = 0.1$ which provokes a minimal buckling load for divers isotropic cylinders. See also Table 4.1 and 4.2.

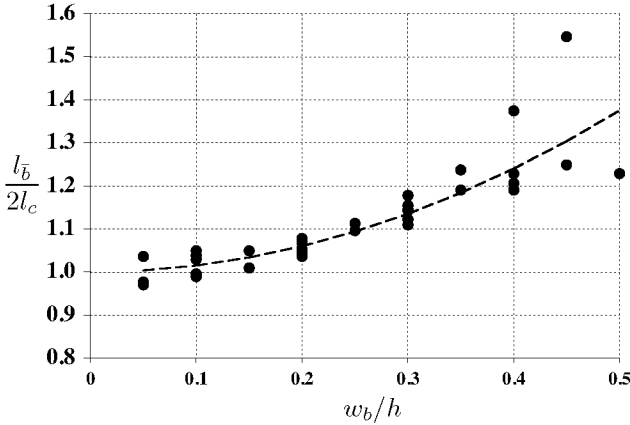


Figure 6.93: Ratio of the initial dent height $l_{\bar{b}}$ to the classical axial wavelength $2l_c$ subject to the initial normalized dent depth w_b/h . Results for six isotropic cylinders of different radius, length and wall thickness.

ratios of the initial dent heights $l_{\bar{b}}^*$ to the wavelength $2l_c$. This formula is given by the following parabolic function:

$$\frac{l_{\bar{b}}^*}{2l_c} = 1.0 + 1.5 \left(\frac{w_b}{h} \right)^2 \quad \forall \quad 0 < w_b < w_b^* \quad (6.11)$$

The lengths $l_{\bar{b}}^*$ approximate the initial heights $l_{\bar{b}}$ which result for *shallow dents*, i.e. for dents with initial depths w_b not deeper than the marginal depth w_b^* . For dents initially deeper than the respective marginal depths w_b^* inconsistent results for the searched initial dent heights $l_{\bar{b}}$ were obtained.

Figure 6.94 displays the marginal depths w_b^* which resulted for dents with lateral dimensions specified for an initial depth of $w_b/h = 0.1$ (black), subject to BATDORF’s parameter Z of some cylinders to which these dents were applied. According to the gray circlelets for dents with 24% longer initial heights l_b and 32% longer initial widths a_b marginal depths w_b^* resulted which are about $0.05h$ deeper. Hence, the marginal depth w_b^* which serves as application range of the formula for the initial dent height $l_{\bar{b}}$ depends also on this length $l_{\bar{b}}$, albeit in a weak way. Though longer initial dent heights led to lower minimum buckling loads $P_{cr \text{ MIN}}/P_{cr \text{ id}}$, the consideration of the trend line along the smaller depths in Figure 6.94 is preferable for an estimate of the marginal depth w_b^* . Figure 6.95 includes the relative deviations $\Delta l_{\bar{b}}$ of the initial dent heights

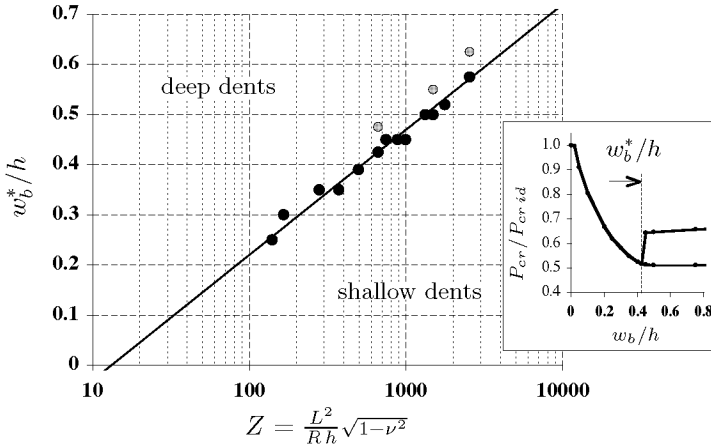


Figure 6.94: Marginal initial depths for shallow dents w_b^*/h versus Batdorf's cylinder parameter Z . Results of nonlinear buckling analyses for some cylinders having a dent with lengths l_b and a_b specified for $w_b/h = 0.1$ (black) or for a dent with a 32 % longer initial width a_b and a 24 % longer initial height l_b (gray).

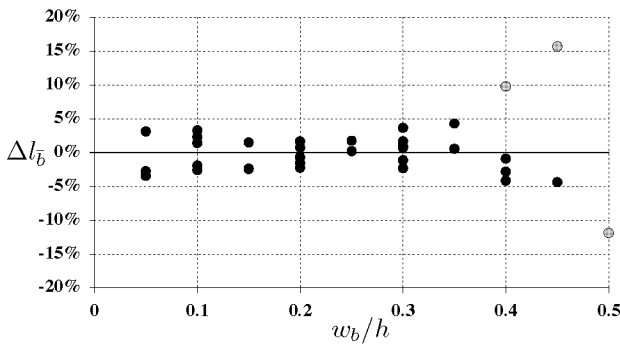


Figure 6.95: Relative deviations Δl_b of the initial dent heights l_b in Fig. 6.93 from the dent heights $l_b^*(w_b^2)$, calculated by means of Equation (6.11), in dependence on the initial dent depth w_b/h .

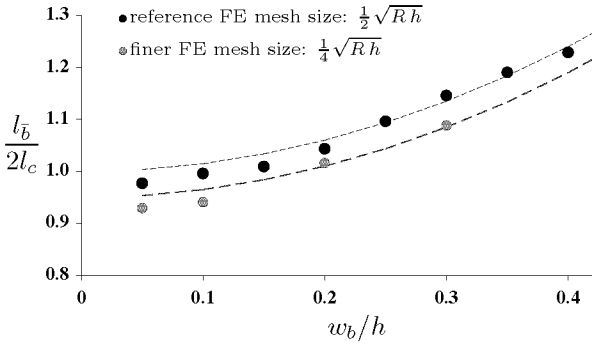


Figure 6.96: Ratio of the initial dent height $l_{\bar{b}}$ to the wavelength $2l_c$ versus the initial dent depth w_b/h for the reference cylinder within the respective application range $w_b < w_b^*$ of the formula $l_{\bar{b}}^*(w_b^*)$ (dashed lines). Results for the standard FE mesh size (black dots) and for a finer mesh size (gray dots) as indicated.

$l_{\bar{b}}$ in Figure 6.93 from the dent heights $l_{\bar{b}}^*$ calculated with Equation (6.11). The bold dots refer to good results with deviations smaller than $\pm 5\%$, whereas the gray markers stand for values with larger differences between prediction and analysis result. The two upper gray dots mark the results for a cylinder with $Z = 279$ and $w_b^*/h = 0.35$, the two lower those for the reference cylinder with $Z = 662$ and $w_b^*/h = 0.425$. Thus, these dent heights with larger deviations ($|\Delta l_{\bar{b}}| \gg 5\%$) exceed the application range $w_b < w_b^*$ for the estimation of the dent height with the formula. For *shallow dents* however the parabolic function in (6.11) yields feasible estimates $l_{\bar{b}}^*$ of the initial meridian heights achievable with nonlinear buckling analyses $l_{\bar{b}}$.

The repetition of the minimum searches for the initial dent height $l_{\bar{b}}$ for the reference cylinder with a finer element mesh size of half the standard size yielded results which confirmed the parabolic progression of the dent-height/wavelength ratio $l_{\bar{b}}/2l_c$ with increasing initial dent depth w_b/h in Figure 6.93. Figure 6.96 shows the ratio of the initial dent height $l_{\bar{b}}$ to the classical axial wavelength $2l_c$ subject to the initial dent depth w_b/h for the reference cylinder and initial dent depths within the application range for this shell ($0 < w_b < 0.425h$). The black dots and the black curve refer to dent heights which were obtained with the standard element mesh size of $0.5\sqrt{Rh}$, whereas the gray dots below mark heights that resulted for a finer mesh of half the element-edge

length: $0.25\sqrt{Rh}$. The heights $l_{\bar{b}}$ resulting for the finer mesh are about 5% shorter than those yielded with the “standard” FE model. The bold dashed line corresponds to the adapted parabolic trend curve for the predicted dent heights $l_{\bar{b}}^*$ for the finer mesh with a constant term (vertical shift) of 0.95 instead of 1.0 in Equation (6.11). Mentionable that the buckling loads P_{cr} resulting for nonlinear buckling analysis with the finer mesh were less than 5% below those obtained with the standard element mesh size, see Section 6.6.7.

The longer initial heights $l_{\bar{b}}$ for a dent with deeper initial depth w_b and also the lower minimum buckling loads resulting for the finer element mesh might be explained with the different initial axial curvatures in the dent with the cosine profile and its more or less coarse discretization with bi-linear finite elements, see Figure 6.8 on page 201: a smaller initial dimple height l_b for a given initial depth w_b/h , for example, leads to smaller initial axial curvatures in the dent; but, changing the axial curvatures and the position of the element nodes along the curved shell means a modification of the states of stress and hence also of the damaging effect of the dents; therefore, depending on the initial dent depth and the element mesh size the length $l_{\bar{b}}$ corresponds to dent height which yielded the axial curvatures with the states of stress damaging the axial stability of the cylinder FE-model the most.

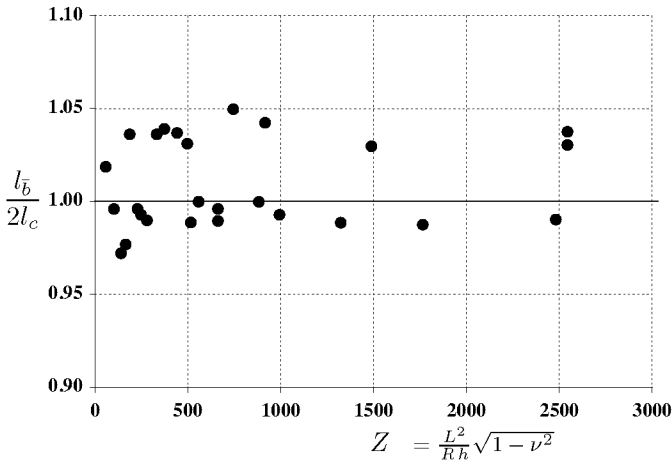


Figure 6.97: Ratio of the initial dent height $l_{\bar{b}}$ to the classical axial wavelength $2l_c$ versus Batdorf's parameter Z . Results for a dent of initial depth $w_b/h = 0.1$ and the isotropic cylinders in Table 6.3.

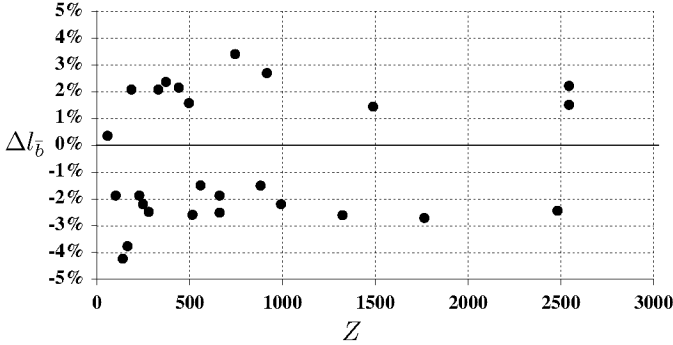


Figure 6.98: Comparison between the initial dent heights $l_{\bar{b}}$ in Fig. 6.97 and the dent heights approximated with $l_{\bar{b}}^* = 1.015 \cdot 2l_c$ for an initial dent depth $w_b/h = 0.1$. Relative deviations $\Delta l_{\bar{b}}$ subject to Batdorf's cylinder parameter Z .

While the application range of the formula for the initial dent height $l_{\bar{b}}$ in Equation (6.11) depends also on the length L of the isotropic cylinder to which the dent is applied, the estimate of the ratio of the dent height to the axial wavelength $l_{\bar{b}}^*/2l_c$ is solely a parabolic function of the initial dent depth normalized with respect to the wall thickness, w_b/h . In Figure 6.97 the dent-height/wavelength ratio $l_{\bar{b}}/2l_c$ for a dent of initial depth $w_b/h = 0.1$ are displayed in dependence of BATDORF's geometry parameter Z for the isotropic cylinders listed in Table 6.3. With Equation (6.11) for standard FE models, the initial depth $w_b/h = 0.1$ on hand, leads to predicted initial dent heights $l_{\bar{b}}^*$ almost equal to the classical axial wavelength; thus: $l_{\bar{b}}^* = 1.015 \cdot 2l_c$ or $l_{\bar{b}}^* \approx 3.51\sqrt{Rh}$ for $\nu = 0.3$. As can be taken from Figure 6.98, for all cylinders above the so approximated dent heights $l_{\bar{b}}^*$ differ less than $\pm 5\%$ from the values $l_{\bar{b}}$ in Figure 6.97 which were calculated with nonlinear buckling analyses. From this follows that for medium long cylinders the initial dent heights $l_{\bar{b}}$ are independent from the cylinder length L .

Initial dent widths $a_{\bar{b}}$:

The initial widths $a_{\bar{b}}$ of dents provoking minimal cylinder buckling loads with an initial depth $w_b/h = 0.1$ listed in Table 6.3 yielded ratios of these widths to the corresponding dent heights, $a_{\bar{b}}/l_{\bar{b}}$ between two and three. Thus, it was found obvious to investigate the dependence of the dent width $a_{\bar{b}}$ on the initial dent depth and cylinder dimensions by means of

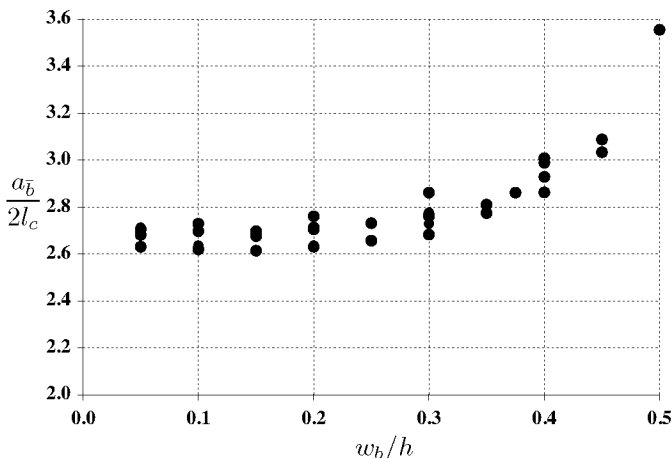


Figure 6.99: Ratio of the initial dent width $a_{\bar{b}}$ to the wavelength $2l_c$ subject to the initial dent depth w_b/h . Results for six isotropic cylinders of different radius, length and wall thickness.

the resulting ratios of the circumferential dent width to the classical axial wavelength $2l_c$, as it was done for the dent height. The behaviour of the width/circumference ratios $a_{\bar{b}}/l_{\bar{b}}$ was considered being less meaningful.

Figure 6.99 reproduces the width/wavelength ratios $a_{\bar{b}}/2l_c$ versus the initial dent depth w_b/h for some isotropic cylinders. For relatively small initial depths up to circa $w_b/h = 0.3$ the ratios $a_{\bar{b}}/2l_c$ are almost constant with a mean value of about 2.7. But for deeper dents with increasing initial dimple amplitude the initial widths $a_{\bar{b}}$ increases. That the initial width is longer for a deeper initial depth is plausible since the arc-length of a circle segment increases also with an increasing segment height. The arc-length \hat{a}_b of a cosine-shaped dent which initially has zero circumferential curvature at its apex ($1/\tilde{r}_A \equiv 0$) depends on the initial dent depth w_b and the cylinder radius R and is given by the equation

$$\hat{a}_b = \frac{2\pi R}{\sqrt{2\left(\frac{w_b}{R} - 1\right)}}. \quad (6.12)$$

Thus, the initial width \hat{a}_b of a dent with an initially flat shell increases as well with increasing initial dent depth w_b . But, according to this formula for $w_b = 0$ the dent width \hat{a}_b is zero, whereas the dent-width/wavelength ratios $a_{\bar{b}}/2l_c$ in Figure 6.99 exceed the level 2.6 also towards the ordinate.

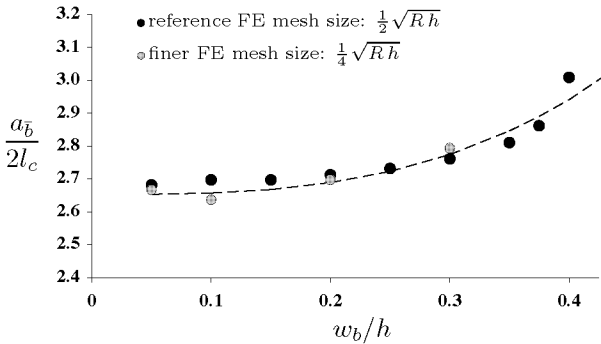


Figure 6.100: Ratio of the initial dent width $a_{\bar{b}}$ to the wavelength $2l_c$ in dependence on the initial dent depth w_b/h . Results for the reference cylinder and with a standard FE mesh size (black dots) and a finer mesh size (gray dots) as indicated. Dashed line refers to a simple cubic formula $a_{\bar{b}}^*(w_b/h)$ for an estimate of the initial dent width.

Moreover, with Equation 6.12 such values for the ratio $\hat{a}_{\bar{b}}/2l_c$ are reached only for initial dent depths deeper than $w_b/h > 4.0$ for $R = 250$ mm. But, with the shallow dents with $w_b/h < w_b^*/h \ll 1.0$, for which the initial widths $a_{\bar{b}}$ resulted, the cylinder shells are not flat in the *initial* state. Shallow dents having initial dent widths $a_{\bar{b}}$ provoke partial shell flattening and states of deformation which are the worst for the cylinder stability *during* the deformation process due to axial cylinder compression. And since initially the complex deformation process including bulging at the initial-dent sides and local buckling is unknown, there is no obvious indication given by the initial cylinder and dent geometry for an analytical approach of the initial dent dimensions resulting in the minimum cylinder stability.

In Figure 6.100 again ratios of the initial dent width $a_{\bar{b}}$ to the axial wavelength $2l_c$ subject to the initial amplitude w_b/h are shown for a FE model with standard mesh size of $0.5\sqrt{Rh}$ and a model with half this mesh size considering the reference cylinder as example. Both shell element dimensions yielded similar initial dent widths $a_{\bar{b}}$. Since the circumferential width $a_{\bar{b}}$ of the cosine wave is more than twice as long as the corresponding initial height and axial wavelength $l_{\bar{b}}$ of the dent, the influence of the mesh size and the resulting dent-profile approximation with linear elements is smaller for the initial dent width $a_{\bar{b}}$ compared to

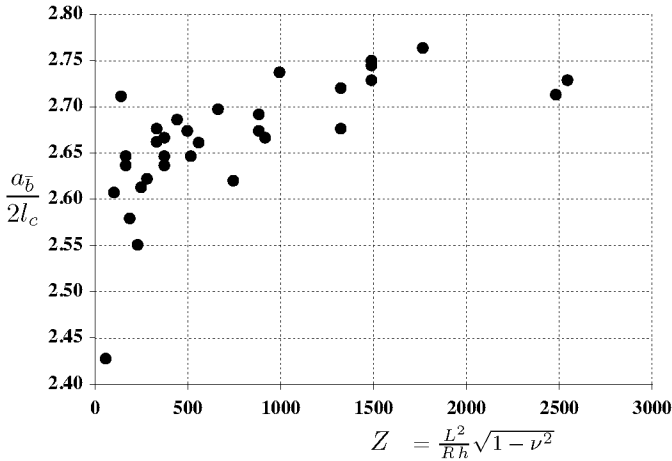


Figure 6.101: Ratio of the initial dent width $a_{\bar{b}}$ to the wavelength $2l_c$ of dents with an initial depth $w_b/h = 0.1$ in dependence on Batdorf's cylinder parameter Z for the isotropic cylinders in Table 6.3.

that for the shorter meridian dent height $l_{\bar{b}}$ (see Figure 6.96).

The dashed line in Figure 6.100 shows an estimate of the initial dent width $a_{\bar{b}}$ by means of a simple cubic function in terms of the initial dent depth w_b/h which fits better with the resulting widths for deeper dent depths than a cubic function like that for the dent heights $l_{\bar{b}}^*$. But in contrast to the initial dent heights the resulting ratios of the initial dent widths to the wavelength $a_{\bar{b}}/2l_c$ exhibit an obvious dependence on the cylinder length L . Figure 6.101 depicts the resulting width/wavelength ratio $a_{\bar{b}}/2l_c$ versus BATDORF's geometry parameter Z for the isotropic cylinders in Table 6.3. It can be seen that for longer cylinders and hence larger Z the ratio $a_{\bar{b}}/2l_c$ is higher. With an additional linear term considering the cylinder dimensions an empirical formula could be devised for estimates of the initial dent width $a_{\bar{b}}$. Together with the mentioned cubic term including the initial dent depth w_b the estimated dent widths $a_{\bar{b}}^*$ are given by the function:

$$\frac{a_{\bar{b}}^*}{2l_c} = 2.62 + 4.5 \left(\frac{w_b}{h} \right)^3 + 5 \cdot 10^{-5} Z \quad \forall \quad 0 < w_b < w_b^* \quad (6.13)$$

The lengths $a_{\bar{b}}^*$ are again approximations of nonlinear buckling analysis results for shallow dents and medium length cylinders. For deep dents with initial depths w_b deeper than the marginal initial depth w_b^* long

widths $a_{\bar{b}}$ resulted with large deviations from the predicted value, see Figure 6.94. Comparisons between the initial dent widths $a_{\bar{b}}$ obtained with minimum searches and the corresponding widths $a_{\bar{b}}^*$ due to the formula above are displayed in Figure 6.102 and Figure 6.103. Almost all relative deviations $\Delta a_{\bar{b}}$ are very small ($|\Delta a_{\bar{b}}| < \pm 5\%$), only for the reference cylinder having a deep dent of initial depth $w_b/h = 0.5$, which exceeds the marginal depth $w_b^*/h = 0.425$, and for a short cylinder with $Z = 57$ and $L/R = 0.4$ larger discrepancies resulted.

In Section 6.6.1 it was demonstrated that for deep dents with $w_b > w_b^*$ the buckling loads P_{cr} decreased with increasing initial dent widths a_b with the loads for the ring-shaped dent as lower bound. For shallow dents with $w_b < w_b^*$ however the buckling loads obtained for dents with shorter initial widths a_b , which had been specified for shallow dents, are smaller than the loads for the wider or axisymmetrical dents. Consequently, the minimum searches after the initial dent width $a_{\bar{b}}$ was performed only for shallow dents, and therefore also the formula for the estimates of the widths $a_{\bar{b}}^*$ is only applicable for dents with initial depths w_b not deeper than w_b^* .

Isotropic Cylinders with Outward Dimples

In contrast to inward dimples, for *outward* dimple imperfections only one unique minimal value could be identified in graphs showing the dependence of the buckling load P_{cr} on the initial dimple width a_b , see Figure 6.104 in comparison to Figure 6.92 for dents. In this chart the nonlinear buckling analyses results for the reference cylinder having a bulge with an initial elevation $w_b/h = -0.3$ and a given meridian height $L/l_b = 8.1$ are shown. The minimum buckling load P_{cr} resulted for the ring-shaped, axisymmetric bulge to be found at the right limit of the admissible range of a_b : the cylinder circumference $2\pi R = 1571$ mm. There is also a local minimum at about $a_b/(2\pi R) = 0.2$ identifiable in the chart, but the ring-shaped bulge caused a notably lower buckling load. In Figure 6.105 the nonlinear buckling analysis results for the reference cylinder having a bulge with an initial elevation $w_b/h = -0.1$ and various initial widths a_b and heights l_b are displayed. As for the dents in Figure 6.90, the shaded surface represent the resulting normalized buckling loads $P_{cr}/P_{cr\ id}$ versus the corresponding initial bulge widths a_b and heights l_b , again with focus on the bulge-length ranges with minimal buckling loads. The thick straight line in the contour plot below the load-surface and parallel to the a_b -axis chains the values for the bulge height l_b which yielded the

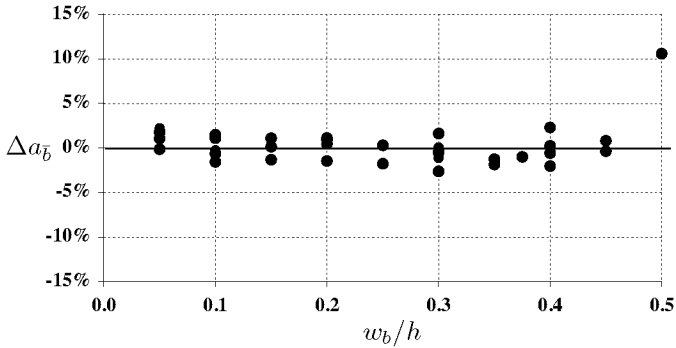


Figure 6.102: Relative deviations $\Delta a_{\bar{b}}$ of the initial dent widths $a_{\bar{b}}$ in Fig. 6.99 from the dent widths $a_{\bar{b}}^*$, estimated by means of Equation (6.13), in dependence on the initial dent depth w_b/h .

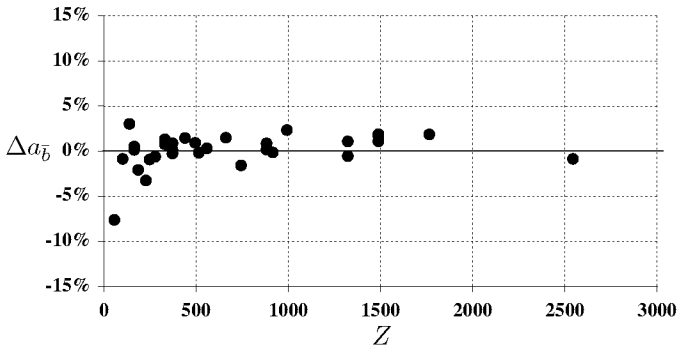


Figure 6.103: Comparison between the initial dent widths $a_{\bar{b}}$ in Fig. 6.101 and the dent widths approximated with Equation (6.13) for an initial dent depth $w_b/h = 0.1$. Relative deviations $\Delta a_{\bar{b}}$ subject to Batdorf's parameter Z .

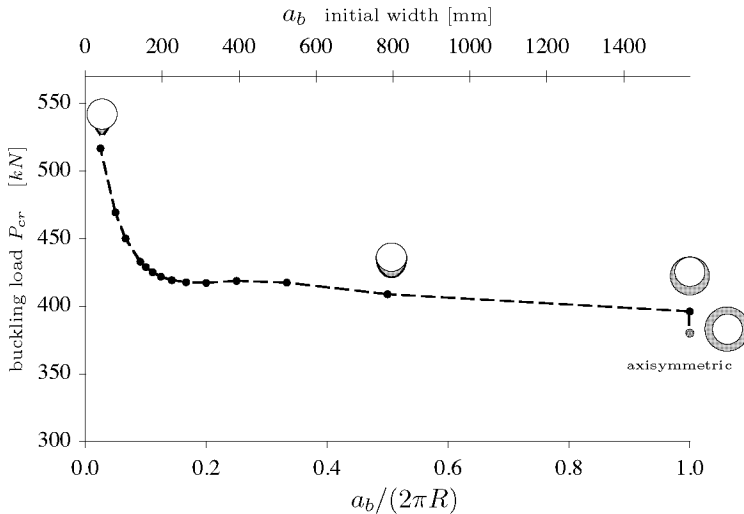


Figure 6.104: Buckling loads of the reference cylinder having a single outward dimple width a given elevation $w_b/h = -0.3$, a fixed initial meridian height $L/l_{\bar{b}} = 8.1$ and a variable initial circumferential width a_b .

smallest buckling loads for the respective initial dimple widths. The line pointing at the minimum values for the initial widths a_b runs top down along the right end of the contour plot.

According to the buckling analysis results for several different isotropic cylinders axisymmetrical outward dimples are more damaging than outward dimples with short initial widths a_b also for small initial dimple amplitudes w_b . Therefore, the initial width $a_{\bar{b}}$ of a bulge equals to the “width” of a ring-shaped bulge, independent of the initial dimple elevation w_b :

$$a_{\bar{b}} = \infty \quad \forall \quad w_b < 0$$

The initial width a_b of the dimples, considered for this thesis, is the full-length of a cosine wave, which is infinity for a constant amplitude. For practical reasons in the graphs above the results for the axisymmetrical bulge were plotted close to those for the bulge with a width a_b identical to the cylinder edge circumference $2\pi R$.

Since the “pessimism bulge” is always axisymmetrical only the initial dimple height which causes the minimum cylinder stability $l_{\bar{b}}$ had to be searched with nonlinear buckling analyses. These minimum searches for

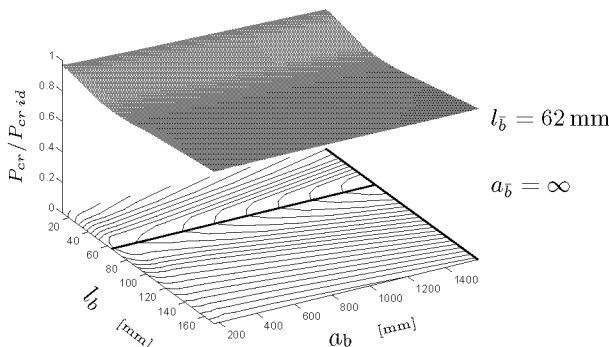
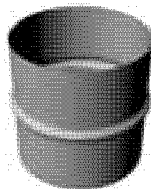


Figure 6.105: Normalized buckling loads $P_{cr}/P_{cr, id}$ of the reference cylinder having a bulge of initial elevation $w_b/h = -0.1$ with different initial meridian heights l_b and initial circumferential widths a_b . Thick lines in the contour plot point to a_b and l_b with minimal load P_{cr} .

the height l_b of bulges yielded curve progressions of the buckling loads P_{cr} versus the varied bulge height l_b similar to the curves for the heights of dents, see e.g. Figure 6.91. Compared with the results for dents, the minimal values for the bulge height l_b are somewhat short-wavier; for example for the reference cylinder in Figure 6.105 and an initial absolute amplitude of $|w_b/h| = 0.1$ the minimal value resulted in $L/l_b = 8.2$ or $l_b = 62$ mm, which is, compared to the dent of like initial amplitude with $l_b = 67$ mm, an about seven percent shorter initial meridian length of the dimple.

The buckling loads of cylinders having axisymmetrical imperfections may not only be calculated with numerical methods but also with analytical formulations. For cosine ring-shaped dimples defined by

$$\begin{aligned} \Delta_R(\zeta) &= \frac{w_b}{2} \left\{ 1 - \cos\left(\frac{2\pi}{l_b}\zeta\right) \right\} & |\zeta| \leq \frac{l_b}{2} \\ &= 0 & |\zeta| > \frac{l_b}{2} \end{aligned} \quad (6.14)$$



(HUTCHINSON, TENNYSON & MUGGERIDGE [51]) presented a solution for the general asymptotic formula

$$\left(1 - \frac{P_{cr}}{P_{cl}}\right)^{3/2} = \frac{3\sqrt{3(1-\nu^2)}}{2^{3/2}} |I_\Delta| \frac{P_{cr}}{P_{cl}} \quad (6.15)$$

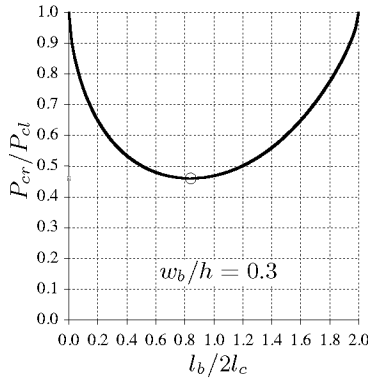


Figure 6.106: Buckling loads of the reference cylinder having an axisymmetric dimple subject to the initial dimple height l_b for a particular initial dimple amplitude. Results of the asymptotic formula in (6.15).

which yields buckling loads for axially compressed, infinitely long cylinders having a single axisymmetrical imperfection of small amplitude, see Section 6.1. The term I_Δ in Equation (6.15) is the FOURIER transformed imperfection function $\Delta_R(\zeta)$ of (6.14), which in present case is given by

$$\begin{aligned}
 |I_\Delta| &= \frac{w_b}{h} \frac{\sin\left(\pi \frac{l_b}{2l_c}\right)}{\left(\frac{l_b}{2l_c}\right)^2 - 1} & \forall \frac{l_b}{2l_c} \neq 1 \\
 |I_\Delta| &= \frac{\pi w_b}{2h} & \forall \frac{l_b}{2l_c} = 1
 \end{aligned} \tag{6.16}$$

This solution yields buckling loads for various initial inward and outward dimple amplitudes w_b and different ratios of the dimple height l_b (full wavelength) to the analytical axial wavelength $2l_c$ for axisymmetrical buckling of perfect cylinders. But the solution¹¹ also allows exact determination of the wavelengths ratio $l_b/2l_c$ which yields the smallest buckling load for a particular initial dimple amplitude! In Figure 6.106 the resulting normalized buckling loads P_{cr}/P_{cl} of a cylinder having an inward *or* an outward dimple of the shape as defined in (6.14) with a given initial amplitude of $w_b/h = 0.3$ are reproduced for different dimple-height to wavelength ratios $l_b/2l_c$. The minimum buckling load $P_{cr}/P_{cl} = 0.46$ results for a normalized dimple height of $l_b/2l_c = 0.84$,

¹¹The explicit power function which solves the asymptotic formula in (6.15) is lengthy and therefore not written out.

but the variation of the buckling loads within the range of the wavelength ratio $l_b/2l_c$ from 0.7 to 1.0 is below 1.5%. This thesis focusses on cylindrical shells with dimple imperfections which are localized in axial as well as in circumferential direction; hence, the behaviour of cylinder having dents and bulges with a full extent in their circumference was not investigated with the same efforts as for the single dimples of smaller wavelengths presented on the previous pages. However, for a few aluminium cylinders having a single axisymmetric cosine bulge the initial bulge height l_b provoking the lowest buckling load P_{cr} was also searched numerically by means of nonlinear buckling analyses in order to compare the FE analysis results with the analytical solution above.

In Figure 6.107 the resulting bulge-height/wavelength ratios $l_b/2l_c$ versus the initial bulge elevation $-w_b/h$ are depicted for some cylinders of different radius, length and wall thickness. It can be seen that for small amplitudes the resulting bulge heights are at about $l_b/2l_c = 0.9$, but with increasing elevation $-w_b/h$ the values grow linearly to about $l_b = 2l_c$ for bulges with amplitudes w_b close to the wall thickness h . The linear function l_b^* , given by

$$\frac{l_b^*}{2l_c} = 0.9 - 0.12 \frac{w_b}{h} \quad \forall \quad w_b < 0 \quad , \quad (6.17)$$

follows the results in Figure 6.107 approximatively and yields feasible estimates for the initial bulge height l_b . The deviations Δl_b of these numerical analyses results from the values due to the linear formula (6.17) are reproduced in Figure 6.108; they are all smaller than $\pm 5\%$.

Compared with the minimum value $l_b/2l_c = 0.84$ obtained with the asymptotic formula the nonlinear buckling analysis results are slightly higher, probably due to the relatively coarse approximation of the cosine-shaped radius variation with only eight bi-linear shell elements in axial direction involved. The gray dots in Figure 6.107 refer to initial bulge heights l_b resulting for the reference cylinder modelled with twice as much bi-linear shell elements in axial and circumferential direction. These two values are about $l_b/2l_c = 0.04$ closer to the asymptotic theory results for very small initial amplitudes compared with the results obtained with the coarser reference mesh size.

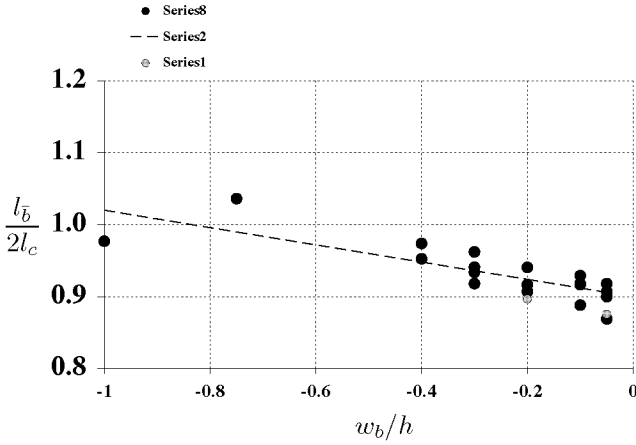


Figure 6.107: Ratio of the initial bulge height $l_{\bar{b}}$ to the classical axial wavelength $2l_c$ subject to the initial bulge amplitude $-w_b/h$. Results for a few isotropic cylinders of different radius, length and wall thickness. Gray dots results for the reference cylinder with half FE mesh size.

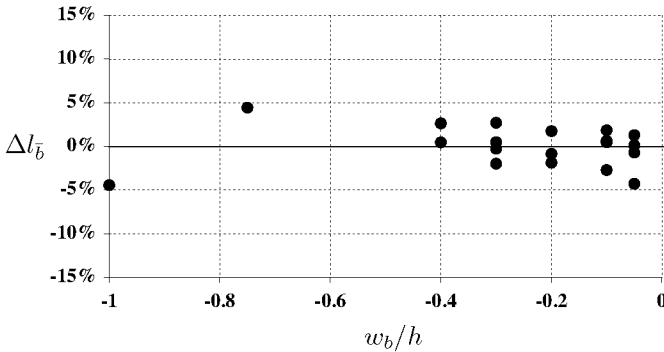
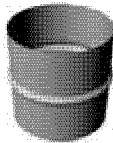


Figure 6.108: Relative deviations of the initial bulge heights $l_{\bar{b}}$ in Fig. 6.107 from the bulge heights $l_{\bar{b}}^*$, approximated by means of Equation (6.17), in dependence on the initial bulge amplitude $-w_b/h$.

6.6.4 Minimum Buckling Loads for Isotropic Cylinders with Single Dimples

In the previous sections the instability behaviour and the buckling loads of isotropic cylinders having a single initial inward or outward dimple was discussed. Section 6.6.1 and 6.6.2 contain the descriptions of buckling analysis results and deformation behaviour patterns of various cylinders with a dent or bulge, respectively, of varied initial amplitude and predefined initial circumferential dimple width and meridian dimple height. Section 6.6.3 includes results for the initial width and height of the dimples which yielded the minimum cylinder buckling resistance for a predefined initial dimple amplitude. For design engineers however the minimum buckling loads to be expected for cylinders with a dimple imperfection might be of more importance than the buckling behaviour and the dimple geometry. Thus, in the following the minimum buckling resistance of isotropic shells with a dent or bulge is discussed and results compared with the values recommended for design by other authors and in standards which base on tests of shells that have some randomly distributed imperfections. Minimum buckling loads of cylinders with a single parametric dent or bulge obtained with nonlinear buckling analyses were already indicated in Section 6.6.1 and are now pointed out to demonstrate the influences of the nominal cylinder geometry and the initial dimple size observed. Finally, the sensitivity to a single initial non-axisymmetric dimple is compared with impact of a single initial ring-shaped dimple as well as with the effect of evenly distributed imperfections that relate to classical or linear buckling modes of perfect cylinders.

With increasing initial amplitude w_b of a single dimple with fixed initial width and height the resulting local buckling load of a cylinder decreased to a minimum value. For further growth of the initial dimple amplitudes again slightly higher buckling load were obtained. In Figure 6.109 the nonlinear buckling analysis results for the reference cylinder with a single dimple are reproduced. The buckling loads are normalized with respect to the buckling load $P_{cr id} = 569$ kN of the perfect aluminium reference cylinder with radius $R = 250$ mm, length $L = 510$ mm, and wall-thickness $h = 1.5$ mm. The minimum buckling load resulted for an inward dimple of initial depth $w_b/h = 0.75$. For this initial depth the nonlinear buckling analysis yielded a local buckling load of $P_{cr MIN} = 290$ kN, or of $P_{cr MIN}/P_{cr id} = 0.51$ if normalized.

The buckling loads reproduced in Figure 6.109 resulted with dimples

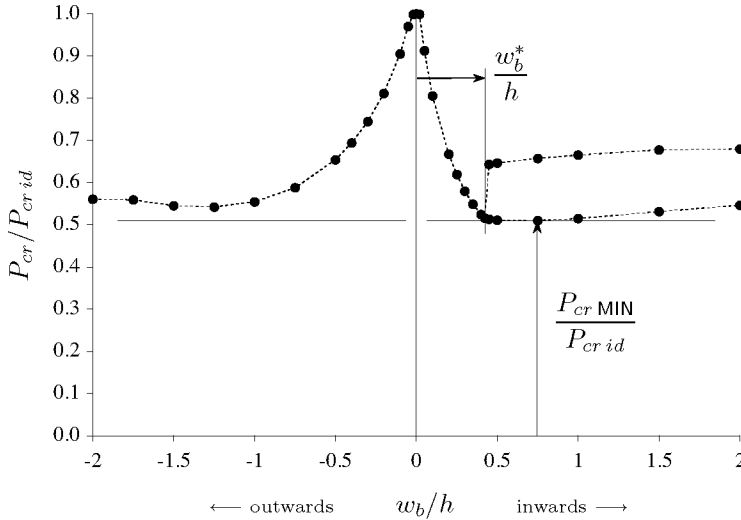


Figure 6.109: Buckling load $P_{cr}/P_{cr id}$ of the reference cylinder having a single dimple against the initial dimple amplitude w_b/h . Results of nonlinear buckling analyses for the initial dimple width $a_{\bar{b}} = 181$ mm and the height $l_{\bar{b}} = 67$ mm. Buckling loads normalized with respect to the result for the perfect cylinder $P_{cr id}$.

having an initial circumferential width of $a_{\bar{b}} = 181$ mm and an initial meridian height of $l_{\bar{b}} = 67$ mm. These dimple dimensions are the result of a systematic search after the initial width $a_{\bar{b}}$ and height $l_{\bar{b}}$ of a dent with an initial depth of $w_b/h = 0.1$ which reduced the reference cylinder buckling resistance the most, see Section 6.6.3. But, for dents with initially longer width $a_b > a_{\bar{b}}$ and height $l_b > l_{\bar{b}}$ the minimum buckling load $P_{cr MIN}/P_{cr id}$ achieved was smaller. In Figure 6.110 the nonlinear buckling analysis results for the reference cylinder having a single dent or bulge given in Figure 6.109 are compared with results for longer initial dimple widths and heights. It can be seen that for the shell with a 32% larger width a_b and a 32% larger height l_b a notably lower minimum buckling load $P_{cr MIN}$ resulted. In this case the normalized minimum is $P_{cr MIN}/P_{cr id} = 0.44$ for an absolute load of $P_{cr MIN} = 253$ kN. This minimum buckling load is 13% below the value for the smaller dent of initial height $l_{\bar{b}}(0.1)$ and width $a_{\bar{b}}(0.1)$ specified with $w_b/h = 0.1$. Further elongations of the initial width a_b alone result in further reductions of the minimum buckling load $P_{cr MIN}$ with the values for the ring-shaped dimple as lower bound.

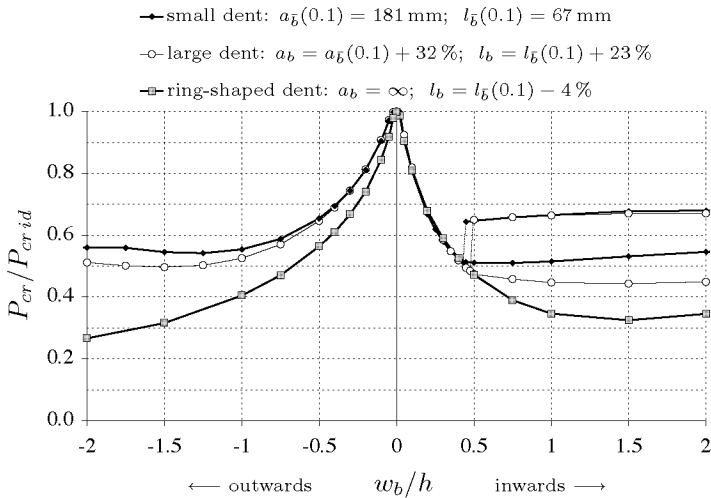


Figure 6.110: Normalized buckling load of the reference cylinder having a single dimple against the initial dimple amplitude w_b/h . Nonlinear buckling analysis results for an initial dimple width a_b and height l_b as indicated.

For the ring-shaped inward dimple also a minimum buckling load could be found, whereas for the ring-shaped outward dimple the buckling loads continuously decreased with increasing initial amplitude. The initial height $l_b = 64 \text{ mm}$ applied for the ring-shaped dimples in Figure 6.110 was specified with such bulges of initial elevation $w_b/h = -0.4$ and is shorter than the dimple heights l_b resulted for the non-axisymmetric dents of similar initial absolute amplitude, see Section 6.6.3. For ring-shaped outward dimples always significantly lower buckling loads were obtained than for outward dimples of small initial widths, contrary to ring-shaped inward dimples for which in case of small initial dimple depths $w_b < w_b^*$ almost or even slightly higher buckling loads resulted than for non-axisymmetric dents.

Provided that the dimple width is small compared to the cylinder circumference, the minimum buckling load for outward dimples is higher than the minimum buckling load $P_{cr \text{ MIN}}$ for inward dimples. From this follows that dents tend to be more damaging than bulges. Therefore the analyses to the lowest critical loads focussed on cylinders with dents of different size. In Figure 6.111 the normalized buckling loads depicted in Figure 6.110 are reproduced for the dents with initial depths up to

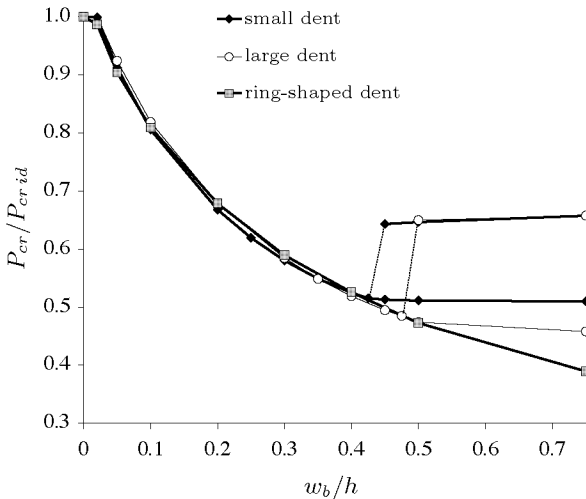
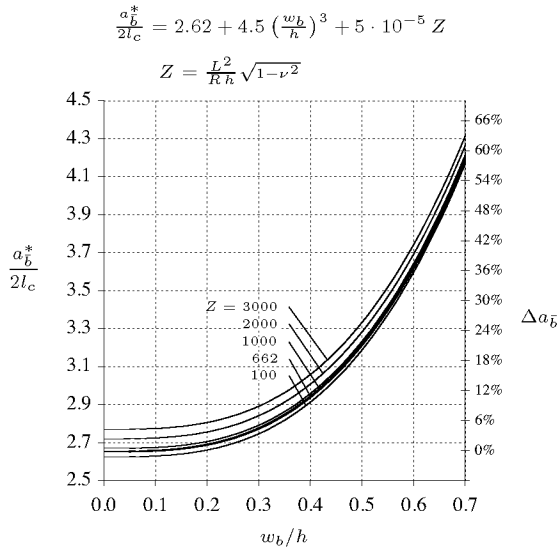


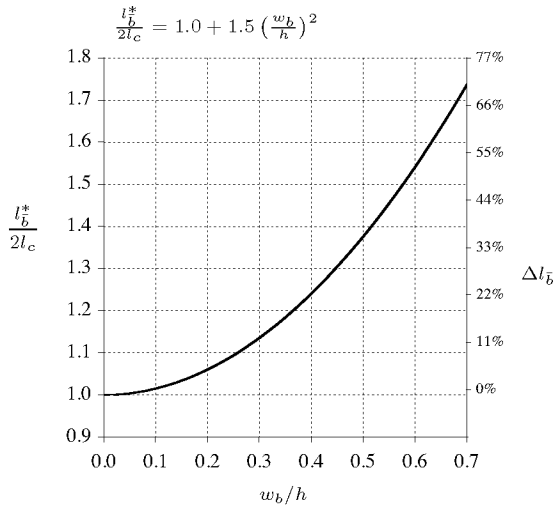
Figure 6.111: Normalized buckling load $P_{cr}/P_{cr,id}$ of the reference cylinder having a single dent versus the initial dent depth w_b/h . Nonlinear buckling analysis results for initial dent widths a_b and heights l_b as indicated. Focus on initial depths of shallow dents. See Figure 6.110.

$w_b/h = 3/4$. It can be seen again that for initial depths w_b/h below the marginal depths w_b^*/h for shallow dents the small dimples with initial width $a_b(0.1)$ and height $l_b(0.1)$ as well as the large dimples with 32% and 23% longer initial width and height, respectively, yielded almost equal or even lower buckling loads $P_{cr}/P_{cr,id}$ than the ring-shaped dents of similar initial height l_b ! Additionally, in this initial-dent-depth range the reduction rate per increasing dimple amplitude and hence the sensitivity to an initial dent is maximal. For deep dents with $w_b > w_b^*$, however, the change in the buckling loads with increasing initial dent depth is small compared with that for shallow dents. But for these initial depths the buckling loads resulting for axisymmetric dents are always smaller than those for non-axisymmetric dents of like initial height. For these reasons, and since the study of cylinders having a localized dimple focussed on small dents which are not ring-shaped, minimum buckling loads $P_{cr,MIN}$ of further isotropic cylinders with an initial dent were calculated solely for dimples of initial width a_b small compared to the cylinder circumference and specified with initial depths $w_b > w_b^*$ of shallow dents.

The initial meridian dent height l_b and the initial circumferential width



(a) *initial dent width*



(b) *initial dent height*

Figure 6.112: Initial dent width and height ratios to the classical axial wavelength versus initial dent depth for isotropic cylinders. Curves approximate solutions for selected shells found with nonlinear buckling analyses.

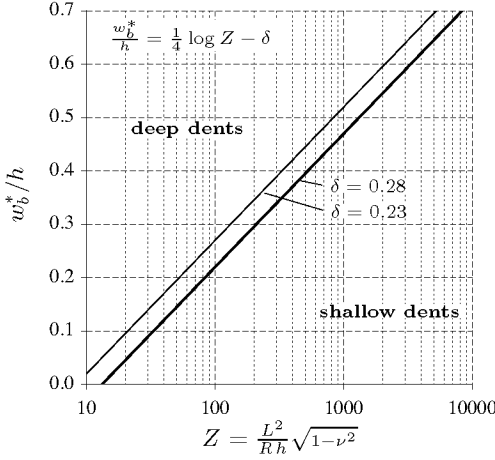


Figure 6.113: Normalized marginal initial depth for shallow dents w_b^*/h against BATDORF's parameter Z . Curves and formula approximate results for small dents of initial height $l_{\bar{b}}$ and width $a_{\bar{b}}$ specified for $w_b/h = 0.1$ (thick line) and for larger dents of 23 % and 32 % longer initial height and width respectively (thin line).

$a_{\bar{b}}$ found with systematic searches depend strongly on the initial dent depth w_b/h for which these lengths were calculated; that is: $a_{\bar{b}} = a_{\bar{b}}(w_b)$ and $l_{\bar{b}} = l_{\bar{b}}(w_b)$. In Figure 6.112 curves for (a) the initial width $a_{\bar{b}}^*$ and (b) the initial height $l_{\bar{b}}^*$ depending on the initial dent depth w_b/h are shown, see Section 6.6.3. In both cases the initial lengths are normalized with respect to the analytical wavelength $2l_c$ for axisymmetric buckling. The curves, i.e. the values $a_{\bar{b}}^*/2l_c$ and $l_{\bar{b}}^*/2l_c$, approximate the lengths $a_{\bar{b}}/2l_c$ and $l_{\bar{b}}/2l_c$ which resulted with nonlinear buckling analyses. The formulas associated with the curves are given above the graphs. Contrary to the initial dent height $l_{\bar{b}}^*/2l_c$ the initial dent width $a_{\bar{b}}^*/2l_c$ is also weakly dependent on BATDORF's cylinder-geometry parameter Z . The bold line in Figure 6.112 (a) refers to initial-width/wavelength ratios for the reference cylinder with $Z = 662$. The initial depth, for which the first and also the most subsequent initial heights $l_{\bar{b}}$ and widths $a_{\bar{b}}$ were specified, was arbitrarily set to $w_b/h = 0.1$. Therefore also the majority of the nonlinear buckling analyses of different shells with varied initial dimple amplitude w_b/h which also yielded minimum buckling loads $P_{cr \text{ MIN}}$ (see Fig. 6.109) was performed with dimples having an initial height $l_{\bar{b}}(0.1)$ and an initial width $a_{\bar{b}}(0.1)$, i.e. specified with $w_b/h = 0.1$. The initial dimple dimensions $l_{\bar{b}}(0.1)$ and $a_{\bar{b}}(0.1)$ of a series of isotropic cylinders

are listed in Table 6.3 on page 331. But, as demonstrated in Figure 6.110 by means of the reference cylinder, for widths and heights larger than $a_{\bar{b}}(0.1)$ and $l_{\bar{b}}(0.1)$, respectively, smaller minimum buckling loads $P_{cr \text{ MIN}}/P_{cr \text{ id}}$ were obtained. Consequently, in order to calculate the lowest minimum loads for cylinders with dents of initial height and width maximal for shallow dents, the initial widths and heights would have been specified which result with the marginal initial depth w_b^*/h for shallow dents, that is: $a_{\bar{b}}(w_b^*)$ and $l_{\bar{b}}(w_b^*)$, see Figure 6.109. In Figure 6.113 the marginal initial depths w_b^*/h are depicted against BATDORF's parameter Z . The curves and the logarithmic formula included approximate the maximum initial depths w_b^*/h which caused termination of nonlinear buckling analyses at the local buckling load, see definitions in Section 6.6.1 on page 275 ff. The thick line again follows from calculations with dents of initial height $l_{\bar{b}}(0.1)$ and width $a_{\bar{b}}(0.1)$ specified for $w_b/h = 0.1$. The thin line refers to slightly higher marginal depths obtained with the 32% and 23% longer initial widths and heights, respectively. Thus, unfortunately like the minimum buckling loads $P_{cr \text{ MIN}}$ the marginal initial depths w_b^*/h depend on the initial width a_b and height l_b of the dents, which in turn depend on the initial depth w_b/h . Therefore, for an exact determination of the marginal initial depths w_b^*/h some iteration loops would have been required, where a new marginal initial depth would have been specified with dents of initial dimensions specified with the first marginal depth, and so on. But so resulting corrections would hardly exceed marginal-depth differences of 0.05. For example, in case of the reference cylinder via the logarithmic formula a marginal initial depth of $w_b^*/h = 0.25 \cdot \log 662 - 0.28 = 0.43$ for small dents and $w_b^*/h = 0.25 \cdot \log 662 - 0.23 = 0.48$ for 32% wider dents results. These depths inserted into the formula for the initial dent dimensions yields $a_{\bar{b}}^*/2l_c = 2.62 + 4.5 \cdot 0.43^3 + 662 \cdot 5 \cdot 10^{-5} = 3.0$ and $a_{\bar{b}}^*/2l_c = 3.14$, for the initial dent widths, and $l_{\bar{b}}^*/2l_c = 1 + 1.5 \cdot 0.43^2 = 1.27$ and $l_{\bar{b}}^*/2l_c = 1.34$ for the initial dent heights. The difference between first, smaller width $a_{\bar{b}}^*/2l_c$ to the width $a_{\bar{b}}^*/2l_c(0.1) = 2.66$ resulting with $w_b/h = 0.1$ is about 13%, that between the second, wider width and the width $a_{\bar{b}}^*/2l_c(0.1) = 2.66$ is about 18%. The heights, in turn, differ in the range of about 30%. Thus, and since the buckling load reduction depends stronger on the initial width than the height, the buckling loads obtained for the *large* dents will be close and slightly below the buckling loads that would result with the initial dimensions above specified for the marginal initial width w_b^*/h , see Figure 6.110 and 6.111. But, due to the only small corrections expected and the vast time exposure additional calculations with dents of initial dimensions specified with w_b^*/h

were not conducted to prove this assumption.

As already mentioned, almost all analyses of the isotropic cylinders having a dent of varied initial depth were performed with initial dent heights and widths which were most damaging for an initial dent depth of $w_b/h = 0.1$, i.e. with $l_{\bar{b}}(0.1)$ and $a_{\bar{b}}(0.1)$. Therefore, also most of the minimum buckling loads $P_{cr \text{ MIN}}/P_{cr id}$ for isotropic cylinders, resulted from these nonlinear buckling analyses with these smaller initial dent sizes. For three cylinders, however, additionally analyses were performed with dents of 32% and 23% longer initial widths and heights, respectively. In Figure 6.114 the normalized minimum buckling loads

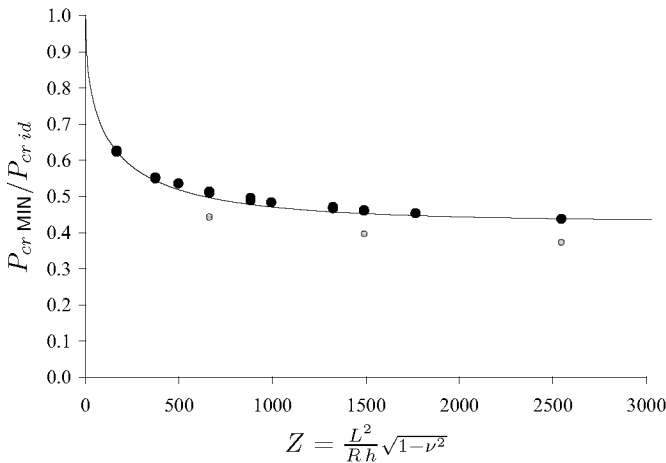


Figure 6.114: Minimum buckling loads $P_{cr \text{ MIN}}/P_{cr id}$ versus BATDORF's parameter Z for isotropic cylinders with a single dent. Results for initial lateral dimple dimensions which caused minimal cylinder stability for an initial dent depth of $w_b/h = 0.1$ (black dots) and for larger dents of 23% and 32% longer initial height and width respectively (gray dots).

$P_{cr \text{ MIN}}/P_{cr id}$ found by means of nonlinear buckling analyses of some cylinders of different length, radius and shell thickness are shown in dependency of BATDORF's cylinder geometry parameter Z . The black dots stand for dents applied to the cylinders with respective lateral lengths $a_{\bar{b}}(0.1)$ and $l_{\bar{b}}(0.1)$ specified with $w_b/h = 0.1$, the three gray dots refer to dents with 32% longer initial widths and 23% longer initial heights, see Figure 6.110 and 6.111. According to these results the normalized minimum buckling loads of the smaller dents differ from those of the larger dents in an about constant vertical shift of circa 0.7 or between

13 and 15 percent. For small Z , i.e. for short cylinders the sensitivity to a dent is smaller than for medium-length cylinders. For longer cylinders with high Z the minimum buckling loads converge to about $P_{cr \text{ MIN}}/P_{cr \text{ id}} \approx 0.37$ in case of the wider dents.

The minimum buckling loads $P_{cr \text{ MIN}}$ in Figure 6.114 were normalized with respect to the buckling loads $P_{cr \text{ id}}$ resulting for the nonlinear buckling analysis of the cylinders without imperfections. In design guidelines however the recommended critical loads refer to the buckling loads of classical analytical solutions, P_{cl} . Figure 6.115 depicts the minimum

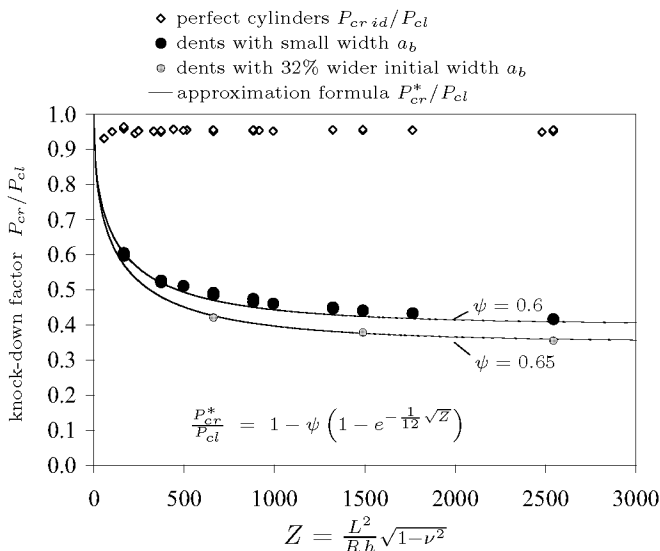


Figure 6.115: Knock-down factors P_{cr}/P_{cl} against BATDORF parameter Z for isotropic cylinders. Nonlinear buckling analysis results for cylinders with perfect geometry and cylinders with a single dent as indicated. Included curves for estimates of the buckling load of isotropic cylinders having a single dents of either small or large initial width and height.

buckling loads $P_{cr \text{ MIN}}$ in the ratio of the classical buckling loads for isotropic cylinders $P_{cl} = 3.8Eh^2$, again plotted against BATDORF's cylinder geometry parameter Z . The small diamonds refer to the load ratios $P_{cr \text{ id}}/P_{cl}$ for the nonlinear buckling analysis results of the cylinders with perfect geometry. These loads $P_{cr \text{ id}}$ were about four to seven percent smaller than the classical buckling loads P_{cl} . Consequently, the minimum-buckling-load ratios P_{cr}/P_{cl} which resulted for the shells with

a dent are slightly smaller than the ratios $P_{cr\text{MIN}}/P_{cr\text{id}}$. The normalized minimum buckling loads $P_{cr\text{MIN}}/P_{cl}$ (black dots) which resulted for dents of initial width $a_{\bar{b}}(0.1)$ and height $l_{\bar{b}}(0.1)$, specified with $w_b/h = 0.1$, may be approximated with the exponential equation $P_{cr}^*(Z)/P_{cl}$

$$\frac{P_{cr}^*}{P_{cl}} = 1 - 0.6 \left(1 - e^{-\frac{1}{12}\sqrt{Z}} \right) \quad (6.18)$$

included in the chart. For the three lower loads obtained with the initially 32% wider and 23% higher dents (gray dots) the approximation

$$\frac{P_{cr}^*}{P_{cl}} = 1 - 0.65 \left(1 - e^{-\frac{1}{12}\sqrt{Z}} \right) \quad (6.19)$$

was derived similarly, which might also serve as lower bound for loads resulting with the aforementioned dents of initial width $a_{\bar{b}}(w_b^*)$ and height $l_{\bar{b}}(w_b^*)$, thus specified with the marginal dent depth for shallow dents w_b^*/h .

The smallest factor to which the lower curve converges, $P_{cr}^*/P_{cl} = 0.35$ is notably higher than the smallest values to be expected due to the knock-down factors recommended for design by the NASA Space Vehicle Design Criteria, SP-8007 [62], for instance, see page 5.2ff.. In Figure 6.116 the curve to these knock-down factors is reproduced which are given by the formula in Equation 5.4 on page 158:

$$\frac{P_{cr}}{P_{cl}} = 1 - 0.902 \left(1 - e^{-\frac{1}{16}\sqrt{\frac{R}{h}}} \right)$$

In this representation the imperfection sensitivity depends on the cylinder radius/wall-thickness ratio R/h , but possible influences of the cylinder length L are ignored. According to the test results of (WEINGARTEN et al. [79]), on which above curve in Figure 6.116 bases, for large R/h buckling loads less than 20 percent of the classical buckling load have to be expected, see page 157 ff.. For comparisons again the buckling loads normalized with respect to the classical buckling load of Figure 6.115 were added using the identical markers for the results with perfect shells and with small or large dents, see legends. It can be seen that for thin cylindrical shells with $R/h > 300$ the reduction of the load carrying capacity due to a single dent was less severe than those caused by the multiple, randomly distributed imperfections in tests. But, for cylinders with a single dent of radius/wall-thickness ratios between $R/h = 100$ and 200 buckling loads considerably below the loads according to the NASA design curve were obtained. These loads may be explained with the

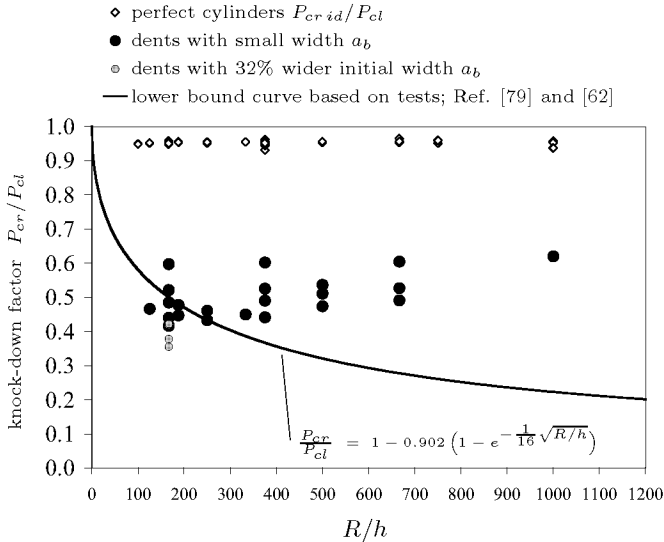


Figure 6.116: Knock-down factors P_{cr}/P_{cl} against radius/wall-thickness ratio R/h for isotropic cylinders. Comparison between values for cylinders with dents as indicated, for cylinders with perfect geometry, and from the curve recommended in the NASA Space Vehicle Design Criteria, Ref. [62]. Design curve derived from test results of cylinders with unspecified, distributed imperfections, see Ref. [79].

relatively larger wall-thickness h of such shells and the associated lower probability that their real imperfection patterns include single dimples as considered in the analyses with initial depths of about half the wall thickness. That is, the imperfections of the tested cylinders with these R/h ratios were probably much smaller and hence also less damaging than the relatively deep dimples associated with the calculated minimum buckling loads. For cylinders with high radius/wall-thickness ratios and thus thin shell walls, in contrast, the presence of small multiple random dents and notches with depths of about only half the wall-thickness is unavoidable and hence very likely. Nevertheless, according to the nonlinear analysis results in Figure 6.116 care has to be taken using the NASA design recommendation for rather thick cylinders with $R/h < 200$ if single dents of dimensions like those considered for the numerical investigations are, or may be present.

In Figure 6.115 the minimum buckling loads ratios of the cylinders hav-

ing a single dent are shown versus BATDORF's geometry parameter Z which takes the radius and the shell wall-thickness as well as the cylinder length into account. This graphic representation of the nonlinear buckling analysis results was found more meaningful than that in Figure 6.116 where the loads are depicted against the radius/wall-thickness ratio R/h . Ignoring the cylinder length L the resulting minimum buckling loads are "arbitrarily" scattered and thus possible correlations between load and cylinder geometry can hardly be detected. The normalized minimum buckling load $P_{cr \text{ MIN}}/P_{cr \text{ id}}$ decreases with increasing cylinder length, see Section 6.6.1 on page 281 ff. And for shells with like length and factor $R \cdot h$ similar buckling loads of cylinders with a dent of equal normalized initial depth and equal initial height and width resulted. In Figure 6.115, the loads plotted subject to the geometry parameter Z , these facts are considered.

Alternatively, the buckling stresses linked with the values of Figure 6.115 were divided by the square of the length/wall thickness ratio $(L/h)^2$ and the bending stiffness parameter D to yield the respective buckling load coefficient k and these again plotted against the parameter Z , see Figure 5.2 on page 156. Figure 6.117 depicts these coefficients k versus Z in logarithmic scales. The chart includes the minimum buckling stresses for the cylinders with a dent of size as indicated and those for the perfect cylinders. The markers correspond with those in the two previous figures, the bold straight line refers to the theory for ideal cylinders. The coefficients k smaller than 10 differ for clamped and hinged cylinder edges and were therefore omitted. The 90 percent probability curve for a ratio $R/h = 100$ finally proposed for shell design by (HARRIS et al. [71]) was added for comparison (thin line). This curve again bases on test results and should yield safe buckling stresses for 90 percent of the cylinders in the shown Z range. The straight line is parallel to the thick perfect-cylinder line, whereas the results for the cylinders with a dent seem to be arranged more along a single line with a smaller gradient (dashed line), indicating that the damaging effect of a single dent increases with increasing Z (or length L). But, in contrast to the NASA design curve in Figure 6.116 the values for the cylinders with dents are always above the design curve recommended by (HARRIS et al. [71]) also for the relatively thicker cylinders of small ratio $R/h = 100$. For larger ratios R/h the researchers recommended other parallel lines with further vertical distances to the thick line. Thus, these design curves are conservative subject to the smallest buckling analysis results with single dents $P_{cr \text{ MIN}}$ for all isotropic cylinders considered in the parameter studies on hand.

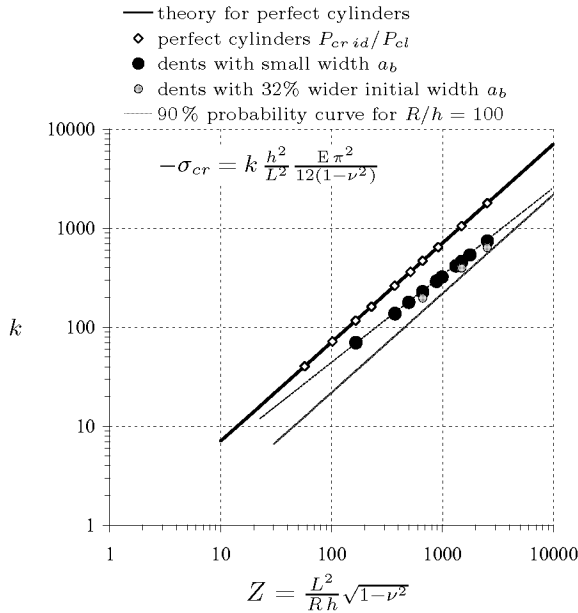
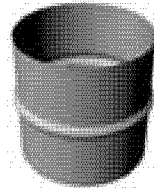


Figure 6.117: Buckling load coefficient k_a against BATDORF's parameter Z for isotropic cylinders. Values resulting for cylinders with perfect geometry, as per theory and nonlinear buckling analyses, and for cylinders with single dents as indicated. Thin line corresponds to the 90 % probability curve for $R/h = 100$ recommended for design by (HARRIS et al. [71]).

The buckling load reductions recommended by the German standard DIN 18800 part 4 could not be reproduced with the analyses of the cylinders having a single initial dimple, see Section 6.1 on page 6.1 ff. Only the axial gauge length for single dimples in the standard with $l_{mx} = 4\sqrt{Rh}$ is close to the axial wavelength for classical axisymmetric buckling $2l_c \approx 3.5\sqrt{Rh}$ and thus also close the initial meridian heights $l_{\bar{b}}$ of dents found with the calculations. For the reference cylinder the gauge length is $l_{mx} = 63$ mm, see example on page 192. The standard stipulates that the initial dimple depth w_b should not exceed 1% of l_{mx} , thus: $w_{b MAX} = 0.63$ mm or $w_{b MAX}/h = 0.42$ with $h = 1.5$ mm. But the nonlinear buckling analyses of the reference cylinders with a dent yielded drastic load-reduction rates for initial depths smaller than this value. For initial depths deeper than this value the buckling load reduction changes only little or even decreases with further increase of the initial depth, see Figure 6.109 on page 348. For single dents which

are initially deeper than the value $0.01 \cdot l_{max}$ a reduction factor is to be applied which depends strongly on the ratio of the classic buckling stress to the yield stress of the shell material. Finally, for imperfection sensitive shells in addition a rather small security factor (e.g. 1.22) is to be applied which should consider small stochastic dimension tolerances. Neither this security factor could be followed nor any source of the reduction factors could be identified by means of the nonlinear buckling analysis results of the cylinders having a single initial dent. Additionally, since the final knock-down factors recommended in DIN 18800 part 4 result from formulas which include not only the shell geometry but also the yield stress, possible correlations between the analysis results $P_{cr \text{ MIN}}/P_{cl}$ and these factors may hardly be found. And a reasonable application of the standard DIN 18800 on cylinders with shells of a material without a “yield stress”, e.g. CFRP laminates, is also not possible.

In Figure 6.110 and 6.111 normalized buckling loads for the reference cylinder with a short-waved localized initial dimple were compared with loads for this cylinder having a single ring-shaped dimples. As already explained in Section 6.6.3, for cosine ring-shaped dimples in isotropic circular cylinder shells an analytical solution exists to predict the buckling loads. (HUTCHINSON, TENNYSON & MUGGERIDGE [51]) published a solution of the general asymptotic formula



$$\left(1 - \frac{P_{cr}}{P_{cl}}\right)^{3/2} = \frac{3\sqrt{3(1-\nu^2)}}{2^{3/2}} |I_{\Delta}| \frac{P_{cr}}{P_{cl}}$$

derived by (AMAZIGO & BUDIANSKY [3]). For a single cosine ring-shaped dimple in infinitely long cylinders under axial load, see Section 6.1, they obtained the FOURIER transformed imperfection function I_{Δ} with

$$|I_{\Delta}| = \frac{w_b}{h} \frac{\sin\left(\pi \frac{l_b}{2l_c}\right)}{\left(\frac{l_b}{2l_c}\right)^2 - 1} \quad \forall \frac{l_b}{2l_c} \neq 1$$

$$|I_{\Delta}| = \frac{\pi w_b}{2 h} \quad \forall \frac{l_b}{2l_c} = 1$$

The solution¹² of the formula above yields knock-down factors P_{cr}/P_{cl} for different initial inward and outward dimple amplitudes w_b and dimple height ratios $l_b/2l_c$, see Section 6.6.3. The knock-down factors P_{cr}/P_{cl}

¹²The explicit power function which solves the asymptotic formula is lengthy and therefore not written out.

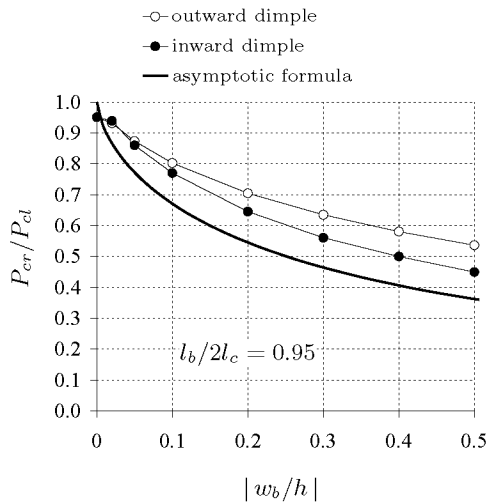


Figure 6.118: *Buckling loads of the reference cylinder having an axisymmetric dimple versus the initial dimple amplitude w_b/h for the particular initial dimple height ratio indicated. Comparisons between results obtained with the asymptotic formula (black line) and with nonlinear buckling analyses (dots) for axisymmetric dents and bulges.*

of cylinders with a ring-shaped dimple due to the asymptotic formula are identical for bulges and for dents. But, calculated with nonlinear buckling analyses the buckling loads resulting for axisymmetric inward dimples are considerably smaller than the buckling loads for axisymmetric outward dimples, see Figure 6.118. In both cases the numerical analyses yielded notably higher loads than the asymptotic theory. However, (HUTCHINSON, TENNYSON & MUGGERIDGE [51]) also conducted numerical calculations of clamped cylinders with ring-shaped dimples with a nonlinear approach (see Section 5.2) and obtained similar results as regards the differences between dents and bulges, as well as between numerical and asymptotic theory results.

Several commercial FE programs (e.g. MARC[®], ABAQUS[®]) provide procedures with which a linear buckling mode or linear combinations of such eigenvectors can be applied to an FE model prior to a buckling analysis. The linear buckling modes involved result from a preceding common linear buckling analysis of the shell having perfect geometry. The application of such notional buckling-mode affine imperfections is found in

the intention to consider the unavoidable presence of any random irregularities also in FE analyses and bases on KOITER's asymptotic theory, see Section 5.1, and on the assumption that such imperfection patterns damage the axial stability of a shell structure the most. To compare the sensitivity of isotropic cylinders to such distributed imperfections with the impact of a single dimple a series of buckling modes that relate to the classical analysis was used as initial deformation patterns for the reference cylinder. In the following the nonlinear buckling analysis results of these additional shells are briefly explained. Figure 6.120 reproduces the nonlinear buckling analysis results for the reference cylinder having a classical buckling mode-affine imperfection of various initial amplitude. In Figure 6.119 (a) the applied pattern given by a bi-harmonic function of 11 half-waves in axial and 7 waves in circumferential direction (m, n) is depicted. As shown in Section 4.2.1, for an ideal isotropic cylinder the classical buckling analysis gives almost the same buckling load for many combinations of m and n . For instance, the classical buckling load of the reference cylinder is $P_{cl} = 599$ kN and results approximatively for axisymmetric buckles with $m = 15$, but also for $m = 13$ together with $n = 8$, and many others more. *However, the mode in Figure 6.119 (a) with $m = 11$ and $n = 7$ yields a 6 % higher buckling load of $P_{cr} = 633$ kN!* But this buckling mode, i.e. this imperfection pattern is the result of a systematic search after the (m, n) -combination which minimizes the buckling load of the simply supported reference cylinder. The search was conducted again with a number of nonlinear buckling analyses for an initial imperfection amplitude w_{mn} of $0.1 h$, similar to the procedure for the initial dimple dimensions described in Section 6.6.3. The reduced buckling load for $m/n = 11/7$ was $P_{cr} = 381$ kN, whereas that for the mode $m/n = 13/8$ –which yields about the classical buckling load– was $P_{cr} = 390$ kN. *Thus, contrary to the mentioned assumption the buckling mode associated with the buckling load of the perfect reference cylinder was not the most damaging imperfection shape for this shell!*

In Figure 6.120 the normalized buckling loads $P_{cr}/P_{cr id}$ achieved for the imperfections pattern in 6.119 (a) of $m/n = 11/7$ are plotted versus the double of the normalized initial amplitude, thus $2 \cdot w_{mn}/h$. By this means for small initial amplitudes the loads correlate with the values for a single dent as well with the results for a single ring-shaped, all of simple initial depth w_b/h . The results for the initial dents of initial widths a_b and heights l_b as indicated correspond to the values already shown in Figure 6.110. Figure 6.119 (b) above gives information about the geometric difference between the amplitude w_{mn} of the bi-harmonic deformation function $w(x, y)$ in the classical analysis (Section 2.2.2, p.

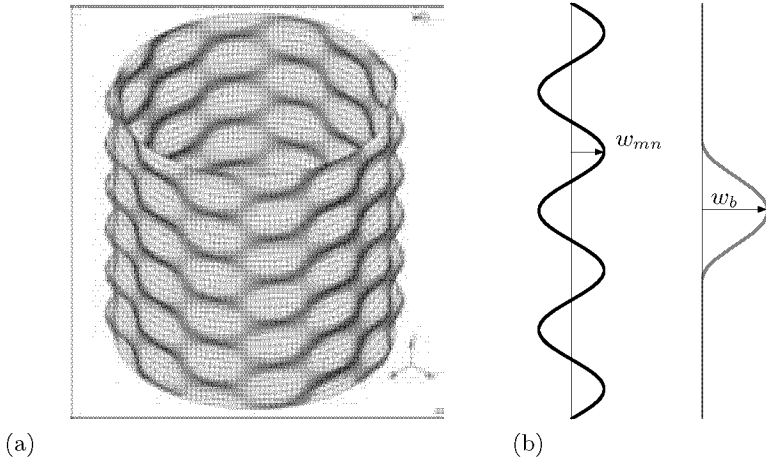


Figure 6.119: (a) classical buckling mode with $m = 11$ half-waves in axial and $n = 7$ waves in circumferential direction, (b) amplitudes of buckling modes (w_{mn}) and of single dimples (w_b).

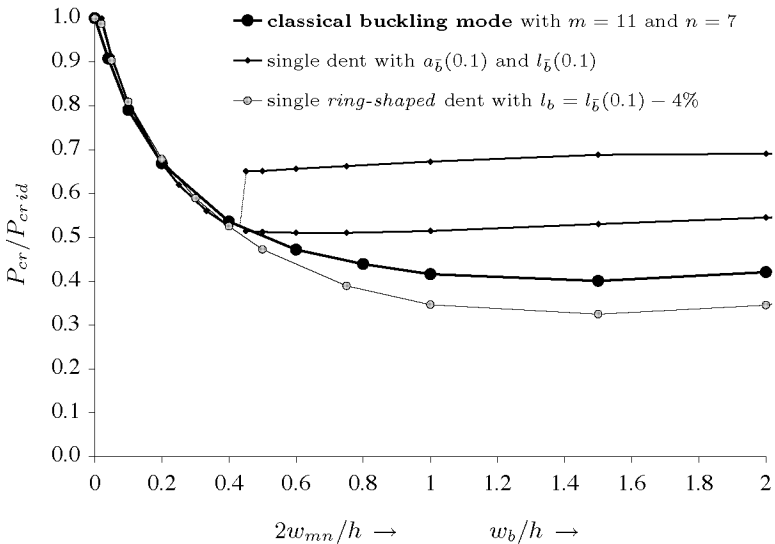


Figure 6.120: Nonlinear buckling analysis results for the reference cylinder having a classical buckling mode-shaped imperfection with wavenumbers as indicated. Comparison with results for a single dent of initial height $l_b = 181$ mm and width $a_b = 67$ mm and a single axisymmetric dent of initial height $l_b = 64$ mm.

51) and the amplitude w_b of the initial dimples defined in Equation 6.4 on page 197. The minimum buckling load obtained for the classical buckling mode of initial amplitude $2w_{mn} = 1.5h$ is $P_{cr \text{ MIN}} = 236 \text{ kN}$. This value lies between the -21% lower minimum for the ring-shaped dimples of $P_{cr \text{ MIN}} = 185 \text{ kN}$ and the 23% higher minimum for deep dents of $P_{cr \text{ MIN}} = 290 \text{ kN}$.

Although the numerical results could not be assured by analytical solutions or tests it was concluded that

- a linear buckling mode, which yields the minimum buckling load for a perfect cylinder, does not necessarily correspond to the most damaging imperfection pattern for a given initial imperfection amplitude, that
- single shallow dents ($w_b < w_b^*$) may reduce the buckling load of a cylinder as much as the initial deformations of double initial amplitude related to a classical buckling mode, and that
- single non-axisymmetric shallow dents with initial heights $l_{\bar{b}}$ and widths $a_{\bar{b}}$ small compared to the cylinder length and circumference tend to reduce the buckling resistance of isotropic cylinders as much as ring-shaped dents of similar initial height.

6.6.5 Stress Distributions

Finite element models are probably most commonly used to detect tensile or compressive stresses which are critical referring to mechanical strength, i.e. yielding or rupture. The searched stress field values have to be calculated from the priorly evaluated nodal displacements by means of the material law and interpolation functions. However, such stress analyses need less computational efforts than buckling analyses since neither for linear nor for nonlinear stress analyses expensive eigenvalue extractions are necessary. But, analysts dealing with lightweight structures are often more confronted with stiffness problems than with material strength limitations, since above all *local* buckling may occur at stresses far below the yield or rupture point of the material. The possible presence of local compressive stresses may give information on the existence of a structural instability problem, but whether the tested loading underpins the critical buckling load remains unknown. The total collapse of

a structure in general leads to very large displacements and hence also to exorbitant strain and stress values, but in cases of localized instability problems excessive displacements may be prevented by the support of stable parts of a structure as a whole. In such a case, the resulting stress values do not point to any instability problem. The eigenmodes to an analysis case, in turn, which result from the eigen problem with the initial stress stiffness matrix, demonstrate the location of possible buckling problems; but these analytical deformation patterns follow from the combination of the stress distributions (see Section 3.5).

Although from stress values no critical buckling loads can be derived directly, the stress and strain fields give valuable information for the investigations of the local buckling behaviour at single dimples in cylinders. The membrane force-per-unit-length distributions show the type of local loading of the shell in and in the vicinity of the dimples in dependency of the axial cylinder compression, and also the varying range of the shell surface influenced by single dimples is indicated. Therefore, this special section was included to present distributions of stresses and membrane forces/unit length in different directions and their alterations during axial loading for some selected cylinder shells with single inward dimples, in addition to the contour-deformation plots of cylinders with dents and bulges already displayed in Section 6.6.1 and 6.6.2.

The strain fields follow from the stress fields via the constitutive law and vice versa; thus, in case of linear material elasticity they would differ in amplitudes and unites, but not in the pattern of their distribution in the shell surface. Therefore, an additional display of strains was not found necessary.

Membrane Forces in a Perfect Circular Cylinder

The deformation pattern of a perfect circular cylinder under axial load prior to its collapse is axially symmetrical and hence the variation of the axial membrane force in the pre-buckling state is also purely axisymmetric. In classical analysis the membrane stress, treated via membrane force per unit length, is separated in a stress of the fundamental state and a stress associated with the shell deflections, see Section 2.2. For *perfect* isotropic circular cylinder under pure axial loading the membrane forces per unit length of the fundamental state are assumed to be the

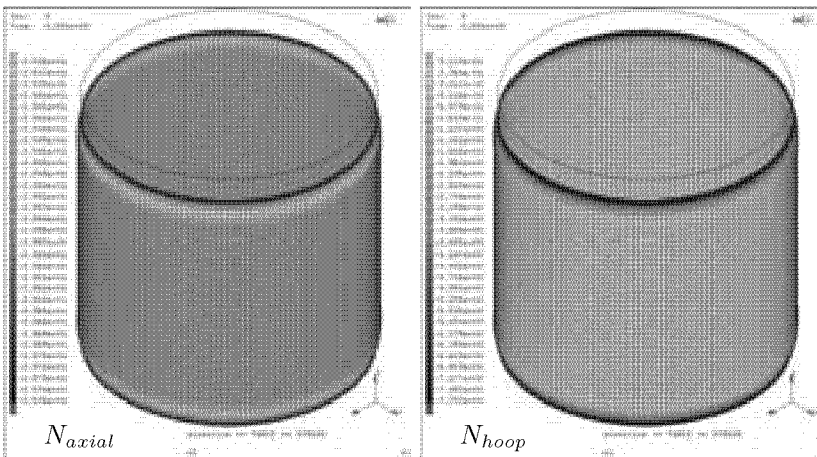
following:

$$\text{axial:} \quad \tilde{N}_x = \frac{-P}{2\pi R};$$

$$\text{circumferential:} \quad \tilde{N}_y = 0;$$

$$\text{shear:} \quad \tilde{N}_{xy} = 0;$$

with P for the axial compressive load. However, axisymmetric radial deflections w produce circumferential membrane forces per unit length of $N_y = w/R \cdot Eh$. Boundary effects neglected and for axial loads P small regarding the buckling load P_{cr} , in ideal cylinders the deflections w are negligibly small and hence the total axial membrane force N_x in the shell is approximatively that of the fundamental state, \tilde{N}_x . In Figure 6.121 the axial and circumferential membrane forces per unit length of the aluminium reference cylinder with perfect geometry are plotted for a small axial load of $P = 40$ kN. The membrane forces were calculated with a nonlinear static analysis and displayed with colour contour plots applied to the cylinder surface with amplified deformations. The nominal axial membrane force for this axial compressive load is



(a) axial membrane forces

(b) circumferential membrane forces

Figure 6.121: Axial and circumferential membrane forces per unit length of an aluminium cylinder with perfect geometry resulting for an applied axial load of $P = 40$ kN. Results of a nonlinear static analysis. Reference cylinder with $R = 250$ mm, $L = 510$ mm, $h = 1.5$ mm; buckling load: $P_{cr} = 569$ kN.

$\tilde{N}_x = -P/(2\pi R) = -25.5 \text{ N/mm}$. In Figure 6.121 (a) the resulting axial membrane force per unit length N_{axial} in the central part of the cylinder shell surface, colored in yellow, agreed well with the nominal value, as can be taken from the colour map at the left side of the plot. But at the two cylinder edges the axial membrane forces deviate a little from the nominal membrane force: at the border of the first and the last element somewhat increased axial membrane forces of about $N_{axial} = -25.8 \text{ N/mm}$ emerged, flanked by slightly relieved elements with minimum compressive forces of $N_{axial} = -25.4 \text{ N/mm}$. These small deviations from the nominal value stem from bending at the clamped cylinder edges where the radial expansion of the shell due to the POISSON'S ratio effect is restrained. The decay length of the deviation measures about the analytical wave-length of the axis-symmetrical buckling mode for this cylinder with $2l_c = 3.46\sqrt{Rh} = 66 \text{ mm}$, see Section 2.2. The resulting circumferential membrane forces per unit length N_{hoop} in the reference cylinder for an axial compressive load of $P = 40 \text{ kN}$ are depicted in Figure 6.121 (b). The light gray colour of the surface with sufficient distance of the cylinder edges stands for values close to zero, in agreement with assumption for quasi zero deflections. Again due to the boundary condition and the restrained radial expansion at the cylinder edges circumferential compressive membrane forces of maximal $N_{hoop} = -7.7 \text{ N/mm}$ and small tensile forces of maximal $N_{hoop} = 0.5 \text{ N/mm}$ resulted. With increasing axial compression the axially symmetrical bulges at the two edges of an ideal cylinder grow and above and below these first dimples slowly further axis-symmetric dents and bulges are formed, until close to buckling the cylinder is filled in its full length with ring-formed buckles of small amplitude and axial wavelength $2l_c$, approximatively. The distribution of the membrane forces per unit length again follow from the state of deformation and hence the axial as well as the circumferential membrane forces vary axis-symmetrically with the distance of the shell edges. In Figure 6.122 again the axial membrane forces N_{axial} and the circumferential membrane forces N_{hoop} of the reference cylinder are reproduced, but for an applied axial load of $P = 568 \text{ kN}$ just prior to the cylinder collapse, which according to nonlinear buckling analyses occurs at a load of $P_{cr} = 569 \text{ kN}$, see Section 4.2.1. The nominal membrane forces per unit length appendant to the applied compressive load P is $\tilde{N}_x = -362 \text{ N/mm}$. The plot in Figure 6.122 (a) demonstrates that the resulting compressive axial membrane force N_{axial} are reduced on the apexes of the outward dimples and amplified in the furrows of the inward dimples, since the neutral surface of the superposed shell bending is shifted from the middle surface towards the cylinder axis. The

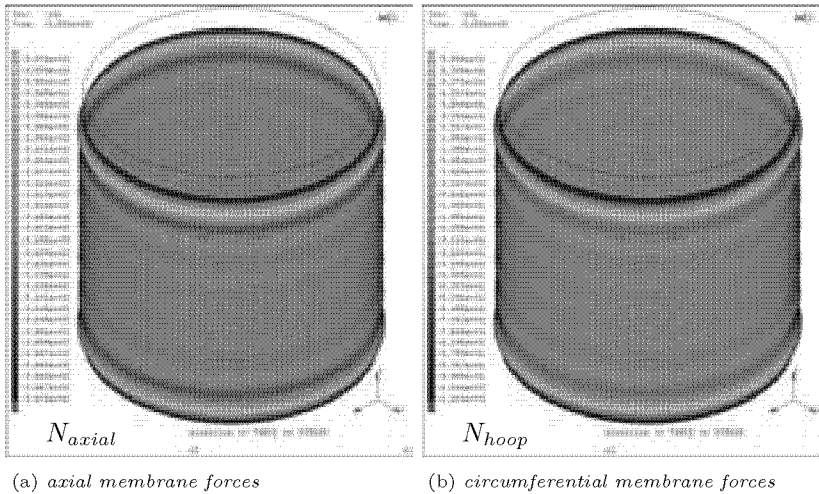


Figure 6.122: Axial and circumferential membrane forces per unit length of the ideal reference cylinder in Figure 6.121 resulting for an applied axial load of $P = 568 \text{ kN}$. State just prior to the buckling of the ideal cylinder at circa $P_{cr} = 569 \text{ kN}$.

circumferential membrane force per unit length N_{hoop} , shown in Figure 6.122 (b), now deviate from zero in the entire cylinder shell. Due to the the POISSON'S ratio effect and thus following the distribution of the flexural stress in axial direction, on the bulges the shell is stretched circumferentially whereas in the dents the shell is compressed. Consequently, tensile circumferential membrane forces $+N_{hoop}$ resulted on the bulges and compressive forces $-N_{hoop}$ in the inward dimples. For both axial forces the resulting shear membrane forces per unit length are very small and vary only marginally owing to numerical inadequacies, that is: $N_{shear} \approx 0$, as expected.

Membrane Forces in Cylinders with a Single Initial Dent

Contrary to perfect cylinders, in cylinders with initial imperfections from the beginning of the axial compression stress distributions emerge with axial membrane forces which may differ considerably from the nominal value, and the circumferential as well as the shear membrane force deviate substantially from zero. Furthermore, during loading the stresses are continuously rearranged according to the actual state of deformation. In

the following, the alteration of the complex stress distributions whilst axial compression of isotropic cylinders afflicted with an initial single inward dimple is detailed again by means of the reference cylinder, but having a single dent of initial depth $w_b/h = 0.3$. This imperfection also exemplified in Section 6.6.1 and has an initial width of $a_b = 181$ mm and an initial meridian height of $l_b = 66$ mm.

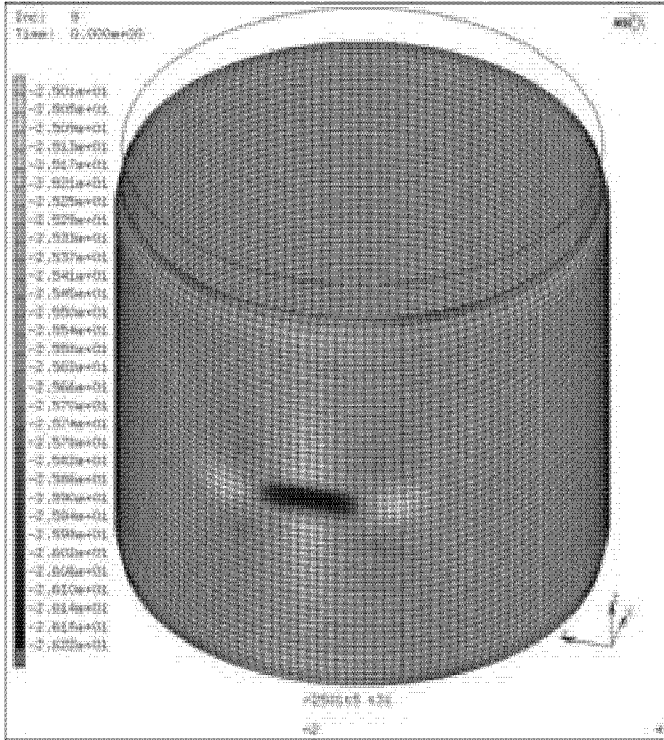


Figure 6.123: Axial membrane forces per unit length N_{axial} of the reference cylinder with $L = 510$ mm, $R = 250$ mm, and $h = 1.5$ mm, having a single inward dimple of initial depth $w_b/h = 0.3$. Result of a nonlinear static stress analysis for an axial load of only $P = 40$ kN.

Figure 6.123 reproduces the axial membrane forces per unit length N_{axial} of this shell resulting for an applied axial compressive load of $P = 40$ kN that equals a nominal membrane force of $\tilde{N}_x = -25.5$ N/mm. The associated resulting distribution of the circumferential membrane forces per unit length N_{hoop} are depicted in Figure 6.124. The stresses and

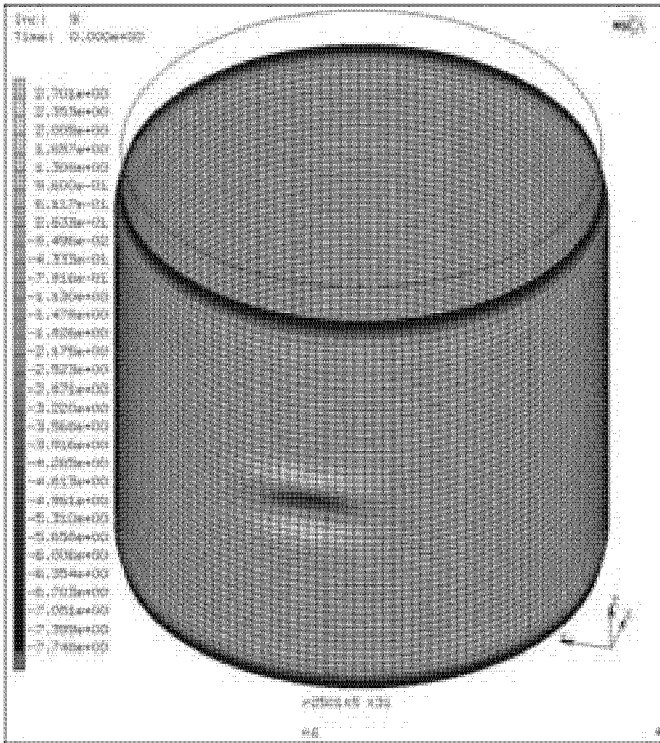


Figure 6.124: Circumferential membrane forces per unit length N_{hoop} resulting for the shell in Fig. 6.123 with a dent of initial depth $w_b/h = 0.3$ and an applied axial load of $P = 40$ kN.

membrane forces were again obtained with a nonlinear static analysis, and the relatively small axial compression corresponds to that of the reference cylinder without imperfections whose membrane force distributions are shown in Figure 6.121. Similar to the ring-formed buckles of the ideal cylinder in Figure 6.122(a) in the dimple the axial membrane force per unit length N_{axial} is increased, whereas at parts where the shell is bulged the membrane force is reduced. According to the colour map in Figure 6.123 the resulting maximum axial compressive membrane force on the vertex of the dent is $N_{axial} = -26.2$ N/mm, which deviate 0.7 N/mm or 2.8% from the nominal value \tilde{N}_x . On the apices of the two bulges on the left and the right of the dent, and also above and below the dent, bright-toned stains indicate shell elements where the analysis yielded axial compressive membrane forces below the absolute nominal

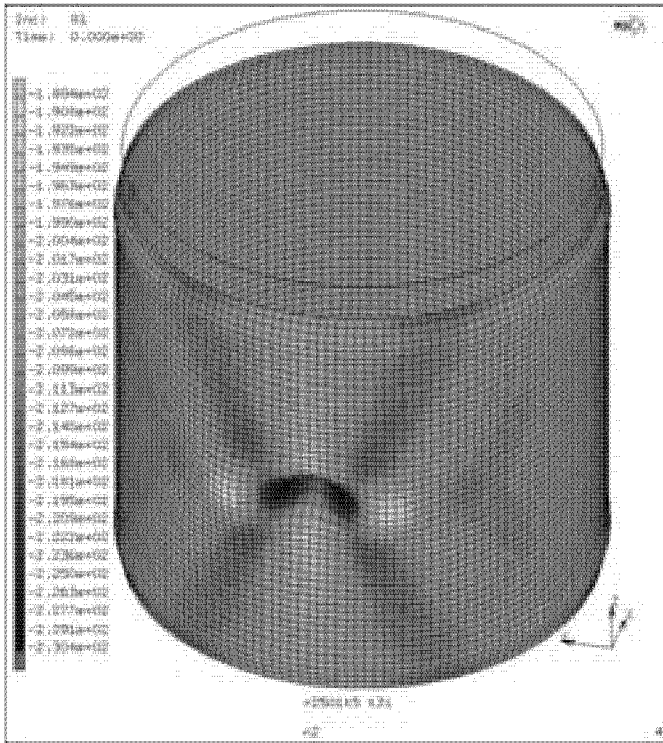


Figure 6.125: Axial membrane forces per unit length N_{axial} of the reference cylinder with a dent of initial depth $w_b/h = 0.3$ resulting for an axial load of $P = 328 \text{ kN}$ close to local buckling ($P_{cr} = 330 \text{ kN}$).

axial membrane force. The minimum value is $N_{axial} = -25.0 \text{ N/mm}$, thus -0.5 N/mm or 1.9% below the nominal value. Above and below the dent the grey to bright yellow colour shows that the curved, almost undeformed zones are relieved. But beside these vertical strips four skew orange shell sectors emerged, radiating from the lateral flanks of the dent, with elements that have slightly increased axial membrane forces. These parts around the imperfection with additional compressive axial loading spreads out to the clamped cylinder edges. That following, above and below the dent at these edges the axial membrane forces are diminished whereas aside these minima they are raised.

With increasing axial loading of the cylinder the amplitudes of the dimples grow and consequently the deviations of the membrane forces from

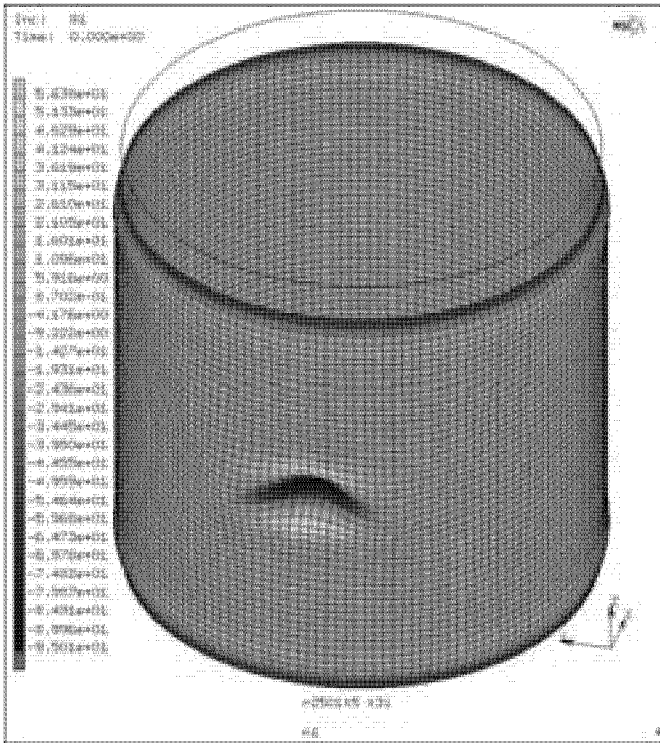


Figure 6.126: Circumferential membrane forces per unit length N_{hoop} resulting for the cylinder shell in Fig. 6.125 with a dent of initial depth $w_b/h = 0.3$ and an applied axial load of $P = 328$ kN close to buckling.

the nominal value increase. Therefore, the distribution of the axial membrane force per unit length N_{axial} with brighter vertical strips of diminished stress below and above the initial dent, with a dominate shell loading in the dent, and with two red \rangle or \langle -formed shell parts of elevated axial loading becomes more distinctive. In the color contour plot of Figure 6.125 the axial membrane forces per unit length N_{axial} of the shell at hand, calculated for an axial load of $P = 328$ kN, are reproduced. This compressive force is close to the local buckling load $P_{cr} = 330$ kN of the reference cylinder with the dent of initial depth $w_b/h = 0.3$, the corresponding nominal membrane force is $\tilde{N}_x = -208.8$ N/mm. Contrary to the shell loaded with only $P = 40$ kN and a single membrane force concentration at the centre of the dent, now two dark spots beside the dimple apex resulted which refer to maximal forces of about

$N_{axial} = -230.4 \text{ N/mm}$. That is, the concentration of axial membrane force at the apex is split into two peaks at the lateral edges of the dimple. On the two bulges on the left and the right of the dimple the axial compressive membrane force was diminished to a minimum value of about $N_{axial} = -189.4 \text{ N/mm}$. The maximum deviation from the nominal value is circa 22 N/mm absolute or about 11% relative. In addition to the spots with extremal values at the dent and the bulges again a bright yellow, vertical strip from the bottom-up with weakened axial membrane forces emerged, flanked by red shell parts with elevated membrane forces which radiate from the dark peaks.

The region of the cylinder shell around the dent, where the circumferential membrane forces per unit length N_{hoop} deviate perceptibly from the nominal value in an perfect cylinder ($N_y = 0$), is much smaller than that for the axial membrane forces described above. The contour deformation plots in Figure 6.126 and 6.124 show the resulting circumferential membrane forces per unit length N_{hoop} for the shell above loaded with an axial compressive load of $P = 328 \text{ kN}$ and $P = 40 \text{ kN}$ accordingly to the plots in Figure 6.125 and 6.123 for the axial membrane forces. For both loads in the dent a concentration of the compressive circumferential membrane force N_{hoop} occurred, in case of the applied axial load close to local buckling with a maximum of circa $N_{hoop} = -95 \text{ N/mm}$. The slight bulging above and below the dent led to tensile circumferential forces, for the higher loading with a maximum of about $N_{hoop} = 56 \text{ N/mm}$. But besides the dent the circumferential membrane forces are almost zero, as in the vertical strip above and below the dent where the axial membrane force is clearly reduced.

In Figure 6.127 the shear membrane forces per unit length N_{shear} for the shell above is shown, again resulting for an applied axial force of $P = 328 \text{ kN}$. The contour deformation plot with the shear membrane forces supplement the similar plots in Figure 6.125 and 6.126 which include the axial and circumferential membrane forces per unit length of the shell with this axial load. The nominal shear membrane force per unit length in an ideal cylinder is zero, but around the dent shear membrane forces resulted with peaks up to $\pm 23 \text{ N/mm}$ placed at the edge of the dimple. The colour pattern in the contour plot give reason for the existence of small shear membrane forces also at the cylinder half opposite to the imperfection, but the coloured spots there are rather a result of numerical inconsistencies due to small numbers.

All the finite element calculations presented so far were conducted for cylinders with controlled axial edge displacements according to the

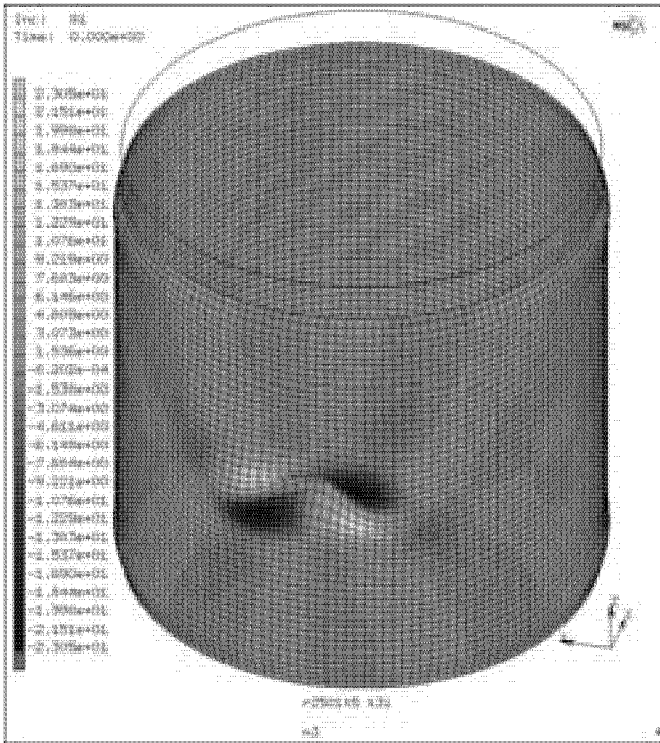


Figure 6.127: Shear membrane forces per unit length N_{shear} resulting for the cylinder shell in the two previous figures with a dent of initial depth $w_b/h = 0.3$ and an applied axial load of $P = 328$ kN.

clamped boundary conditions CC_4 in the shell calculus. Both edges are clamped retaining all rotations, the radial and the circumferential displacements of the nodes along the cylinder boundaries. By means of a central auxiliary node tied to the edge nodes, rigid, plane parallel end plates were simulated, see Section 6.4. Consequently, an axial compression of such a cylinder model by application of either given cylinder end-shortenings ΔL or total axial compressive loads P on the auxiliary node provokes axial displacements u identical for all edge nodes but potentially non-uniformly distributed axial membrane forces N_{axial} along the cylinder edges. In Figure 6.128 the axial membrane forces per unit length \bar{N}_{axial} in the elements along the path over the dent apex at $L/2$ around the reference cylinder with the dent of initial depth $w_b/h = 0.3$ are shown again for an applied axial load of $P = 328$ kN. The axial mem-

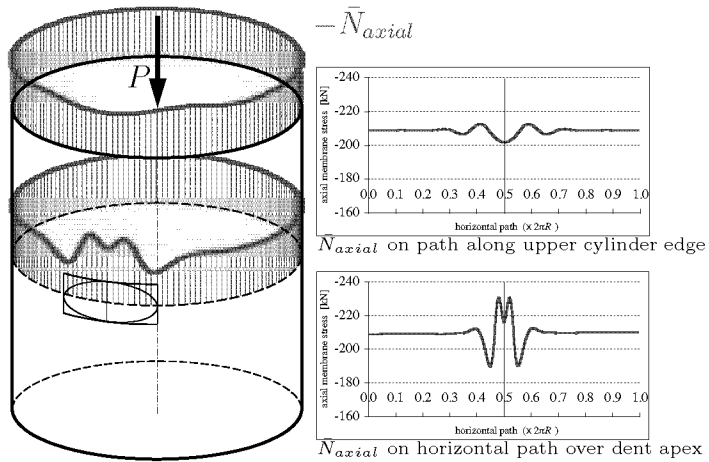


Figure 6.128: Axial membrane forces per unit length \bar{N}_{axial} in the elements along the upper cylinder edge and along the horizontal path over the dent of initial depth $w_b/h = 0.3$ applied to the reference cylinder. Results of a non-linear static analysis at an applied axial compressive load of $P = 328$ kN and for cylinder edges with the clamped boundary conditions CC_4 which simulate rigid, plane parallel endplates with resulting uniform axial edge displacements of $\Delta L = -1.01$ mm.

brane forces N_{axial} in this cylinder shell resulting for this load close to the local buckling load were already presented in the contour-deformation plot of Figure 6.125, page 371. Additional to the progression of the membrane forces along the path over the dent apex also that around the upper cylinder edge was included for comparison. At the right of the drawn cylinder with a more qualitative indication of the membrane force-per-unit-length distribution applied, in two charts the respective uncoiled membrane-force curves around the shell are reproduced with an adapted scale. It can be seen that the resulting axial membrane forces per unit length \bar{N}_{axial} along the upper edge vary in a similar way to the forces distributed along the path over the dent, albeit with lower deviations from the nominal value. As already mentioned, whilst axial cylinder compression the membrane force in the vertical strip over the dent from the bottom cylinder edge up to its top edge diminishes. During this stress relief at the dent centre, the axial compressive membrane force concentration is split into two peaks to the left and the right of the dent vertex. Two small peaks of compressive membrane force emerged also along the cylinder edge, but the distance of these peaks from the

dent apex (at $0.5 \times 2\pi R$) is larger compared with that of the two peaks at the lateral dent sides. From Figure 6.125 it can be taken that this longer distance stems from the shape of the four red zones of higher compressive axial membrane forces which radiate slantwise from the peaks beside the dent apex up to the cylinder edges.

As detailed in the previous sections, during axial cylinder compression the depth of an inward dimple continuously increases and at the edges of the initial dimple further bulges and dents emerge. Then, depending on the width and the depth of the so deformed dimple the cylinder shell is flattened locally. As a consequence thereof, within the vertical strip from bottom-up over the dent the axial stiffness due to the shell curvature vanishes. With decreasing curvature in the dimple the axial membrane force in the shell strip diminishes as well, whereas the two lateral flanks of the dent are additionally stressed. That is, the axial membrane force is transferred from the flattened vertical strip over the dent to the curved shell parts between the inward and the two outward dimples. To demonstrate the positions of the membrane-force maxima and minima whilst axial cylinder compression in Figure 6.129 the axial membrane forces per unit length in the shell elements \bar{N}_{axial} along a horizontal path are shown in comparison to the curvatures $1/\tilde{r}_k$ and the radii r_k of the nodes along this path, see Section 6.5.3. These values are results of a transient dynamic analysis of the reference cylinder afflicted with dent above of initial depth $w_b/h = 0.3$, initial arc-length $a_b = 181$ mm, and initial height $l_b = 66$ mm. In contrast to nonlinear buckling analyses the transient dynamic analyses enables to display membrane-force distributions after the local buckling of the shell at hand with only minor deviations of static analysis results due to damping. The axial membrane force per unit length \bar{N}_{axial} plotted in the bottom chart resulted for axial compressions ΔL of 1.012 mm, 1.030 mm, and 1.039 mm which yielded the reaction forces P of 328 kN, 333 kN, and 326 kN, respectively, as indicated. The first load is before, the third after the sudden shell flattening during the local buckling. The values are axial membrane forces per unit length averaged in each element of the path which starts at the apex of the dent and runs counterclockwise around the half cylinder circumference, as indicated with the small sketch in the centre of Figure 6.129 or as introduced in Section 6.5.3. In the top chart the local radii r_k and in the chart below the approximated local curvatures $1/\tilde{r}_k$ along the nodal path corresponding to the element path for the membrane forces are plotted which result for the aforementioned axial loadings. The thin lines with circlets show the radii and curvatures of the unloaded initial configuration. The vertical dash-dotted line in all

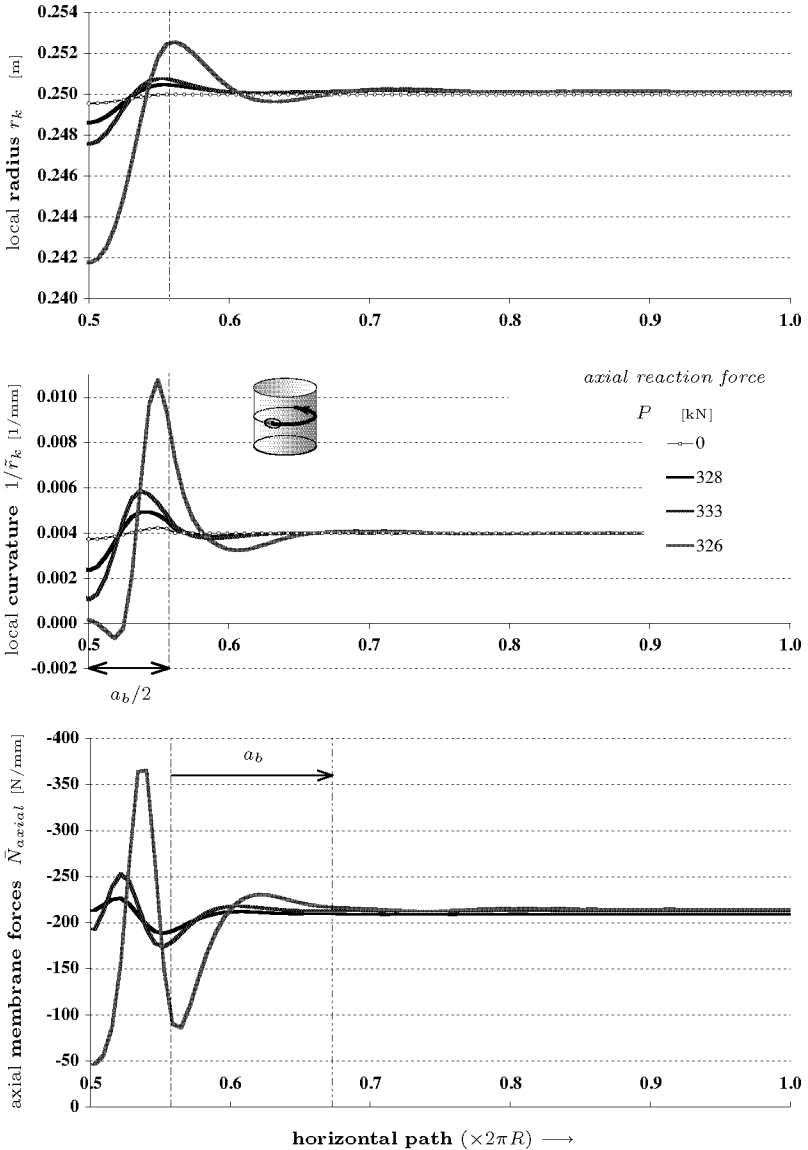


Figure 6.129: Axial membrane forces per unit length \bar{N}_{axial} , approximated curvatures $1/\bar{r}_k$, and radii r_k along the horizontal path from the apex of the dent (\rightarrow small sketch). Results of an transient dynamic analysis referring to axial loads P as indicated. Reference cylinder having an initial dent with $w_b/h = 0.3$, $a_b = 181$ mm, $l_b = 66$ mm.

three charts give the distance from the initial lateral end of the dent to the apex of the applied dent, in the present case $a_b/2 = 90.5$ mm. According to the distributions of the membrane forces per unit length and the respective local curvature and radii for the three load levels the peaks with the highest compressive axial membrane forces per unit length \bar{N}_{axial} are shifted to the element where the respective curve for the local-curvatures $1/\tilde{r}_k$ crosses the thin line with circlets for the initial state. That is, the shell elements at the lateral flanks of the dent had to sustain additional axial membrane loading where the shell curvature is about that of the unloaded state. After local buckling (red lines) the approximated curvatures at the first four nodes beside dent centre fell to quasi-zero and also the axial membrane forces were reduced to a minimum of less than -50 N/mm, thus about $1/4$ of the nominal value of -208 N/mm. The radius r_k at the lateral edges of the dent (vertical dash-dotted line) increases whilst cylinder compression since new bulges are formed where the axial membrane force diminishes. And again adjacent to these bulges further inward dimples emerge which slightly raise the axial membrane force locally.

The main deviations of the axial membrane forces as well as of the local radius and the curvature from the values for the ideal cylinder, prior to the total cylinder collapse, are decayed after a lateral distance from the initial dent of about $1.5 a_b$, as denoted with the second vertical, thin dash-dotted line in the bottom chart.

The alteration of the radii and curvatures of the nodes along the horizontal path above with increasing axial compression of the reference cylinder with the dent of initial amplitude $w_b/h = 0.3$ is also shown in Section 6.6.1 by means of surface plots which are formed by a sequence of curvature or radius curves similar to the curves in the upper two charts in Figure 6.129. In Figure 6.130 the progressions of the axial membrane forces per unit length \bar{N}_{axial} in the elements along the horizontal path from the dent apex around half the cylinder circumference are plotted also sequenced bottom-up for increasing axial loading. The uncoiled path again serves as x-axis from left to right of the surface plots with the dent apex at the left end. The y-axis from the bottom up indicates the applied axial compression ΔL . Figure 6.130 (a) shows the runs of the axial membrane forces for the deformation process whilst local buckling, and plot (b) below for that during total cylinder collapse. The runs of the radii r_k of the nodes along the path resulting for the analysis at hand and for the sequence of load steps ΔL in plot (a) are presented with a similar surface plot in Figure 6.43, page 258, and the radii for the

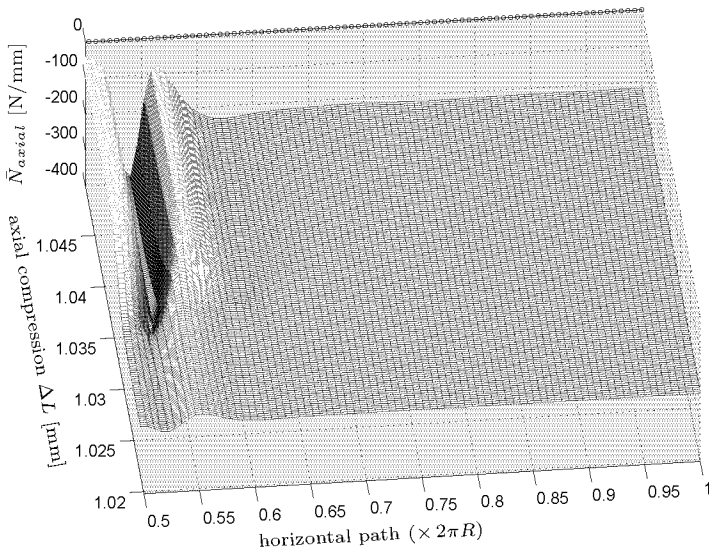
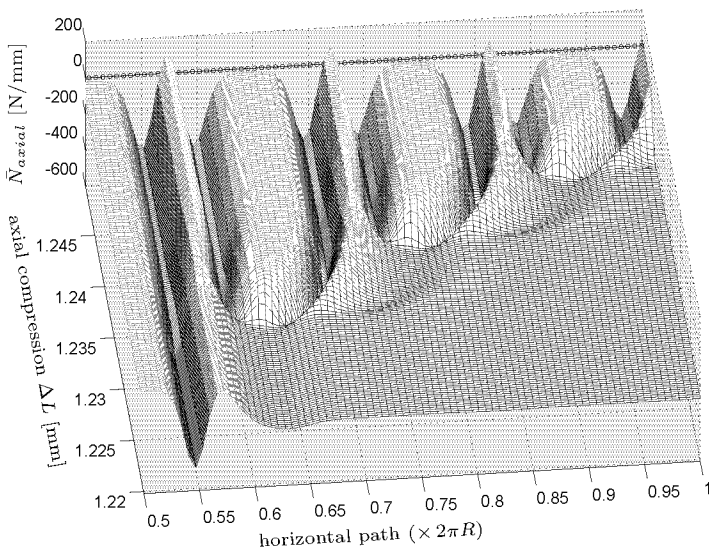
(a) Part 1: *local buckling*(b) Part 2: *cylinder collapse*

Figure 6.130: Sequenced progressions of the axial membrane forces per unit length \bar{N}_{axial} along the horizontal path between the dimple apex and its opposite point for a dent of initial depth $w_b/h = 0.3$ applied to the isotropic reference cylinder.

sequence of ΔL during cylinder collapse in plot (b) are given similarly in Figure 6.46, page 260. The approximated curvatures $1/\tilde{r}_k$ along the path according to the surface plots in Figure 6.130(a) and (b) are displayed in Figure 6.44, page 259, and Figure 6.47, page 261, respectively, again in similar surface plots. The axial membrane forces \bar{N}_{axial} are results of the same transient dynamic analysis as the values in the bottom chart of Figure 6.129, but in the surface plots negative values standing for compressive loading are oriented downward. The line \dashrightarrow serves to indicate the upper edge of a plane in the plot with zero axial membrane force $\bar{N}_{axial} = 0$. The curve made up by the lower boundary of the “surface” in Figure 6.130(a) resembles the black membrane-force curve in the bottom chart of Figure 6.129 for the state of stress and deformation prior to local buckling but is upside down, i.e. mirrored with respect to $\bar{N}_{axial} = 0$. The curve to the upper “surface” boundary of the surface plot accordingly is similar to the inverted red curve in the line chart representing the state of a partially flattened shell after local buckling. In the successively deepening and flattening dent, close to the y-axis of the surface plot (a), the axial membrane force is significantly reduced and hence the surface grid lines there change from red to yellow. The adjacent black valley in the “surface” depicts the high concentration of axial compressive membrane force arisen at the right flank of the dent. In Figure 6.130(b) also the alteration of the axial membrane forces per unit length along the path during the total collapse of the cylinder is shown. After the collapse, in the cavities of the applied dent and the laterally formed new dimples the axial membrane force is almost zero, what can be taken from the yellow tops of the wider “hills” in the “surface”. The black furrows at each side of these quasi-zero-load segments refer to the elements at the lateral flanks of the buckles which are massively stressed. Between these compressive force peaks, on the top of the narrow bulges formed between the inward dimples, due to outward bending small tensile axial membrane forces $+\bar{N}_{axial}$ resulted, which in the surface plot are represented by light-coloured “pinnacles”.

Influence of the initial dent depth w_b/h

The deviation values of the membrane forces in an isotropic cylinder with a single initial dimple from the their values for the ideal cylinder depend on the applied axial load and on the actual size and amplitude of the dents and bulges in the shell. The alteration of the shell geometry during loading, in turn, follows from the initial dimensions of the applied dimple

and of the cylinder. The influences of the initial dimple amplitude, the initial width and height of the dimple, as well as of the cylinder length, radius and wall thickness on the deformation process and the reduced axial buckling load of the cylinder are explained in Section 6.6.1 for dents and 6.6.2 for bulges. To demonstrate the impact of the initial dent depth w_b on the axial load at which the shell flattens partially, and on the process of this local stiffness reduction (e.g. local buckling), in Section 6.6.1 additional to the analysis results for the dent of initial depth $w_b/h = 0.3$ also the resulting critical loads and deformation states for the dents with $w_b/h = 0.1$ or $w_b/h = 0.5$ but otherwise identical geometry are depicted. These exemplary dents with an initial width of $a_b = 181$ mm and height $l_b = 66$ mm were added to the reference aluminium cylinder above with length $L = 510$ mm, radius $R = 250$ mm and shell thickness $h = 1.5$ mm. Already there the axial membrane forces per unit length N_{axial} together with the circumferential membrane forces N_{hoop} for these three dents were reproduced in contour deformation plots: in Figure 6.35 on page 247 the membrane forces for the dent of initial depth $w_b/h = 0.1$, in Figure 6.41 on page 255 those for the dent of initial depth $w_b/h = 0.3$, and finally in Figure 6.50 on page 266 those for the dent of initial depth $w_b/h = 0.5$. These distributions are results of nonlinear static analyses with constant load step size for axial compression forces close to local buckling or to the lowest critical load referring to local shell flattening.

In contrast to the two shallower dents the dimple with $w_b/h = 0.5$ provoked a continuous convergence to a flattened shell at the dent. Thus the given membrane forces in Figure 6.50 resulted for a load and state of strain with an already flattened shell strip. This shell geometry leads to rearrangements of the axial compressive stress with a more distinctive relief at the centre of the dent and peaks at the lateral dent flanks.

But a more significant difference between the resulting force distributions for the dent with initial depth $w_b/h = 0.5$ in Figure 6.50, p. 266, and those for the dent with $w_b/h = 0.3$ in Figure 6.41, p. 255, may be detected for the circumferential membrane forces N_{hoop} : in the case of the dent with $w_b/h = 0.3$ prior to local collapse in the centre of the dent resulted a single concentration of compressive circumferential membrane forces $-N_{hoop}$, whereas in the case of the already flattened dent of initial depth $w_b/h = 0.5$ two separate peaks of $-N_{hoop}$ at the flanks of the dent emerged, in the plot identifiably by the two dark stains. To enlighten this particular type of membrane-force distribution, in Figure 6.131 the circumferential membrane forces N_{hoop} and the axial membrane forces N_{axial} for a deep dent of initial depth $w_b/h = 1$ are depicted which were

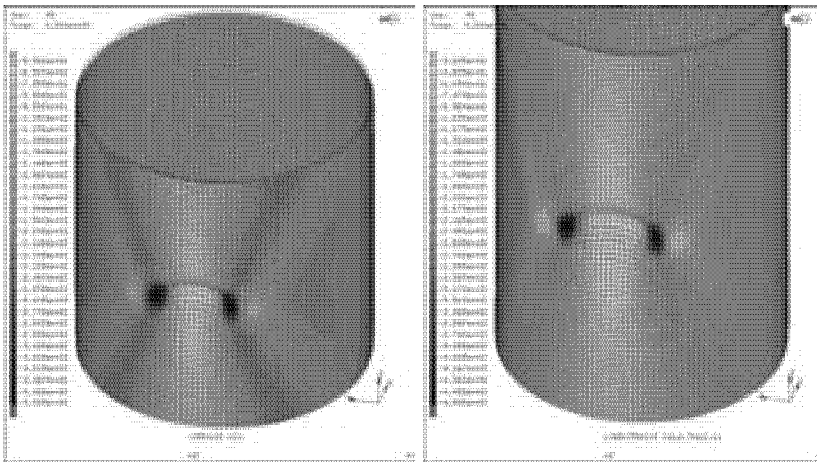
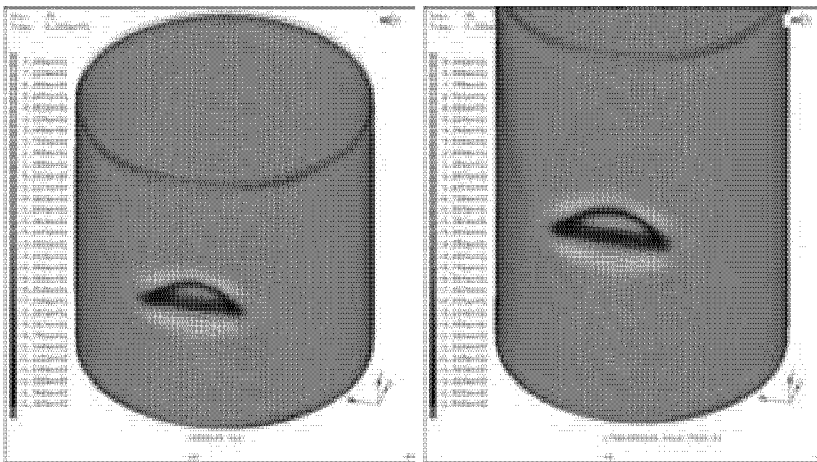
(a) *axial membrane forces N_{axial}* (b) *circumferential membrane forces N_{hoop}*

Figure 6.131: *Axial and circumferential membrane forces per unit length resulting for a dent of initial depth $w_b = h$ applied to the reference cylinder with length $L = 510$ mm (left column) and to the 50% longer cylinder with length $L = 765$ mm (right column). Results of nonlinear static analyses for an applied load of $P = 304$ kN. Wall thickness and radius for both cylinders $h = 1.5$ mm and $R = 250$ respectively. The initial width of the dent is $w_b = 181$ mm for both cases, the initial height $l_b = 66$ mm for the left and 69 mm for the right shell.*

yielded with a nonlinear static analysis for an axial load of $P = 304 \text{ kN}$ in the range of already accomplished shell flattening. Thus, this load is above the lower buckling load for local instability $P_{crL} = 293 \text{ kN}$ which resulted from a nonlinear buckling analysis of the mid-long reference cylinder having this dent ($L = 510 \text{ mm}$, left column), see Section 6.6.1. On the left contour-deformation plot of Figure 6.131 (b) for the circumferential membrane force distribution two separate dark stains can be recognized which denote a high compressive-force maximum of $N_{hoop} = -142 \text{ N/mm}$ at the lateral, far apart dent sides. But whereas in the centre of the dent the compressive force is small (orange coloured), at the upper and the lower side of the dent further “dark zones” with high compressive forces. The dent is again framed by tensile circumferential membrane forces with their maximum of about $N_{hoop} = +79 \text{ N/mm}$ above and below the dent. Thus, in this state the horizontal flattened strip from dent side to dent side resembles a longish plate which is loaded lengthwise at its narrow edges. Since the deformation plot were created with amplified radial displacements the actually flat shell strip in the initial dent is shown with an unreal curvature. The buckling mode in Figure 6.49 (d), Section 6.6.1, page 265, with a dent flanked by bulge follows from this particular local state of stress and deformation; it corresponds to the first buckling mode of a longish plate with respective boundary conditions and loading.

The nominal axial membrane force per unit length to the applied compressive load is $\tilde{N}_x = -193.5 \text{ N/mm}$. In the left contour-deformation plot of Figure 6.131 (a) the two dark spots for maximal axial compressive membrane force $-N_{axial}$ are separated by a wide vertical light-coloured strip with only small compressive axial forces. The resulting maximum compressive force at the flanks of the dent is $N_{axial} = -353 \text{ N/mm}$, thus about 82% in excess of the nominal value above. In contrast to the axial membrane force distribution for the dent with $w_b/h = 0.3$, a minimal axial membrane force of $N_{axial} = -59 \text{ N/mm}$ has settled in the centre of the wide vertical strip and not on the also relieved bulges at the left and the right side of the dent. This minimum value means a reduction to less than one third of the nominal value.

Influence of the Cylinder Dimensions L , R , and h

In Figure 6.131 the contour-deformation plots with the axial and the circumferential membrane forces/unit length for the 50% longer cylinder of length $L = 765 \text{ mm}$ afflicted with the dent of initial depth $w_b/h = 1$

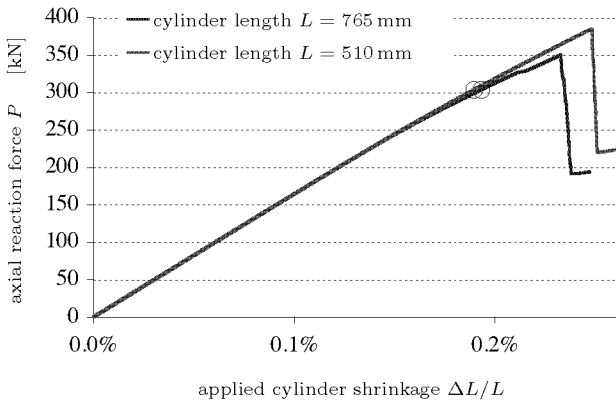


Figure 6.132: *Transient dynamic analysis results for a single dent of initial depth $w_b = h$ in two cylinders with lengths as indicated, radius $R = 250$ mm, and shell thickness $h = 1.5$ mm. Shells identical to those in Figure 6.131.*

and also loaded with $P = 304$ kN were added for comparisons (right column) to the plots for the reference cylinder with this dent (left column). This shell resulted a first buckling load of $P_{cr L} = 265$ kN with a nonlinear buckling analysis, but a transient dynamic analysis led to the observation of a second local buckling event at an axial load of circa $P = 320$ kN including a lateral shift of the dent to the left or the right of its initial position according to the aforementioned buckling mode of the compressed horizontal flattened strip, see Section 6.6.1. In Figure 6.132 the transient dynamic analysis results for the two shells of different length L in Figure 6.131 are charted. The two circlets indicate the axial load level $P = 304$ kN for which the membrane forces are shown above. It can be seen that the membrane forces in Figure 6.131 were obtained for an axial load below the second local buckling load in case of $L = 765$ mm and above the load (≈ 250 kN) at which both curves start to differ from a straight line due to the loss in axial stiffness in the flattened shell strip. The curves give the resulting axial reaction force P for the applied *normalized* axial compression $\Delta L/L$. The small offset in the blue curve left below the peak load stems from the mentioned second local buckling event during compression of the longer cylinder. This behaviour could not be observed for the shorter reference cylinder and hence the red curve is also bend but without any zig-zag course of the ascending curve prior to the cylinder collapse load. On the influences of the cylinder length L on the buckling behaviour of cylinders with a single

initial dimple it was already reported in Section 6.6.1. For both cylinder lengths the initial width of the dent was specified as $a_b = 181$ mm, enabling direct comparison of the resulting state of stress and deformation of the two cylinder shells with different lengths but otherwise like shell and imperfection geometry. For the identical applied axial load of $P = 304$ kN the sized distance between the clamped cylinder edges of the longer shell leads to larger radial displacements at the mid-length of the shell without a higher bending energy needed. Thus, the critical state of a partially flat shell and also the total collapse of the cylinder with $L = 765$ mm occurs at lower axial loads, as can be recognized in Figure 6.132 with the blue curve. The larger resulting displacements yield also higher deviations of the axial membrane forces per unit length N_{axial} in Figure 6.131 (a) as well as the circumferential membrane forces per unit length N_{hoop} in (b) from the same nominal values. The maximum axial membrane force, again located at the lateral sides of the dent, with $N_{axial} = -460$ N/mm is circa 30% higher than the maximum value for the reference cylinder with $L = 510$ mm. In the vertical flattened strip, which is somewhat wider than that of the mid-long reference shell, and the bulges at the dent sides again the axial membrane force is considerably reduced to a minimum of only $N_{axial} = -32$ N/mm, thus to about the half of the minimum value of the reference shell. However, probably more distinctive differences between the two cylinders may be found in the circumferential membrane force distributions in Figure 6.131 (b). In both cases high compressive forces/unit length $-N_{hoop}$ settled around the four dent sides with two peaks at the lateral flanks of the dimple; but in contrast to the reference cylinder, at the dent apex and centre of the flattened shell small tensile forces $+N_{hoop}$ resulted; the maximum compressive circumferential force of $N_{hoop} = -159$ N/mm is 12%, the maximum tensile force of $N_{hoop} = +94$ N/mm 18% in excess of the maximum value for the reference cylinder. The mentioned main differences between the distributions in left plots and those in the right plots of Figure 6.131 were probably decisive that a further axial compression of the longer cylinder led to the occurrence of the mentioned second local buckling incident, whereas that for the reference cylinder did not.

Nevertheless, the cylinder radius R and the shell wall thickness h exert the major influence on the absolute deviation values of the membrane forces in a cylinder having a dent. According to the formula for the buckling stress of perfect isotropic cylinder, $\sigma_{cr} = 0.6 E h/R$, cylinders with a larger radius have basically a smaller critical stress than cylinders with smaller diameter and otherwise like wall thickness and material. Therefore also local peak stresses are smaller for imperfect cylindrical shells

with larger radius. And at a given axial load for larger cylinder circumferences smaller stresses and membrane forces result. However, the extremal values of membrane forces in different cylinders, all having a dimple imperfection of a given initial amplitude, resulting for axial compressions always relative to the respective buckling loads become almost identical if normalized with respect to the corresponding nominal membrane forces \tilde{N}_x . That is, for example, the maximal *relative* deviation of the compressive axial membrane force per unit length resulting for an applied axial load of 90% of the collapse load, $P = 0.9 P_{cr}$, from the nominal membrane force \tilde{N}_x is identical for all cylinders having a dent with like initial depth and adequate initial lateral dimensions.

cylinder				dent		buckling loads		applied loads	
R	h	L	\sqrt{Rh}	a_b	l_b	P_{crL}	P_{crU}	P	\tilde{N}_x
[mm]	[mm]	[mm]	[mm]	[mm]	[mm]	[kN]	[kN]	[kN]	[N/mm]
187.5	1.0	382.5	13.7	124	50	127	157	156	-132
250	1.5	510	19.4	181	66	291	368	368	-234
500	0.75	510	19.4	181	66	74	97	97	-31
				width	height	local	cylinder	force	nominal

Table 6.4: Dimensions of three aluminium cylinders and initial lateral lengths of their dent with initial depth $w_b/h = 0.5$. Resulting local buckling and cylinder-collapse loads. Applied axial loads P related to the nominal axial membrane forces/unit length \tilde{N}_{axial} used for Figure 6.133.

In Table 6.4 the radius, the length and the shell thickness of the reference cylinder and two further exemplary aluminum cylinders are listed. The shells have a single inward dimple of initial depth $w_b/h = 0.5$ whose appropriate initial width a_b and initial height l_b are given in the table. Furthermore, the lower buckling loads P_{crL} referring to local shell flattening and the total collapse loads P_{crU} , both obtained with nonlinear buckling analyses, can be taken. The first two cylinders have both a diameter $2R$ almost as long as their length L , compared to the last shell with a diameter/length ratio $2R/L$ of about 0.5. And, all three shells differ in the radius/wall thickness ratio R/h . For the consideration of the axial membrane forces close to the total collapse of these three cylinder shells again nonlinear static analyses were performed and the resulting values along the horizontal path over the dent vertex listed. For the reference cylinder in the second row of Table 6.4, for instance, at an applied axial load of $P = 368$ kN just prior to the cylinder buckling P_{crU} (see penultimate column) the calculation yielded a maximum compressive

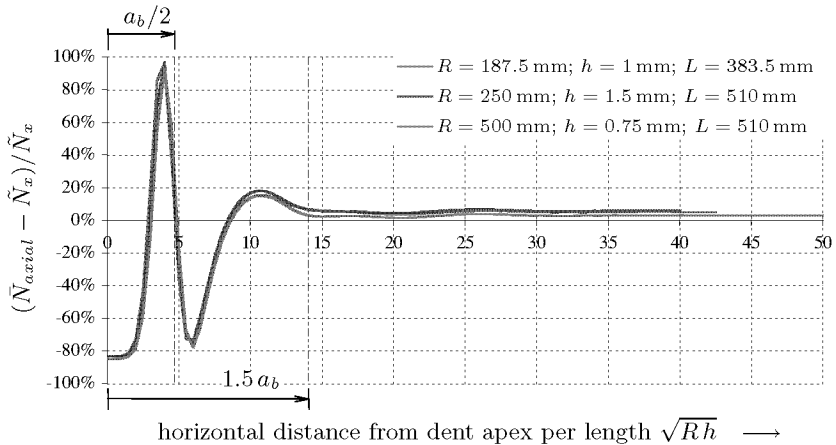


Figure 6.133: *Relative deviations of the compressive axial membrane forces per unit length $-\bar{N}_{axial}$ from the nominal compressive membrane force $-\tilde{N}_x$ along a horizontal path for three cylinders as indicated with a dent of initial depth $w_b/h = 0.5$. Distances from the dent apex in ratio to the length \sqrt{Rh} . Corresponding initial dent lengths a_b and l_b , and applied axial loads P listed in Table 6.4.*

axial membrane force of $\bar{N}_{axial} = -461$ N/mm. This peak value means a deviation from the nominal axial membrane force $\tilde{N}_x = -234$ N/mm (last column) of $\Delta N = -227$ N/mm. The corresponding relative deviation with respect to the nominal value results in $\Delta N/\tilde{N}_x = +97\%$. The similar calculation for the shell of radius $R = 500$ mm in the last row at an axial load of $P = 97$ kN yielded a peak of compressive axial membrane force of $\bar{N}_{axial} = -60$ N/mm and an deviation from $\tilde{N}_x = -31$ N/mm of only $\Delta N = -29$ N/mm. Compared with the reference cylinder, the radius/wall thickness ratio R/h of this wider shell is four times larger; therefore, the membrane forces as well as their extremal values are only a fourth of that of the reference shell. However, the relative deviation of the peak value above for the wider cylinder is $\Delta N/\tilde{N}_x = +94\%$, hence very close to the previous relative tolerance resulting for the reference cylinder.

In Figure 6.133 the relative deviations of the compressive axial membrane forces per unit length with respect to the nominal value $\Delta N/\tilde{N}_x$ of the three cylinders in Table 6.4 with a dent of initial depth $w_b/h = 0.5$ and applied axial loads just before collapse are depicted. To the left of the first vertical dash-dotted line, which indicates the initial right side of

the dent, the peaks with large relative deviations between 90 and 100 % for the reference cylinder (red line) and the wider shell with $R = 500$ mm (green line) can be relocated. As abscissa of the chart serves the distance of the elements in the horizontal path from the dent apex normalized in terms of the “wave-length” \sqrt{Rh} . As already repeatedly mentioned, during axial compression the zone of maximal axial compressive membrane force is shifted from the dent centre to its lateral flanks, and in the dent as well as on the bulges beside the dent the axial membrane force is diminished. The initial arc-length a_b and the initial meridian height l_b of the dent applied to the three cylinders, see Table 6.4, are the initial lateral dent lengths which resulted in the smallest buckling loads for an initial depth of $w_b/h = 0.1$, see Section 6.6.3. According to the results for the considered cylinders with common isotropic material both dent dimensions can be related to the wavelength $2l_c = 3.46\sqrt{Rh}$ for the axis-symmetric buckling of ideal isotropic cylinders. Consequently, the position of these extremal values measured in arc-length per root \sqrt{Rh} for isotropic cylinders with an accordant dent will be identical, and hence the runs of the three relative-deviation curves in Figure 6.133 agree almost completely.

From these results follows that isotropic cylinders of moderate length having a single dimple of a given normalized initial amplitude w_b/h , and axially compressed with a load at a given percentage to the buckling load P/P_{cr} , yield identical peak values and distributions of relative axial-membrane-force deviations $\Delta N/\tilde{N}_x$ in dependency of the length \sqrt{Rh} . That is, with results for a cylinder such as given in Figure 6.133 and known buckling loads it is possible to make good estimates of the axial membrane loading in any other cylinder with equal dimple amplitude w_b/h , appropriate dimple dimensions a_b and l_b , similar normalized axial load P/P_{cr} , and adequate cylinder length L . But due to the aforementioned impact of the cylinder length L on the force amplitudes, for the comparisons of cylinders with different wavelength \sqrt{Rh} , a similar length/radius ratio L/R or nondimensional parameter L/\sqrt{Rh} is provided, otherwise a larger underestimate of the peak membrane forces is probable.

The right dash-dotted line in Figure 6.133 horizontally distant $1.5 \cdot a_b$ from the dent apex indicates that the main \tilde{N}_{axial} -deviations along the path over the dent with $w_b = h/2$ close to cylinder collapse are limited within an arc of a length three times the initial dimple width, $3 \cdot a_b$. This approximative decay length along the horizontal path can be considered as a maximum lateral spread of the stress or membrane-force distur-

bances for applied axial loads below the collapse load of an isotropic cylinder with a single dimple imperfection.

Stress Distributions in Selected Shell Cross-Sections

Membrane forces per unit length stem from the mean stresses in cross sections of a shell. Thus, with the reproduction of membrane forces the peak stress values within a shell remain hidden. In case of pure shell bending, for example, the membrane force is zero despite high stresses at the outer skins of the shell.

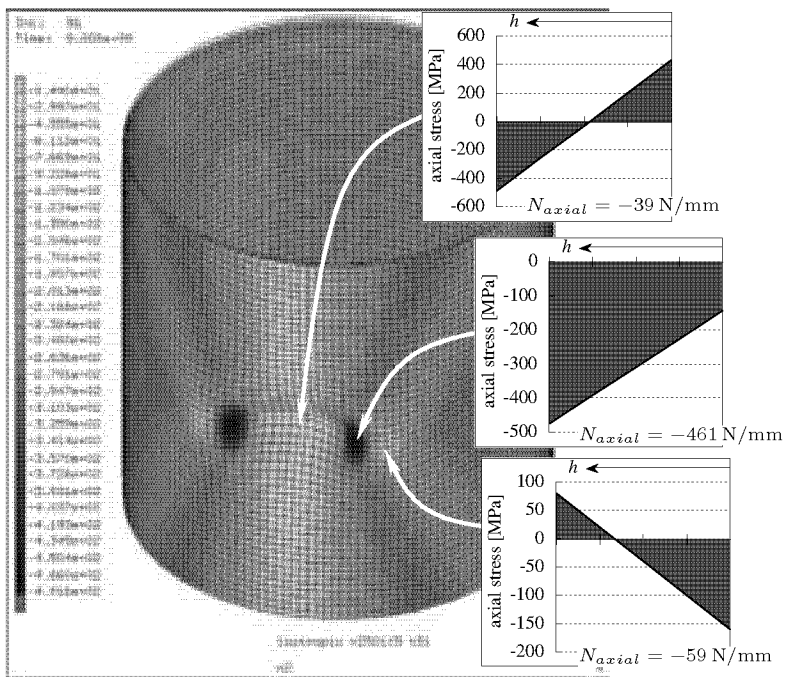


Figure 6.134: Distributions of the axial stress σ_{axial} in the shell cross section at three selected spots in the reference cylinder with a dent of initial depth $w_b/h = 0.5$ as indicated, resulting for an applied axial force of $P = 368 \text{ kN}$. CAUCHY stresses obtained with a nonlinear static analysis. Contour-deformation plot in background to display the respective axial membrane forces per unit length N_{axial} .

Since the cylinder shells with initial dents are not only compressed but

also considerably bent, in Figure 6.134 the distributions of the axial CAUCHY stress σ_{axial} in three shell cross sections are depicted again resulting for the reference cylinder with a dent of initial depth $w_b/h = 0.5$ as given in the second row of Table 6.4. The stresses in the charts σ_{axial} as well as the axial membrane forces/unit length N_{axial} are results of a nonlinear static analysis at an applied axial load of $P = 368$ kN. The cylinder, the dent and the applied load agree with those which yielded the red \bar{N}_{axial} -deviations curve in Figure 6.133. The selected cross sections are located at spots with maximal or minimal compressive membrane forces N_{axial} , as indicated with white arrows in the contour-deformation plot. The membrane forces associated with the stresses in the cross sections are given at the lower chart border. The stresses σ_{axial} at the outer shell skin are left at the ordinates, that of the inner surface at the right side of the stress charts. Thus, from the slope of the straight line joining the axial stresses in the second chart follows that there, additionally to axial compressive stresses, high bending stresses due to the indentation are superposed. In the centre of the dent the shell is almost flat; however, during the deformation process at the dent apex high bending stresses are formed at small membrane forces, see first chart. The tensile stresses are located at the inner shell skin, hence the stresses are result of the bending whilst the continuous deepening of the dent. In the third chart, in contrast, the tensile stress are at the outer shell skin, and thus in this case the moderate bending stresses result for the bulging of the shell at the lateral dent sides.

Similarly, in Figure 6.135 the distributions of the circumferential CAUCHY stress σ_{hoop} in three shell cross sections again for the shell and load level as in Figure 6.134 are shown. The resulting circumferential membrane forces N_{hoop} at the selected spots in the shell, again marked with arrows, are indicated at the right or below the stress charts. The stresses σ_{hoop} at the outer shell surface are now at the top, that of the inner surface at the bottom of the charts. At the centre of the dent the *compressive* circumferential membrane force \bar{N}_{hoop} is small, nevertheless large bending stresses of more than $\sigma_{hoop} = -300$ MPa resulted (top chart). Although in the configuration of the cylinder on hand the shell in the dent is quasi flat, during axial compression the dent deepened, the shell bended and thus tensile stresses at the inner shell side emerged. But at the lateral flanks of the dent and on the adjacent small bulges at its inner surface the shell was compressed due to bulging. At the spot with maximal circumferential membrane force (second chart) large compressive hoop stresses of about $\sigma_{hoop} = -250$ MPa accumulated at the inner shell skin but only small tensile stresses at the outer. On the bulges (third chart),

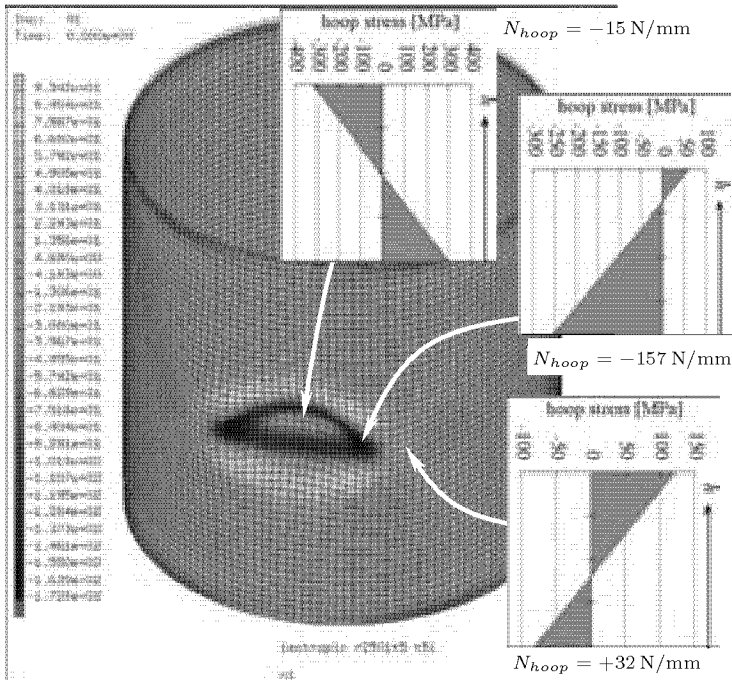


Figure 6.135: Distributions of the circumferential stress σ_{hoop} in the shell cross section at three selected spots in the reference cylinder with a dent of initial depth $w_b/h = 0.5$ as indicated, resulting for an applied axial force of $P = 368$ kN. CAUCHY stresses obtained with a nonlinear static analysis. Contour-deformation plot in background to display the respective axial membrane forces N_{hoop} .

in turn, larger tensile stresses at the outer surface front and smaller compressive stresses at the inner arose; therefore, as indicated, a small tensile membrane force per unit length N_{hoop} resulted.

For all calculations linear elastic material was provided; that is, it was presumed that possible yielding in the cylinder shells can be ignored. With the resulting stress values up to almost 500 MPa in the aluminium shell as presented in Figure 6.135, the validity of this assumption has to be questioned, since also the top yield stresses of high-strength aluminium alloys are below this value. Thus, during a compression test of the aluminium reference cylinder with radius $R = 250$ mm and wall thickness $h = 1.5$ mm, prior to the total collapse permanent plastic strain

at edges of a deeper dent has to be expected. However, the cylinder with a wall thickness of only $h = 0.75$ mm, a radius of $R = 500$ mm, and a length equal to the reference cylinder yielded stress values in the shell that are solely a fourth of those in the reference cylinder, despite the equally sized dimple imperfection, the same buckling behaviour, and the similar relative stress deviations. This shell has half the wall thickness and double the radius of the reference cylinder and hence an identical wave-length \sqrt{Rh} , yet its radius/wall thickness ratio R/h is four times bigger. Concerning the buckling behaviour, the qualitative differences between this cylinder and the reference cylinder are negligible, due to the constant wave-length \sqrt{Rh} and identical length L . Moreover, the absolute initial depths of the dimples are specified in relation to h and both the used initial widths and the heights of the dimples depend on the length \sqrt{Rh} . Thus, by means of a reduction of the wall thickness h and an appropriate increase of the radius R always new shells with equal \sqrt{Rh} can be specified which have the identical buckling behaviour and the same relative deviations of the membrane forces, but whose maximum stresses are arbitrarily reduced and therefore underrun the lowest existing yield stress. For instance, with peak stresses in the range of 125 MPa for the shell above with $R = 500$ mm, yielding of the shell prior to cylinder collapse will be unlikely. For this reason, additional buckling analyses under consideration of plasticity were not performed. Since the edge lengths of the finite shell elements in the used models have the length $0.5\sqrt{Rh}$, the reduction of the wall thickness and thus also of the stresses has the disadvantage that with the required increase of the radius also the number of shell elements in the circumference accumulate. The cylinder with $h = 1.5$ mm and $R = 250$ mm was selected as reference shell due to its smaller number of elements and thus shorter computing times, and not because of the resulting high “academic” peak stresses.

Cylinders with Uniformly Distributed Edge Loads

As aforementioned, the finite element calculations presented so far were conducted for cylinders with controlled axial edge displacements according to the clamped boundary conditions CC4 in the shell calculus. Thus, the axial displacement around the cylinder edge is identical for all edge nodes but potentially, whereas axial membrane forces per unit length N_{axial} along the cylinder edges non-uniformly distributed. Alternatively to the application of the loading on an auxiliary node tied to the edge nodes, the force may also be distributed directly to the edge nodes in

equal shares. Contrary to the boundary conditions CC4 above, in such a case the now uniformly distributed edge load is given by the nominal compressive axial membrane force $\tilde{N}_x = -P/2\pi R$. Retaining all rotations as well as the radial and the circumferential displacements of the edge nodes, a clamped but axially flexible cylinder end is simulated. Such a setting corresponds to the analytical boundary condition set CC3 for clamped edges with controlled axial edge loads \tilde{N}_x and resulting potentially non-uniformly distributed axial edge displacements.

—> *For cylinders having a dimple important discrepancies of the buckling behaviour and the buckling loads between the conditions CC4 and CC3 may result.*

⇒ Buckling analysis results (loads and stresses) for clamped boundary conditions CC3 with controlled axial edge load are detailed in Section 6.6.7, page 426.

Remarks on Measures to Prevent Local Buckling of a Dent

The lower buckling loads of cylinders having an initial dent compared to those of perfect cylinders stem from local variations of the stress distribution related to local buckling at the imperfection prior to the cylinder collapse. These variations in the stress fields in turn are caused by the imperfection and change with particular shell deformations. The linear buckling modes (eigenvectors) follow from these stress fields. End effects ignored in perfect cylinders the stresses are constant and their linear buckling modes consist in evenly distributed dimples of equal size. In the cylinders with an initial dent however stress peaks result and their linear buckling modes contain a few single, large dimples at the imperfection, whereas the rest of the shell is “dimpleless”. Hence, measures to prevent local instability prior to cylinder collapse may be successful if they anticipate the appearance of local stress variations within the shell.

Probably the first measures which come into mind to remove local stress peaks in an axially compressed cylinder having a dent is to reduce the stiffness or to increase the wall thickness locally. But the amplitude as well as the positions of the stress peaks in the shell change continuously during cylinder compression. Thus, a local change in wall thickness for instance may be successful at a particular load level, but will be idle or even impairing at an other load.

Nevertheless, local changes in the wall thickness yielded remarkable increases of the buckling loads considering the initial dent geometry and dimensions instead of the stress disturbances: by attaching a shell strip on the outer cylinder surface over the dent the damaging effect of the dent could be compensated. Without much additional calculation effort a few series of nonlinear buckling analyses of the reference cylinder with a single dent of initial depth $w_b/h = 0.2$ or $w_b/h = 0.5$ and a shell strip of different wall thickness affixed over the dent were conducted. The dents had an initial width of $a_b = 185$ mm and an initial height of $l_b = 64$ mm. With a width of 194 mm and a of height of 77 mm the strip or tape overlapped the dent edges somewhat to match the additional shell elements, with which the tape was modeled (8×20 elements), with the elements of the cylinder (52×162 elements). The nodes of the tape elements were linked with the adjacent nodes of the cylinder elements by means of rigid beam elements. The length of these elements were given by half the wall thickness of the tape and the cylinder. In this manner ideal bonding between tape and cylinder was simulated, additionally the eccentric loading of the tape due to its larger mean radius

compared to that of the coaxial cylinder shell was taken into account. In Figure 6.136 the shell strip applied on the outer cylinder surface is

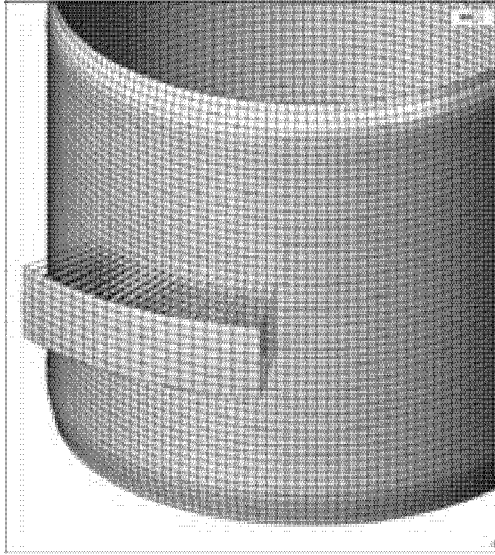


Figure 6.136: *Cylinder model under axial load with a small shell strip applied over the dent on the outer cylinder surface. Rigid beam elements to model perfect cylinder-strip bonding elongated for illustration.*

depicted with drastically elongated beam elements to clarify the configuration with the additional finite elements. The effect of the tape was investigated for different initial tape thicknesses h_t , either constant for the entire tape or thicker in the tape centre and zero along its four edges. In case of the tapes with variable shell thickness distribution different values h_t were specified on each of the four integration points per shell element using cosine formulas similar to those for the dent geometry in Equation 6.4 on page 197. The material of the tape was the same than that of the reference cylinder shell (aluminium).

Figure 6.137 depicts the nonlinear buckling analysis results of the shells with a tape of sinusoidal thickness distribution for an initial dent depth of $w_b/h = 0.2$ and of $w_b/h = 0.5$. The buckling loads normalized with respect to the perfect cylinder are shown against the amplitude h_t of the tape thickness normalized with respect to the initial dent depths w_b . It can be seen that for a tape-thickness amplitude h_t almost equal to the initial dent depth w_b the buckling load of the cylinders with a

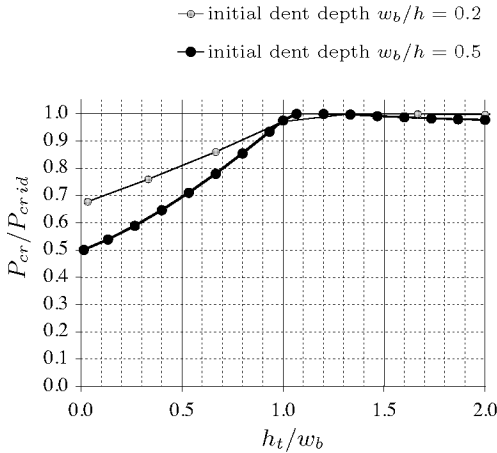


Figure 6.137: Buckling loads of the reference cylinder having a dent of initial depth as indicated and a **tape** affixed over the dent versus the amplitude h_t of the **variable** tape thickness. Results for a tape of thickness h_t at its centre and zero at its edge. Buckling loads normalized with respect to that of the perfect cylinder $P_{cr id}$; tape thickness amplitude normalized with respect to the initial dent depth w_b .

dent and a tape is about that of the cylinder with perfect geometry. This tape thickness distribution corresponds to the complete filling of the dent furrow with shell material, resulting in a local swelling inwards of the cylinder shell instead of the concave inward dimple. Additional tape thickness or cylinder swelling did not yield better results: the tape with $h_t/w_b \approx 1$ is the optimum.

With a tape of *constant thickness*, however, the buckling load of the cylinder with a dent could be increased only up to 94 or 91 % of the load of the perfect cylinder. In case of the shallow dent the former higher maximum resulted again for $h_t/w_b = 1$, but for the deep dent the latter lower maximum was at about $h_t/w_b \approx 3/4$. The smaller efficiency of the tape with constant thickness compared with that of the tape with variable thickness distribution is probably due to the saltus of the shell stiffness at its edges and any associated stress peaks at these edges.

The tapes discussed above are all of isotropic material. For tapes with constant thickness also the effect of *orthotropic* shell stiffness was investigated. For this purpose unidirectional laminated CFRP strips were modeled with the ply properties known from the DEVILS cylinder shells:

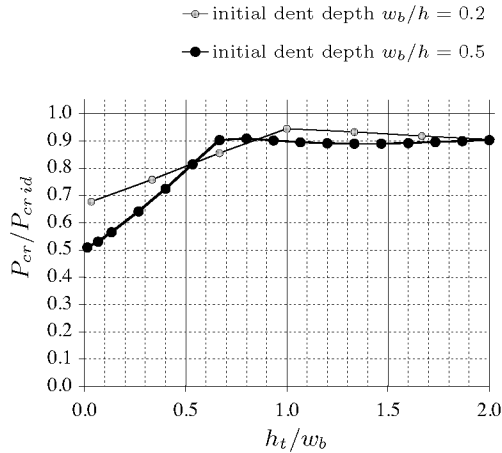


Figure 6.138: Buckling loads of the reference cylinder having a dent of initial depth as indicated and a **tape** affixed over the dent versus the **constant** tape thickness h_t . Buckling loads normalized with respect to that of the perfect cylinder $P_{cr id}$; tape thickness normalized with respect to the initial dent depth w_b .

$E_{axial} = 123550$ MPa, $E_{hoop} = 8708$ MPa, $\nu_{ah} = 0.32$, $G_{ah} = 5695$ MPa, see Section 4.1.2. These laminated tapes of height and width given above were again affixed to the isotropic aluminum reference cylinder with $E = 70000$ MPa and $\nu = 0.3$. Figure 6.139 depicts normalized buckling loads of the cylinder having a deep dent of initial depth $w_b/h = 0.5$ with an unidirectional laminated tape affixed over the dent on the outer cylinder surface. All carbon fibres of the tape were either oriented in axial direction (red) or in circumferential direction (blue). The loads were again plotted against the constant tape thickness h_t normalized with respect to the initial dent depth $w_b = 0.75$ mm. Due to the different and more arbitrarily selected tape material stiffness these structure configurations are “academic”; hence the analysis results should be considered only qualitatively. *Nevertheless, it is surely of some importance that the tape with high circumferential stiffness (blue) was more successful in increasing the buckling load than the tape with high axial stiffness (red). Consequently, in the design of frames, tapes or other countermeasures against local imperfections in axially compressed cylinders the circumferential stiffness should receive attention.*

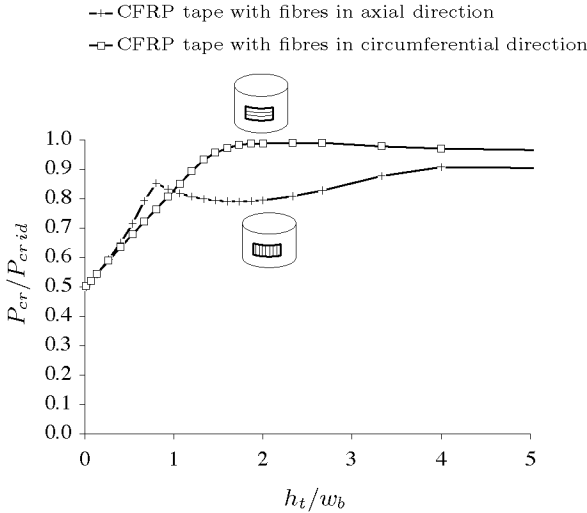


Figure 6.139: *Buckling loads of the reference cylinder having a dent of initial depth $w_b/h = 0.5$ and a laminated CFRP tape affixed over the dent versus the constant tape thickness h_t . Buckling loads normalized with respect to that of the perfect cylinder $P_{cr,ld}$; tape thickness normalized with respect to the initial dent depth w_b .*

6.6.6 Isotropic Cylinders with Two Dents

In the previous sections the damaging effect of a single dimple imperfection to the axial stability of isotropic cylinders was described. In this section the buckling analysis results for cylinders with two inward dimples are discussed. These calculations were performed to investigate if an additional dimple may cause a further reduction of the axial stability of a cylinder already reduced by a similar dimple, and under what conditions and with what amount. The investigation was limited to nonlinear buckling analyses with isotropic cylinders and inward dimples. Both dents in a cylinder are always initially of the same size, their initial width and height correspond to the length $a_{\bar{b}}$ and $l_{\bar{b}}$ respectively to be found in Table 6.3, p. 331, specified by means of the procedure detailed in Section 6.6.3. The dents were located in the cylinders by specification of the axial distance of the dent apexes from the cylinder edges and the circumferential spacing Δ_{φ} between the dent apexes, see Figure 6.140. Only two axial distances were analysed: (I) both dents arranged around

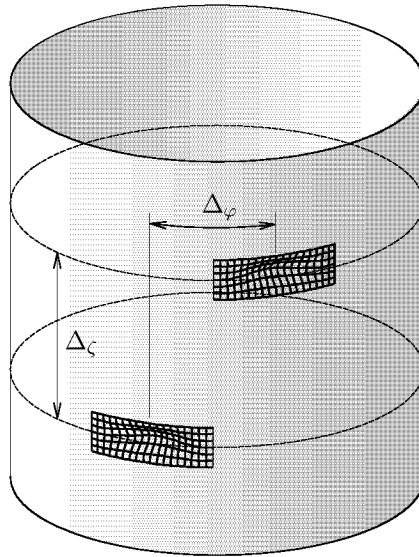


Figure 6.140: *Cylinder with two inward dimple imperfections. Layout of the dents by specification of the vertical and circumferential spacing between the dimple apices, Δ_ζ and Δ_φ respectively.*

the circumference at half the cylinder length $L/2$, and (II) each dent located around a circumference with a distance from the cylinder edge of $L/3$. In the former case the axial spacing between the dent peaks Δ_ζ is zero, in the latter $0.4L$. With the so predefined axial distances the circumferential spacing Δ_φ was varied in steps of ten or twenty degrees for the set-up of the series of the additional cylinder shells.

In Section 6.6.5 stress and membrane-force distributions were shown which resulted for isotropic cylinders with a single dimple. The extent of the stress disturbance around a dent and the kind of stress distribution is of vital importance for the interaction of two dents in a shell. Thus, to explain the analysis results it was found sufficient to consider the resulting differences in the interfering membrane forces. The arrangement of the dents was rather arbitrary ignoring the particular distribution of the membrane stress peaks in and at a dent, see Section 6.6.5. Hence, other configurations with two dents in a cylinder causing a larger impact on the cylinder stability cannot be excluded; a systematic search for extremal values was not conducted in this context.

In the majority of cases, the nonlinear buckling analyses performed with the finite element model of the isotropic reference cylinder simulating clamped edges and rigid, plane-parallel endplates. Thus, unless otherwise noted the cylinder ends were set for boundary condition CC4, see Section 6.4. For the reference cylinder with a length $L = 510$ mm, a radius $R = 250$ mm, and a shell wall thickness $h = 1.5$ mm the calculations described in Section 6.6.3 with a dent of initial depth $w_b/h = 0.1$ yielded the initial circumferential dent width $a_{\bar{b}} = 181$ mm and the initial meridian dent height $l_{\bar{b}} = 66$ mm. These lateral dent lengths were used for all dents in the reference cylinder.

In the following first the results for the series with two dents located in one row around the circumference at half the cylinder length are presented, followed by those for series with two axially distant dents located in two rows. Finally, the numerical analysis results are compared with test data available for thin epoxy cylinders having one, two or multiple deep V-shaped notches.

I. Both Dents along the Cylinder Circumference at $L/2$

In Figure 6.141 the buckling loads of the reference cylinder having two dents of initial depth $w_b/h = 0.2$, which are both located around the circumference at $L/2$, are plotted against the circumferential spacing between the dent apices. The buckling loads P_{cr} are normalized with respect to the buckling load of the ideal perfect cylinder $P_{cr id}$. The result leftmost for zero spacing is identical with the result for the shell with only one single dent, and the rightmost value denotes the case with two dents each located diagonally opposite to the other. The buckling load for a circumferential spacing $\Delta_\varphi = 20^\circ$ is 6% higher than the load for only one dent, the buckling load for a spacing $\Delta_\varphi = 40^\circ$ in turn is 3% lower. For circumferential spacings $\Delta_\varphi = 60^\circ$ and above the difference in the resulted buckling load is negligible small. In the following pages, for the case with only one dent and for the spacings $\Delta_\varphi = 20^\circ, 40^\circ, 60^\circ$, and 180° the distributions of the axial and the circumferential membrane forces per unit length, N_{axial} and N_{hoop} respectively, for the axial load $P = 360$ kN are pictured by means of contour-deformation plots as introduced in Section 6.6.5. On the left below these figures additionally the local radii r_k of the nodes in the path around the full circumference of the cylinder at $L/2$ are depicted for the initial unloaded state, for an axial load of $P = 200$ kN, and for an axial load of $P = 360$ kN. On the right finally the deviations of the axial membrane forces $\Delta N = \bar{N}_{axial} - \bar{N}_x$,

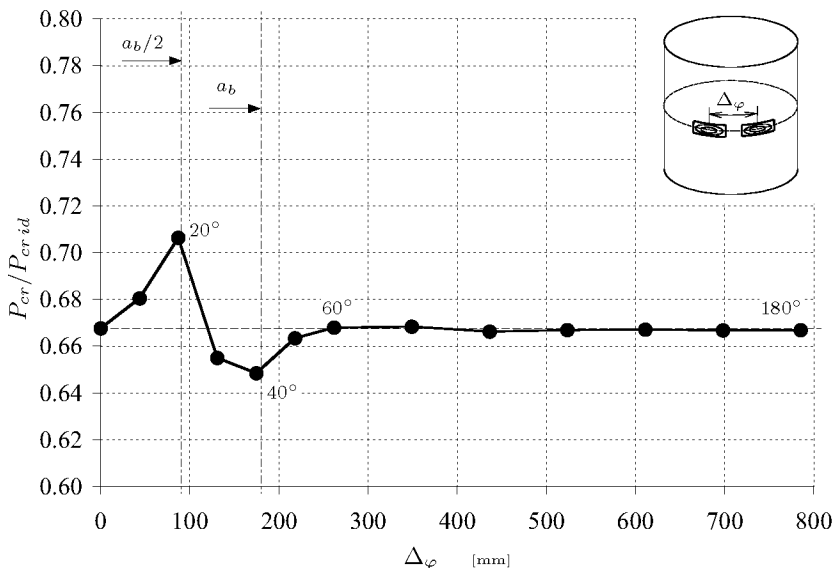


Figure 6.141: Normalized buckling loads for the isotropic reference cylinder having 2 dents, both of initial depth $w_b/h = 0.2$, width $a_b = 181$ mm and height $l_b = 66$ mm. Loads versus circumferential spacing Δ_φ between the apexes of the dents arranged around the circumference at $L/2$.

relative to the nominal force per unit length $\tilde{N}_x = -P/(2\pi R)$, in the middle of the shell elements in the circumferential path at $L/2$ are diagrammed again for the two mentioned loaded states. The reference cylinder with a single dent of initial depth $w_b/h = 0.2$, width $a_b = 181$ mm and height $l_b = 66$ mm yielded a buckling load of $P_{cr} = 380$ kN; thus, the higher load used for the graphs is close to buckling.

In Figure 6.142 and 6.143 on page 404 the results for the reference cylinder having a single dent with an initial depth $w_b/h = 0.2$ are displayed. The membrane-force distributions and the deformation progress typical for isotropic cylinders with such a dent were detailed in the previous sections: The dent centre moves to the cylinder axis whereas the lateral sides of the dent are bulged outwards; this is also reflected in the axial membrane forces which in case of $P = 360$ kN form a twin peak of an about +4.3% deviation from the nominal value flanked by peaks of reduced loading with 4.9% smaller values. The maximum axial membrane force in the contour plot is $N_{axial} = -242$ N/mm.

Figure 6.144 and 6.145 on page 405 depict the results for a circumferential spacing between the apexes of the two dents of $\Delta_\varphi = 20^\circ$ or $\Delta_\varphi = 87\text{ mm}$. The initial width of the dents is $a_b = 181\text{ mm}$ hence the apex of one dent is located close to the lateral boundary of the other dent. That is, one flank of each dent is replaced by the peak of the adjacent dent. The buckling load for this configuration is $P_{cr} = 402\text{ kN}$ and thus 6% *above* that for the cylinder with only one dent. Since the peaks of maximum axial membrane force N_{axial} in a single dent are located at these flanks for the case at hand the membrane force peaks in a dent are abated by the other dent. The maximum axial membrane force along the circumferential path is now only 2.6% higher than the nominal membrane force, and with $N_{axial} = -238\text{ N/mm}$ the maximum in the contour plot is about 2% smaller than that for a single dent.

In Figure 6.146 and 6.147 on page 406 the effect due to two dents with a circumferential spacing between the dent apexes of $\Delta_\varphi = 40^\circ$ or $\Delta_\varphi = 175\text{ mm}$ is demonstrated. In this case the two dents adjoin to each other. Since the initial width of the dents a_b is somewhat longer than the spacing Δ_φ the left boundary of one dent overlap the right boundary of the other. The buckling load for this configuration is $P_{cr} = 369\text{ kN}$ and thus 3% *below* that for the cylinder with only one dent. This configuration leads to a larger increase in the depth of the dents and in the elevation of the bulges during axial cylinder compression in comparison to the shell with a single dent. Above all the bigger bulging of the shell lying in between the two dents strike. Consequently, the axial membrane force in the larger bulge is about twice as much reduced compared with the bulges for a single dent. The maximum axial membrane force along the circumferential path resulted 5.3% higher than the nominal value, and with $N_{axial} = -245\text{ N/mm}$ the maximum in the contour plot is almost 1% above that for a single dent. According to Figure 6.141 the smallest buckling load with two dents of that size arranged around the cylinder circumference will probably be obtained with a spacing equal to the dent width, i.e. for $\Delta_\varphi = a_b$.

In Figure 6.148 and 6.149 on page 407 the effect due to two dents with a circumferential spacing between the dent apexes of $\Delta_\varphi = 60^\circ$ or $\Delta_\varphi = 262\text{ mm}$ is demonstrated. In this case the two dents adjoin to each other. Since the initial width of the dents a_b is somewhat longer than the spacing Δ_φ the left boundary of one dent overlap the right boundary of the other. For this configuration the buckling load is $P_{cr} = 380\text{ kN}$ and thus almost identical with that for the cylinder with only one dent. With $N_{axial} = -242\text{ N/mm}$ the maximum in the contour plot also ap-

proximates that for a single dent. The dents are so far apart that the stress-raising area of one dent does not overlap with that of the other dent in a way that the peak values increase. Only close to the cylinder edge the shell parts of elevated axial membrane force aslope radiating from the flanks of the two dents interfere with each other positively, i.e. they increase the membrane force locally due to superposition of the undulating stress distribution with amplitudes in equal direction.

Figure 6.150 on page 408 finally depicts the results for two dents with a circumferential spacing between the dent apexes of $\Delta_\varphi = 180^\circ$, i.e. for two dents arranged diagonally opposite. These plots were added only for demonstration of the geometric conditions and that the minor difference in the buckling load between a single dent and two opposing dents obviously comes along with quasi identical membrane force peak values. Thus, the local radii r_k and the axial membrane force/unit length \bar{N}_{axial} along the circumferential path obtained for this configuration were not included and can be derived from those for a single dent (Fig. 6.143).

The differences in the distribution of the circumferential membrane force per unit length N_{hoop} for these dent configurations are less impressive than those for the axial membrane force, the plots including the circumferential membrane forces were added for the sake of completeness. The maximum circumferential membrane forces per unit length N_{hoop} , tensile and compressive, resulted for an circumferential spacing of $\Delta_\varphi = 40^\circ$, the minimum N_{hoop} for $\Delta_\varphi = 20^\circ$.

Single Dent: $\Delta_\zeta = 0$; $\Delta_\varphi = 0$:

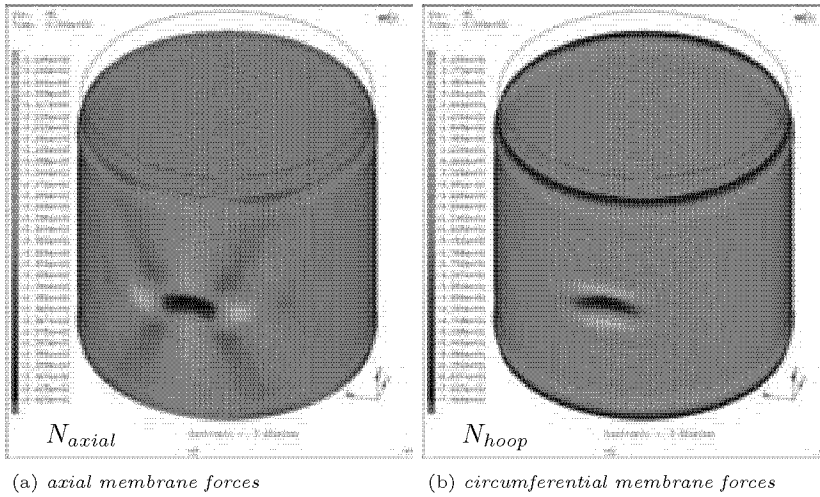


Figure 6.142: Axial and circumferential membrane forces per unit length of the reference cylinder with a single dent of initial depth $w_b/h = 0.2$, width $a_b = 181$ mm and height $l_b = 66$ mm. Results of a nonlinear static analysis for an axial load of $P = 360$ kN.

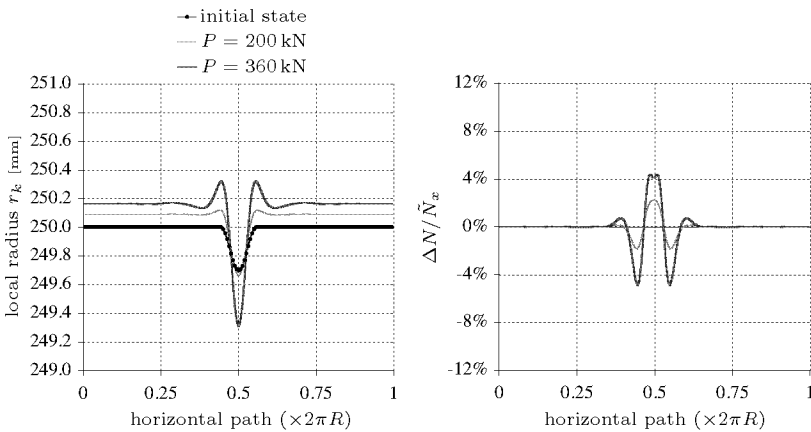


Figure 6.143: Local radii r_k and deviations of the axial membrane forces/unit length from the nominal values $\Delta N / \bar{N}_x$ for a cylinder with a single dent as shown in the Figure above. Results for axial loads P as indicated.

2 Dents: $\Delta_\zeta = 0$; $\Delta_\varphi = 20^\circ$:

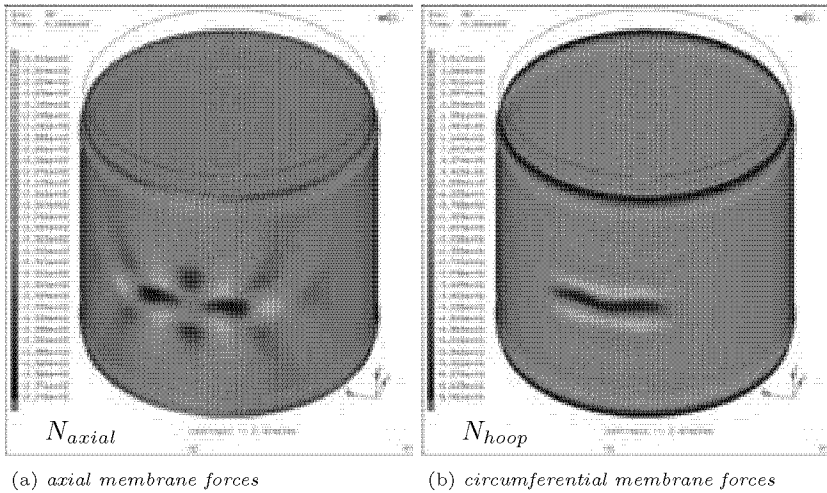


Figure 6.144: Axial and circumferential membrane forces per unit length of the reference cylinder with two dents of initial depth $w_b/h = 0.2$, width $a_b = 181$ mm and height $l_b = 66$ mm. Spacing between dent apices $\Delta_\varphi = 20^\circ$ or $\Delta_\varphi = 87$ mm. Results of a nonlinear static analysis for an axial load of $P = 360$ kN.

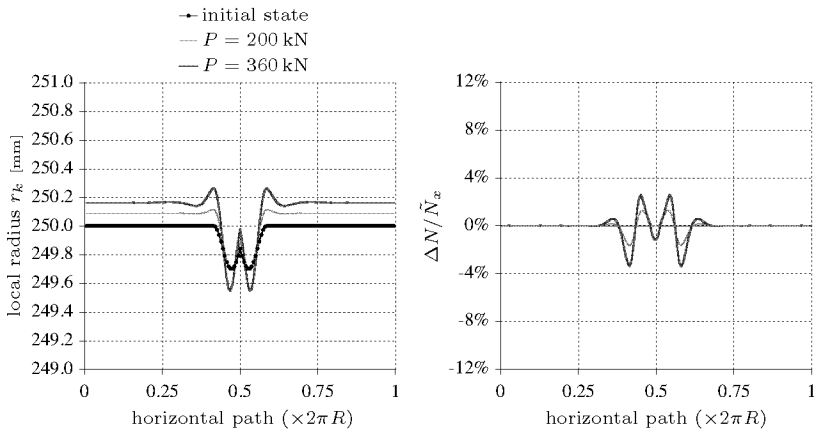


Figure 6.145: Local radii r_k and deviations of the axial membrane forces per unit length from the nominal values $\Delta N / \tilde{N}_x$ for a cylinder with two dents as shown in the Figure above. Results for axial loads P as indicated.

2 Dents: $\Delta_\zeta = 0$; $\Delta_\varphi = 40^\circ$:

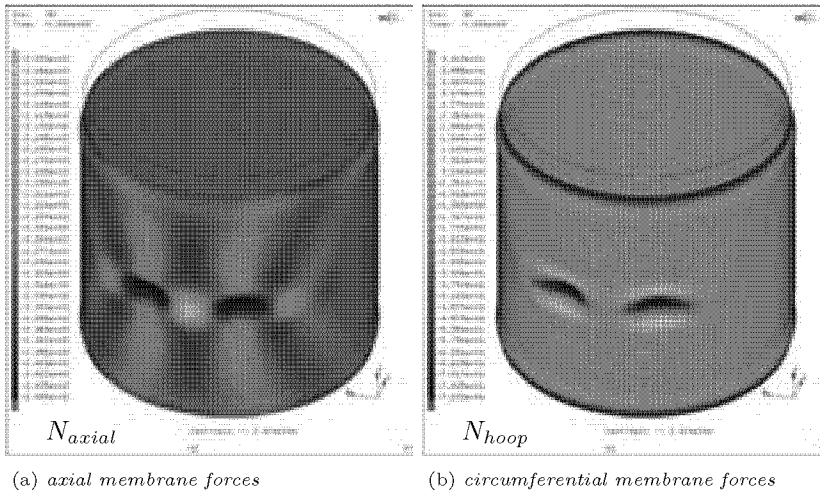


Figure 6.146: Axial and circumferential membrane forces per unit length of the reference cylinder with two dents of initial depth $w_b/h = 0.2$, width $a_b = 181$ mm and height $l_b = 66$ mm. Spacing between dent apices $\Delta_\varphi = 40^\circ$ or $\Delta_\varphi = 175$ mm. Results of a nonlinear static analysis for an axial load of $P = 360$ kN.

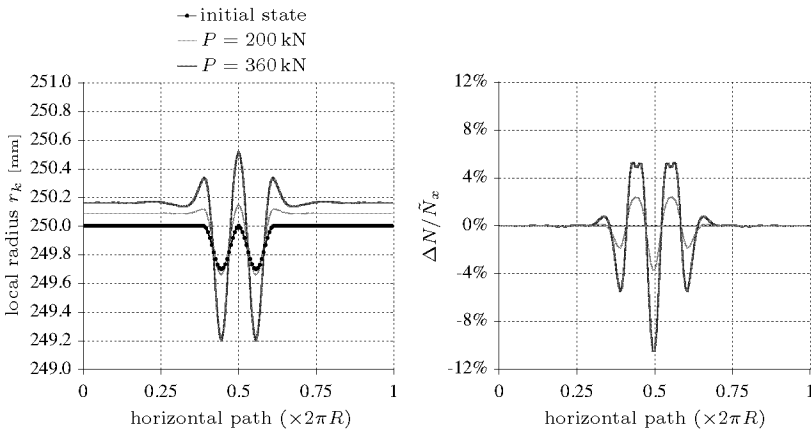


Figure 6.147: Local radii r_k and deviations of the axial membrane forces per unit length from the nominal values $\Delta N / \tilde{N}_x$ for a cylinder with two dents as shown in the Figure above. Results for axial loads P as indicated.

2 Dents: $\Delta_\zeta = 0$; $\Delta_\varphi = 60^\circ$:

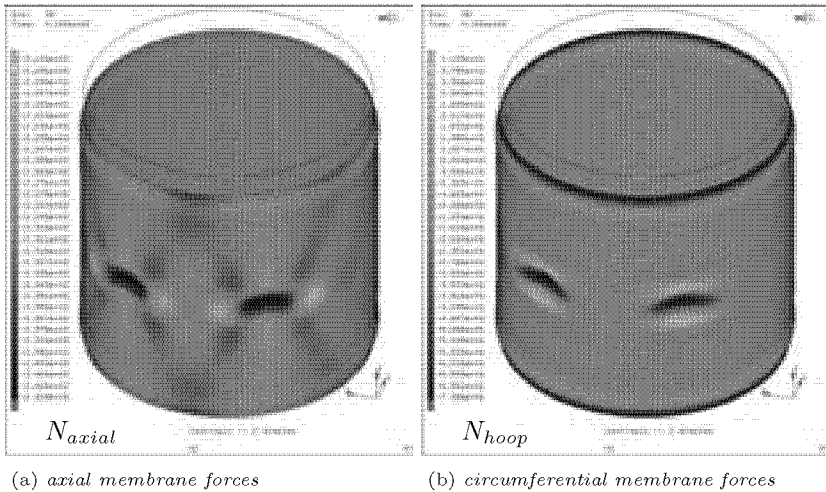


Figure 6.148: Axial and circumferential membrane forces per unit length of the reference cylinder with two dents of initial depth $w_b/h = 0.2$, width $a_b = 181$ mm and height $l_b = 66$ mm. Spacing between dent apices $\Delta_\varphi = 60^\circ$ or $\Delta_\varphi = 262$ mm. Results of a nonlinear static analysis for an axial load of $P = 360$ kN.

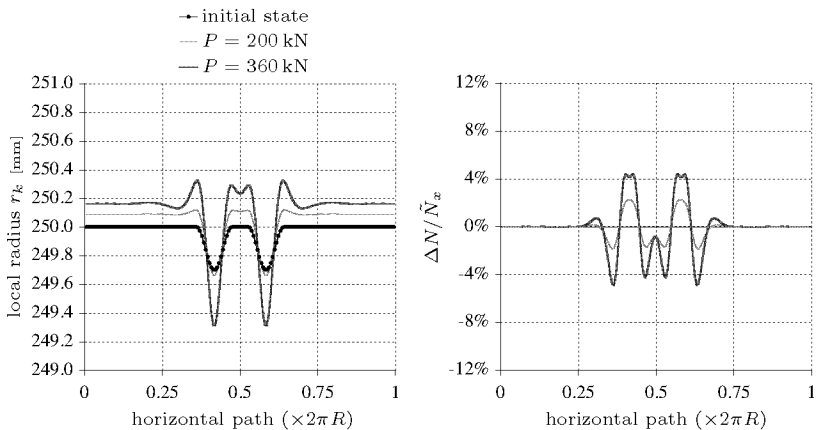


Figure 6.149: Local radii r_k and deviations of the axial membrane forces per unit length from the nominal values $\Delta N / \tilde{N}_x$ for a cylinder with two dents as shown in the Figure above. Results for axial loads P as indicated.

2 Dents: $\Delta_\zeta = 0$; $\Delta_\varphi = 180^\circ$:

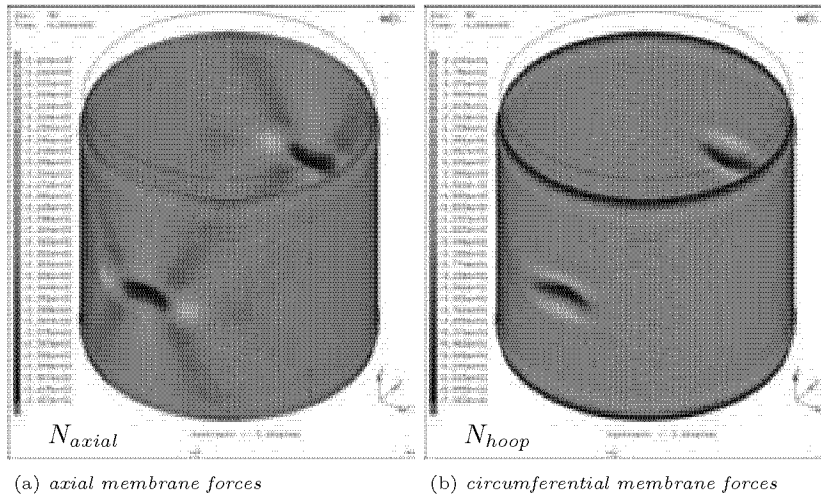


Figure 6.150: Axial and circumferential membrane forces per unit length of the reference cylinder with two dents of initial depth $w_b/h = 0.2$, width $a_b = 181$ mm and height $l_b = 66$ mm. Spacing between dent apexes $\Delta_\varphi = 180^\circ$ or $\Delta_\varphi = 785$ mm. Results of a nonlinear static analysis for an axial load of $P = 360$ kN.

In Section 6.6.5 the importance of the “wavelength” \sqrt{Rh} was already demonstrated by means of the analogy between the accordingly modified distributions of the relative deviation of the axial membrane force N_{axial} for three isotropic cylinders of different radius, length and wall thickness, see Figure 6.133 on page 387. Additional to the reference cylinder the effects of two dents with an initial depth of $w_b/h = 0.2$ in a row in dependence on their spacing were calculated also for the cylinder with radius $R = 500$ mm and for that with radius $R = 187.5$ mm. The data to these shells are listed in subsequent Table 6.5. Figure 6.151 shows the normalized buckling loads $P_{cr}/P_{cr id}$ for these three cylinders with two dents of initial depth $w_b/h = 0.2$ located around the cylinder circumference at half the cylinder length. The buckling loads are plotted against the ratio of the circumferential spacing Δ_φ to the length \sqrt{Rh} . Similar to the results for the membrane force deviations in Figure 6.133 the variation in the buckling load with increasing relative dimple distance for the reference cylinder accords well with those for the two other

cylinder				dents	
R	h	L	\sqrt{Rh}	a_b	l_b
[mm]	[mm]	[mm]	[mm]	[mm]	[mm]
187.5	1.0	382.5	13.7	124	50
250	1.5	510	19.4	181	66
500	0.75	510	19.4	181	66
				width	height

Table 6.5: Dimensions of three aluminium cylinders and initial lateral lengths of their dents with an initial depth $w_b/h = 0.2$.

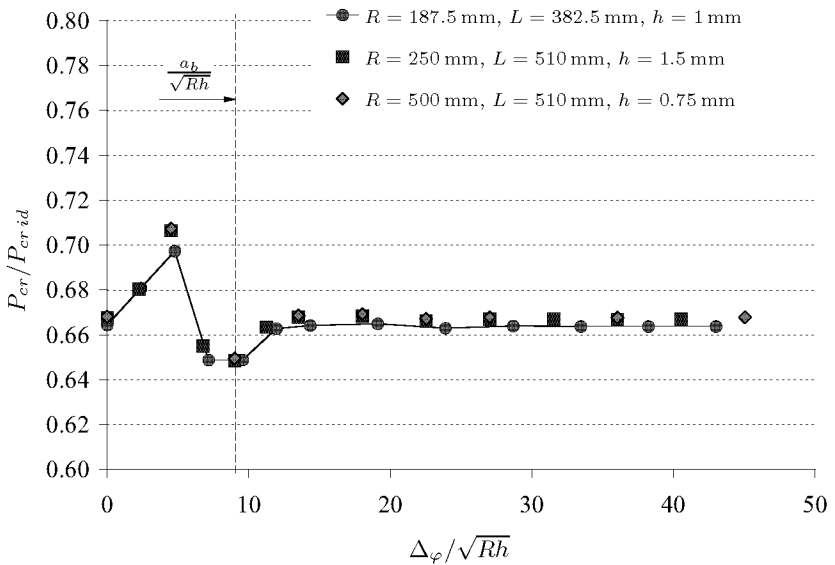


Figure 6.151: Normalized buckling loads for three isotropic cylinders as indicated having two dents of initial depth $w_b/h = 0.2$ in a row around the cylinder circumferences at $L/2$ in dependence on the ratio of the circumferential spacing between the dent apices Δ_φ to the length \sqrt{Rh} . Dimple dimensions listed in Table 6.5.

cylinders. For all three shells the decay lengths of the load variations is about 1.5 times the initial dent widths a_b .

The results for two dents of initial depth $w_b/h = 0.2$ arranged around the circumference of the reference cylinder with boundary condition CC4 (constant axial edge displacements) could also be compared with results for the same shells but with distributed axial edge loads (condition CC3 at the loaded side). The difference between the buckling loads are negligible, since initially the applied dents are shallow; the buckling loads for the reference cylinder with distributed edge loads and one dent of that initial depth are also only little below the respective results for the reference boundary condition CC4, see Section 2.2.

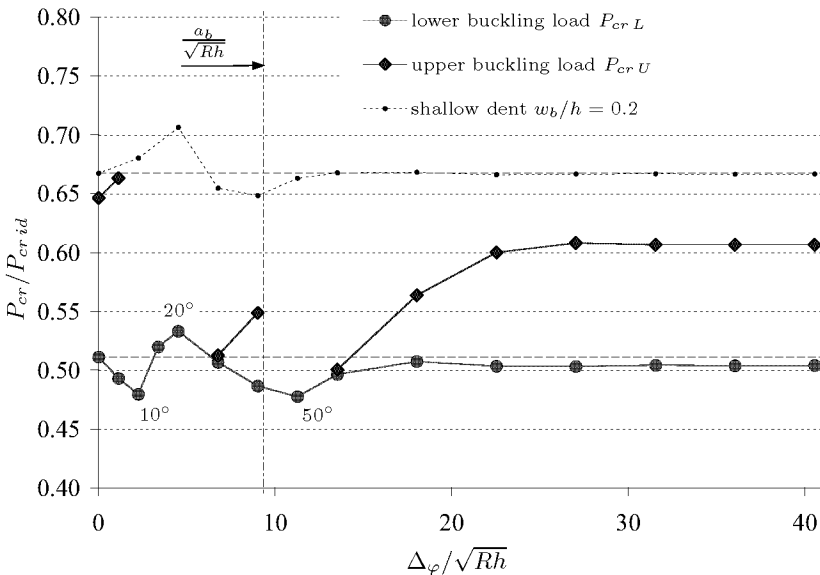


Figure 6.152: Normalized buckling loads for the reference cylinder having two deep dents of initial depth $w_b/h = 0.5$ arranged around the cylinder circumference at $L/2$ in dependence on the ratio of the circumferential spacing between the dent apices Δ_φ to the length \sqrt{Rh} . Cylinder dimensions: $R = 250$ mm, $L = 510$ mm, $h = 1.5$ mm; initial dent dimensions: $a_b = 181$ mm, $l_b = 66$ mm.

Nonlinear buckling analyses with the reference cylinder having two deep dents in a row around the cylinder circumference yielded results which include some additional complexity. Figure 6.152 depicts the normalized buckling loads for this cylinder with two dents of initial depth

$w_b/h = 0.5$. The loads are again plotted against the ratio of the circumferential spacing between the dent apexes to the length, Δ_φ/\sqrt{Rh} . Note that the initial height l_b and the initial width a_b of these dents equal those for the shallower dents of initial depth $w_b/h = 0.2$ which were used for the previously described analyses. The additional, probably somewhat irritating markers in the graph (blue diamonds), joint with interrupts, denote upper buckling loads $P_{cr U}$, i.e. loads for total cylinder collapse. The red circlets mark the lower buckling loads $P_{cr L}$ associated with local instability events. As detailed in Section 6.6.1, depending on the initial size of the applied dent and the associated dynamic of the shell deformation process a nonlinear buckling analysis is either aborted when reaching the lower buckling load or continued until reaching the total cylinder collapse load. The result leftmost for zero dent spacing Δ_φ again is that for the single dent: the lower normalized buckling load is $P_{cr L}/P_{cr id} = 0.51$, the upper $P_{cr U}/P_{cr id} = 0.65$. For dent spacings Δ_φ between 5° and 30° as well as between 40° and 60° no upper buckling loads were obtained, since probably the associated initial shell configurations led to particular local deformation processes with sudden shell flattening. The upper buckling load for dent spacings $\Delta_\varphi = 120^\circ$ and longer with $P_{cr U}/P_{cr id} = 0.61$ are 6% below the value for the single dent. The lower buckling loads for these dimple spacings in contrast differ only 1%. The larger sensitivity of the upper buckling loads $P_{cr U}$ to variations of the initial dimple geometry and the cylinder dimensions in comparison to the lower buckling load was already observed by means of the nonlinear buckling analysis results for single dents as presented in Section 6.6.1. The larger load reduction for two opposing dents and the somewhat higher upper buckling load for a spacing of only 5° confirm these observations. Better insights into the deformation processes which are involved in the peculiar variation of the upper buckling load could be provided by a series of transient dynamic analyses. But not only the upper buckling loads strike, there are also noticeable differences in the variation of the lower buckling loads $P_{cr L}$ between the deep dents with $w_b/h = 0.5$ and the shallow dents with $w_b/h = 0.2$, see Figure 6.152. The minimum lower buckling load resulted for a dent spacing of $\Delta_\varphi = 50^\circ$ or 218mm and is 6% below the value for one dent. This reduction of the load $P_{cr L}$ is twice as much as the minimum buckling load for the two shallow dents, which was obtained for a dent spacing of only 40° . The maximum buckling load resulted again for the dent spacing $\Delta_\varphi = 20^\circ$ or 87mm and is 4% higher than the load for the single dent. Thus, compared to the elevation of 6% for the shallow dents the positive effect due to the two deeper dents with like spacing is consid-

erably smaller. But, above all the particular additional minimum for a spacing of $\Delta_\varphi = 10^\circ$ attracts attention. For such dent spacings shorter than half the initial dent width the shallow dents caused buckling loads even higher than for the single shallow dent. The initial width used for the dents is $a_b = 181$ mm, but the initial width which causes minimal stability for the initial depth $w_b/h = 0.5$ is much longer ($a_{\bar{b}} = 238$ mm; +32%). A spacing of only $\Delta_\varphi = 10^\circ$ or 44 mm between the two dent apices forms a single dent with a twin cusp and a total width of 225 mm. That is, with this configuration a wider dent is formed which matches better with the dent of initial depth $w_b/h = 0.5$ that reduces the cylinder stability the most. Consequently, the buckling load is smaller than that for the dent with the shorter width. The difference between the initial dent width a_b applied and the wider width for minimal stability $a_{\bar{b}}$ might also explain the longer spacing $\Delta_\varphi = 50^\circ$ for the minimum load in comparison to the normalized length a_b/\sqrt{Rh} . Calculations with two dents of this initial depth but with the wider initial width $a_{\bar{b}}$ would probably result in load variations similar to that for the shallow dents, thus with one maximum load at $\Delta_\varphi = 1/2 a_{\bar{b}}$ and one minimum load only at $\Delta_\varphi = a_{\bar{b}}$. Nevertheless, the explanations given for the results in Figure 6.152 base on the experience with cylinders having one single dent of different initial depths; further static stress or transient dynamic analyses with two deep dents in a cylinder were not performed for their verification.

II. Two Dents with Axial and Circumferential Spacing

The buckling analysis results above include cylinders with two dents in a single row around the cylinder circumference at half the cylinder length, thus shells having dents without axial spacing between their apices. To deal also with cylinders having two dents with circumferential spacing Δ_φ as well as with axial spacing Δ_ζ between the dent tops, again on the basis of the isotropic reference cylinder a series of shells having two dents with a constant axial spacing of $\Delta_\zeta = 2/5 L$ was created, arranging one dent around the cylinder circumference at $0.3 L$ and the other around the circumference at $0.7 L$ again with varied circumferential spacing Δ_φ . Both dents have an initial depth of $w_b/h = 0.2$ and an initial width and height of $a_b = 181$ mm and $l_b = 66$ mm respectively. Figure 6.153 depicts the normalized buckling loads for the reference cylinder with $L = 510$ mm having such two dents located accordingly. The loads are once again plotted against the circumferential spacing Δ_φ between the

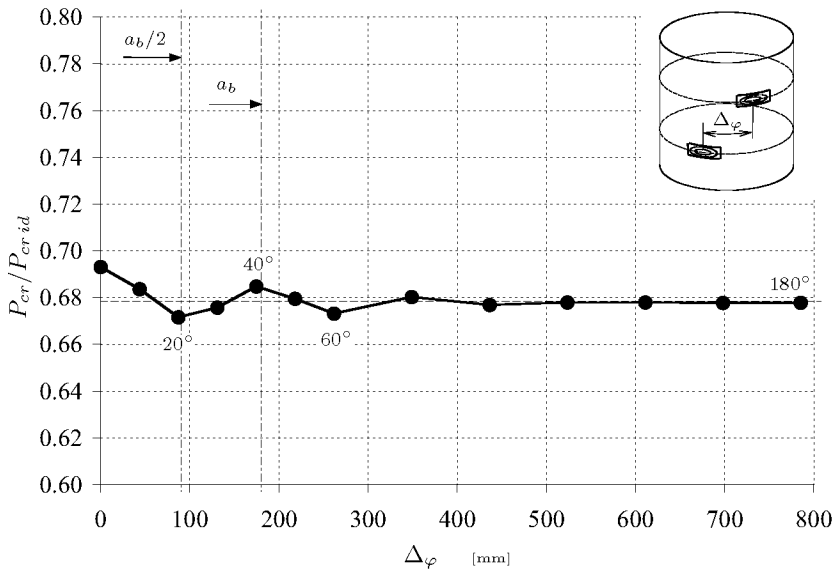


Figure 6.153: Normalized buckling loads for the isotropic reference cylinder having 2 dents, both of initial depth $w_b/h = 0.2$, width $a_b = 181$ mm and height $l_b = 66$ mm. Loads versus circumferential spacing Δ_φ between the apexes of the dents which are located around the circumferences at $0.3L$ and $0.7L$ resulting in an axial spacing of $\Delta_\zeta = 2/5L$.

dent apexes. In the graph the result leftmost with zero circumferential spacing denotes the configuration with two dents arranged in a single column one upon the other. The axial spacing between the two dent apexes is $\Delta_\zeta = 2/5L = 204$ mm and the distance of the dent apexes from closer cylinder edge $0.3L = 153$ mm. The associated buckling load is the maximum value among these results and 2% above the load for the cylinder with one dent of that depth located at $0.3L$ or $0.7L$. Contrary to the cases without axial spacing including maximum loads for the circumferential spacing $\Delta_\varphi = 20^\circ$ and minimum loads for $\Delta_\varphi = 40^\circ$ (see Fig. 6.141, p. 401), the nonlinear buckling analyses of the reference cylinder with the axial spacing $\Delta_\zeta = 2/5L$ yielded a second peak of higher buckling load for a circumferential spacing of $\Delta_\varphi = 40^\circ$ and two minimum values for the spacings $\Delta_\varphi = 20^\circ$ and 60° . That is, in Figure 6.153 a minimum resulted for a spacing where in Figure 6.141 a maximum was obtained and vice versa. But the maximum and the minimum buckling loads differ about three times less from the values for

the cylinder with the single dent located at $0.3L$ or $0.7L$ compared with cylinder having the dents all at $L/2$, see Figure 6.141: the maximum load elevation is 2% and the maximum load reduction 1%, against 6% resp. 3% for the dents in a row at $L/2$. Additionally, the decay length of the buckling load variation is longer than $1.5a_b$, i.e. that for two dents around one circumference. The reasons for these differences lie in the interacting, undulating membrane force fields in the cylinder shell area above and below the two dents which differ from the undulating membrane force fields directly to the left and to the right of the two dents in amplitude and phase. In the subsequent contour-deformation plots the distributions of the axial and the circumferential membrane forces per unit length, N_{axial} and N_{hoop} resp., are displayed for the circumferential dent spacings $\Delta_\varphi = 0^\circ, 20^\circ, 40^\circ$, and 180° which are results of nonlinear static analyses for an axial load of $P = 360\text{ kN}$. For the first and the last case additionally the local radii r_k and deviations of the axial membrane forces from the nominal values $\Delta N/\tilde{N}_x$ along the axial path over the apex of the lower dent are graphed.

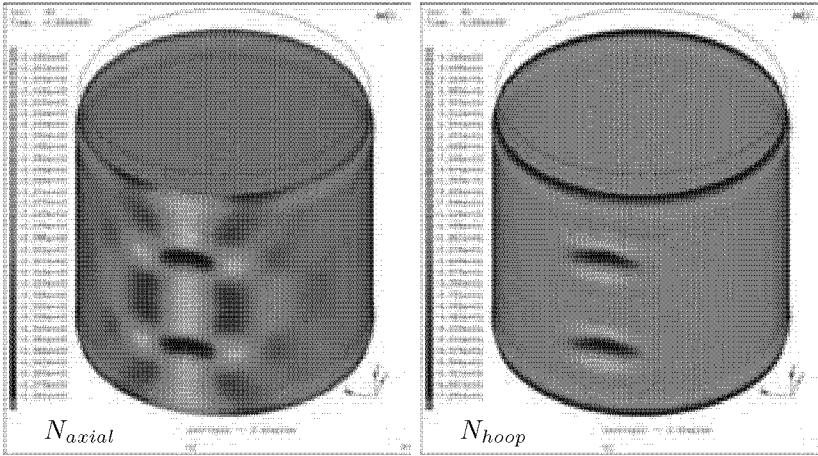
In Figure 6.154 and 6.155 on page 416 the results for the reference cylinder having two dents arranged in a single column one upon the other ($\Delta_\varphi = 0$) are displayed. The buckling load is $P_{cr} = 395\text{ kN}$ which is 2% above the load for the cylinder with one dent of that initial size at $0.3L$ or $0.7L$. Thus, latter cylinder resulted in a buckling load of $P_{cr} = 386\text{ kN}$ which in turn is 1.6% above the load $P_{cr} = 380\text{ kN}$ for the shell also with a single dent of this initial size but located at half the cylinder length. The higher buckling load for the dent closer to the cylinder edge can be explained with the smaller increase in dimple and shell deformations during axial compression due to the shorter shell length above or below the dent free for radial shell displacements. For similar reasons the cylinder with two dents in a single column one upon the other resulted in a higher buckling load than the shell with only one dent at $0.3L$ or $0.7L$. The states of stress and deformation for the cylinder with a single dent approximate those for the cylinder having two dents of equal initial size with an circumferential spacing of $\Delta_\varphi = 180^\circ$. The results for this configuration are depicted in Figure 6.159 and 6.160 on page 419. For better comparisons between the stress and deformation fields of the shell with two dents in a column and of that with only one dent in Figure 6.155 and 6.160 on the left the local radii r_k of the nodes in the axial path over the dent apexes are depicted for the unloaded state, for an axial load of $P = 200\text{ kN}$, and for an axial load of $P = 360\text{ kN}$ close to the buckling load of the cylinders (95% P_{cr}). To the right in these figures the deviations of the axial membrane forces per unit length $\Delta N = \tilde{N}_{axial} - \tilde{N}_x$,

relative to the nominal value $\tilde{N}_x = -P/(2\pi R)$, in the middle of the shell elements in the axial path are shown for the two mentioned loaded states. It can be seen that in case with only one dent the axial membrane force peak in the dent apex is higher: $N_{axial} = -241 \text{ N/mm}$ compared with $N_{axial} = -238 \text{ N/mm}$ for $P = 360 \text{ kN}$, thus plus one percent. Additionally, in the free surface above the single dent the axial membrane force is less reduced than that for the shell with the second dent above the other.

Figure 6.156 on page 417 shows the membrane forces for the cylinder having two dents arranged with a circumferential spacing of $\Delta_\varphi = 20^\circ$ or $\Delta_\varphi = 87 \text{ mm}$. The initial width of the dents is $a_b = 181 \text{ mm}$, hence about twice the spacing Δ_φ . That is, the right edge of the upper dent lies about in a vertical line over the apex of the upper dent and vice versa. With a buckling load of $P_{cr} = 383 \text{ kN}$ this dimple configuration yielded the minimum value for the dents located around these two circumferences. According to the plot in Figure 6.156(a) the circumferential spacing on hand makes a bulge with reduced N_{axial} at a flank of one dent to lie directly in an axial straight line over the apex with maximum N_{axial} of the other dent. Due to axial bending, at this axial positions above and below the dents the shell tend to move outwards, and the bulges formed by the other dent amplify this bulging. The increased radial displacements are accompanied by an increased axial membrane force relief (bright coloured areas) in the bulged shell and by the somewhat higher peak values in the dents.

In Figure 6.157 on page 417 the membrane forces for the cylinder with two dents having a circumferential spacing of $\Delta_\varphi = 40^\circ$ or $\Delta_\varphi = 175 \text{ mm}$. Since Δ_φ is only little shorter than the initial width of the dents $a_b = 181 \text{ mm}$ the left boundary of the upper dent is located directly above the right boundary of the lower dent. This configuration yielded the second maximum buckling load of $P_{cr} = 390 \text{ kN}$ among these shells, since in this case the apexes of the bulges at the lateral dent flanks lie in a vertical straight line, and so do their adjacent inward dimples. Thus, the shallow inward dimples formed above and below the initial dents act like the two dents in a single column one upon the other presented above but with a smaller positive effect contrary to the bulging above or below a single dent.

Figure 6.158 on page 418 finally depicts the results for the cylinder having two dents arranged with a circumferential spacing of $\Delta_\varphi = 60^\circ$ or $\Delta_\varphi = 262 \text{ mm}$. This means a lateral distance between the boundary of one dent and that of the other of about half the initial dent width. Since



(a) axial membrane forces

(b) circumferential membrane forces

Figure 6.154: Membrane forces per unit length for the reference cylinder with two dents of initial depth $w_b/h = 0.2$, width $a_b = 181$ mm and height $l_b = 66$ mm and an axial load of $P = 360$ kN. Axial spacing between dent apexes $\Delta\zeta = 2/5L$ or $\Delta\zeta = 204$ mm, circumferential spacing $\Delta\varphi = 0$.

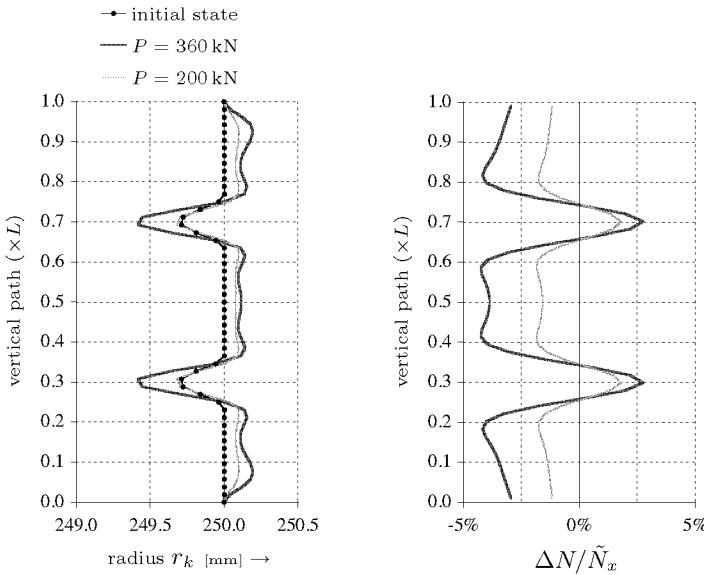


Figure 6.155: Local radii r_k and deviations of the axial membrane forces per unit length from the nominal values $\Delta N/\tilde{N}_x$ for a cylinder with two dents as shown in the Figure above. Results for axial loads P as indicated.

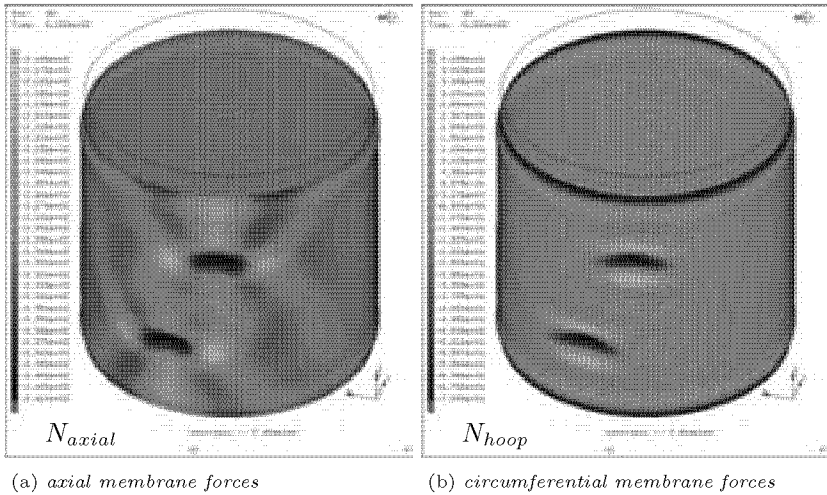


Figure 6.156: Membrane forces per unit length for two dents of initial depth $w_b/h = 0.2$ and an axial load of $P = 360$ kN. Axial spacing between dent apices $\Delta_\xi = 2/5L$, circumferential spacing $\Delta_\varphi = 20^\circ$ or $\Delta_\varphi = 87$ mm.

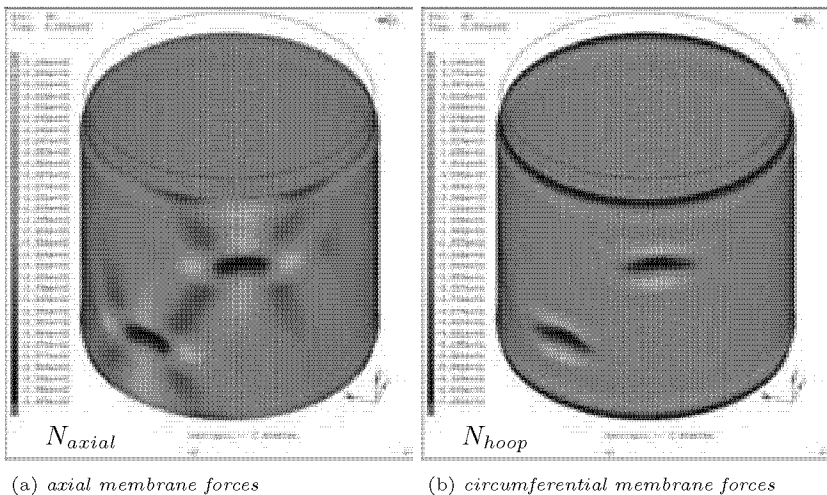


Figure 6.157: Membrane forces per unit length for two dents of initial depth $w_b/h = 0.2$ and an axial load of $P = 360$ kN. Axial spacing between dent apices $\Delta_\xi = 2/5L$, circumferential spacing $\Delta_\varphi = 40^\circ$ or $\Delta_\varphi = 175$ mm.

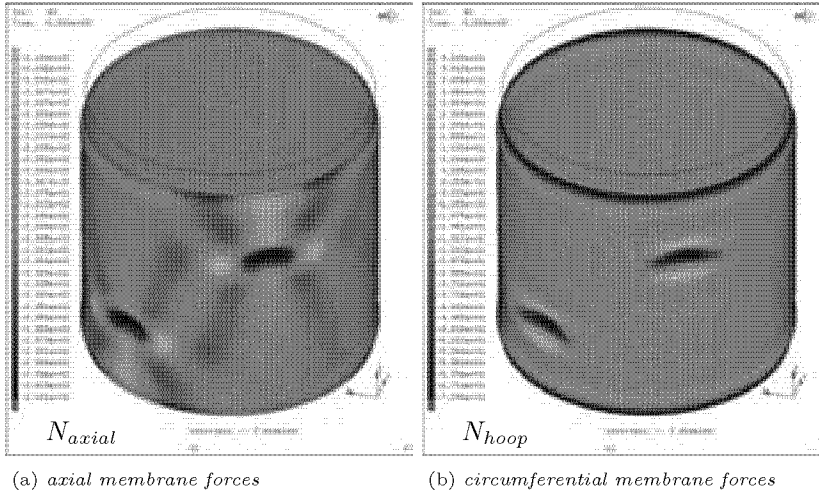
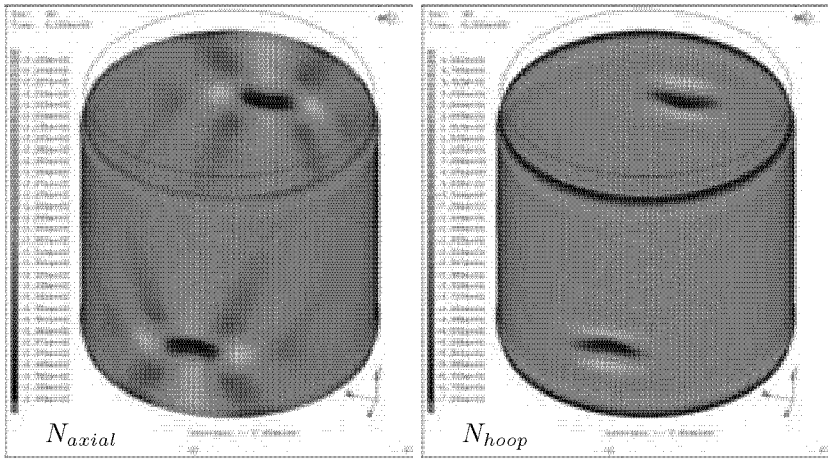


Figure 6.158: Membrane forces per unit length for two dents of initial depth $w_b/h = 0.2$ and an axial load of $P = 360$ kN. Axial spacing between dent apices $\Delta_\zeta = 2/5L$, circumferential spacing $\Delta_\varphi = 60^\circ$ or $\Delta_\varphi = 262$ mm.

the undulating axial membrane force distribution along the circumference over the apex of the upper dent is again in antiphase with that along the circumference over the apex of the lower dent, for the reasons mentioned above for the circumferential spacing $\Delta_\varphi = 20^\circ$ this configuration yielded also a minor buckling load close to the value for that spacing, i.e. $P_{cr} = 383$ kN.

As for the two dents arranged without axial spacing the distributions of the circumferential membrane force N_{hoop} in these figures differ only marginally. Thus, the interactions of the N_{hoop} in and around the dents may be neglected.

The effects of two dents of initial depth $w_b/h = 0.2$ with an axial spacing of $2/5L$ were also analysed for the isotropic cylinder 50 percent longer than the reference cylinder but with equal radius and wall thickness, thus: $L = 765$ mm, $R = 250$ mm, $h = 1.5$ mm. The initial width and the initial height of the two dents are equal or almost equal to those in the reference cylinder: $a_b = 181$ mm, $l_b = 67$ mm. The dents were arranged around cylinder circumferences with an axial spacing between the two dent apices $\Delta_\zeta = 2/5L = 306$ mm and a distance of the dent apices from closer cylinder edge $0.3L = 230$ mm. The nonlinear buckling analyses for this longer cylinder were again conducted for clamped



(a) axial membrane forces (b) circumferential membrane forces

Figure 6.159: Membrane forces for the reference cylinder with two dents of initial depth $w_b/h = 0.2$, width $a_b = 181$ mm and height $l_b = 66$ mm and an axial load of $P = 360$ kN. Axial spacing between dent apexes $\Delta_\zeta = 2/5L$, circumferential spacing $\Delta_\varphi = 180^\circ$ or $\Delta_\varphi = 785$ mm.

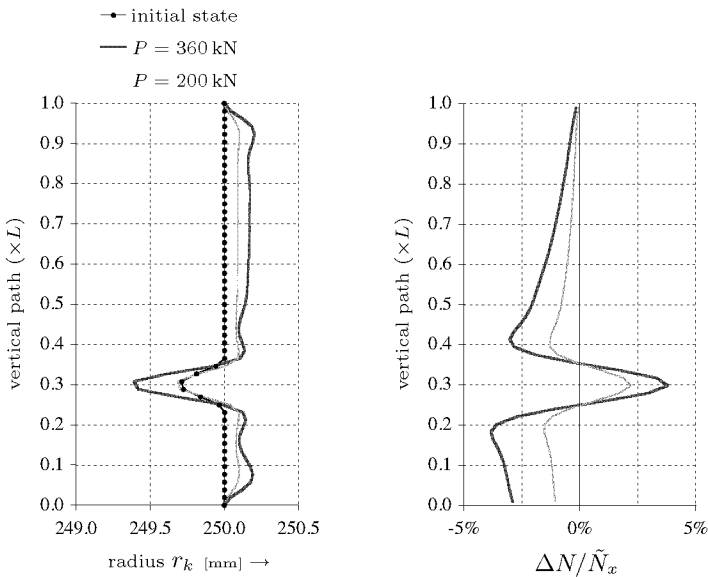


Figure 6.160: Local radii r_k and deviations of the axial membrane forces from the nominal values $\Delta N/\tilde{N}_x$ for a cylinder with two dents as shown in the Figure above. Results for axial loads P as indicated.

edges (boundary condition CC4) and the resulting normalized buckling loads are plotted in Figure 6.161 against the ratio of the circumferential spacing Δ_φ to the term \sqrt{Rh} . The graph also includes the results

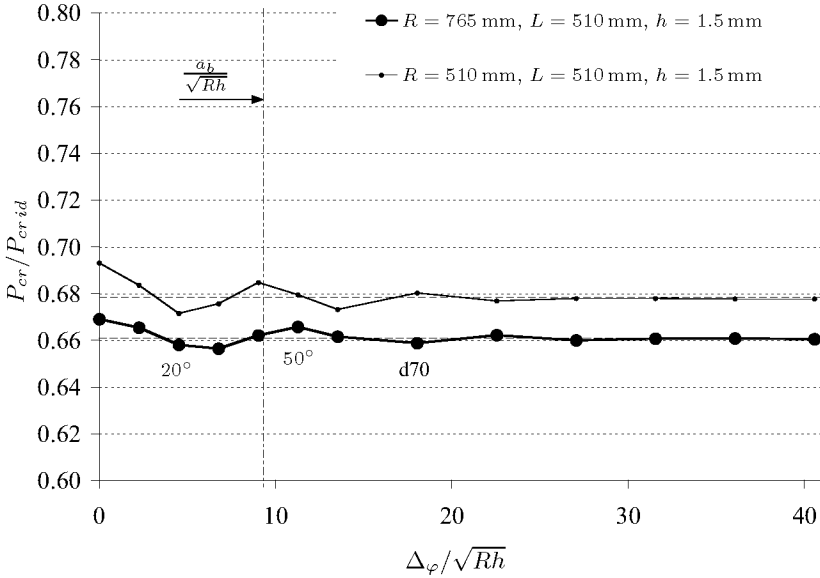


Figure 6.161: Normalized buckling loads for the reference cylinder and the 50 % longer cylinder having two dents of initial depth $w_b/h = 0.2$ arranged around the cylinder circumferences at $0.3L$ and $0.7L$ in dependence on the ratio of the circumferential spacing between the dent apexes Δ_φ to the length \sqrt{Rh} . Initial dent dimensions $a_b = 181 \text{ mm}$, $l_b = 67 \text{ mm}$. (66 mm).

for the reference cylinder for comparisons. The buckling loads obtained for the longer cylinder are slightly below those for the reference cylinder due to the larger radial displacements at like bending efforts for longer cylinders, see Section 6.6.1 page 281. Since in the longer cylinder the dents have a longer axial distance the effects due interaction of the stress fields around the dents is smaller, and hence the amplitudes of the buckling load variation in Figure 6.161 are somewhat smaller compared with those for the reference cylinder above. The shift of the maximum and the minimum buckling loads towards longer circumferential spacings Δ_φ probably stem from the different axial positions of the formed dents and bulges and the therefore different resulting interference patterns in the stress and the displacement fields. With equal radius and wall thickness the lengths of the waves in the undulating stress and the

displacement fields are identical. The axial positions $0.3L$ and $0.7L$ of the dents were set arbitrarily and the resulting absolute axial distances of the dents are different for different cylinder lengths L . That is, the constant wavelength of the displacement field was ignored. Thus, the waves of the shells formed in circumferential direction are superposed with those formed in axial direction differently for the different absolute axial dent spacings, or similarly only by pure coincidence.

Comparisons with Test Results for Multiple Local Imperfections

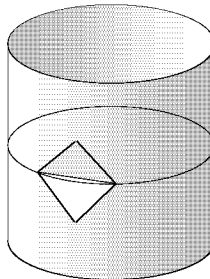


Figure 6.162: *Diamond shaped dent as applied by (KRISHNAKUMAR & FOSTER [57]) for experimental investigations on epoxy cylinders having one or multiple dents of this type.*

As already mentioned in Section 6.1 (KRISHNAKUMAR & FOSTER [57]) conducted tests of cylindrical spun-cast epoxy shells having one or more deep diamond or V-shaped dents, see Figure 6.162 and 6.6 on page 195. These more than forty thin cylinders had a mean radius of $R = 77$ mm, a length L between 70 and 90 mm, and a wall thickness h from 0.13 to 0.39 mm. The dents were introduced into the cylinders by local softening of the epoxy shells with heat from a hairdryer, whereby the shell around the dent was protected with a cardboard mask. The size of the dimples was controlled by the size of the V-shaped notch cut into a wooden mandril [57, 38]. Thus, the width of the imperfection was always close to the length of the straight intersection line of the two flat faces of the notch. Additionally, the initial depth w_n of the imperfections were also determined by the intersection line and the cylinder radius R . Three different sizes of such dents or notches were applied to their specimens, specified by their initial height l_n and width a_n . In the table below

the dimensions of the notches denoted with D1, D2, and D3 are listed according to the notation used herein:

	θ	a_n [mm]	l_n [mm]	w_n [mm]
D1	21°	28	24	1.3
D2	27°	36	30	2.1
D3	42°	57	50	5.0

The angle θ defined the width of the notches with $a_n = \theta \cdot (2\pi R)/360^\circ$. The actual size of the notch in the epoxy shells was usually smaller than that of the template listed above and later measured accurately from photographs. Each of the three notches above was added to 12 cylinders. Most of the shells had one or two of such imperfections, but four cylinders were tested with eight or nine notches around the circumference at half the cylinder length. In the cases with two notches the second notch was located either adjacent or diagonally opposite to the first. Both notches were arranged at $L/2$, or in a way that the directly adjacent second notch was located above or below with an axial offset $\Delta\zeta$ of $l_n/2$. The axial wavelengths $2l_c$ of the analytical axisymmetric buckling patterns of these epoxy cylinders lie between 11 and 19 mm. Thus, the three notches listed above are notably higher than the initial meridian heights $l_b \approx 2l_c$ for double-cosine dimples that would have been used for numerical buckling analyses such as described above. The initial widths of the notches in turn are close to their heights; hence, the width/height ratio is much smaller than the mean value obtained for the double-cosine dents in isotropic cylinders of about 2.7. But above all, with depth ratios from $w_b/h = 3$ up to about $w_b/h = 30$ (!) the notches are very deep in comparison to those of the dents in the FE models above with only $w_b/h = 0.2$ or 0.5 .

The shells were subjected to several buckling tests in a screw operated loading frame, first without notch, and then with a first a notch and subsequently again with a second, and so on [57]. Figure 6.163 depicts the test results for the epoxy cylinders having two of the notches above with positions as indicated. The normalized buckling loads vary between $P_{cr}/P_{cl} = 0.5$ and 0.8 , but experiments with a single notch yielded loads in the same range [57]. Variations of the buckling load due to different distances between the notches as shown in Figure 6.151 could not be

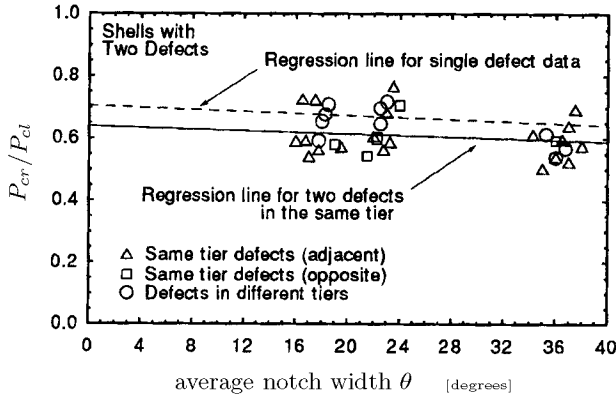


Figure 6.163: Test results of thin epoxy cylinders having two deep, diamond shaped notches located as indicated. Buckling loads normalized with respect to the analytical buckling loads for ideal cylinders and plotted against the measured notch size. From (KRISHNAKUMAR & FOSTER [57]).

spotted, i.e. two notches adjacent or diagonally apposite appeared to have the same effect. A comparison of the test results for the epoxy shells having deep V-shaped notches with the buckling loads of the own numerical analyses for different isotropic shells having relatively shallow double-cosine dents was hardly possible. For the epoxy shells own numerical nonlinear buckling or transient dynamic analyses were not performed. However, as regards the relative reduction of the buckling resistance due to one and two local imperfections at least the test results of (KRISHNAKUMAR & FOSTER [57]) are not contrary to the own nonlinear buckling analysis results. The drop of the buckling load due to a first notches is much more drastic than the further load reduction caused by a second notch. The linear regression lines in Figure 6.163 fitted to the test results for one and two notches indicate an additional reduction in the buckling load due to the second notch of 5 to 6%, which matches with the maximum load reduction obtained for the nonlinear buckling analyses of the reference cylinder having two adjacent double-cosine dents.

The regression lines to the test data of (KRISHNAKUMAR & FOSTER [57]) indicate a reduction in the buckling load of about 5% with increasing notch size. The nominal geometry of the cylinder in turn seemed to have no influence on the damaging effect of the notches. On the basis of these results with one, two and multiple notches the two researchers

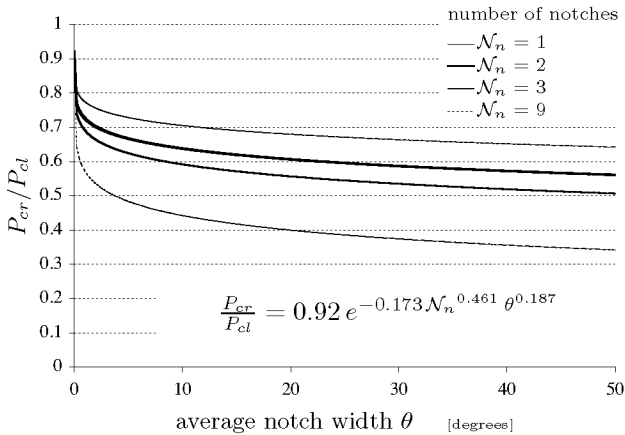


Figure 6.164: Empirical relation by (KRISHNAKUMAR & FOSTER [57]) for the normalized axial buckling load of isotropic cylinders having multiple notches considering their number \mathcal{N}_n and their average width θ .

finally derived an empirical relation for the normalized axial buckling load of isotropic cylinders having one and more diamond-shaped notches considering their number \mathcal{N}_n and their average width θ . Figure 6.164 includes this formula and shows the so calculated buckling loads for various numbers of notches as indicated and for notch widths θ up to 50° . The drastic reduction of the buckling load due to a single notch might stem from the presence of stress concentrations in the shells at the edges of the notches. This would explain the large gaps also for very small notch sizes [57]. But the further smaller load reductions caused by additional imperfections depend on the increase in the width of the shell section affected by the stress disturbance. Within the imperfections the axial membrane force is reduced and the added loading has to be carried by the area at the edges of the dimples and the shell outside the imperfections. According to this, since the remaining width of the shell unaffected by imperfections decreases with increasing total width of all imperfections the reduction of the buckling load should be direct proportional to the number and size of the imperfections.

The numerical buckling analyses were performed only with one or two double-cosine dents. The initial width $a_b = 181$ mm of the dents in the reference cylinder with $R = 250$ mm corresponds approximately to an angle $\theta = a_b \cdot 360^\circ / (2\pi R) \approx 40^\circ$. According to the stress analysis results in Section 6.6.5 the width of the shell strip with noticeable axial

membrane force variations prior to buckling is about 3 times the initial dent width. Hence, for two dents arranged around a circumference the total width with relevant membrane-force variations is circa $6 \cdot a_b$ or 240° and the remaining width of the unaffected shell area is 120° or a third of the circumference. Since in the numerical simulations the contribution of the shells above or below the dents to the loading is not zero but only reduced and the effective width of the area with axial membrane forces below the nominal value¹³ is smaller and closer to the initial width of the dents, for the cylinder with the boundary condition considered the dimension of the shell remaining unaffected is less reduced by a second dent than the considerations above probably would expect.

Extremal values are attained for KRISHNAKUMAR & FOSTER's formula if the entire cylinder circumference is filled up with dents or notches. For example, having a width of $\theta = 40^\circ$ *nine* notches arranged around the circumference would yield the minimum buckling load. In Figure 6.164 the lowest curve denotes the expected buckling loads for a cylinder with nine notches. For the exemplifying notch size a load of $P_{cr}/P_{cl} = 0.36$ result. This configuration resembles the cylinder having a single deep ring-shaped inward dimple. A nonlinear buckling analysis of the reference cylinder having a deep axisymmetric dent with an initial depth $w_b = 2h$ and an initial height l_b close to the classic-analysis wavelength $2l_c$ yielded also a minor buckling load of about $P_{cr}/P_{cr id} = 0.3$. This value may be considered being the lower bound for this cylinder having one or more localized dimple imperfections.

Worth mentioning finally that with the reference cylinder having one or two dents of initial depth w_b/h normalized buckling loads were obtained below $P_{cr}/P_{cr id} = 0.5$. These results are below the loads calculated with KRISHNAKUMAR & FOSTER's formula for a imperfection width of $\theta = 40^\circ$, despite the much smaller initial depth and height of the used dents in comparison to the notches applied for the tests. But, it contrast to the size of their notches the height and the width of the dents used for the numerical calculations are results of minimum searches and critical for the geometry of the cylinder involved.

¹³The variations in the shell of width $3 \cdot a_b$ also include the maximum peak values.

6.6.7 Alternative Conditions and Models

During the modeling of a structure with finite elements prior to any analysis the suitable type(s) of elements, the adequate element mesh size and the set of boundary conditions have to be selected, which influence the analysis results. The choice of such parameters and options should be performed under consideration of the geometries, the materials, the analysis case, and the expected structural behaviour as well as the available hard- and software. The manner how the cylinders were simulated for the studies presented herein bases on the experience with the buckling analyses of the laminated cylinders during the DEVILS project. This section deals with the buckling analysis results of isotropic cylinders having a single dimple imperfection which were obtained with boundary conditions, mesh size, dimple geometry, and dimple positions which differ from those always used for the analyses above. The reference shape of the dimples and cylinder modeling is subject of Section 6.4 on page 200 ff. The reasons for the reference options and parameters in general are founded on the accuracy and the comparability of the results and the time consumption of the calculation.

The possible influences of the parameters to the transient dynamic analysis of axially compressed cylinders was described in connection with the analysis of cylinders with perfect geometry in Section 4.3, p. 143, and is not further followed up.

All analyses presented in this section were made with the isotropic reference cylinder with radius $R = 250$ mm, length $L = 510$ mm, and wall thickness $h = 1.5$ mm. The initial circumferential width and meridian height of the dimples applied are always $a_b = 181$ mm and $l_b = 66$ mm, respectively.

Other Boundary Conditions

The test results for the laminated cylinders of the DEVILS project were used for the calibration of the numerical analysis settings. These specimens were clamped in endplates. Thus, for the numerical buckling analyses the clamped boundary conditions CC4 were applied simulating ideal rigid and plane-parallel end plates, see Section 6.4 and 2.2.1. Afterwards, these boundary conditions were also adopted for the numerical analysis of cylinders with dimple imperfections.

The boundary conditions CC4 and SS4 were simulated with auxiliary

nodes on the cylinder axis whose degrees of freedom were joint with the nodes on an edge. The loading was applied on one of these auxiliary nodes which was linked with the nodes on the loaded edge in the form of algebraic equations. These enforced the translations and rotations of the edge nodes to follow those of the guiding auxiliary node on the axis. Consequently, the displacements of all edge nodes are identical, also the non-zero axial displacements. The clamped boundary conditions CC4 with uniform edge displacements and all rotations, the radial and the circumferential displacements retained are the reference conditions and were applied for all numerical analyses presented in this work so far.

Alternatively, the axial load may also be applied directly by means of equal forces on the edge nodes. With such a setting the boundary conditions CC3 or SS3 of the shell calculus are simulated with uniform membrane forces along the edges but with potentially non-uniform axial edge displacements, see 2.2.1.

In the following (a) the important differences in the buckling behaviour and buckling loads between uniform edge membrane forces (CC3) and uniform edge displacements (CC4) are detailed. That followed, (b) the results obtained for the simply supported boundary conditions SS4, i.e. with unconstrained rotations, are compared with results for the clamped reference conditions CC4.

(a) Controlled cylinder edge loads \rightarrow boundary conditions CC3

All the finite element calculations presented so far were conducted with boundary conditions CC4 applied for clamped cylinder edges with controlled axial edge displacements. Consequently, axial compression of such a cylinder model with rigid and plane-parallel endplates simulated provokes axial displacements u identical for all edge nodes but potentially non-uniformly distributed axial membrane forces per unit length N_x along the cylinder edges.

The direct application of the compressive load via equal forces on the edge nodes, however, causes uniformly distributed axial membrane forces N_x along the edges but potentially non-uniformly distributed axial edge displacements u . For a simulation of the clamped boundary conditions CC3 on the edge nodes all rotations, the radial and the circumferential displacements are retained without any use of an auxiliary node on the cylinder axis. The controlled axial membrane force N_x linearly distributed along the edge is the membrane force/unit length of the fundamental state $-\tilde{N}_x$ and applied on the k edge nodes B_k with equal

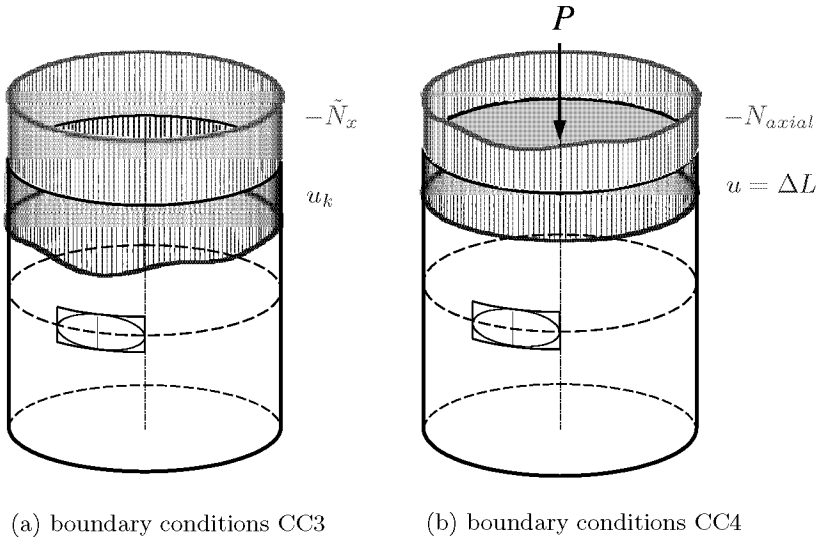


Figure 6.165: *Runs of the axial membrane force per unit length (red) and the axial displacement (blue) around the upper cylinder edge for (a) boundary conditions CC3 with constant axial membrane forces per unit length \tilde{N}_x and for (b) boundary conditions CC4 with constant axial displacements u simulating rigid, plane-parallel endplates. Qualitative representations for a cylinder with a single dent.*

compressive forces $P^{(B_k)}$. With the applied total force P the k nodal forces are given by

$$P^{(B_k)} = \frac{P}{k} \quad (6.20)$$

where $P = -\tilde{N}_x (2\pi R)$, see Figure 6.9 on page 202. In Figure 6.165 the distribution of the axial membrane force and the axial displacement around the loaded cylinder edge for the boundary conditions CC3 (a) is compared with the distributions for the reference boundary conditions CC4 (b). The curves are qualitative representations of results for a cylinder with a single dent. In case of the conditions CC3 the axial membrane forces along the edge $N_{axial} = \tilde{N}_x$ (red) are uniform ($\partial N_x / \partial y = 0$) and the resulting axial edge displacements u (blue) are non-uniform ($\partial u / \partial y \neq 0$), whereas in case of the conditions CC4 the axial membrane forces/unit length along the edge N_{axial} are non-uniform

($\partial N_x/\partial y \neq 0$) and the resulting axial edge displacements u are uniform ($\partial u/\partial y = 0$).

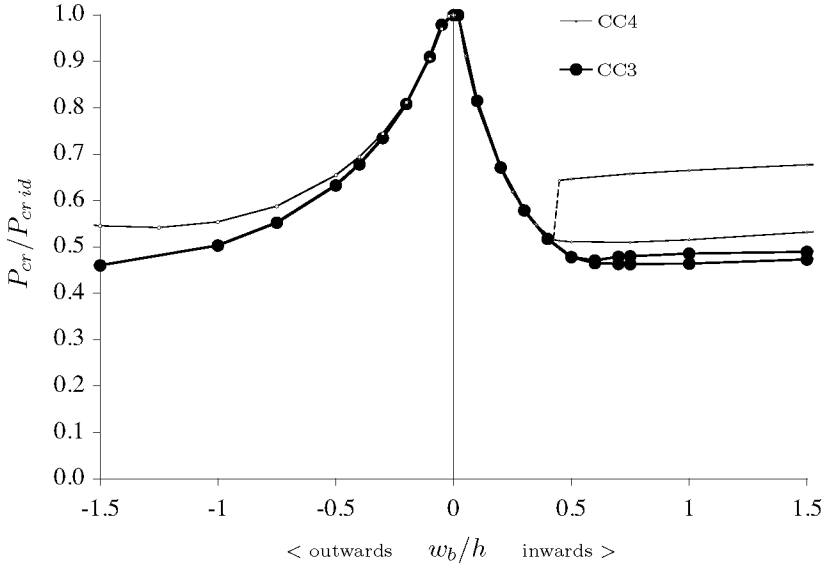


Figure 6.166: Normalized buckling loads for the reference cylinder having a dimple with an initial amplitude w_b/h as indicated. Results for boundary conditions CC3 (uniform axial edge load) and for boundary conditions CC4 (uniform axial edge displacement) as indicated. Dents and bulges of initial width $a_b = 181$ mm and height $l_b = 66$ mm.

Figure 6.166 depicts the normalized buckling loads $P_{cr}/P_{cr id}$ resulting for the reference cylinder having a single dimple of initial width $a_b = 181$ mm and height $l_b = 66$ mm in dependence of the initial dimple amplitude w_b/h . The black bold marks denote the results of nonlinear buckling analyses with clamped boundary conditions CC3 on the loaded edge but CC4 on the unloaded. That is, contrary to the conditions CC3 in the classical analysis only along the loaded edge the axial membrane force/unit length is uniform; to simplify matters, along the unloaded edge the axial displacement was constrained and hence the axial membrane force per unit length along this edge is not necessarily uniform. The thin line shows the results of analyses with the reference conditions CC4 described in the previous sections. The loads $P_{cr}/P_{cr id}$ were normalized with the buckling load obtained for the reference cylinder with ideal geometry and with the reference conditions CC3 applied,

$P_{cr\ id} = 558\text{ kN}$. This buckling load is only 2 percent smaller than the load $P_{cr\ id} = 569\text{ kN}$ that resulted accordingly with the reference conditions CC4. For shallow inward dimples ($w_b/h \leq 0.45$) the difference between the normalized buckling loads for CC3 and CC4 are less than 5 percent. But the smallest buckling load achieved for dents and CC3 is $P_{cr\ L} = 258\text{ kN}$ for $w_b/h = 0.75$, which is about 12% below the smallest load $P_{cr\ L} = 290\text{ kN}$ for dents and CC4. With the reference boundary conditions CC4 applied the nonlinear buckling analyses of cylinders with shallow dents yielded a lower buckling load $P_{cr\ L}$, associated with local buckling, and additionally a higher buckling $P_{cr\ U}$, associated with the cylinder collapse, see Section 6.6.1. During compression the depth of a shallow dent is continuously increased and the circumferential curvature at the dent apex decreased until at a load $P_{cr\ L}$ flattened vertical strip over the dent is formed with locally reduced axial buckling resistance. Since with the boundary conditions CC4 the axial edge displacement of the flattened strip is controlled and identical with the edge displacement of the still unaffected cylinder shell, this local buckling is *not* immediately followed by the total cylinder collapse due to excessive axial displacement of the edge over the dent. But, in case of a cylinder with the boundary conditions CC3 after having reached the state with a flattened strip the axial edge displacement is not controlled but the axial load, and hence after the local buckling the shell strip including the deepened dent is more compressed than the rest of the cylinder. The cylinder edge tilts rapidly towards the initial dent and shortly afterwards the cylinder collapses totally. As can be taken from Figure 6.166, for deep dents with initial depths between $w_b/h = 0.6$ and 2.0 also with the boundary conditions CC3 second buckling loads $P_{cr\ U}$, which are slightly higher than the local-buckling loads $P_{cr\ L}$, were obtained. These loads denote the total cylinder collapse and are probably somewhat above the local-buckling load because of the relatively slow local shell flattening and the therefore only later accelerated shell deformations.

The results for the nonlinear buckling analyses of the reference cylinder with a single *outward* dimple performed with the boundary conditions CC3 are also included in Figure 6.166. The variations between these loads and the results for the reference conditions CC4 increase continuously with increasing initial bulge amplitude. For bulges with initial amplitudes above $w_b/h = -0.4$ deviations of more than 5 percent resulted. The bulge with $w_b/h = -1.5$ yielded a deviation of more than 20%. Additionally, the minimum buckling load of the reference cylinder having a bulge with this initial width and height results for a larger initial amplitude compared with that obtained with the conditions CC4.

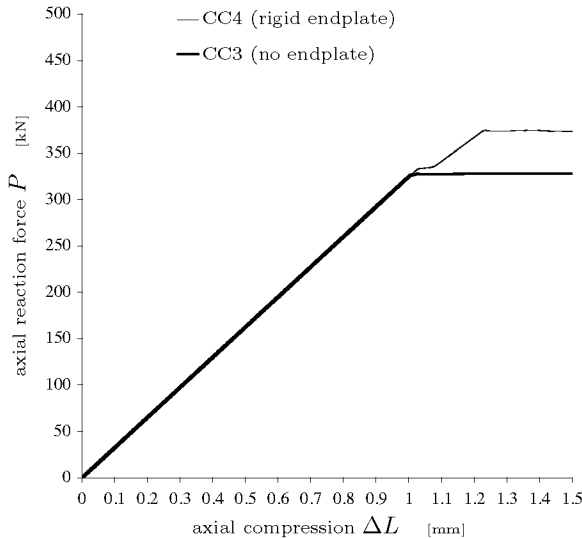


Figure 6.167: Results of transient dynamic analyses of the reference cylinder having an inward dimple of initial depth $w_b/h = 0.3$, width $a_b = 181$ mm, and height $l_b = 66$ mm. Calculations with applied axial forces simulating either boundary conditions CC3 (uniform edge loads) or CC4 (uniform edge displacements).

In Figure 6.167 and 6.168 the results of a dynamic transient analysis of the reference cylinder with a single dent of initial depth $w_b/h = 0.3$, width $a_b = 181$ mm, and height $l_b = 66$ mm are displayed. The upper edge is clamped with the conditions CC3 applied and hence loaded by means of increasing nodal forces, whereas the bottom unloaded edge is clamped with the conditions CC4. The reference conditions CC4 applied, nonlinear buckling analyses of the reference cylinder having this dent of initial depth $w_b/h = 0.3$ yielded only one buckling load ($P_{cr} = 330$ kN). Due to a distinctive local buckling the nonlinear buckling analyses were aborted when reaching this load. With transient dynamic analyses and controlled edge displacements, however, for this shell a collapse load of about $P_{crU} = 374$ kN could be reached. But the transient dynamic analysis with the conditions CC3 resulted that with uncontrolled edge displacements already directly after local buckling total cylinder collapse occurs. In Figure 6.167 the load-axial displacement curve (bold line) resulting for this analysis is shown. After reaching the local buckling load the uncontrolled edge displacements increase rapidly at an almost con-

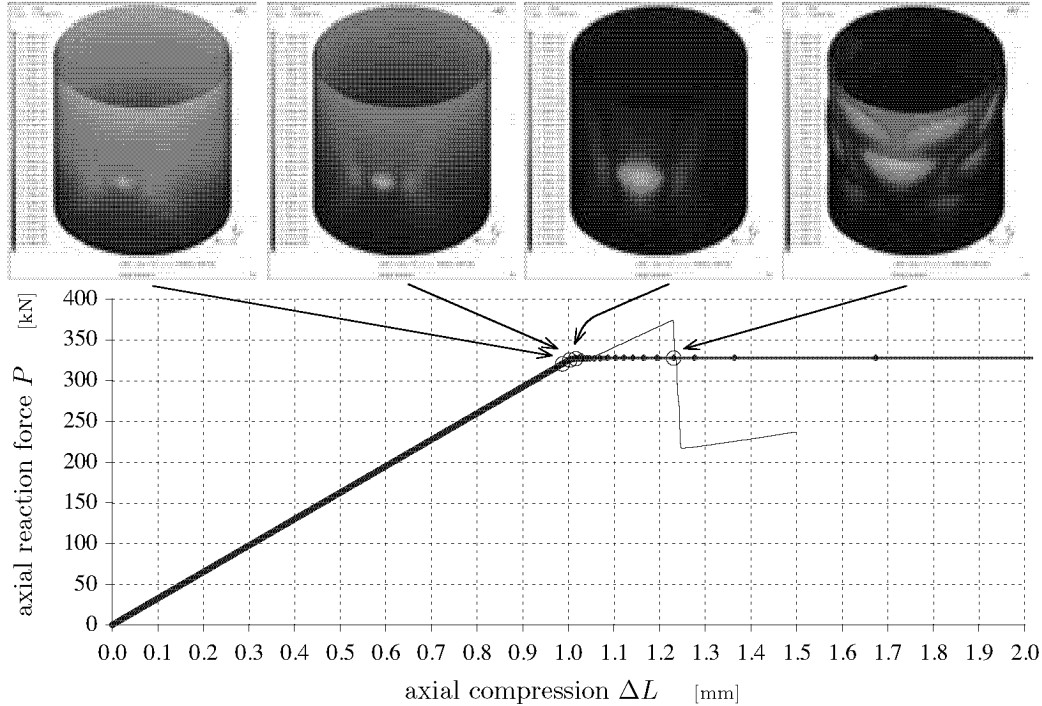


Figure 6.168: Results of a transient dynamic analysis for the reference cylinder having a dent of initial depth $w_b/h = 0.3$. Analysis with clamped boundary conditions CC3 (controlled axial edge load $-\tilde{N}_x$) for the upper cylinder end and CC4 (all degrees of freedom fixed) for the bottom. Thin line results of an edge displacement controlled calculation. Deformations in the pictures displayed without magnification; contour color maps refer to total-displacement vector lengths in metres.

stant load. The horizontal load curve indicates a rapid displacement of the upper edge towards the bottom. In Figure 6.168 the four small included plots depict selected deformation states prior, at, and immediately after local buckling. It can be seen, that after local buckling unilaterally new large dimples were performed and that the upper cylinder edge tilted towards the initial dent. In Figure 6.167 the results of a transient dynamic analysis of this shell with the conditions CC4 (uniform edge displacement) but with the total axial force P as loading parameter are reproduced (thin line) for comparison. In the resulting load-axial displacement curve at the load for local buckling a kink resulted, indicating that after the shell flattening the axial cylinder stiffness is reduced. But in this case, shortly afterwards the load reincreases up to the remarkable higher collapse load. Only having passed this peak load again the upper edge is rapidly displaced towards the bottom.

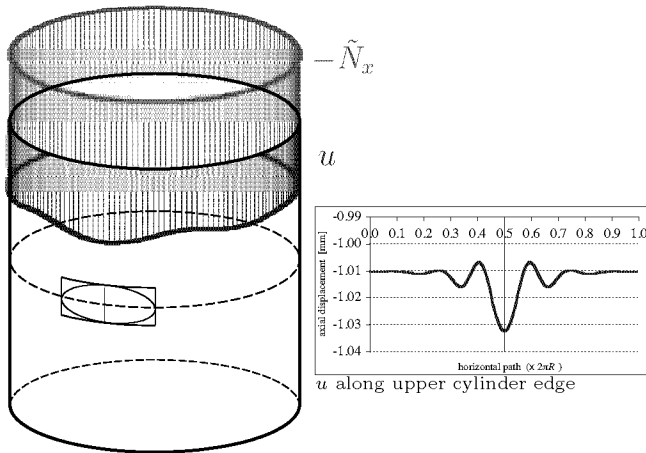
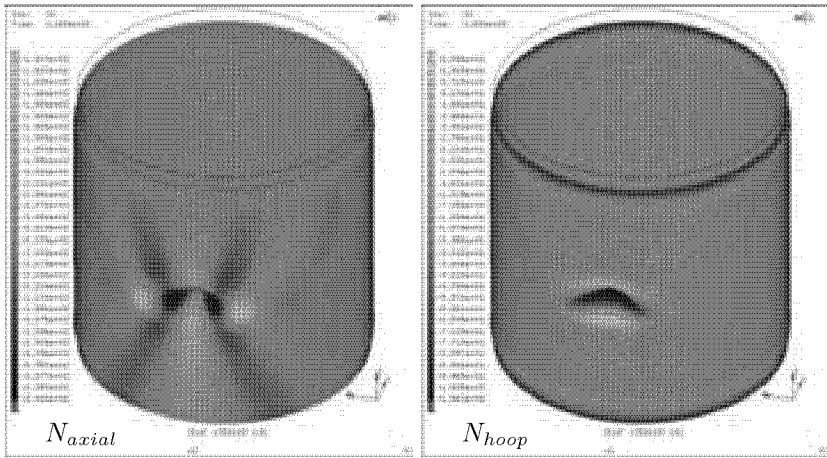


Figure 6.169: Varying axial displacements u of the nodes along the upper edge of the reference cylinder having a dent of initial depth $w_b/h = 0.3$. Results of a nonlinear static analysis at an uniformly distributed axial membrane force per unit length of $\tilde{N}_x = -208.8 \text{ N/mm}$ applied to the upper edge. Total external compressive force $P = 328 \text{ kN}$. Upper cylinder edge with clamped boundary conditions CC3, lower edge with CC4.

In Figure 6.169 the axial edge displacements u along the upper edge of the shell above are depicted which resulted from a nonlinear stress analysis for an uniformly distributed load of $\tilde{N}_x = -208.8 \text{ N/mm}$ applied to the upper cylinder edge. The resulting axial compressive load for

this axial membrane force/unit length is $P = 328 \text{ kN}$, which is identical to the applied axial load P for the analysis case in Figure 6.125 on page 371 with uniform edge displacements (CC4). The red “railing” of constant height on the upper edge of the drawn cylinder stands for the with conditions CC3 evenly distributed compressive edge load $-\tilde{N}_x$; the blue ring “hanging” below shows the varying axial displacement u with a maximal local compression located above the dent apex and two minima formed on the left and the right of the lateral dent sides. The nominal axial displacement of the upper reference cylinder edge for the shell without imperfection and the axial load on hand is $\Delta L = 1.01 \text{ mm}$. To the right of the drawn cylinder in Figure 6.169 the uncoiled blue curve around the upper shell edge is reproduced in a chart with an adapted scale for a better visibility of the resulting axial displacement variations. At the cylinder edge diagonally opposite to the dent (at 0 or $2\pi R$) the nominal value of cylinder contraction ΔL was achieved, whereas above the dent with $u = -1.032 \text{ mm}$ a maximum local compression of about 2% above the nominal value was obtained. Without a guidance of the axial edge displacement, due to the continuous increase of the dent depth and the that following the axial contraction of the vertical shell strip over the dent, the cylinder edge sags more above the dent. The bulges at the dent sides, in turn, increase the axial stiffness of the shell locally and hence the axial edge displacement above these bulges underruns the nominal value.

Figure 6.170 finally represents the axial membrane forces N_{axial} and the circumferential membrane forces N_{hoop} , both again per unit length, resulting for above shell, boundary conditions CC3 and uniformly distributed edge load \tilde{N}_x applied on the upper edge. Since in contrast to the upper edge nodes the axial displacement of the lower edge nodes are fixed, a direct comparison between results for cylinders boundaries modeled according to the analytical conditions CC3 and such according to the conditions CC4 is enabled. In the lower cylinder half of the contour deformation plot (b), similar to the results in Figure 6.125 on page 371, the red zones of higher axial membrane forces N_{axial} radiating slantwise from the lateral dent flanks reach the cylinder bottom, and consequently the axial membrane force along the edge is non-uniform. In the upper shell half, in contrast, the red zones of higher axial membrane forces are faded away some element rows below the shell boundary since there the axial membrane force N_{axial} equals the given edge load \tilde{N}_x . The local extremal deviations of the axial membrane forces N_{axial} from the nominal value \tilde{N}_x are slightly higher compared with the values in Figure 6.125 due to the somewhat larger deformations. The differ-



(a) axial membrane forces

(b) circumferential membrane forces

Figure 6.170: Axial and circumferential membrane forces per unit length of the reference cylinder with a dent of initial depth $w_b/h = 0.3$ resulting for an evenly distributed axial membrane force of $\tilde{N}_x = -208.8 \text{ N/mm}$, a total load of $P = 328 \text{ kN}$. Results of a nonlinear static analysis for a clamped lower cylinder edge and a flexible upper edge with boundary condition set CC3. See Fig. 6.169 and Section 6.4.

ences between the circumferential membrane forces/unit length N_{hoop} in Figure 6.170 (b) and those in Figure 6.126 are negligibly small, considering the colour distribution as well as the maximal compressive and tensile membrane forces. Therefore, the change from the cylinder edge modeling with boundary conditions CC4 to that with conditions CC3 affected the axial membrane forces N_{axial} within the cylinder shell only close to the cylinder edge substantially; the resulting differences in the tangential membrane forces N_{hoop} and the axial membrane forces N_{axial} around the dent are both negligibly small.

The numerical analyses of cylinders having a single dimple yielded considerably lower buckling loads if performed with uniform edge loads (CC3) than the calculations with uniform, controlled edge displacements (CC4) applied. Hence, a more conservative investigation on the minimum loads of cylinders with single dimples would have required to apply the boundary conditions CC3 as reference for the parameter studies to this thesis. But, the reasons for the application of the other conditions CC4 as ref-

erence lie in the better comparability with test results and the interest in the particular behaviour of the shells after local buckling which is rarely observable using the conditions CC3 due to instantaneous total collapse.

(b) Simply supported cylinder edges \rightarrow boundary conditions SS4

To investigate how much buckling loads of cylinders with hinged edges differ from those with clamped edges, the nonlinear buckling analyses of the reference cylinder having a dent or bulge at half the cylinder length and of varied initial amplitude w_b was repeated with the boundary conditions SS4 applied. For these conditions the rotational degrees of freedom were left free, but the translations were treated identically to clamped edges by means of tied nodes and application of the load on an auxiliary node on the cylinder axis, see Section 6.4.

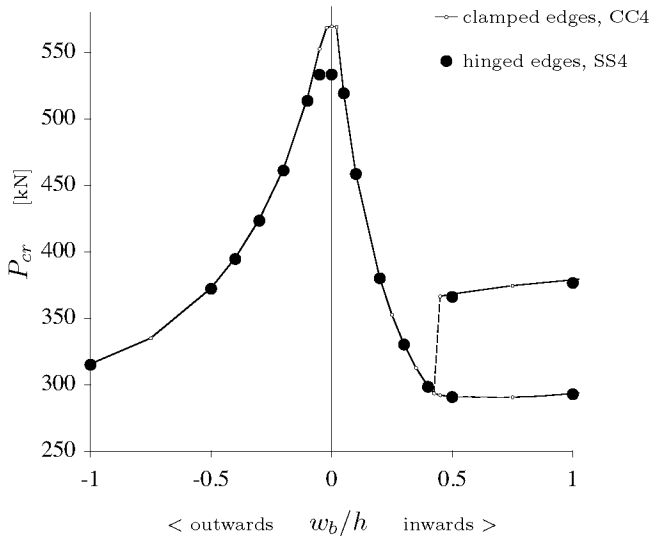


Figure 6.171: Buckling loads P_{cr} for the reference cylinder having a dimple with an initial amplitude w_b/h as indicated. Results for hinged and for clamped cylinder edges. Dents and bulges located at half the cylinder length and of initial width $a_b = 181$ mm and height $l_b = 66$ mm.

In Figure 6.171 the resulting buckling loads are depicted. It may be seen that for the perfect cylinder ($w_b = 0$) a difference in the load of about seven percent between clamped and hinged edges may be iden-

tified, whereas for the dimples with amplitudes above $|w_b/h| = 0.1$ the loads are almost identical. Consequently, the sensitivity to single dimples, given by the ratio $P_{cr}/P_{cr id}$, is larger for clamped edges since in this case the buckling load for the ideal geometry $P_{cr id}$ is higher and the buckling loads with dents are equal to those for hinged edges. Therefore, buckling analyses of cylinders with clamped boundary conditions CC4 applied having an initial dimple yield more conservative results than with hinged conditions SS4. But, it has to be pointed out that the dimples were located at half the cylinder length $L/2$, thus with sufficient distance to the edges to ignore end-effects. Similar calculations with hinged conditions and dimples close to a cylinder edge were not performed; hence, for such cases the different influence of the boundary conditions CC4 and SS4 could not be estimated.

Finite Element Mesh Size

The finite element mesh sizes of the analysed cylinders, i.e. the edge length of the almost square finite elements in the models, was specified by the length $0.5\sqrt{Rh}$, see Section 4.1.3. This element size bases on the decay length of edge bending disturbances and is recommended for bilinear MINDLIN-type shell elements in FE models established for buckling analyses of axially compressed cylinders. Buckling analyses of perfect circular cylinders with finer mesh sizes yields slightly lower buckling loads. But, the only small improvement of the results would hardly justify the increase of the computation costs involved.

Figure 4.3 on page 123 contains linear buckling analysis results for two laminated cylinders with ideal geometry and demonstrates the only very small buckling-load reduction for a 50 percent shorter mesh size.

In Figure 6.172 the buckling loads P_{cr} of the isotropic reference cylinder having a single dimple are graphed which resulted either for the standard mesh-size of $0.5\sqrt{Rh}$ or for half this mesh-size. With the standard element length the reference cylinder contained $162 \times 52 = 8424$ elements, whereas with half this length four times more elements were needed: $324 \times 104 = 33\,696$ elements. Because of the vast time-consumption of the nonlinear buckling analyses with the shorter element edge length, only for the ideal reference cylinder and for dimples with small initial amplitudes not larger than $|w_b/h| = 0.4$ such additional analyses were performed. Within this range the deviation of the buckling load that resulted with the standard element mesh from those achieved with the

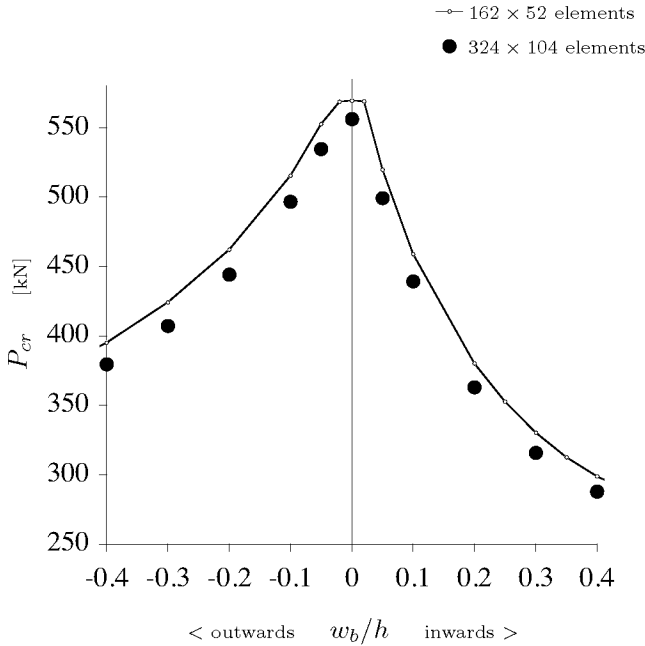


Figure 6.172: Nonlinear buckling analysis results for the reference cylinder having a dimple with an initial amplitude w_b/h as indicated, a width $a_b = 181$ mm, and a height $l_b = 66$ mm. Buckling loads obtained with 162×52 bilinear finite shell elements for a mesh size of $0.5\sqrt{Rh}$, and with 324×104 elements for half this mesh size.

finer mesh seems to be independent of the initial dimple amplitude. Additionally, the deviations vary solely between 2 and 5 percent.

The finite element mesh-size also influences the initial circumferential width $a_{\bar{b}}$ and initial meridian height $l_{\bar{b}}$ of shallow dents for maximum buckling load reduction which were obtained by means of minimum searches for given initial dimple amplitudes w_b , see Section 6.6.3. In Figure 6.173 the initial heights $l_{\bar{b}}$ and the initial widths $a_{\bar{b}}$ of shallow dents in the reference cylinder achieved for a fine FE mesh-size of $0.25\sqrt{Rh}$ (324×104 elements) are compared with those obtained for the standard mesh-size of $0.5\sqrt{Rh}$ (162×52 elements). The initial dent heights $l_{\bar{b}}$ which resulted for the fine mesh-size are 6% or less shorter than the heights that yielded the analyses for the standard mesh-size. The differences between the initial dent widths $a_{\bar{b}}$, finally, are 2% or smaller and

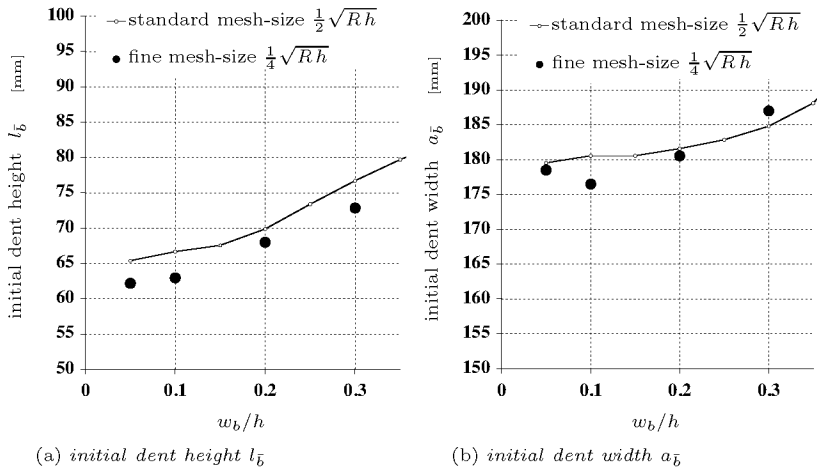


Figure 6.173: Initial meridian dent height $l_{\bar{b}}$ and initial circumferential dent width $a_{\bar{b}}$ against the initial dent depth w_b/h . Results for the reference cylinder with 162×52 elements (standard mesh) and 324×104 elements (fine mesh).

can therefore be neglected.

Dimple Shape

The element mesh-size also affects the initial geometry of the surface in the dimple imperfections. The multiply curved cylinder shell surface was approximated by a mesh of almost square plate-like elements. Since the mesh-size equals the length of their straight edges it determined the accuracy of the approximation by the resulting polygon-surface. The shape of the dimples used for the studies was defined by a “double-cosine” function. The initial cosine profiles of these dimples were then approximated with polygons, see Section 6.2. Additionally, for comparison a series of nonlinear buckling analyses were performed of the reference cylinder with dimples having V-shaped profiles in axial direction. That is, in axial direction the dimple geometry is given by linear equations instead of a cosine. But, in circumferential direction the profiles of these dimples were identical with those of the cosine-shaped reference dimples. Like the dimensions of these reference dimples, the initial width a_b , the initial height l_b , as well as the initial amplitude w_b of the V-shaped dimples are independent variables. Contrary to the flat faces of the diamond shaped dent in a YOSHIMURA buckling pattern, the two faces of these V-shaped

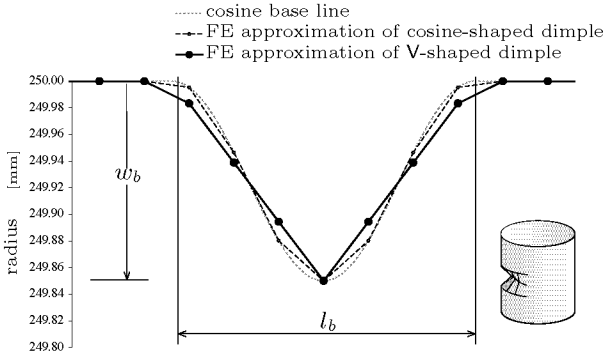


Figure 6.174: Radial and axial positions of nodes on the path over the apex of a dimple with amplitude $w_b = 0.15$ mm and meridian height $l_b = 66$ mm. Profiles of the cosine dimple and of the V-shaped dimple for FE approximations with a mesh-size of 9.7 mm.

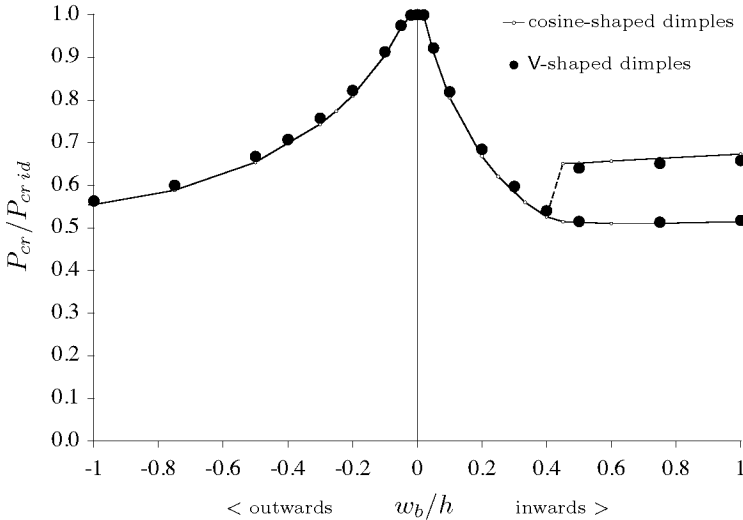


Figure 6.175: Nonlinear buckling analysis results of the reference cylinder having a dimple of shape and initial depth as indicated. Initial circumferential width of the dimples $a_b = 181$ mm. Initial meridian height of the cosine dimples $l_b = 66$ mm, that of the V-shaped dimples $l_b = 59$ mm.

dimples are elliptically curved. In Figure 6.174 the exemplary axial profile of a V-shaped dent is shown. A minimum search with the reference cylinder having a V-shaped dent of initial depth $w_b/h = 0.1$ yielded that the lowest buckling load is obtained for an initial width of $a_{\bar{b}} = 181$ mm and an initial height of $l_{\bar{b}} = 66$ mm, thus for lengths identical to those of the cosine-shaped dent associated to that initial depth. Figure 6.175 depicts the normalized buckling loads of the reference cylinder having a dimple imperfection of various initial amplitude w_b and with the lateral lengths $a_{\bar{b}}$ and $l_{\bar{b}}$ mentioned. The graph compares the nonlinear buckling analysis results for the reference cosine-shaped dimple geometry with those for the V-shaped dimples. It can be seen that almost all buckling loads obtained with V-shaped dimples are somewhat higher than the loads resulted with the reference dimples. Only for deep dents the upper, i.e. cylinder collapse loads the results for V-shaped dimples are slightly below the reference values.

The initial heights $l_{\bar{b}}$ of the dimples which provoke minimal buckling resistance of isotropic cylinders correlate approximatively with the analytical axial wavelength $2l_c \approx 3.5\sqrt{Rh}$. The length of the shell element edges is about $0.5\sqrt{Rh}$. Therefore, for dimples of initial height $l_{\bar{b}}$ in axial direction only seven element nodes are involved to form polygons to the axial dimple profile, see Figure 6.174. In case of the reference cosine-shaped dimples this polygon yields a rather rough approximations of the associated cosine base lines. Thus the difference between the initial dimple geometries with V-shapes and that with polygons is very small also for large amplitudes. Moreover, after first cylinder compression in the deformed shell the resemblance between the dimple geometries is even better. But, the cosine-shaped dimples was preferred to the V-shaped, mainly because of the better analytical comparability with the common bi-harmonic buckling patterns for ideal cylinders.

Axial Position of Dimple Apex

The analyses for the investigation on the buckling behaviour of cylinders having a single initial dimple were conducted with such dimples all located at half the cylinder length L . On the one hand to minimize the influence of the clamped cylinder edges, on the other hand because of the lower buckling loads obtained for dents at $L/2$ compared to those resulted for identical dents located closer to a cylinder edge. In Figure 6.176 the normalized buckling loads of the reference cylinder (clamped, CC4) having a dent of initial depth $w_b/h = 0.2$ are graphed for different

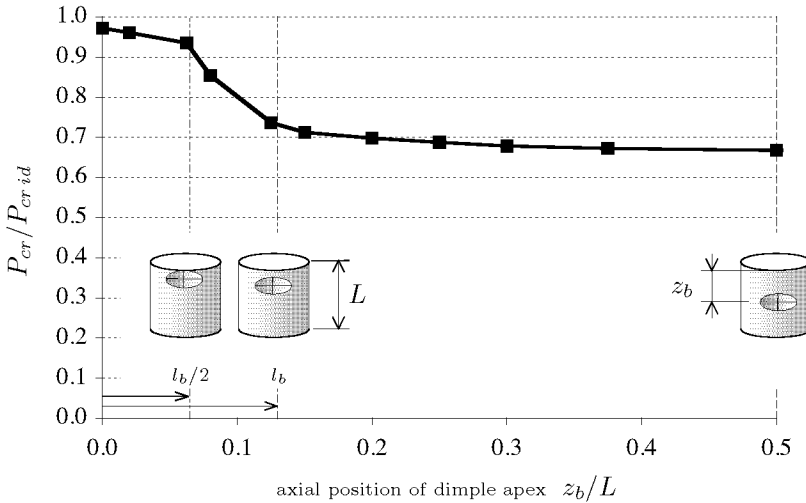


Figure 6.176: *Nonlinear buckling analysis results for the clamped reference cylinder having a dent of initial depth $w_b/h = 0.2$, initial circumferential width $a_b = 181$ mm, and meridian height $l_b = 66$ mm. Normalized buckling load versus the ratio of the axial position of the dent apex to the cylinder length L .*

axial positions of the dent. The loads, again obtained with nonlinear buckling analyses, are plotted against the ratio of initial axial dimple-apex position z_b to the cylinder length L . The shell with the dent located at half the cylinder length $z_b/L = 0.5$, in fact, yielded the lowest load. With decreasing edge distance z_b the buckling load increases. The buckling loads that resulted for distances from the dent apex to the closer cylinder edge longer than the initial dent height l_b are only little above the minimum value. An axial position of $z_b = l_b/2$ means that one edge of the dent matches with the cylinder edge. The buckling loads obtained for this apex position and for dent apexes closer to the cylinder edge are almost that of the perfect cylinder. For axial positions $z_b < l_b/2$ the geometry of the cylinder edge is also affected by the dent, i.e. the shape of the edge is not that of perfect circle. But, despite the imperfect edge these dimple imperfections at a cylinder edge are much less damaging than in the middle of the shell surface.

Close to the edge axial compression leads to axisymmetrical bulging of the clamped cylinder because of the prevented radial expansion due to POISSON'S effect. The height of these axisymmetrical bulges is about the

classical wavelength $2l_c$ for axisymmetric buckling. Since the height of the dent is also close to $2l_c$ the height of the bulge is also about that of the applied dent. For $z_b = l_b/2$ the applied inward dimple locally compensates the ring-shaped bulging and hence the damaging effect the dent on hand is reduced. Additionally, due to their support close to the edges the lateral displacements are smaller than in the middle of the shell, and therefore the increase in stress due to bending at and in a dent close to the cylinder edges is also smaller than for an identical dent at half the cylinder length. However, the review whether axially compressed cylinders tend to be more sensitive to dents in the middle of the shell than to such close to an edge was limited to calculations with (i) inward dimples, (ii) with a dimple size close to $2l_c$, (iii) with the mid-long reference cylinder, and (iv) with clamped boundary conditions. Searches for the initial heights and widths of dents or bulges close to a cylinder edge with minimum buckling loads were not performed. Consequently, the existence of dimples close to a cylinder end with particular size and/or geometry different to the dent considered which cause considerable reduction of the axial buckling resistance can not be excluded.

Linear Versus Nonlinear Buckling Analysis

Design engineers and stress analysts are confronted with not necessarily pleasant questions about the time and the costs needed for their calculations. In case of structural stability sometimes the operation of nonlinear buckling analyses with incremental-iterative solutions of equilibrium equations and a few tens of eigenvalue extractions have to be justified, since with the linear buckling analysis a much faster method with only one eigenvalue extraction is available. In Figure 6.177 the normalized buckling analyses $P_{cr}/P_{cr id}$ of the reference cylinder with a single dimple calculated with either linear or nonlinear buckling analyses are shown for different initial dimple amplitudes w_b/h . The buckling loads were normalized with respect to the buckling load of the ideal cylinder $P_{cr id}$ calculated with the relating analysis method; the buckling load of the ideal reference cylinder is $P_{cr id} = 569 \text{ kN}$ with a nonlinear buckling analysis and $P_{cr id} = 617 \text{ kN}$ (+8%) with a linear buckling analysis. It can easily be recognized that above all for very small initial dimple amplitudes the discrepancies between the results of linear and nonlinear analyses are dramatic. A dent with an initial depth of only $w_b/h = 0.1$ already yielded loads with a deviation of 24%, and a dent with $w_b/h = 0.4$ gave a difference of about 40%. Moreover, with linear

buckling analyses the behaviour of deep dents between the local buckling and the cylinder collapse may not be analysed. Already during the DEVILS project the important finding was confirmed that the inclusion of imperfections demands the use of nonlinear analysis methods which consider large displacements and rotations.

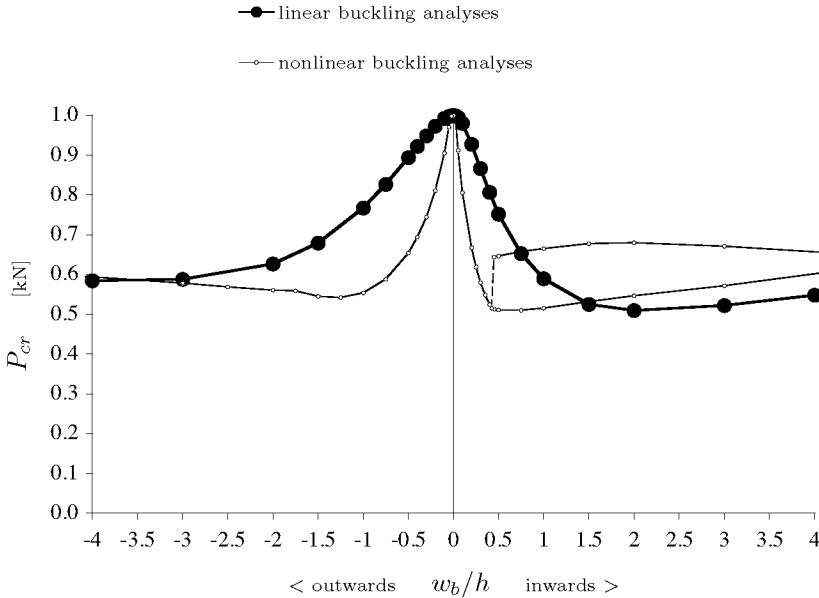


Figure 6.177: Results of linear buckling analyses and nonlinear buckling analyses. Buckling loads P_{cr} for the reference cylinder having a dimple with an initial amplitude w_b/h as indicated, normalized with respect to the particular load of the perfect cylinder $P_{cr id}$. Dents and bulges of initial width $a_b = 181$ mm and height $l_b = 66$ mm.

Thus, the reason for the consequent use of the more sophisticated and time-consuming nonlinear buckling analysis for the parameter studies of dimples in cylinders founds on the obvious quasi-uselessness of the linear buckling analysis for circular cylinders which differ from their perfect geometry! The extraordinary generous allocation of computing and human resources for the present thesis was condition but not reason for the use of the more expensive analysis methods.

6.7 Laminated Cylinders with Dimples

In the previous sections buckling analysis results for *isotropic* cylinders of medium length having a single inward or outward dimple were discussed. The changes in the axial buckling loads due to the variation of the initial dimple amplitude at given lateral dimple lengths were detailed. Further, the initial dent widths and heights of the dimples which yielded the minimum buckling loads for a particular initial amplitude were presented for different cylinder radii, wall thicknesses and lengths. According to these results the instability behaviour of such isotropic cylinders with a single dent or bulge, the resulting progressions of the normalized buckling loads and the initial sizes of the most damaging dimple depend on the normalized initial dimple amplitude w_b/h , the length \sqrt{Rh} , and the cylinder length L . The stiffness of the shell material however has no influence on the sensitivity of isotropic cylinders to dimple imperfections. In design guidelines or standards for isotropic cylinder shells the imperfection sensitivity and critical measures of imperfections are taken into account similarly being functions of the cylinder radius R , the cylinder length L , and the shell wall thickness h , but not of the YOUNG's modulus E for isotropic ideal-elastic material. On the basis of the experiences with the numerical buckling analysis of imperfect CFRP cylinders, see Section 5.3, it was aimed at investigating if for *laminated* cylinders of medium length similar design guidelines can be derived which include the impact to the axial stability and the critical size of single dimples, and which parameters influence these limits the most. The buckling load as well as the buckling mode of laminated cylinders with perfect shell geometry strongly depend on the fibre orientations of the laminate layers and their stacking sequence. This led to the assumption that the buckling behaviour of laminated cylinders with local dimples and the dimensions of dimples provoking minimum axial stability also depend on the laminate stacking and the resulting material stiffness ratios, and not only on the nominal cylinder geometry. This section deals with the buckling analysis results for laminated CFRP cylinders having a single dent or bulge which confirm the assumption mentioned above widely.

The specifications of the eccentrically laminated cylinders Z28, Z30, Z32, and Z33 of the project DEVILS as well as of the series of additional shells which exemplified for FE calculations were introduced in Section 4.1.2, page 119 ff. The analysis results for these cylinders with perfect shell geometry, including explanations of the effects observed, were detailed in Section 4.2.2, page 131 ff. These laminated CFRP cylinders

have a length L of 510 mm and a radius of R of 250 mm. The shell wall thickness h is 1.25 mm in case of the DEVILS cylinders with ten layers, and 1.0 mm in case of the additional cylinders with eight layers, see Section 4.1.2. Thus, the computations of the buckling loads of laminated cylinders afflicted with single dimples were confined to shells which differ in the material parameters and the initial dimple size. In contrast to the analyses for isotropic cylinders, where the impacts also due to the variation of the cylinder length and radius and the wall thickness were of interest, for the laminated cylinders the influences of the fibre orientations and stacking sequences were focussed. It was assumed that the influence of the cylinder dimensions observed for isotropic cylinders apply also for laminated cylinders and that they are independent of the material parameters. That is, according to this assumption the effects of a change in the length of a laminated cylinder, for instance, is similar to that of isotropic shells and superimposable over the effect of a change in the material parameter such as due to a variation of the layer stacking.

For the FE calculations exclusively the standard conditions and models were used, see Section 6.6.7. That is, the edges of the cylinder models were clamped for the boundary conditions CC4 to simulate rigid end-plates, the shell-element edge length was given by $0.5\sqrt{Rh}$, the dimples of cosine-shape were always arranged at half the cylinder length, and only nonlinear buckling analyses and transient dynamic analyses were performed.

In the following first the resulting change in the buckling loads due to the variation of the initial dimple amplitude w_b at given lateral dimple lengths l_b and a_b is described for selected laminated cylinders. Afterwards, the initial meridian heights $l_{\bar{b}}$ and circumferential widths $a_{\bar{b}}$ of the inward dimples are dealt with which yielded minimum buckling loads for a given initial dimple amplitude w_b . Finally, the minimum buckling loads $P_{cr \text{ MIN}}$ which resulted from the nonlinear buckling analyses with inward dimples of various initial depth are discussed.

6.7.1 Variation of the Initial Dimple Amplitude

In order to investigate the change in the reduction of the axial buckling resistance exclusively due to the variation of the initial amplitude of a single dimple, for a few laminated cylinders a series of nonlinear buckling analyses were performed with a dent or a bulge of constant initial dimple width a_b and height l_b . For all selected cylinders and priorly specified respective initial dimple widths and heights sets of shells were established with the initial dimple amplitude as the only stepwise varied sampling parameter. This procedure is similar to that for the isotropic cylinders having a dent described in Section 6.6.1. After a few calculations for dimples with an initial height and width of ten percent of the cylinder length and of the circumference respectively, the particular initial widths $a_{\bar{b}}$ and the initial heights $l_{\bar{b}}$ of the dents which yielded minimum cylinder stability for an initial depth $w_b/h = 0.1$ were applied for the analyses. The initial widths $a_{\bar{b}}$ and heights $l_{\bar{b}}$ of the “pessimum” dents which resulted for the laminated cylinders are subject of the subsequent Section 6.7.2.

The investigations described in this section were motivated by the experiences with the buckling analyses of DEVILS cylinder Z33 with its measured imperfection pattern which includes some small dents or notches, see Section 5.3. Therefore, the first computations with a parametric “cosine”-dimple added to a laminated cylinder were conducted also with cylinder Z33 [81]. The results were then compared with those obtained for Cylinder Z32 with the reversed layer stacking (i.e. axially stiff layers outside), but also with cylinder Z28 and Z30 with maximised buckling loads for perfect circular cylinder geometry.

	stacking	$P_{cr id}$ [kN]
Z28	$\pm 53^\circ, \pm 8^\circ, \pm 90^\circ, \pm 68^\circ, \pm 38^\circ$	269
Z30	$\pm 53^\circ, \pm 38^\circ, \pm 22^\circ, \pm 90^\circ, \pm 30^\circ$	265
Z32	$\pm 0^\circ, \pm 19^\circ, \pm 37^\circ, \pm 45^\circ, \pm 51^\circ$	105
Z33	$\pm 51^\circ, \pm 45^\circ, \pm 37^\circ, \pm 19^\circ, \pm 0^\circ$	199

Table 6.6: Identification of the DEVILS cylinders, their stacking sequences from outside to inside layers (0° : axial), and the buckling loads for the perfect cylinders obtained with nonlinear buckling analyses. See Figure 4.1, page 121.

In Table 6.6 the stacking sequences of the four DEVILS cylinders con-

sidered are listed together with the buckling loads for the ideal cylinders $P_{cr id}$ obtained with nonlinear buckling analyses. The ply properties of these carbon fibre reinforced laminates are given in Section 4.1.2, page 121. Cylinder Z30 was designed as the shell with the highest buckling load among the DEVILS shells, whereas cylinder Z32 is the one with the lowest buckling load. The stacking sequence of cylinder Z33 was provided by reversing the ply order of cylinder Z32. In Section 4.2.2 it was pointed out that the perfect cylinder Z33 with axially stiff layers at the inner side buckles at about double the load compared with the “pessimism” cylinder Z32 with axially stiff layers at the outer side. The optimization of the buckling resistance was performed by means of an analytical solution as introduced in Section 2.2.3 which yielded a buckling load $P_{cl} = 287$ kN for cylinder Z30 and only 255 kN for cylinder Z28. Nonlinear buckling analyses however resulted in almost equal buckling loads for these two shells, see Section 4.2.2.

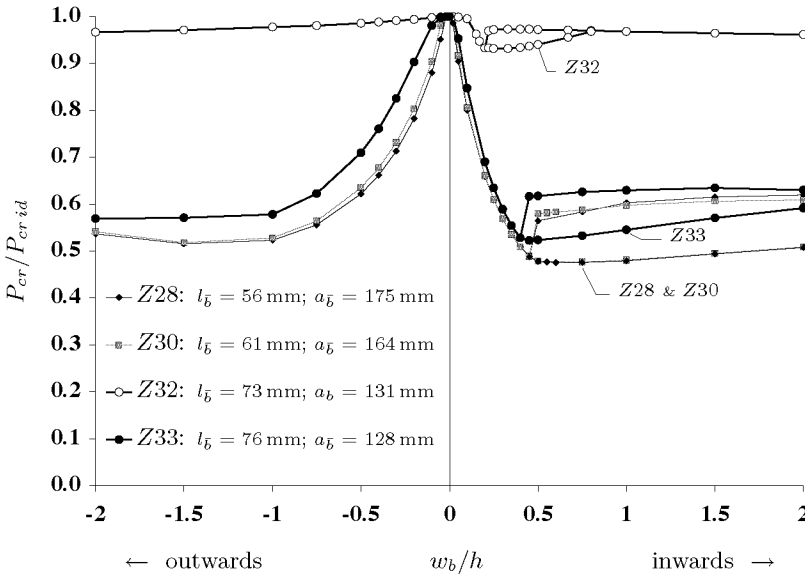


Figure 6.178: Normalized buckling loads for the laminated DEVILS cylinders Z28, Z30, Z32, and Z33 having a single inward or outward dimple versus the initial dimple amplitude w_b/h . Results of nonlinear buckling analyses for dimples with initial widths $a_{\bar{b}}$ and heights $l_{\bar{b}}$ as indicated.

As different the buckling loads and the buckling modes of these cylin-

ders of perfect geometry are, as different is their sensitivity to a single localized dimple: in Figure 6.178 the buckling loads P_{cr} normalized with respect to the buckling load of the ideal shell $P_{cr id}$ are depicted versus the normalized initial amplitude w_b/h of an inward or outward dimple applied to these four DEVILS cylinders. The loads are nonlinear buckling analysis results for dimples with initial circumferential widths a_b and meridian heights l_b as indicated. In case of cylinder Z28, Z30, and Z33 these lengths equal those widths and heights of a dent with initial depth $w_b/h = 0.1$ which provoked minimum cylinder stability, i.e. $a_{\bar{b}}$ and $l_{\bar{b}}$ respectively, see subsequent Section 6.7.2. Cylinder Z32 without imperfections buckles axisymmetrically ($n_c = 0$), and also the “pessimism” single dents are axial symmetrical, i.e. $a_{\bar{b}} = \infty$; hence, the initial height l_b used for shell Z32 is the height $l_{\bar{b}}$ of the ring-shaped dent specified with $w_b/h = 0.1$, whereas the selected width a_b is about 1/12 of the circumference, close to the width $a_{\bar{b}}$ of cylinder Z33.

The progressions of the reduction of the buckling loads $P_{cr}/P_{cr id}$ with increasing initial dimple amplitude w_b are similar to the curves which resulted for the isotropic reference cylinder with like radius and length, as displayed in Figure 6.19, page 223, for instance. As it can be seen in the right half of the diagram (i.e. for dents), for the laminated cylinders there are also limit dent depths which separate the analyses results in shallow dents with a distinct local buckling and deep dents with a slow, continuous local shell flattening prior to the cylinder collapse as it was described in Section 6.6.1 for various isotropic cylinders. In the former cases the nonlinear buckling analyses are stopped at the load where the shell in the dimple suddenly snaps inward to form a configuration with a locally flat shell strip. In the latter case two buckling loads can be specified: a first $P_{cr L}$ for the axial stiffness reduction due to local shell flattening and a second for the cylinder collapse $P_{cr U}$. With dynamic transient analyses the distinct local snapping of shallow dents could be reproduced, whereas the lower buckling load $P_{cr L}$ of deep dents could not be associated with a significant change in the run of resulting axial load-displacement curves. Figure 6.179 shows the results of a transient dynamic analysis for cylinder Z33 having a dent with various initial depths w_b/h and with an initial height of 10% of the cylinder length and an initial width of 10% of the cylinder circumference. The buckling loads are again normalized with respect to the nonlinear buckling analysis result for the perfect cylinder Z33. The corresponding nonlinear buckling analysis results are added to the chart and connected with thin lines. As for the transient dynamic analyses for the DEVILS cylinders without and with measured imperfections the compression velocity was

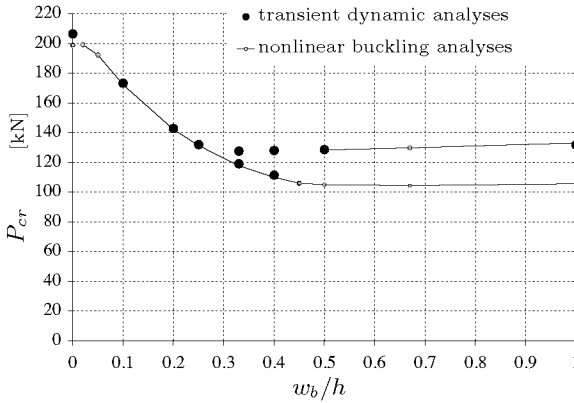


Figure 6.179: *Transient dynamic analysis results for cylinder Z33 having a dent of various initial depth w_b/h , an initial height $l_b = 51$ mm, and an initial width $a_b = 157$ mm. Corresponding buckling loads due to nonlinear buckling analyses added (thin lines) for comparison.*

0.1 mm and the damping matrix 25000 times the mass matrix. The dynamic transient analysis results for cylinder Z30, Z32, and Z33 with ideal geometry and with measured imperfections were presented in Section 4.3, page 143 et seq., and Section 5.3.2, page 179 ff, respectively. Similar to the example with the isotropic reference cylinder having a dent of different initial depth shown in Figure 6.24, page 231, within a first range single buckling loads resulted for nonlinear buckling as well as for transient dynamic analyses; then, for deeper but still shallow dents two buckling loads were obtained with transient dynamic analyses but only the lower with nonlinear buckling analyses; for deep dents finally with dynamic transient analyses only the cylinder collapse load could be identified whereas the nonlinear buckling analyses yielded two buckling loads. Hence, the different deformation processes for laminated cylinders having a dimple with particular local buckling phenomena do not differ notably from those observed for isotropic cylinders. It may therefore be assumed that the explanations given in Section 6.6.1 for the effects observed for isotropic cylinders with a dent or a bulge of various initial amplitude also apply for laminated cylinders having such dimple imperfections.

With a minimum buckling load of $P_{cr}/P_{cr id} = 0.48$ the two cylinders Z28 and Z30 having a dimple yielded the maximal buckling-load reduction among the four DEVILS cylinders, see Figure 6.178. With perfect

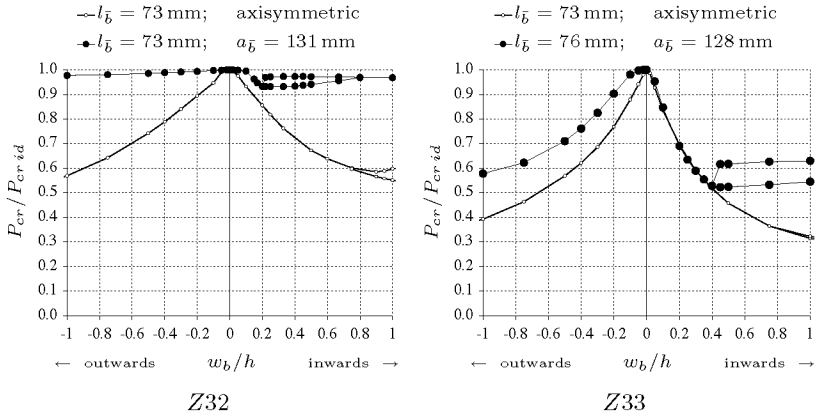


Figure 6.180: Normalized buckling loads for cylinder Z32 and Z33 having a ring-shaped dimple (bold line) or a localized dimple (bold dots) versus the normalized dimple amplitude. Results of nonlinear buckling analyses for dimples with particular initial widths $a_{\bar{b}}$ and heights $l_{\bar{b}}$ as indicated.

cylinder geometry these two laminates yielded also the highest buckling load $P_{cr id}$. Thus, the calculations with single dimples in the DEVILS cylinders confirmed the finding that cylinders with maximised buckling resistance tend to be maximal imperfection sensitive, as already demonstrated on the basis of these cylinders with measured imperfection surfaces considered for their initial geometry, see Section 5.3. Cylinder Z32 in contrast, the DEVILS shell with minimal buckling load in case of ideal geometry, is almost not affected due to single dimples of initial height $l_b = 73$ mm and initial width $a_b = 131$ mm: the resulted minimum buckling is $P_{cr}/P_{cr id} = 0.93$. These dimples however have not the shape of the dimple which reduced the buckling resistance of cylinder Z32 the most. As mentioned above, for this cylinder the maximum reduction is reached with ring-shaped dimples. Figure 6.180 (left) depicts the buckling loads resulting for Z32 with either the localized, short-waved dimples in Figure 6.178 or with single ring-shaped dimples of initial height $l_{\bar{b}} = 73$ mm again in dependency of the initial dimple amplitude w_b/h . In the right chart the buckling loads which resulted for the inversely laminated cylinder Z33 having axisymmetric dimples or dimples of limited width are similarly graphed. Having an axisymmetric inward dimple of initial height $l_{\bar{b}}$ the buckling resistance of cylinder Z32 is notably reduced down to a minimum normalized buckling load of $P_{cr}/P_{cr id} = 0.53$ close to the minimum buckling load for cylinder Z33 with a non-axisymmetric

dent. But, the minimum for *Z32* was obtained for a ring-shaped dent of initial depth $w_b/h = 1.4$ (out of displayed range), whereas that for *Z33* resulted for $w_b/h = 0.45$. For outward dimples the bold line for the buckling loads due to axisymmetric dents in *Z32* follows approximatively the thin line for the short-width dimple in *Z33*. Consequently, ignoring the initial dimple amplitude involved, in comparison to the other DEVILS shells cylinder *Z32* may only be denoted as “insensitive to single dimples” only for short-waved dents or bulges of non-axisymmetric shape.

Cylinder *Z33* having a ring-shaped dimple yielded normalized buckling loads somewhat higher than the loads due to localized dimples in case of shallow dents with initial depths between $w_b/h = 0.3$ and 0.4 . For deep ring-shaped dents and axisymmetric bulges considerably lower loads were achieved compared with the non-axisymmetric dimples in *Z33*, but also compared with the axisymmetric dimples in *Z32*.

In contrast to outward ring-shaped dimples, for inward ring-shaped dimples with varied initial dimple amplitude minimum buckling loads were found, similar to non-axisymmetric dents. Additionally, also results with an upper and a lower buckling load were obtained, see black buckling-load curves for $w_b/h > 0.75$ in Figure 6.180. For isotropic cylinders with a ring-shaped dimple also an analytical approach is available on basis of the asymptotic theory (see Section 6.6.3), which however yields normalized buckling loads independent of the sign of the dimple amplitude and which ignores the special progressions of the buckling resistance of deep ring-shaped inward dimples observed with the numerical analyses. Transient dynamic analyses of isotropic cylinders with deep axisymmetric dents resulted that the lower buckling load is probably associated with the formation of short-waved, non-axisymmetric dimples in the furrow of the initial dent which change the axial cylinder stiffness. But, since the main focus of this thesis lies in the investigation of cylinders afflicted with localized dimples no further time-consuming computations like transient dynamic analyses were conducted to ascertain the buckling behaviour and the different states of stress and deformation for cylinders with axially symmetrical dimples.

The analysis results for the only four eccentrically laminated DEVILS cylinders are not sufficient for a general statement on the sensitivity of laminated cylinders to single dimples. Therefore, similar nonlinear buckling analyses were also conducted for some selected shells of the series of laminated CFRP cylinders *Z0.α* and *Zα.0* with inward dimples of different initial depth. The length, the radius and the ply properties of these laminate shells equal those of the DEVILS cylinder, but their

wall thickness is only $h = 1.0$ mm. Near either the inner or the outer shell surface four of the eight unidirectional layers are always oriented in cylinder axis direction, whereas the orientation of the other four layers is given by the ply angle $\pm\alpha$, see Section 4.1.2, page 122. The cylinders $Z0.\alpha$ with stacking sequences $[0^\circ_4, (+\alpha, -\alpha)_2]$ have the axially stiff layers at the outer laminate side, the cylinders $Z\alpha.0$ with stacking sequences $[(-\alpha, +\alpha)_2, 0^\circ_4]$ at the inner side. In Figure 6.181 the buckling loads

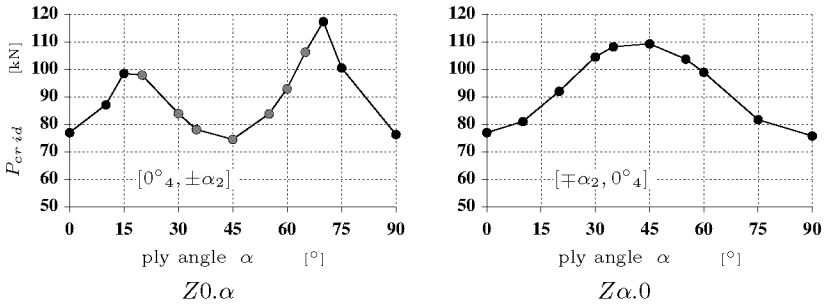


Figure 6.181: Buckling loads for the laminated cylinders $Z0.\alpha$ and $Z\alpha.0$ without imperfections for various ply angles α . Results of nonlinear buckling analyses. Gray circlets mark cylinders with ring-shaped buckling.

P_{cr_id} resulting for nonlinear buckling analyses of cylinders $Z0.\alpha$ (left) and $Z\alpha.0$ (right) having *perfect geometry* are depicted versus the ply angle α between 0° and 90° . The gray circlets refer to solutions with axisymmetric buckling. Section 4.2.2, page 131 ff, details the different buckling loads and modes of cylinder $Z0.45$ versus the cylinder $Z45.0$ as well as the similar behaviour of cylinders $Z0.90$ and $Z90.0$ and give a mechanical explanation for the observed effects.

For those cylinders with limit values or extremal buckling loads in the two cylinder series $Z0.\alpha$ and $Z\alpha.0$ in Figure 6.181 the impact of a single dent with various initial depth and particular initial lateral dimension was investigated. As it was observed for isotropic cylinders, the reduction of the buckling resistance which resulted for the laminated cylinders due to an outward dimple is less severe compared with that due to an inward dimple; consequently, the additional computations were restricted to shells with dents. The normalized buckling loads P_{cr}/P_{cr_id} resulting for nonlinear buckling analyses of cylinders with $\alpha = 0^\circ, 45^\circ, 70^\circ$, and 90° all having a single dent of initial height $l_{\bar{b}}$ and width $a_{\bar{b}}$ are included in Figure 6.182 for different initial dent depths w_b/h . The initial meridian heights $l_{\bar{b}}$ and circumferential widths $a_{\bar{b}}$ indicated in the

charts are once again the lateral dimensions of the dents of initial depth $w_b/h = 0.1$ which provoked minimum buckling loads. Cylinder Z0.70 with axially stiff layers near the outer laminate surface and a ply angle of $\alpha = 70^\circ$ yielded the highest buckling load for ideal shell geometry $P_{cr id}$ among the cylinders in Figure 6.181. Confirming the results for cylinder Z30, also with maximum buckling resistance, cylinder Z0.70 resulted in maximal sensitivity to a single dimple imperfection. With a minimum normalized buckling load of $P_{cr MIN}/P_{cr id} = 0.51$ for this laminate, see upper chart of Figure 6.182, the lowest resulting normalized buckling load of the considered shells was obtained for $w_b/h \leq 1$. For the three shells with axially stiff layer at the inner side in the lower chart, likewise the cylinder Z45.0 with $\alpha = 45^\circ$ and the highest buckling load $P_{cr id}$ of the cylinders $Z\alpha.0$ gave the lowest normalized buckling load among these cylinders: $P_{cr MIN}/P_{cr id} = 0.57$. Cylinder Z0.45, also with $\alpha = 45^\circ$ but with axially stiff layer at the outer side, having perfect geometry buckles axisymmetrically at a relatively low buckling load. Similar to the cylinder Z32, the worst single dent to this shell is also ring-shaped. The progression of the buckling loads with increasing dent depth, which resulted for Z0.45 with such axisymmetric dents, resembles that of cylinder Z32: the minimum normalized buckling load $P_{cr MIN}/P_{cr id}$ is about 0.51 and hence about as low as that of the cylinder Z0.70, but for a considerably deeper initial dent depth which is out of the displayed range. The three cylinders Z0.0, Z0.90, and Z90.0, finally, with a half of the carbon fibres in circumferential direction in the two latter cases or with fibres solely in axial direction in the former case resulted in low buckling loads for ideal shell geometry. In turn, their sensitivity to single dents is low compared with that of Z0.70 and Z45.0: the minimum normalized buckling loads is above $P_{cr MIN}/P_{cr id} = 0.7$. As these three cylinders yielded very similar buckling loads for ideal geometry, the runs of the lower normalized buckling loads resulting for $\alpha = 0^\circ$ and 90° resemble each other. However, the level of the upper buckling loads $P_{cr U}/P_{cr id}$ for cylinder Z0.90 as well as for Z90.0 are considerably higher than those for Z0.0. This might be explained with the much higher circumferential elasticity of the shell after partial flattening in case of Z0.0 and the therefore reduced resistance to the total collapse of the partially flattened cylinder; the curved shell part adjacent to the strip including the flattened dent serves as an “elastic foundation” of the strip which depends directly on the tangential stiffness of the shell.

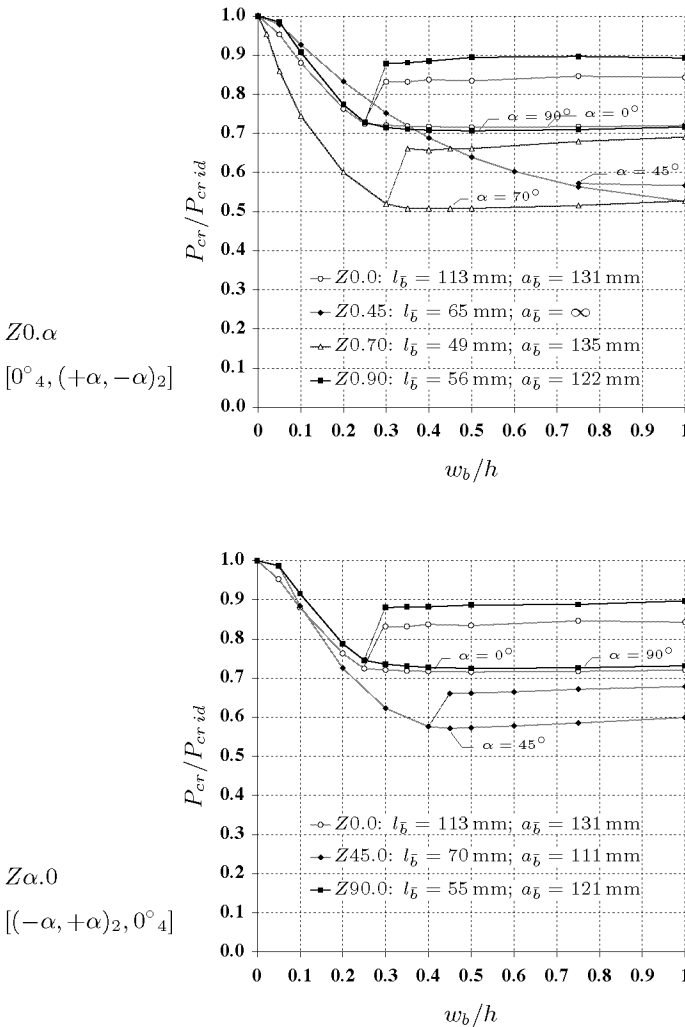


Figure 6.182: Normalized buckling loads $P_{cr}/P_{cr,ld}$ of eccentrically laminated cylinders having an initial single inward dimple of appropriate size versus the initial dimple depth w_b/h . Nonlinear buckling analysis results for cylinders $Z0.\alpha$ with axially stiff layers at the outer laminate side (top) and for cylinders $Z\alpha.0$ with axially stiff layers at the inner side (bottom). Lateral dent dimensions $a_{\bar{b}}$ and $l_{\bar{b}}$ as indicated.

6.7.2 Lateral Dimensions of Dimples Provoking Minimal Cylinder Stability

The dents above with varied initial depth w_b in eccentrically laminated cylinders have predefined initial meridian heights l_b and initial circumferential widths a_b . In the following the determination of these two lateral dimple lengths is described for a series of laminated cylinders with different ply angles and laminate stacking. Similar to the dimple dimensions for isotropic shells discussed in Section 6.6.3, page 325, by means of nonlinear buckling analyses the initial dimple widths $a_{\bar{b}}$ and initial dimple heights $l_{\bar{b}}$ were specified which reduced the axial stability of the laminated cylinders the most for a given initial amplitude w_b . Again first the initial height $l_{\bar{b}}$ for minimal stability was searched with an also fixed initial width a_b , estimated as close to $a_{\bar{b}}$ as possible. Subsequently, the initial width $a_{\bar{b}}$ was calculated accordingly using the previously found initial height $l_{\bar{b}}$.

For the isotropic shells in Section 6.6.3 the investigations focussed on the impact of the ideal cylinder dimensions L , R , and h on the “pessimism” dimple dimensions $l_{\bar{b}}$ and $a_{\bar{b}}$, whereas for the laminated cylinders mainly the influence of the material parameters on these imperfections dimensions was of interest.

Laminated Cylinders with Inward Dimples

Table 6.7 contains the initial meridian heights $l_{\bar{b}}$ and circumferential widths $a_{\bar{b}}$ of a single dent in the four laminated DEVILS cylinders which resulted for an initial dimple depth $w_b/h = 0.1$. Additionally the number of axial half-waves m_c and complete circumferential waves n_c of the buckling pattern are listed which were obtained with the classical analysis for axially compressed laminated circular cylinders of perfect geometry introduced in Section 2.2.3. Furthermore, the axial wavelength for axisymmetric buckling $2l_c$ of these shells can be taken, calculated with Equation 2.63

$$l_c = \pi \sqrt{R \sqrt{\tilde{D}_{11} a_{22} + b_{21}^2}}$$

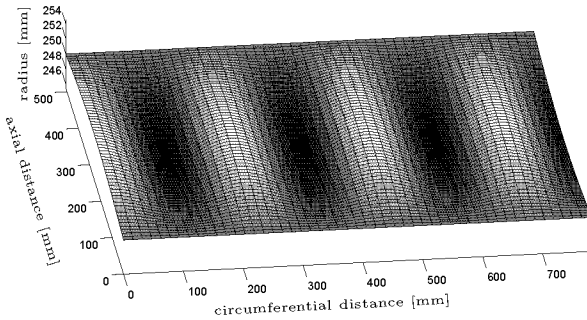
considering the cylinder radius R , the laminate eccentricity term b_{21} , the modified axial bending stiffness \tilde{D}_{11} , and the circumferential flexibility a_{22} , see Section 2.1.2, page 39, and 2.2.3, page 54. The initial dent heights $l_{\bar{b}}$ of the DEVILS cylinders resulting for nonlinear buckling

	classic analysis			initial dent height			initial dent width		
	m_c	n_c	$2l_c$ [mm]	$l_{\bar{b}}$ [mm]	$\frac{L}{m_c}$ [mm]	$\frac{l_{\bar{b}}}{2l_c}$	$a_{\bar{b}}$ [mm]	$\frac{2\pi R}{n_c}$ [mm]	$\frac{a_{\bar{b}}}{2l_c}$
Z28	1	6	56	56	510	1.00	175	262	3.12
Z30	8	13	61	61	64	0.99	164	121	2.67
Z32	13	0	76	70	39	0.92	∞	∞	∞
Z33	1	7	76	76	510	1.01	128	224	1.69

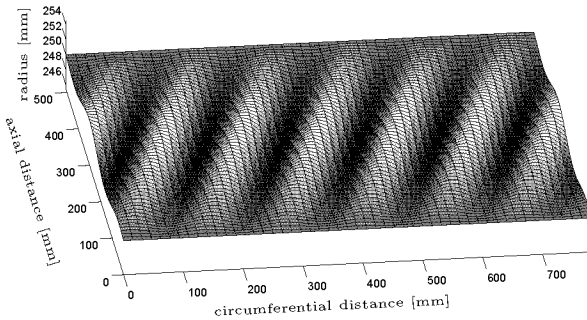
Table 6.7: *Initial meridian dent height $l_{\bar{b}}$ and initial circumferential dent width $a_{\bar{b}}$ of the four laminated DEVILS cylinders resulting from nonlinear buckling analyses for the initial dent depth $w_b/h = 0.1$. Values listed together with the number of half-waves in axial and of complete waves in circumferential direction, m_c and n_c respectively, and the axial wavelengths for axisymmetric buckling $2l_c$, which yielded the classic analysis for laminated cylinders under axial loading.*

analyses (FE) are very close to the axial wavelength for axisymmetric buckling $2l_c$. Only cylinder Z32 with an axisymmetric dent ($a_{\bar{b}} = \infty$) yielded a ratio $l_{\bar{b}}/2l_c$ of only 0.92, but this value fits with the heights $l_{\bar{b}}$ of flat axisymmetric outward dimples in isotropic shells, see Figure 6.107 on page 346. The axial half-wave lengths L/m_c of the cylinder Z28 and Z33 obviously do not correlate with the initial dent heights $l_{\bar{b}}$. With $m_c = 8$ for shell Z30, however, the axial half-wave length $L/m_c = 64$ mm is close to the dimple size $l_{\bar{b}} = 61$ mm. And for Z32 the full-wave length $2 \cdot L/m_c = 78$ mm differs only a little from the axial wave-length for axisymmetric buckling with $2l_c = 76$ mm. Thus, for the initial dimple heights $l_{\bar{b}}$ of the DEVILS cylinders on basis of the axial wavelengths for the ideal shells good approximations could be derived. But, apart from shell Z32 for the resulting initial circumferential widths $a_{\bar{b}}$ considerable differences to the wavelengths $2\pi R/n_c$ derived from the buckling modes for perfect shell geometry resulted. Also the dent width/height ratios $a_{\bar{b}}/2l_c$ vary apparently in an arbitrary way.

The important irregularities between the calculated initial dent widths $a_{\bar{b}}$ and the axial wavelengths of the analytical buckling mode of the eccentrically laminated cylinders may stem from the discrepancy between the analytical buckling patterns, given by bi-harmonic functions, and those yielded with linear buckling analyses of FE models. The FE analyses of ideal laminated cylinders often resulted in some spiral shape. Cylinder Z33, for instance, according to the classic analysis buckles in one dimple in axial direction ($m_c = 1$) and in seven dents in the circumference



(a) Classic analysis result: $m_c = 1$, $n_c = 7$



(b) Linear buckling analysis result: spiral pattern with helix angle $\theta = 23^\circ$

Figure 6.183: Buckling modes for cylinder Z33 with ideal geometry resulting for (a) a classic analysis and (b) a linear buckling analysis with a finite element model. Uncoiled circular cylinder shell; only half the circumference displayed.

($n_c = 7$). In Figure 6.183(a) this mode is depicted by means of the uncoiled half shell. In the picture (b) below the pattern resulting from a linear buckling analysis (eigenmode) is accordingly represented. This buckling shape with 12 long skew dents corresponds to that in Figure 4.11 (right) on page 134 and was reproduced mathematically with the coupled bi-harmonic function

$$\begin{aligned}
 w(x, y) &= w_{mn} \sin\left(\frac{m\pi}{L} x - \Theta_x y\right) \cos\left(\frac{n}{R} y - \Theta_y x\right) \\
 \Theta_y &= \frac{n}{R} \tan \theta \\
 \Theta_x &= \frac{m\pi}{L} \frac{\Theta_y}{2\pi R} \left(L - \frac{L}{m}\right)
 \end{aligned} \tag{6.21}$$

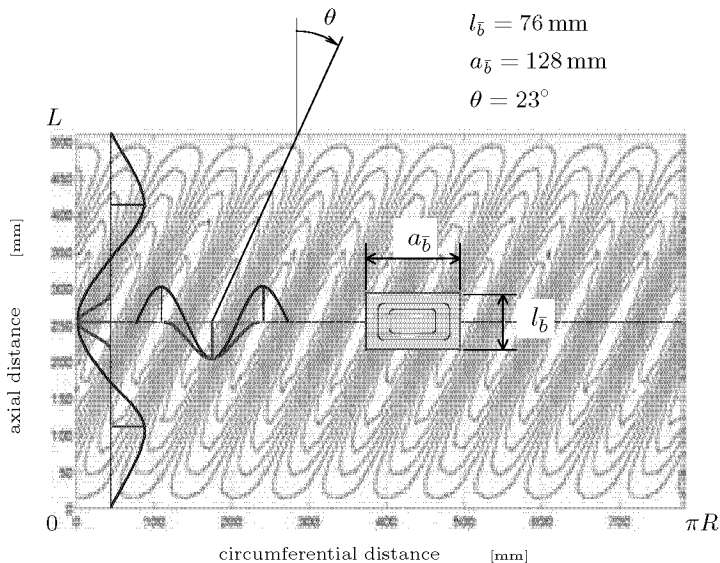


Figure 6.184: *Contour plot of the buckling mode for cylinder Z33 with perfect shell geometry and lateral lengths $l_{\bar{b}}$ and $a_{\bar{b}}$ of the inward dimple with initial depth $w_{\bar{b}}/h = 0.1$ which provoked the minimum buckling load. The frame of the dent is drawn to scale and placed around the cylinder median to fit best with the skew buckles for the ideal cylinder. Red sinuous lines indicate the axial and circumferential wavelike shape of the dent, blue ones those of the buckles for the ideal cylinder.*

using the helix angle θ to define the local phase shifts. In case of cylinder Z33 the helix angle is approximately $\theta = 23^\circ$. Thus, due to the potentially skew configurations of the buckles the meridian as well as the circumferential distances between two wave peaks may differ from the analytical wavelengths given by m_c and n_c also in case of identical number of resulting buckles. To demonstrate this effect, a single dent with the initial height and the initial width in Table 6.7 was placed in the buckling mode of the ideal cylinder Z33 with skew buckles. In Figure 6.184 the contour plot of the pattern in Figure 6.183 (b) is shown with the frame of the dent given by $l_{\bar{b}}$ and $a_{\bar{b}}$ which was drawn to scale and positioned around the cylinder meridian appropriately to the configuration of the skew inward or outward dimples of the buckling mode. The resulting axial and circumferential progressions of the wave lines over the apices of the skew buckles are plotted in blue colour at the left side of

the dent, in comparison to the red coloured complete wave of the dent. It can be seen that the circumferential width of the dent $a_{\bar{b}}$ matches with the horizontal or circumferential wavelength of the skew dimples. And, in vertical or axial direction the dent height $l_{\bar{b}}$ approximate the half length of the vertical half-wave of the skew buckles. Hence, in case of cylinder Z33 the initial circumferential width $a_{\bar{b}}$ of dent which caused minimal stability for an initial depth of $w_b/h = 0.1$ follows from the buckling mode obtained with a linear buckling analysis of the ideal shell (eigenvector).

label	α	b_{21} [mm]	$\frac{\tilde{D}_{11}}{\tilde{D}_{22}}$	classic analysis			initial dent height			initial dent width		
				m_c	n_c	$2l_c$ [mm]	$l_{\bar{b}}$ [mm]	$\frac{L}{m_c}$ [mm]	$\frac{l_{\bar{b}}}{2l_c}$	$a_{\bar{b}}$ [mm]	$\frac{2\pi R}{n_c}$ [mm]	$\frac{a_{\bar{b}}}{2l_c}$
Z0.0	0°	0.0000	14.2	5	14	104	113	102	1.09	131	112	1.26
Z0.10	10°	0.0467	13.4	5	14	103	104	102	1.01	133	112	1.30
Z0.15	15°	0.1007	12.4	7	13	101	98	73	0.97	143	121	1.41
Z0.20	20°	0.1656	10.9	10	0	98	85	51	0.86	∞	∞	∞
Z0.30	30°	0.2729	7.1	11	0	90	81	46	0.90	∞	∞	∞
Z0.35	35°	0.2898	5.4	12	0	84	74	43	0.88	∞	∞	∞
Z0.45	45°	0.2465	3.1	14	0	71	65	36	0.93	∞	∞	∞
Z0.55	55°	0.1607	1.9	17	0	59	53	30	0.91	∞	∞	∞
Z0.60	60°	0.1201	1.6	19	0	54	51	27	0.95	∞	∞	∞
Z0.65	65°	0.0854	1.4	20	0	50	51	26	1.02	153	∞	3.05
Z0.70	70°	0.0573	1.2	22	0	47	49	23	1.04	135	∞	2.87
Z0.75	75°	0.0359	1.1	12	15	45	52	43	1.14	124	105	2.73
Z0.90	90°	0.0092	1.0	10	15	43	56	51	1.29	122	105	2.81
Z0.0	0°	0.0000	14.2	5	14	104	113	102	1.09	131	112	1.26
Z10.0	10°	-0.0467	13.4	5	14	103	111	102	1.08	129	112	1.25
Z20.0	20°	-0.1656	10.9	5	15	98	100	102	1.02	125	105	1.27
Z30.0	30°	-0.2729	7.1	5	15	90	91	102	1.01	117	105	1.30
Z35.0	35°	-0.2898	5.4	5	15	84	84	102	1.00	115	105	1.37
Z45.0	45°	-0.2465	3.1	6	16	71	70	85	0.99	111	98	1.58
Z55.0	55°	-0.1607	1.9	7	16	59	67	73	1.15	106	98	1.81
Z60.0	60°	-0.1201	1.6	8	16	54	65	64	1.20	106	98	1.97
Z75.0	75°	-0.0359	1.1	9	15	45	57	57	1.25	113	105	2.49
Z90.0	90°	-0.0092	1.0	9	14	43	55	57	1.28	121	112	2.79

Table 6.8: Ply angle α , eccentricity term b_{21} , and modified bending stiffness ratio $\tilde{D}_{11}/\tilde{D}_{22}$ for the eccentrically laminated cylinders Z0. α and Z α .0 and their resulting initial meridian height $l_{\bar{b}}$ and the initial circumferential width $a_{\bar{b}}$ of a single dent causing minimal stability for the initial depth $w_b/h = 0.1$. For comparison the buckling mode with m_c half-waves in axial and n_c complete waves in circumferential direction as well as the axial wavelength $2l_c$ for axisymmetric buckling resulting from classic analysis.

For a systematic investigation into the importance of the ply angle and the layer stacking of eccentrically laminated cylinders to the lateral dent dimensions the minimum searches with nonlinear buckling analyses were

also applied to the two series of CFRP cylinders $Z0.\alpha$ and $Z\alpha.0$ with clearly eccentric stackings, see Section 4.1.2 and 4.2.2. In Table 6.8 the initial circumferential widths $a_{\bar{b}}$ and the initial meridian heights $l_{\bar{b}}$ resulting for these cylinder shells are listed. These dent widths and heights are again the dimensions which gave minimum buckling loads for an initial dent depth of $w_{\bar{b}}/h = 0.1$. In the upper block are the results of the cylinders $Z0.\alpha$ with laminates $[0^{\circ}_4, (+\alpha, -\alpha)_2]$ and axially stiff layers near the outer shell surface, in the lower those of the cylinders $Z\alpha.0$ with laminates $[(-\alpha, +\alpha)_2, 0^{\circ}_4]$ and axially stiff layers near the inner surface, always depending on the given ply angle α . The table also includes the buckling mode of classic analyses according to Section 2.2.3 with m_c half-waves in axial and n_c waves in circumferential direction as well as the axial wavelength $2l_c$ for axisymmetric buckling. The values of the eccentricity term b_{21} and the modified bending stiffness ratio $\bar{D}_{11}/\bar{D}_{22}$ in the third and fourth table column are later used for comparisons with other laminated as well as with isotropic shells.

The initial heights $l_{\bar{b}}$ yielded for the cylinders $Z0.\alpha$ are close to the analytical axial wavelengths $2l_c$ only for some ply angles α near 10° and 70° . For the solutions with ring-shaped dents ($a_{\bar{b}} = \infty$) and small ply angles the dimple heights $l_{\bar{b}}$ are notably below the respective $2l_c$ values, and the cylinders with angles near 90° yielded dent heights more than 25% longer than the associated analytical wavelengths $2l_c$. In the latter case the half-wave length L/m_c of the classic buckling mode is closer to the dent height $l_{\bar{b}}$ found with numerical analyses. In Figure 6.185 the initial dent heights $l_{\bar{b}}$ listed in Table 6.8 are compared with the analytical axial wavelengths $2l_c$ and the axial half-wave lengths L/m_c of the classic analysis which resulted for the cylinders $Z0.\alpha$ (left) and $Z\alpha.0$ (right) of different ply angle α . The initial heights $l_{\bar{b}}$ for the shells $Z\alpha.0$ with ply angles from $\alpha = 20^{\circ}$ to 45° are in accordance with the wavelength $2l_c$, whereas for angles between $\alpha = 55^{\circ}$ and 90° the lengths $l_{\bar{b}}$ match better with the half-wave length L/m_c . For the cylinder $Z0.0$ the deviation of the initial dent height $l_{\bar{b}}$ from the axial wavelength $2l_c$ is about 10%, for the cylinders $Z0.90$ and $Z90.0$ about 29%. The differences between the axial wavelength $2l_c$ and the dent height $l_{\bar{b}}$ in dependence of the ply angle is readily identifiable in Figure 6.186 by means of the wavelength ratios $l_{\bar{b}}/2l_c$ resulting for the shells $Z0.\alpha$ and $Z\alpha.0$. Small values between 0.95 and 0.86 were obtained for cylinders $Z0.\alpha$ having a ring-shaped dent (gray markers). Large ratios $l_{\bar{b}}/2l_c$ above 1.1, in turn, up to 1.29 resulted for laminates with ply angles between $\alpha = 45^{\circ}$ and 90° .

The initial circumferential dent widths $a_{\bar{b}}$ of the two series of laminated

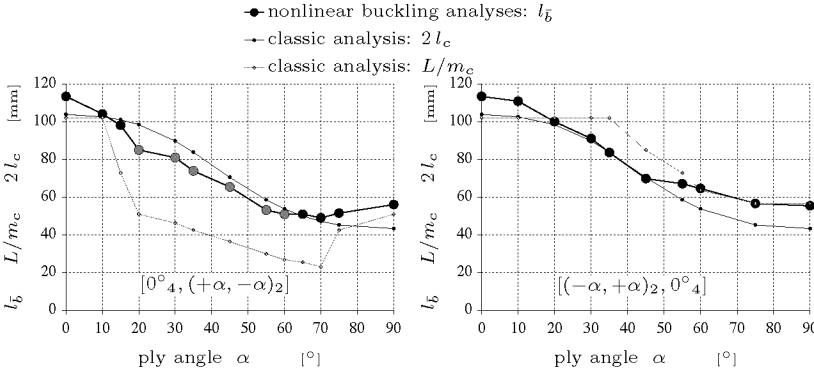


Figure 6.185: Resulting initial meridian heights $l_{\bar{b}}$ for cylinders $Z0.\alpha$ (left) and $Z\alpha.0$ (right) subject to the ply angle α in comparison to the half-wave lengths L/m_c and wavelengths $2l_c$ for axisymmetric buckling due to the classic analysis. Gray circlets denote solutions with a ring-shaped dent.

cylinders in Table 6.8 vary between 106 and 153 mm, thus the variation range of the widths $a_{\bar{b}}$ is much smaller compared with that of the initial meridian dent heights $l_{\bar{b}}$ which vary between 49 and 113 mm. But, all listed widths $l_{\bar{b}}$ are notably wider than the circumferential wavelengths $2\pi R/n_c$ that resulted from the buckling modes of the classic analyses. Maximum deviations were obtained for small ply angles α with initial widths $l_{\bar{b}}$ about 20 % longer than the classical wavelengths $2\pi R/n_c$. But above all the results for cylinder $Z0.65$ and $Z0.70$ strike: the classic analyses yielded axisymmetric buckling modes associated to the lowest stability for ideal geometry ($n_c = 0$), but the calculated initial shape of the “pessimum dent” is non-axisymmetric, i.e. $a_{\bar{b}} \neq \infty$. In Figure 6.187 the initial circumferential dent widths $a_{\bar{b}}$ listed in Table 6.8 are compared with the circumferential wavelengths $2\pi R/n_c$ of the classic analysis which resulted for the cylinders $Z0.\alpha$ (left) and $Z\alpha.0$ (right) of different ply angle α . The widths $a_{\bar{b}}$ that approximate the classical wavelengths $2\pi R/n_c$ the best are for shells $Z\alpha.0$ with ply angles α between 60° and 90° whose resulting deviations are about circa 8 %. But, the differences between the lengths $a_{\bar{b}}$ and $2\pi R/n_c$ of the cylinders $Z\alpha.0$ and $Z0.\alpha$ in Table 6.8 are smaller than those between the DEVILS cylinders, which measures more than 40 % in case of shell Z33. One reason for these discrepancies may lie in the difference between the buckling patterns for the ideal cylinders resulting from the classic analyses, specified by m_c and n_c , and those from the FE analyses. As demonstrated by means

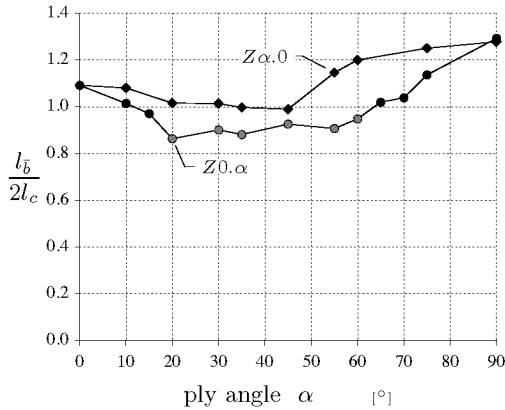


Figure 6.186: Ratios of the initial dent heights $l_{\bar{b}}$ to the classical axial wavelength $2l_c$ which resulted for the laminated cylinders $Z_{\alpha.0}$ and $Z_{0.\alpha}$ plotted against the ply angle α . Gray markers for results of shells $Z_{0.\alpha}$ with a ring-shaped dent.

of the buckling modes for cylinder Z_{33} in Figure 6.183 and 6.184 with the bi-harmonic functions of the classic analysis the often spiral-shaped linear buckling modes cannot be described. Only cylinder $Z_{0.0}$, $Z_{0.90}$, and $Z_{90.0}$ yielded linear buckling modes with multiple staggered rows of dimples as predicted by the classic analysis (see Fig. 4.14, p. 136), all other shells in Table 6.8 gave either axisymmetric patterns or modes with spiral shapes and long skew buckles (see Figure 4.13, p. 136). It is also of crucial importance that the linear buckling modes result from the stress distributions in the perfect shell prior to collapse. The stress distribution in and around an applied single dent in an otherwise perfect cylinder shell result in different stress distributions with stress concentrations located differently to those associated with the pre-buckling states of perfect cylinders, see Section 6.6.5. The calculated dent widths $a_{\bar{b}}$ finally stem from the stress distributions for a particular single dimple imperfection, and not from those for a perfect shell. This may explain the considerable discrepancy between the dent width $a_{\bar{b}}$ and the analytical wavelength $2\pi R/n_c$ also for the cylinders which yielded linear buckling modes without skew or spiral-shaped buckles. Consequently, in general the wavelengths $2\pi R/n_c$ of the classic analysis will be inappropriate for a prediction of the initial dent width $a_{\bar{b}}$. More encouraging results in this context were obtained with the ratios of the initial circumferential dent width $a_{\bar{b}}$ to the classical axial wavelength $2l_c$ in dependence of the

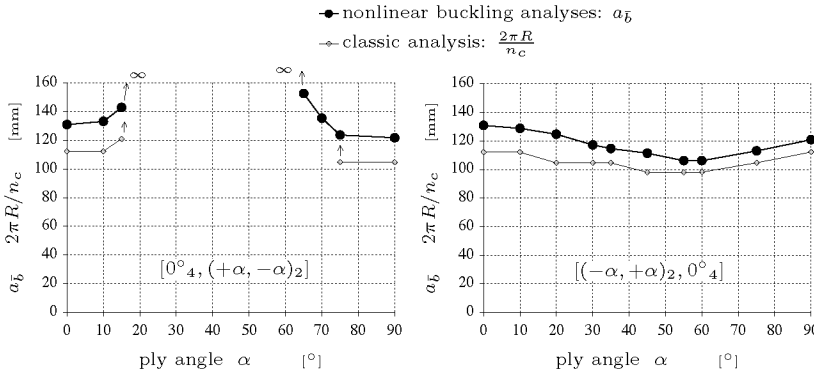


Figure 6.187: Resulting initial circumferential widths $a_{\bar{b}}$ for cylinders $Z0.\alpha$ (left) and $Z\alpha.0$ (right) subject to the ply angle α in comparison to the wave-lengths $2\pi R/n_c$ due to the classic analysis.

laminate parameters. This dent-width/axial-wavelength ratio $a_{\bar{b}}/2l_c$ was already used for the quantification of the different dimple dimensions for isotropic cylinders, see Section 6.6.3; hence, it was obvious to test its application also for the laminated shells. In Figure 6.188 the ratios $a_{\bar{b}}/2l_c$ which resulted for the laminated cylinders $Z0.\alpha$ and $Z\alpha.0$ are shown, again subject to the ply angle α . As can be taken from Figure 6.186 the meridian heights of non-axisymmetric dents calculated for these shells vary between about $l_{\bar{b}} = 2l_c$ and $l_{\bar{b}} = 1.3 \cdot 2l_c$. Therefore, for small angles α with dent-width/axial-wavelength ratios of only circa $a_{\bar{b}}/2l_c = 1.2$ the resulting “pessimum” dent for these laminates and an initial dent depth of $w_b/h = 0.1$ is of almost square shape. For the isotropic cylinders, in contrast, width/height ratios $a_{\bar{b}}/l_{\bar{b}}$ resulted between 2.4 and 2.8 for wider dimples. Wider non-axisymmetric dents were obtained also for the laminated cylinders of large ply angles α up to 90° with resulting initial dent width/height ratios $a_{\bar{b}}/l_{\bar{b}}$ of about 3.0.

The DEVILS cylinders as well as the two series of cylinders $Z0.\alpha$ and $Z\alpha.0$ are eccentrically laminated, i.e. they have CFRP laminates with layer stackings asymmetric in respect of the middle shell surface. The cylinders $Z0.\alpha$ and $Z\alpha.0$ are more “academic” since shells with such laminates will distort already during the fabrication. Therefore, two symmetric laminates both composed of eight layers with ply angles either $\alpha = 0^\circ$ or 60° were added to the calculations. Cylinder $Z60.0s$ with the symmetric laminate $[\pm 60^\circ, 0^\circ_4, \mp 60^\circ]$ has the axially stiff layers in the

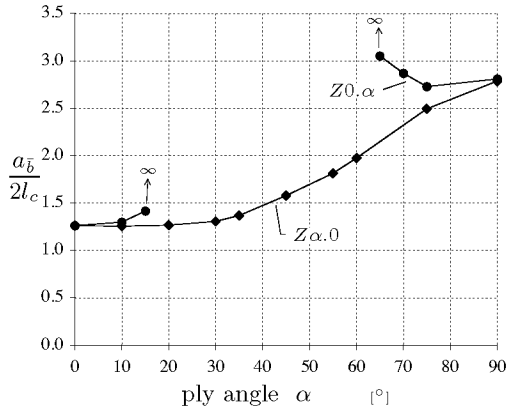


Figure 6.188: Ratios of the initial dent widths $a_{\bar{b}}$ to the classical axial wavelength $2l_c$ which resulted for the laminated cylinders $Z\alpha.0$ and $Z0.\alpha$, plotted against the ply angle α .

core of the shell, whereas the cylinder $Z0.60s$ with its symmetric laminate $[0^\circ_2, \pm 60^\circ, \mp 60^\circ, 0^\circ_2]$ has the axially stiff layers close to the two shell surfaces. In Table 6.9 the initial meridian heights $l_{\bar{b}}$ and circumfer-

	b_{12}		classic analysis			initial dent height			initial dent width		
	$\frac{\tilde{D}_{11}}{D_{22}}$	$\frac{\tilde{D}_{22}}{D_{11}}$	m_c	n_c	$2l_c$	$l_{\bar{b}}$	$\frac{L}{m_c}$	$\frac{l_{\bar{b}}}{2l_c}$	$a_{\bar{b}}$	$\frac{2\pi R}{n_c}$	$\frac{a_{\bar{b}}}{2l_c}$
	[mm]				[mm]	[mm]	[mm]		[mm]	[mm]	
Z60.0s	0.00	0.5	20	0	50	49	26	0.97	∞	∞	∞
Z0.60s	0.00	6.5	2	10	69	77	255	1.12	98	157	1.43
Z0.60	0.12	1.6	19	0	54	51	27	0.95	∞	∞	∞
Z60.0	-0.12	1.6	8	16	54	65	64	1.20	106	98	1.97

Table 6.9: Resulting initial meridian height $l_{\bar{b}}$ and circumferential width $a_{\bar{b}}$ of a dent provoking minimal stability of the symmetrically laminated cylinders $Z60.0s$ with laminate $[\pm 60^\circ_2, 0^\circ_2]_S$ and $Z0.60s$ with laminate $[0^\circ_2, \pm 60^\circ_2]_S$ for an initial dent depth $w_b/h = 0.1$. Values to the eccentrically laminated cylinders $Z0.60$ and $Z60.0$ added below for comparisons.

ential widths $a_{\bar{b}}$ of a dent in these two cylinders, again provoking minimal stability for $w_b/h = 0.1$, are listed together with the terms of eccentricity b_{21} , the bending stiffness ratios $\tilde{D}_{11}/\tilde{D}_{22}$, and the buckling modes and axial wavelengths $2l_c$ of the classic analysis. The buckling modes and loads of these two cylinders are described in Section 4.2.2, page 131. The

respective values for the cylinders Z0.60 and Z60.0 also with ply angles $\alpha = 0^\circ$ and 60° but eccentrically laminated, see Table 6.8, were attached for direct comparisons and are in the last two table rows. Since with symmetric layer stackings for cylinder Z60.0s as well as for Z0.60s the term of eccentricity b_{21} is zero. But, in contrast to the two eccentric shells, their axial/circumferential bending stiffness ratio $\tilde{D}_{11}/\tilde{D}_{22}$ differ from each other. In case of Z60.0 the axial bending stiffness is smaller than the circumferential one, and without imperfections the cylinder buckles axisymmetrically ($n_c = 0$). The initial meridian dent height yielded for this shell is very close to the wavelength $2l_c$ for classic axisymmetric buckling and also to the full-wave length $2 \cdot L/m_c$ of the classic analysis. The initial dent width $a_{\bar{b}}$ is infinite, as expected due to the linear buckling mode and the classic analysis for the ideal cylinder. Cylinder Z060s has a bending stiffness ratio of $\tilde{D}_{11}/\tilde{D}_{22} = 6.5$, thus for the shell with axially stiff layers lying outside in axial direction the bending stiffness is higher than that in circumferential direction. In this case, the buckling mode for perfect geometry is non-axisymmetric, and also the initial dent width is not infinity resulting in $a_{\bar{b}} = 98$ mm. This length, however, is again far from the wavelength $2\pi R/n_c$ given by the classic analysis. Additionally a considerable deviation between the resulting initial dent height $l_{\bar{b}}$ and the analytical axial wavelength $2l_c$ (+12%) was obtained for this laminate.

For the isotropic cylinders simple formulas in terms of the initial dent depth w_b and BATDORF's parameter Z , considering the ideal cylinder geometry, could be derived to predict the initial widths $a_{\bar{b}}$ and heights $l_{\bar{b}}$ of dents and bulges quite accurately, see Section 6.6.3. Finally the question came up whether, despite the large variations in the resulting dent sizes, for arbitrarily laminated cylinder also rules may be derived considering the material parameters, additionally to those for the perfect cylinder geometry. For this purpose many parameters and ratios were tested, but with little success. However, with the term of eccentricity b_{21} and the modified bending stiffness ratio $\tilde{D}_{11}/\tilde{D}_{22}$ at least rough approximations of the dent dimensions should be possible for laminated cylinders such as presented herein. As already mentioned, the cylinder geometry, i.e. the cylinder length L , the radius R , and the wall thickness h , was fixed for the investigation of dents in laminated cylinders, their influence on the worst dimple size was presumed independent of the shell material and to be taken into account separately.

Figure 6.189 and 6.190 depict the ratios of the initial meridian dent height $l_{\bar{b}}$ to the classical axial wavelength $2l_c$ for the laminated DEVILS

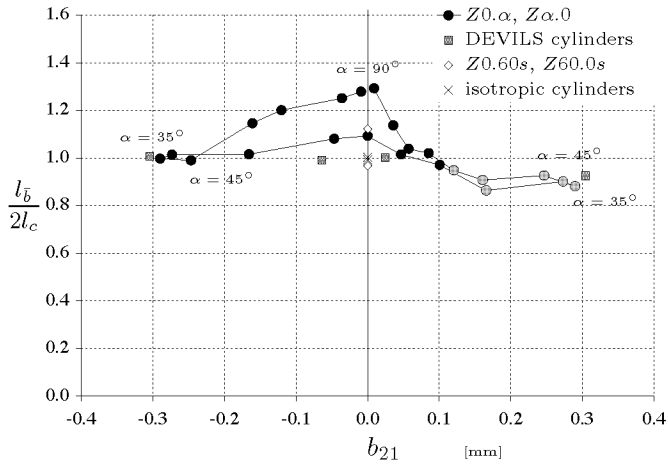


Figure 6.189: Ratios of the initial meridian dent height $l_{\bar{b}}$ to the classical axial wavelength $2l_c$ for a series of laminated or isotropic cylinders as indicated with equal length and radius. Dent-height ratio versus term of eccentricity b_{21} . Gray circlets denote ratios for shells $Z0.\alpha$ with a ring-shaped dent.

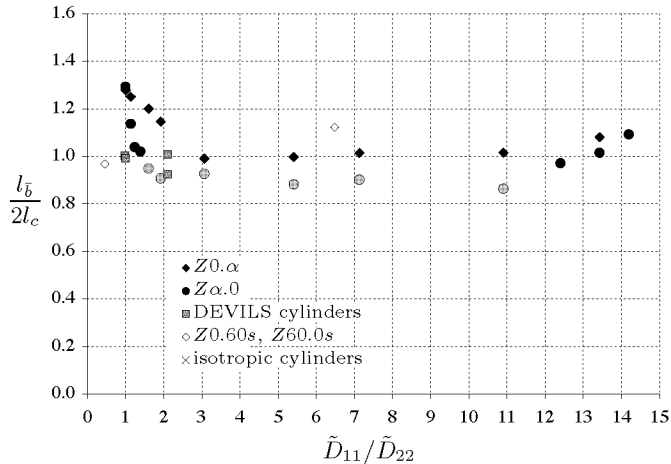


Figure 6.190: Ratios of the initial dent height $l_{\bar{b}}$ to the classical axial wavelength $2l_c$ for a series of laminated or isotropic cylinders as indicated. Dent-height ratio versus the modified axial/circumferential bending stiffness ratio $\tilde{D}_{11}/\tilde{D}_{22}$. Gray circlets denote values for shells $Z0.\alpha$ with a ring-shaped dent.

cylinders, the also eccentrically laminated cylinders $Z0.\alpha$ and $Z\alpha.0$, the symmetric cylinders $Z0.60s$ and $Z60.0$, as well as for two isotropic cylinders, all with $L = 510\text{ mm}$ and $R = 250\text{ mm}$. In Figure 6.189 the axial dent-height/ wavelength ratios $l_{\bar{b}}/2l_c$ are plotted against the eccentricity term b_{21} and in Figure 6.190 against the modified axial/circumferential bending stiffness ratio $\tilde{D}_{11}/\tilde{D}_{22}$. With the term b_{21} useful statements can be made only for eccentric laminate stackings. For cylinders with b_{21} larger than 0.1 mm the pessimum dents are ring-shaped and the initial height $l_{\bar{b}}$ is small compared to that for the other dent patterns. The dent height ratios for the DEVILS cylinders $Z28$ and $Z30$ (gray quadrats) with small b_{21} follow more the results for the cylinders $Z0.\alpha$ and $Z90.0$ with ply angles α below 45° . For symmetrically laminated and isotropic cylinders ($b_{21} = 0$) however no one-to-one assignment can be conducted since three different ratio ranges at about $l_{\bar{b}}/2l_c = 1.0$, 1.1 , and 1.3 resulted. In contrast to the eccentricity term b_{21} with the bending stiffness ratio $\tilde{D}_{11}/\tilde{D}_{22}$ also for the two symmetric cylinders $Z0.60s$ and $Z60.0s$ (diamonds) a determination of the resulting initial dent height $l_{\bar{b}}$ can be made. Unfortunately, their result, as plotted in the diagram of Figure 6.190, are not close to the ratios for the other cylinders. Again, for ring-shaped dents a group with length ratios below 1.0 resulted, and for stiffness ratios between $\tilde{D}_{11}/\tilde{D}_{22} = 1$ and 2 a cluster of results, including the isotropic and the DEVILS shells, was obtained. The dent-height/wavelength ratios for all considered cylinders vary between $l_{\bar{b}}/2l_c = 0.86$ and 1.29 with a mean value of $\overline{l_{\bar{b}}/2l_c} = 1.04$. The variations of the dent heights $l_{\bar{b}}$ from the mean are $\pm 20\%$. Hence, since no other useful trend line subject to one of the material parameter (ratios) could be found the mean value above had to be sufficient for a rough prediction of the dent-height/wavelength ratio $l_{\bar{b}}^*/2l_c$, of the initial dent height $l_{\bar{b}}$ respectively for a given cylinder shell material:

$$\frac{l_{\bar{b}}^*}{2l_c} = 1.04 .$$

Similarly to the initial dent heights, in Figure 6.191 and the 6.192 the ratios of the initial circumferential dent width $a_{\bar{b}}$ to the classical axial wavelength $2l_c$ that resulted for the investigated laminated and isotropic cylinders with $L = 510\text{ mm}$ and $R = 250\text{ mm}$ are plotted versus either the eccentricity term b_{21} or the modified axial/circumferential bending stiffness ratio $\tilde{D}_{11}/\tilde{D}_{22}$. The cylinders with ring-shaped dents have infinite dent widths and were therefore not included in the graphs. In Figure 6.191 the dent-width/axial-wavelength ratios $a_{\bar{b}}/2l_c$ yielded for the DEVILS cylinders $Z28$, $Z30$, and $Z33$ are about 0.3 higher than the

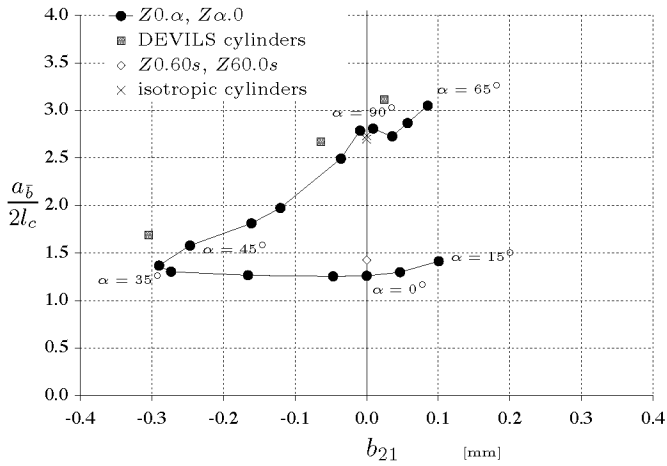


Figure 6.191: Ratios of the initial circumferential dent width $a_{\bar{b}}$ to the classical axial wavelength $2l_c$ for a series of laminated or isotropic cylinders with equal length and radius. Dent-height ratio versus eccentricity term b_{21} .

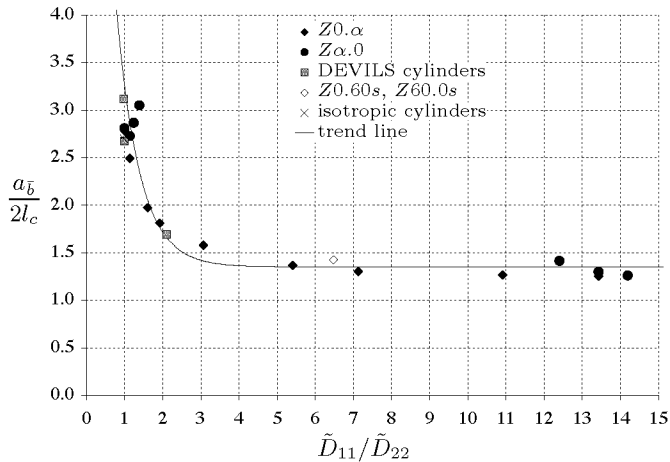


Figure 6.192: Ratios of the initial dent width $a_{\bar{b}}$ to the classical axial wavelength $2l_c$ for a series of laminated or isotropic cylinders as indicated. Dent-height ratio versus modified axial/circumferential bending stiffness ratio $\tilde{D}_{11}/\tilde{D}_{22}$.

values for the cylinders $Z\alpha.0$ and $Z0.\alpha$ with ply angles larger than 45° ; in contrast to the ratios $l_{\bar{b}}/2l_c$ above which match better for angles smaller than 45° . But, as for the dent height for the symmetrical cylinder $Z0.60s$ with zero eccentricity term b_{21} the ratio $a_{\bar{b}}/2l_c$ resulted closer to the ratio for cylinder $Z0.0$ with alike $b_{21} = 0$ than to the cylinders with $\alpha = 90^\circ$. More significant marker positions to the width/wavelength ratios $a_{\bar{b}}/2l_c$ in a graph resulted for the analysed cylinders were achieved with the bending stiffness ratio $\tilde{D}_{11}/\tilde{D}_{22}$ as axis of abscissae, see Figure 6.192. Ratios $\tilde{D}_{11}/\tilde{D}_{22}$ near 1.0, i.e. for the isotropic cylinders and cylinders $Z\alpha.0$ and $Z0.\alpha$ of ply angles α at 90 degrees, yielded long initial widths with ratios $a_{\bar{b}}/2l_c$ above 2.5. For large bending stiffness ratios $\tilde{D}_{11}/\tilde{D}_{22}$ (i.e. $\alpha \rightarrow 0$), in turn, shorter dent widths for more square dents resulted in width/wavelength ratios $a_{\bar{b}}/2l_c$ less than 1.5. With the exponential function

$$\frac{a_{\bar{b}}^*}{2l_c} = 1.35 + 10 e^{-1.65 \frac{\tilde{D}_{11}}{\tilde{D}_{22}}}$$

that was introduced as trend line in Figure 6.192, approximations of the FE calculations are enabled. But the maximum deviations which result between the dent widths $a_{\bar{b}}$ and $a_{\bar{b}}^*$ are still at about $\pm 25\%$.

The cylinders above have all a length of $L = 510$ mm. For the laminates $Z0.10$ and $Z0.70$ the initial dent width $a_{\bar{b}}$ and the initial height $l_{\bar{b}}$ for a initial depth $w_b = 0.1$ was additionally calculated for a 50% longer cylinder length, i.e. for $L = 765$ mm. The so achieved lateral dent lengths differ less than 3%. According to these results, for first estimates of the dent size and shape considering the ideal cylinder geometry (parameter Z) the rules in Section 6.6.3 may be used, since the errors due to the inclusion of material parameters will be more important.

With cylinder $Z0.70$ the influence of the initial dimple amplitude w_b on the initial lateral dimple lengths $l_{\bar{b}}$ and $a_{\bar{b}}$ was investigated briefly also for laminated shells. The calculations for $Z0.70$ and an initial dent depth $w_b/h = 0.1$ yielded a height and a width as listed in Table 6.9, thus a dent-height/axial-wavelength ratio of $l_{\bar{b}}/2l_c = 1.04$ and a dent-width/axial-wavelength ratio of $a_{\bar{b}}/2l_c = 2.87$. Accordingly, for an initial dent depth $w_b/h = 0.3$ resulted a dent-height/axial-wavelength ratio of $l_{\bar{b}}/2l_c = 1.32$ and a dent-width/axial-wavelength ratio of $a_{\bar{b}}/2l_c = 3.03$. The new height is 27%, the new width 5% above the value for $w_b/h = 0.1$. The amplitude $w_b/h = 0.3$ corresponds to the marginal value w_b^* for shallow dents, see Figure 6.182 on page 455. The impact of the dent depth is more important for this laminated cylinder than for the analysed isotropic cylinders: with the Equation 6.11 introduced in

Section 6.6.3 for $w_b/h = 0.3$ a predicted ratio of $l_b^*/2l_c = 1.14$ results. This discrepancy would have justified further calculations with more cylinders, but due to the vast variations within the dent dimensions specified with $w_b/h = 0.1$ no further attempts were made for closer approximations considering the laminated-cylinder material parameters.

Laminated Cylinders with Outward Dimples

As for isotropic cylinders in cases of outward dimples the axisymmetric shapes always cause the lowest buckling load independent of the initial bulge elevation w_b , therefore the calculations on laminated cylinders were limited to inward dimples. That is, there are no analysis results for the heights and widths of bulges in laminated cylinders to be discussed.

6.7.3 Minimum Buckling Loads for Laminated Cylinders with Single Dimples

Comprising the nonlinear buckling analysis results for laminated cylinders with a single dent of different initial depth discussed in the previous sections, mainly the minimum buckling loads $P_{cr \text{ MIN}}$ interested. Since these shells differ in their material parameters but not in the nominal cylinder dimensions (R, L, h) it was attempted to derive reliable predictions of the worst possible buckling resistance of arbitrary laminated cylinders solely by means of their shell material. Section 6.6.4 deals with the minimum buckling loads $P_{cr \text{ MIN}}$ resulting for isotropic cylinders which depend solely on the shell geometry. In this section finally the minimum buckling loads which resulted for a series of laminated cylinders were compiled and their dependencies on laminate stiffness components observed are discussed.

In the lower charts of Figure 6.193 the minimum normalized buckling loads $P_{cr \text{ MIN}}/P_{cr \text{ id}}$ found for a few laminated cylinders are plotted against the ratio of the axial to the circumferential modified¹⁴ bending stiffness $\tilde{D}_{11}/\tilde{D}_{22}$ (left) and against the term of eccentricity b_{21} (right). In the two charts above, the buckling loads $P_{cr \text{ id}}$ of the two series of eccentrically laminated cylinders $Z0.\alpha$ and $Z\alpha.0$ of ideal geometry are displayed with the same abscissae, see Figure 4.16 page 139. Diamonds denote the minimum loads $P_{cr \text{ MIN}}/P_{cr \text{ id}}$ which resulted for cylinders

¹⁴In fact, the differences between D_{11}/D_{22} and $\tilde{D}_{11}/\tilde{D}_{22}$ are negligible.

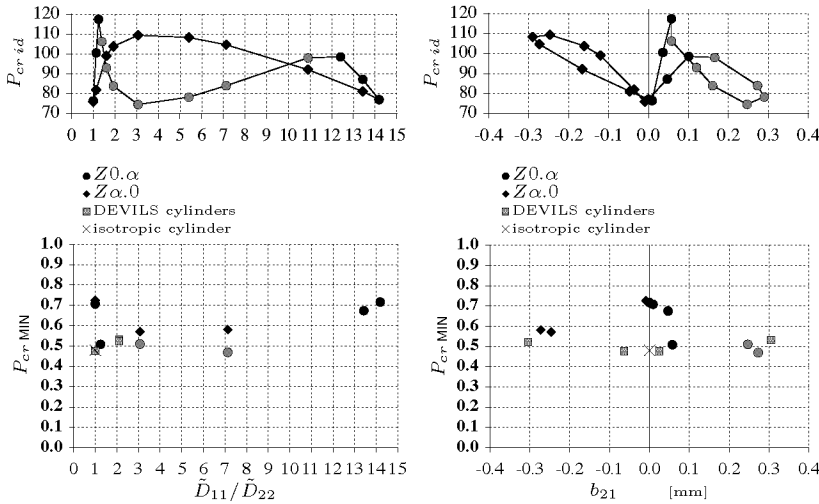


Figure 6.193: Minimal normalized buckling loads $P_{cr MIN}/P_{cr id}$ versus the modified bending stiffness ratio $\tilde{D}_{11}/\tilde{D}_{22}$ (left) and versus the eccentricity term b_{21} (right) for the laminated cylinders $Z0.\alpha$ and $Z\alpha.0$ having a single dent of initial height $l_{\bar{b}}$ and width $a_{\bar{b}}$. Includes also solutions for an isotropic cylinder of identical dimensions and the four DEVILS cylinder. Above accordingly the buckling loads of the cylinders without imperfections $P_{cr id}$. Gray circlets mark solutions with axisymmetric buckling.

$Z\alpha.0$, circlets those for cylinders $Z0.\alpha$. Gray circlets identify solutions with axisymmetric buckling. The charts also include the minima obtained for the four DEVILS cylinders and the load which resulted for the isotropic cylinder with dimensions equal to that of $Z0.\alpha$ and $Z\alpha.0$. The loads vary between $P_{cr MIN}/P_{cr id} = 0.48$ and 0.72 . High values resulted for cylinders $Z0.\alpha$ and $Z\alpha.0$ with low buckling resistances in case of perfect geometry and non-axisymmetrical buckling; that is, for laminates with small $|b_{21}|$ as well as for maximal and minimal bending stiffness ratios ($\alpha = 0^\circ$ and 90°). Low values in turn were obtained for the isotropic and the DEVILS cylinders as well as for $Z0.70$ with the maximal buckling load of $P_{cr id} = 117$ kN in the upper charts for $b_{21} = 0.06$ mm and $\tilde{D}_{11}/\tilde{D}_{22} = 1.3$.

This consideration includes the special cases of a ring-shaped dent applied to cylinders with axisymmetric buckling in absence of imperfections ($Z32$ or gray circlets) which yielded small buckling resistances $P_{cr id}$ without, but also low normalized buckling loads $P_{cr MIN}/P_{cr id}$ with an

imperfection. Thus, solutions with ring-shaped buckles ignored, the obvious fact that the laminates and the associated material parameters for maximal classical buckling loads also lead to maximal sensitivity to localized dimple imperfections was confirmed. However, one-to-one relationships between material parameters and the minimum buckling loads could not be found for reliable, quantitative predictions of the factors $P_{cr \text{ MIN}}/P_{cr \text{ id}}$ for arbitrarily laminated cylinders. Material parameters and stiffness ratios alternative to those used for Figure 6.193 gave not more significant diagrams. The markers to the load for the DEVILS and the isotropic cylinders were always apart from those to the cylinders $Z\alpha.0$ and $Z0.\alpha$, as shown in the chart for the term b_{21} . After all, there was no indication found that laminated cylinders are more sensitive to dimples than isotropic cylinders with similar nominal shell geometry and imperfection shape.

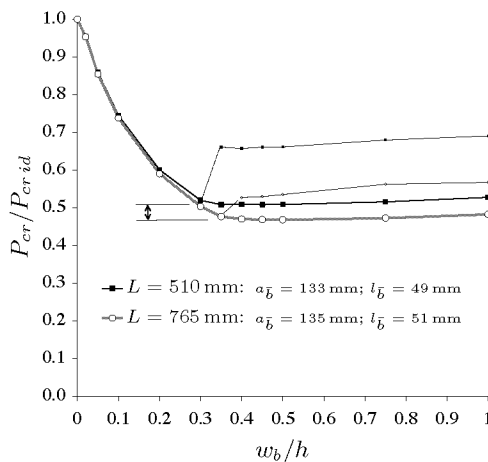


Figure 6.194: Normalized buckling loads versus initial dent depth for the cylinder $Z0.70$ with the reference length L and for the 50% longer version, both having a dent of initial width a_b and height l_b as indicated.

In addition to the important effect of the material parameters, the minimum buckling load $P_{cr \text{ MIN}}$ of a laminated cylinder with a dimple is also determined by the nominal cylinder dimensions, above all the length L , and the initial dimple width and height. All laminated cylinders used for the calculations and described above have the length $L = 510 \text{ mm}$. Figure 6.194 depicts the buckling loads $P_{cr}/P_{cr \text{ id}}$ which resulted for cylinder $Z0.70$ having a dent of different initial depth w_b/h and for a

cylinder with the identical laminate stacking $[0^{\circ}_4, \pm 70^{\circ}_2]$ but a 50 percent longer shell ($L = 765$ mm), likewise having a dent of different depth. The radius and the wall thickness of both shells are identical, the initial lateral dent dimensions to the two cylinder lengths are indicated in the graph and differ only a little. With a minimum buckling load of $P_{cr \text{ MIN}}/P_{cr \text{ id}} = 0.47$ the longer cylinder yielded an about 0.05 lower value compared to cylinder with the shorter reference length. Analyses of cylinders with the laminate of shell Z0.10 and the two lengths, 510 and 765 mm, resulted a similar vertical distance between their lowest buckling load levels $P_{cr \text{ MIN}}/P_{cr \text{ id}}$. In Section 6.6.1, page 281 ff, especially the influence of the cylinder length L to the axial buckling resistance and behaviour of isotropic cylinders was detailed. In case of isotropic shell material the material stiffness does not affect the normalized buckling loads, and the other important parameters either remained unvaried or were adapted to the particular length L . Figure 6.63 on page 282 includes the normalized buckling loads which resulted for the isotropic reference cylinder with $L = 510$ mm and also for a longer shell of length $L = 765$ mm, both having a dent of various depth. The curve progressions of these isotropic shells resemble those of the laminate cylinders above with the same two lengths. Furthermore, the vertical distance which resulted between the minimum loads $P_{cr \text{ MIN}}/P_{cr \text{ id}}$ of the isotropic reference cylinder and that of its 50% longer alternative is about 0.05, hence of the same size than the value resulting for the laminated shells. Alike it was observed for the longer isotropic cylinder, in case of the longer laminated cylinder in Figure 6.194 the vertical distance between the lower and the upper buckling load, i.e. between thick and thin lines ($P_{cr U} - P_{cr L}$), is notably smaller than the distance for the shorter shell. Consequently, the particular local buckling incident with a lateral displacement of the dimple described in Section 6.6.1 has also to be expected for laminated cylinders of arbitrary, medium length. However, calculations with cylinders of both lengths $L = 510$ and 765 mm but with the laminate Z0.10 (lower buckling load $P_{cr \text{ id}}$) yielded curve progressions for the normalized buckling loads similar to the results for shorter isotropic cylinders without the characteristic associated with the mentioned local-buckling phenomenon; thus: larger differences between $P_{cr U}$ and $P_{cr L}$ at higher minima $P_{cr \text{ MIN}}/P_{cr \text{ id}}$.

The large variation range of the minimum normalized buckling loads $P_{cr \text{ MIN}}/P_{cr \text{ id}}$ of the laminated cylinders Z0. α and Z α .0 solely due to different ply angles α in addition to the similar variation range resulting for various cylinder dimensions, as found for isotropic shells, and comparisons with the results for the DEVILS cylinders led to the aban-

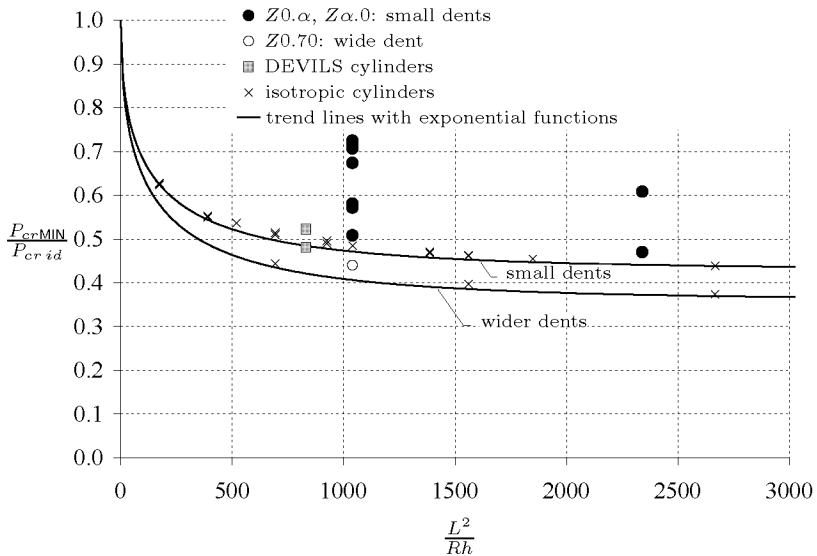


Figure 6.195: Minimum normalized buckling load versus cylinder geometry parameter L^2/Rh for laminated and isotropic cylinders. Nonlinear buckling analysis results for shells as indicated. Trend lines according to analysis results for isotropic shells with either small dents ($\alpha_{\bar{b}}(0.1)$) or wider dents ($\alpha_{\bar{b}}(0.1) + 30\%$). Axisymmetric dimples not considered.

document of the task to derive a formula for the minimum buckling loads $P_{cr \text{ MIN}}/P_{cr \text{ id}}$ versus a suitable material parameter as well as of the cylinder length L , radius R , and wall thickness h . But, according to the analysis results above, the influences of the cylinder length and of the initial dimple dimensions to the minimum loads for laminated cylinders accord with those of the isotropic shells and are hence independent of the shell material properties. And, ignoring the results with axisymmetric dimples there is no indication that an arbitrarily laminated cylinder results in a notably lower minimum load $P_{cr \text{ MIN}}/P_{cr \text{ id}}$ than an isotropic cylinder with identical L , R and h . Consequently, for a prediction of the minimum axial buckling load $P_{cr \text{ MIN}}/P_{cr \text{ id}}$ to be expected as the worst case for a laminated cylinder the rules for isotropic shells may be used to consider the cylinder length L , radius R , and wall thickness h , see Section 6.6.4.

Figure 6.195 includes the minimum normalized buckling loads $P_{cr \text{ MIN}}/P_{cr \text{ id}}$

which resulted for the isotropic cylinders and the laminated cylinders as indicated, all having a single, non-axisymmetric dent. The loads are plotted against the geometry parameter L^2/Rh which equals BATDORF's parameter Z but without the root term that takes the transverse contraction of the shell material into account. The dents referred to as "small" have initial circumferential widths $a_{\bar{b}}(0.1)$ and meridian heights $l_{\bar{b}}(0.1)$ which provoked minimal buckling resistance for an initial dent depth of $w_b = 0.1$, the other dents have about 30% wider initial widths and also similarly longer heights, see previous Section 6.7.2. Deep dents have longer lateral dimensions for smallest buckling resistance than shallow dents; and, in turn, longer initial dent widths cause lower minimum buckling loads $P_{cr\text{ MIN}}/P_{cr\text{ id}}$ than smaller widths, with the results for ring-shaped dents as lower bound. The initial widths and heights $a_{\bar{b}}$ and $l_{\bar{b}}$ found for laminated cylinders are subject of the preceding section. According to the analysis results, again under consideration of the numerical modelling and the boundary conditions, the minimum normalized buckling load $P_{cr\text{ MIN}}/P_{cr\text{ id}}$ of a medium length *isotropic* cylinder with the dimensions L , R , and h having a non-axisymmetrical dent of initial width and height as specified for shallow dents will result about between the values

$$\begin{aligned} \frac{P_{cr\text{ MIN}}}{P_{cr\text{ id}}} &= 1 - 0.57 \left(1 - e^{-\frac{1}{12} \frac{L}{\sqrt{Rh}}} \right) && \text{for small dents, and} \\ \frac{P_{cr\text{ MIN}}}{P_{cr\text{ id}}} &= 1 - 0.64 \left(1 - e^{-\frac{1}{12} \frac{L}{\sqrt{Rh}}} \right) && \text{for wider dents.} \end{aligned} \quad (6.22)$$

solely with the cylinder dimensions taken into account, see Section 6.6.4. For a laminated cylinder, again having a non-axisymmetrical dent of appropriate initial width and height, a minimum buckling load $P_{cr\text{ MIN}}/P_{cr\text{ id}}$ for the identically dimensioned isotropic cylinder or a value above will result with nonlinear buckling analyses, depending on the material parameters (i.e. layer angles and stacking) of the shell.

The vast imperfection sensitivity of axially compressed cylinders compared to cylinders subjected to external pressure or torsion was explained with the substantially larger number of periodic buckling modes m_c and n_c in in the classical theory for isotropic cylinders that are associated with the same or almost the same buckling load. The classical analysis of laminated cylinders under axial load in contrast yields also only a single buckling mode to the lowest buckling load of a shell and a smaller group of modes associated with slightly higher buckling loads. This might justify the assumption that laminated cylinders are rather less imperfection-sensitive than axially compressed isotropic cylinders of equal size.

A single, local axisymmetric dent in a laminated or isotropic cylinder will cause a significantly lower minimum buckling load $P_{cr \text{ MIN}}/P_{cr \text{ id}}$ than a non-axisymmetric dent, also for shells which in absence of imperfections buckle non-axisymmetrically. Cylinders, in turn, whose classical buckling mode is axially symmetrical are relatively insensitive to dents of initial width a_b small compared to the cylinder circumference (e.g. shell Z32). This may be used to design cylindrical shells tolerant to shallow, localized dimple imperfections, whose unintentional presence in a real shell is more likely than that of ring-shaped dimples of short meridian height as applied to cylinder Z32 or Z0.45.

As already mentioned, the buckling analyses results of the laminated cylinders did not allow to develop any relationship between minimum buckling load $P_{cr \text{ MIN}}/P_{cr \text{ id}}$ and a material parameter consistent for all analysed laminated as well as isotropic cylinders and usable to predict the $P_{cr \text{ MIN}}/P_{cr \text{ id}}$ only on basis of the shell material data. According to the results obtained for non-axisymmetric dents, the minimum buckling load $P_{cr \text{ MIN}}/P_{cr \text{ id}}$ of a laminated cylinder having a dent will not be smaller than that of a isotropic cylinder with like dimensions having a dent of similar size. Further, the non-axisymmetric dimples reduce the load carrying capacity of axially compressed cylinders—laminated or isotropic—less than local ring-shaped dimples of like initial amplitude. For safe shell design this is of importance since by means of the cylinder length, radius and wall thickness the lowest buckling load to be expected for a laminated cylinder may therefore be taken from the knock-down factors and recommendations provided for isotropic cylinders, see Section 6.6.4. But with adequately designed layer stacking sequences and fibre orientations the sensitivity of a laminated cylinder to localized dimples may effectively be reduced to save weight. In order to utilize this possibility to dimension light-weight shell structures with larger reduction factors some calculation effort is needed to find a reasonable compromise between shell stiffness and sensitivity to dents and bulges. The lowest buckling load of a laminated cylinder to be designed finally may only be quantified by means of *nonlinear* finite element analyses¹⁵ considering either measured imperfection patterns, if available, or a single dent which approximates the “worst single dimple” that might occur in reality. Dimensions for such critical single initial dimples were discussed in Section 6.7.2.

¹⁵Imperfections imply nonlinear analyses as introduced in Section 3.3 and 3.5.

Chapter 7

Conclusions

Finite element analysis results of thin-walled, unstiffened isotropic and laminated composite cylinders under pure axial compression with initial dimple imperfections were discussed and pictured with several examples. By means of nonlinear static buckling and transient dynamic analyses the critical loads and the particular states of deformation and stress were calculated for a series of such shells having a single inward or outward dimple. Parameter studies were conducted for a number of cylinders with dimples of different initial amplitude w_b but fixed initial circumferential width a_b and axial height l_b , see Figure 1.5 on page 18. In addition, for a few cylinders and for some predefined initial amplitudes the initial axial height $l_{\bar{b}}$ and circumferential width $a_{\bar{b}}$ of the dimple was specified which reduced the buckling load the most. Finally, the influence of the relative position of a second, initially identical inward dimple to the load-carrying capacity was investigated.

The finite element models of the shells were analysed under consideration of nonlinear deformations using Lagrangian formulations with geometry update as incorporated in MARC[®]. To manage the large number of shells with different buckling loads and behaviour considered, a nonlinear buckling analysis with adaptive load step control was developed which utilized linear eigenvalues, intermediately calculated after a selected number of small loading steps to determine the stability of pre-buckling states of stress and deformation. The transient dynamic finite element analyses were performed with significant inertia damping introduced, using the implicit single-step Houbolt operator for time integration implemented

into MARC[®].

The laminated composite cylinders considered were already investigated for a Brite-Euram project which focussed on the correlation of buckling loads of test cylinders with analytical and numerical predictions. It has been demonstrated that carefully conducted tests including extremely careful equalization of load introduction, implementation of actual radial geometries and consideration of non-linear deformations yielded an *excellent agreement between analysed and experimental buckling loads*. The finite element analyses of these shells have shown that for such cylinders buckling loads close to test values may be attained with accuracies which differ barely from those resulting for other types of FE analyses.

According to the investigations of the cylinders with perfect geometry, with measured imperfections, and finally with dimple imperfections considered, the following conclusions concerning the finite element modeling and the analysis methods have been drawn:

- i. Considering imperfections in FE analyses nonlinear procedures are mandatory! However, for perfect cylinders the application of nonlinear procedures yields hardly notably different results than that of linear methods. → Figure 6.177, page 444.
- ii. In nonlinear buckling analyses the continuous monitoring of the lowest eigenvalue throughout the iteration is recommended to understand the situation close to buckling. → Section 6.5.1, page 204.
- iii. The modified nonlinear buckling analysis with adaptive load step control enabled consistent extraction of the buckling load from the incremental results and minimized the pre-processing effort for adjustments to each new shell. → Section 6.5, page 203.
- iv. The relatively large time exposure for a nonlinear buckling analysis was dominated by the eigenvalue calculations at selected load steps. Thus, further development of fast but still reliable and accurate eigenvalue extraction methods suitable also for nonlinear buckling analyses would be beneficial.
- v. Additional data extracted by user subroutines developed for post-processing, e.g. local curvatures, purpose to help to understand the behaviour of the investigated cylinder. The effort to generate such codes appears to be feasible in case of large number of imperfection parameters, and hence different shells to be analysed.

- vi. Numerical buckling simulations by means of transient dynamic analysis are possible but time consuming. The choice of adequate damping parameters is the most demanding part, as the calculation time has to be kept to reasonable limits (CPU time in days). However, such analyses help to study the buckling as well as the post-buckling behaviour.
- vii. For the transient dynamic analyses the use of an implicit operator was preferred as for the rather slow compression velocities assumed the number of time steps needed to guarantee equilibrium is significantly smaller than needed using an explicit operator. The explicit operators are only stable for very small time steps; thus, their use can not be recommended as long as the structure is not an object of a crash analysis which deals with much higher deformation velocities and shorter process durations.
→ Section 3.5.3, page 112.
- viii. The use of arc-length methods without continuous control of the system matrix to ascertain the axial buckling load of a perfect cylinder is not advisable, since at the bifurcation points of such shells the equilibrium paths often intersect with a small acute angle. The correct path may then be traced beyond buckling only with very small load steps and arc-lengths. Moreover, any indication whether the largest load found in the results correlates with the effective buckling load is not provided.
→ Figure 6.15, page 214.
- ix. FE cylinder models with square bi-linear shell elements should have a mesh size not wider than $0.5\sqrt{R h}$. The use of higher-order shell elements in nonlinear buckling analyses is not recommended.
→ Section 4.1.3, page 123, and Figure 6.172, page 438.
- x. The differences between buckling loads for cylinders under axial load with clamped or hinged boundary conditions are negligible as long as the radial as well as the tangential edge displacements are restrained (i.e. SS3, SS4, CC3, or CC4). This applies for perfect cylinders and cylinders with distributed imperfections only.
→ Item (xvi) below and Section 4.2.2, page 131.

The positive experience with the FE analyses of cylinders having perfect geometry or measured imperfections set the stage for the subsequent calculations of such cylinders but with a single initial parametric dent or bulge. These dimple imperfections were applied to the cylinders by

means of user-subroutines, developed for the pre-processing in which the coordinates of all element nodes of a cylinder model were specified via mathematic formulas. In general, the shape of the dents or bulges was predefined with a cosine function in axial and one in circumferential direction, enabling arbitrary variation of the initial amplitude w_b as well as of the initial circumferential width a_b and of the initial axial height l_b of the dimple. Any local initial stress disturbance in the shell or variation of the shell-wall thickness, in turn, was not considered.

The influence of the initial dimple size and of the cylinder dimensions on the instability behaviour was investigated systematically with several parameter studies of accordingly established FE models. Such studies were performed for linear-elastic isotropic cylinders (aluminium) of different cylinder radius R , length L and wall-thickness h , but also for laminated composite cylinders (carbon fibre reinforced epoxy). For both shell materials the influence of the initial amplitude w_b of a dimple with a given initial width a_b and a given initial height l_b on the buckling behaviour and the buckling loads was analysed. Furthermore, for fixed initial amplitudes the initial width a_b and the initial height l_b of the dimple were searched which give the minimum axial stability for a selected cylinder. Finally, only for an isotropic reference cylinder having an initial dent the impact of a second, identical initial dent was investigated for different relative positions in the cylinder surface.

The FE analyses of the cylinders having a localized initial dimple yielded particular deformation processes including different local buckling phenomena which were hardly known from circular monocoque cylinders with neither perfect geometry nor with imperfections distributed over the entire shell surface. Nevertheless, by means of systematic variation of the shell parameters some interrelationships between the results and the nominal dimensions of the cylinder and the dimple could be derived.

As for the concluding remarks on the numerical analysis methods above, afterwards compiled the conclusions drawn from the observations of the shells with single local dents and bulges:

- xi. The design recommendations in standards and literature considered for thin-walled, unstiffened isotropic cylinders under pure axial compression seem to be conservative if the nominal cylinder length L , radius R , and wall-thickness h are taken into account. The buckling loads found for a given cylinder having a single dimple were higher compared to the values provided for the dimples of amplitude and geometry whose occurrence in the corresponding

real random imperfection surface cannot be excluded. But the load reduction factors recommended in the German standard DIN 18800 (usable solely for isotropic shells) could not be reproduced with the FE analyses as therein the related formulas consider the cylinder geometry together with the yield stress.

→ Section 6.6.4, page 347.

- xii. Axisymmetric, i.e. ring-shaped dimples are more damaging than non-axisymmetric dimples of like amplitude w_b . Only localized inward dimples of small initial amplitude and particular initial width a_b and height l_b reduce the buckling load as much as ring-shaped inward dimples of identical, small initial amplitude.
→ Figure 6.110, page 349.
- xiii. Localized outward dimples (bulges) reduce the load carrying capacity less than localized inward dimples (dents) of like absolute amplitude $|w_b|$, initial width a_b and initial height l_b . The amplitude of bulges increases only little during cylinder compression, but above and below the initial bulge inward dimples of increasing depth are formed instead which cause local loss in stability similarly to the processes observed for initial dents.
→ Section 6.6.2, page 296.
- xiv. According to the deformation behaviour patterns of the cylinder shells observed, inward dimples may be divided into *shallow dents* and *deep dents*. Shallow dents with an initial amplitude smaller than a certain marginal depth w_b^* provoke a distinct *local buckling* with a snapping inwards of the dent to form a local, flattened shell strip of reduced geometric axial stiffness. Deep dents with an initial amplitude larger than w_b^* , in turn, result in a continuous flattening of the shell, if not initially flattened, without dynamic local-buckling incident prior to the total *cylinder collapse*.
→ Section 6.6.1, page 225; extra: Figs. 6.59 & 6.60, page 276.
- xv. A non-axisymmetric, shallow dent of adequate initial width and height may be as damaging as an evenly distributed imperfection-pattern that is given by a classical buckling mode of initial amplitude w_{mn} that is half the initial amplitude w_b of the dent with $w_b = 2 \cdot w_{mn}$. → Figure 6.120, page 363.
- xvi. The difference between *uniform edge loads* (boundary conditions SS3 and CC3) and *uniform edge displacements* (SS4 and CC4) is important for cylinders having a single deep dimple. For uniform edge loads after local loss in stability of the flattened dimple

the edge tilts towards the imperfection and the cylinder collapses directly. With controlled edge displacement, in turn, after local flattening of the shell within the dimple the cylinder is still stable and further compression is possible up to the cylinder collapse. But the difference between the effects due to a single dimple at half the cylinder length for *clamped* cylinder edges (CC4) and those for *hinged* boundary conditions (SS4) is negligible.

→ Section 6.6.7, page 426.

- xvii. The rate in decrease of the load carrying capacity with increasing initial amplitude w_b is greatest for small amplitudes. The decline is maximal for shallow dents, whereas for deep dents the local buckling load, i.e. the load associated with local instability, decreases only little or even increases with increasing depth w_b .
→ Figure 6.22, page 228.
- xviii. The cylinder length L exerts important influence on the buckling loads of cylinders with a single dimple. The minimum buckling loads of such shells decrease with increasing cylinder length, and the deformation behaviour pattern prior to collapse of a partially flattened cylinder shell depends also on the length L . Predictions of the critical loads for cylinders having a single dimple are more accurate if referenced to BATDORF's cylinder geometry parameter $Z = L^2/(Rh)\sqrt{1-\nu^2}$ than if only referenced to the nominal cylinder radius R and wall thickness h . → Section 6.6.4, page 347.
- xix. For large parameter Z the minimum buckling load $P_{cr\ MIN}$ of isotropic cylinders with a single, non-axisymmetric dimple converges to about 35% of the classic buckling load of the perfect cylinder P_{cl} . → Figure 6.115, page 355.
- xx. The marginal initial depth w_b^* , i.e. the maximum dent depth for which distinct local buckling of the dent occurs, varied between $0.25h$ for small Z and $0.58h$ for Z above 2500. The depth w_b^* depends also weakly on the initial width a_b of the dent.
→ Figure 6.113, page 352.
- xxi. For isotropic cylinders the initial axial heights $l_{\bar{b}}$ of *dents* that reduced the buckling load the most for a preselected initial depth w_b varied between $l_{\bar{b}} = 3.4\sqrt{Rh}$ and $4.3\sqrt{Rh}$. The height $l_{\bar{b}}$ is thus close to the wavelength for classical axisymmetric buckling of a perfect cylinder, $2l_c = 3.46\sqrt{Rh}$, and increases with increasing initial depth w_b .

For *bulges* somewhat smaller initial dimple heights $l_{\bar{b}}$ between $3.0\sqrt{Rh}$ and $3.6\sqrt{Rh}$ were found. The heights $l_{\bar{b}}$ for bulges are only little affected by the dimple amplitude.

The initial widths $a_{\bar{b}}$ of the “pessimism” *dents* resulted between 2 to 3 times the initial height $l_{\bar{b}}$. The width $a_{\bar{b}}$ of a dent increases faster with increasing initial depth w_b and depends also weakly on the cylinder geometry parameter Z .

The worst *bulge* is always axisymmetric ($a_{\bar{b}} = \infty$), independent from the initial amplitude.

→ Section 6.6.3, page 325.

- xxii. Isotropic cylinders of moderate length having a single dimple of a given *normalized* initial amplitude w_b/h which are axially compressed by a load at a given percentage to the buckling load P/P_{cr} yielded identical values and distributions of the relative axial-membrane-load deviations, *normalized* with respect to the nominal axial compressive membrane force per unit length $\tilde{N}_x = -P/(2\pi R)$, in dependency of the length \sqrt{Rh} . Consequently, having stress analysis results for one cylinder and with known buckling loads P_{cr} the axial membrane load distribution and peak values in any other cylinder of equal dimple amplitude w_b/h , appropriate dimple dimensions, similar *normalized* axial load P/P_{cr} , and adequate cylinder length L can be predicted.

→ Figure 6.133, page 387.

- xxiii. The buckling load of a cylinder with single dent is only little different from that of a cylinder having *two dents* of identical size. The buckling loads depend on the relative position of the two dimples and the resulting interference between the single displacement and stress fields caused by the dents. Compared with the load for a single deep dent the load for a second was maximal 6 percent smaller if one dent was arranged directly adjacent to the other around a single row. → Section 6.6.6, page 398.

- xxiv. *Laminated composite cylinders* with maximised buckling resistance tend to be imperfection sensitive in buckling analyses. Laminates associated with relatively small load-carrying capacity in turn may be used to design imperfection tolerant shell structures.

→ Section 6.7, page 445.

- xxv. For many laminated cylinders of perfect geometry *helical* buckling patterns were obtained which could not be described by means of the bi-harmonic deflection functions usually considered in classical

analyses. → Figure 6.183, page 458, and Figure 4.11, page 134.

- xxvi. For the laminated cylinders accurate and general predictions of the minimum buckling loads and of critical dimple dimensions could not be derived on the basis of the cylinder geometry alone as the buckling behaviour patterns of such shells depend strongly on the laminate stacking. However, there was no indication that any laminated cylinder with any non-axisymmetric dimple will result in a smaller buckling load than an isotropic cylinder of identical radius, length and wall thickness also having a non-axisymmetric dimple. → Fig. 6.190, p. 467, Fig. 6.192, p. 469, and Fig. 6.195, p. 475.

The subsequent **answers** to the **questions** of the Introduction serve to recap the prime conclusions:

- Are there single, localized initial dimples which reduce the nominal axial buckling load of an unstiffened circular cylinder more than imperfections derived from classical buckling patterns for ideal shells?
- ⇒ *No, but a shallow dent of initial depth w_b and adequate initial width and height may be as damaging as a classical-buckling-mode affine imperfection pattern of initial amplitude $w_{mn} = w_b/2$.*
- Is there a *worst geometry* of such a single dimple imperfection? That is, are there initial aspect ratios of the dimple that damage the most?
- ⇒ *Yes, for isotropic cylinders the initial axial height l_b of the worst dents is close to the wavelength for classical axisymmetric buckling of ideal cylinders, $2l_c = 3.46\sqrt{Rh}$. The initial widths a_b of the “pessimum” dents are between 2 to 3 times the initial height. The worst bulge is always axisymmetric. For laminated composite cylinders such “pessimum” dimples exist as well; but, if not axisymmetric their initial shape can only be estimated roughly on the basis of the nominal cylinder geometry as well as the material parameters.*
- Is the effect of inward dimples (dents) on the axial cylinder stability the same as of outward dimples (bulges)?
- ⇒ *No, localized bulges are less damaging than localized dents of same initial width a_b , height l_b , and absolute amplitude $|w_b|$.*

- Is the instability behaviour the same for *isotropic* shells as for *laminated composite* shells (anisotropic) having such a localized dimple imperfection?
- ⇒ *No, for laminates whose classical buckling pattern is axisymmetric the sensitivity to localized, non-axisymmetric dimples is small. A single localized dimple reduces the axial stability of a laminated cylinder maximal as much as the axial stability of an isotropic cylinder of same nominal L , R , and h . And: yes, the effects of localized dimples in laminated cylinders on the deformation process is similar to those for isotropic cylinders (e.g. local buckling due to local shell flattening).*
- Is there an important interaction between *two* initial dimples?
- ⇒ *No, the further reduction of the axial cylinder stability caused by a second dent of identical size to the first one is small. Compared with the load for a single deep dent the load for a second was maximal 6 percent smaller if one dent was arranged directly adjacent to the other.*

To make allowance for the extraordinary sensitivity to imperfections of unstiffened cylinders under axial load, in many commercial FE programs procedures have been implemented with which after a linear buckling analysis scaled buckling modes can be added to the initial shell geometry for subsequent nonlinear analyses. However, for save shell design the pattern which yields the minimum buckling load has to be considered, though in general the wave numbers as well as the amplitudes of the buckling modes which contribute to this pattern are not known a priori. Best analysis results may be achieved introducing measured imperfections, but these are available only with substantial effort or are unavailable for structures that exist only virtually in design. The thesis on hand deals with localized dimples which were initially added to otherwise perfect cylinders. With this alternative notional type of imperfection hopefully a contribution to the solution of the difficulties in specifying suitable imperfection patterns for shells could be made. The application of the “worst dimple”, whose possible appearance under operation condition may not be excluded, could provide a basis for a more realistic critical scenario already in the design of a structure. In addition, according to the analysis results discussed herein, for isotropic cylinders

the initial shape and size of a single dimple that minimizes the axial stability the most is given by the nominal cylinder dimensions alone. That is, the critical initial aspect ratio and amplitude of the single dent to be applied can easily be specified prior to a buckling analysis as they follow solely from the nominal cylinder radius, length and wall thickness. For laminated cylinders, however, a few numerical analyses will be unavoidable for the specification of the critical dimple geometry; anyway, after a linear analysis of the ideal shell, e.g., at least good initial estimates of the appropriate aspect ratio and amplitude should be possible.

In leaflets about commercial FE programs sometimes the ease of use of linear buckling analyses is pointed out, although in practice for cylindrical shells this method can be used only for a first estimate of the critical load level, in order to get appropriate parameter settings for subsequent nonlinear buckling analyses. With nonlinear buckling and transient dynamic analyses convincing results can be obtained, but they are time consuming and hence quite expensive. Using these nonlinear FE methods the analyst is confronted with several input parameters (e.g. load step sizes, damping) which are difficult to specify a priori. Nevertheless, their application is possible and the effort appears manageable. In addition, nonlinear FE analysis basically requires the choice of the right type of finite elements, mesh size, boundary conditions, loading incrementation, material parameters, and so on. Hence, correct introduction of adequate imperfections provided, nonlinear buckling analyses of cylindrical shells are not more elaborate than other nonlinear analyses as for contact or thermal-mechanical coupled problems, for instance. Finally, although the time exposure of numerical buckling test simulations is still discouraging, presuming that the boost of the CPU rates proceeds as hitherto, in the not so far future the transient dynamic FE analysis method might become a widely used tool for buckling problems, albeit as a complement to static analyses.

The dissertation covered the application of single dent and bulges in order to initially weaken thin-walled, unstiffened circular cylinders. However, the usability of such localized dimple imperfections for buckling analyses of other, more commonly used shell structures (e.g. stiffened panels) has not been investigated. Furthermore, the study was limited to ideal, linear elastic shell material. Hence, further efforts could aim in the consideration of yielding, laminate failure, or rupture throughout the simulation of buckling processes of cylindrical shells, as well as of other shell structures.

Bibliography

- [1] B. O. ALMROTH, *Influence of imperfections and edge restraint on the buckling of axially compressed cylinders*, Tech. Rep. CR-432, NASA, 1966.
- [2] B. O. ALMROTH, E. MELLER, AND F. A. BROGAN, *Computer solutions for static and dynamic buckling of shells*, in *Buckling of Structures*, B. Budiansky, ed., New York, 1976, IUTAM Symposium Cambridge/USA June 1974, Springer, pp. 52 – 66.
- [3] J. C. AMAZIGO AND B. BUDIANSKY, *Asymptotic formulas for the buckling stresses of axially compressed cylinders with localized or random axisymmetric imperfections*, *Journal of Applied Mechanics*, (1972), pp. 179 – 184.
- [4] E. ANDERHEGGEN, *Lineare Finite-Elemente-Methoden: Eine Einführung fr Ingenieure*. Lecture script.
- [5] J. ARBOCZ, *Towards an improved design procedure for buckling critical structures*, in *Buckling of shell structures on land in the sea and in the air*, J. F. Jullien, ed., Elsevier Science Publishers Ltd., 1992, pp. 270 – 276.
- [6] J. ARBOCZ AND J. C. D. BABCOCK, *The effect of general imperfections on the buckling of cylindrical shells*, *Journal of Applied Mechanics*, (1969), pp. 28 – 38.
- [7] J. ARBOCZ AND J. C. D. BABCOCK, *Prediction of buckling loads based on experimentally measured initial imperfections*, in *Buckling of Structures*, B. Budiansky, ed., New York, 1976, IUTAM Symposium Cambridge/USA June 1974, Springer, pp. 291 – 311.

- [8] J. ARBOCZ AND J. M. A. M. HOL, *Koiter's stability theory in a computer aided engineering (CAE) environment*, Int. J. Solids and Structures, 26 (1990), pp. 945 – 973.
- [9] J. ARBOCZ AND J. M. A. M. HOL, *Collapse of axially compressed cylindrical shells with random imperfections*, Thin-Walled Structures, 23 (1995), pp. 131 – 158.
- [10] J. ARBOCZ AND J. G. WILLIAMS, *Imperfection surveys on a 10-ft-diameter shell structure*, AIAA Journal, 15 (1977), pp. 949 – 956.
- [11] Y. BAŞAR AND D. WEICHERT, *Nonlinear Continuum Mechanics of Solids*, Springer, Berlin and Heidelberg, 2000.
- [12] S. B. BATDORF, *A simplified method of elastic-stability analysis for thin cylindrical shells*, Tech. Rep. 874, NACA, 1947.
- [13] S. B. BATDORF, M. SCHILDCROUT, AND M. STEIN, *Critical stress of thin-walled cylinders in axial compression*, Tech. Rep. 887, NACA, 1947.
- [14] K.-J. BATHE, *Finite-Elemente-Methoden*, Springer, Berlin and Heidelberg, 1990.
- [15] Z. P. BAŽANT AND L. CEDOLIN, *Stability of Structures*, The Oxford engineering science series, Oxford University Press, New York, 1991.
- [16] C. BISAGNI, *Numerical analysis and experimental correlation of composite shell buckling and post-buckling*, Composites: part B, 31 (2000), pp. 655 – 667.
- [17] B. BRENDDEL, *Zur geometrisch nichtlinearen Elastostabilität*, PhD thesis, Universität Stuttgart, 1979.
- [18] D. O. BRUSH AND B. O. ALMROTH, *Buckling of bars, plates and shells*, McGraw-Hill Book Company Inc., New York, 1975.
- [19] B. BUDIANSKY, *Theory of buckling and post-buckling behaviour of elastic structures*, Advances in Applied Mechanics, 14 (1974), pp. 1 – 65.
- [20] B. BUDIANSKY AND J. W. HUTCHINSON, *A survey of some buckling problems*, AIAA Journal, 4 (1966), pp. 1505 – 1510.

- [21] D. BUSHNELL, *Computerized buckling analysis of shells*, no. 9 in Mechanics of elastic stability, Martinus Nijhoff Publishers, Dordrecht, NL, 1985.
- [22] M. K. CHRYSSANTHOPOULOS, V. GIAVOTTO, AND C. POGGI, *Characterization of manufacturing effects for buckling-sensitive composite cylinders*, Composites Manufacturing, 6 (1995), pp. 93 – 101.
- [23] J. CHUNG AND G. M. HULBERT, *A family of single-step houbolt time integration algorithms for structural dynamics*, Comput. Methods Appl. Mech. Engrg., 118 (1994), pp. 1 – 11.
- [24] G. A. COHEN, *Effect of a nonlinear prebuckling state on the post-buckling behavior and imperfection sensitivity of elastic structures*, AIAA Journal, 6 (1968), pp. 1616 – 1619.
- [25] COLUMN RESEARCH COMMITTEE OF JAPAN, *Handbook of structural stability*, 1971. Corona Publishing Company, Japan.
- [26] M. A. CRISFIELD, *A fast incremental/iterative solution procedure that handles "snap-through"*, Computers & Structures, 13 (1981), pp. 55 – 62.
- [27] M. A. CRISFIELD, *Non-linear Finite Element Analysis of Solids and Structures*, vol. 1, Essentials, John Wiley & Sons Ltd., Chichester, UK, 1991.
- [28] DIN DEUTSCHES INSTITUT FÜR NORMUNG E.V., *Stahlbauten*, 1990. DIN 18 800.
- [29] L. H. DONNELL, *A new theory for the buckling of thin cylinders under axial compression and bending*, Transactions of the ASME, 56 (1934), pp. 795 – 806.
- [30] L. H. DONNELL AND C. C. WAN, *Effect of imperfections on buckling of thin cylinders and columns under axial compression*, Journal of Applied Mechanics, (1950), pp. 73 – 83.
- [31] J. F. DOYLE, *Nonlinear Analysis of Thin-Walled Structures*, mechanical engineering series, Springer, New York, 2001.
- [32] B. EDLUND, *Thin-Walled Cylindrical Shells under Axial Compression*, PhD thesis, Calmers University of Technology Göteborg, 1974.

- [33] I. ELISHAKOFF, *Uncertain buckling: its past, present and future*, Int. J. of Solids and Structures, 37 (2000), pp. 6869 – 6889.
- [34] P. ERMANNI, *Leichtbau III*. Lecture notes, 2002. ETH Zürich, Institute of Mechanical Systems IMES, Structure Technologies.
- [35] M. ESSLINGER, *Hochgeschwindigkeitsaufnahmen vom Beulvorgang dünnwandiger, axialbelasteter Zylinder*, Der Stahlbau, 39 (1970).
- [36] M. ESSLINGER AND H.-R. MEYER-PIENING, *Beulen und Nachbeulen dünnwandiger Schalen - Isotroper Kreiszyylinder unter Axiallast*. Institut für den wissenschaftlichen Film, Göttingen, Germany. B 1050T.
- [37] J. R. FITCH, *The buckling and post-buckling behavior of spherical caps under concentrated load*, Int. J. Solids Structures, 4 (1968), pp. 421 – 446.
- [38] C. G. FOSTER, *Axial compression buckling of conical and cylindrical shells*, Experimental Mechanics, (September 1987), pp. 255 – 261.
- [39] B. GEIER, *A method to compute koiter's b-factor of anisotropic panels*, Int. J. of Non-linear Mechanics, 37 (2002), pp. 699 – 707.
- [40] B. GEIER, H.-R. MEYER-PIENING, AND R. ZIMMERMANN, *On the influence of laminate stacking on buckling of composite cylindrical shells subjected to axial compression*, Composite Structures, 55 (2002), pp. 467 – 474.
- [41] B. GEIER AND G. SINGH, *Some simple solutions for buckling loads of thin and moderately thick cylindrical shells and panels made of laminated composite material*, Aerospace Science and Technology, 1 (1997), pp. 47 – 63.
- [42] G. GERARD AND H. BECKER, *Handbook of structural stability, part III, buckling of curved plates and shells*, TN 3783, NACA, 1957.
- [43] D. GROSS, W. HAUGER, W. SCHNELL, AND P. WRIGGERS, *Technische Mechanik*, vol. 4, Springer, Berlin and Heidelberg, third ed., 1999.
- [44] J. S. HANSEN, *General random imperfections in the buckling of axially loaded cylindrical shells*, AIAA Journal, 15 (1972), pp. 1250 – 1255.

- [45] HIBBITT, KARLSSON & SORENSEN, INC., *ABAQUS Theory Manual, Version 5.8*, 1998.
- [46] E. HINTON, ed., *NAFEMS Introduction to Nonlinear Finite Element Analysis*, Glasgow, 1992, NAFEMS Ltd.
- [47] N. J. HOFF, *The accuracy of donnell's equations*, J. Appl. Mech., 22 (1955), pp. 329 – 334.
- [48] N. J. HOFF AND L. W. REHFELD, *Buckling of axially compressed circular cylindrical shells at stresses smaller than the classical critical value*, Transactions of the ASME, J. Appl. Mech., 32 (1965), pp. 542 – 552.
- [49] J. W. HUTCHINSON, *Axial buckling of pressurized imperfect cylindrical shells*, AIAA Journal, 3 (1965), pp. 1461 – 1466.
- [50] J. W. HUTCHINSON AND J. C. FRAUENTHAL, *Elastic postbuckling behaviour of stiffened and barreled cylindrical shells*, Journal of Applied Mechanics, (1969), pp. 784 – 790.
- [51] J. W. HUTCHINSON, R. C. TENNYSON, AND D. B. MUGGERIDGE, *Effect of a local axisymmetric imperfection on the buckling behaviour of a circular cylindrical shell under axial compression*, AIAA Journal, 9 (1971), pp. 48 – 52.
- [52] B. KLEIN, *FEM Grundlagen und Anwendungen der Finite-Element-Methode*, Friedr. Vieweg & Sohn Verlagsgesellschaft mbH, Braunschweig, 1997.
- [53] K. KNOTHE AND H. WESSELS, *Finite Elemente*, Springer, Berlin and Heidelberg, second ed., 1992.
- [54] W. T. KOITER, *On the stability of elastic equilibrium*, PhD thesis, TU Delft, 1945. Original in Dutch. English translation as NASA TT F-10833, 1967.
- [55] W. T. KOITER, *The effect of axisymmetric imperfections on the buckling of cylindrical shells under axial compression*, Koninkl. Ned. Akad. Wetenschap. Proc., B66 (1963), pp. 265 – 279.
- [56] W. B. KRÄTZIG, *Time-invariant instability problems*, in Nonlinear Stability of Structures, A. N. Kounadis and W. B. Krätzig, eds., no. 342 in CISM Courses and Lectures, Springer, 1995, pp. 313 – 336.

- [57] S. KRISHNAKUMAR AND C. G. FOSTER, *Buckling of axially compressed cylindrical shells with local geometric imperfections*, in *Buckling of shell structures on land in the sea and in the air*, J. F. Jullien, ed., Elsevier Science Publishers Ltd., 1992, pp. 33 – 42.
- [58] B. KRÖPLIN AND D. DINKLER, *Dynamic versus static buckling analysis of thin walled shell structures*, in *Finite Element Methods for Plate and Shell Structures*, T. J. R. Hughes and E. Hinton, eds., vol. 2, Pineridge Press Ltd., Mumbles, Swansea, UK, 1986.
- [59] H.-R. MEYER-PIENING, *Theoretische und experimentelle Untersuchung des Nachbeulverhaltens dünnwandiger Kreiszyylinder mit eingespannter Rändern unter Aussendruckbelastung*, PhD thesis, Technische Universität Carolo-Wilhelmina zu Braunschweig, 1968.
- [60] H.-R. MEYER-PIENING, M. FARSHAD, B. GEIER, AND R. ZIMMERMANN, *Buckling loads of CFRP composite cylinders under combined axial and torsion loading - experiments and computations*, *Composite Structures*, 53 (2001), pp. 427 – 435.
- [61] MSC.SOFTWARE CORPORATION, *MSC.Marc Volume A: Theory and User Information, Version 2000*, 2000.
- [62] NATIONAL AERONAUTICS AND SPACE ADMINISTRATION, *Buckling of Thin-Walled Circular Cylinders*, 1968. NASA SP-8007, NASA Space Vehicle Design Criteria.
- [63] P. T. PEDERSEN, *Buckling of unstiffened and ring stiffened cylindrical shells under axial compression*, *Int. J. of Solids and Structures*, 9 (1973), pp. 671 – 691.
- [64] W. H. PRESS, S. A. TEUKOLSKY, W. T. VETTERLING, AND B. P. FLANNERY, *Numerical Recipes in C: The Art of Scientific Computing*, Cambridge University Press, second ed., 1993.
- [65] E. RAMM, *Geometrisch nichtlineare Elastostatik und Finite Elemente*, professorial dissertation, Universität Stuttgart, 1976.
- [66] E. RAMM, *Strategies for tracing the non-linear response near limit points*, in *Non-linear Finite Element Analysis in Structural Mechanics*, W. Wunderlich, E. Stein, and K.-J. Bathe, eds., Springer, Berlin, 1981, pp. 63 – 89.
- [67] J. N. REDDY, *Mechanics of laminated composite plates: theory and analysis*, CRC Press Inc., 1997.

- [68] J. D. REID, R. W. BIELENBERG, AND B. A. COON, *Indenting buckling and piercing of aluminium beverage cans*, Finite Elements in Analysis and Design, 37 (2001), pp. 131 – 144.
- [69] E. RIKS, *An incremental approach to the solution of snapping and buckling problems*, J. Solids Structures, 15 (1979), pp. 529 – 551.
- [70] J. ROORDA, *Buckling of Elastic Structures*, Solid Mechanics Division, University of Waterloo Press, 1980.
- [71] L. A. SARRIS, H. S. SUER, W. T. SKENE, AND R. J. BENJAMIN, *The stability of thin-walled unstiffened circular cylinders under axial compression including the effect of internal pressure*, Journal of the Aeronautical Sciences, 24 (1957), pp. 587 – 596.
- [72] H. R. SCHWARZ, *Methode der Finite Elemente*, no. 47 in Leitfäden der angewandten Mathematik und Mechanik, Teubner, third ed., 1991.
- [73] I. SHEINMAN AND Y. GOLDFELD, *Buckling of laminated cylindrical shells in terms of different theories and formulations*, AIAA Journal, 39 (2001), pp. 1773 – 1781.
- [74] I. SHEINMAN AND G. J. SIMITSES, *Buckling of imperfect stiffened cylinders under destabilizing loads including torsion*, AIAA Journal, 15 (1977), pp. 1699 – 1703.
- [75] J. SINGER AND H. ABRAMOVICH, *The development of shell imperfections measurement techniques*, Thin-Walled Structures, 23 (1995), pp. 379 – 398.
- [76] S. P. TIMOSHENKO AND J. M. GERE, *Theory of Elastic Stability*, McGraw-Hill Book Company Inc., New York, 1961.
- [77] T. VON KÁRMÁN, L. G. DUNN, AND H.-S. TSIEN, *The influence of curvature on the buckling characteristics of structures*, Journal of the Aeronautical Sciences, 7 (1940), pp. 276 – 289.
- [78] Š. MARKUŠ, *The Mechanics of Vibrations of Cylindrical Shells*, studies in applied mechanics 17, Elsevier, Bratislava, 1988.
- [79] V. I. WEINGARTEN, E. J. MORGAN, AND P. SEIDE, *Elastic stability of thin-walled cylindrical and conical shells under axial compression*, AIAA Journal, 3 (1965), pp. 500 – 505.

- [80] P. WRIGGERS, *Nichtlineare Finite-Element-Methoden*, Springer, Berlin and Heidelberg, 2001.
- [81] L. WULLSCHLEGER AND H.-R. MEYER-PIENING, *Buckling of geometrically imperfect cylindrical shells - definition of a buckling load*, Int. J. of Non-linear Mechanics, 37 (2002), pp. 645 – 657.
- [82] S. YAMADA AND J. G. A. CROLL, *Contributions to understanding the behaviour of axially compressed cylinders*, Journal of Applied Mechanics, 66 (1999), pp. 299 – 309.
- [83] Y. YOSHIMURA, *On the mechanism of buckling of a circular cylindrical shell under axial compression*, technical memorandum 1390, NACA, 1955.
- [84] O. C. ZIENKIEWICZ, *The Finite Element Method in Engineering Science*, McGraw-Hill, London, second ed., 1971.

Appendix A

Nonlinear Continuum Mechanics

Nonlinearity in mechanics of deformable bodies is either physical or geometrical; that is, the theory is concerned either with the stress-strain relations or with expressions which represent the influence of rotations of structural elements on the behaviour of the structure. In this thesis ideal linear elasticity is assumed for the stress-strain relations; hence, the nonlinearity is purely geometrical [18].

A.1 Deformation and Rotation

The description of macroscopic deformations of a body requires beneath the knowledge of its current position also information about its initial position. A particle ${}_0P$ of the initial configuration ${}_0B$ of an arbitrary body, relative to the origin of a orthogonal Cartesian coordinate system in a three dimensional Euclidean space, may be identified by the position vector

$$\mathbf{X} = {}_0x_1\mathbf{e}_1 + {}_0x_2\mathbf{e}_2 + {}_0x_3\mathbf{e}_3 \quad (\text{A.1})$$

where ${}_0x_i$: ${}_0x_1, {}_0x_2, {}_0x_3$ are LAGRANGIAN or **material coordinates** and \mathbf{e}_i are unit vectors along the ${}_0x_i$ -axes (Fig. A.1). The configuration ${}_0B$ is supposed to be unloaded and undeformed. At a certain time t the body takes the current configuration B , i.e. the particle ${}_0P$ is moved

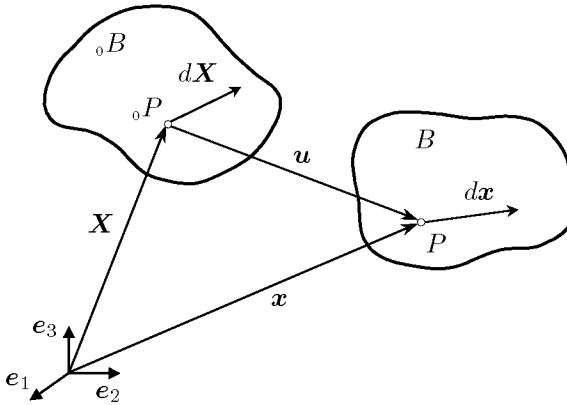


Figure A.1: Particle kinematics

into the position P which can be described by the vector

$$\mathbf{x} = x_1\mathbf{e}_1 + x_2\mathbf{e}_2 + x_3\mathbf{e}_3 \quad (\text{A.2})$$

where x_i : x_1, x_2, x_3 are EULERIAN or **spatial coordinates**.

The motion of the particle may be specified in two different ways: in a LAGRANGIAN or material description all behaviour is expressed with respect to the initial particle coordinates \mathbf{X} , whereas in a EULERIAN or spatial system all description is expressed with respect to the current coordinates \mathbf{x} of the particle:

$$\mathbf{x} = \mathbf{x}(\mathbf{X}, t) \quad \Longleftrightarrow \quad \mathbf{X} = \mathbf{X}(\mathbf{x}, t) \quad (\text{A.3})$$

In other words, in the material system a particle is constantly labelled with coordinates \mathbf{X} , whereas in a spatial system the coordinates of a particle are continuously changing when it moves from one spatial coordinate to another. The material system is more common in structural analysis, in contrast to the spatial system which is usually applied in fluid mechanics.

A deformation of a body is always a comparison of two configurations. The **displacement vector** \mathbf{u} may be defined by the position vector of particle P relative to ${}_0P$ (Fig. A.1):

$$\mathbf{u} = \mathbf{u}(\mathbf{X}, t) = \mathbf{u}(\mathbf{x}, t) = \mathbf{x} - \mathbf{X} \quad (\text{A.4})$$

For later use and a distinction between rigid body motions and deformations the distance of two neighbouring particles of the body is defined by $d\mathbf{X}$ in the initial configuration ${}_0B$ and $d\mathbf{x}$ in the current configuration B . With (A.3) the relation between these two “fibre” lengths may be described as

$$d\mathbf{x} = \mathbf{F} \cdot d\mathbf{X} \quad (\text{A.5})$$

with

$$\mathbf{F} = \frac{\partial \mathbf{x}}{\partial \mathbf{X}} \quad (\text{A.6})$$

The so-called **deformation gradient tensor** \mathbf{F} is the fundamental measurement describing deformations of a solid. The second-order tensor written out in matrix form is

$$[F_{ij}] = \begin{bmatrix} \frac{\partial x_1}{\partial_0 x_1} & \frac{\partial x_1}{\partial_0 x_2} & \frac{\partial x_1}{\partial_0 x_3} \\ \frac{\partial x_2}{\partial_0 x_1} & \frac{\partial x_2}{\partial_0 x_2} & \frac{\partial x_2}{\partial_0 x_3} \\ \frac{\partial x_3}{\partial_0 x_1} & \frac{\partial x_3}{\partial_0 x_2} & \frac{\partial x_3}{\partial_0 x_3} \end{bmatrix}$$

With $\mathbf{x} = \mathbf{X} + \mathbf{u}(\mathbf{X}, t)$ and (A.6) the deformation gradient may alternatively be expressed in terms of displacements \mathbf{u} :

$$\mathbf{F} = \left[\mathbf{I} + \frac{\partial \mathbf{u}}{\partial \mathbf{X}} \right] \quad (\text{A.7})$$

In general \mathbf{F} is asymmetric. According to the polar decomposition theorem \mathbf{F} may be multiplicatively decomposed into a orthogonal *rotation tensor* \mathbf{R} and a symmetric *stretch tensor* \mathbf{U} :

$$\mathbf{F} = \mathbf{R} \cdot \mathbf{U} \quad (\text{A.8})$$

Thus, the deformation gradient tensor contains not only information on stretch but also on rotation.

With an elemental volume ${}_0dV$ prior to deformation and such a volume dV after deformation the JACOBIAN *determinant* is defined by

$$J = \frac{dV}{{}_0dV} = \det \mathbf{F} \quad (\text{A.9})$$

This scalar measure corresponds to the third invariant of \mathbf{F} and has to be positive, otherwise the corresponding deformation is physically not

possible. Mass conservation during a deformation of a solid demands that

$$\rho dV = {}_0\rho_0 dV$$

Thus, it is additionally:

$$J = \frac{{}_0\rho}{\rho} \quad (\text{A.10})$$

A.2 Strain Measures

As already mentioned, the deformation gradient tensor includes also information on rigid body motions. Thus, \mathbf{F} does not vanish for rigid body movements of a body which may consist of a rotation and a translation and can therefore not be used as an *objective* strain measure.

To define an objective strain measure the change of the distance between two particles shall be examined. With (A.5) the square of the length in the initial configuration is defined by $d\mathbf{X}^T \cdot d\mathbf{X}$ and $d\mathbf{x}^T \cdot d\mathbf{x}$ in the current state, respectively. Using the *right* CAUCHY-GREEN *tensor* $\hat{\mathbf{c}}$ with ¹

$$\hat{\mathbf{c}} = \mathbf{F}^T \cdot \mathbf{F} = \mathbf{U}^2 \quad (\text{A.11})$$

the squared current “fibre” length may be expressed in terms of the initial lengths $d\mathbf{X}$, i.e.

$$d\mathbf{x}^T \cdot d\mathbf{x} = d\mathbf{X}^T \cdot \hat{\mathbf{c}} \cdot d\mathbf{X} \quad (\text{A.12})$$

The difference between these lengths ($d\mathbf{x}^T \cdot d\mathbf{x} - d\mathbf{X}^T \cdot d\mathbf{X}$) may then be written as

$$d\mathbf{X}^T \cdot \hat{\mathbf{c}} \cdot d\mathbf{X} - d\mathbf{X}^T \cdot d\mathbf{X} = d\mathbf{X}^T (\hat{\mathbf{c}} - \mathbf{I}) d\mathbf{X} = d\mathbf{X}^T (2\mathbf{E}) d\mathbf{X} \quad (\text{A.13})$$

The right side of (A.13) together with (A.11) finally yields the following definition of the **GREEN-LAGRANGE strain tensor** \mathbf{E} :

$$\mathbf{E} = \frac{1}{2} \left[\mathbf{F}^T \cdot \mathbf{F} - \mathbf{I} \right] \quad (\text{A.14})$$

¹In literature often referred to as \mathbf{C} . The “unorthodox” notation was chosen to prevent possible confusions with the constitutive tensor.

With expression (A.7) for \mathbf{F} the *symmetric* GREEN-LAGRANGE strain tensor may be expressed in terms of displacements. In index notation this second-order tensor consequently is given by

$$E_{ij} = \frac{1}{2} \left[\frac{\partial u_i}{\partial_0 x_j} + \frac{\partial u_j}{\partial_0 x_i} + \sum_k \frac{\partial u_k}{\partial_0 x_i} \frac{\partial u_k}{\partial_0 x_j} \right] \quad (\text{A.15})$$

Note the presence of nonlinear terms. The components E_{ij} are defined with respect to the undeformed configuration.

The tensor \mathbf{E} is an *objective* strain measure: it vanishes if the body in the initial configuration ${}_0B$ is subjected to a pure translation as well as in case of pure rotation.

Similar to the derivation above a *spatial* “counterpart” to the *material* strains \mathbf{E} may be defined. The difference between the “fibre” lengths now expressed with respect to the spatial vector $d\mathbf{x}$, yields the **EULARIAN** or **ALMANSI strain tensor** \mathbf{e} , which is given by

$$\mathbf{e} = \frac{1}{2} [\mathbf{I} - (\mathbf{F}^{-1})^T \cdot \mathbf{F}^{-1}] \quad (\text{A.16})$$

Again, the symmetric strain tensor alternatively expressed in terms of displacements and in index notation:

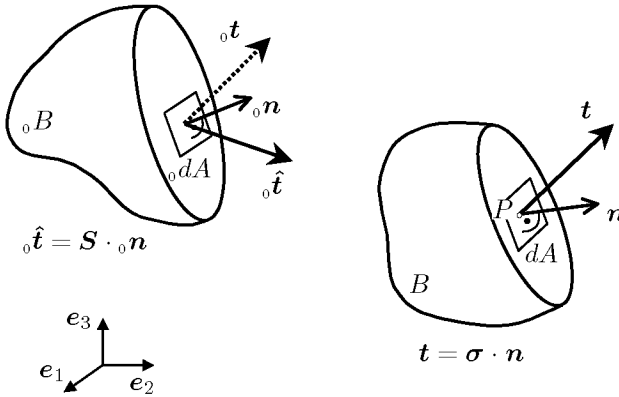
$$e_{ij} = \frac{1}{2} \left[\frac{\partial u_i}{\partial x_j} + \frac{\partial u_j}{\partial x_i} - \sum_k \frac{\partial u_k}{\partial x_i} \frac{\partial u_k}{\partial x_j} \right] \quad (\text{A.17})$$

The ALMANSI strain tensor of second order is an *objective* measure as well, i.e. \mathbf{e} will remain unaffected by rigid body motions.

If the displacement gradients ($\partial \mathbf{u} / \partial \mathbf{x}$) are small then the nonlinear term in (A.17) may be neglected. What remains is the familiar **linear strain tensor** $\boldsymbol{\varepsilon}$, expressed as

$$\varepsilon_{ij} = \frac{1}{2} \left[\frac{\partial u_i}{\partial x_j} + \frac{\partial u_j}{\partial x_i} \right] \quad (\text{A.18})$$

It has to be emphasized that this strain measure is only appropriate if both the strains and the rotations are small. Viz, a body subjected to pure rotation cause components ε_{ij} which become nonzero as the rotation increases.

Figure A.2: *Material and spatial stresses*

A.3 Stresses

Be P an arbitrary point inside a homogeneous body in its deformed configuration B , in which external forces induce internal forces. Furthermore, ΔA is defined by the surface element of the slice plane passing P with \mathbf{n} as the outward unit normal to ΔA at P . With $\Delta \mathbf{p}$ as the internal force fraction across the area ΔA the **stress vector** \mathbf{t} is defined by the following limit

$$\mathbf{t} = \lim_{\Delta A \rightarrow 0} \frac{\Delta \mathbf{p}}{\Delta A} \quad (\text{A.19})$$

The stress vector represents a force per unit area of the deformed surface. \mathbf{t} is invariant regarding the selection of coordinates.

The **CAUCHY stress tensor** $\boldsymbol{\sigma}$ is defined by

$$\mathbf{t} = \boldsymbol{\sigma} \cdot \mathbf{n} \quad (\text{A.20})$$

The spatial CAUCHY stress tensor includes the familiar “true stresses”. According to the *CAUCHY theorem*, $\boldsymbol{\sigma}$ is the symmetric second-order tensor which transforms the field of the normal vector \mathbf{n} to the stress vector \mathbf{t} acting on dA (Fig. A.2).

To define further useful stress tensors the spatial stress vector \mathbf{t} may be “pulled back” from the deformed state to the initial basis (Fig. A.2)

with

$${}_0\mathbf{t} = \frac{dA}{{}_0dA}\mathbf{t}$$

Since ${}_0\mathbf{t}$ describes the actual force upon the undeformed area ${}_0dA$ it is named *pseudo stress vector*. The material stress tensor related to ${}_0\mathbf{t}$ is called the *nominal* or *1st PIOLA-KIRCHHOFF stress tensor* \mathbf{P} :

$${}_0\mathbf{t} = \mathbf{P} \cdot {}_0\mathbf{n}$$

Accordingly, by a purely mathematical transformation the **2nd PIOLA-KIRCHHOFF stress tensor** \mathbf{S} may be introduced as

$${}_0\hat{\mathbf{t}} = \mathbf{S} \cdot {}_0\mathbf{n} \tag{A.21}$$

with (see Fig. A.2)

$${}_0\hat{\mathbf{t}} = \mathbf{F}^{-1} \cdot {}_0\mathbf{t} \quad \text{resp.} \quad {}_0\hat{\mathbf{t}} = \frac{dA}{{}_0dA}\mathbf{F}^{-1} \cdot \mathbf{t}$$

The 2nd PIOLA-KIRCHHOFF stress gives the *transformed* current force per unit undeformed area. Despite its absence of a real physical meaning, the 2nd PIOLA-KIRCHHOFF stress tensor \mathbf{S} is widely used, especially in a Total Lagrangian nonlinear analysis.

One reason for the popularity of 2nd PIOLA-KIRCHHOFF stress tensor \mathbf{S} might be its invariance to rigid body motions; in contrast to the CAUCHY stress tensor the components of the 2nd PIOLA-KIRCHHOFF stress tensor does not change due to pure rotations. In addition, contrary to the first PIOLA-KIRCHHOFF stress tensor \mathbf{P} , the second, \mathbf{S} , is symmetric.

Despite the above-mentioned advantages of the 2nd PIOLA-KIRCHHOFF stresses, at the end of any analysis “true” CAUCHY stresses have to be calculated. For this purpose, with

$${}_0\hat{\mathbf{t}} = \frac{dA}{{}_0dA}\mathbf{F}^{-1} \cdot \mathbf{t} = \frac{dA}{{}_0dA}\mathbf{F}^{-1} \cdot \boldsymbol{\sigma} \cdot \mathbf{n} = J\mathbf{F}^{-1} \cdot \boldsymbol{\sigma} \cdot \mathbf{F}^{-T} \cdot {}_0\mathbf{n} \tag{A.22}$$

the following relations between $\boldsymbol{\sigma}$ and \mathbf{S} may be deduced:

$$\begin{aligned} \mathbf{S} &= J\mathbf{F}^{-1} \cdot \boldsymbol{\sigma} \cdot \mathbf{F}^{-T} \\ \boldsymbol{\sigma} &= J^{-1}\mathbf{F} \cdot \mathbf{S} \cdot \mathbf{F}^T \end{aligned} \tag{A.23}$$

A.4 The Principle of Virtual Displacements

Based on NEWTON's second law the equation of motions for an arbitrary deformable body can be expressed as

$$\int_A \mathbf{t} dA + \int_V \mathbf{b} dV = \int_V \rho \ddot{\mathbf{u}} dV \quad (\text{A.24})$$

where \mathbf{t} is the surface traction vector, \mathbf{b} the body force vector, and $\ddot{\mathbf{u}}$ the acceleration vector. The explanations in this section are confined to time independent measures. Thus, the inertia term at the right side is neglected in the subsequent equations. In the remaining *translational equilibrium equation* the traction \mathbf{t} may be replaced by CAUCHY stresses according to (A.20). Moreover, by applying the divergence theorem the surface integral may be transformed into a volume integral, consequently [11, 31, 46]:

$$\int_A \boldsymbol{\sigma} \cdot \mathbf{n} dA + \int_V \mathbf{b} dV = \int_V \operatorname{div} \boldsymbol{\sigma} dV + \int_V \mathbf{b} dV = 0 \quad (\text{A.25})$$

Since equilibrium has to apply to the whole body, the integral over the arbitrary volume V must vanish and the *spatial differential equilibrium equation* finally may be expressed as

$$\mathbf{r} = \operatorname{div} \boldsymbol{\sigma} + \mathbf{b} = 0 \quad (\text{A.26})$$

with \mathbf{r} introduced as *residual* force vector.

The partial differential equation system in the form of (A.26) is *not* suitable for the construction of a numerical system of equations! Therefore, the differential equation is transformed into an energy expression. The *virtual work* formulation of equilibrium delivers a scalar value with which it is easier to handle if, for numeric reasons, equilibrium may only be reached approximatively.

Consider vector \mathbf{r} to be the forces which act on an arbitrary body. This body is displaced by an imaginary or *virtual displacement* $\delta \mathbf{u}$. According to (A.4) an *infinitesimal* virtual displacement field may be defined by

$$\delta \mathbf{u} = \delta \mathbf{u}(\mathbf{X}) = \delta \mathbf{u}(\mathbf{x}, t) \quad (\text{A.27})$$

Note that *virtual* displacements are independent of *real* forces of the real deformation process, but should not violate boundary conditions.

The virtual work is defined by the scalar product

$$\delta W = \int_V \mathbf{r} \cdot \delta \mathbf{u} dV = 0 \quad (\text{A.28})$$

Thus, if $\delta W = 0$ for any kinematically permitted $\delta \mathbf{u}$, the stress state satisfies the equilibrium conditions. Now, by replacing \mathbf{r} in (A.28) the differential equilibrium equation (A.26) is transformed into a *weak* formulation:

$$\delta W = \int_V [\text{div } \boldsymbol{\sigma} + \mathbf{b}] \cdot \delta \mathbf{u} dV = 0 \quad (\text{A.29})$$

With the chain rule follows that

$$\text{div} [\boldsymbol{\sigma} \cdot \delta \mathbf{u}] = [\text{div } \boldsymbol{\sigma}] \cdot \delta \mathbf{u} + \boldsymbol{\sigma} : \left(\frac{\partial \delta \mathbf{u}}{\partial \mathbf{x}} \right)$$

where two dots “:” denote a double scalar product of two second-order tensors² (double contraction).

Thus, it is

$$\begin{aligned} \int_V [\text{div } \boldsymbol{\sigma}] \cdot \delta \mathbf{u} dV &= \int_V \text{div} [\boldsymbol{\sigma} \cdot \delta \mathbf{u}] - \boldsymbol{\sigma} : \left(\frac{\partial \delta \mathbf{u}}{\partial \mathbf{x}} \right) dV \quad , \text{ or} \\ &= \int_A \boldsymbol{\sigma} \cdot \mathbf{n} \cdot \delta \mathbf{u} dA - \int_V \boldsymbol{\sigma} : \left(\frac{\partial \delta \mathbf{u}}{\partial \mathbf{x}} \right) dV \end{aligned}$$

using the divergence theorem.

The first term may be transformed according to the definition of CAUCHY stress. The virtual work formulation, again supplemented with the body force, consequently becomes

$$\delta W = \int_{A_\sigma} \mathbf{t} \cdot \delta \mathbf{u} dA_\sigma - \int_V \boldsymbol{\sigma} : \left(\frac{\partial \delta \mathbf{u}}{\partial \mathbf{x}} \right) dV + \int_V \mathbf{b} \cdot \delta \mathbf{u} dV = 0 \quad (\text{A.30})$$

As mentioned in Section A.1 the deformation gradient \mathbf{F} may be decomposed into a symmetric stretch tensor and a antisymmetric rotation tensor (A.8). Similarly, the virtual deformation gradient $(\partial \delta \mathbf{u} / \partial \mathbf{x})$ is decomposed into a symmetric virtual strain tensor $\delta \boldsymbol{\epsilon}$ and a antisymmetric virtual rotation tensor $\delta \boldsymbol{\omega}$. Since a contraction (“: -product”) of a antisymmetric tensor with a symmetric one (the stress tensor) is zero, (A.30) can be rewritten in the familiar form

$$\delta W = \int_V \boldsymbol{\sigma} : \delta \boldsymbol{\epsilon} dV - \int_V \mathbf{b} \cdot \delta \mathbf{u} dV - \int_{A_\sigma} \mathbf{t} \cdot \delta \mathbf{u} dA_\sigma = 0 \quad (\text{A.31})$$

² $\mathbf{A} : \mathbf{B} = \sum_i \sum_j A_{ij} B_{ij}$

The first integral is the *virtual strain energy* δU and the last two terms give the *virtual external work* δW_{ex} . Thus, the principle of virtual displacements states briefly that equilibrium applies if

$$\delta W = \delta U - \delta W_{ex} = 0 \quad (\text{A.32})$$

For numerical procedures, as presented in the sections to come, it is found to be unfortunate that the weak variational equilibrium equation above is expressed in terms of integrals over an *unknown* and varying volume V and surface area A_σ . Therefore, the virtual work expression is transformed in terms of a *known*, e.g. undeformed configuration. For constant volume and surface area or small changes the definition in (A.28) becomes:

$$\delta W = \int_{\text{}_0V} \text{}_0\mathbf{r} \cdot \delta \mathbf{u}_0 dV = 0 \quad \text{with } \text{}_0\mathbf{r} = \mathbf{J} \mathbf{r} \quad (\text{A.33})$$

The energies have to be the same regardless of the state the integrals are taken. Thus, in order to make δU invariant, different virtual strain measures require respective stresses to be paired with, i.e. the stress and virtual strain measures have to be *work conjugate*. Ultimately, it applies [31]

$$\int_V \boldsymbol{\sigma} : \delta \boldsymbol{\epsilon} dV = \int_{\text{}_0V} \mathbf{S} : \delta \mathbf{E}_0 dV \quad (\text{A.34})$$

with the 2nd PIOLA-KIRCHHOFF stress tensor \mathbf{S} and the virtual GREEN-LAGRANGE strain tensor $\delta \mathbf{E}$, according to the measures presented in Section A.3 and A.2 respectively. Finally, the entire virtual work expression with respect to the undeformed, initial configuration can be completed and becomes

$$\delta W = \int_{\text{}_0V} \mathbf{S} : \delta \mathbf{E}_0 dV - \int_{\text{}_0V} \text{}_0\mathbf{b} \cdot \delta \mathbf{u}_0 dV - \int_{\text{}_0A_\sigma} \text{}_0\mathbf{t} \cdot \delta \mathbf{u}_0 dA_\sigma = 0 \quad (\text{A.35})$$

with $\text{}_0\mathbf{b} = \mathbf{J} \mathbf{b}$ and $\text{}_0\mathbf{t} = (dA/\text{}_0dA) \mathbf{t}$. In contrast to the differential equation system (A.26), there are no problems to use the undeformed state as reference. In addition, during a deformation process, the reference configuration can be any one of the previous, thus known equilibrium states and not necessarily the original, unloaded state. This is used in the incremental updated LAGRANGE procedure for numerical simulations.

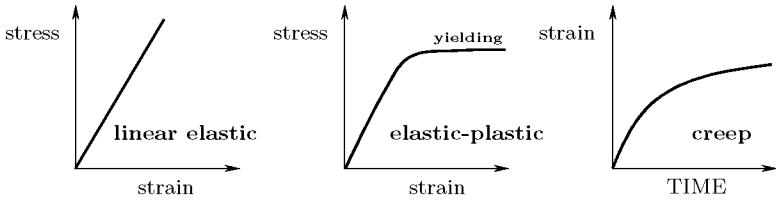


Figure A.3: *Typical material behaviour patterns.*

A.5 Constitutive Equations

To complete the collection of the “ingredients” necessary for structural analyses and to construct numerical procedures, the relations between stresses and strains are to be arranged which are given by the material behaviour. Since the present work is restricted to geometrically non-linear behaviour of thin-walled structures, the procedures of which the derivations are described consider possible *large displacements and rotations* but *small strains*. Therefore, material nonlinearities, like yielding or creep (see Figure A.3), are not taken into account herein; and from a description of nonlinear elasticity models, plasticity models or creep laws could be refrained.

The used materials are assumed to be **linear elastic**. The **HOOKEAN law** for elastic material describes the relationship between the 2nd PIOLA-KIRCHHOFF stress tensor S_{ij} and the GREEN-LAGRANGE strain tensor E_{kl} by the forth-order tensor C_{ijkl} :

$$S_{ij} = \sum_{k,l} C_{ijkl} E_{kl} \quad \text{resp.} \quad \mathbf{S} = \mathbf{C} : \mathbf{E} \quad (\text{A.36})$$

Since both the strain tensor and the stress tensor are invariant to rotations only the current strain of the material affects the components of the stress tensor. Thus, as long as the strains are small, the general relation for elastic materials above may be used also for geometrically nonlinear problems.

In (A.36) the HOOKEAN law is specified with respect to the initial configuration of an arbitrary deformable body. For the case of *linear* elasticity it is assumed that the strains are small and that the material tensor \mathbf{C} remains constant during the deformation process. Therefore, the relation can also be expressed in terms of the current state by $\boldsymbol{\sigma} = \mathbf{C} : \mathbf{e}$ with the CAUCHY stress tensor $\boldsymbol{\sigma}$ and the ALMANZI strain tensor \mathbf{e} . For larger

strains the constitutive tensor has to be “pushed forward”, i.e. transformed by the adequate use of the transformation gradient [14, 17]. But in case of infinitesimal small displacements the stresses are connected with the *linear* strains $\boldsymbol{\varepsilon}$ in the form

$$\boldsymbol{\sigma} = \mathbf{C} : \boldsymbol{\varepsilon} \quad (\text{A.37})$$

This relation, applicable in linear continuum mechanics, is probably the best known version of the HOOKEAN material law.

Due to the symmetry in \mathbf{S} and \mathbf{E} the number of independent coefficients C_{ijkl} reduces from 81 to 36. Furthermore, the rule of \mathbf{C} as derivative of the strain energy density function gives that

$$C_{ijkl} = C_{klij}$$

which yields a further reduction to 21 constants.

The constitutive relation of the general linear elastic, **anisotropic** material in (A.36) can also be expressed in matrix form:

$$\begin{Bmatrix} S_{11} \\ S_{22} \\ S_{33} \\ S_{23} \\ S_{13} \\ S_{12} \end{Bmatrix} = \begin{bmatrix} C_{11} & C_{12} & C_{13} & C_{14} & C_{15} & C_{16} \\ C_{21} & C_{22} & C_{23} & C_{24} & C_{25} & C_{26} \\ C_{31} & C_{32} & C_{33} & C_{34} & C_{35} & C_{36} \\ C_{41} & C_{42} & C_{43} & C_{44} & C_{45} & C_{46} \\ C_{51} & C_{52} & C_{53} & C_{54} & C_{55} & C_{56} \\ C_{61} & C_{62} & C_{63} & C_{64} & C_{65} & C_{66} \end{bmatrix} \begin{Bmatrix} E_{11} \\ E_{22} \\ E_{33} \\ 2E_{23} \\ 2E_{13} \\ 2E_{12} \end{Bmatrix} \quad (\text{A.38})$$

or in common abbreviated form:

$$\{S_{ij}\} = \mathbf{C} \{E_{ij}\} \quad (\text{A.39})$$

with the symmetric 6×6 material matrix \mathbf{C} and the stresses $\{S_{ij}\}$ and strains $\{E_{ij}\}$ in vector form.

Special materials have reduced forms of the relation above. **Orthotropic** materials for instance have three planes of symmetry which reduces the number of material coefficients to nine. The *flexibility matrix* \mathbf{C}^{-1} , i.e. the inverse of the elastic matrix \mathbf{C} , for orthotropic materials is given by

$$\{E_{ij}\} = \mathbf{C}^{-1} \{S_{ij}\} \quad (\text{A.40})$$

$$\mathbf{C}^{-1} = \begin{bmatrix} \frac{1}{E_1} & -\frac{\nu_{21}}{E_2} & -\frac{\nu_{31}}{E_3} & 0 & 0 & 0 \\ -\frac{\nu_{12}}{E_1} & \frac{1}{E_2} & -\frac{\nu_{32}}{E_3} & 0 & 0 & 0 \\ -\frac{\nu_{13}}{E_1} & -\frac{\nu_{23}}{E_2} & \frac{1}{E_3} & 0 & 0 & 0 \\ 0 & 0 & 0 & \frac{1}{G_{23}} & 0 & 0 \\ 0 & 0 & 0 & 0 & \frac{1}{G_{13}} & 0 \\ 0 & 0 & 0 & 0 & 0 & \frac{1}{G_{12}} \end{bmatrix} \quad (\text{A.41})$$

with the material constants relative to the symmetry planes, which are the YOUNG’S moduli E_1 , E_2 , and E_3 , the shear moduli G_{23} , G_{13} , and G_{12} , as well as the POISSON ratios

$$\nu_{ij} = -\frac{E_{jj}}{E_{ii}}$$

Furthermore, due to the symmetry of \mathbf{C} and \mathbf{C}^{-1} it applies:

$$\frac{\nu_{ij}}{E_{ii}} = \frac{\nu_{ji}}{E_{jj}}$$

and thus only three of the six POISSON’S ratios have to be specified.

Transversally isotropic materials need only five constants in the matrices \mathbf{C} and \mathbf{C}^{-1} for their constitutive description, because $C_{55} = C_{66}$ and $C_{44} = \frac{1}{2}(C_{11} - C_{12})$ [31]. A single ply of a laminated composite shell for instance is usually considered to be transversally isotropic and homogeneous. In this case, the material constants are given with respect to local coordinate systems which are given by the particular fiber orientation of the ply.

Isotropic materials finally may be specified by only two independent constants, since in this special case every plane is a plane of symmetry and every axis an axis of symmetry [31]. Alternatively to (A.36) the according constitutive relation is often expressed in the form

$$S_{ij} = 2G E_{ij} + \lambda \delta_{ij} \sum_k E_{kk} \quad (\text{A.42})$$

with the LAMÉ constant λ and the shear modulus G . The YOUNG’S modulus E and the POISSON’S ratio ν are related to these two coefficients by

$$E = \frac{G(3\lambda + 2G)}{G + \lambda} \quad \text{and} \quad \nu = \frac{\lambda}{2(G + \lambda)}$$

respectively.

In analysis of thin-walled structures the special case of **plane stress** arise, where the stress orthogonal to the middle surface of a plate or shell is approximately zero such that $S_{33} \approx 0$ [31]. Infinitesimal changes in the wall thickness are therefore given by the two in-plane stresses, viz:

$$E_{33} = - \left(\frac{\nu_{13}}{E_1} S_{11} + \frac{\nu_{23}}{E_2} S_{22} \right) \quad (\text{A.43})$$

for orthotropic materials. Furthermore, for thin laminated composite shells it is assumed that the shear strains E_{23} and E_{13} as well as the shear stresses S_{23} and S_{13} may be neglected (KIRCHHOFF hypothesis; see Section B). Hence, for plane stress and *transversally isotropic* material the constitutive equations (A.41) and (A.38) are further reduced to

$$\begin{Bmatrix} E_{11} \\ E_{22} \\ 2E_{12} \end{Bmatrix} = \begin{bmatrix} \frac{1}{E_1} & -\frac{\nu_{21}}{E_2} & 0 \\ -\frac{\nu_{12}}{E_1} & \frac{1}{E_2} & 0 \\ 0 & 0 & \frac{1}{G_{12}} \end{bmatrix} \begin{Bmatrix} S_{11} \\ S_{22} \\ S_{12} \end{Bmatrix} \quad (\text{A.44})$$

for the strain-stress relation $\{E_{ij}\} = \mathbf{C}^{-1}\{S_{ij}\}$, and by inversion

$$\begin{Bmatrix} S_{11} \\ S_{22} \\ S_{12} \end{Bmatrix} = \begin{bmatrix} \frac{E_1}{1-\nu_{12}\nu_{21}} & \frac{\nu_{12}E_2}{1-\nu_{12}\nu_{21}} & 0 \\ \frac{\nu_{21}E_1}{1-\nu_{12}\nu_{21}} & \frac{E_2}{1-\nu_{12}\nu_{21}} & 0 \\ 0 & 0 & G_{12} \end{bmatrix} \begin{Bmatrix} E_{11} \\ E_{22} \\ 2E_{12} \end{Bmatrix} \quad (\text{A.45})$$

for the stress-strain relation $\{S_{ij}\} = \mathbf{Q}\{E_{ij}\}$. The material matrix \mathbf{Q} is the *reduced elastic* matrix for plane stress and thin, transversally isotropic plates or shells, i.e. a reduced version of the elastic matrix \mathbf{C} .

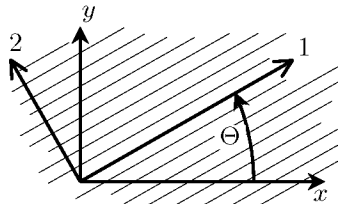


Figure A.4: *Positive rotation from the structure reference coordinates (x, y) to the local ply coordinates $(1, 2)$*

As aforementioned, the material constants of laminated shells are given with respect to local ply coordinate systems, which are given by the

particular fibre orientation, i.e. the reduced material stiffnesses \mathbf{Q}_k of a single ply are specified in terms of the particular principle axes (1, 2). In order to describe the contribution of the plies to the stiffness of the laminate consistently, in the classical lamination theory the constants of each ply are transformed from the ply coordinate system (1, 2) to the reference coordinate system of the laminate (x, y), see Figure A.4. This transformation consists of a rotation about the shell normal, which with the *transformation matrix* \mathbf{T} may be written in form of a matrix manipulation; first for the stresses:

$$\begin{Bmatrix} S_{xx} \\ S_{yy} \\ S_{xy} \end{Bmatrix} = \begin{bmatrix} \cos^2 \Theta & \sin^2 \Theta & 2 \sin \Theta \cos \Theta \\ \sin^2 \Theta & \cos^2 \Theta & -2 \sin \Theta \cos \Theta \\ -\sin \Theta \cos \Theta & \sin \Theta \cos \Theta & \cos^2 \Theta - \sin^2 \Theta \end{bmatrix}^{-1} \begin{Bmatrix} S_{11} \\ S_{22} \\ S_{12} \end{Bmatrix} \quad (\text{A.46})$$

Since it may be assumed that the in-plane deformations of laminated shells remain small, in general the constitutive equations are formulated with components of the linear strain tensor and CAUCHY stress tensor.

For the transformation of the strains the transformation matrix \mathbf{T} in (A.46) has possibly to be modified to consider that the common shearing strains γ_{ij} correspond to the double shear distortions, $2E_{ij}$ [34]. With the rotation matrix \mathbf{T}_ε for the strains (in present case identical with \mathbf{T}) the transformation of the stress-strain relation may finally be written in the following form:

$$\begin{Bmatrix} S_{xx} \\ S_{yy} \\ S_{xy} \end{Bmatrix} = \mathbf{T}^{-1} \mathbf{Q} \mathbf{T}_\varepsilon \begin{Bmatrix} E_{xx} \\ E_{yy} \\ 2E_{xy} \end{Bmatrix} \quad (\text{A.47})$$

Hence, the transformed reduced stiffness matrix for single ply is given by

$$\bar{\mathbf{Q}} = \mathbf{T}^{-1} \mathbf{Q} \mathbf{T}_\varepsilon \quad (\text{A.48})$$

Finally, the constitutive equation (A.46) may be rewritten in short form as

$$\boldsymbol{\sigma} = \bar{\mathbf{Q}} \boldsymbol{\varepsilon} \quad (\text{A.49})$$

In the classical lamination theory this equation is used to determine the stress-strain relation for each layer in laminated composite.

Appendix B

Bending of Plates

Plates are structure elements where one of the dimensions, the plate thickness, is considerably smaller than the other two. In three-dimensional thin-walled structures the plates may support both in-plane and out-of-plane loading. Since plates are thin, also when the structure are three-dimensional the local behaviour is two-dimensional under plane stress. Furthermore, the plate thickness h is assumed to be constant.

The comments on plates herein are restricted to Cartesian coordinates with the axes x and y lying in the middle surface of the undeformed structure. The z -axis is perpendicular to the middle surface. The coordinates x , y and z correspond to the spatial coordinates x_1 , x_2 , and x_3 , respectively, defined in Appendix A.1. Accordingly, the displacement components u_1 , u_2 , and u_3 of the displacements vector \mathbf{u} are assigned to u , v and w , respectively.

In order to emphasize the essentials, primarily the deflections and the strains are assumed to remain small. Therefore and since the plate is thin the displacements may approximatively be described by

$$\begin{aligned}u(x, y, z) &\approx \bar{u}(x, y) + z \phi_x(x, y) \\v(x, y, z) &\approx \bar{v}(x, y) + z \phi_y(x, y) \\w(x, y, z) &\approx \bar{w}(x, y)\end{aligned}\tag{B.1}$$

Thus, the deformation is controlled by the in-plane displacements $\bar{u}(x, y)$ and $\bar{v}(x, y)$, the out-of-plane displacement $\bar{w}(x, y)$ and the rotations of the middle surface $\phi_x(x, y)$ and $\phi_y(x, y)$. The middle surface of the plate

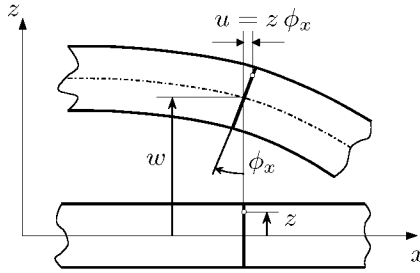


Figure B.1: Displacement in x direction due to rotation ϕ_x

is specified at $z = 0$. The rotations ϕ_x and ϕ_y describe the slope of the middle surface normal to its initial direction (see Fig. B.1).

In accordance with the definition of the linear ALMANSI strain tensor ε (Eq. A.18), the *normal strains* ε_{ii} and the *shear strains* γ_{ij} relating to the deformations above are given by

$$\begin{aligned} \varepsilon_{xx} &= \frac{\partial u}{\partial x} = \frac{\partial \bar{u}}{\partial x} + z \frac{\partial \phi_x}{\partial x}, & \varepsilon_{yy} &= \frac{\partial v}{\partial y} = \frac{\partial \bar{v}}{\partial y} + z \frac{\partial \phi_y}{\partial y}, \\ \gamma_{xy} &= \frac{\partial u}{\partial y} + \frac{\partial v}{\partial x} = \left(\frac{\partial \bar{u}}{\partial y} + \frac{\partial \bar{v}}{\partial x} \right) + z \left(\frac{\partial \phi_x}{\partial y} + \frac{\partial \phi_y}{\partial x} \right), & (B.2) \\ \gamma_{xz} &= \frac{\partial u}{\partial z} + \frac{\partial w}{\partial x} = \phi_x + \frac{\partial \bar{w}}{\partial x}, & \gamma_{yz} &= \frac{\partial v}{\partial z} + \frac{\partial w}{\partial y} = \phi_y + \frac{\partial \bar{w}}{\partial y} \end{aligned}$$

For thin plates the stress in z -direction may be neglected. Thus, a state of plane stress with a (CAUCHY) *stress* $\sigma_{zz} = 0$ is assumed. The HOOKEAN law (see Appendix A.5) for plane stress and isotropic materials connects the *normal stresses* σ_{ii} with the strains ε_{ii} by

$$\sigma_{xx} = \frac{E}{1 - \nu^2} (\varepsilon_{xx} + \nu \varepsilon_{yy}), \quad \sigma_{yy} = \frac{E}{1 - \nu^2} (\varepsilon_{yy} + \nu \varepsilon_{xx}) \quad (B.3)$$

The *shear stresses* τ_{ij} are specified by

$$\tau_{xy} = G \gamma_{xy}, \quad \tau_{yz} = G \gamma_{yz}, \quad \tau_{zx} = G \gamma_{zx} \quad (B.4)$$

where E stands for the YOUNG modulus, G for the shear modulus and ν for the POISSON'S ratio. Thereby it is additionally assumed that the plate thickness does not change due to deformation, thus: $\varepsilon_{zz} = 0$.

With the strain definitions in (B.2) the stresses may be written as

$$\begin{aligned}
 \sigma_{xx} &= \frac{E}{1-\nu^2} \left[\left(\frac{\partial \bar{u}}{\partial x} + \nu \frac{\partial \bar{v}}{\partial y} \right) + z \left(\frac{\partial \phi_x}{\partial x} + \nu \frac{\partial \phi_y}{\partial y} \right) \right] \\
 \sigma_{yy} &= \frac{E}{1-\nu^2} \left[\left(\frac{\partial \bar{v}}{\partial y} + \nu \frac{\partial \bar{u}}{\partial x} \right) + z \left(\frac{\partial \phi_y}{\partial y} + \nu \frac{\partial \phi_x}{\partial x} \right) \right] \\
 \tau_{xy} &= G \left[\left(\frac{\partial \bar{u}}{\partial y} + \frac{\partial \bar{v}}{\partial x} \right) + z \left(\frac{\partial \phi_x}{\partial y} + \nu \frac{\partial \phi_y}{\partial x} \right) \right] \\
 \tau_{xz} &= G \left[\phi_x + \frac{\partial \bar{w}}{\partial x} \right], \quad \bar{\tau}_{yz} = G \left[\phi_y + \frac{\partial \bar{w}}{\partial y} \right],
 \end{aligned}
 \tag{B.5}$$

B.1 Pure bending of plates

To derive the equilibrium equations a plate element with all acting lateral loads and stress resultants is considered as shown in Figure B.2. For the stress resultants the integrations are conducted over the plate

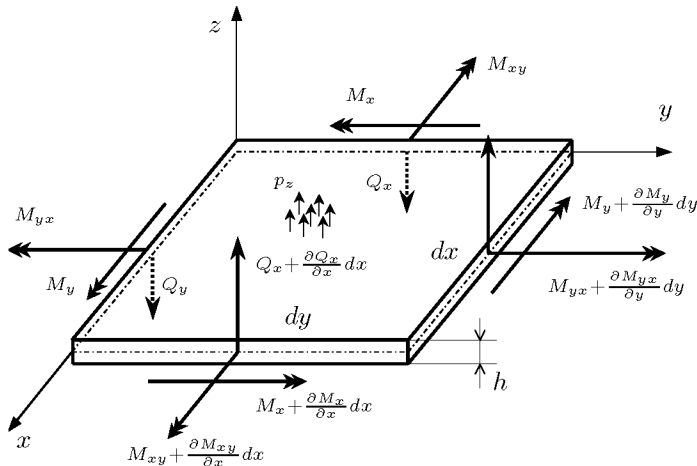


Figure B.2: Segment of a plate

thickness, thus, the dimensions are force per length and moment per length. In the classical *linear plate theory* for small displacements in-plane loads are ignored or treated separately as a *membrane problem*, consequently in the strain and stress expressions in (B.2) and (B.5) the terms with in-plane displacements u or v are omitted. The remaining

resultants are

$$\begin{aligned}
 \text{Shearing forces:} \quad Q_x &= \int_{-h/2}^{h/2} \tau_{xz} \, dz, & Q_y &= \int_{-h/2}^{h/2} \tau_{yz} \, dz \\
 \text{Bending moments:} \quad M_x &= \int_{-h/2}^{h/2} \sigma_{xx} z \, dz, & M_y &= \int_{-h/2}^{h/2} \sigma_{yy} z \, dz \\
 \text{Torsional moments:} \quad M_{xy} &= - \int_{-h/2}^{h/2} \tau_{xy} z \, dz = -M_{yx}
 \end{aligned} \tag{B.6}$$

The balance of forces in z -direction yields

$$\frac{\partial Q_x}{\partial x} + \frac{\partial Q_y}{\partial y} = -p_z \tag{B.7}$$

Accordingly, the balance of moments about the x and the y axis gives

$$\begin{aligned}
 \frac{\partial M_x}{\partial x} + \frac{\partial M_{yx}}{\partial y} &= Q_x \\
 \frac{\partial M_y}{\partial y} - \frac{\partial M_{xy}}{\partial x} &= Q_y
 \end{aligned} \tag{B.8}$$

By inserting Q_x and Q_y from (B.8) into (B.7) and with $M_{xy} = -M_{yx}$ the following equilibrium equation may be determined [76]:

$$\frac{\partial^2 M_x}{\partial x^2} - 2 \frac{\partial^2 M_{xy}}{\partial x \partial y} + \frac{\partial^2 M_y}{\partial y^2} = -p_z \tag{B.9}$$

B.1.1 Mindlin-Reissner plate theory

The stress expressions (B.5) inserted into the formulas for the stress resultants in (B.6) special elasticity relations may be defined. For instance (neglecting the in-plane strains):

$$\begin{aligned}
 M_x &= \int_{-h/2}^{h/2} \sigma_{xx} z \, dz = \frac{E}{1-\nu^2} \left(\frac{\partial \phi_x}{\partial x} + \nu \frac{\partial \phi_y}{\partial y} \right) \int_{-h/2}^{h/2} z^2 \, dz \\
 &= \frac{E h^3}{12(1-\nu^2)} \left(\frac{\partial \phi_x}{\partial x} + \nu \frac{\partial \phi_y}{\partial y} \right)
 \end{aligned} \tag{B.10}$$

The term¹

$$D = \frac{E}{1 - \nu^2} \int_{-h/2}^{h/2} z^2 dz = \frac{E h^3}{12(1 - \nu^2)} \quad (\text{B.11})$$

is called the *flexural rigidity of the plate* [76] or *plate bending stiffness* [31]. Accordingly, the elasticity relations of all stress resultants may be obtained

$$\begin{aligned} Q_x &= G h \left[\phi_x + \frac{\partial \bar{w}}{\partial x} \right], & Q_y &= G h \left[\phi_y + \frac{\partial \bar{w}}{\partial y} \right], \\ M_x &= D \left(\frac{\partial \phi_x}{\partial x} + \nu \frac{\partial \phi_y}{\partial y} \right), & M_y &= D \left(\frac{\partial \phi_y}{\partial y} + \nu \frac{\partial \phi_x}{\partial x} \right), \\ M_{xy} &= \frac{D}{2} \left(\frac{\partial \phi_y}{\partial x} + \nu \frac{\partial \phi_x}{\partial y} \right) (1 - \nu) \end{aligned} \quad (\text{B.12})$$

With the three equilibrium equations (B.7) and (B.8) and the five elasticity relations in (B.12) eight equations are available to specify the eight unknown, i.e. the five stress resultants and the three kinematic measures \bar{w} , ϕ_x and ϕ_y . The plate theory based hereunto is called after E. REISSNER and R.D. MINDLIN [43]. Important is that this theory considers also the transverse shear elasticity of “thick” or sandwich plates.

B.1.2 Kirchhoff thin-plate theory

Since the partial differential equations including the transverse shear influence is difficult to solve for “thin” plates additional simplifications are done by assuming that the shear stiffness is infinite. Because the transverse forces remain finite, with the first row of (B.12) it follows that

$$\gamma_{xz} = \phi_x + \frac{\partial \bar{w}}{\partial x} = 0, \quad \gamma_{yz} = \phi_y + \frac{\partial \bar{w}}{\partial y} = 0. \quad (\text{B.13})$$

Consequently, a vector perpendicular to the undeformed middle surface is also perpendicular to the deformed middle surface. The corresponding theory of “thin”, shear stiff plates traces back to G. KIRCHHOFF [43].

According to (B.13) the rotations ϕ_x and ϕ_y are given by $\phi_x = -\partial \bar{w} / \partial x$ and $\phi_y = -\partial \bar{w} / \partial y$ respectively. Hence, in accordance to (B.1) the dis-

¹To simplify matters the plate material is assumed to be homogeneous and isotropic.

placements for the flexural motion may be approximated as

$$\begin{aligned} u(x, y, z) &\approx -z \frac{\partial \bar{w}}{\partial x}(x, y), & v(x, y, z) &\approx -z \frac{\partial \bar{w}}{\partial y}(x, y), \\ w(x, y, z) &\approx \bar{w}(x, y) \end{aligned} \quad (\text{B.14})$$

Assuming that the strains of the middle surface are negligibly small the linear strains corresponding to small deflections are given by

$$\begin{aligned} \varepsilon_{xx} &= \frac{\partial u}{\partial x} = -z \frac{\partial^2 w}{\partial x^2}, & \varepsilon_{yy} &= \frac{\partial v}{\partial y} = -z \frac{\partial^2 w}{\partial y^2}, \\ \gamma_{xy} &= \frac{\partial u}{\partial y} + \frac{\partial v}{\partial x} = -z 2 \frac{\partial^2 w}{\partial x \partial y}, & \gamma_{xz} &= 0, & \gamma_{yz} &= 0 \end{aligned} \quad (\text{B.15})$$

assuming that $w = \bar{w}$. These strains inserted into the HOOKEAN law for plane stress yields, similarly to (B.5), the following stress expressions:

$$\begin{aligned} \sigma_{xx} &= -\frac{Ez}{1-\nu^2} \left(\frac{\partial^2 w}{\partial x^2} + \nu \frac{\partial^2 w}{\partial y^2} \right), & \sigma_{yy} &= -\frac{Ez}{1-\nu^2} \left(\frac{\partial^2 w}{\partial y^2} + \nu \frac{\partial^2 w}{\partial x^2} \right), \\ \tau_{xy} &= -2Gz \frac{\partial^2 w}{\partial x \partial y} \end{aligned} \quad (\text{B.16})$$

The elasticity relations of the stress resultants in (B.6) may also be modified for the case of pure plate bending. The moments written in terms of curvatures are

$$\begin{aligned} M_x &= -D \left(\frac{\partial^2 w}{\partial x^2} + \nu \frac{\partial^2 w}{\partial y^2} \right), & M_y &= -D \left(\frac{\partial^2 w}{\partial y^2} + \nu \frac{\partial^2 w}{\partial x^2} \right), \\ M_{xy} &= D(1-\nu) \frac{\partial^2 w}{\partial x \partial y} = -M_{yx} \end{aligned} \quad (\text{B.17})$$

For the transverse forces Q_x and Q_y there is no elasticity relation in the KIRCHHOFF thin plate theory. They are ascertainable by the use of the equilibrium equations (B.8).

With the equilibrium equation (B.9) and the moments in (B.17) above four equations are available to specify the the four unknown (the deflection w and three moments) [43]. The expressions (B.17) inserted into (B.9) finally yields the common KIRCHHOFF differential equation for thin, flat plates and small deformations

$$\frac{\partial^4 w}{\partial x^4} + 2 \frac{\partial^4 w}{\partial x^2 \partial y^2} + \frac{\partial^4 w}{\partial y^4} = \frac{p_z}{D} \quad (\text{B.18})$$

B.2 Combination of bending and in-plane loading

In the plate theories presented above it is assumed that the plates are bent by lateral loads and that the deflections are so small that any strain of the middle surface of the plate may be neglected. The middle surface is considered as the neutral plane of the plate. If in addition to the lateral loads in-plane forces are acting at the middle surface, then stretching of the middle surface is provoked and the corresponding stresses are to be considered [76].

Ignoring any lateral load the pure in-plane *membrane* behaviour may be considered. Then the resultants of the normal and shear stresses on the cross section of an undeformed plate or “membrane” element are defined as

$$\begin{aligned}
 N_x &= \int_{-h/2}^{h/2} \sigma_{xx} dz = \frac{E}{1-\nu^2} \left[\frac{\partial u}{\partial x} + \nu \frac{\partial v}{\partial y} \right] h = \bar{\sigma}_{xx} h \\
 N_y &= \int_{-h/2}^{h/2} \sigma_{yy} dz = \frac{E}{1-\nu^2} \left[\frac{\partial v}{\partial y} + \nu \frac{\partial u}{\partial x} \right] h = \bar{\sigma}_{yy} h \\
 N_{xy} &= \int_{-h/2}^{h/2} \tau_{xy} dz = G \left[\frac{\partial u}{\partial y} + \frac{\partial v}{\partial x} \right] h = \bar{\tau}_{xy} h
 \end{aligned} \tag{B.19}$$

These are the in-plane or *membrane forces* per unit length due to the stresses acting on the edge faces, see Figure B.3.

Projecting the forces shown in Figure B.3 in the x - and y -axes the following equilibrium equations may be obtained:

$$\begin{aligned}
 \frac{\partial N_x}{\partial x} + \frac{\partial N_{xy}}{\partial y} &= 0 \\
 \frac{\partial N_y}{\partial y} + \frac{\partial N_{xy}}{\partial x} &= 0
 \end{aligned} \tag{B.20}$$

Inertia and body forces were set to zero to shorten subsequent formulations. Above equations are independent of deflections and moments. Thus, as long as the plate remains flat, the equilibrium equations of a membrane above may be treated separately of the equilibrium equations of lateral loaded plates. But, if the stresses in the middle surface are not small their effect of bending of the plate has to be considered [76]. Respecting the projection of the forces shown in Figure B.3 in z -direction,

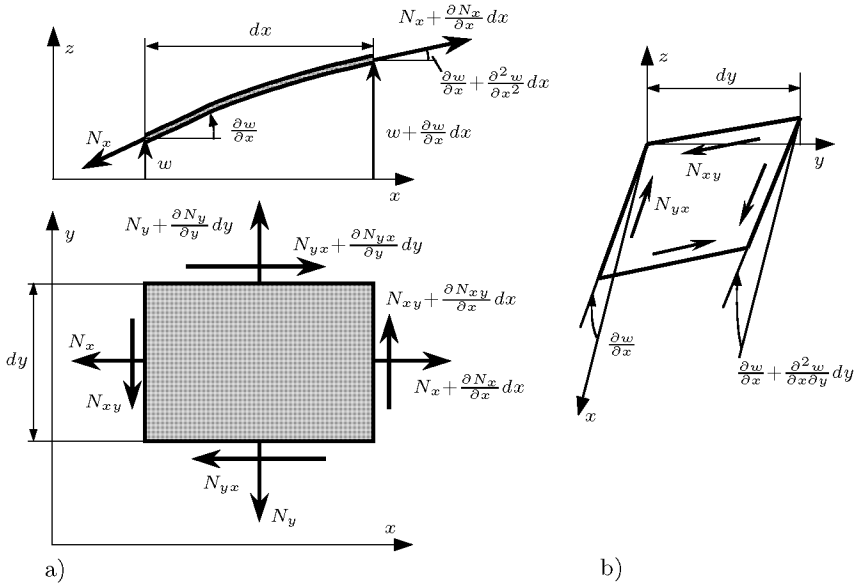


Figure B.3: Membrane forces with deflections

the deflection of the plate has to be taken into account. The deflection is still assumed to be small and the applied forces remain therefore unchanged. Thus, due to the different slopes at x and at $x + dx$ of the deformed plate segment the membrane force N_x generates a resulting force on the z -axis of

$$-N_x dy \frac{\partial w}{\partial x} + \left(N_x + \frac{\partial N_x}{\partial x} dx \right) \left(\frac{\partial w}{\partial x} + \frac{\partial^2 w}{\partial x^2} dx \right) dy$$

After neglecting the small member of higher order it remains

$$N_x \frac{\partial^2 w}{\partial x^2} dx dy + \frac{\partial N_x}{\partial x} \frac{\partial w}{\partial x} dx dy \quad (\text{B.21})$$

The projection of the membrane force N_y on the z axis yields similarly

$$N_y \frac{\partial^2 w}{\partial y^2} dx dy + \frac{\partial N_y}{\partial y} \frac{\partial w}{\partial y} dx dy \quad (\text{B.22})$$

With the angles $\frac{\partial w}{\partial y}$ and $\frac{\partial w}{\partial y} + \frac{\partial^2 w}{\partial x \partial y} dx$ about the x axis and $\frac{\partial w}{\partial x}$ and $\frac{\partial w}{\partial x} + \frac{\partial^2 w}{\partial x \partial y} dx$ about the y axis, the z components of the shear forces N_{xy}

and N_{yx} may be obtained as

$$N_{xy} \frac{\partial^2 w}{\partial x \partial y} dx dy + \frac{\partial N_{xy}}{\partial x} \frac{\partial w}{\partial y} dx dy, \quad \text{resp.}$$

$$N_{yx} \frac{\partial^2 w}{\partial x \partial y} dx dy + \frac{\partial N_{yx}}{\partial y} \frac{\partial w}{\partial x} dx dy$$

With $N_{xy} = N_{yx}$ one expression for all shear forces projected on the z -axis is given by

$$2N_{xy} \frac{\partial^2 w}{\partial x \partial y} dx dy + \frac{\partial N_{xy}}{\partial x} \frac{\partial w}{\partial y} dx dy + \frac{\partial N_{xy}}{\partial y} \frac{\partial w}{\partial x} dx dy \quad (\text{B.23})$$

Now, the expressions in (B.21), (B.22) and (B.23) may be added to the equilibrium equation (B.7) of the plate. According to (B.20) the first derivatives of the membrane forces disappear. Finally, the following equilibrium equation remains:

$$\frac{\partial Q_x}{\partial x} + \frac{\partial Q_y}{\partial y} + N_x \frac{\partial^2 w}{\partial x^2} + 2N_{xy} \frac{\partial^2 w}{\partial x \partial y} + N_y \frac{\partial^2 w}{\partial y^2} = -p_z \quad (\text{B.24})$$

With the balance of moments (B.8) the transverse shear resultants may be eliminated and the differential equation of equilibrium may be expressed as

$$\frac{\partial^2 M_x}{\partial x^2} - 2 \frac{\partial^2 M_{xy}}{\partial x \partial y} + \frac{\partial^2 M_y}{\partial y^2} = - \left(p_z + N_x \frac{\partial^2 w}{\partial x^2} + 2N_{xy} \frac{\partial^2 w}{\partial x \partial y} + N_y \frac{\partial^2 w}{\partial y^2} \right) \quad (\text{B.25})$$

With the elasticity relations in (B.17), which is still valid for small displacements, the moments may be replaced by terms of deflection, that is

$$\frac{\partial^4 w}{\partial x^4} + 2 \frac{\partial^4 w}{\partial x^2 \partial y^2} + \frac{\partial^4 w}{\partial y^4} = \frac{1}{D} \left(p_z + N_x \frac{\partial^2 w}{\partial x^2} + 2N_{xy} \frac{\partial^2 w}{\partial x \partial y} + N_y \frac{\partial^2 w}{\partial y^2} \right) \quad (\text{B.26})$$

This common differential equation of equilibrium, which traces back to SAINT VENANT, is to be used instead of the KIRCHHOFF plate equation (Eq. B.18) if the membrane forces N_x , N_y and N_{xy} are not small compared to critical (compression) forces [76].

B.2.1 Large deflections of plates

To calculate the lateral deflections of a plate which is combined loaded laterally and in the middle surface, the ST. VENANT differential equation (B.26) may be solved by determining bi-harmonic functions, which satisfy the boundary conditions, only if the deflections are small in comparison with the plate thickness. In the plate theories for small deflections it is assumed that stretching of the middle surface may be neglected in case of pure bending or that the strain of the middle surface is given by external membrane forces. After TIMOSHENKO the stretching of the middle surface of a plate due to bending has to be taken into account in the cases where the deflection exceeds about 40 percent of the wall thickness [76]. Considering large deflections of plates the ST. VENANT differential equation (B.26) may be used but the membrane forces N_x , N_y and N_{xy} now depend not only on the external loads applied in the middle surface but also on the strain of the middle surface due to bending.

Since in the equation system of equilibrium (B.20) there are three unknown membrane forces N_x , N_y and N_{xy} an additional equation has to be specified to determine them [76]. To do so, the strain in the middle surface of a plate during bending is considered: the elongation of a

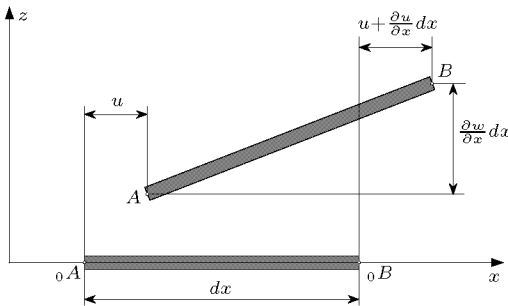


Figure B.4: *Elongation of a plate element due to large deflection [76].*

linear plate element $0A_0B$ (see Fig. B.4) due to the displacement u in x -direction is $(\partial u/\partial x) dx$. The z component of the distance between A and B due to the rotation angle $\partial w/\partial x$ is $(\partial w/\partial x) dx$. Thus, the new

length ds of the element is

$$\begin{aligned}
 ds &= \sqrt{\left(dx + \frac{\partial u}{\partial x} dx\right)^2 + \left(\frac{\partial w}{\partial x} dx\right)^2} = \\
 &dx \sqrt{1 + 2\frac{\partial u}{\partial x} + \left(\frac{\partial u}{\partial x}\right)^2 + \left(\frac{\partial w}{\partial x}\right)^2} \quad (\text{B.27}) \\
 &\approx dx \left\{1 + \frac{\partial u}{\partial x} + \frac{1}{2} \left(\frac{\partial w}{\partial x}\right)^2 + \dots\right\}
 \end{aligned}$$

using the approximation $\sqrt{1 + \xi} \approx 1 + \frac{1}{2}\xi - \frac{1}{8}\xi^2 + \dots$.

With the initial element length dx and the new length ds a strain measure may be defined as

$$\varepsilon_x = \frac{ds - dx}{dx} = \frac{\partial u}{\partial x} + \frac{1}{2} \left(\frac{\partial w}{\partial x}\right)^2 \quad (\text{B.28})$$

truncating the series as of the mixed terms and those to the power of three. The expressions for the other in-plane components follow accordingly:

$$\varepsilon_y = \frac{\partial v}{\partial y} + \frac{1}{2} \left(\frac{\partial w}{\partial y}\right)^2 \quad \gamma_{xy} = \frac{\partial u}{\partial y} + \frac{\partial v}{\partial x} + \frac{\partial w}{\partial x} \frac{\partial w}{\partial y} \quad (\text{B.29})$$

The same strain measures are obtained by considering the GREEN-LAGRANGE strain tensor (Eq. (A.15) in Appendix A.2). The x -component of this tensor for example is

$$E_{xx} = \frac{\partial u}{\partial_0 x} + \frac{1}{2} \left[\left(\frac{\partial u}{\partial_0 x}\right)^2 + \left(\frac{\partial v}{\partial_0 x}\right)^2 + \left(\frac{\partial w}{\partial_0 x}\right)^2 \right] \quad (\text{B.30})$$

using the large displacements coordinate description introduced in Appendix A, thus, the differences refer to the initial configuration of a body. Now, assuming that the lateral deflection w is substantially larger than the in-plane displacements u and v the corresponding first two square terms in (B.30) are omitted and the remaining expression correlates with the strain component in (B.28):

$$E_{xx} = \frac{\partial u}{\partial_0 x} + \frac{1}{2} \left(\frac{\partial w}{\partial_0 x}\right)^2 \quad (\text{B.31})$$

Nevertheless, without the square term in w a small rigid body rotation about the y -axis of the element in the (x, z) -plane of Figure B.4 would

lead to a strain in x -direction different from zero. In case of large rotations the two omitted square terms have to be retained. Thus, using the strains (B.28) and (B.29) the deflections are considered to be not small in comparison to the plate thickness, but still small enough for simplified expressions for curvatures [76].

By differentiating the strain expressions in (B.28) and (B.29) it follows that

$$\frac{\partial^2 \varepsilon_x}{\partial y^2} + \frac{\partial^2 \varepsilon_y}{\partial x^2} - \frac{\partial^2 \gamma_{xy}}{\partial x \partial y} = \left(\frac{\partial^2 w}{\partial x \partial y} \right)^2 - \frac{\partial^2 w}{\partial x^2} \frac{\partial^2 w}{\partial y^2} \quad (\text{B.32})$$

After replacing the strain components by their expressions in terms of the membrane forces the third equation in terms of N_x , N_y and N_{xy} is obtained.

By introducing an AIRY *stress function* $\mathcal{F}(x, y)$ the concurrent solution of the three equations in (B.20) and (B.32) may be simplified [76]. With the definitions

$$N_x = \frac{\partial^2 \mathcal{F}}{\partial y^2}, \quad N_y = \frac{\partial^2 \mathcal{F}}{\partial x^2}, \quad N_{xy} = -\frac{\partial^2 \mathcal{F}}{\partial x \partial y} \quad (\text{B.33})$$

the two equations in (B.20) are identically satisfied [76]. Thus, for homogeneous isotropic material the strain components in terms of the stress function are

$$\begin{aligned} \varepsilon_x &= \frac{1}{hE} (N_x - \nu N_y) = \frac{1}{hE} \left(\frac{\partial^2 \mathcal{F}}{\partial y^2} - \nu \frac{\partial^2 \mathcal{F}}{\partial x^2} \right) \\ \varepsilon_y &= \frac{1}{hE} (N_y - \nu N_x) = \frac{1}{hE} \left(\frac{\partial^2 \mathcal{F}}{\partial x^2} - \nu \frac{\partial^2 \mathcal{F}}{\partial y^2} \right) \\ \gamma_{xy} &= \frac{1}{hG} N_{xy} = -\frac{2(1+\nu)}{hE} \frac{\partial^2 \mathcal{F}}{\partial x \partial y} \end{aligned} \quad (\text{B.34})$$

These expressions² inserted into (B.32) yields the *compatibility equation*

$$\frac{\partial^4 \mathcal{F}}{\partial x^4} + 2 \frac{\partial^4 \mathcal{F}}{\partial x^2 \partial y^2} + \frac{\partial^4 \mathcal{F}}{\partial y^4} = E h \left[\left(\frac{\partial^2 w}{\partial x \partial y} \right)^2 - \frac{\partial^2 w}{\partial x^2} \frac{\partial^2 w}{\partial y^2} \right] \quad (\text{B.35})$$

²Note that in literature the derivatives of \mathcal{F} are sometimes multiplied with the wall thickness h [76]

Compliance of this differential equation satisfies the condition that the strains are “compatible” and that the contributions of the strains and the (small) rotations to the deflections are considered.

By the use of the stress function definitions in (B.33) the ST. VENANT differential equation of equilibrium becomes:

$$\frac{\partial^4 w}{\partial x^4} + 2 \frac{\partial^4 w}{\partial x^2 \partial y^2} + \frac{\partial^4 w}{\partial y^4} = \frac{1}{D} \left(\frac{p_z}{h} + \frac{\partial^2 \mathcal{F}}{\partial y^2} \frac{\partial^2 w}{\partial x^2} - 2 \frac{\partial^2 \mathcal{F}}{\partial x \partial y} \frac{\partial^2 w}{\partial x \partial y} + \frac{\partial^2 \mathcal{F}}{\partial x^2} \frac{\partial^2 w}{\partial y^2} \right) \quad (\text{B.36})$$

The use of stress functions reduces the analysis of large deflections to the solution of only two equations, the equilibrium equation (B.36) and the compatibility equation (B.35), which are to be solved simultaneously together with the boundary conditions. This system of coupled differential equations determine the two functions $\mathcal{F}(x, y)$ and $w(x, y)$. For some simple cases, with approaches of the function $w(x, y)$ and $\mathcal{F}(x, y)$ the compatibility condition is primarily solved exactly. Then, the equilibrium condition is solved at least approximatively. Solutions with approaches in form of functions for u , v and w fulfilling both the equilibrium and the compatibility equations without inclusion of a stress function might be found but the particular specification of unknown coefficients is much more demanding.

B.3 Buckling of plates

The calculation of the critical values of the membrane forces at which the flat form of equilibrium becomes unstable and the plate begins to buckle is surely one of the most important applications of the differential equilibrium equation (B.26). The critical forces, i.e. the *buckling forces*, acting in the middle surface of a plate may be obtained by assuming that the plate has some initial curvature or some lateral loading. Then, the membrane forces at which the deflections tend to grow indefinitely are usually the searched critically values [76]. Thus, for the purpose of a buckling load estimation of a plate the integration of the differential equilibrium equation (B.26) with $p_z = 0$ may be used. However, close-form solutions of these equations which fulfill the boundary conditions may only be found for some special cases.

For instance, in the case where a simply supported rectangular plate is loaded uniformly only in one direction the truncated differential equation for isotropic materials is with $N_y = N_{xy} = 0$

$$\frac{\partial^4 w}{\partial x^4} + 2 \frac{\partial^4 w}{\partial x^2 \partial y^2} + \frac{\partial^4 w}{\partial y^4} = \frac{N_x}{D} \frac{\partial^2 w}{\partial x^2} \quad (\text{B.37})$$

The deflection surface of the buckled, simply supported plate with edge lengths a and b may be represented by the double series:

$$w(x, y) = \sum_{m=1}^{\infty} \sum_{n=1}^{\infty} w_{mn} \sin \frac{m\pi x}{a} \sin \frac{n\pi y}{b} \quad m, n = 1, 2, \dots \quad (\text{B.38})$$

This basic approach fulfills the boundary conditions $w = M_x = M_y = 0$ at all four edges. Equation (B.38) derivated several times and inserted into (B.37) yields [43]

$$\sum_{m=1}^{\infty} \sum_{n=1}^{\infty} \left\{ D \left[\left(\frac{m\pi}{a} \right)^2 + \left(\frac{n\pi}{b} \right)^2 \right]^2 + N_x \left(\frac{m\pi}{a} \right)^2 \right\} w_{mn} \sin \frac{m\pi x}{a} \sin \frac{n\pi y}{b} = 0 \quad (\text{B.39})$$

At least one coefficient w_{mn} has to be different from zero, thus the expression in curly brackets has to vanish. Consequently, the searched membrane force is given by

$$-N_x = \frac{D \left[\left(\frac{m\pi}{a} \right)^2 + \left(\frac{n\pi}{b} \right)^2 \right]^2}{\left(\frac{m\pi}{a} \right)^2} \quad (\text{B.40})$$

The buckling load is found by the search after the combination of the number of half-waves m and n which gives the lowest compressive force $|-N_x|$. For instance, with $n = 1$ for all width-to-height ratios a/b and with $w = 1$ in the case of a square plate the following formula may be specified which is analogous to the common EULER equation for buckling of columns [76]:

$$-N_{cr} = 4 \frac{D \pi^2}{a^2} \quad (\text{B.41})$$

where $-N_{cr}$ is the critical *compressive* membrane force $-N_x$.

Appendix C

Initial Stress Stiffness Matrices for Plate Elements

For the finite element analysis of the instability behaviour of shell structures the generation of the contribution of the nonlinear displacement terms to the tangent stiffness matrix is essential. For a better survey the formulations of the nonlinear or initial stress stiffness matrix are explained on basis of a flat plate.

The deformations of plates which are loaded below the load where buckling occurs are not infinitesimal but also not excessively large [84]. As mentioned in Section B.2.1 the lateral deflections then combine bending strains with membrane strains. According to Appendix A and B as well as Section 3.3, the GREEN-LAGRANGIAN strains at increment $s + 1$ may be expressed as

$$\{ {}^{\ell} \bar{E}_{ij}^{s+1} \} = \{ {}^{\ell} \bar{E}_{ij}^s \} + \{ {}^{\ell} \bar{E}_{ij} \} + z {}^{\ell} \mathbf{\kappa} + \{ {}^{\ell} \eta_{ij} \} \quad (\text{C.1})$$

where ℓ marks the reference state of a LAGRANGIAN formulation. In an *Updated* Lagrangian formulation ($\ell = s$) the vector $\{ {}^{\ell} \bar{E}_{ij} \}$ includes the membrane strain increments of the reference surface

$$\{ {}^s \bar{E}_{ij} \}^T = \left\{ \frac{\partial \bar{u}}{\partial_s x}, \frac{\partial \bar{v}}{\partial_s y}, \frac{\partial \bar{u}}{\partial_s y} + \frac{\partial \bar{v}}{\partial_s x} \right\} \quad (\text{C.2})$$

and in ${}_s\boldsymbol{\kappa}_{ij}$ are the increments of the curvatures and the twist

$${}_s\boldsymbol{\kappa}^T = \left\{ \frac{\partial\phi_x}{\partial_s x}, \frac{\partial\phi_y}{\partial_s y}, \frac{\partial\phi_x}{\partial_s y} + \frac{\partial\phi_y}{\partial_s x} \right\} \quad (\text{C.3})$$

where \bar{u} and \bar{v} are the membrane displacement increments in the reference surface and ϕ_x and ϕ_y are the rotations about the local x -axis and y -axis, respectively¹. A possible contribution of transverse shear deformations is neglected. For a better comparison with (3.19) and (3.50) the linear and nonlinear components of the strain vector are separated, that is,

$$\{ {}_s\bar{E}_{ij}^{s+1} \} = \{ {}_\ell\bar{E}_{ij}^s \} + \{ {}_s\bar{E}_{ij} + z {}_s\boldsymbol{\kappa} \} + \{ {}_s\eta_{ij} \} \quad (\text{C.4})$$

The *nonlinear* term $\{ {}_\ell\eta_{ij} \}$ is, any initial curvature ignored, given by

$$\{ {}_s\eta_{ij} \}^T = \left\{ \frac{1}{2} \left(\frac{\partial w}{\partial_s x} \right)^2, \frac{1}{2} \left(\frac{\partial w}{\partial_s y} \right)^2, \frac{\partial^2 w}{\partial_s x \partial_s y} \right\} \quad (\text{C.5})$$

The virtual work expressions (see Section 3.3) need also the virtual variants of the strain components. The virtual vectors $\{ \delta_s \bar{E}_{ij} \}$ and $\{ \delta_s \boldsymbol{\kappa}_{ij} \}$ only differ from their “real” counterpart in the “ δ ” at the displacement and curvature increment components. The nonlinear virtual strain contribution in turn may be written as

$$\{ \delta_s \eta_{ij} \} = \left\{ \begin{array}{c} \frac{\partial\delta w}{\partial_s x} \frac{\partial w}{\partial_s x} \\ \frac{\partial\delta w}{\partial_s y} \frac{\partial w}{\partial_s y} \\ \frac{\partial\delta w}{\partial_s x} \frac{\partial w}{\partial_s y} + \frac{\partial w}{\partial_s x} \frac{\partial\delta w}{\partial_s y} \end{array} \right\} = \begin{bmatrix} \frac{\partial w}{\partial_s x} & 0 \\ 0 & \frac{\partial w}{\partial_s y} \\ \frac{\partial w}{\partial_s y} & \frac{\partial w}{\partial_s x} \end{bmatrix} \left\{ \begin{array}{c} \frac{\partial\delta w}{\partial_s x} \\ \frac{\partial\delta w}{\partial_s y} \end{array} \right\} \quad (\text{C.6})$$

It can be assumed that for all kinematic variable \bar{u} , \bar{v} , w , ϕ_x , and ϕ_y the same shape functions H_i are defined (as for the geometry); thus, with the matrix \mathbf{H} containing the shape functions it is

$$\mathbf{u} = \mathbf{H} \bar{\mathbf{u}} \quad (\text{C.7})$$

whereby \mathbf{u} stands for the displacement field and rotations field vector

$$\mathbf{u} = \{ u, v, w, \phi_x, \phi_y \} \quad (\text{C.8})$$

¹In a *Total Lagrangian* formulation contributions of *initial displacements* have to be considered (see Section 3.3, Eq. 3.20)

and $\tilde{\mathbf{u}}$ includes the degrees of freedom at the N element nodes

$$\tilde{\mathbf{u}} = \{u^{(1)}, v^{(1)}, w^{(1)}, \phi_x^{(1)}, \phi_y^{(1)}, \dots, u^{(N)}, v^{(N)}, w^{(N)}, \phi_x^{(N)}, \phi_y^{(N)}\} \quad (\text{C.9})$$

(see Section 3.2). For later use the vector $\tilde{\mathbf{u}}$ is split into a vector containing the displacements in the element reference surface $\tilde{\mathbf{u}}_m$, one including the rotations $\tilde{\mathbf{u}}_\phi$, and finally a vector $\tilde{\mathbf{u}}_w$ which contains the lateral displacements at the nodes [27]:

$$\begin{aligned} \tilde{\mathbf{u}}_m &= \{u^{(1)}, v^{(1)}, \dots, u^{(N)}, v^{(N)}\} & \tilde{\mathbf{u}}_\phi &= \{\phi_x^{(1)}, \phi_y^{(1)}, \dots, \phi_x^{(N)}, \phi_y^{(N)}\} \\ \tilde{\mathbf{u}}_w &= \{w^{(1)}, \dots, w^{(N)}\} \end{aligned} \quad (\text{C.10})$$

With the corresponding derivatives of the shape functions relations between the nodal degrees of freedom and the strain components may be found:

$$\begin{aligned} \{ {}_s \bar{E}_{ij} \} &= {}_s \mathcal{B}_l \tilde{\mathbf{u}}_m & \{ \delta_s \bar{E}_{ij} \} &= {}_s \mathcal{B}_l \delta \tilde{\mathbf{u}}_m \\ {}_s \boldsymbol{\kappa} &= {}_s \mathcal{B}_l \tilde{\mathbf{u}}_\phi & \delta_s \boldsymbol{\kappa} &= {}_s \mathcal{B}_l \delta \tilde{\mathbf{u}}_\phi \end{aligned} \quad (\text{C.11})$$

Similarly, the relations between the slopes and the lateral deflection w may be expressed as

$$\left\{ \frac{\partial w}{\partial_s x_i} \right\} = {}_s \mathcal{B}_w \tilde{\mathbf{u}}_w \quad \text{resp.} \quad \left\{ \frac{\partial \delta w}{\partial_s x_i} \right\} = {}_s \mathcal{B}_w \delta \tilde{\mathbf{u}}_w \quad (\text{C.12})$$

With these expressions the nonlinear strains in (C.5) and (C.6) may be rewritten as

$$\{ {}_s \eta \} = \left[\frac{\partial w}{\partial_s x_i} \right] \left\{ \frac{\partial w}{\partial_s x_i} \right\} = \left[\frac{\partial w}{\partial_s x_i} \right] {}_s \mathcal{B}_w \tilde{\mathbf{u}}_w \quad \{ \delta_s \eta \} = \left[\frac{\partial w}{\partial_s x_i} \right] {}_s \mathcal{B}_w \delta \tilde{\mathbf{u}}_w \quad (\text{C.13})$$

The slope $\partial w / \partial_s x_i$ and the rotations ϕ_i are linked to each other via the transverse shear strains. Thus, the “ \mathcal{B} -matrices” have to respect the continuity conditions according to the choice of the element type (e.g. “Mindlin” or “Discrete Kirchhoff” element, see Ref. [4, 84]).

In an Updated Lagrangian formulation, as in present case, the 2nd PIOLA-KIRCHHOFF stresses ${}_s \mathbf{S}$ are equal to CAUCHY stresses $\boldsymbol{\sigma}$ (see Eq. (3.51) in Section 3.3). Consequently, according to (3.25) in Section 3.3 the virtual strain energy may be expressed as

$$\int_{{}_s V} (\{ \sigma_{ij} \} + {}_s \mathbf{S})^T \delta (\{ {}_s \bar{E}_{ij} + z {}_s \boldsymbol{\kappa} \} + \{ {}_s \eta_{ij} \}) {}_s dV = \delta_s W_{ex}^{s+1} \quad (\text{C.14})$$

The expression above expanded becomes

$$\int_{sV} \{\sigma_{ij}\}^T \{\delta_s \bar{E}_{ij} + z \delta_s \boldsymbol{\kappa}\} {}_s dV + \int_{sV} \{\sigma_{ij}\}^T \{\delta_s \eta_{ij}\} {}_s dV + \int_{sV} {}_s \mathbf{S}^T \{\delta_s \bar{E}_{ij} + z \delta_s \boldsymbol{\kappa}\} {}_s dV = \delta_s \bar{W}_{ex}^{s+1} \quad (\text{C.15})$$

whereby the term with ${}_s \mathbf{S}^T \{\delta_s \eta_{ij}\}$ is neglected (see Section 3.3).

The constitutive relation between an increment of the 2nd PIOLA-KIRCHHOFF stresses and an increment of the GREEN-LAGRANGIAN strains are given by

$${}_s \mathbf{S} = {}_s \mathbf{C} (\{{}_s \bar{E}_{ij} + z {}_s \boldsymbol{\kappa}\} + \{{}_s \eta_{ij}\}) \quad (\text{C.16})$$

with the linear elastic material matrix ${}_s \mathbf{C}$. In order to obtain the stress resultants the equation above is integrated through the thickness coordinate z [27]. Thus,

$$\begin{aligned} \{{}_s N_{ij}\} &= \int_{-h/2}^{h/2} {}_s \mathbf{S} dz = \int_{-h/2}^{h/2} {}_s \mathbf{C} (\{{}_s \bar{E}_{ij} + z {}_s \boldsymbol{\kappa}\} + \{{}_s \eta_{ij}\}) dz \\ &= {}_s \mathbf{C}_A \{{}_s \bar{E}_{ij} + {}_s \eta_{ij}\} + {}_s \mathbf{C}_B {}_s \boldsymbol{\kappa} \\ \{{}_s M_{ij}\} &= \int_{-h/2}^{h/2} {}_s \mathbf{S} z dz = \int_{-h/2}^{h/2} {}_s \mathbf{C} (\{{}_s \bar{E}_{ij} + z {}_s \boldsymbol{\kappa}\} + \{{}_s \eta_{ij}\}) z dz \\ &= {}_s \mathbf{C}_B \{{}_s \bar{E}_{ij} + {}_s \eta_{ij}\} + {}_s \mathbf{C}_D {}_s \boldsymbol{\kappa} \end{aligned} \quad (\text{C.17})$$

where ${}_s \mathbf{C}_A$ is the membrane stiffness matrix, ${}_s \mathbf{C}_B$ the coupling stiffness matrix and ${}_s \mathbf{C}_D$ the bending stiffness matrix [27]. When the reference surface of the plate correlates with the neutral surface, where bending stresses vanish, coupling between membrane deformations and bending may be neglected (i.e. ${}_s \mathbf{C}_B = 0$); For the sake of simplification in the following it is assumed that ${}_s \mathbf{C}_B = 0$. Since in an Updated Lagrangian formulation $\{{}_s \bar{N}_{ij}\}$ and the moments $\{{}_s \bar{M}_{ij}\}$ at increment s are composed of CAUCHY stresses, the membrane forces $\{{}_s \bar{N}_{ij}\}$ and their increments $\{{}_s N_{ij}\}$ may be also be written as

$$\begin{pmatrix} {}_s \bar{N}_{xx} \\ {}_s \bar{N}_{yy} \\ {}_s \bar{N}_{xy} \end{pmatrix} = \begin{pmatrix} \bar{\sigma}_{xx} h \\ \bar{\sigma}_{yy} h \\ \bar{\sigma}_{xy} h \end{pmatrix} \quad \text{resp.} \quad \begin{pmatrix} {}_s N_{xx} \\ {}_s N_{yy} \\ {}_s N_{xy} \end{pmatrix} = \begin{pmatrix} {}_s \bar{S}_{xx} h \\ {}_s \bar{S}_{yy} h \\ {}_s \bar{S}_{xy} h \end{pmatrix} \quad (\text{C.18})$$

with the average membrane stresses $\bar{\sigma}_{ij}$ and ${}_s\bar{S}_{ij}$, respectively, and the wall thickness h .

The third term in (C.15) gives the linear contribution to the tangent stiffness matrix. Neglecting the nonlinear term in (C.16) and (C.17) it applies accordingly

$$\begin{aligned} \int_{{}_sV} {}_s\mathbf{S}^T \{ \delta_s \bar{E}_{ij} + z {}_s\boldsymbol{\kappa} \} {}_s dV &= \int_{{}_sA} \{ {}_sN_{ij} \}^T \{ \delta_s \bar{E}_{ij} \} + \{ {}_sM_{ij} \}^T \delta_s \boldsymbol{\kappa} {}_s dA \\ &\Rightarrow \int_{{}_sA} \delta \tilde{\mathbf{u}}_m^T {}_s\mathbf{B}_l^T {}_s\mathbf{C}_A {}_s\mathbf{B}_l \tilde{\mathbf{u}}_m + \delta \tilde{\mathbf{u}}_\phi^T {}_s\mathbf{B}_l^T {}_s\mathbf{C}_D {}_s\mathbf{B}_l \tilde{\mathbf{u}}_\phi {}_s dA \end{aligned} \quad (\text{C.19})$$

where the definitions of the stress resultants in (C.17) and the definitions of the \mathbf{B} matrices in (C.11) were used.

The second term in (C.15) finally yields the searched initial stress stiffness matrix. With (C.13) the nonlinear contribution to the virtual strain may be written as

$$\begin{aligned} \int_{{}_sV} \{ \sigma_{ij} \}^T \{ \delta_s \eta_{ij} \} {}_s dV &= \int_{{}_sA} \{ \delta_s \eta_{ij} \}^T \{ {}_sN_{ij} \} {}_s dA = \\ &= \int_{{}_sA} \delta \tilde{\mathbf{u}}_w^T {}_s\mathbf{B}_w^T \left[\frac{\partial w}{\partial {}_s x} \right]^T \{ {}_sN_{ij} \} {}_s dA \end{aligned} \quad (\text{C.20})$$

It can be shown that, because of a special property of the transposed matrix $[\partial w / \partial {}_s x_i]^T$ [84], the following transformation is allowed:

$$\left[\begin{array}{ccc} \frac{\partial w}{\partial {}_s x} & 0 & \frac{\partial w}{\partial {}_s y} \\ 0 & \frac{\partial w}{\partial {}_s y} & \frac{\partial w}{\partial {}_s x} \end{array} \right] \left\{ \begin{array}{c} {}_sN_{xx} \\ {}_sN_{yy} \\ {}_sN_{xy} \end{array} \right\} \Rightarrow \left[\begin{array}{cc} {}_sN_{xx} & {}_sN_{xy} \\ {}_sN_{xy} & {}_sN_{yy} \end{array} \right] \left\{ \begin{array}{c} \frac{\partial w}{\partial {}_s x} \\ \frac{\partial w}{\partial {}_s y} \end{array} \right\} \quad (\text{C.21})$$

Insertion of the expression above into (C.20) yields

$$\begin{aligned} \int_{{}_sA} \delta \tilde{\mathbf{u}}_w^T {}_s\mathbf{B}_w^T \left[\frac{\partial w}{\partial {}_s x} \right]^T \{ {}_sN_{ij} \} {}_s dA \\ = \int_{{}_sA} \delta \tilde{\mathbf{u}}_w^T {}_s\mathbf{B}_w^T \left[\begin{array}{cc} {}_sN_{xx} & {}_sN_{xy} \\ {}_sN_{xy} & {}_sN_{yy} \end{array} \right] \left\{ \frac{\partial w}{\partial {}_s x_i} \right\} {}_s dA \end{aligned} \quad (\text{C.22})$$

or with (C.12)

$$= \int_{sA} \delta \tilde{\mathbf{u}}_w^T {}_s \mathbf{B}_w^T \begin{bmatrix} {}_s N_{xx} & {}_s N_{xy} \\ {}_s N_{xy} & {}_s N_{yy} \end{bmatrix} {}_s \mathbf{B}_w \tilde{\mathbf{u}}_w {}_s dA \quad (\text{C.23})$$

Now, in accordance with the formulations in Section 3.3 a nonlinear stiffness matrix may be specified:

$${}_s \mathbf{K}_{nlw} = \int_{sA} {}_s \mathbf{B}_w^T \begin{bmatrix} {}_s N_{xx} & {}_s N_{xy} \\ {}_s N_{xy} & {}_s N_{yy} \end{bmatrix} {}_s \mathbf{B}_w {}_s dA \quad (\text{C.24})$$

This matrix is only combined with the lateral nodal displacements $\tilde{\mathbf{u}}_w$; thus in connection with the complete nodal degrees of freedom vector $\tilde{\mathbf{u}}$ the stiffness matrix above, as a sub-matrix, has to be placed accordingly in the larger initial stress stiffness matrix of an plate or flat shell element [84]. Alternatively, for a general formulation the relation between the slopes and the nodal degrees of freedom in (C.12) and (C.13) is redefined as

$$\left\{ \frac{\partial w}{\partial_s x_i} \right\} = {}_s \mathbf{B}_{nl} \tilde{\mathbf{u}} \quad \text{resp.} \quad \left\{ \frac{\partial \delta w}{\partial_s x_i} \right\} = {}_s \mathbf{B}_{nl} \delta \tilde{\mathbf{u}} \quad (\text{C.25})$$

simultaneously allowing for any displacement constraints stemming from the relationship between the slope, the rotations and possible transverse shear deformations [27]. With this, finally the element initial stress stiffness matrix in a general form, similar to that given in Section 3.3, is obtained:

$${}_s \mathbf{K}_{nl} = \int_{sA} {}_s \mathbf{B}_{nl}^T \begin{bmatrix} {}_s N_{ij} \end{bmatrix} {}_s \mathbf{B}_{nl} {}_s dA \quad (\text{C.26})$$

In a Total Lagrangian formulation the matrix is obtained similarly. The nonlinear stiffness matrix is mostly called either **geometric stiffness matrix** or **initial stress stiffness matrix**. The components of the matrix depend on the applied loads, in present case on the membrane forces. A central feature of the nonlinear stiffness matrix is that for its specification a precedent static analysis is necessary where the reaction of the structure due to a given loading is calculated. Further, in a finite element analysis the deflections and thus also the slopes, i.e. the geometric variables which bring the nonlinearity, are finally members of the searched nodal degrees of freedom vector.

Curriculum Vitae

Luc Wullschleger

- | | |
|-------------------|--|
| 11th of June 1970 | Birth in Binningen, Switzerland |
| 1977 – 1987 | Primary and secondary school in Binningen, Canton Baselland, Switzerland |
| 1987 – 1990 | Grammar school in Oberwil, Canton Baselland, Switzerland, Matura (school leaving examination) |
| 1991 – 1997 | Studies of Mechanical Engineering at the Swiss Federal Institute of Technology ETH in Zürich, Switzerland |
| 1997 | Diploma degree in Mechanical Engineering from ETH Zürich (MSc ETH) |
| 1997 – 2002 | Research and Teaching Assistant to Prof. Meyer-Piening (emeritus), Institute for Mechanical Systems IMES, former Institute for Lightweight Structures and Ropeways ILS, ETH Zürich |
| 2002 – 2003 | Teaching Assistant to Prof. Ermanni, Institute for Mechanical Systems IMES, Structure Technologies, ETH Zürich |
| 2004 | CAD Engineer at Helbling Technik AG in Aarau, Switzerland |
| 2004 – | CAD Engineer at the Swiss Federal Laboratories for Materials Testing and Research Empa in Dübendorf, Switzerland |